RISK-BASED SEISMIC PERFORMANCE ASSESSMENT OF EXISTING TALL STEEL FRAMED BUILDINGS

Thesis submitted for the degree of
Doctor of Philosophy in Earthquake Engineering

Carlos Molina Hutt, PE, CEng MICE

University College London
Civil, Environmental and Geomatic Engineering Department
2017

This page is intentionally left blank.

I, Carlos Molina Hutt, confirm that the work presented in this thesis is my own. Where information has been derived from other sources, I confirm that this has been indicated in the thesis.

This page is intentionally left blank.

"The final challenge is not in predicting performance or estimating losses; it is in contributing effectively to the reduction of losses and the improvement of safety. We must never forget this."

Allin Cornell and Helmut Krawinkler

This page is intentionally left blank.

Abstract

One of the major concerns in earthquake disaster resilience is understanding the risk posed by existing buildings that are not conformant with modern building codes. A related challenge is how, if necessary, to mitigate the risk through retrofit policies or other measures in a cost effective manner. For some types of buildings, such as unreinforced masonry, the risks are so obviously large, that mandatory laws have been enacted to assess and retrofit the buildings. However, in other cases, such as with non-ductile concrete buildings or older tall steel buildings, the risks and mitigation strategies are not as clear cut. This research addresses the risks posed by older seismically deficient steel buildings, which constitute a significant portion of tall buildings in western US cities with high seismic hazard. These buildings include many steel moment resisting frames (MRF), constructed during the late 1960's through mid-1990's, with the type of welded connections that experienced sudden brittle fractures during the 1994 Northridge earthquake.

This work applies performance-based earthquake engineering (PBEE) tools to this potential seismic safety problem. San Francisco is selected as a case study city in order to permit engagement with the city's ongoing earthquake safety initiatives. The performance of existing 1970s tall steel MRF buildings is evaluated through the development of archetype buildings. A series of studies that progressively explore the performance of individual archetype buildings, within a probabilistic framework, are carried out, including scenario-based, intensity-based and time-based assessments. Additionally, a method is proposed to extend such assessments to evaluate clusters of buildings and how their performance may impact the resilience of the community; going beyond individual building performance, towards more holistic seismic performance evaluations. The results of this body of research are communicated not only in terms of structural response, but also in terms of direct economic losses, downtime and recovery, which are more accessible to decision makers.

The scenario-based and intensity-based evaluations are carried out to assess performance under an expected earthquake scenario, and design level shaking, respectively. The results indicate that, while the archetype buildings considered are expected to guarantee the life-safety of occupants, the associated economic losses and downtime entail a costly and slow recovery, which can, additionally, result in considerable indirect losses. The impact of adopting structural retrofit schemes, enhanced non-structural building components, and seismic mitigation measures is explored. The results indicate that, through a combination of these interventions, significant reductions, in both losses and downtime, under the earthquake ground motion shaking intensities considered, can be achieved.

In order to benchmark the performance of 1970s steel MRFs versus modern design standards, a comparative time-based evaluation is carried out. The results indicate that the probabilities of collapse of the 1970s archetype buildings considered are well in excess of the 1% in 50 year target implicit in modern design standards. The results also illustrate that while modern designs result in performance that complies with the code intended collapse-safety margin, the level of damage control may be insufficient to enable a swift recovery and ensure the seismic resilience of these buildings.

A methodology to assess the earthquake risk of existing tall buildings on the urban community is proposed. This method is implemented in a simple case study of a cluster of tall steel MRF buildings in downtown San Francisco. The results suggest that under a range of realistic earthquake scenarios, a considerable loss of occupancy and functionality is expected in buildings consistent with the 1970s archetype. Furthermore, permanent deformations in these buildings can result in large cordons around the damaged structures, which would prevent access to other buildings within a considerable area.

The results of this research serve to inform the debate over the expected seismic performance of existing 1970s tall steel MRF buildings. This work provides an array of results from different types of assessment that can be informative to different parties including design practitioners, building owners, policy makers and the insurance sector.

Acknowledgements

I offer my most sincere gratitude to my supervisor Professor Tiziana Rossetto (University College London), for her guidance, enthusiasm and encouragement. The opportunities she has afforded me throughout my PhD studies, many of which go beyond the scope of this thesis, are helping me grow towards my goal of becoming a well-rounded earthquake engineer.

I am grateful to Professor Gregory Deierlein (Stanford University), who agreed to co-supervise this research, and who has, despite the distance, provided continuous guidance and support.

I would like to thank my former employer Arup, where I initiated this research through their 'Arup University' scheme. In particular, I would like to thank Michael Willford and Ibbi Almufti for supporting and believing in this work, as well as Damian Grant and Adam Pearce for their technical guidance and encouragement when I first expressed interest in working with Arup's Advanced Technology and Research group. I would also like to thank Tabitha Tavolaro, my line manager during my four years at Arup, who challenged me and inspired me to become a better engineer.

I am grateful to Professor Dina D'Ayala (University College London), who, as my line manager, ensured I was able to balance my duties as a full-time Teaching Fellow in the Civil, Environmental and Geomatic Engineering Department with the demands of a part-time PhD.

I would also like to thank my colleague and office-mate, Dr. Lena Ciric, for her charisma, uniqueness, nerve and talent, but more importantly for her endless patience putting up with me over the past five years.

Last, but not least, I would like to thank my family and friends for their continuous love and support, without whom I would have never completed this work. In particular, I would like to thank my mother, Judith, my father, Carlos, and my sister, Ana, who are my foundation. I would also like to thank my partner, Diego, for his endless love, support and encouragement.

This page is intentionally left blank.

Contents

1 Introduction 1
1.1 Background and motivation 1
1.2 Aim, objectives and scope 3
1.3 Thesis structure 5
1.4 Publications 6
2 Literature Review 9
2.1 Seismic vulnerability of existing tall steel buildings in the US 9
2.1.1 Seismic design evolution of building codes 9
2.1.2 Welded steel moment resisting frame (WSMRF) vulnerabilities 12
2.1.3 Seismic design of tall buildings 14
2.1.4 Loss assessment of tall buildings from a vulnerability perspective 15
2.2 Seismic performance assessment of buildings and FEMA P58 16
2.2.1 Performance-based earthquake engineering (PBEE) 18
2.2.2 Seismic hazard analysis 19
2.2.3 Structural response simulation 21
2.2.4 Damage and consequence estimation 24
2.2.5 PBEE for risk management 26
2.3 Seismic resilience and frameworks for evaluation 27
2.4 Point of departure 32
3 Methodology 35
3.1 Index buildings and modelling approaches 37
3.2 Building specific performance evaluations (BSPE) 38
3.2.1 BSPE: Scenario-based assessment 40
3.2.2 BSPE: Intensity-based assessment 41
3.2.3 BSPE: Time-based assessment 41
3.3 Beyond individual building evaluations 42
3.4 Transferability of method 44
4 Archetype Buildings and Numerical Modelling 45
4.1 Archetype tall building selection 45
4.1.1 Design requirements per UBC 1973 vs IBC 2012 49
4.1.2 Design summary of 40- and 20-storey 1970s archetype buildings 67
4.1.3 Tall buildings in other US west coast cities 71
4.2 Non-linear response history analysis (NLRHA) models 73
4.2.1 Non-linear beams 74
4.2.2 Non-linear columns 76

4.2.3 Non-linear panel zones 80
4.2.4 Other analysis assumptions 81
4.2.5 Global response: comparison against instrumented buildings 81
4.2.6 Collapse simulation 82
4.2.7 Adjustments for 40- and 20-storey archetypes 84
4.3 Building performance model 85
4.3.1 Loss assessment methodology 86
4.3.2 Downtime assessment methodology 92
4.3.3 Recovery functions 96
5 BSPE: Scenario-based Assessment 103
5.1 HayWired scenario ground motions 105
5.2 Non-linear dynamic analysis results 110
5.2.1 Impact of fracture distribution 119
5.2.2 Impact of building orientation 120
5.3 Expected direct economic losses and downtime 122
5.4 Summary and conclusions 123
6 BSPE: Intensity-based Assessment 125
6.1 Seismic hazard and ground motions 126
6.2 40-storey archetype building and strategies for increased resilience 130
6.3 Summary and conclusions 145
7 BSPE: Time-based Assessment 147
7.1 Methodology 147
7.2 Seismic hazard and ground motions 149
7.3 Structural performance assessment 156
7.4 Time-based assessment 166
7.4.1 Collapse risk 167
7.4.2 Performance functions 172
7.5 Loss assessment 176
7.5.1 Loss function and average annual loss 183
7.5.2 Seismic vulnerability function 182
7.6 Recovery functions 190
7.7 Implications of results on deaths and injuries 201
7.8 Summary and conclusions 203
8 Beyond Individual Building Evaluations 205
8.1 Overview 205
8.2 Methodology 205
8.2.1 Vulnerability curves for resilience-based evaluations 206

8.3 Comprehensive scenario-based assessments 210
8.4 Building cluster assessment 219
8.5 Conclusions 228
9 Summary and Conclusions 229
9.1 Overview 229
9.2 Summary of findings and conclusions 230
9.2.1 BSPE: Scenario-based evaluation 230
9.2.2 BSPE: Intensity-based evaluation 231
9.2.3 BSPE: Time-based evaluation 232
9.2.4 Beyond individual building evaluations 234
9.3 Reflections on transferability 234
9.4 Limitations and future research 237
9.5 Concluding remarks 241
References 243
Appendix A 257
Appendix B 309
Appendix C 329
Appendix D 373
Appendix E 393
Appendix F 403
Appendix G 415
Appendix H 437

This page is intentionally left blank.

List of Figures

Figure 1-1: Building height distribution in Los Angeles, San Francisco, and Seattle. 2
Figure 2-1: Design spectra for UBC 1973 to 1994 versus modern building codes. 11
Figure 2-2: Schematic illustration of standard levels of seismic performance. 17
Figure 2-3: Schematic of PEER methodology. 18
Figure 2-4: Conceptual resilience function. 28
Figure 2-5: Target states of recovery for San Francisco's building and infrastructure..... 30
Figure 2-6: CAPSS Earthquake Safety Implementation Program Phase C. 31
Figure 3-1: General methodology flowchart. 36
Figure 3-2: Index building and modelling approaches flowchart. 38
Figure 3-3: Flowchart for building specific evaluations including general evaluation procedure, scenario-based, intensity-based and time-based evaluations. 39
Figure 3-4: Framework for assessing the earthquake risk of tall buildings to cities and the impact of different retrofit risk mitigation strategies..... 43
Figure 4-1: Spatial distribution of existing tall buildings in downtown San Francisco. 46
Figure 4-2: Number of tall buildings built in San Francisco per decade between 1900 and 2010 (a) and lateral resisting system types for tall buildings built between 1960 and 1990 (b)... 47
Figure 4-3: Images of existing tall buildings in downtown San Francisco greater than 35 storeys, built between 1960 and 1990, whose lateral system is believed to be a steel MRF. 48
Figure 4-4: 1973 and 2012 archetype building plan drawings of lateral resisting system illustrating typical cross section shapes. 50
Figure 4-5: UBC 1973 seismic zone map of the United States..... 52
Figure 4-6: IBC 2012 design spectra. 54
Figure 4-7: UBC 1973 wind pressure map of the United States. 55
Figure 4-8: Design wind pressure distribution per UBC 1973 and IBC 2012. 56
Figure 4-9: Design compliance of archetype building with interstorey drift requirements per (a) UBC 1973 and (b) IBC 2012. 57
Figure 4-10: 1973 and 2012 archetype building elevation drawings of lateral resisting system illustrating typical section sizes in beams and columns. 60
Figure 4-11: Typical details observed in existing building drawings: typical moment connection plan view (a) and elevation (b); typical splice connection (c). 63
Figure 4-12: Dynamic properties of the UBC 1973 archetype building (only lateral resisting system shown). 65

Figure 4-13: Dynamic properties of the IBC 2012 archetype building (only lateral resisting system shown). 66
Figure 4-14: Archetype 40-storey office building plan (a) and isometric (b). 68
Figure 4-15: Structural models for the 40- and 20-storey 1973 archetype buildings..... 69
Figure 4-16: Construction material of existing tall buildings constructed between 1960 and 1990 in (a) Los Angeles, (b) Seattle, (c) San Francisco (d) San Diego and (e) Oakland. 72
Figure 4-17: Isometric of 40-storey analytical model and close-up of component models (boxed in red). 73
Figure 4-18: Sample analytical versus experimental hysteretic moment-rotation response in a (a) RBS and (b) non-RBS beam-to-column connection consistent with pre-qualified detailing. 75
Figure 4-19: Impact of introduction of fracture variable in the moment-rotation response of beams, shown against ASCE 41 recommendations..... 76
Figure 4-20: Sample analytical versus experimental column moment-rotation hysteretic response under varying ALR: 0.1(a) and 0.3 (b). 78
Figure 4-21: Sample analytical versus experimental response of panel zones in W (a) and HSS (b) column sections. 80
Figure 4-22: Design response spectrum versus ground motion spectra recorded at the base of the Chevron Building during 1989 Loma Prieta Earthquake. 82
Figure 4-23: Collapse realization results including contour plot illustrating ASCE 41 rotation performance levels as well as sample hysteretic response of a sample beam, panel zone and column in the storeys in which a collapse mechanism is observed.... 83
Figure 4-24: Probability distributions CDF (a) and PDF (b), and sample hysteretic response of moment rotation in beam to column moment connections under different levels of plastic rotation at fracture: 0.005 rad (c) and 0.015 (d). 85
Figure 4-25: Loss and downtime assessment methodology. 87
Figure 4-26: Fragility function (and repair consequence) for a standard partition wall. 91
Figure 4-27: Simplified tri-linear recovery path to re-occupancy or functional-recovery..... 96
Figure 4-28: Illustration of the Repair Time (RT) matrix or dataset to enable the development of recovery functions. 98
Figure 4-29: Illustration of the Repair Class Database (RCD) matrix or dataset to enable the development of recovery functions. 98
Figure 4-30: Illustration of the Damage State (DS) matrix or dataset to enable the development of recovery functions. 98
Figure 4-31: Illustration of the Repair Class (RC) matrix or dataset to enable the development of recovery functions. 98

Figure 5-1: USGS shakemap of the San Francisco bay area under the HayWired earthquake scenario, a M_w 7.0 earthquake on the Hayward fault. 104
Figure 5-2: HayWired earthquake scenario assessment locations in downtown San Francisco (red pin) and downtown Oakland (green pin). 105
Figure 5-3 Acceleration, velocity and displacement time histories of the east-west and north-south components of the HayWired scenario earthquake in San Francisco. ... 106
Figure 5-4: Acceleration, velocity and displacement time histories of the east-west and north-south components of HayWired scenario earthquake in Oakland. 107
Figure 5-5: Uniform hazard spectrum and conditional spectra (mean, variance and ground motion suite) at a representative site in downtown San Francisco versus ground motion spectra from earthquake scenarios: HayWired (at San Francisco and Oakland sites) and 1989 Loma Prieta (Chevron Building, San Francisco). 109
Figure 5-6: Illustration of damageable drift calculation. 110
Figure 5-7: Archetype 40-storey (a, b) and 20-storey (c, d) building interstorey drift ratio (IDR) in the short (a, c) and long (b, d) building directions in Oakland. 111
Figure 5-8: Archetype 40-storey (a, b) and 20-storey (c, d) building peak floor acceleration (PFA) in the short (a, c) and long (b, d) building directions in Oakland. 112
Figure 5-9: Archetype 40-storey (a, b) and 20-storey (c, d) building interstorey drift ratio (IDR) in the short (a, c) and long (b, d) building directions in San Francisco. 113
Figure 5-10: Archetype 40-storey (a, b) and 20-storey (c, d) building peak floor acceleration (PFA) in the short (a, c) and long (b, d) building directions in San Francisco. 114
Figure 5-11: Archetype 40-storey (a, b) and 20-storey (c, d) building beam performance for sample long (a, c) and short (b, d) building elevations in Oakland. 115
Figure 5-12: Archetype 40-storey (a, b) and 20-storey (c, d) building beam performance for sample long (a, c) and short (b, d) building elevations in San Francisco. 116
Figure 5-13: Archetype 40-storey (a, b) and 20-storey (c, d) building column performance (ASCE 41 thresholds) for sample long (a, c) and short (b, d) building elevations in Oakland. 117
Figure 5-14: Archetype 40-storey (a, b) and 20-storey (c, d) building column performance (ASCE 41 thresholds) for sample long (a, c) and short (b, d) building elevations in San Francisco. 118
Figure 6-1: Compliance with ASCE 7 for site-specific ground motions. 128
Figure 6-2: Mean of maximum and minimum demand response spectra and individual components for the short period (a) and long period (b) suites of ground motions. 129

Figure 6-3: Demand parameters for the archetype building: transient and residual drifts (i.e. IDR) and accelerations (i.e. PFA) at each storey in each building direction... 133
Figure 6-4: Demand parameters for the elastic spine retrofit: transient and residual drifts (i.e. IDR) and accelerations (i.e. PFA) at each storey in each building direction... 133
Figure 6-5: Demand parameters for the base isolation retrofit: transient and residual drifts (i.e. IDR) and accelerations (i.e. PFA) at each storey in each building direction. 133
Figure 6-6: Fragility functions for standard (solid line) versus enhanced (dashed line) partitions walls. 134
Figure 6-7: Loss estimates for archetype building (baseline), elastic spine, and base isolation retrofit schemes with standard and enhanced non-structural components: (a) with consideration of residual drifts; (b) without consideration of residual drifts. 139
Figure 6-8: Contribution to losses of building components for the following: (a) archetype building (baseline); (b) elastic spine retrofit scheme; (c) base isolation retrofit scheme with standard and enhanced non-structural components. 140
Figure 6-9: Probability distribution of residual drifts for archetype building (baseline), elastic spine, and base isolation retrofit schemes and associated FEMA damage states. 142
Figure 6-10: Downtime contributors for re-occupancy (a) and functional recovery (b) and sample de-aggregation of impeding factors for the archetype building (baseline) using standard non-structural components and no mitigation measures to minimize impeding factors versus enhanced non-structural components and mitigation measures to minimize impeding factors..... 144
Figure 7-1: Methodology adopted in the time-based assessment of the 1973 and 2012 50-storey archetype buildings. 148
Figure 7-2: Seismic hazard curve at the representative site in downtown San Francisco (V_{s30}=260m/s, T=5sec.) illustrating the earthquake ground motion intensities (e_i) considered in the time-based assessment. 150
Figure 7-3: Target conditional mean, variance, ground motion records and corresponding the UHS for the intensity levels considered in the time based assessment including SA, AFE, return periods and de-aggregation data (M, R and ε). The geomean spectra of a Loma Prieta ground motion record is also shown for comparison. 154
Figure 7-4: Revised earthquake ground motion intensities (e_i) considered in the time-based assessment for (a) the 1973 50-storey archetype building and (b) the 2012 50-storey archetype building. 155

Figure 7-5: Peak transient storey drift results from non-linear dynamic analysis for all intensity levels considered. Probabilities of no collapse at each earthquake intensity specified atop. 157
Figure 7-6: Peak residual storey drifts results from non-linear dynamic analysis for all intensity levels considered. Probabilities of no collapse at each earthquake intensity specified atop. 158
Figure 7-7: Peak floor acceleration results from non-linear dynamic analysis for all intensity levels considered. Probabilities of no collapse at each earthquake intensity specified atop. 159
Figure 7-8: Peak beam plastic rotation results from non-linear dynamic analysis for all intensity levels considered. Probabilities of no collapse at each earthquake intensity specified atop. 160
Figure 7-9: Peak column plastic rotation results from non-linear dynamic analysis for all intensity levels considered. Probabilities of no collapse at each earthquake intensity specified atop. 161
Figure 7-10: Peak panel zone rotation results from non-linear dynamic analysis for all intensity levels considered. Probabilities of no collapse at each earthquake intensity specified atop. 162
Figure 7-11: UBC 1973 design storey drifts, shear and overturning moment versus peak storey results from non-linear dynamic analysis subject to ground motions consistent with a 72 year return period event. 166
Figure 7-12: Multiple stripe analysis results (a) for collapse fragility derivation (b) of the 1973 and 2012 archetype buildings. 168
Figure 7-13: Graphical illustration of mean annual frequency of collapse calculation and collapse de-aggregation for the 1973 and 2012 archetype buildings. 171
Figure 7-14: Peak Interstorey Drift Ratio (IDR) (a) dynamic analysis results and (b) associated performance functions for 1973 and 2012 50-storey archetype buildings. 173
Figure 7-15: Peak Residual Interstorey Drift Ratio (IDR) (a) dynamic analysis results and (b) associated performance functions for 1973 and 2012 50-storey archetype buildings. 174
Figure 7-16: Peak floor acceleration (PFA) (a) dynamic analysis results and (b) associated performance functions for 1973 and 2012 50-storey archetype buildings. 175
Figure 7-17: Loss realizations and fitted loss curves under earthquake intensities considered in the time-based assessment for the 1973 50-storey archetype building. 178
Figure 7-18: Loss realizations and fitted loss curves under earthquake intensities considered in the time-based assessment for the 2012 50-storey archetype building. 179

Figure 7-19: Contribution of drift and acceleration sensitive components to repairable damage at different intensities of ground motion shaking for the (a) 1973 and (b) 2012 50-storey archetype buildings..... 181
Figure 7-20: Contribution of different building component categories to repairable damage at different intensities of ground motion shaking for the (a) 1973 and (b) 2012 50-storey archetype buildings..... 181
Figure 7-21: Contribution of (a) acceleration versus drift-sensitive and (b) different building component categories to repairable damage under earthquake ground motion intensity e_{2A} for the 1973 archetype. 182
Figure 7-22: Probabilities of observing repairable damage, irreparable damage or collapse at different intensities of ground motion shaking for the (a) 1973 and (b) 2012 50-storey archetype buildings..... 183
Figure 7-23: Loss curves for the (a) 1973 and (b) 2012 50-storey archetype buildings..... 185
Figure 7-24: Contribution of repairable damage, irreparable damage and collapse to the average annual loss (AAL) for the (a) 1973 and (b) 2012 50-storey archetype buildings..... 186
Figure 7-25: Contribution of different earthquake ground motion intensities to the cumulative 1973 50-storey archetype building loss curve. 187
Figure 7-26: Contribution of different earthquake ground motion intensities to the cumulative 2012 50-storey archetype building loss curve. 187
Figure 7-27: Seismic vulnerability functions for the (a) 1973 and the (b) 2012 50-storey archetype buildings illustrating loss contribution from collapse, repairable and irreparable damage. 189
Figure 7-28: Re-occupancy recovery curves under the earthquake intensities considered in the time-based assessment for the 1973 50-storey archetype building showing mean and sample realizations (10^{th}, 20^{th} 30^{th}, 40^{th}, 50^{th}, 60^{th}, 70^{th}, 80^{th}, 90^{th} percentile estimates) for realizations where damage is repairable.. 191
Figure 7-29: Functionality recovery curves under the earthquake intensities considered in the time-based assessment for the 1973 50-storey archetype building showing mean and sample realizations (10^{th}, 20^{th} 30^{th}, 40^{th}, 50^{th}, 60^{th}, 70^{th}, 80^{th}, 90^{th} percentile estimates) for realizations where damage is repairable. 192
Figure 7-30: Re-occupancy recovery curves under the earthquake intensities considered in the time-based assessment for the 2012 50-storey archetype building showing mean and sample realizations (10^{th}, 20^{th} 30^{th}, 40^{th}, 50^{th}, 60^{th}, 70^{th}, 80^{th}, 90^{th} percentile estimates) for realizations where damage is repairable. 193
Figure 7-31: Functionality recovery curves under the earthquake intensities considered in the time-based assessment for the 2012 50-storey archetype building showing mean

and sample realizations (10^{th}, 20^{th} 30^{th}, 40^{th}, 50^{th}, 60^{th}, 70^{th}, 80^{th}, 90^{th} percentile estimates) for realizations where damage is repairable. 194
Figure 7-32: Downtime curves to re-occupancy for the 1973 and 2012 50-storey archetype buildings. 197
Figure 7-33: Downtime curves to functional recovery for the 1973 and 2012 50-storey archetype buildings..... 197
Figure 7-34: Impeding factors, structural repairs, non-structural repairs, residual drift and collapse contribution to the 1973 50-storey archetype building's downtime curve to (a) re-occupancy and (b) functional recovery. 198
Figure 7-35: Impeding factors, structural repairs, non-structural repairs, residual drift and collapse contribution to the 2012 50-storey archetype building's downtime curve to (a) re-occupancy and (b) functional recovery. 199
Figure 7-36: Contribution of repairable damage, irreparable damage from residual IDRs and collapse to the average annual downtime (AAD) to (a, c) re-occupancy and (b, d) functional recovery for the (a, b) 1973 and (c, d) 2012 50-storey archetype buildings. 200
Figure 8-1: 1973 50-storey archetype building vulnerability curves for resilience-based evaluations. 208
Figure 8-2: 2012 50-storey archetype building vulnerability curves for resilience-based evaluations. 208
Figure 8-3: Median spectra for earthquake scenarios ranging from M7 to M8. 214
Figure 8-4: Distribution of sampled spectral intensities at a 5 second period for earthquake scenarios ranging from M7 to M8 at the site of interest. 215
Figure 8-5: UBC 1973 mean recovery curves to (a) re-occupancy and (b) functional recovery, as well as expected cordon radius and duration (c) for earthquake scenarios ranging from M7 to M8. 216
Figure 8-6: IBC 2012 mean recovery curves to (a) re-occupancy and (b) functional recovery, as well as expected cordon radius and duration (c) for earthquake scenarios ranging from M7 to M8. 217
Figure 8-7: Location of buildings sites in downtown San Francisco. 220
Figure 8-8: Distribution of spectral intensities for earthquake scenario with M7.5 at buildings sites A through E considered in the building cluster assessment. 221
Figure 8-9: Mean recovery curves to (a to d) re-occupancy and (e to h) functional recovery, (a, b, e, f) normalized and (c, d, g, h) in absolute terms, for (a, c, e, g) individual buildings and (b, d, f, h) the overall cluster under a M7.5 earthquake scenario assuming UBC 1973 archetypes. 222

Figure 8-10: Mean recovery curves to (a to d) re-occupancy and (e to h) functional recovery, (a, b, e, f) normalized and (c, d, g, h) in absolute terms, for (a, c, e, g) individual buildings and (b, d, f, h) the overall cluster under a M7.5 earthquake scenario assuming IBC 2012 archetypes. 223
Figure 8-11: Mean cordon preventing access to surrounding areas under a M7.5 earthquake scenario assuming (a) UBC 1973 and (b) IBC 2012 archetypes. 224
Figure 8-12: Probability of cordon with a mean radius equal to the building height and duration equal to the building demolition time under a M7.5 earthquake scenario assuming UBC 1973 archetypes integrated with GIS map. 227
Figure 8-13: Probability of cordon with a mean radius equal to the building height and duration equal to the building demolition time under a M7.5 earthquake scenario assuming IBC 2012 archetypes integrated with GIS map. 227

Figures included within the Appendices are listed on the first page of each Appendix.

List of Tables

Table 2-1: Key specifications from UBC 1973, 1985 and 1994 related to seismic principles and steel MRF design. 11
Table 4-1 Gravity loading criteria. 51
Table 4-2: IBC 2012 wind design parameters. 55
Table 4-3: Comparison in load combinations per UBC 1973 and IBC 2012. 61
Table 4-4: Comparison of steel ASD stress limits in UBC 1973 versus LRFD strength checks in IBC 2012. 61
Table 4-5. Dynamic properties of the UBC 1973 and IBC 2012 50-storey archetype buildings. 64
Table 4-6. Effective wind and seismic design base shears for the 1973 40- and 20-storey archetype buildings. 68
Table 4-7: Dynamic properties of the 40- and 20-storey 1973 archetype buildings. 69
Table 4-8: Lateral resisting system section sizes for the 1973 40-storey archetype building. 70
Table 4-9: Lateral resisting system section sizes for the 1973 20-storey archetype building. 70
Table 4-10: Non-linear beam and column modelling parameters for 1973 and 2012 building archetypes. 79
Table 4-11: Mean peak storey acceleration (PFA) and displacement (D) comparison between the instrumented Chevron building and the 1973 archetype building during Loma Prieta earthquake.. 82
Table 4-12: Fragility numbers, category, description and source for a sample of components included in the 50-storey 1973 archetype building performance model. 90
Table 4-13: Assumed delays associated with impeding factors. 95
Table 4-14: Assumed labour allocation parameters for repair time estimates. 95
Table 5-1: Impact of ground motion directionality on 40-storey archetype peak interstorey drift ratios (IDRs) and peak floor accelerations (PFAs) in Oakland. 121
Table 5-2: Impact of ground motion directionality on 20-storey archetype peak interstorey drift ratios (IDRs) and peak floor accelerations (PFAs) in Oakland. 121
Table 5-3 Impact of ground motion directionality on 40-storey archetype peak interstorey drift ratios (IDRs) and peak floor accelerations (PFAs) in San Francisco. 121
Table 5-4: Impact of ground motion directionality on 20-storey archetype peak interstorey drift ratios (IDRs) and peak floor accelerations (PFAs) in Oakland. 121
Table 5-5: Abbreviation for case study buildings for which estimates of direct economic losses and downtime are conducted. 122

Table 5-6: Direct economic loss estimates (50th and 90th percentile) expressed USD and percentage of replacement cost for the case study buildings considered. 123
Table 5-7: Downtime estimates to re-occupancy and functional (50th and 90th percentile) for the case study buildings considered. 123
Table 6-1: Assumed delays associated with impeding factors..... 136
Table 6-2: Expected loss estimates for the baseline building and enhanced performance schemes with consideration of residual drifts. 138
Table 6-3: Expected loss estimates for the baseline building and enhanced performance schemes without consideration of residual drifts. 138
Table 6-4: Downtime estimates for the baseline building and enhanced performance schemes for re-occupancy. 142
Table 6-5: Downtime estimates for the baseline building and enhanced performance schemes for functional recovery. 142
Table 7-1: SAs at a 5 second period, AFEs, return periods and magnitude (M), distance (R) and epsilon (ε) de-aggregation results for the ground motion intensities considered in the time-based assessment. 151
Table 7-2: SAs at a 5 second period, AFEs, return periods and magnitude, distance and epsilon de-aggregation results for the ground motion intensities considered in the time-based assessment. 153
Table 7-3: Maximum of peak storey results from non-linear dynamic analysis: interstorey drift ratio (IDR), residual IDR, peak floor acceleration (PFA), beam plastic rotation, column plastic rotation and panel zone rotations for the 1973 and 2012 50-storey archetype buildings..... 163
Table 7-4: Probabilities of collapse over different periods of time for a range of codes and structural systems. 170
Table 7-5. Time-based performance assessment metrics related to peak IDRs, peak residual IDRs and maximum PFAs for the 1973 and 2012 archetype buildings. CP denotes collapse. 176
Table 7-6: Median (μ) and dispersion (β) of time to re-occupancy estimates in key recovery phases for the 1973 and 2012 50-storey archetype building. 195
Table 7-7: Median (μ) and dispersion (β) of time to functional recovery in key recovery phases for the 1973 and 2012 50-storey archetype buildings. 196
Table 8-1: Summary of time-based assessment results for the 1973 50-storey archetype building that enable the development of vulnerability curves for resilience-based evaluations (number of realizations or probability of observing each limit state). 207

Table 8-2: Summary of time-based assessment results for the 2012 50-storey archetype building that enable the development of vulnerability curves for resilience-based evaluations (number of realizations or probability of observing each limit state). 207
Table 8-3: UBC 1973 limit state consequence data as a function of earthquake ground motion intensity. 212
Table 8-4: IBC 2012 limit state consequence data as a function of earthquake ground motion intensity. 213
Table 8-5: Probabilities of observing a building cordon with an average radius equal to the building height and a time equal to the demolition time (R=192.8 m, t=300 days) for the IBC 2012 and UBC 1973 archetypes under different scenarios. 218
Table 8-6: Site labels, coordinates and distances to epicentre for the buildings selected to evaluate impact on the urban community. 219

Tables included within the Appendices are listed on the first page of each Appendix.

This page is intentionally left blank.

Glossary of Terms

Abbreviations	Definitions
AACE	Association for the Advancement of Cost Engineering
AAD	Average Annual Downtime
AAL	Average Annual Loss
AFE	Annual Frequency of Exceedance
AISC	American Institute of Steel Construction
AISI	American Iron and Steel Institute
ASCE	American Society of Civil Engineers
ASD	Allowable Stress Design
BORP	Building Occupancy Resumption Program
BSPE	Building Specific Performance Evaluations
CAPSS	Community Action Plan for Seismic Safety
CBD	Central Business District
CMS	Conditional Mean Spectrum
CP	Collapse Prevention (Limit State)
CS	Conditional Spectrum
DBE	Design Basis Earthquake or Design Level Earthquake
DBI	Department of Building Inspection
DM	Damage Measure
DS	Damage State or Damage State matrix
DS_i	Damage State i
DV	Decision Variable
EDP	Engineering Demand Parameter
EMMD	Enveloppe of Mean of Maximum Demand
EPS	Earthquake Protection Systems
FEMA	Federal Emergency Management Agency
GIS	Geographical Information System
GM	Ground Motion
GMPE	Ground Motion Prediction Equation
HVAC	Heating, Ventilation, Air Conditioning
IBC	International Building Code
IDR	Interstorey Drift Ratio
IM	Earthquake Intensity Measure
IO	Immediate Occupancy (Limit State)
LL	Live Load
LRFD	Load and Resistance Factor Design
LS	Life Safety (Limit State)
M or M_w	Earthquake moment magnitude
MCE	Maximum Considered Earthquake
MCE_R	Risk-targeted Maximum Considered Earthquake
MEP	Mechanical, Electrical and Plumbing
MF	Moment-resisting Frame
MRF	Moment Resisting Frames
MSA	Multiple Strip Analysis
NGA	Next Generation Attenuation

Abbreviations	Definitions *(Continued)*
NIST	National Institute of Standards and Technology
NLRHA	Non-Linear Response History Analysis
PBEE	Performance-Based Earthquake Engineering
PBSD	Performance-Based Seismic Design
PEER	Pacific Earthquake Engineering Research Centre
PFA	Peak Floor Acceleration
PGA	Peak Ground Acceleration
PNC	Percentage of Non-Collapsed simualtions
PSHA	Probabilistic Seismic Hazard Analysis
RBS	Reduced Beam Section
RC	Reinforced Concrete
RC	Repair Class matrix
RCD	Repair Class Database matrix
REDi	Resilience-based Earthquake Design Initiative
RSCB	Replaceable Steel Coupling Beam
RT	Repair Time matrix
SA	Spectral Acceleration
SA_{MAX}	Maximum Spectral Acceleration
SA_{MIN}	Minimum Spectral Acceleration
SA_{T1}	Spectral Acceleration at T_1 (fundamental period of a structure)
SDL	Superimposed Dead Load
SEAOC	Structural Engineers Association of California
SEAONC	Structural Engineers Association of Northern California
SFPIM	San Francisco Property Information Map
SLE	Service Level Earthquake
SPUR	San Francisco Planning and Urban Research Association
UBC	Uniform Building Code
UHS	Uniform Hazard Spectrum
USD	United States Dollar ($)
USGS	United States Geological Survey
VRE	Very Rare Earthquake
WGCEP	Working Group on California Earthquake Probabilities
WSMRF	Welded Steel Moment Resisting Frame
2D	Two-dimensional
3D	Three-dimensional

List of Symbols

Abbreviations	Definitions
A_g	Gross cross sectional area (Table 4-4)
ALR	Axial load-to-capacity ratios (Section 4.2)
A_{SPLICE}	Ratio of splice to column tensile capacity (Section 4.2)
A_w	Web area (Table 4-4)
C	Period dependent factor (Table 2.1, Equations 4-1 and 4-2)
C	Exposure category (Table 4-2)
C	Collapse (Equations 7-1, 7-3 and 7-4)
C_c	Column slenderness ratio (Table 4-4)
C_d	Displacement amplification factor (Section 4.1.1)
CDF	Cumulative Distribution Function (Figure 4-24)
C_p	External pressure coefficient (Table 4-2)
C_s	Seismic response coefficient (Section 4.1.1)
C_t	Factor for period estimation (Table 2.1)
C_v	Web shear coefficient (Table 4-4)
D	Dead load (Table 4-3)
D	Peak storey displacement (Table 4-11)
D or D_s	Width of the lateral resisting system (Table 2.1 and Equation 4-3)
Dir.	Direction (Table 4-7)
E	Earthquake load (Tables 4-3 and 4-6)
ε	Epsilon (Tables 7-1 and 7-2)
e or e_i	Earthquake ground motion shaking intensity (i) (Figure 7-2)
E/T	Effective over total mass (Table 4-7)
ε_{ij}	Intra-event residual mean (Equation 8-1)
EL.	Elevation (Tables 4-8 and 4-9)
ER	Exceedance rate (Equation 7-6)
ϕ	Strength reduction factor (Table 4-4)
F_a	Allowable compressive stress (Table 4-4)
F_b	Allowable bending stress (Table 4-4)
F_{cr}	Critical stress (Table 4-4)
F_i	Seismic force at storey i (Table 2.1)
FS	Factor of safety (Table 4-4)
F_t	Allowable tensile stress (Table 4-4)
F_t	Seismic force atop the building (Table 2.1, Equations 4-3 and 4-4)
F_v	Allowable shear stress (Table 4-4)
F_x	Seismic force at storey x (Equation 4-4)
F_y	Specified minimum yield stress (Table 4-4)
G(A|B)	Conditional probability of A given B (Equation 2-1)
GC_{pi}	Internal pressure coefficient (Table 4-2)
G_f	Gust effect factor (Table 4-2)
h_n	Height of the building (Table 2.1 and Equation 4-3)
h_x or h_i or h_{sx}	Height of storey x or i (Figure 5-6, Table 2.1, Equations 4-4 and 4-11)
I or I_e	Occupancy importance factor (Table 2.1 and Section 4.1.1)
K or R_w or R	Response modification factor (Table 2.1, Equation 4-1 and Section 4.1.1)
K_d	Wind directionality factor (Table 4-2)

Abbreviations	Definitions *(Continued)*
Kl	Effective length (Table 4-4)
K_{zt}	Topography factor (Table 4-2)
L	Live load (Table 4-3)
L or L_i	Loss (at intensity level i) (Equation 7-3 and 7-5)
l_{ij}	Width of panel j at storey i (Figure 5-6)
m, n or p	Matrix dimensions (Figures 4-28 to 4-31)
M_n	Nominal flexural strength (Table 4-4)
M_p	Plastic bending moment (Table 4-4)
MRC	Mean repair cost (Section 4.3.1)
MRT	Mean repair time (Section 4.3.1)
M_y	Yield moment (Section 4.2)
N or n	Number of storeys (Table 2.1 and Equation 4-4)
NC, NR	Non-collapse, non-repairable damage (Equation 7-4)
NC, R	Non-collapse, repairable damage (Equation 7-4)
NDS	Number of Damage States (Section 4.3.1)
$P_{Collapse}$	Probability of collapse (Equation 7-2)
PDF	Probability Density Function (Figure 4-24)
P_n	Nominal axial strength (Table 4-4)
P_t	Tensile capacity of column(Section 4.2)
P_x	Total vertical design load above level x (Equation 4-11)
θ	Stability coefficient for p-delta effects (Equation 4-11)
Q(t)	Quality of system (Section 2.3)
θ_π	Pre-capping plastic rotation (Section 4.2)
$\theta_{\pi\chi}$	Post-capping plastic rotation (Section 4.2)
$\theta_{\pi-\phi\rho\alpha\chi\tau}$	Plastic rotation threshold for fracture (Section 4.2)
Qty	Quantity (Section 4.3.1)
r	Radius of gyration (Table 4-4)
R	Distance (Table 7-1 and 7-2)
S	Site coefficient (Table 2.1)
S_1	MCE_R spectral response acceleration at 1-second period (Section 4.1.1)
S_{D1}	Design spectral response acceleration at 1-second period (Section 4.1.1)
S_{DS}	Design spectral response acceleration at short periods (Section 4.1.1)
t	Time in years (Equation 7-2)
T or T_1	Fundamental period (Equation 4-2, Tables 2-1 and 4-7)
T_L	Mapped long period transition (Equation 4-8)
V	Design base shear (Table 2.1, Section 4.1.1, Equations 4-1 and 4-4)
V	Basic Wind Speed (Table 4-2)
V_n	Nominal shear strength (Table 4-4)
V_{S30}	Shear wave velocity in top 30 meters of soil (Figure 7-2)
V_t	Base shear estimated from modal response (Section 4.1.1)
V_x	Seismic shear force at the storey under consideration (Equation 4-11)
W	Weight of the structure or seismic weight (Table 2.1 and Equation 4-1)
W	Wind load (Tables 4-3 and 4-6)
w_x or w_i	Weight of storey x or i respectively (Equation 4-4)
Y_{ij}	Ground motion parameter of interest (Equation 8-1)
$\bar{Y}_{ij}$	Ground motion model median prediction (Equation 8-1)

Abbreviations	Definitions *(Continued)*
Z	Seismic zone factor (Table 2.1 and Equation 4-1)
Z_{SPLICE}	Ratio of splice to column bending capacity (Section 4.2)
Z_x	Plastic section modulus (Table 4-4)
β	Ratio of shear demand to capacity of the storey (Equation 4-11)
β_{IF}	Dispersion, impeding factors (Tables 7-6 and 7-8)
$\beta_{Non\text{-}Struct}$	Dispersion, non-structural repairs (Tables 7-6 and 7-8)
β_{Struct}	Dispersion, structural repairs (Tables 7-6 and 7-8)
γ_{ij}	Damageable storey drift (Figure 5-6)
γ_p	Plastic rotation (Figure 4-21)
γ_y	Yield rotation (Figure 4-21)
Δ	Storey drift (Equation 4-11)
Δe_i	Earthquake ground motion intensity interval (Figure 7-2)
Δu_{ij}	Horizontal displacement at storey i along width of panel j (Figure 5-6)
Δv_{ij}	Vertical displacement at storey i along width of panel j (Figure 5-6)
$\Delta\lambda_i$	Annual rate of occurrence of intensity level I (Figure 7-2)
$\Delta\lambda_i$	Annual rate of occurrence of interval i (Figure 7-2)
η_{ij}	Inter-event residual mean (Equation 8-1)
θ_{ij}	Floor rotation at storey i along width of panel j (Figure 5-6)
Λ	Cumulative plastic rotation capacity (Section 4.2)
$\lambda(e)$	Annual frequency of exceedance of e (Figure 7-2)
λ_c	Mean annual rate of collapse (Equation 7-1)
μ_{IF}	Median, impeding factors (Tables 7-6 and 7-8)
$\mu_{Non\text{-}Struct}$	Median, non-structural repairs (Tables 7-6 and 7-8)
μ_{Struct}	Median, structural repairs (Tables 7-6 and 7-8)
σ_{ij}	Intra-event residual standard deviation (Equation 8-1)
τ_{ij}	Inter-event residual standard deviation (Equation 8-1)

This page is intentionally left blank.

Chapter 1

Introduction

1.1 Background and motivation

Throughout the world, tall buildings play an important role in the socio-economic activity of major metropolitan areas. They are consistently a part of the economic structure in high performing financial and business services cities (Buchanan et al. 2008) and their resilience is vital to ensuring an effective recovery after major disasters. Events such as the Canterbury earthquake in 2011 have highlighted the impact of poor performing buildings on the business continuity of downtown districts, where tall buildings are typically clustered together. Following the 2011 earthquake, Christchurch's Central Business District (CBD) red zone covered a significant area of the city and more than 60% of the businesses were displaced (CERC 2012). Buildings such as the 26-storey Hotel Grand Chancellor sustained significant damage and residual deformations, prompting authorities to cordon off an area with a radius that was roughly equal to its height (NZPA 2011). Thus, in addition to the direct economic losses in the Hotel Grand Chancellor, there were significant indirect losses attributed to business disruption in surrounding buildings.

Until the introduction of Performance-Based Seismic Design (PBSD) in the 1990s, most tall buildings in highly seismic regions were designed following a prescriptive force-based approach (SEAOC 1995). The performance of buildings designed following code prescriptive seismic design requirements, during major earthquakes, is not explicitly quantified in the design process, but rather assumed to be sufficient because the standards specified by the code are met. To address this limitation, the Pacific Earthquake Engineering Research Centre (PEER) developed a framework for Performance-Based Earthquake Engineering (PBEE), which considers uncertainties in the seismic hazard and structural response, and enables the quantification of the seismic performance of new and existing buildings in a more rigorous manner than previously. Following developments in PBEE, several jurisdictions in the United States, including Los Angeles and San Francisco, have adopted performance-based approaches for the design of new tall buildings (e.g., PEER 2010a). Whilst modern tall buildings follow a more adequate approach, at present, little is known about the seismic performance of older existing tall buildings that were designed prior to the adoption of PBSD (Molina Hutt et al. 2015, Wang et al. 2017).

Figure 1-1 shows the building height distribution in western US cities such as Los Angeles, San Francisco and Seattle, where damage to tall buildings has the potential to affect a large number of people and can have significant consequences on surrounding areas. Many of these existing tall buildings were designed following building codes from the late 1960's through mid-1990's, which did not specify drift limits, and prescribed design forces that were significantly lower than those in modern building codes. Such tall buildings include many steel moment frame buildings constructed with the type of welded connections that experienced sudden brittle fractures during the 1994 Northridge earthquake. Furthermore, there are several other significant considerations in modern design codes and practice, which were not adopted in older design standards, and have drastically improved seismic performance, including (1) capacity design principles, (2) prequalified seismic connection details to ensure ductile component behavior, (3) treatment of multi-mode response using response spectrum analysis methods, (4) consideration of bi-directional force components, and other factors.

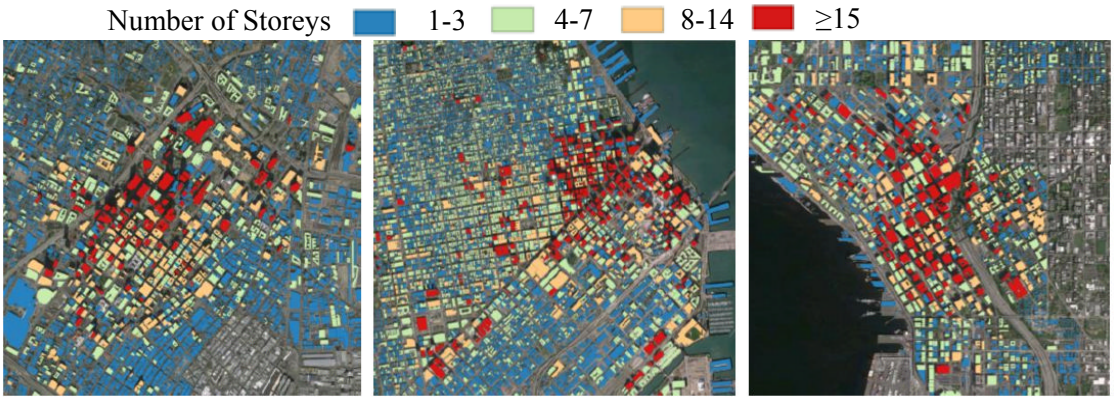

Figure 1-1: Building height distribution in Los Angeles, San Francisco, and Seattle. Source: Eads et al. (2017).

While there are currently no mandatory requirements for the routine assessment or retrofit of existing steel moment frame buildings, San Francisco, Los Angeles and other US cities do have ordinances that require assessments and retrofit during substantial building renovation or within a specified time horizon, e.g. ordinances 183893 and 184081 in Los Angeles for pre-1978 wood-frame soft-storey and non-ductile concrete buildings, respectively. Looking towards the future, San Francisco's Earthquake Safety Implementation Program (CAPSS 2011) has plans to develop assessment requirements for existing low-performance steel buildings. Just as with current programs for wood-frame or concrete buildings, the development and implementation of an effective program for steel buildings will require guidelines for screening and assessment of steel moment frames, along with practical and cost effective retrofit solutions, which this research aims to explore.

1.2 Aim, objectives and scope

Engineering seismologists, seismic, structural and geotechnical engineers have demonstrated that through PBEE, detailed assessments of individual building performance can be conducted through complex Non-Linear Response History Analysis (NLRHA) by subjecting a structural model to different ground motions at various intensity levels, e.g. Krawinkler (2004), Wang et al. (2017), Hwang and Lignos (2017). Advances in computational power and the development of models that can more accurately reproduce the behaviour of structural components have made such assessments possible. These tools can be used both for new design and for the assessment and retrofit of existing buildings in order to ensure adequate performance under seismic events of a specified return period. Estimates of the monetary losses associated with the performance of buildings can also now be conducted through approaches such as that in FEMA P58 (FEMA 2012), implemented in tools such as PACT (2012) or SP3 (2017). Furthermore, recent developments in downtime assessment methodologies for buildings (e.g. Almufti and Willford 2013) provide a framework for identifying the likely causes of downtime such that these can be mitigated to achieve a more resilient seismic performance. Despite significant progress, existing cost and downtime estimation tools limit these detailed performance assessments to individual buildings and neglect the impact of the assessed building on surrounding areas.

The overall aim of this research project is to characterize the earthquake risk of existing tall buildings in West Coast US cities that were designed following code-prescriptive guidelines developed before modern seismic building codes, and to explore retrofit techniques for enhancing their structural performance and resilience. A central component of this work is to apply the framework and latest advancements of PBEE to assess the potential risks of existing tall steel moment frame buildings. Performance is assessed through dynamic analysis of non-linear numerical models, where the results of these simulations are used to estimate damage in the building, as well as the associated consequences (direct economic loss, downtime, etc.). Collapse risk and the potential for the damaged building to be deemed irreparable is a necessary part of this process, as these potential outcomes contribute to the expected economic losses resulting from a seismic event. Such evaluations enable assessing collapse safety and whether the exhibited seismic performance has consequences on the surrounding area. As part of this work, comprehensive risk-based assessments are carried out to enable the development of risk metrics that can be used to advise policy and decision making, allowing building owners to explicitly manage seismic risk through the use of quantitative metrics. Furthermore, this project aims to integrate PBEE tools and

Geographical Information Systems (GIS) to develop a framework that enables analysis and visualization of the seismic performance assessment beyond individual buildings. This framework can help highlight critical risk hotspots, e.g., where building damage is most likely to have disproportionate impacts on the urban community, and the broader socio-economic factors that affect resilience (e.g., services provided by the affected buildings to the community). To this end, the key research objectives of the project are as follows:

1. To quantify the expected seismic performance, in terms of structural response, of existing tall steel moment frame buildings under a scenario earthquake specifically developed to assess impact on the built environment.
2. To quantify the expected seismic performance of these buildings under earthquake intensities consistent with a Design Basis Earthquake (DBE), in terms of structural performance, direct economic losses and downtime to re-occupancy and functional recovery.
3. To evaluate the impact of different strategies including innovative structural retrofits, non-structural enhancements or other measures, that can be adopted to minimize damage, direct economic losses and downtime in these buildings.
4. To assess performance under a wider range of intensities of earthquake ground motion shaking, including levels at which collapse or large permanent deformations my result in the complete loss of these buildings, their content, and their function.
5. To develop comprehensive risks metrics that can be used to help communicate the seismic performance of these buildings including: the mean annual frequency of collapse, expected annualized losses, and expected annualized downtime.
6. To benchmark the seismic performance and associated risk metrics of these existing buildings against equivalent modern code-based designs.
7. To evaluate how different types of building-specific assessments, namely scenario, intensity or time-based assessments, can be formulated to address the specific decision making needs of various stakeholders.
8. To propose a framework that integrates PBEE with GIS tools to extend detailed seismic performance assessments beyond individual buildings, towards a framework for evaluating resilience at city-level.

The study targets districts in areas of high seismicity in the US, where a large number of tall buildings are clustered together (see Figure 1-1) and where significant damage to a single building could compromise the business continuity of surrounding areas. San Francisco is selected as a case study for most of this work, in order to permit engagement and support of ongoing efforts of the city's Earthquake Safety Implementation Program (CAPSS 2011).

1.3 Thesis structure

This dissertation addresses the risks posed by the older seismically deficient steel buildings. Chapter 1 provides the background and motivation for this work, its objectives and scope, as well as the overall organization of the thesis.

Chapter 2 provides a literature review with a focus on the seismic design evolution of building codes in the US, and a review of PBEE for seismic performance assessment of buildings. The latter includes aspects related to seismic hazard estimation and ground motion selection, structural response simulation, and methods for estimating damage and associated consequences. A review of existing frameworks that enable an evaluation of seismic resilience is also provided.

Chapter 3 outlines the methodology adopted to address the research questions outlined in this work. The research questions are addressed through a number of risk-based assessments that evaluate expected seismic performance of individual buildings, as well as through a framework developed to enable evaluating the impact of buildings on surrounding areas and the urban community.

Chapter 4 describes key characteristics of the archetype buildings developed including geometry, structural detailing, occupancy and other relevant parameters that can affect seismic performance. This chapter also outlines the numerical models developed to obtain structural response parameters via NLRHA. It includes calibration of key structural components against experimental test data, as well as global checks against data from instrumented buildings consistent with the archetypes considered. Chapter 4 also describes the building performance models used to estimate the consequences of building response in terms of damage, economic losses and downtime. A method to extend existing assessments to enable the development of probabilistic recovery functions is proposed.

Chapter 5 presents a scenario-based seismic performance assessment of two archetype tall steel buildings. Scenario assessments evaluate building performance subject to an earthquake scenario, with a specific magnitude and location. The HayWired scenario, a M_w 7.0 earthquake on the Hayward fault, developed to study impacts on the San Francisco Bay area is used in this study. This chapter addresses objective No. 1 as outlined in Section 1.2.

Chapter 6 presents an intensity-based seismic performance assessment of an archetype tall steel building. It evaluates building performance under a specified earthquake shaking intensity consistent with a DBE. It evaluates the impact of a number of retrofit schemes, structural and non-structural, developed to achieve increased levels of resilience. This chapter addresses objectives No. 2 and 3 as outlined in Section 1.2.

Chapter 7 presents a comprehensive time-based seismic performance assessment of an archetype tall steel building. It consists of the evaluation of a number of intensity-based performance assessments under a range of ground motion intensity levels, which are then combined with seismic hazard data to provide the annual rates of exceedance of different performance measures. Performance is benchmarked against an equivalent modern code-based design. This chapter addresses objectives No. 4, 5 and 6 as outlined in Section 1.2.

Chapter 8 proposes a framework to assess the risk of existing tall steel buildings and the implications on urban resilience. The proposed framework integrates PBEE tools and seismic risk assessment methodologies into GIS, to enable an analysis and visualization of the seismic performance assessment of business districts. This chapter addresses objectives No. 7 and 8 as outlined in Section 1.2.

Chapter 9 presents the summary and major conclusions of this work. It also provides a reflection on the transferability of the method, it describes the limitations of the present study and provides recommendations for future work.

1.4 Publications

The work presented in this thesis has yielded a number of journal and conference publications. The following journal publications have already been published and are included for reference in Appendix A.

A1. **Molina Hutt C.**, Almufti I., Willford M. and Deierlein G. (2015). "Seismic loss and downtime assessment of existing tall steel-framed buildings and strategies for increased resilience." American Society of Civil Engineers, Journal of Structural Engineering, Special Issue Resilience-Based Analysis and Design of Structures and Infrastructure Systems. Available at: http://dx.doi.org/10.1061/(ASCE)ST.1943-541X.0001314

This publication draws largely on content presented in Chapters 4 and 6.

A2. Ji X., Liu D., Ya S. and **Molina Hutt C.** (2016). "Seismic performance assessment of a hybrid coupled wall system with replaceable steel coupling beams versus traditional RC coupling beams." Journal of Earthquake Engineering and Structural Dynamics. Available at: http://dx.doi.org/10.1002/eqe.2801

This publication is the result of a collaboration with Tsinghua University in Beijing, China funded through a Royal Academy of Engineering Newton Fund Award. While the results of the publication are not included within the body of the thesis, this study enables a reflection on the transferability of the methods used in this thesis to different contexts. This reflection is included in Chapter 9.

A3. Goretti A., **Molina Hutt C.** and Hedelung L. (2017). "Post-earthquake safety evaluation of buildings in Portoviejo, Manabí following the M7.8 coastal Ecuador earthquake of 16 April 2016." International Journal of Disaster Risk Reduction. Available at: https://doi.org/10.1016/j.ijdrr.2017.06.011

This publication summarizes field work carried out in Ecuador following the April 2016 earthquake within the EU Civil Protection Mechanism. It does not relate directly to the thesis contents. However, it provides context and inspiration, particularly for Chapter 8, as it highlights the value of GIS in the seismic performance evaluation of buildings.

Content presented in Chapters 4 and 5 is also included in a peer reviewed report prepared in collaboration with Arup (www.arup.com) as part of the United States Geological Survey (USGS) HayWired Scenario – Tall Building Performance project (RFP – Reference Number G16PS00702).

Additionally, a number of journal publications, which draw on material directly presented in this thesis, are currently in preparation and are listed below.

- **Molina Hutt C.**, Rossetto T. and Deierlein G. (2017a). "Comparative risk-based seismic performance assessment of 1970s vs modern tall steel moment resisting frames."

  This publication draws largely on content presented in Chapters 4 and 7.

- **Molina Hutt C.**, Rossetto T. and Deierlein G. (2017b) "A framework for assessing the impact of tall building performance on the resilience of business districts."

  This publication draws largely on content presented in Chapter 8.

- Ji X., Liu D. and **Molina Hutt C.** (2017). "Evaluating the impact of replaceable steel coupling beams versus traditional RC coupling beams on the seismic recovery of buildings."

  This publication is an extension of the study presented in Appendix A2, which applies some of the methods developed in this thesis to new construction.

A number of conference papers have also been accepted and presented at international conferences. In most cases, these papers consist of preliminary results of work compiled in this thesis.

- **Molina Hutt C.** (2017). "A comparative study on the seismic vulnerability of 1970s vs modern tall steel moment-resisting frame buildings." *Proc., 16th World Conference of Earthquake Engineering,* Santiago, Chile (oral presentation).

- Eads L., **Molina Hutt C.** and Menun C. (2017). "Loss assessment of tall buildings from a vulnerability perspective." *Proc., 16th World Conference of Earthquake Engineering,* Santiago, Chile (oral presentation).
- **Molina Hutt C.**, Almufti I., Willford M. and Deierlein G. (2015). "Risk-based seismic performance assessment of existing tall steel-framed buildings in San Francisco." *Proc., SECED 2015 Conference: Earthquake Risk and Engineering towards a Resilient World,* Cambridge, UK (oral presentation).
- **Molina Hutt C.**, Almufti I., Willford M. and Deierlein G. (2014). "Seismic loss and downtime estimates of existing tall buildings and strategies for increased resilience." *Proc., 2nd European Conference of Earthquake Engineering and Seismology,* Istanbul, Turkey (oral presentation).
- **Molina Hutt C.** (2013). "Non-Linear time history analysis of tall steel moment frame buildings in LS-DYNA." *Proc., 9th European LS-DYNA Conference,* Manchester, UK (oral presentation).
- Almufti I., **Molina Hutt C.**, Willford M. and Deierlein G. (2012). "Seismic assessment of typical 1970s tall steel moment frame buildings in downtown San Francisco." *Proc., 15th World Conference of Earthquake Engineering,* Lisbon, Portugal (oral presentation).
- **Molina Hutt C.** (2011). "Seismic assessment and retrofit recommendations for tall steel moment frame buildings in San Francisco." *Proc., Arup University 2011 Doctoral College Conference*, London, UK (oral presentation).

Throughout my time at UCL, I have had the opportunity to engage on a number of activities which, whilst not directly related to the work presented in this thesis, have provided inspiration to the later chapters and valuable insight into other areas of earthquake engineering research. Some of the associated outputs and publications are listed below.

- Perez-Fuentes G., **Molina Hutt C.**, Rossetto T. and Joffe H. (2017). "Are residents of Seattle ready for 'the big one'? An intervention study to change earthquake preparedness." *Proc., 16th World Conference of Earthquake Engineering,* Santiago, Chile (oral presentation).
- EEFIT (2013). "The M_w9.0 Tōhoku earthquake and tsunami of 11th March 2011 - return mission." Institution of Structural Engineers.
- ECHO (2016). "Earthquake in Ecuador." European Commission, Humanitarian Aid and Civil Protection, ECHO's Next - Newsletter for Civil Protection National Experts, Issue 12, June/July 2016.
- **Molina Hutt C.** (2016). "The guardians of public safety in Ecuador." The Blog of the Institution of Structural Engineers.

Chapter 2

Literature Review

This chapter presents a review of the literature with a focus on three distinct areas. The first section provides a historical overview of seismic design provisions in US building codes, vulnerabilities in steel moment frame buildings with welded beam-to-column connections, and considerations related to the seismic design of tall buildings and associated loss evaluations. The second section provides an overview of state of the art methods for seismic performance assessment of buildings with a focus on the PEER PBEE framework and its implementation to enable decision making for seismic risk mitigation. The last section provides a review of methods for evaluation and quantification of seismic resilience. Overall, this review provides context, identifies research needs and sets the point of departure for this work.

2.1 Seismic vulnerability of existing tall steel buildings in the US

2.1.1 Seismic design evolution of building codes

The seismology committee of the Structural Engineers Association of California (SEAOC) is the originator of seismic design provisions in the US. Since 1959, this committee published a number of editions of "Recommended Lateral Force Requirements and Commentary," informally referred to as the 'SEAOC Blue Book'. These recommendations, which had no legal standing, progressively made their way into the building code regulations, the Uniform Building Code (UBC). The Blue Book of 1959 (SEAOC 1959) already established performance goals, which are still today found in building codes. The objective of the lateral force requirements outlined in the Blue Book of 1959 is to produce structures capable of resisting: minor earthquakes without damage, moderate earthquakes without structural damage, but some non-structural damage and major earthquakes without collapse, but possibly both structural and non-structural damage. At the time of publication, knowledge was insufficient to provide rigorous criteria to ensure these performance goals, hence they were achieved by empirical base shear equations intended to account for different complex phenomena. These equations in conjunction with elastic drift limits and detailing requirements were intended to provide collapse safety and damage control. These principles are still present in modern codes in the form of ductility, achieved through seismic detailing, and capacity design principles where enough ductility cannot be achieved.

Significant changes to US building codes came about in the 1970s, mainly in terms of how seismic inputs were defined. Principles of seismic hazard analysis from Cornell (1968) were implemented to develop hazard maps with effective peak accelerations for a 475 year return period event. These mapped parameters, in conjunction with soil profile coefficients, were used to derive ground motion spectra (ATC 1978). Force-based design requirements, based on the first mode lateral force coefficient, were the predominant method of design, along with the concept of a response modification factor, to permit elastic force design requirements for systems that are expected to behave inelastically. These design principles were based strictly on elastic behaviour without consideration of the deformation capacity of different systems. These concepts are still present in modern building codes. However, they are significantly more detailed and the seismic inputs for design, in the US, have shifted toward a 2475 year return period event, defined as the Maximum Considered Earthquake (MCE), which is later scaled by two-thirds to define the DBE. The notion of a response modification factor is still present and is currently specified for roughly 70 different structural system types in ASCE 7 (ASCE 2010).

Lee and Foutch (2000) conducted a review of seismic design provisions for all editions of the UBC from 1958 to 1994. Based on changes to the provisions for seismic design, these editions of the UBC can be subdivided into three main groups: UBC 1958 to 1973, UBC 1976 to 1985, and UBC 1988 to 1994. Changes to the design methodology, highlighting design considerations for steel Moment Resisting Frames (MRF), are summarized below and illustrated in Table 2-1.

- From 1958 to 1973 seismic and steel design requirements in the UBC did not undergo significant changes. A horizontal force factor of 0.67 was used for MRF structures, regardless of material. This factor is analogous to the response modification factor previously discussed, which is introduced to permit elastic force design requirements. Regarding steel MRFs, two requirements were introduced: (i) capacity design for moment connections and (ii) the use of compact sections for members that were intended to develop plastic hinges.
- From 1976 to 1985, a site coefficient and an importance factor were introduced in order to emphasize the impact of a building's site and occupancy respectively. A new seismic zone was introduced. Most importantly, an interstorey drift limit of 0.005 under the seismic forces defined in the code was introduced. The distribution of lateral forces was modified by re-defining the lateral force applied atop the building. This change resulted in considerably larger forces atop the building for tall and slender structures, such as steel MRFs, than those in prior codes.

- From 1988 to 1994, seismic regulations adopted the recommendations of the SEAOC Blue Book of 1988. The response modification factor was changed to reflect the energy dissipation and ductility of different structural systems and the seismic zone factor was changed to represent the effective peak ground acceleration representative of a 475 year return period event. From a steel design point of view, panel zone provisions were included in the code, as well as strong column-weak beam requirements.

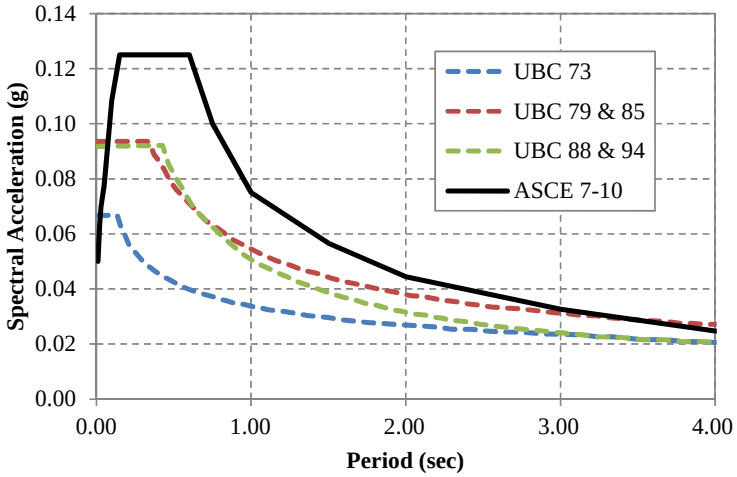

Figure 2-1: Design spectra for UBC 1973 to 1994 versus modern building codes. Sources: Lee and Foutch (2000) and ASCE (2010).

Table 2-1: Key specifications from UBC 1973, 1985 and 1994 related to seismic principles and steel MRF design.
Source: Adapted from Lee and Foutch (2000)

	UBC 1973	UBC 1985	UBC 1994
Allowable Stress	Allowable stresses can be increased by 1/3 when considering earthquake forces.		
Seismic Zones	3	4	4
Base Shear	$V=Z\cdot K\cdot C\cdot W$ $C=0.05/T^{1/3}$ K=0.67 for MRF	$V=Z\cdot I\cdot K\cdot C\cdot S\cdot W$ $C=1/(15\cdot T^{1/2})$ K=0.67 for MRF	$V=Z\cdot I\cdot C\cdot W/R_w$ $C=1.25\cdot S/T^{2/3}$ R_w=12 for MRF
Period	0.1N for steel MRF		$T=C_t\cdot h_n^{3/4}$
Distribution of forces	$V=F_t+\sum F_i$ $F_t=0.004V\cdot(h_n/D)^2$	$V=F_t+\sum F_i$ $F_t=0.07T\cdot V$	
Drift Limits	In accordance with accepted engineering practice	Storey drift < 0.005 with displacement amplified by (1/K)	For T>0.7 sec Limit = $0.03/R_w$ or $0.004*h_i$
Steel MRF Requirements	-Connections able to develop full plastic capacity -Local buckling to satisfy plastic design		-Panel zone strength and thickness -Strength Ratio (strong column-weak beam)

See List of Symbols for variable definitions.

This review highlights that steel MRFs built based on the UBC provisions from 1973 or earlier are characterized by the lack of interstorey drift limits, lack of panel zone design requirements, lack of strong column-weak beam provisions and low design base shear, as illustrated in Figure 2-1. These deficiencies were progressively eliminated through the incorporation of additional code requirements as described earlier.

2.1.2 Welded steel moment resisting frame (WSMRF) vulnerabilities

In the 1960s, engineers began to regard WSMRFs as being among the most ductile systems contained in the building code (FEMA 2000a). It was thought that when subject to earthquake shaking, WSMRFs would have limited damage due to ductile yielding of members and connections. Engineers regarded the potential collapse of such structures as impossible. This led to widespread construction of many WSMRFs particularly in the western United States (FEMA 2000a). Following the 1994 Northridge earthquake, many WSMRFs experienced brittle fractures of beam-to-column connections, even in areas with moderate ground shaking. Damage surveys indicated that brittle fractures initiated within the connections at very low levels of plastic demand, or in some cases within the elastic range, and progressed along a number of paths inducing a significant loss in strength and stiffness (Youssef et al. 1995). Prior to Northridge, the major problem in trying to gauge the past performance of WSMRFs is the lack of data. A few successes, or rather the lack of any notorious failures, established the reputation that WSMRFs have particularly good earthquake resistance characteristics (FEMA 2000b). Until Loma Prieta in 1989, only a handful of modern WSMRFs had been shaken by a major earthquake. Fewer than a dozen were closely inspected after the 1985 Mexico City, 1971 San Fernando and 1964 Prince William Sound earthquakes combined (FEMA 2000b).

Following the 1994 Northridge earthquake, the SAC Joint Venture, the American Institute of Steel Construction (AISC), the American Iron and Steel Institute (AISI) and the National Institute of Standards and Technology (NIST) convened an international workshop to coordinate efforts for the investigation and resolution of this challenge (FEMA 2000c), which led to a massive research program funded by the US Federal Management Emergency Agency (FEMA). This work was aimed at inspecting and assessing damage to WSMRFs, studying repair and upgrade of these buildings for improved performance, and providing guidelines for their design with reliable seismic performance. As a result, many studies have been conducted to assess the performance of pre- and post-Northridge WSMRFs (Gupta and Krawinkler 1999, Seung-Yul et al. 2002, Medina and Krawinkler 2005, and Maison and Bonowitz 1999 amongst

others). While these studies assess the performance of WSMRF buildings, they only evaluated building heights up to 20-storeys, and under limited earthquake ground motion intensities. Furthermore, they focused on structural performance alone, which provides valuable information for the structural engineering community, but fails to provide measures of risk associated with direct economic losses or other metrics used by stakeholders for decision making.

Later studies (Muto and Krishnan 2011, Krishnan et al. 2006) evaluated the response of tall WSMRF buildings subject to a M7.8-7.9 earthquake scenario on the San Andreas fault in Los Angeles and San Diego. They analysed 18-storey buildings using three-dimensional (3D) non-linear finite element models to simulate the expected behaviour throughout the region. The results of their study revealed that 5% of the buildings would collapse, 10% would be red-tagged, 15% with damage scenarios capable of causing loss of life and 20% with significant damage to trigger building closures. While these detailed studies provide insightful information related to the expected structural response of existing WSMRFs, they are conditioned on isolated earthquake scenario events, failing to provide more informative risk metrics, which enable an understanding of performance under other earthquake ground motion intensities. Other studies have assessed the performance of WSMRF buildings up to 40-storeys (Jayaram and Shome 2012) and estimated economic losses associated with building performance (Shome et al. 2013). However, these studies employed simplified single bay two-dimensional structural analysis models and did not consider the potential for fracture in the beam-to-column connections as previously discussed. In the words of Krishnan et al. (2006): "No detailed analyses have been performed to confirm the safety of high-rise buildings 40-storeys and taller during either large distant earthquakes or moderate near-source earthquakes."

During the 1994 Northridge earthquake, tall buildings in downtown Los Angeles were not directly affected by the event. Following the earthquake, reconnaissance missions (EEFIT 1994, EERI 1994) were unaware of damage to WSMRFs. Subsequent inspections revealed that there had been cracking in the beam-to-column joint welds in low and medium rise structures, though none in the tall buildings in the downtown area due to considerably lower seismic demands. In 1995, the Los Angeles City Council passed ordinance number 170406, mandating connection inspections and repairs in WSMRF buildings. The final ordinance covered a specific geographic area that excluded some parts of the city, in particular, the existing tall buildings in the downtown area were excluded (FEMA 2000b). Outside of Southern California, the Northridge damage prompted investigations of some WSMRF

buildings in San Francisco that had been subject to strong ground motions in the 1989 Loma Prieta earthquake. However, no inspections were mandated.

2.1.3 Seismic design of tall buildings

Tall buildings have unique seismic response characteristics including fundamental translation periods of vibration well in excess of 1 second, significant mass participation and lateral response in higher modes of vibration, as well as seismic resisting systems with slender aspect ratios (PEER 2010a). Consideration of period dependent seismic demands dates back to the Blue Book of 1959 (SEAOC 1959) where the design lateral force coefficient contained a $T^{-1/3}$ term, where T is the fundamental period of the structure, also shown for later UBC editions as seen in Table 2-1. The argument for this exponent is that it raises the long period force demand to account for higher modal participation and gives a larger load factor for tall buildings (Freeman 2007). This period dependent seismic coefficient is introduced in the 1961 edition of the UBC. While some consideration to higher mode effects is inherent in the building codes as early 1961, modal response spectrum analysis, which accounts for mass participation and response in higher modes, is not introduced into the code provisions for seismic design until 1978 (ATC 1978).

Even with the introduction of modal response spectrum analysis into building codes, the limitation of code prescriptive requirements to tall building design is apparent through height limitations associated with certain lateral resisting systems, typically with a threshold of approximately 50 meters (160 feet) (ASCE 2010). In recognition of the shortcomings of prescriptive code requirements for tall building design, a number of PBSD guidelines have been developed for tall building design including AB-083 (SEAONC 2007), adopted in San Francisco, LATBSDC (2011), adopted in Los Angeles, PEER (2010a), originally developed for use in the western United States, but applicable to other regions and CTBUH (2010). Modern codes traditionally permit the use of such alternative analysis and design methods provided that these follow well established principles of mechanics (Gerges et al. 2012). These guidelines, developed within the framework of PBEE, later described in Section 2.2.1, have widespread use for the design of new tall buildings. However, while these design guidelines follow an alternate approach to that of the code, they are intended to provide equivalent performance to that provided by prescriptive building code requirements (PEER 2010a). This raises the question whether tall buildings, due to their high occupancies and potential consequences from earthquake damage should be designed to higher standards than low rise buildings (Krawinkler and Deierlein 2014).

2.1.4 Loss assessment of tall buildings from a vulnerability perspective

Low rise buildings, with a seismic response dominated by the first mode of vibration, tend to have similar interstorey drift ratios (IDR) along their height. As a result, the damage to structural and non-structural drift sensitive components, which can represent well over 50% of the total building value in commercial and residential buildings (HAZUS 2014), is well distributed along the height. In contrast, due to the significant participation of higher modes, the response in tall buildings often leads to a non-uniform distribution of IDRs along the height (Eads et al. 2017). Shome et al. (2015) and Ramirez et al. (2012) observed such concentrations of IDRs in just a few stories. The Canterbury earthquake in 2011 provides some examples of tall buildings that were demolished due to concentrated damage sustained during the earthquake (Eads et al. 2017), as outlined below:

- The 26-storey Hotel Grand Chancellor was demolished after a local failure at the base of a shear wall, which caused the southeast corner at the top of the structure to displace 0.8 m (2.6 ft) vertically and 1.3 m (4.3 ft) laterally (CERC 2012).
- The 20-storey Clarendon Tower was demolished after it sustained extensive cracking in the floor diaphragms, as well as damage caused by frame elongation (CERC 2012). The frame damage was most extensive at the mid-height stories, where peak IDRs were estimated to reach 1.3-2.8% (Zimmerman and Holmes 2012, Walsh et al. 2016).
- The 22-storey PricewaterhouseCoopers building was demolished after it was deemed too costly to repair. The most severe damage occurred at the mid-height stories, including the formation of plastic hinges in the beams of the reinforced concrete (RC) frame on levels 6 to 8 (Bayer 2012).

The concentration of large IDRs has important implications for building vulnerability and loss assessment, as it leads to a large proportion of damage and loss resulting from a relatively small number of stories (Eads et al. 2017). As a result, normalized seismic losses, defined as the expected repair costs over the total building value, tend to be lower in tall buildings. If using this metric to evaluate seismic performance, one would consider tall buildings to be less vulnerable than shorter buildings at low to moderate levels of ground shaking. However, at higher ground motion intensities, despite low normalized loss ratios, tall buildings can be rendered irreparable due to excessive permanent deformations in just a small number of stories, suggesting that tall buildings may be more vulnerable than shorter buildings (Eads et al. 2017). Furthermore, at higher ground motion intensities, concentration of damage also leads to a higher risk of sidesway collapse in taller buildings compared to shorter buildings (Ramirez et al. 2012).

2.2 Seismic performance assessment of buildings and FEMA P58

With the introduction of code provisions for seismic design in the 1960s, as discussed in Section 2.1.1, came the realization that many buildings had not been engineered to resist seismic forces. Concerns for seismic rehabilitation of existing buildings grew considerably following the 1971 San Fernando earthquake (Moehle 2000). However, in the US, the issue of seismic risk from existing buildings did not reach a national stage until FEMA launched its 'Program to Reduce the Seismic Hazards of Existing Buildings' in 1985 (Holmes 2009), gaining further impetus following the 1989 Loma Prieta and 1994 Northridge earthquakes. Other than mandated retrofits, seismic upgrades of buildings typically take place through the use of mechanisms referred to as "triggers," such as a change of use or ownership, or when a building is subject to significant alterations (Hoover 1992).

ATC-14 (1987) and FEMA 273 (1997) were both landmark documents in the history of seismic retrofit guidelines (Pekelnicky and Poland 2012, Hamburger 2009). ATC-14 (1987) provides engineers with a standard methodology by which buildings can be evaluated to detect the presence of significant life safety hazards. FEMA 273 (1997) formulates analytical procedures for seismic performance assessment, a linear methodology that uses inelastic demand ratios, and the capacity-spectrum method of inelastic analysis. The assessment and design procedures included in these documents are often referred to as the first generation of PBEE (Moehle and Deierlein 2004). Following their publication, FEMA began efforts to transition those documents from guidelines into national standards. The standardization efforts culminated with the publication of ASCE 31: Seismic Evaluation of Existing Buildings (2003) and ASCE 41: Seismic Rehabilitation of Existing Buildings (2006).

Modern retrofit practice is typically based on the procedures and acceptance criteria outlined in ASCE 41 (2006, 2013). The basic concept of these procedures is shown in Figure 2-2, where a building is being loaded by earthquake-induced lateral forces that result in non-linear response and damage. Relations are then established between structural response indices (IDRs, inelastic component deformations, and member forces) and performance-oriented descriptions such as Immediate Occupancy (IO), Life Safety (LS) and Collapse Prevention (CP), as seen in Figure 2-2. While these measures are suggestive of performance objectives, in reality they are poor at providing the ability to answer the question of how the building will truly perform (Hamburger 2009) as they don't directly address the risk of incurring life loss, economic loss or occupancy disruption.

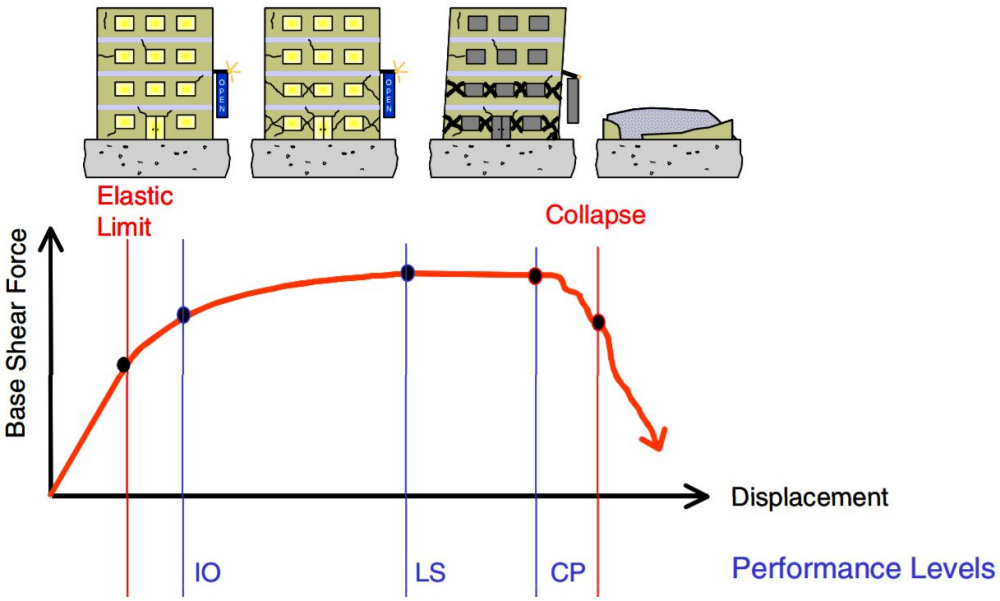

Figure 2-2: Schematic illustration of standard levels of seismic performance.
Source: Moehle and Deierlein (2004)

In recognition of these limitations, the FEMA P58 project (FEMA 2012) developed tools and guidelines for the next-generation PBSD and retrofit of buildings that enables performance to be expressed in terms of probable financial, human and occupancy disruption losses caused by earthquake damage to best suit the decision making criteria of stakeholders (Hamburger 2004). Therefore, efficient designs or retrofit techniques are those that do not focus on structural performance alone, but rather minimize losses to meet the performance targets of stakeholders by limiting both structural and non-structural damage (Lavan 2010). The evaluation procedures follow the PBEE framework, in which probable earthquake losses are calculated by integrating over the ground shaking hazard, probable structural response given intensity, probable damage given response, and probable loss given damage (Deierlein 2004).

The FEMA P58 project is a major departure from prior performance-based approaches, where performance is expressed in terms of arbitrary performance levels (IO, LS or CP), and truly enables more transparent design and decision making than available through prescriptive design. Its implementation takes advantage of the latest research developments in characterizing earthquake ground motion hazards, simulating structural behaviour, and assessing earthquake damage and its consequences (Moehle and Deierlein 2004). At present, “the PBEE framework developed by PEER and implemented in FEMA P58 is the cornerstone for assessing the seismic performance of individual buildings and facilities” (Burton et al. 2015).

2.2.1 Performance-based earthquake engineering (PBEE)

PBEE aims to improve seismic risk decision-making by means of assessment and design methods with a strong scientific basis that express outcomes in metrics that can be understood by stakeholders (Cornell and Krawinkler 2000, Moehle and Deierlein 2004; Krawinler and Miranda 2004). The performance assessment process follows a logical progression of steps that can be studied and resolved in a rigorous and consistent manner, starting with (i) seismic hazard characterization, followed by (ii) simulation of structural response, (iii) damage assessment, and (iv) loss modelling, as illustrated in Figure 2-3.

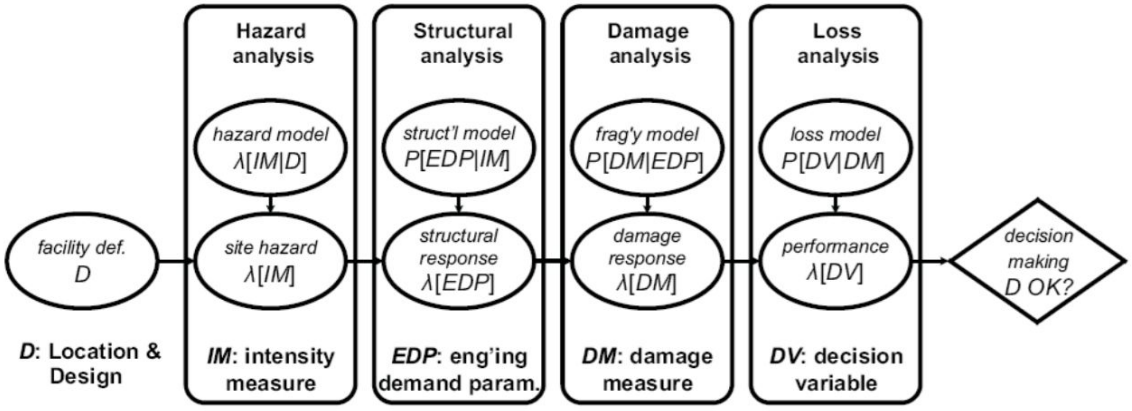

Figure 2-3: Schematic of PEER methodology.
Source: Porter (2003)

Each step yields an output, which enables a systematic transfer of information from a step of the process to the next. The outcomes of each step are represented through generalized variables: (i) the earthquake *Intensity Measure* (IM) which defines in a probabilistic sense the features of the ground motion hazard that affect structural response; (ii) *Engineering Demand Parameters* (EDPs) quantify the structural response in terms of deformations, accelerations, or other response quantities calculated by simulation of the building to the input ground motions; *Damage Measures* (DMs) describe the physical states of the structure and its components as a function of the EDPs; *Decision Variables* (DVs) inferred from the DMs translate the damage into metrics that can be understood by stakeholders for decision marking, e.g. economic losses. A rigorous probabilistic framework permits consistent characterization of the inherent uncertainties throughout the process. The probabilistic expressions of the PBEE methodology components (IM, EDP, DM, and DV) can be integrated by the total probability theorem, expressed conceptually in Equation 2-1 (Deierlein 2004, Cornell and Krawinkler 2000, Moehle and Deierlein 2004; Krawinler and Miranda 2004).

$$\lambda(DV) = \iiint G(DV|DM)\, dG(DM|EDP)\, dG(EDP|IM)\, d\lambda(IM) \qquad \text{Equation 2-1}$$

Where $\lambda(IM)$ represents the mean annual frequencies of exceedance for IM, the intermediate terms G(A|B) are conditional probabilities for the methodology components EDP, DM, and DV, and $\lambda(DV)$ is the probabilistic description of the performance metrics, e.g. the mean annual frequency, Y, that the direct economic loss will exceed X percent of the building replacement cost, i.e. $Y = \lambda$ (Loss > X% replacement cost).

While conceptually straightforward, there are many details associated with the implementation of the framework that are fairly complex. Key elements of the framework are elaborated on in the next sections; for further information, the reader is referred to Krawinkler and Miranda (2004), Krawinkler (2004), Miranda and Aslani (2003), Baker and Cornell (2006), Comerio (2004), Ibarra and Krawinkler (2004), Miranda et al. (2004) and Porter et al. (2001).

2.2.2 Seismic hazard analysis

The performance assessment process initiates with a characterization of the site hazard, that is, the probability that the building will experience various levels of ground shaking, characterized by an IM. The earthquake IM is the primary parameter through which the seismic hazard is defined. Traditional IMs include the peak ground acceleration (PGA), or the spectral acceleration at a particular period of vibration, such as the fundamental period of the structure under consideration (SA_{T1}). These IMs are readily available through Probabilistic Seismic Hazard Analysis (PSHA), which aims to quantify uncertainties in the location, size and shaking intensity of future earthquakes, and combine these to produce an explicit description of the distribution of future shaking that may occur at a site. As outlined in Baker (2008), this calculation can be broken down into five basic steps as follows: identify earthquake sources; characterize the distribution of earthquake magnitudes from each source; characterize the distribution of source-to-site distances from each source; predict the resulting distribution of ground motion intensity; and combine these to compute the annual rate of exceeding an IM. The last step yields a seismic hazard curve, which describes the mean annual frequency of exceeding a certain earthquake IM.

In addition to quantifying the earthquake IM, the hazard analysis involves characterization of appropriate ground motion input records for response history analyses. Deierlein (2004) argues that one of the important questions in choosing an IM relates to how well it represents

the damaging effects of earthquake ground motions on structures. Different ground motions result in a scatter in structural response predictions due to so-called record-to-record variability, resulting from the fact that a particular IM, such as SA_{T1}, may not fully capture all the damaging features of the earthquake records. The PBEE framework can account for this variability; though, it is most advantageous to identify IMs that reduce the variability and capture significant features of the seismic hazard at the site. While it is generally acceptable to select ground motions based on their spectral acceleration intensity, there is continued exploration of ways to incorporate frequency content, duration and other aspects to the ground motion selection process (Deierlein and Krawinkler 2014).

Input ground motions for structural response simulation are typically obtained by selecting and modifying accelerograms to match a target spectrum. Seismic hazard curves at multiple periods enable the development of target response spectra. A response spectrum in which each ordinate has the same rate of exceedance is defined as a uniform hazard spectrum (UHS). By selecting different rates of exceedance, target spectra for different intensities of ground motion shaking can be constructed. NEHRP (2011) provides a thorough review of the state of the practice with regards to selecting and scaling ground motions for NLRHA of buildings and the impacts of different ground motion selection considerations. Two important aspects highlighted by NEHRP (2011) are briefly discussed below: selection of ground motions based on the Conditional Spectrum (CS), which accounts for correlation of ground motion intensities at multiple periods, as opposed to the UHS; and ongoing research on near fault directivity effects.

UHS, derived from probabilistic seismic hazard curves, accounts for the contributions of all seismic sources that may affect the site, but are usually not representative of any one earthquake. Actual time history records show significant variations in spectral ordinates from that of the UHS, and the frequency characteristics of time history records, which control higher mode effects and to some extent inelastic response of structures, are masked by period specific spectral hazard analysis (Krawinkler 1999). For this reason, alternatives to the UHS have been developed such as the Conditional Mean Spectrum (CMS) (Baker 2011) and the related CS (Jayaram et al. 2011). These spectra condition the spectrum calculation on spectral acceleration at a single period, referred to as the conditioning period, and then compute associated spectral acceleration values at all other periods. This ensures that ground motions selected to match that spectrum have appropriate properties for naturally occurring ground motions that would occur at the site of interest (NEHRP 2011).

Earthquake ground motions recorded at small site-to-source distances can have significantly different characteristics than those recorded at larger distances. Sites in the near-fault region may experience shaking described as forward-directivity (rupture towards the site) or backward-directivity (rupture away from the site), which induce intense pulse-like ground motions. These motions can have an adverse effect on the seismic performance of structures (NEHRP 2011). Baker (2007) developed a method for quantitatively identifying ground motions containing strong velocity pulses, such as those caused by near-fault directivity. Furthermore, Shahi and Baker (2011) and Almufti et al. (2013) have developed frameworks for incorporating velocity pulses in PSHA such that they can be accounted for in developing design ground motions for NLRHA.

2.2.3 Structural response simulation

Response history analyses are used to simulate EDPs that can be used as predictors of the damage sustained by the structure and prediction of the intensity of demands placed on non-structural elements and systems supported by the structure, at different intensities of ground motion shaking. Even though buildings are expected to undergo inelastic deformations when subject to large earthquakes, linear elastic analyses are often used to design buildings for seismic resistance, as discussed in Section 2.1.1. In contrast, non-linear analyses enable the calculation of structural response beyond the elastic range, including strength and stiffness deterioration associated with inelastic material behaviour and large displacements. As such, non-linear analysis can play an important role in the design of new buildings and assessment or retrofit of existing buildings (Deierlein et al. 2010). Due to the complex nature of non-linear analysis, its application in earthquake engineering is typically limited to the following cases (Deierlein et al. 2010): (i) assess and design seismic retrofit solutions for existing buildings; (ii) design of new buildings that don’t comply with code requirements, with particular emphasis on tall building design in high seismic regions; (iii) performance assessment for owner or stakeholder decision making.

The first widespread practical applications of non-linear analyses in earthquake engineering in the US were to assess and retrofit existing buildings. As discussed earlier, guidelines such as FEMA 273 (FEMA 1997) focused primarily on non-linear static analysis, also known as pushover analysis. These recommendations developed into ASCE 41 (ASCE 2006, 2013), which introduce the non-linear dynamic procedure, or NLRHA, in addition to the non-linear static analysis. NLRHA simulation provides a more accurate calculation of the structural response to strong ground shaking than non-linear static analysis as it incorporates inelastic

member behaviour that explicitly simulates hysteretic energy dissipation in the non-linear range. The response is computed for input earthquake ground motions, which result in time history data throughout the simulation (Deierlein et al. 2010). As outlined in PEER (2010b), NLRHA is the best tool currently available for predicting building response at varying levels of ground motion intensity. The key objective of NLRHA is to understand behaviour rather than fulfil code prescriptive requirements (Krawinkler 2006).

Many studies have demonstrated the capability of non-linear dynamic analyses to predict the response of structures subjected to earthquake ground motions. For instance, Roger and Jirsa (1998) conducted a NLRHA simulation of an instrumented reinforced concrete structure damaged during 1994 Northridge earthquake. The results of their simulations match closely those recorded during the event. Anderson and Bertero (1998) simulated the response of an instrumented 42 storey steel moment resisting space frame in San Francisco obtaining similar behaviour in their simulations compared to parameters recorded during the 1989 Loma Prieta earthquake. More recent studies have demonstrated the capability of non-linear dynamic analysis to predict structural collapse. Lignos et al. (2010) predicted and validated the sidesway collapse of a 4-storey steel moment frame. As part of this study, Lignos et al. (2010) concluded that relatively simple analytical models can be used to predict the behaviour of moment frames up to collapse, provided that the deterioration characteristics of critical components are adequately represented in the analytical models. While significant progress has been made, the accuracy of models to precisely determine demand parameters such as local deformations, residual drifts, and floor accelerations has not been fully validated (Deierlein and Krawinkler 2014).

In order to accurately capture the behaviour of complex structural systems, it is essential to accurately capture the behaviour of individual components. In steel MRFs the key structural components are beams, panel zones and columns. Many studies have been conducted to analytically represent the true hysteretic response of these structural components. Mathematical models to describe the behaviour of the panel zone, in terms of shear force-shear distortion relationships, have been proposed by many researchers, including Krawinkler (1978), Tsai and Popov (1988), Kim and Engelhardt (1995), and Jin and El-Tawil (2005), based on either experimental observations or finite element modelling. Lignos and Krawinkler (2011) calibrated and validated analytical models to capture the cyclic moment-rotation relationship at the plastic hinge of steel beams against a large database of experimental tests with over 300 specimens. Furthermore, on the basis of information deduced from the steel component database, empirical relationships for modelling such response as a function of

cross section geometry and material properties were developed. Fewer tests are available for steel elements subjected to combined axial load and inelastic deformations caused by cyclic bending moments (PEER 2010b). Analytical modelling, therefore, must be based on a combination of incomplete column test data, principles of mechanics, and extrapolation from beam test results. In order to address this research gap, Kurata et al. (2005) conducted tests to determine the cyclic deformation of hollow steel column sections. Later, Lignos and Krawinkler (2010) used such experimental data for the development of a database including more than 120 axial-bending cyclic tests on tubular hollow square steel columns. This database was used to calibrate the hysteretic response and develop empirical relationships for modelling similar to those developed for beams. While these models capture strength and stiffness degradation, the modelling capabilities are limited to certain behavioural effects and by calibration of phenomenological parameters (Deierlein and Krawinkler 2014).

For building structures, the most common EDPs simulated via NLRHA are storey drift ratios, inelastic component deformations and floor accelerations. Both peak and residual deformations are of interest, as the latter impact decisions on post-earthquake repair, as discussed in Section 2.1.4. The choice of EDP is driven primarily by how it correlates with relevant damage predictions over the full range of behaviour, from small levels of deformation through to collapse. Selecting and modifying accelerograms to match a target spectrum, representative of a particular rate of exceedance, enables characterizing the relationships between EDPs and IMs. These relationships are described by the conditional probability, P(EDP|IM), which captures the variability in the prediction of response. The probability distribution, P(EDP|IM), describes the EDPs conditioned on a particular hazard intensity or IM. However, the variability is solely the result of the ground motion characteristics, described earlier as the record-to-record variability. Ground motion and hazard characterization are known to be a primary source of uncertainties (Deierlein 2004). However, the simulations and resulting probability distributions should also account for other uncertainties in the structural model itself, e.g. variation of material properties, uncertainties associated with the strength and deformation characteristics of structural components, variations in dead loads and seismic mass, etc. While the most likely values for these parameters can be generally well estimated, in fact, the true values are rarely ever known. Since the values for modelling parameters used in the analyses are never fully accurate, the resulting structural response function for the building may either over-predict or under-predict response at a given ground motion intensity. The effect of these additional uncertainties is to broaden the scatter associated with the predicted response. For a real structure, the task of defining these uncertainty bounds, considering the numerous random variables involved, is a complex process requiring many

analyses. As an alternative to this process, FEMA P58 proposes estimating confidence bounds by assuming that the variability can be represented by a standard distribution, typically lognormal, and by selecting a coefficient of variation based on either expert judgment or the variability observed in analysis of a limited number of standard structures (FEMA 2012).

2.2.4 Damage and consequence estimation

In the late 1980s, well founded loss estimation methods began to be employed in the insurance industry and in the 1990s, these were supported by FEMA through the development of the HAZUS (2017) earthquake loss estimation software. These developments were primarily directed to the insurance and re-insurance industry (Khater et al. 2002) as HAZUS attempts to address regional impacts of earthquakes. Numerous researchers have since developed approaches to improve loss estimating methods for individual buildings (Comerio 2006). For instance, Porter and Kiremidjian (2001) proposed a methodology to evaluate the seismic vulnerability of buildings on a building specific basis, by treating the building as a collection of standard assemblies with probabilistic fragility. Miranda and Aslani (2003) proposed including a probabilistic seismic structural response analysis as a main step in the loss evaluation, enabling the assessment of building specific loss estimation to be expressed probabilistically. Mitrani-Reiser (2007) proposed the mathematical foundation for the damage and loss evaluation accounting for the propagation of uncertainties in the prediction.

These methodologies are integrated into the FEMA P58 project (FEMA 2012), which enables estimates of direct losses attributable to earthquake damage to an individual building, as well as the repair or reconstruction time. FEMA P58 uses concepts of fragility and consequence functions to assess the probability that earthquake loss in a building may occur, given that it experiences certain response as measured by EDPs. Fragility functions are mathematical expressions of the probability that a structural or non-structural element will experience damage of a specified type, DM, conditioned on the occurrence of a specific EDP, expressed either as structural force, deformation quantity, acceleration or velocity. Consequence functions are mathematical expressions of the probability that a given loss (life loss, repair cost or repair time) will occur, conditioned on the occurrence of an element being damaged. It is necessary to express both damage and consequence probabilistically because it is impossible to predict their occurrence with certainty (Hamburger 2009).
As described in Deierlein (2004), the DMs provide explicit descriptions of damage to structural and non-structural elements. These descriptions must be relevant, and in sufficient detail, to enable subsequent quantification of the necessary repairs, disruption of function, and

safety hazards (e.g. falling hazards, release of hazardous substances, etc.). As with the IM-EDP relationships, the associations between EDP and DM account for uncertainty in the damage predictions. Using data from earthquake damage assessments, through laboratory testing programs, and in some cases, through analytical simulations, PEER researchers have compiled a number of damage fragility curves for structural and non-structural building components (e.g. Taghavi and Miranda 2003, Aslani and Miranda 2003, Krawinkler 2004, Pagni and Lowes 2006, Hutchinson and Chaudhuri 2004, Eberhard et al. 2001). In this context, non-structural components refer to elements and systems that are not part of the building structure, including architectural (cladding, ceilings, doors, windows, partitions, etc.) and mechanical, electrical, and plumbing (MEP) components (elevators, lights, piping, ducts, security systems, fire protection systems, communication systems, heating, ventilation and air conditioning (HVAC) systems, etc.). Consideration of non-structural components is essential to the loss estimates as they represent the majority of building construction cost, and of earthquake repair costs (Farokhnia and Porter 2012). However, in order to fully realize the potential of PBEE, further work is required to validate and expand the available literature of damage data and fragility functions (Deierlein and Krawinkler 2014).

FEMA P58 parameterizes damage by tracking the condition of individual structural elements and components, as well as by tracking the global state of the building structure. The consequences of each of these individual damage measures are then aggregated on a system basis, over the entire building. This final step in the assessment enables the calculation of DVs in terms that are meaningful for decision makers, e.g. direct dollar losses, repair time, or life safety risks. In a similar manner as was done for the other variables, the DVs are expressed through probabilities of DV conditioned on DM, P(DV|DM). Within FEMA P58, most emphasis has been on calculating direct costs associated with repair of damage through repair costs, developed by professional cost estimators, for each component damage function.

While the FEMA P58 project has made significant progress in utilizing direct economic losses as a DV, evaluation of the other two main decision variables, downtime and casualty risks, are more complicated and not as far advanced as modelling of repair costs (Deierlein 2004). Repair durations are an obvious contributor to downtime predictions, though experience suggests that other factors may be more significant, including post-earthquake safety of the structure and its impact on accessibility to the building, availability of financial and other necessary resources for repairs, plus a host of even less predictable issues, such as the influence of external management or socio-political factors. The main challenge in quantifying downtime are the uncertainties associated with availability of labour, materials, capital and

relating damage and repair needs in building components with lack of functionality (Krawinkler and Miranda 2004). The HAZUS method earlier discussed includes a subroutine for calculating downtime. However, this downtime estimate is derived from the direct economic loss estimate. Recognizing this essential component of loss modelling, Comerio (2006) identifies various factors that affect building downtime and divides components contributing to downtime into so-called "rational" and "irrational" components. Rational components are those related to repair work whereas irrational components are those related to resource mobilization. More recently, Almufti and Willford (2013) proposed a detailed downtime assessment methodology by accounting for both direct repairs and impeding factors (analogous to Comerio's rational and irrational components), where estimates of the different components that contribute to downtime are expressed probabilistically.

2.2.5 PBEE for risk management

Seismic risk decisions are generally avoided due to reliance on minimum building code requirements. May (2001), in a report on organizational and societal considerations regarding risk decision making, dismisses the notion of defining performance in terms of an "acceptable risk" and, instead, promotes an approach that supports decision making based on trade-offs. How these trade-offs are decided, and what the priorities are, can differ dramatically depending on the circumstances (Krawinkler 2004, Comerio 2004). Deierlein (2004) argues that while there are a multitude of opinions on seismic risk decision making, PBEE provides stakeholders with information to make better informed decisions. PBEE enables an improved capability to manage seismic risks effectively and efficiently from a business perspective, as the characterization of performance is technically sound and practical from an engineering perspective (Comartin 2004). Furthermore, the results can be formulated to address the specific decision making needs of various stakeholders.

Financial and insurance organizations are comfortable dealing with mean annual expected losses or mean annual frequencies of exceedance of loss. However, other stakeholders prefer more intuitive measures, such as likely losses or downtimes from one or more earthquake scenarios. In some cases, stakeholders may evaluate earthquake hazard mitigation through structural retrofit as one alternative among other strategies (such as insurance) to manage their risk. PBEE can assist in quantifying trade-offs between the cost-benefits of earthquake mitigation compared to other business or societal needs and priorities. The PBEE methodology permits alternative descriptions of the performance metrics. Thus, the final expression of the PBEE decision variables can be translated into different formats. This

flexibility is important to enable communicating results in a way that is meaningful and useful to decision makers, which can be building developers, facility managers, risk managers, lenders, insurers, public agencies, regulators or individual members of the public (Hamburger 2004).

2.3 Seismic resilience and frameworks for evaluation

The PBEE framework discussed in Section 2.2.1 represents a major step forward toward quantifying and managing earthquake risks of individual buildings. However, a much broader interpretation of performance is needed to understand how communities will be affected, and recover from devastating earthquakes (Krawinkler and Deierlein 2014). More recently, earthquake engineering researchers and practitioners have embraced the concept of seismic resilience as a measure of a community's ability to contain the effects of an earthquake and achieve a timely recovery (Burton et al. 2015).

Seismic resilience describes the loss and loss recovery required to maintain the function of a system with minimal disruption (Cimellaro et al. 2006). A resilient system is one that illustrates reduced failure probabilities, reduced consequence from failures (loss of life, damage, etc.) and reduced recovery time (restored functionality) (Bruneau and Reinhorn 2006). Bruneau et al. (2003) developed a conceptual framework for quantifying seismic resilience and defined four properties (robustness, redundancy, resourcefulness, and rapidity) and four dimensions of resilience (technical, organizational, social, and economic). Resilience is quantified by using a multidimensional space of performance measures that includes the probability of failure, the consequences of failure, and time to recovery. Studies such as Bruneau et al. (2003), Cimellaro et al. (2006) and Bruneau and Reinhorn (2006) offer a definition of resilience to cover all actions that minimize losses from hazard, considering mitigation and recovery, making it possible to relate probability functions, fragilities, and resilience in a single integrated approach such that resilience can be quantified. Cimellaro et al. (2010) extended these resilience concepts in a unified terminology for a common reference framework for quantification of disaster resilience by means of resilience functions, which provide a comprehensive understanding of damage, response, and recovery as they illustrate the time variation of damage as well as its relationship to response and recovery. Within this framework, a number of studies have explored the seismic resilience of different systems such as healthcare facilities (Bruneau and Reinhorn 2007), water resource systems (Wang and Blackmore 2009) or natural gas distribution networks (Cimellaro et al. 2014).

Seismic resilience is defined as the ability of a system to reduce the chances of a shock, to absorb a shock if it occurs (abrupt reduction of performance) and to recover quickly after a shock (re-establish normal performance), as described in Bruneau et al. (2003). Bruneau and Reinhorn (2004) propose expressing resilience, based on the notion that a measure, Q(t), which varies with time, can be defined to represent the quality of a system or infrastructure. Specifically, performance can range from 0% to 100%, where 100% means no degradation in quality and 0% means total loss as illustrated in Figure 2-4, with restoration expected to occur over time.

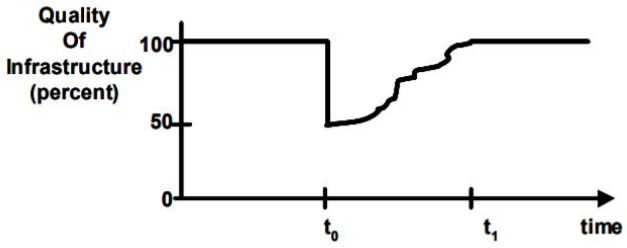

Figure 2-4: Conceptual resilience function.
Adapted from Bruneau and Reinhorn (2004).

Miles and Chang (2011) developed a model of community recovery (ResilUS) built by characterizing the attributes and behaviours of economic agents within a community, such as households and businesses, and describing relationships between agents themselves and relationships with their environment, such as buildings of residence and transportation networks. Twigg (2009) and Cutter et al. (2010) identify different components of resilience, grouped into thematic areas, which measure the resilience of communities to disasters. Mieler et al. (2015) developed a conceptual framework for connecting specific performance targets for the built environment to community resilience goals. The framework proposes (1) specifying a performance goal at the community level, (2) identifying an undesirable outcome and acceptable level of risk associated with the occurrence of this outcome, (3) identifying vital community functions that must be maintained to prevent the undesirable outcome, and (4) using probabilistic risk assessment to establish a relationship between the probability of losing these vital functions and the occurrence of the undesirable outcome.

As outlined in Burton et al. (2015), most of the previous approaches rely on the generic damage states used in loss estimation (e.g. none, slight, and moderate), which are not related to recovery. A rigorous evaluation of seismic resilience requires methods for incorporating the probabilistic assessment of multiple limit states, which are explicitly linked to recovery of the building inventory. As concluded by Bruneau and Reinhorn (2004), research is most needed to develop tools, such that the resilience objectives defined by a community can be

evaluated by decision makers for compliance. “However, in formulating policies anchored in quantitative resilience targets, one must recognize that resilience targets, while important objectives, are not to be taken as absolutes. This points to the need for a quantitative probabilistic framework and tools anchored in engineering procedures to guide decision makers in consideration of policies, rather than to focus on numerical values in a one-size fits all approach” (Bruneau and Reinhorn 2004).

The seismic resilience of a building may be described as its ability to respond to and recover from a damaging earthquake event. It can be measured as the time needed to restore basic operations. In a building resilience curve, such as the one illustrated in Figure 2-4, the vertical axis represents the loss in functionality due to earthquake damage and the horizontal axis represents the time for recovery. The total impact is a combination of direct repair costs for rebuilding and the cumulative loss in functionality, which can be measured by the integration of loss in function over recovery time. The cumulative loss depends on the combined effects of the amount of damage and the speed of recovery. Thus, resilience can be improved by both reducing the amount of damage incurred and taking measures to accelerate recovery. Existing standards for seismic evaluation do not explicitly address recovery time. Bonowitz (2009) proposes new evaluation criteria to address questions of resilience, with a strong emphasis on recovery time, where more resilience means the ability to recover basic operations faster. The San Francisco Planning and Urban Research Association (SPUR) outlined outline a set of performance objectives for buildings and lifeline infrastructure in San Francisco, under an ‘expected’ earthquake, necessary to increase the seismic resilience of the city (Poland 2009). Seismic performance targets are defined based on their implication to post-earthquake functionality and recovery, considering city wide needs. As illustrated in Figure 2-5, building damage is characterized by the following performance categories: (1) safe and operational, (2) safe and usable during repair, (3) safe and usable after repair. Undesirable outcomes, not considered in Figure 2-5, include (4) safe but not repairable or (5) unsafe. In addition to establishing these specific target goals, Poland (2009) estimates the performance of the current inventory, albeit based largely on “educated guesses about current standards for recovery time” (Burton et al. 2015).

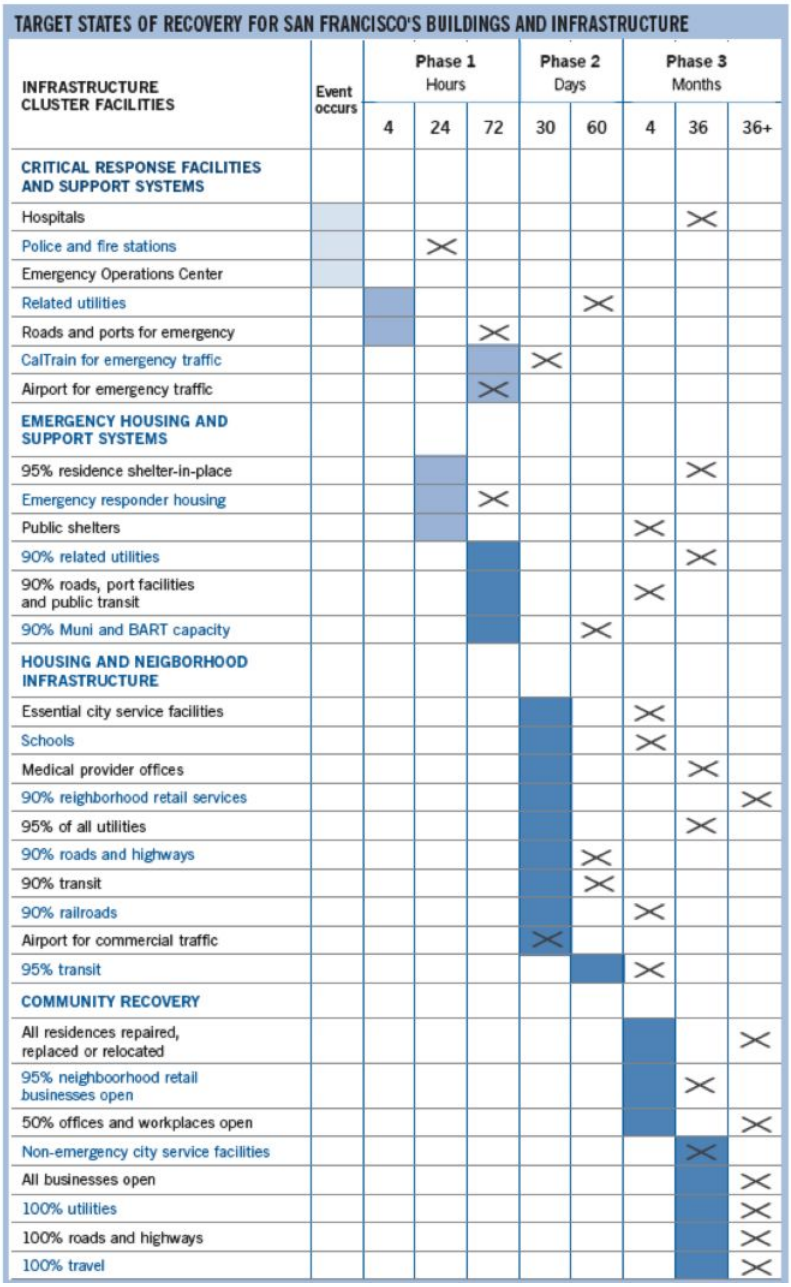

Figure 2-5: Target states of recovery for San Francisco's building and infrastructure. Source: Adapted from Poland (2009).

In recognition of the deficiencies associated with existing WSMRF buildings, as discussed in Section 2.1.2, San Francisco's Earthquake Safety Implementation Program (CAPSS 2011) has plans to develop mandatory evaluation and retrofit requirements for 'low-performance steel buildings', as illustrated in task C2.d of their 30 year plan, illustrated in Figure 2-6. According to Bonowitz (2009), San Francisco's resilience targets for commercial buildings are collapse prevention, to limit response demands, and damage control to limit job loss, and expedite recovery (50% of offices open within 4 months according to the Community Recovery Section in Figure 2-5).

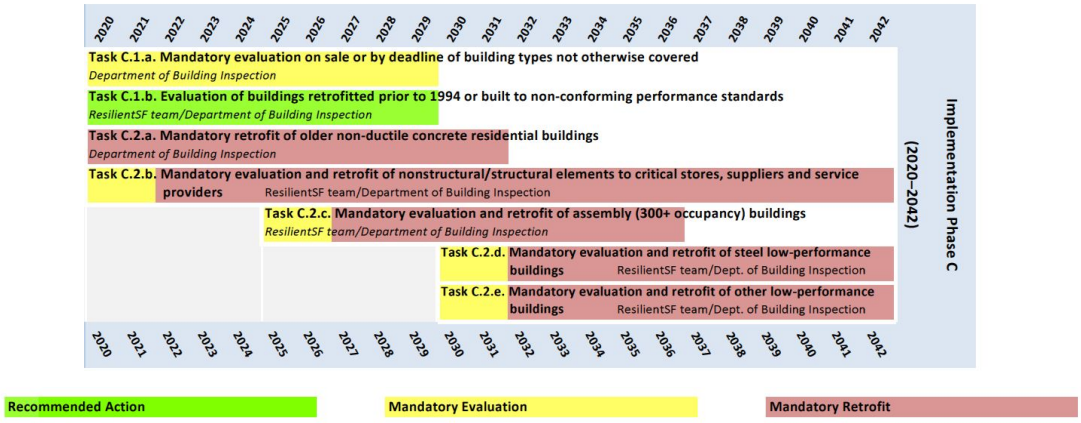

Figure 2-6: CAPSS Earthquake Safety Implementation Program Phase C.
Source: Adapted from CAPSS (2011).

Bonowitz (2009) highlights the need for a resilience assessment methodology that enables engineering resilience. In view of this demand, the Structural Engineers Association of Northern California (SEAONC) proposed a rating system for earthquake performance which consists of a scale of 1 through 5 stars, in each of the following three dimensions: safety, repair cost, and time to re-occupy. While the proposed system defines the star rating of each point in the scale, a method by which to derive the rating value from outputs of various accepted standards for evaluation of a building is yet to be proposed (SEAONC 2009). More recently, Almufti and Willford (2013) have proposed a resilience-based earthquake design approach as a holistic process which identifies and mitigates earthquake-induced risks to enable swift recovery in the aftermath of a major earthquake. The approach acknowledges that direct losses, which include the financial costs of post-earthquake repair or reconstruction, make up a significant percentage of earthquake losses, but that the most significant vulnerability may be indirect losses due to downtime. As Almufti and Willford (2013) note: "designing buildings to sustain less damage in earthquakes is a key component of resilience-based design. This significantly decreases the uncertainty in the behaviour of the building and increases the confidence that the building will perform as intended. Resilience-based design explicitly

incorporates the design and performance verification of the structure and all non-structural components […]. However, one of the key differentiators of resilience-based design is preparedness for post-earthquake recovery to ensure continued operation immediately after the earthquake. This process considers the performance of the building (and contents) and the threats posed by the post-earthquake environment which could hinder the primary functions of the organization." This approach to resilience-based earthquake design is the first to consider indicators of resilience in the form of downtime.

Performance-based methods clearly have an important role in assessing and designing for community resilience. However, to effectively serve this role, PBEE research must expand beyond the current emphasis on calculating direct losses and place greater attention on post-earthquake functionality and repair (Deierlein and Krawinkler 2014). Burton et al. (2015) propose an initial approach to how the current PBEE framework can be adapted and incorporated into a resilience framework to model recovery at the individual building and community scales. It incorporates the assessment of a set of building performance limit states that specifically inform community seismic resilience. However, the proposed method does not directly link to results from the FEMA P58 methodology, such that it can be systematically extended into a method for resilience evaluations. The method does not explicitly account for externalities, such as impeding factors, on recovery, and does not account for the expected variability in the delays associated with different limit states with increasing earthquake ground motion intensities.

2.4 Point of departure

As discussed in Section 2.1, a review of the evolution of seismic design codes highlights a number of potential deficiencies in steel MRFs, particularly in existing tall buildings designed following code-prescriptive guidelines, such as those from the Uniform Building Codes from the late 1960's through mid-1990's. Compounding these deficiencies, are the fracture-prone beam-to-column connections identified following the 1994 Northridge earthquake. Despite the massive research programme aimed at addressing these vulnerabilities following the Northridge event, a review of the literature highlights a need to evaluate the impact of these deficiencies, as they apply to existing tall WSMRF buildings, particularly with regards to providing measures of risk associated with direct economic losses or other metrics for decision making. As outlined in Section 2.2, PBEE has developed considerably, to the point that formal methods and tools are now available to reliably assess seismic performance of individual buildings for seismic risk mitigation and provide a wide range of metrics for different

stakeholders. While the overall framework is well-established, details of the procedures are continuously being further developed and refined, particularly in the move beyond the evaluation of direct economic losses to consider factors that relate to recovery, such as downtime. As discussed in Section 2.3, society has become more concerned with ensuring the resilience of communities, particularly large cities with high population density. For example, the city of San Francisco has established a seismic resilience program that specifies target performance expectations for buildings and infrastructure to help ensure recovery following a large earthquake. While conceptual frameworks for the evaluation of seismic resilience are available in the literature, no tools are readily available and more work is needed to relate building-specific measures to community-wide concerns. The literature review presented in this chapter sets the point of departure for this research, which, as set out in Chapter 1, aims to characterize the seismic risk of existing tall WSMRF buildings in West Coast US cities, particularly in business districts, where large numbers of tall buildings are clustered together and where significant damage to a single building can have disproportionate consequences on the business continuity of surrounding areas.

This page is intentionally left blank.

Chapter 3

Methodology

A central component of this work is to apply the framework and latest advancements of PBEE to assess the potential risks of existing WSMRF buildings and to propose a framework to evaluate the implications of seismic performance on urban resilience. The first step consists of the development of index buildings and numerical modelling approaches to simulate seismic response. In order to characterize seismic performance, while formulating results to address specific decision making needs of various stakeholders, the next step consists of an array of high-fidelity building specific assessments. Three types of building-specific performance evaluations (BSPE) are conducted:

- Scenario-based;
- Intensity-based;
- Time-based assessments.

Each of these types of assessment, with increasing levels of complexity, has a specific usefulness to groups of stakeholders accustomed to certain analysis results. The last step consists of the development and application of a framework for resilience-based evaluations that enables extending building-specific evaluations, to consider impact of the assessed buildings on surrounding areas. The methodology flowchart is illustrated in Figure 3-1.

Through this series of progressive steps, the thesis objectives, as set out in Section 1.2, are addressed. The justification of each step and its intended outcome is presented in the next sections. San Francisco is selected as a case study location for this work, in order to permit engagement and support of ongoing efforts of the city's Earthquake Safety Implementation Program (CAPSS 2011), which has plans to (i) characterize the seismic performance of existing tall buildings, (ii) address seismic risks that are disproportionately associated with tall buildings with recommendations for new policy and further research, and (iii) evaluate barriers to post-earthquake re-occupancy of tall buildings (Gregory Deierlein, personal communication, 2017). A reflection on the transferability of the methodology implemented throughout this thesis to different structural systems and different geographical areas is also provided by comparing the work here presented on existing tall WSMRF buildings to a related study that evaluates the use of innovative structural systems versus conventional construction methods.

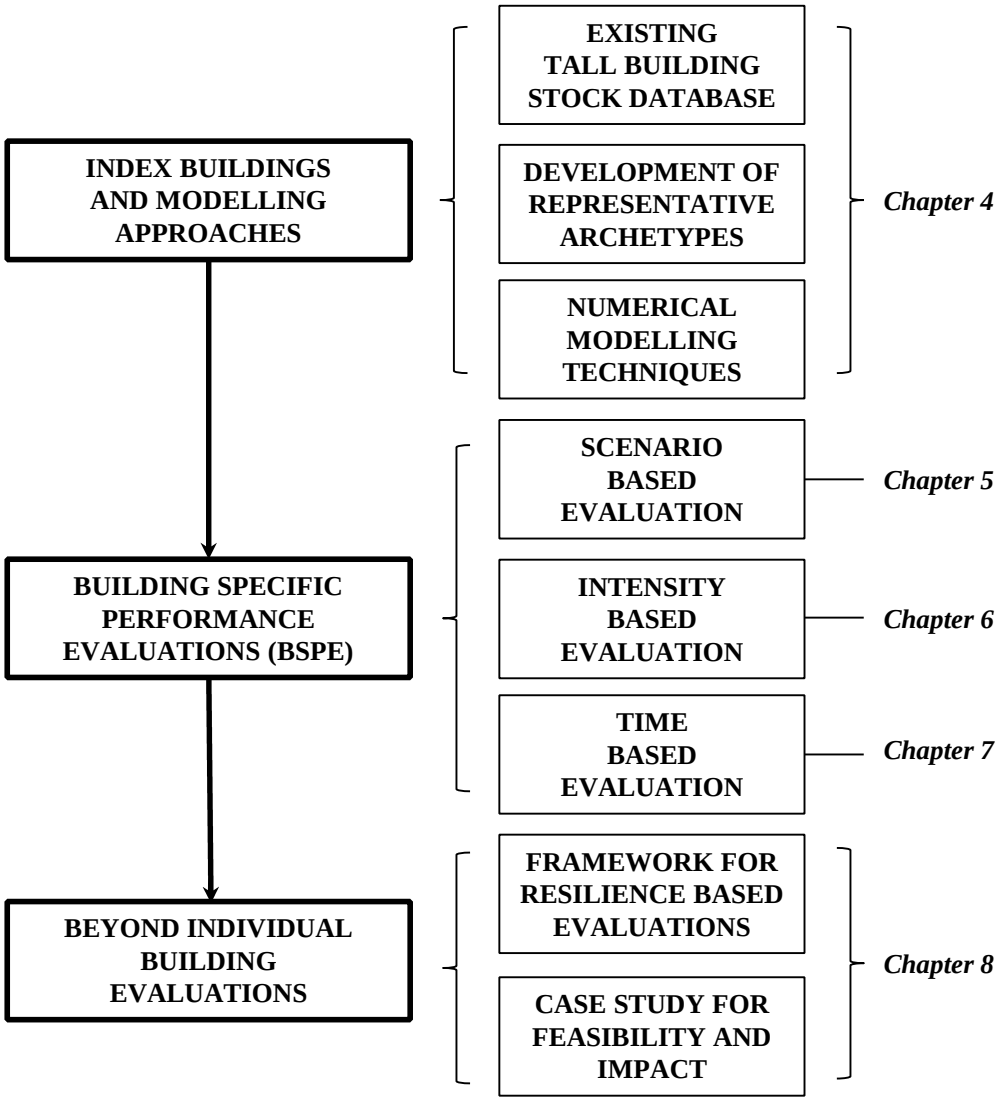

Figure 3-1: General methodology flowchart.

3.1 Index buildings and modelling approaches

This research seeks to characterize the expected seismic performance of existing tall WSMRFs by means of archetype buildings. In order to inform the selection and design of prototype buildings, a database of the existing tall building stock in the case study city, San Francisco, is compiled and analysed. The archetype buildings are selected based on the building characteristics, the geographical distribution of the existing tall building database, and designed to comply with historic code-prescriptive requirements from the UBC. To gain insight into the impact of code evolution on the expected seismic performance of tall buildings, one analogous archetype is developed following modern design requirements, the International Building Code (IBC), in order to provide a benchmark for comparison.

Numerical modelling techniques focus on the structural response simulation and building performance. As discussed in Section 2.2.3, NLRHA is the best tool currently available for predicting structural response at varying levels of ground motion intensity. Therefore, numerical models are developed to enable structural response simulation via NLRHA. Additionally, as discussed in Section 2.2.5, PBEE enables an improved capability to manage seismic risks effectively as the results can be formulated to address the specific decision making needs of various stakeholders. Therefore, the PBEE framework is adopted to carry out the proposed BSPEs. More specifically, the PBEE framework, as developed through the FEMA P58 (FEMA 2012) project, is implemented to assess damage and economic losses associated with the results from the structural response simulation. For the purpose of estimating downtime, the methodology proposed by Almufti and Wilford (2013) is adopted because it enables extending the results of the FEMA P58 assessment to carry out downtime estimates.

In order to further extend existing tools to provide more comprehensive indicators of resilience, a method is proposed to develop recovery curves, which express re-occupancy and functionality ratios against time, analogous to the resilience function illustrated in Figure 2-4. In this study, these curves are termed ‘recovery’ curves rather than ‘resilience’ curves, as it is believed that a single curve is unable to fully characterize resilience, hence the term recovery, which is a indicator of resilience, is more adequate. These curves provide a useful link to relate building-specific measures to community-wide concerns.

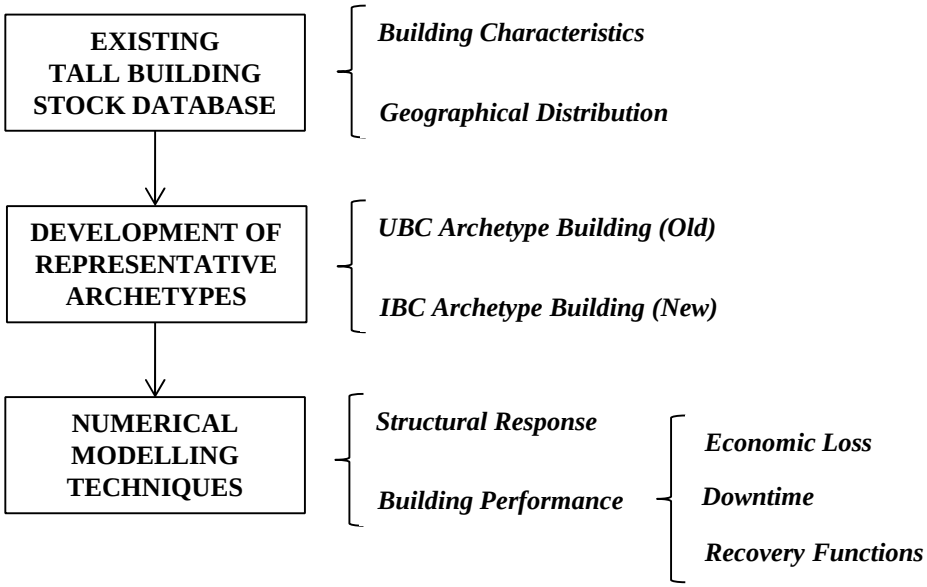

Figure 3-2: Index building and modelling approaches flowchart.

Numerical models for building response estimation via NLRHA, as well as the development of building performance models used to estimate economic losses, downtime and the proposed method to construct recovery functions are described in detail in Chapter 4. A flowchart of the index building selection and modelling approaches is illustrated in Figure 3-2.

3.2 Building specific performance evaluations (BSPE)

In order to characterize seismic performance while formulating results to address specific decision making needs of various stakeholders, three types of building-specific evaluations are conducted:

- Scenario-based;
- Intensity-based;
- Time-based assessments.

A flowchart of the general BSPE procedure, as well as that corresponding to the scenario-based, intensity-based and time-based evaluations, is illustrated in Figure 3-3. While the overall flowchart and performance metrics, which are direct outputs of the numerical modelling approaches previously described, are similar, the results are conditioned on the occurrence of different events, as described in more detail in the following sections.

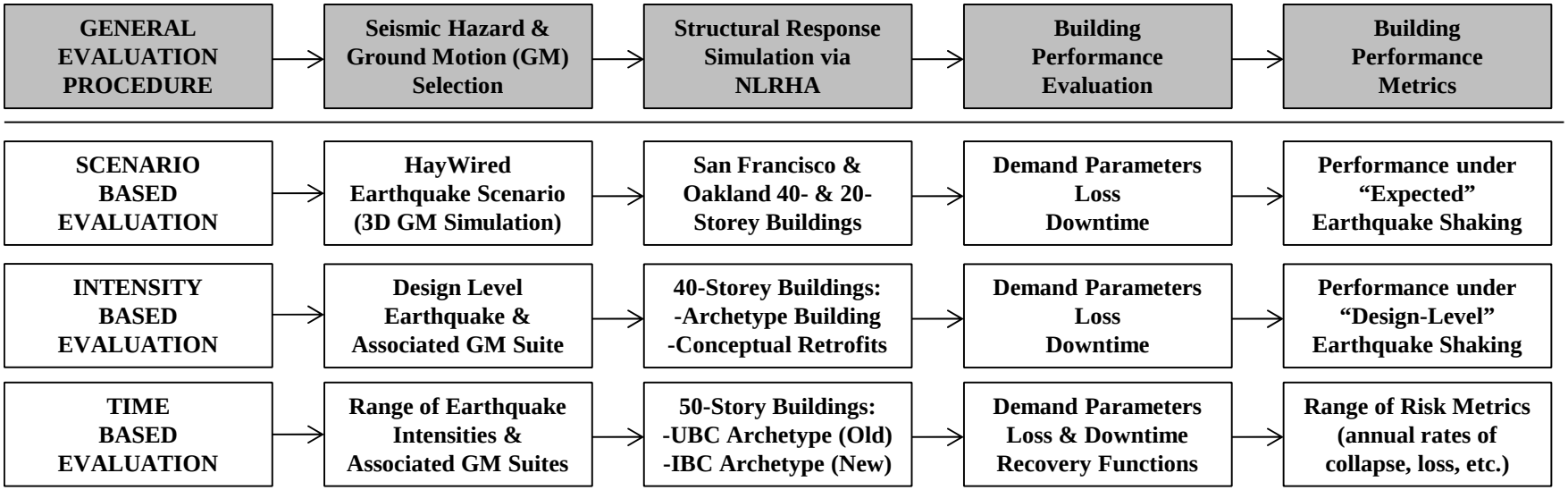

Figure 3-3: Flowchart for building specific evaluations including general evaluation procedure, scenario-based, intensity-based and time-based evaluations.

3.2.1 BSPE: Scenario-based assessment

Scenario-based assessments evaluate the expected performance of a building subjected to a user-specified earthquake event, consisting of a specific magnitude earthquake occurring in a specific seismic source, at a specific location (distance) relative to the building site. In general, it is easier for communities at risk and policymakers to relate to the results of a scenario-based assessment than to other evaluations which express earthquake occurrence probabilistically (SPUR 2012). Scenario-based assessments are useful for buildings located in close proximity to active faults and can also be used to evaluate performance under a historic earthquake (Whittaker et al. 2007). The HayWired scenario, a M_w 7.0 earthquake on the Hayward fault, developed to study impacts on the San Francisco Bay area (Detweiler and Wein 2017) is selected for this evaluation. The hypothetical HayWired earthquake is used to examine the well-known earthquake hazard of the Hayward Fault, with a focus on newly emerging vulnerabilities (Hudnut et al. 2017). The focus of the assessment is in the evaluation of response parameters such as peak transient and residual drifts in each storey, peak storey accelerations and inelastic deformations in fracture-prone beam-to-column moment connections. These response parameters are selected, as described in Section 2.2.3, because of how well they correlate with damage predictions. A summary of the economic loss and downtime estimates associated with the computed response parameters is also provided as part of this assessment. The scenario-based assessment provides an initial understanding of the expected performance of tall WSMRF buildings in the San Francisco Bay area under a realistic earthquake, highlighting the likely impacts on these structures such that steps can be taken, if necessary, to change negative outcomes and reduce future risk (objective 1, as outlined in section 1.2).

This scenario-based evaluation provides an understanding of seismic performance conditioned on a single event developed to provide science for decision-making, and to engage potential users of the information throughout the scenario development process (Hudnut et al. 2017). Furthermore, the results of this evaluation provide a reference point against more comprehensive risk-based evaluations such as intensity-based or time-based assessments. The scenario earthquake ground motions are developed through a 3D numerical simulation. The 3D model is conditioned on one particular hypocentre, one realization of slip distribution, and one particular simulation of high-frequency motion (Porter 2017). It aims to provide a single outcome in terms of shaking. This method is different from the more common approach to study earthquake scenarios by means of ground motion prediction equations (GMPEs), which is also be utilized later in this study (Chapter 8).

3.2.2 BSPE: Intensity-based assessment

Intensity-based assessments evaluate the expected performance of a building conditioned on a specified intensity of ground shaking. For instance, performance can be evaluated under a shaking intensity, defined by a target response spectrum, representative of the expected shaking under a specified return period, e.g. 475 years. These evaluations are frequently used in the engineering community to evaluate the seismic performance of existing buildings or for new designs. This type of assessment can be used to evaluate performance under the design earthquake shaking specified within a building code. The objective of this evaluation is to enable an understanding of the expected behaviour of existing WSMRF buildings under a ground motion shaking intensity consistent with the design earthquake hazard level defined in modern building codes (IBC 2012) (objective 2, as outlined in section 1.2). The results of such evaluation enable understanding whether expected performance complies with the objectives implicit in code-prescriptive design standards. In order to influence decision making, the results report the expected consequences in terms of direct economic losses, and downtime. Additionally, a number of strategies to achieve increased levels of resilience, including seismic improvements to the structural system, enhancement of non-structural components and systems, as well as mitigation measures to minimize recovery times are evaluated under the same intensity of ground motion shaking (objective 3, as outlined in section 1.2). The focus of the chapter is on the explicit consideration of downtime in the assessment methodology, going beyond damage and direct economic losses to consider repair and recovery times for an existing archetype building and an array of retrofit interventions. These results help design practitioners understand how different types of intervention influence the seismic performance of existing tall WSMRF buildings.

3.2.3 BSPE: Time-based assessment

Time-based assessments are the most comprehensive of the approaches, considering all earthquakes affecting a site and their risk of occurrence over a specified period of time. The period of time is generally one year (results indicate the annual rate of exceedance of a performance measure) or the design life of the building (50 to 100 years). This type of assessment is more comprehensive than a scenario or intensity-based assessment, as it evaluates performance over a range of ground motion levels, i.e. it consists of an array of intensity-based assessments. In this study, a time-based seismic performance assessment of two archetype tall buildings is carried out: a WSMRF designed following the requirements of the 1973 Uniform Building Code (UBC 1973), and a WSMRF designed following the 2012 International Building Code (IBC 2012). The goal of this work is to benchmark the performance of older existing tall

WSMRF buildings against modern designs (objective 6, as outlined in section 1.2). Furthermore, this work intends to verify compliance with the life-safety objective of modern codes under extreme events and provide an understanding of expected performance at other earthquake intensities. The study aims to evaluate performance at an array of earthquake intensities from levels that cause no damage up to levels that trigger collapse (objective 4, as outlined in section 1.2) in order to provide more advanced risk metrics, such as collapse rates, average annual loss (AAL) or average annual downtime (AAD) (objective 5, as outlined in section 1.2), than those obtained under a scenario-based or intensity-based assessment. Generally, the output of these evaluations are useful to catastrophe modellers and the insurance market. However, certain metrics inferred from such assessment, such as the annual rate of collapse (λ_c), can also provide valuable information to policy makers. Time-based assessments are also referred to as risk-based assessments (NEHRP 2011). In this study, the term time-based is preferred over risk-based because it is believed that the other BSPEs considered, such as the scenario-based or the intensity-based, are also risk-based assessments. If adopting the NEHRP (2011) nomenclature, the term 'comprehensive risk-based' assessment rather than simply risk-based assessment is believed to be more accurate when used to describe time-based assessments.

3.3 Beyond individual building evaluations

The scenario-based, intensity-based and time-based assessments described earlier are building specific evaluations of expected seismic performance. These evaluations consider individual buildings in isolation and neglect the impact of damage to these buildings on neighbouring buildings and overall community resilience. To address these limitations, this step of the methodology aims to develop a framework to assess earthquake risk of existing tall WSMRF buildings, considering implications for both individual buildings and their impact on surrounding buildings and the urban community as illustrated in Figure 3-4 (objective 7, as outlined in section 1.2). The framework proposed in Figure 3-4, integrates PBEE tools and seismic risk assessment methodologies into a GIS platform that enables visualization of impact of the building typology under consideration on an entire business district. This framework enables highlighting risk hotspots, e.g. where building damage is most likely to have disproportionate impact on the urban community and the broader socio-economic factors that affect resilience (e.g. services provided in the affected buildings to the community). Furthermore, it enables evaluating the impact of different seismic retrofits or enhancements, which can be used to broadly evaluate the impact of mandatory seismic retrofit policies.

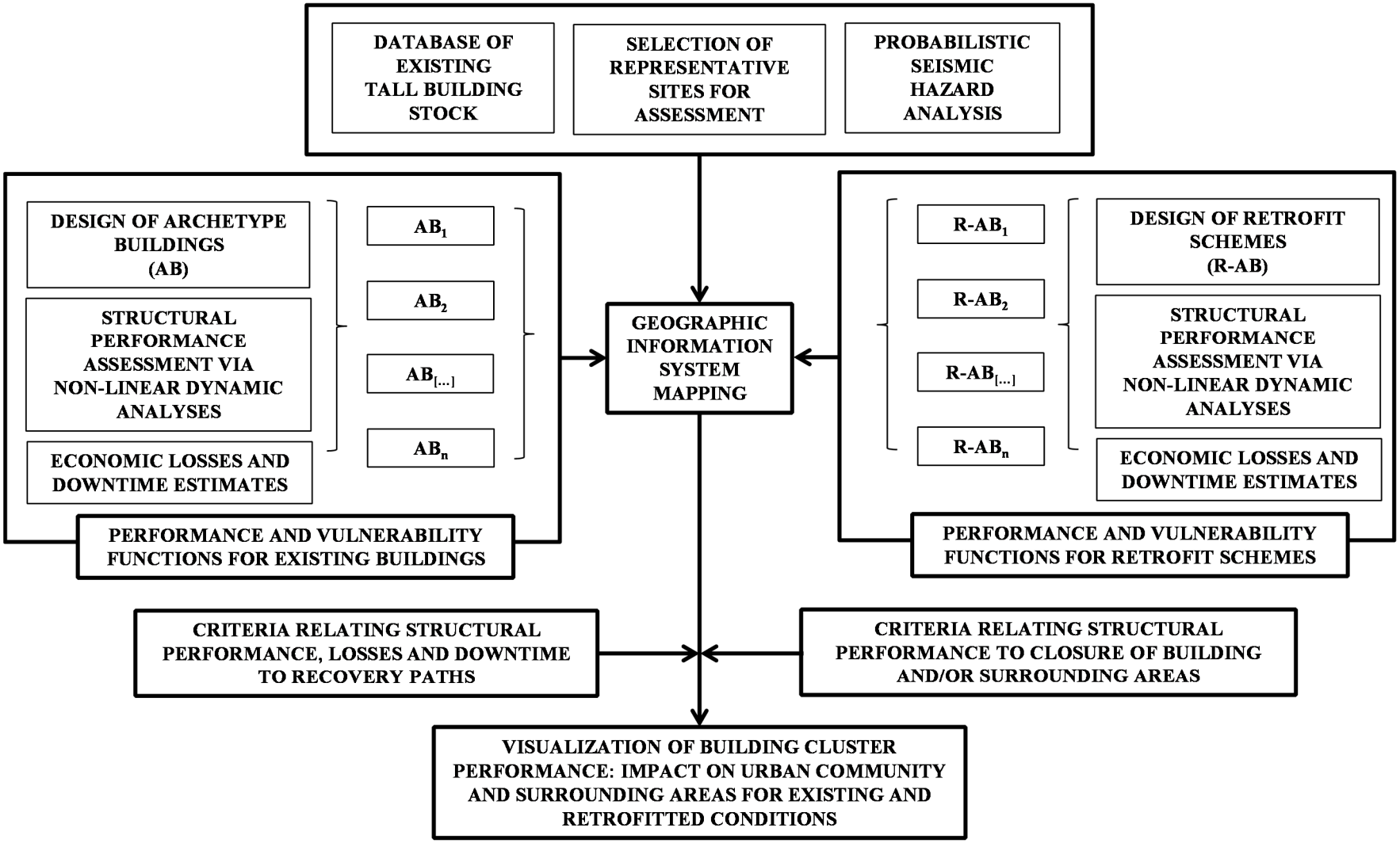

Figure 3-4: Framework for assessing the earthquake risk of tall buildings to cities and the impact of different retrofit risk mitigation strategies.

In this section, the aim is to develop an early demonstrator of the feasibility and usefulness of this technique, which is illustrated through a case study. As part of the case study, the outputs of the different BSPEs considered, namely scenario-based, intensity-based and time-based assessments, are reviewed to evaluate their suitability for use in a city-level evaluation (objective 8, as outlined in section 1.2).

3.4 Transferability of method

The work proposed thus far aims to inform the debate over the expected seismic performance of older tall WSMRF buildings. While a modern WSMRF design is also developed as part of this work to provide a benchmark for comparison, in reality, modern tall WSMRF buildings are extremely rare due the flexibility of the structural system. In modern high rise construction, coupled RC wall systems are more common due to their superior strength and stiffness over other systems. However, even though modern coupled RC wall systems are believed to behave well in terms of life safety, post-earthquake repair can be costly and time consuming due to considerable seismic damage levels in RC coupling beams. Ji et al. (2016) evaluate the expected seismic performance of modern RC coupled wall systems through a number of intensity-based assessments. Furthermore, the impact of incorporating innovative structural components such as replaceable steel coupling beams (RSCBs), which concentrate seismic damage in easily replaceable elements, allowing for a swift recovery after earthquakes, is also evaluated in the study. Rather than assessing and benchmarking performance of older buildings, the purpose of this evaluation is to incentivize the use of novel structural systems that enable enhanced seismic performance over conventional construction methods. The proposed system was implemented in a recently completed project in Beijing, China and used as a case study. Even though the study itself is not embedded in this thesis, it is used to provide a reflection on the transferability of the method used here to evaluate existing tall WSMRF buildings in San Francisco, to a different structural system and geographical area. The reflection is provided in the conclusions (Chapter 9) and the published journal paper used for this comparison is included in Appendix A2.

Chapter 4

Archetype Buildings and Numerical Modelling

This chapter discusses the archetype tall building selection, the development of numerical models for NLRHA, and the development of building performance models used to conduct loss and downtime estimates throughout this thesis. Part of the work presented has been published in Molina Hutt et al. (2015) and Molina Hutt et al. (2017), as referenced throughout the chapter. The author was the key contributor to the referenced journal papers.

4.1 Archetype tall building selection

As discussed in Chapter 1, this work targets districts in areas of high seismicity in the US, where a large number of tall buildings are clustered together, and where significant damage to a single building could compromise the business continuity of surrounding areas. San Francisco is selected as a case study for most of this work, in order to permit engagement and support of ongoing efforts of the city's Earthquake Safety Implementation Program (CAPSS 2011), which has plans to develop assessment and retrofit guidelines for existing tall buildings. The extent to which the proposed archetypes are representative of construction practice in other US west coast cities with high seismic hazard, such as Los Angeles, Seattle, San Diego or Oakland, is also discussed in this section.

In order to identify representative tall buildings, it is necessary to understand the composition of the existing tall building stock. The SEAONC Committee on PBSD of Tall Buildings developed a database of all buildings in San Francisco taller than 50m (~160 ft). The database tabulates building characteristics by location, height, number of storeys, year built, and lateral system type. Approximately 230 buildings greater than 50m (~160 ft) in height are identified in this database. This height threshold is selected because it is the modern code (IBC 2012) limit above which certain structural systems are not permitted. Appendix B summarizes and validates the inventory in the SEAONC tall building database against data from the City and County of San Francisco's Planning Department (SFPIM 2017) and sources such as Emporis (2000). Figure 4-1 illustrates the spatial distribution of existing tall buildings in downtown San Francisco. The downtown area is located approximately 14 km from the San Andreas Fault and 16 km from the Hayward Fault. These faults are the greatest contributors to the seismic hazard in the city (see Appendix E).

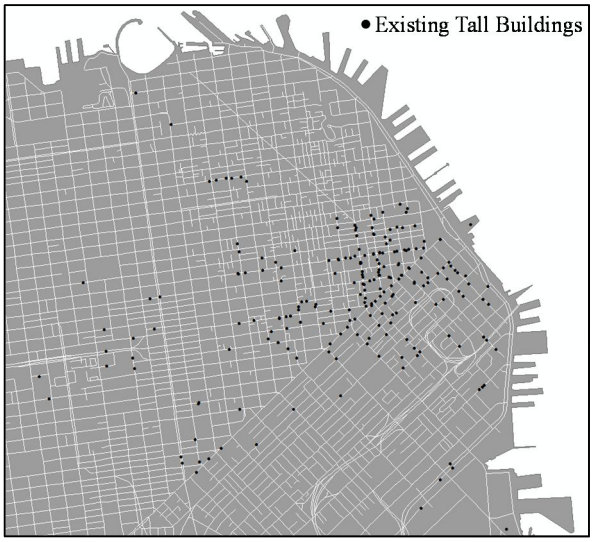

Figure 4-1: Spatial distribution of existing tall buildings in downtown San Francisco.

In order to select prototype buildings for this work, the data from the existing tall building database was de-aggregated. Figure 4-2a illustrates the number of tall buildings built each decade between 1900 and 2010. Interviews with practicing engineers and a partial database gathered previously by the SEAONC Committee (personal communication, Arup 2011) revealed information on the lateral system type for some of these buildings. Information on the remaining buildings was obtained by personally viewing construction documents available at the San Francisco Department of Building Inspection (DBI). The database identifies the lateral load resisting system type for approximately 80 out of the 240 buildings. The lateral load resisting system type of many buildings remains unknown because, whilst drawings of existing buildings are available for viewing at the DBI (California Health and Safety Code 19850), access to drawings is limited by the difficulty in locating relevant structural information within the large microfilm archive.

Figure 4-2b shows the lateral load resisting system type for tall buildings built between 1960 and 1990. The subcategory termed as “other system” means that the lateral load resisting system of the building is known and it is not a steel MRF, while the subcategory termed as “unknown system” is designated for all buildings for which the lateral load resisting system is unknown. This data reveals that the steel MRF system was the most prevalent type in pre-1990s construction for buildings greater than 35 storeys in height. It was also frequently used for buildings in the 20- to 30-storey height range. A sidewalk survey of a random sample of these tall buildings revealed that most are regular in shape, although some have setbacks up the height and others lack corner columns. Images of some of these existing tall buildings are shown in Figure 4-3.

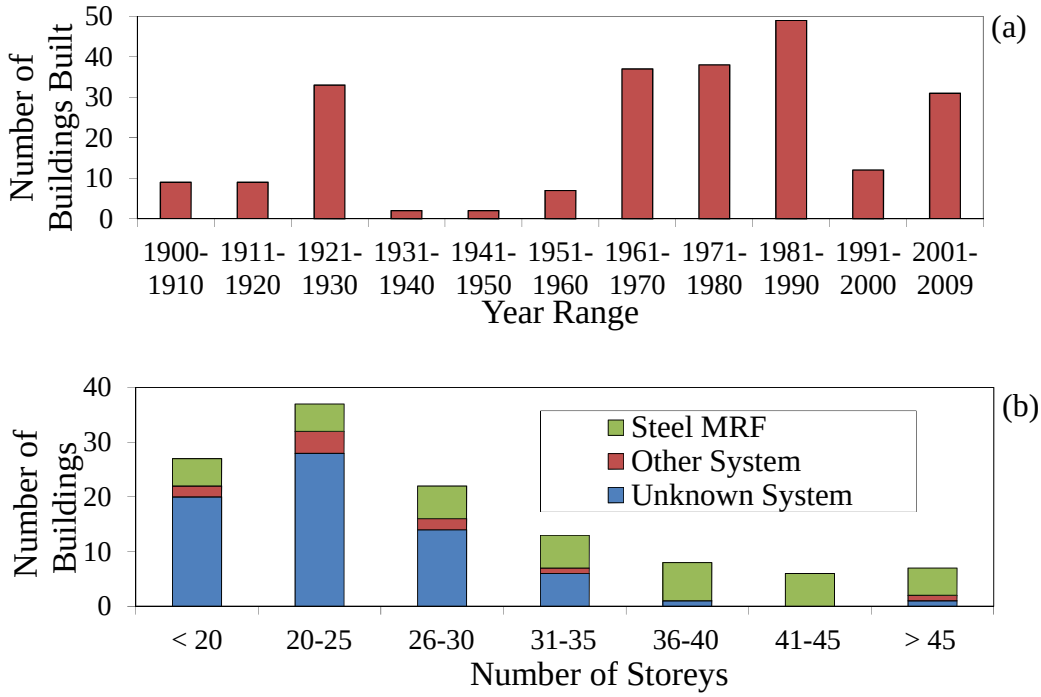

Figure 4-2: Number of tall buildings built in San Francisco per decade between 1900 and 2010 (a) and lateral resisting system types for tall buildings built between 1960 and 1990 (b).
Source: Molina Hutt et al. (2015).

Based on this information, a number of archetype steel MRFs are developed to represent the state of design and construction practice for tall buildings in San Francisco from the mid-1970s to the mid-1980s including buildings with 20-, 40- and 50-storeys in height. The archetype buildings are designed per UBC 1973. The design of a 50-storey archetype building is illustrated in detail in this chapter. Furthermore, an illustration of how the design process compares to that of an equivalent modern code conforming steel MRF building is also provided, by carrying out an equivalent design per IBC 2012. A summary of the design and the dynamic properties of the 20- and 40-storey 1970s archetypes, which follow the same methodology as for the 50-storey building are also provided in Section 4.1.2.

As discussed in Chapter 2, PBSD, by definition, implies that pre-defined seismic performance objectives are met at different intensities of ground motion shaking. Rather than adopting a PBSD approach for the equivalent modern building archetype and verifying pre-defined performance objectives, a design per IBC 2012 is adopted for comparison. This approach enables verifying compliance with the seismic performance objectives implicit in modern building codes.

Figure 4-3: Images of existing tall buildings in downtown San Francisco greater than 35 storeys, built between 1960 and 1990, whose lateral system is believed to be a steel MRF.

4.1.1 Design requirements per UBC 1973 vs IBC 2012

This section describes the assumed geometry, occupancy, relevant code requirements prescribed by UBC 1973 and IBC 2012, as well as the resulting steel MRF design section sizes and typical details for a 50-storey building. The building is assumed regular in plan and the occupancy is that of a commercial office with two levels for mechanical equipment, one at mid-height, and one at the top floor, consistent with observations in existing tall buildings in downtown San Francisco. Typical storey heights are 3.8 m (12.5 ft), except at the lobby with height 6.1 m (20 ft). The overall height of the structure is 192.8 m (632.5 ft) above ground. The building width is 51.2 m (168 ft), and consists of 6 bays of 8.5 m (28 ft) in each direction. The design of the 1973 archetype building is in accordance with the provisions of UBC 1973 and the SEAOC Bluebook of 1973 (SEAOC 1973), which was commonly employed to supplement minimum design requirements. The design of the modern archetype building follows IBC 2012 and ASCE 7 (ASCE 2010) requirements.

The lateral resisting system of the modern archetype building is also a steel MRF, but incorporates a perimeter frame as opposed to a space frame, as shown in Figure 4-4. The lateral resisting system for the 1973 archetype building consists of 7 frames in each direction, whereas the 2012 archetype building consists of only two frames in each direction. In the 1970s, it was customary to have moment connections in all beam-to-column intersections, but this practice was ultimately abandoned for economic reasons and replaced with the use of perimeter frame structures in which only two frame lines in each direction are moment-resisting, and the interior is used to resist gravity loading (Jayaram et al. 2012).

Typical section shapes, sizes and connection details for the 1973 archetype building are selected based on those observed in available existing tall steel MRF building drawings. Consistent with these records, built-up box columns (denoted R in Figure 4-10), wide flange beams, and welded beam-to-column connections are selected for the prototype building. In the case of the 2012 archetype building, built-up I sections (denoted I in Figure 4-10) are selected for the columns and wide flange sections are selected for the beams, with reduced beam section (RBS) moment connections, where portions of the beam flange are trimmed in the region adjacent to the beam-to-column connection such that the plastic hinge in the beams forms in the trimmed region, away from the column face. These connections are prequalified for use in special steel MRF systems (AISC 2010b).

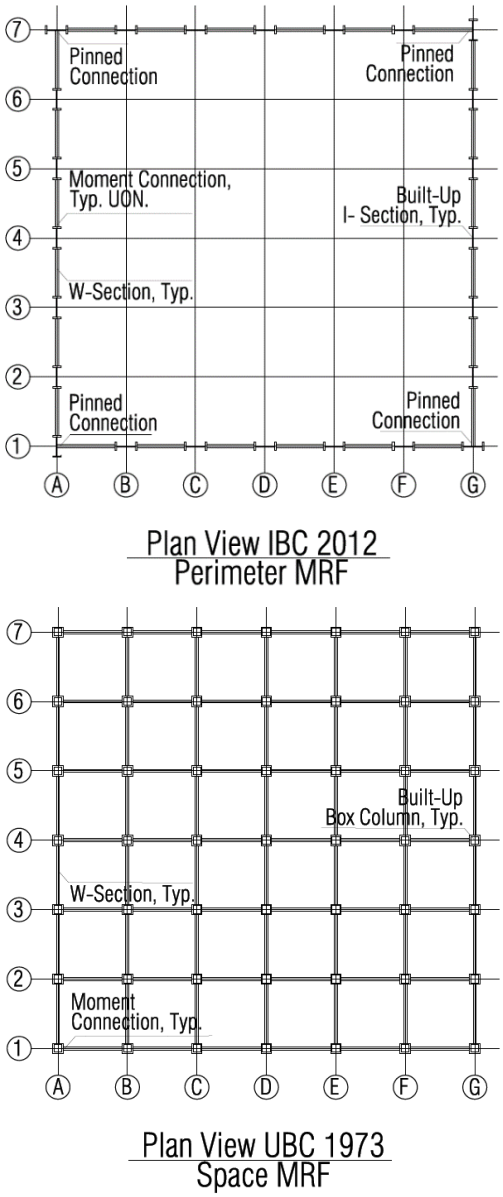

Figure 4-4: 1973 and 2012 archetype building plan drawings of lateral resisting system illustrating typical cross section shapes.
Source: Molina Hutt et al. (2017).

The building enclosure is assumed to be composed of precast concrete panels and glass windows, as seen in many of the buildings in Figure 4-3. The floor system is composed of a concrete slab of 76.2 mm (3 in.) thickness over a metal deck of 63.5 mm (2.5 in.) thickness supported by steel beams of ASTM A36 [248 MPa (36 ksi)], and steel columns of ASTM A572 [345MPa (50 ksi)]. Both the 1973 and the 2012 archetypes are assumed to have the same steel grade specification, i.e. ASTM A36 for beams and A572 for columns. The gravity load requirements (Superimposed Dead Load or SDL; Live Load or LL) of UBC 1973 (as specified in section 2302 of the code) and IBC 2012 (as specified in section 1607 of the code) do not differ greatly and are summarized in Table 4-1.

Table 4-1 Gravity loading criteria.

Use	SDL		LL	
	(kPa)	(psf)	(kPa)	(psf)
Parking	0.7	15	2.5	50
Lobby	4.3	90	4.8	100
Office	1.9	40	2.7	56
Mechanical	6.5	135	2.7	56
Roof	4.1	85	1.5	32
Façade	2.0	41	-	-

With regards to the seismic design requirements, UBC 1973 follows an equivalent lateral force procedure, with minimum earthquake design forces (as specified in section 2314 of the code), as illustrated in Equation 4-1. Where V is the total lateral force, Z is a numerical coefficient based on the seismic zone, K is the horizontal force factor, prescribed by the code as a function of the lateral resisting system type, and C is a numerical coefficient for base shear determined as a function of the fundamental period of the structure, T, as specified in Equation 4-2. W is the effective seismic weight, defined as the total dead load.

$$V = Z \cdot K \cdot C \cdot W \qquad \text{Equation 4-1}$$

$$C = 0.05 / T^{1/3} \qquad \text{Equation 4-2}$$

The seismic zone map in UBC 1973 is illustrated in Figure 4-5. Major cities in the west coast of the US, including Los Angeles, Seattle, San Francisco, San Diego or Oakland, all correspond to Seismic Zone 3, for which Z takes a value of 1. The value of K for buildings with a ductile space MRF system (as specified in UBC 1973 Table 23-I) takes a value of 0.67. According to UBC 1973, the value of T in MRF systems used for computing the value of C, is equal to 0.1 times the number of storeys, which corresponds to a period of 5 seconds for a 50-storey building. The resulting value of C is 0.029. Therefore, the resulting seismic lateral force for design is just under 2% of the total dead load of the building. This calculation highlights the lack of consideration for site amplification or soil type within the UBC 1973 seismic load calculation.

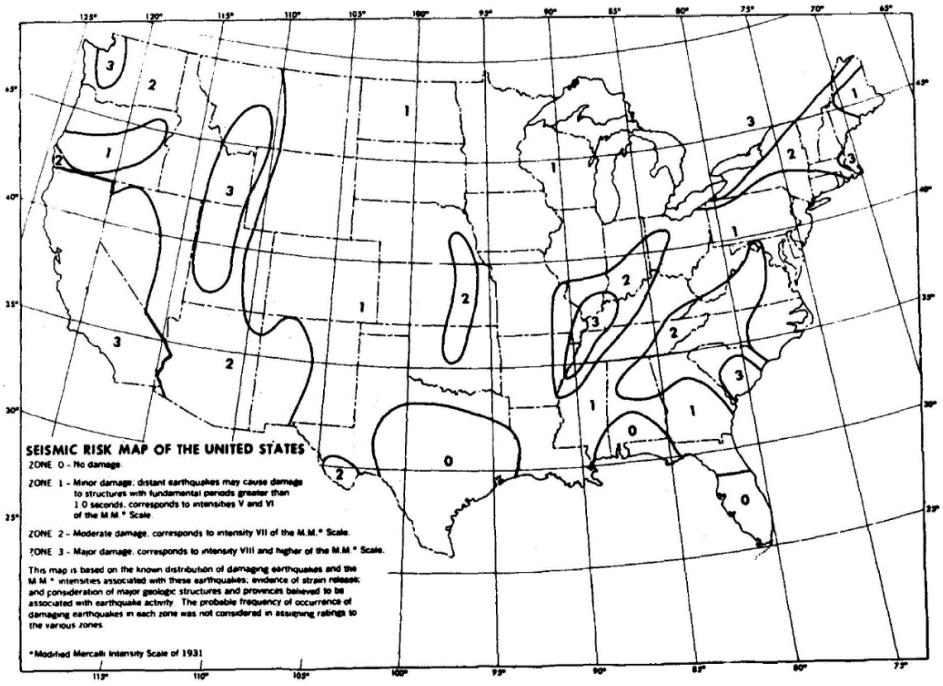

Figure 4-5: UBC 1973 seismic zone map of the United States.
Source: UBC 1973.

The lateral force V is then distributed up the height of the building as illustrated in Equations 4-3 and 4-4, which define the force to be applied at the top of the structure (F_t), and the distribution of the remaining storey forces, F_x, respectively. F_x denotes the force at the storey of interest.

$$F_t = 0.004 \cdot V \cdot (h_n/D_s)^2 \qquad \text{Equation 4-3}$$

$$F_x = (V - F_t) \cdot w_x \cdot h_x \,/\, \sum_{i=1}^{n} (w_i \cdot h_i) \qquad \text{Equation 4-4}$$

Where h_n is the height of the building, D_s is the plan dimension of the lateral force resisting system in the direction considered, w_x and w_i is the weight at level x or i, respectively, h_x and h_i is the height at level x or i, respectively, and n is the number of storeys in the building under consideration. The resulting force distribution is strictly based on the first mode translation response of the structure, without consideration of higher mode effects. This calculation is to be carried out in both of the building's principal directions. For the 50-storey archetype building here considered, the resulting forces are identical in both directions.

A code-based design of the archetype building per IBC 2012 requires a modal response spectrum analysis, as it does not permit the use of an equivalent lateral force procedure for buildings above ~50m (160 ft) in height. The design response spectrum per IBC 2012 is defined as two-thirds of the risk-targeted Maximum Considered Earthquake (MCE_R). Mapped five-

percent MCE_R spectral accelerations at periods of 0.2 and 1 seconds, which form the basis for constructing the response spectrum, are provided by the code for different site classes. The site class is defined as a function of the soil properties at the site. The majority of tall buildings in San Francisco are located in areas with subsurface ground conditions consistent with Site Class D (as defined in ASCE 2010), which is also the site class recommended by the code when soil properties at the site are unknown. The code also defines the seismic design category of any structure, as a function of the risk category and the mapped MCE_R parameters. The risk category is a categorization of buildings for the determination of loads based on the risk associated with unacceptable performance. A commercial office building corresponds to a risk category of II (ASCE 7 Table 1.5-1). Based on the risk category and MCE_R values, the archetype building falls under seismic design category D.

To estimate the seismic design forces, the design spectrum (i.e. two-thirds of the MCE_R spectrum) is divided by R/I_e, where R is the response modification factor and I_e is the importance factor. In order to estimate displacements, the spectrum for design force calculation is subsequently multiplied by C_d/I_e, where C_d is the displacement amplification factor. The importance factor accounts for the degree of risk to human life associated with damage to the building. For the building under consideration, the importance factor takes a value of 1. The response modification coefficient and the displacement amplification factors are dependent on the ductility of the lateral resisting system. These values are tabulated in ASCE 7 Table 12.2-1, and for special steel MRF systems correspond to an R value of 8 and a C_d value of 5.5. Figure 4-6 illustrates the MCE_R spectrum, the design spectrum, and the spectrum for force demand and displacement demand calculations. The curves are also shown in log-log axis to facilite evaluation of spectral accelerations at long periods

With regards to wind forces, the minimum horizontal wind pressures to be taken upon the gross area of the vertical projection of the building are defined per UBC 1973 (Table 23-F) for different height zones above ground as a function of the wind pressure map at 9.1m (30 ft) above ground, as seen in Figure 4-7. The mapped wind pressure for all of California is 0.95 kPa (20 psf). The resulting wind pressure distribution in the archetype building varies from 0.72 kPa (15 psf) at ground level to 1.68 kPa (35 psf) at roof level. The resulting base shear expressed as a function of the total dead load of the building (for comparison with the seismic base shear) is 1.80%.

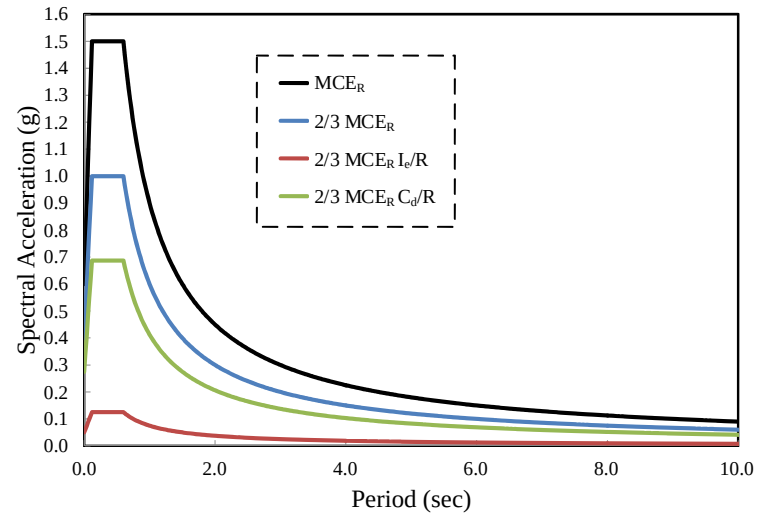

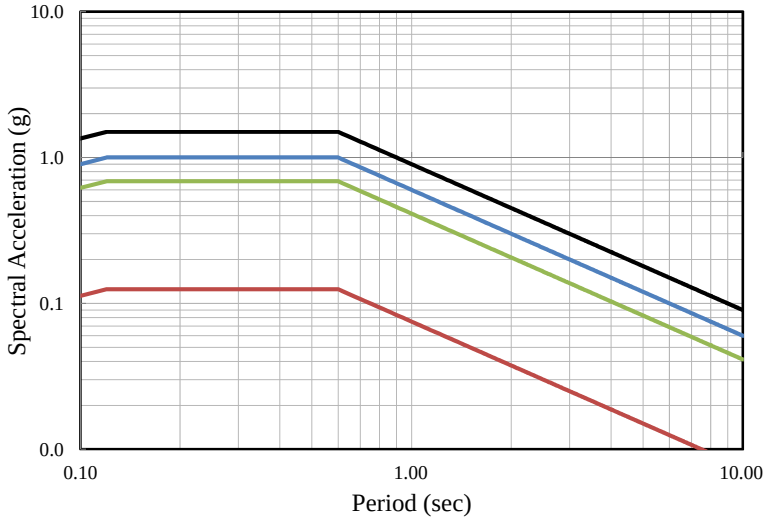

Figure 4-6: IBC 2012 design spectra.

The wind design forces per IBC 2012 are dependent on a number of parameters provided by the code. One of the key parameters is the basic wind speed, which is used in conjunction with other parameters to determine the wind loads based on a directional procedure permitted in the design of buildings of all heights. The basic wind speed is a mapped parameter corresponding to a 3 second gust speed at 10 m (33 ft) above ground in exposure category C, corresponding to a 7% probability of exceedance in 50 years. For the western US, this value corresponds to 49 m/s (110 mph). Additional parameters along with relevant sections of the code are shown in Table 4-2. Those parameters enable the calculation of the velocity pressure and design wind loads up the building height. Figure 4-8 provides a comparison of the resulting wind pressures as calculated per UBC 1973 and IBC 2012 up the building height.

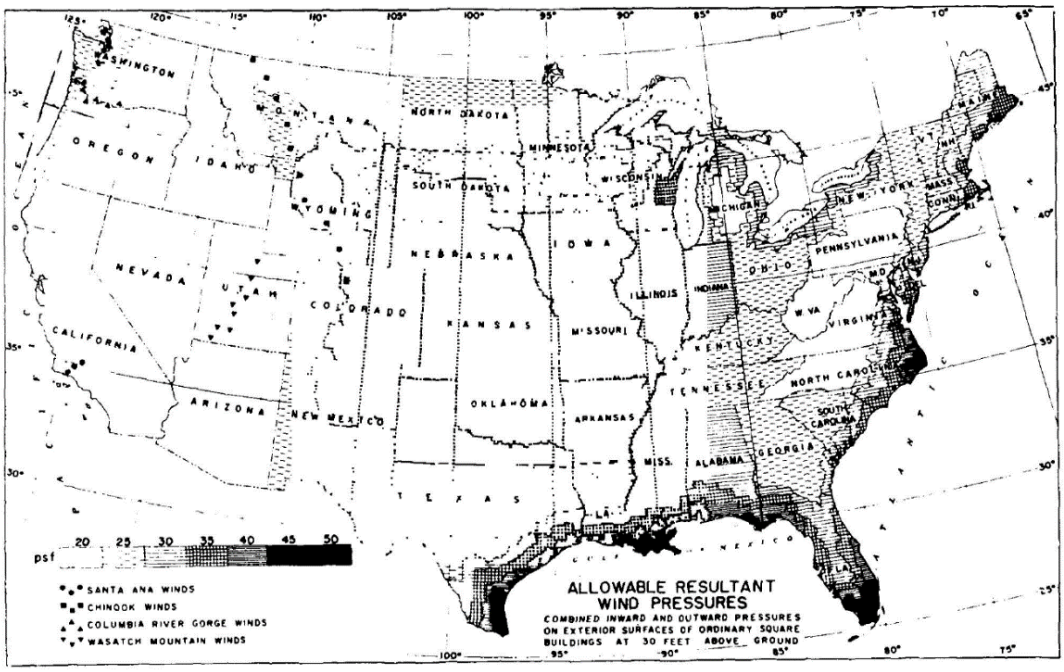

Figure 4-7: UBC 1973 wind pressure map of the United States.
Source: UBC 1973.

Table 4-2: IBC 2012 wind design parameters.

Design Parameter	Value	ASCE 7 Reference
Basic Wind Speed (V)	49 m/s (110 mph)	Figure 26.5-1
Wind Directionality Factor (K_d)	0.85	Table 26.6-1
Exposure Category	C	Section 26.7.3
Topography Factor (K_{zt})	1	Figure 26.8-1
Gust Effect Factor (G_f)	1	Section 26.9
Enclosure Classification	Enclosed	Section 26.10
Internal Pressure Coefficient (GC_{pi})	0.18	Table 26.11-1
External Pressure Coefficient (C_p) Windward	0.8	Section 27.4
External Pressure Coefficient (C_p) Leeward	0.5	Section 27.4
External Pressure Coefficient (C_p) Side Walls	0.7	Section 27.4

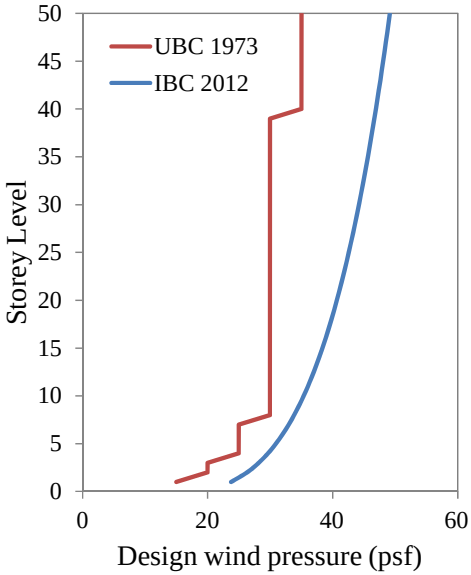

Figure 4-8: Design wind pressure distribution per UBC 1973 and IBC 2012.

Based on discussions with engineers knowledgeable of the design practice in the 1970s (H.J. Brunnier Associates, Degenkolb Engineers, Rutherford and Chekene, personal communication 2012), even though UBC 1973 did not specify drift limits, design offices would have implemented drift limits established by their firm's practice or those obtained from the Bluebook (SEAOC 1973). In this work, the drift limit recommendations from Appendix D of the Bluebook for buildings taller than 13 storeys are used, which equal 0.0025 and 0.005 for wind and seismic loads, respectively. IBC 2012 requirements result in a slightly more stringent seismic drift limit of approximately 0.004; the change in lateral deflection between two adjacent storeys divided by the storey height (i.e. IDR) should be less than 0.020, but the deflection amplification factor, C_d, with a value of 5.5, as prescribed for special steel MRF (ASCE 2010), should be applied to the lateral deflection.

Figure 4-9 illustrates compliance with storey drift requirements in both archetype buildings. It is worth noting that presently, IBC 2012 does not specify wind drift limits. When used in design, these are mainly to check against damage (e.g. leakage of the curtain wall). In this example, the service drift limit of 0.005, as recommended by the PEER Tall Buildings Initiative (PEER 2010a), is used for compliance verification.

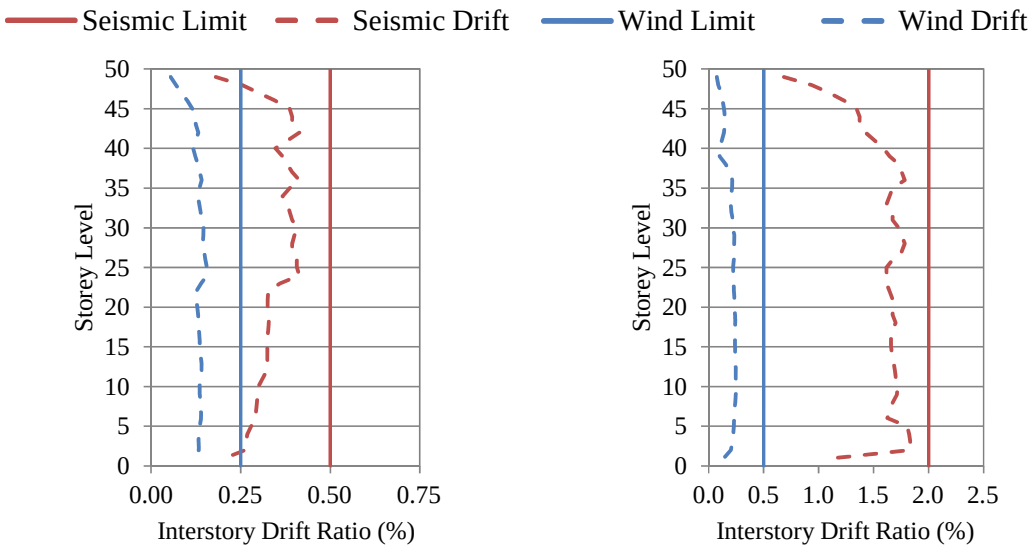

Figure 4-9: Design compliance of archetype building with interstorey drift requirements per (a) UBC 1973 and (b) IBC 2012.

Even though the seismic drift limits do not appear to be drastically different between UBC 1973 and IBC 2012, it is important to note that the design forces are significantly larger in modern building codes than they were in the 1970s. Per UBC 1973 design requirements, the effective wind base shear and effective seismic base shear are 1.80% and 1.96% of the total building dead load, respectively. Instead, per IBC 2012 requirements, the effective wind base shear and effective seismic base shear are 4.26% and 3.74% of the total building dead load. While the wind pressures and seismic forces previously discussed may not appear to differ drastically between the UBC 1973 and IBC 2012 provisions, there are a number of additional considerations in IBC 2012 that drastically increase the design forces. Regarding the wind design forces, the pressures prescribed per UBC 1973 are considered as the final resulting lateral pressures exerted on the building face. However, when considering those prescribed by IBC 2012, these are amplified due to considerations of windward, leeward and internal pressures acting simultaneously. In the case of seismic forces, the spectral accelerations at long periods shown in Figure 4-6 are relatively low; for instance in the response spectrum curve used to estimate design forces, the spectral acceleration at a 5 second period is equal to 0.015g. This would appear to be less than the 2% of the total building dead load, as required per UBC 1973 seismic design requirements. However, the resulting base shear per IBC 2012 is higher due to contribution of higher modes and the scaling of forces required to meet minimum base shear requirements, which are not included in the UBC 1973 design regulations.

In modern design standards, where the combined response for the modal base shear is less than 85% of the calculated base shear using the equivalent lateral force procedure, the forces shall be multiplied by 0.85 V/V_t, where V is the base shear calculated per the equivalent lateral force procedure and V_t is the base shear estimated from modal response. In IBC 2012, V per the equivalent lateral force procedure is calculated as illustrated in Equation 4-5, where C_s is the seismic response coefficient, defined in Equation 4-6, and W is the effective seismic weight, defined as the total dead load of the building.

$$V = C_s \cdot W \qquad \text{Equation 4-5}$$

$$C_s = S_{DS} / (R/I_e) \qquad \text{Equation 4-6}$$

In Equation 4-6, S_{DS} is the design spectral response acceleration at short periods, and R and I_e are as defined previously. The value of C_s is bound by the maxima set by Equations 4-7 and 4-8 and the minima set by Equations 4-9 and 4-10, where S_{D1} is the design spectral response acceleration at a 1-second period, T_L is the mapped long period transition and S_1 is the mapped MCE_R spectral acceleration at a 1 second period (ASCE 7 Figures 22-12 and 22-2). All other variables are as previously defined. The resulting value of C_s is equal to 0.044 g.

$$C_s = S_{D1} / (T \cdot R/I_e) \quad \text{for } T \leq T_L \qquad \text{Equation 4-7}$$

$$C_s = S_{D1} \cdot T_L / (T^2 \cdot R/I_e) \quad \text{for } T \geq T_L \qquad \text{Equation 4-8}$$

$$C_s = 0.044 \cdot S_{DS} \cdot I_e \geq 0.01 \qquad \text{Equation 4-9}$$

$$C_s = 0.5 \cdot S_1 / (R/I_e) \quad \text{if } S_1 \geq 0.6g \qquad \text{Equation 4-10}$$

The scaling of forces required to meet minimum base shear requirements is also applied to the calculation of drifts. Additionally, these must be further amplified to account for p-delta effects (ASCE 7 Section 12.8.7). The scaling due to p-delta effects is checked on a storey per storey basis. When the stability coefficient, θ, defined per Equation 4-11, exceeds 0.10, the amplification due to p-delta effects is applied by multiplying displacements by $1/(1-\theta)$. The stability coefficient need not exceed the value set by Equation 4-12.

$$\theta = P_x \cdot \Delta \cdot I_e / (V_x \cdot h_{sx} \cdot C_d) \qquad \text{Equation 4-11}$$

$$\theta = 0.5 / (\beta \cdot C_d) \leq 0.25 \qquad \text{Equation 4-12}$$

Where P_x is the total vertical design load above level x, Δ is the storey drift, V_x is the seismic shear force at the storey under consideration, h_{sx} is the storey height, β is the ratio of shear demand to capacity of the storey, and C_d and I_e are as previously defined.

For the archetype building, this scaling of forces and displacements results in a scale factor of 3.74, which is applied to the forces and displacements obtained from response spectrum analysis. Furthermore, consideration of p-delta effects results in an additional increase of up to 30%, particularly in the lower storeys.

The overall seismic weight, defined as the total building dead load, of the 1973 archetype building is 784,220 kN (176,300 kips), whereas the seismic weight of the modern design is 825,145 kN (185,500 kips). The 5% discrepancy in seismic weight between the two archetypes is a reflection of the differences in the steel self-weight (more material is required for the modern archetype to comply with design requirements). While one may expect a greater tonnage increase in the modern archetype, because the system consists of a perimeter frame, which is considerably more efficient than a space frame, the resulting tonnages are relatively consistent between the two designs. The resulting section sizes for a typical frame in both the 1973 and 2012 archetype buildings are shown in Figure 4-10.

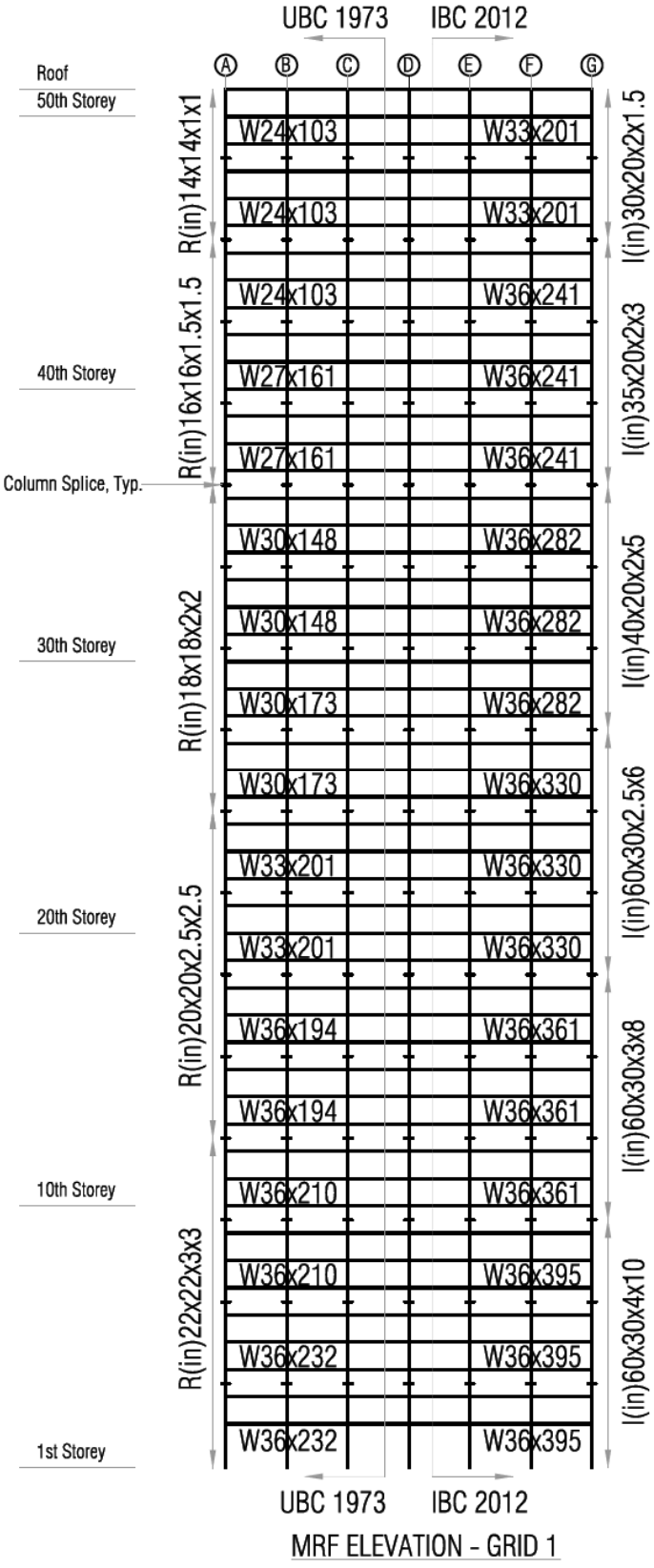

Figure 4-10: 1973 and 2012 archetype building elevation drawings of lateral resisting system illustrating typical section sizes in beams and columns.
Source: Molina Hutt et al. (2017).

While the design of both archetypes is controlled by drift requirements, it is worth noting the differences in strength checks associated with designs from the 1970s versus modern design standards. UBC 1973 follows an Allowable Stress Design (ASD) approach, whereas IBC 2012 follows a Load and Resistance Factor Design (LRFD). The approach followed in ASD is to check actual versus allowable stress. This implies that there are no factors associated with the loading criteria. LRFD compares the required strength versus actual strengths, and applies safety factors on the loads as well as on the strength calculations. Tables 4-3 and 4-4 illustrate a comparison between load combinations and basic strength checks associated with both UBC 1973 and IBC 2012 (ASCE 2010 for load combinations and AISC 2010a for steel design) relevant to the design of the archetype buildings considered.

Table 4-3: Comparison in load combinations per UBC 1973 and IBC 2012.

UBC 1973	IBC 2012	Load Definition
	1.4D	
D	1.2D +1.6L	D: dead
D + L	1.2D + 1.0W + L	L: live
D + L + W	1.2D + 1.0E + L	W: wind
D + L + E	0.9D + 1.0W	E: Earthquake
	0.9D + 1.0E	

Table 4-4: Comparison of steel ASD stress limits in UBC 1973 versus LRFD strength checks in IBC 2012.

Check	UBC 1973[*,^] (Code Section Reference)	AISC 2010a[^] (Code Section Reference)
Tension	$F_t=0.60F_y$ (Sec. 2702.1)	$\phi P_n=\phi F_y A_g$ (16.1 D2-1)
Compression	$F_a=[1-(Kl/r)^2/(2C_c^2)]F_y/FS$ (Sec. 2702.3)	$\phi P_n=\phi F_{cr} A_g$ (16.1 E3-1)
Bending	$F_b=0.66F_y$ (Sec. 2702.4)	$\phi M_n=\phi M_p=\phi F_y Z_x$ (16.1 F2-1)
Shear	$F_v=0.4F_y$ (Sec. 2702.2)	$\phi V_n=\phi 0.6F_y A_w C_v$ (16.1 G2-1)
Combined Action	Considered (Sec. 2703.a)	Considered (16.1 H1)

[*] *All allowable stresses can be increased by 1/3 when considering seismic and wind forces.*
[^] *See List of Symbols for variable definitions.*

UBC 1973 does not require consideration of lateral forces acting in perpendicular directions to act simultaneously, whereas IBC 2012 requires consideration of 100% of the lateral forces in one direction in conjunction with 30% of the forces acting perpendicularly. Under the load combinations prescribed in Table 4-3, and the stress and strength limits in Table 4-4, the maximum utilization ratios (demand to capacity) in the columns per UBC 1973 requirements are as follows: 0.38 under axial loads, 0.19 under shear, 0.36 in bending and 0.83 under

combined axial load and biaxial bending. Similarly, the maximum utilization ratios per IBC 2012 requirements are: 0.31 under axial loads, 0.05 under shear, 0.33 in bending and 0.49 under combined axial load and bending. For beams, UBC 1973 utilization ratios are 0.69 in bending and 0.10 in shear versus 0.80 in bending and 0.33 in shear per IBC 2012.

Additional requirements to ensure adequate seismic performance per UBC 1973 include: (i) individual frames must be capable of carrying 25% of the total seismic loads, (ii) beam-to-column moment connections must be capable of developing the full capacity of the beam, and (iii) cross sections width-to-thickness ratios must ensure that sections can reach their plastic capacity. Figure 4-11 illustrates some of the typical details frequently observed in existing building drawings from the 1970s. There are many aspects not considered in the designs of the 1970s, which are present in modern design standards, that drastically improve seismic performance, including: i) response spectrum analysis method as opposed to equivalent lateral force procedure based on the first mode translation response; ii) consideration of lateral forces acting simultaneously in both building directions; iii) consideration of accidental torsion; iv) minimum base shear requirements (scaling of forces and displacements); v) p-delta effects (scaling of forces and displacements); vi) consideration of vertical and horizontal irregularities; vii) strong column weak beam consideration; viii) panel zone consideration; ix) capacity design principles; and x) prequalified seismic connection details.

In addition to these design deficiencies, other aspects are also expected to negatively affect the seismic performance of the 1970s archetype buildings. Since the switch in the weld process that led to welds with very low toughness, as evidenced by fractures observed in the 1994 Northridge earthquake, took place in the mid-1960s (FEMA 2000), it is assumed that that fracture-prone pre-Northridge moment connections are common in designs from the 1970s. Designs of the 1970s did not include consideration of panel zone flexibility or strong column-weak beam principles. The panel zone model proposed by Krawinkler was not developed until 1978 (PEER 2010b) and strong column-weak beam requirements were not introduced in the UBC provisions until 1988 (SAC 2000). Column splices are typically located 1.2 m (4 ft) above the floor level approximately every three floors. Observed typical splice connection details consist of partial joint penetration welds of roughly half the thickness of the smaller section being connected. When subject to tensile forces, these splices can only carry a fraction of the moment capacity and/or axial tension capacity of the smallest section size being connected. Furthermore, experimental tests on heavy steel section welded splices have illustrated sudden failures with limited ductility (Bruneau and Mahin 1990). Based on this evidence, column splice failures are considered in the assessment. Because modern design standards for steel

special MRF require that columns splices are capable of developing the full capacity of the smallest section being connected, a reduced capacity of column splices need not be considered in the assessment of the 2012 archetype building.

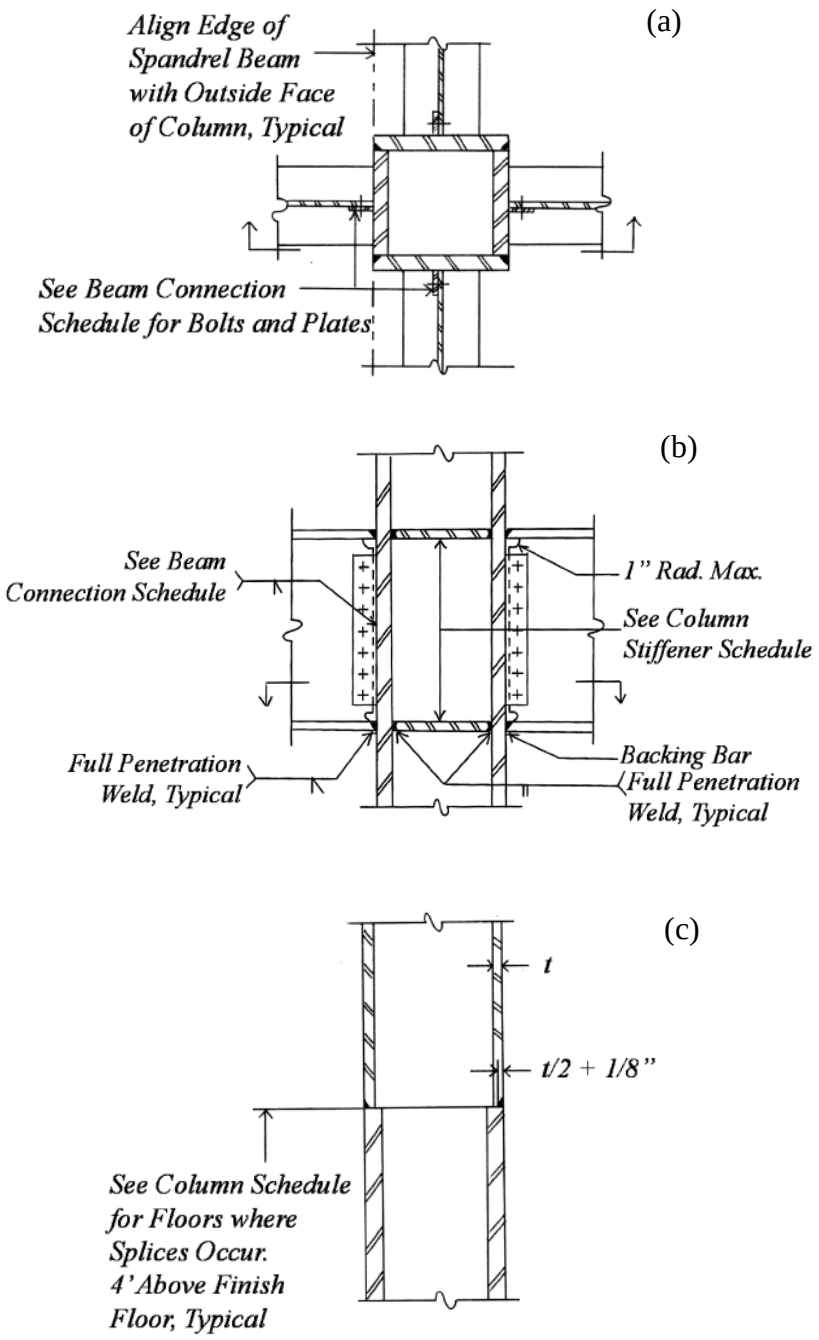

Figure 4-11: Typical details observed in existing building drawings: typical moment connection plan view (a) and elevation (b); typical splice connection (c).
Source: Molina Hutt et al. (2015).

The details illustrated in Figure 4-11 indicate that the 1970s steel MRF archetype buildings considered have welded beam-to-column connections, denoted WSMRFs in Section 2.1.2. Unless otherwise noted, throughout the rest of the thesis, when referring to steel MRFs, it is implied that these have welded beam-to-column connections, i.e. they are WSMRFs.

The dynamic properties of the 50-storey archetype buildings are illustrated in Figures 4-12 and 4-13, and summarized in Table 4-5. These properties are estimated considering only the seismic mass associated with the total building dead load and accounting for panel zone flexibility. Consideration of panel zone flexibility is important in calculating the dynamic properties, particularly given the considerable depth of the beam and column sections in the archetype buildings considered. A centreline model that neglects the effect of panel zones would result in an average increase of 30% in the fundamental periods estimated in Table 4-5. The clear heights and spans captured by centreline models become unrealistic when deep beam and column sections are used.

Table 4-5. Dynamic properties of the UBC 1973 and IBC 2012 50-storey archetype buildings. Source: Molina Hutt et al. (2017).

Mode	IBC 2012		UBC 1973	
	Period [s]	Effective / total mass [%]	Period [s]	Effective / total mass [%]
1	5.01	74.26	5.68	70.59
2	5.01	74.26	5.68	70.59
3	2.88	-	4.85	-
4	1.84	12.54	2.18	15.61
5	1.84	12.54	2.18	15.61
6	1.09	-	1.97	-

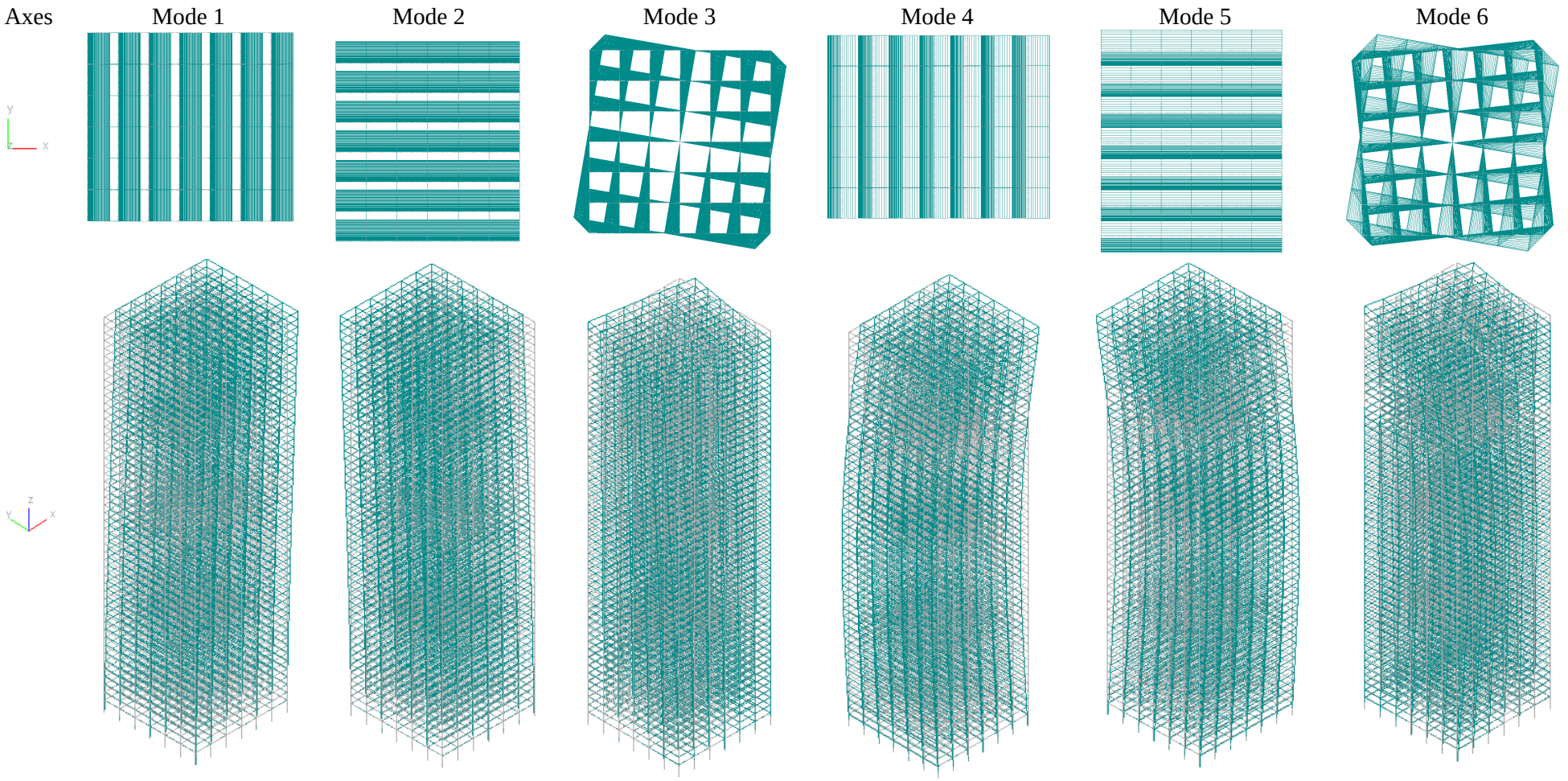

Figure 4-12: Dynamic properties of the UBC 1973 archetype building (only lateral resisting system shown).

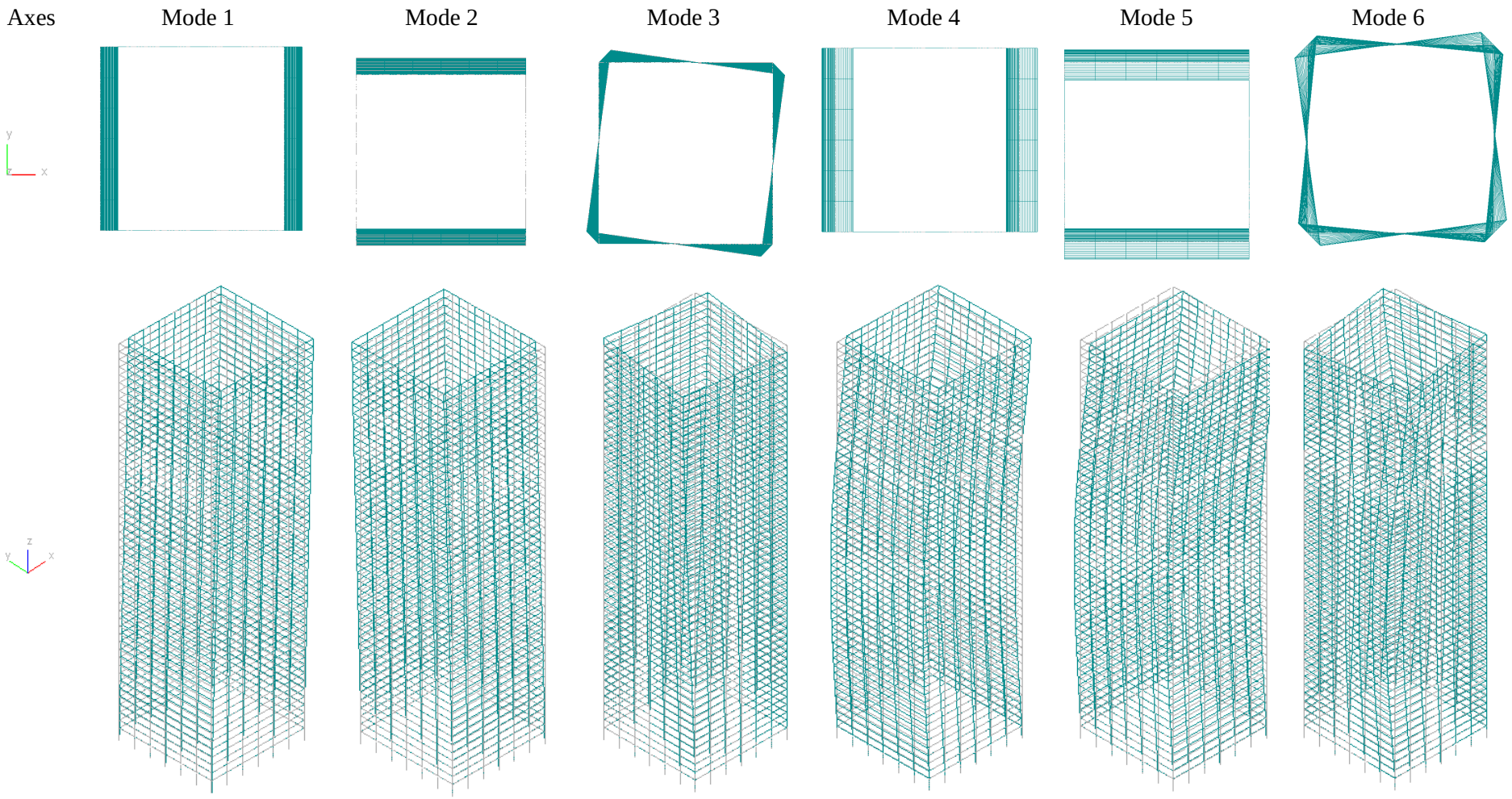

Figure 4-13: Dynamic properties of the IBC 2012 archetype building (only lateral resisting system shown).

4.1.2 Design summary of 40- and 20-storey 1970s archetype buildings

The same methodology described in section 4.1.1 is used in the design of the 40- and 20- storey 1970s archetype buildings. Occupancy is also assumed to be that of a commercial office with two levels for mechanical equipment, one at mid-height, and one at the top floor. These additional archetype buildings are designed with a small number of basement levels for parking, as observed in some of these existing tall buildings. The number of parking levels assumed is n-1, where n is the number of storeys in each archetype. Typical storey heights are 3.8 m (12.5 ft), 6.1 m (20 ft) at the lobby and 3 m (10 ft) for basement levels. The overall height of the structures above ground is 154.7 m (507.5 ft) and 78.5 m (257.5 ft) for the 40- and 20-storey buildings, respectively. The overall height of the structures below ground is 9 m (30 ft) and 3 m (10 ft) for the 40- and 20-storey buildings, respectively. The structural system of the archetypes consists of a steel space MRF with 6.1 to 12.2 m spans (20 to 40 ft) using wide flange beams, built up box columns and welded beam-to-column connections. The building width is 36.6 m (120 ft) in the long direction and 24.4 m (80 ft) in the short direction. Figure 4-14 illustrates a plan view and isometric of the 40-storey archetype. Figure 4-15 illustrates the analytical models used in design. The gravity load requirements, building enclosure, floor system and material grades are consistent with those described for the 50-storey archetype building. A summary of the resulting designs is shown in Tables 4-8 and 4-9 for the 40- and 20-storey buildings, respectively. Additionally, a summary of the dynamic properties and seismic weight of the buildings is also shown in Table 4-7.

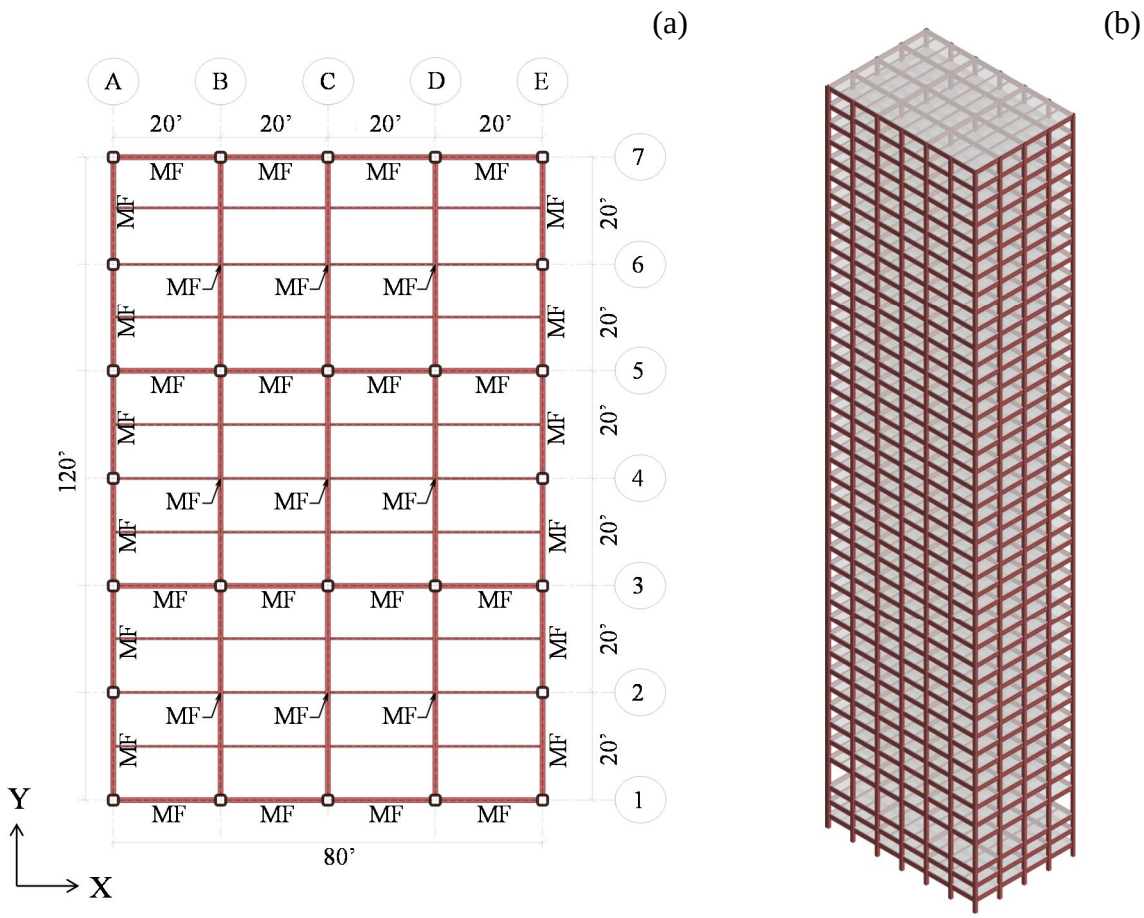

Figure 4-14: Archetype 40-storey office building plan (a) and isometric (b).
Source: Molina Hutt et al. (2015).

Table 4-6. Effective wind and seismic design base shears for the 1973 40- and 20-storey archetype buildings.

Archetype	Direction*	W [%]	E [%]	Seismic Weight [kN (kips)]
40-storey	X	3.25	2.06	286,065 (64,310)
	Y	2.17	2.06	
20-storey	X	2.73	2.62	137,894 (31,000)
	Y	1.82	2.62	

W: Wind; S: Seismic. Refer to Figure 4-14.

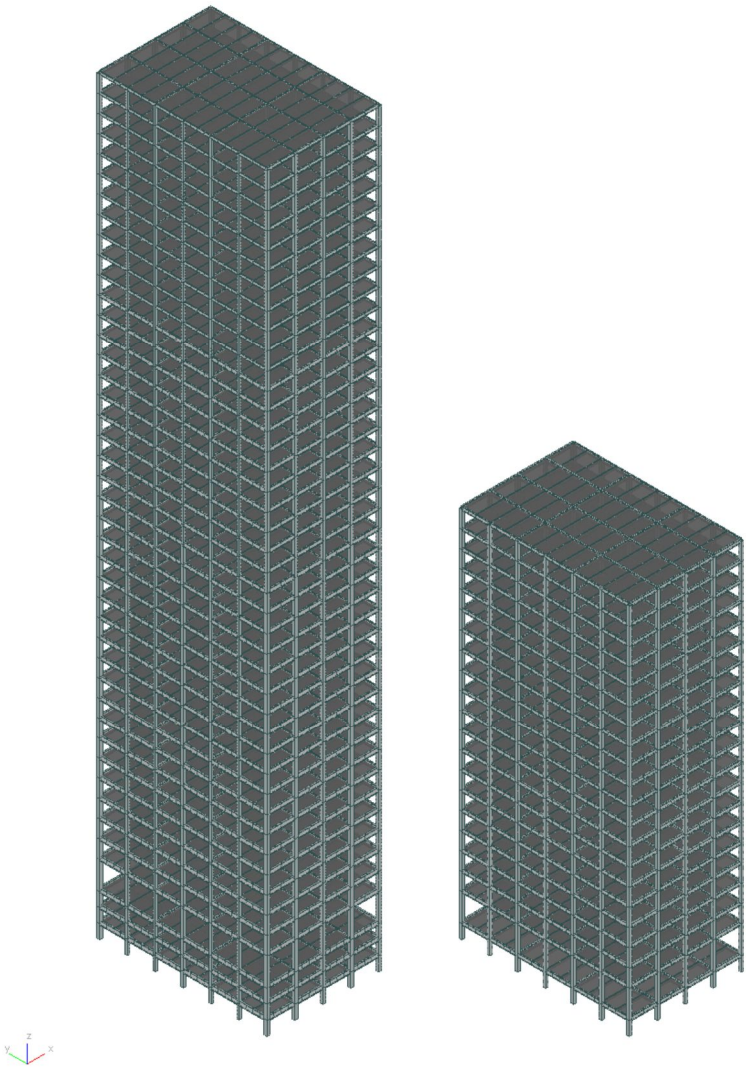

Figure 4-15: Structural models for the 40- and 20-storey 1973 archetype buildings.

Table 4-7: Dynamic properties of the 40- and 20-storey 1973 archetype buildings.

Mode	40-storey		20-storey	
	T [s]	E / T (Dir) [%]	T [s]	E / T (Dir) [%]
1	4.88	60.24 (X)	2.30	77.82 (X)
2	4.86	63.11 (Y)	2.01	74.74 (Y)
3	2.85	-	1.40	-
4	1.59	20.36 (X)	0.74	11.49 (X)
5	1.13	19.82 (Y)	0.63	14.74 (Y)
6	1.05	-	0.46	-

T: Period; E/T: Effective over total mass; Dir: Direction. Refer to Figure 4-14.

Table 4-8: Lateral resisting system section sizes for the 1973 40-storey archetype building. Source: Molina Hutt et al. (2015).

Level Range	Wide Flange Beams			Box Columns		
	Exterior Short Span	Interior Short Span	Interior Long Span	Interior	Ext. Short EL. (x)	Ext. Long EL. (y)
Base to 10	W36x256	W36x282	W30x124	22x22” t=3”	26x26” t=3”	20x20” t=2.5”
11 to 20	W33x169	W36x194	W27x84	20x20” t=2”	26x26” t=2.5”	20x20” t=2”
21 to 30	W33x118	W33x169	W27x84	18x18” t=1”	24x24” t=1.5”	18x18” t=1”
30 to Roof	W24x62	W27x84	W24x76	18x18” t=0.75”	24x24” t=1”	18x18” t=0.75”

EL: Elevation; Ext: Exterior.

Table 4-9: Lateral resisting system section sizes for the 1973 20-storey archetype building.

Level Range	Wide Flange Beams			Box Columns		
	Exterior Short Span	Interior Short Span	Interior Long Span	Interior	Ext. Short EL. (x)	Ext. Long EL. (y)
Base to 10	W30x148	W30x173	W30x211	22x22” t=2”	22x22” t=2.5”	22x22” t=1.5”
11 to 20	W27x129	W27x146	W30x191	22x22” t=1.5”	22x22” t=2.0”	22x22” t=1”

EL: Elevation; Ext: Exterior.

4.1.3 Tall buildings in other US west coast cities

The design criteria followed in the development of the 1970s archetype buildings is equivalent in other US west coast cities with high seismic hazard including Seattle, Los Angeles, Oakland or San Diego. Any of these locations fall within the same seismic and wind zones specified by UBC 1973 (see Figure 4-5 and Figure 4-7). However, the properties (height, plan dimensions, typical sections, steel grades, etc.) of the archetype buildings presented in this study are developed exclusively on an inventory of the existing tall building stock in San Francisco, which may differ from the existing tall building stock in other cities.

In order to understand how these archetype buildings may also be representative of existing tall buildings in other western US cities, a database of tall buildings constructed between 1960 and 1990 was compiled using Emporis (2000). San Francisco is also included to provide a comparison between the data from Emporis and the more detailed database discussed in Section 4.1.1 and included in Appendix B.

Figure 4-16 illustrates the breakdown of existing tall buildings constructed between 1960 and 1990 in Los Angeles, Seattle, San Francisco, San Diego and Oakland. These results indicate that the 20-, 40- and 50-storey building archetypes developed for San Francisco, could also be used to represent construction practice in cities such as Seattle or Los Angeles. The 20-storey archetype developed for San Francisco could also be used to represent buildings in Oakland and San Diego. However, for cities other than San Francisco, a more thorough review of the existing tall building stock would enable the development of archetype buildings that better represent construction in each one of these cities. Particularly since the information provided in Figure 4-16 reflects the construction material, but does not explicitly classify the lateral resisting system of the buildings considered.

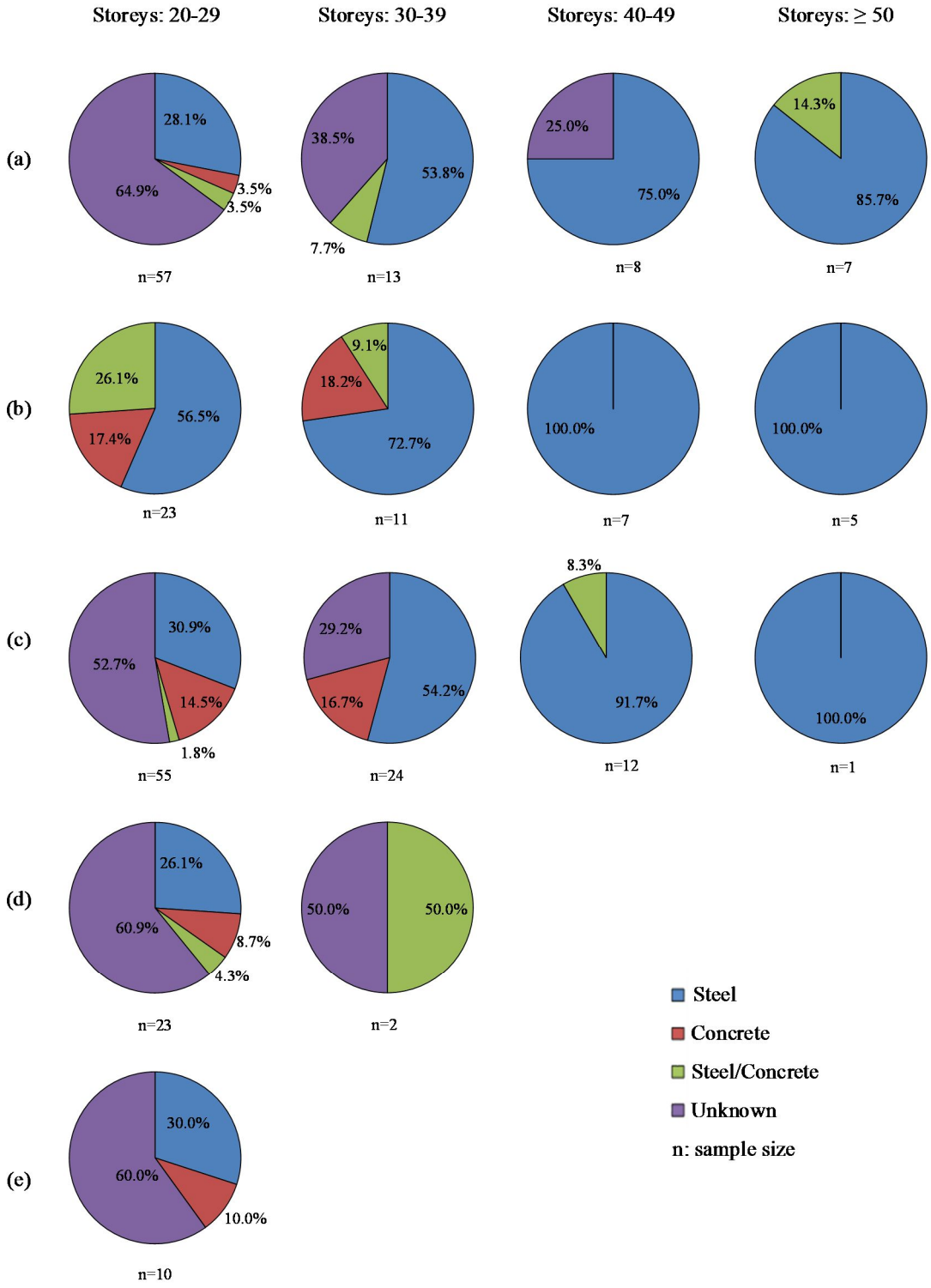

Figure 4-16: Construction material of existing tall buildings constructed between 1960 and 1990 in (a) Los Angeles, (b) Seattle, (c) San Francisco (d) San Diego and (e) Oakland.

4.2 Non-linear response history analysis (NLRHA) models

In order to conduct non-linear dynamic analysis of the archetype buildings, finite element models capable of capturing the response of all structural elements that significantly contribute to the strength and stiffness of the system are developed. The numerical models for simulation are developed in LS-DYNA (LSTC 2011), a multi-purpose explicit and implicit finite element program used to analyse the non-linear response of structures. Component models to represent the response of non-linear beams, columns and panel zones are calibrated, where possible, against available experimental test data for validation. These component models are illustrated in Figure 4-17 for the 40-storey archetype building. The colour coding of floors represents the different use associated with each space: (i) green for parking, (ii) dark blue for lobby area, (iii) light blue for office space, (iv) pink for MEP levels and (v) yellow for the roof.

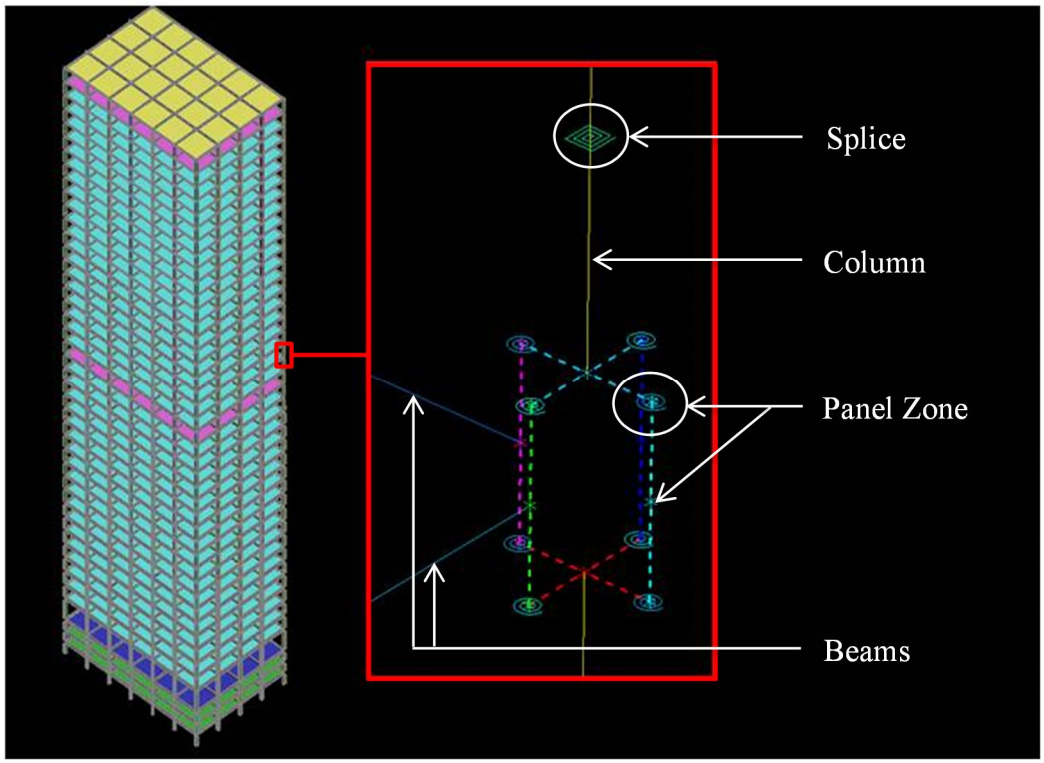

Figure 4-17: Isometric of 40-storey analytical model and close-up of component models (boxed in red).

As in section 4.1, the development of the non-linear dynamic analysis models for the 50 storey archetype buildings (UBC 1973 and IBC 2012) is illustrated in detail in this section. First, the discussion focuses on the structural response at the component level, with an emphasis on the key structural elements in steel MRFs (beams, columns and panel zones) and other analysis assumptions. Next, the discussion shifts to global behaviour, where the global response of the archetype buildings is compared with the response of a similar building instrumented in past

earthquakes, as an approximate check of the numerical model. Additionally, because this work includes seismic assessments at intensities of ground motion shaking that trigger collapse, the ability of the models to explicitly simulate lateral instability, accelerated due to strength and stiffness deterioration, is also illustrated. Lastly, a description of how the procedure is adjusted for the 40- and 20-storey buildings is provided.

4.2.1 Non-linear beams

Beams are modelled as lumped plasticity beam elements. The key difference in expected response, in terms of moment-rotation behaviour, between prequalified moment connections in modern construction, assumed in the 2012 archetype building, and fracture-prone pre-Northridge moment connections, assumed in the 1973 archetype building, is discussed here.

In support of enabling reliable assessments of structural systems under earthquake loading, Lignos and Krawinkler (2011) develop empirical relationships for modelling steel beams, with and without RBS detailing, based on a large database of experimental tests. For the 2012 archetype building, beams follow these modelling recommendations for RBS connections. These guidelines define the moment-rotation response as a function of the yield moment M_y, pre-capping plastic rotation θ_p, post-capping plastic rotation θ_{pc} and cumulative plastic rotation capacity Λ; all of which can be defined as a function of beam geometry and material properties. Figure 4-18a illustrates a comparison between the analytical (LS-DYNA) and experimental (obtained from Lignos 2013) moment-rotation response of a beam with an RBS connection. Figure 4-18b illustrates a similar calibration exercise for non-RBS beams. The results shown in Figures 4-18 illustrate good agreement between the analytical and the experimental results for both beams with and without RBS detailing.

For the 1973 archetype building model, consistent with pre-Northridge moment connections, the hysteretic response of the beams accounts for fracture based on ASCE 41 (ASCE 2013) recommendations. The modelling procedure is similar to that used for the 2012 archetype, but adjusted for non-RBS connections and introducing a plastic rotation threshold $\theta_{p\text{-}fract}$ at which fracture is set to occur in the connections. Figure 4-19 illustrates the impact of introducing the fracture variable in the moment rotation response of the components previously illustrated in Figure 4-18. The envelope of the hysteretic responses in Figure 4-19 illustrates good agreement with the recommended ASCE 41 (ASCE 2013) backbone curves. Table 4-10 summarizes the modelling parameters used for beams in both archetype building models.

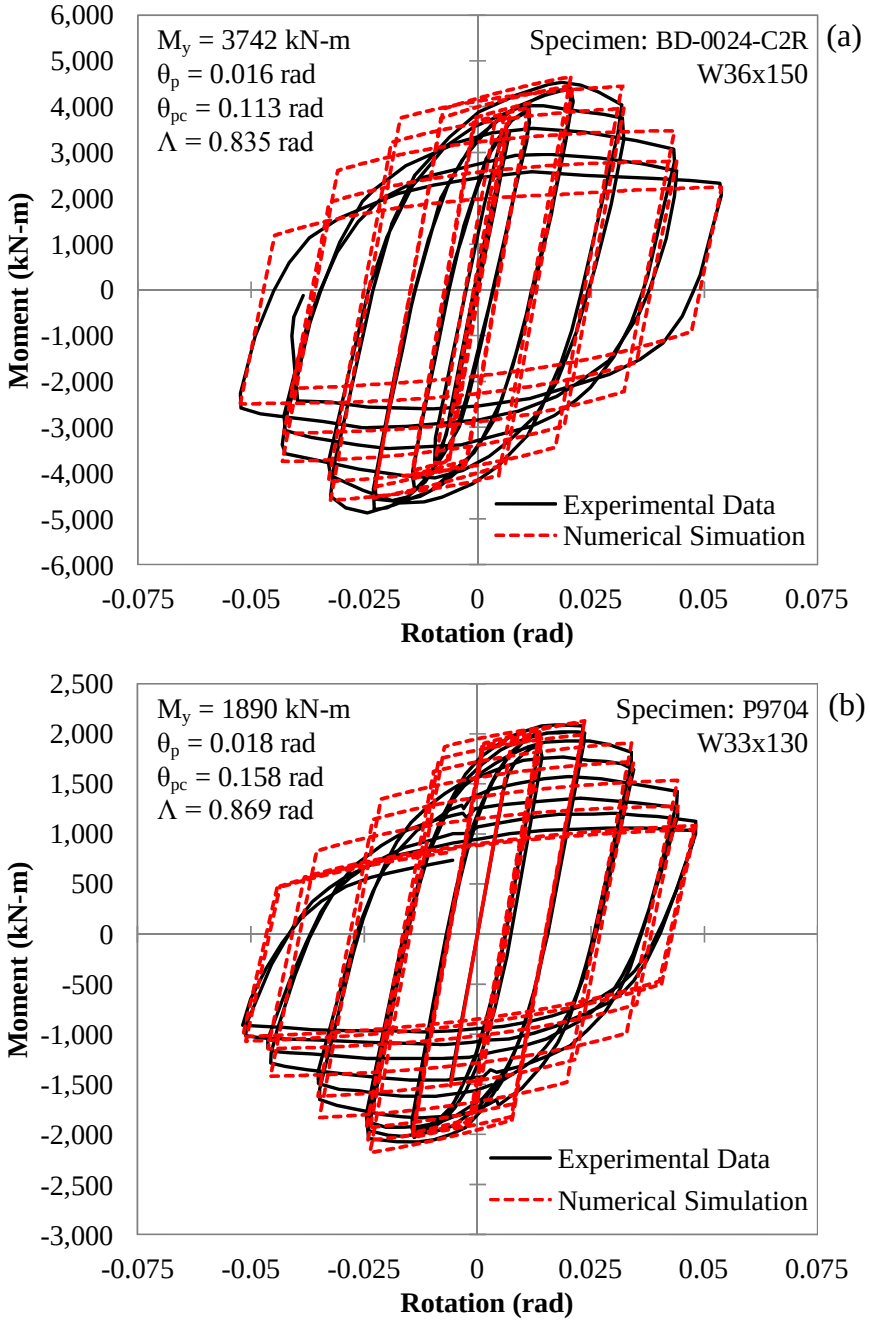

Figure 4-18: Sample analytical versus experimental hysteretic moment-rotation response in a (a) RBS and (b) non-RBS beam-to-column connection consistent with pre-qualified detailing. Source: Molina Hutt et al. (2017).

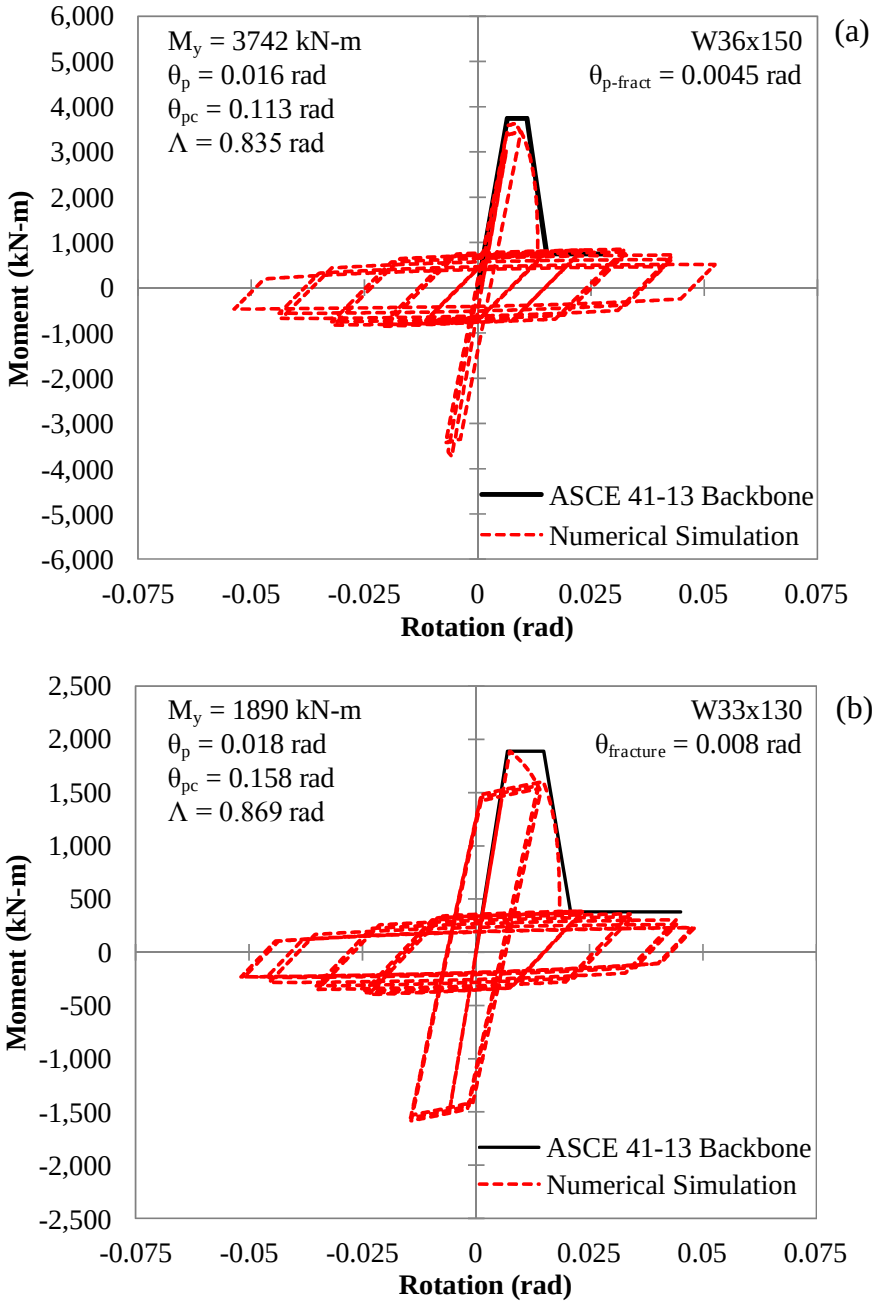

Figure 4-19: Impact of introduction of fracture variable in the moment-rotation response of beams, shown against ASCE 41 recommendations.
Source: Molina Hutt et al. (2017).

4.2.2 Non-linear columns

Columns are modelled as lumped plasticity beam elements with yield surfaces capable of capturing interactions between bending moment and axial force. Under low levels of axial load, the moment-rotation response of columns is similar to that of beams. However, under axial load-to-capacity ratios (ALR) greater than 0.2, the moment-rotation response experiences a greater rate of degradation. For the 1973 archetype building, degradation parameters for the moment-rotation response under cyclic loads are calibrated based on experimental tests of tubular steel columns (Kurata et al. 2005) in accordance with the guidelines for tubular hollow steel columns under varying levels of axial load (Lignos and Krawinkler 2010). Similar to the beam modelling procedure, these guidelines define the moment-rotation response not only as a function of the yield moment M_y, pre-capping plastic rotation $\theta_{p,}$ post-capping plastic rotation θ_{pc} and cumulative plastic rotation capacity Λ based on cross section geometry and material properties, but also as a function of ALR. Figures 4-20a and 4-20b illustrate the component deterioration calibration results for two column samples with ALR of 0.1 and 0.3, respectively. The 1973 archetype column sections are modelled following this approach. For the 2012 archetype, due to the low axial demands in the columns under expected gravity loads, which range from 7 to 11%, degradation parameters for the moment-rotation response under cyclic loads are assumed to be equivalent to those outlined in Lignos and Krawinkler (2011) for steel beams, as recommended by PEER (2010b). For the 1973 archetype, axial demands in the columns under expected gravity loads range from 20 to 30%, hence degradation parameters that account for ALR are considered. The results illustrated in Figure 4-20 show good agreement between the analytical and experimental response. Table 4-10 summarizes the modelling parameters used for columns in both archetype buildings.

For the 1973 archetype building, column splices are modelled consistent with columns, but adjusted to their nominal capacity when subject to tension and/or bending as noted in Table 4-10. In the latter table the variables A_{SPLICE} and Z_{SPLICE} indicate the ratio of the tensile and bending capacity, respectively, of the splice to the smallest column section connected. In Table 4-10, the estimated tensile capacity is denoted by variable P_t. The splices are modelled to reach their nominal capacity after which they fail in a brittle manner. These assumptions have the intent of capturing the limited ductility observed in experimental texts on heavy steel section welded splices in Bruneau and Mahin (1990). Full column capacity is assumed in compression since this is achieved by direct bearing. For the 2012 archetype building, splices can develop the full capacity of the smallest section being connected, as required by the code.

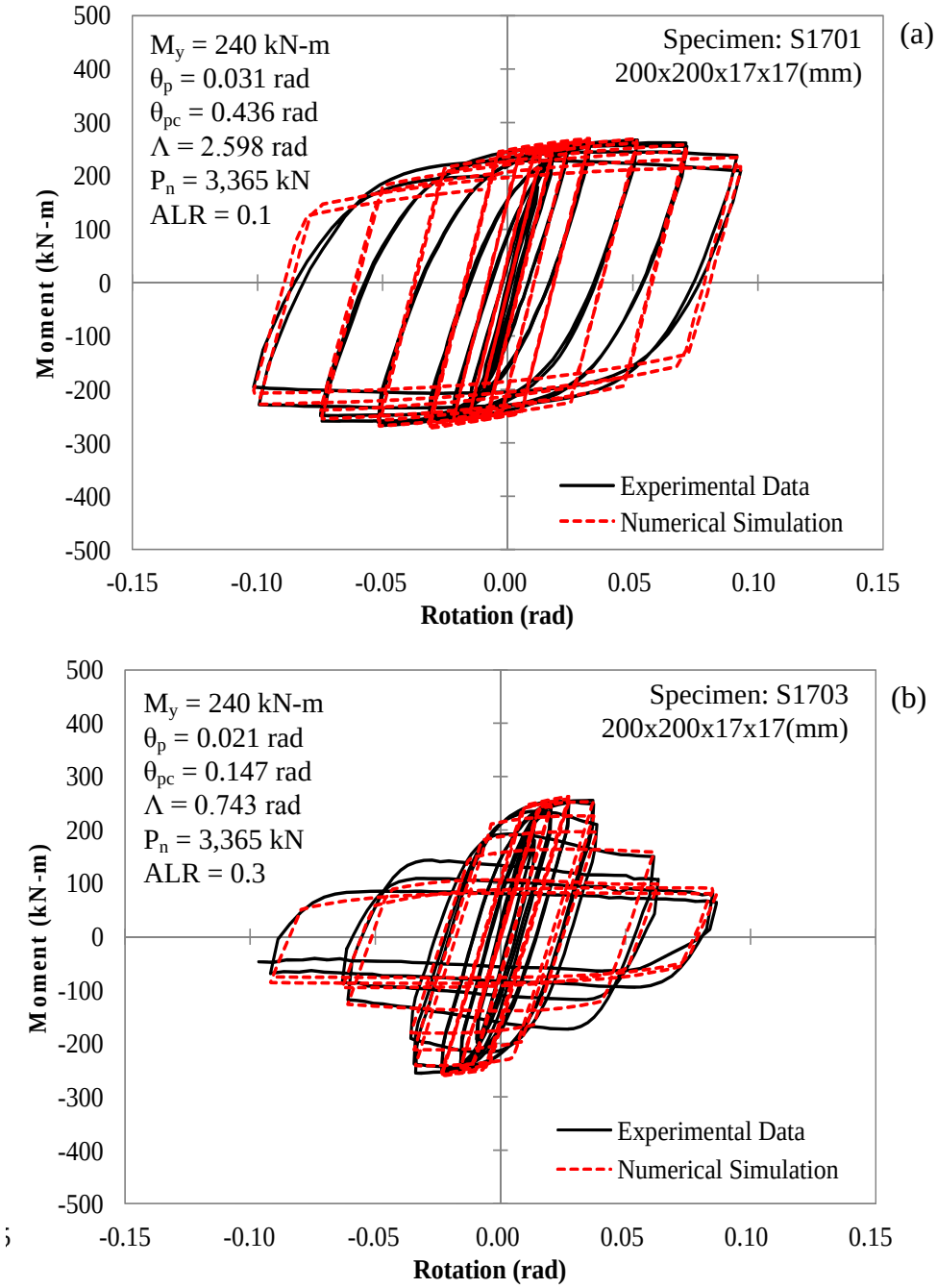

Figure 4-20: Sample analytical versus experimental column moment-rotation hysteretic response under varying ALR: 0.1(a) and 0.3 (b).
Source: Molina Hutt et al. (2017).

Table 4-10: Non-linear beam and column modelling parameters for 1973 and 2012 building archetypes. Source: Molina Hutt et al. (2017).

Section	M_y (kN-m)	θ_p (rad)	θ_{pc} (rad)	Λ (rad)	$\theta_{p-fract}$ (rad)	ALR (-)	P_t(kN)	A_{SPLICE} (%)	Z_{SPLICE} (%)
W36x232	4,758	0.023	0.175	1.51	0.003	-	-	-	-
W36x210	4,260	0.022	0.152	1.31	0.003	-	-	-	-
W36x194	3,918	0.020	0.138	1.15	0.004	-	-	-	-
W33x201	3,949	0.019	0.114	1.01	0.007	-	-	-	-
W30x173	3,094	0.020	0.115	1.02	0.011	-	-	-	-
W30x148	2,547	0.023	0.150	1.20	0.011	-	-	-	-
W27x161	2,625	0.023	0.132	1.23	0.015	-	-	-	-
W24x103	1,427	0.025	0.155	1.25	0.019	-	-	-	-
R(in) 22x22x3x3	11,197	0.046	0.340	4.91	-	0.3	55,782	58	73
R(in) 20x20x2.5x2.5	7,903	0.043	0.320	4.17	-	0.3	42,815	59	74
R(in) 18x18x2x2	5,277	0.041	0.350	4.00	-	0.3	31,316	59	74
R(in) 16x16x1.5x1.5	3,245	0.038	0.350	3.32	-	0.2	21,285	61	76
R(in) 14x14x1x1	1,736	0.031	0.310	2.19	-	0.2	12,722	64	78
W36x395	7,603	0.019	0.338	2.37	-	-	-	-	-
W36x361	6,905	0.019	0.301	2.04	-	-	-	-	-
W36x330	6,275	0.018	0.268	1.75	-	-	-	-	-
W36x330	6,275	0.018	0.268	1.75	-	-	-	-	-
W36x282	5,302	0.017	0.216	1.34	-	-	-	-	-
W33x241	4,188	0.018	0.203	1.28	-	-	-	-	-
W33x201	3,475	0.017	0.160	0.96	-	-	-	-	-
I(in) 60x30x4x10	113,475	0.019	0.638	10.08	-	0.1	185,942	100	100
I(in) 60x30x3x8	95,237	0.017	0.454	6.00	-	0.1	149,732	100	100
I(in) 60x30x2.5x6	76,288	0.015	0.325	3.96	-	0.1	117,437	100	100
I(in) 40x20x2x5	27,001	0.025	0.483	5.78	-	0.1	63,612	100	100
I(in) 35x20x2x3	15,999	0.029	0.359	5.10	-	0.1	43,550	100	100
I(in) 30x20x2x1.5	9,389	0.030	0.251	3.35	-	0.1	29,115	100	100

4.2.3 Non-linear panel zones

Panel zones are modelled using the Krawinkler model as outlined in PEER (2010b), which incorporates an assembly of rigid links and rotational springs. The rigid links extend out to represent the true dimensions of the panel zone. The non-linear springs are calibrated to capture the trilinear shear force-deformation relation based on the geometric and material properties. Panel zones are assumed to be non-degrading. Figure 4-21 illustrates sample calibrations between the analytical models (LS-DYNA) and experimental test data (obtained from Lignos 2013) for a W column section, consistent with the modern archetype, and HSS section, consistent with the 1973 archetype. These results indicate good agreement between the analytical simulations and the experimental tests.

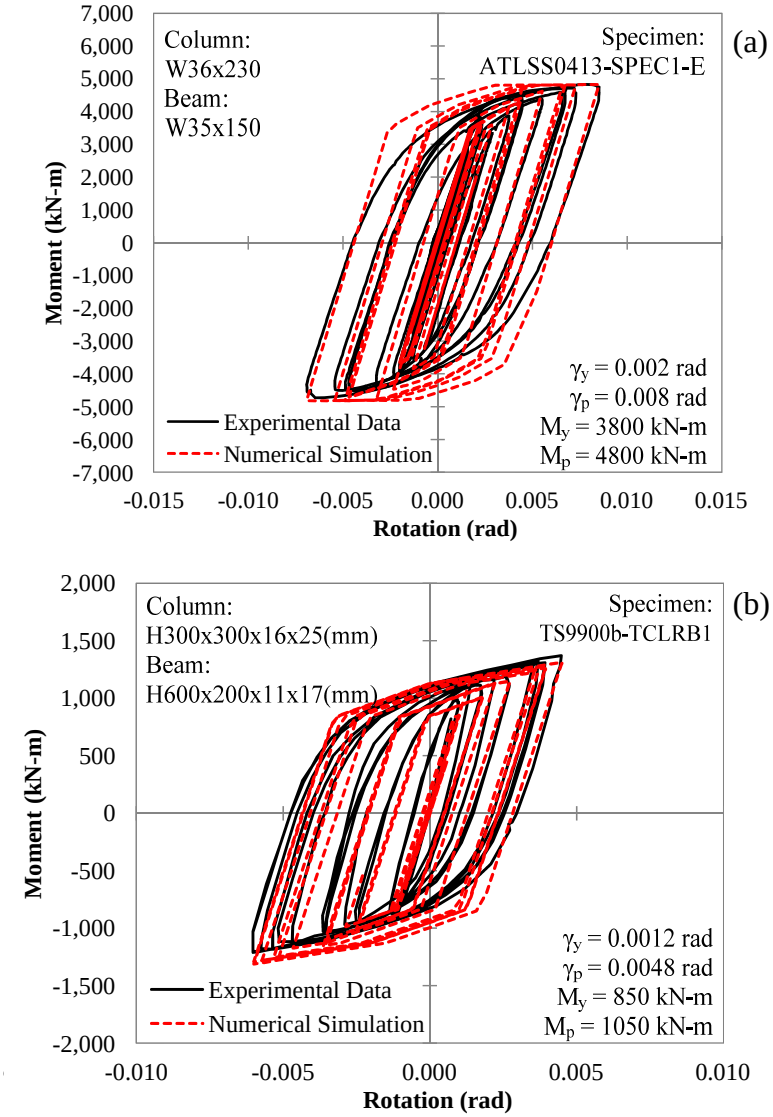

Figure 4-21: Sample analytical versus experimental response of panel zones in W (a) and HSS (b) column sections.
Source: Molina Hutt et al. (2017).

4.2.4 Other analysis assumptions

For analysis purposes, two-dimensional (2D) models of a representative frame are used in the study of the 50-storey 1973 and 2012 archetype buildings. This approach is commonly employed in the literature for analytical studies of moment frame buildings in which a large number of simulations are employed, e.g. as Sattar and Liel (2016), Hwang and Lignos (2017), Haselton et al (2011), etc. Analytical models are subject to ground motions in conjunction with expected gravity loads associated with the seismic weight of the structure. In these analysis simulations, the seismic weight includes self-weight, superimposed dead load, and 25% of the unreduced live loads as recommended by PEER (2010a). For the 1973 archetype building (space frame), the seismic weight is approximately that of the corresponding tributary area of the frame. However, for the 2012 archetype building (perimeter frame), the seismic weight corresponding to a representative frame is greater than its tributary area. Therefore, a leaning column is included in the modern archetype building model to support the corresponding seismic weight and include relevant p-delta effects in the analysis. The leaning column approach is also adopted in the sample studies previously mentioned in order to capture p-delta effects. A value of 2.5% damping is assumed in the analysis as recommended by PEER (2010a). A fixed base is assumed at ground level and soil-structure interaction is not considered.

4.2.5 Global response: comparison against instrumented buildings

In order to check whether the response of the 1973 archetype building is representative of the existing tall building stock, its response is compared to that of an instrumented 1970s 42-storey steel MRF building in downtown San Francisco: The Chevron building, whose response during the 1989 Loma Prieta earthquake was instrumented (CESMD 2007) at an epicentral distance of 96 km. The Chevron building has an overall height of 167 m (550 ft) and is rectangular in plan: 24 m (79 ft) by 46 m (151 ft). The first three modal periods of the structure are 5.4, 1.8 and 1.1 seconds in the short building direction, and 5.1, 1.7 and 1.0 seconds in the long building direction (Anderson and Bertero 1998). Construction of the Chevron building was completed in 1975; hence its design is believed to be consistent with the requirements of the 1973 UBC. The acceleration time histories recorded during Loma Prieta at the base of the building were obtained from (CESMD 2007) at USGS Station 1446 and used as inputs at the base of the analytical model of the 1973 50-storey archetype. The ground motion spectra recorded at the site has spectral acceleration values at long periods that are well below the design earthquake response spectrum as shown in Figure 4-22.

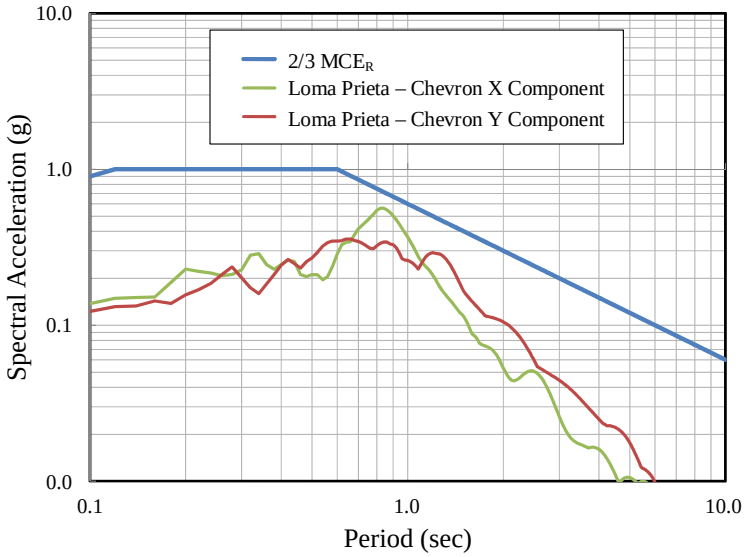

Figure 4-22: Design response spectrum versus ground motion spectra recorded at the base of the Chevron Building during 1989 Loma Prieta Earthquake.

Table 4-11 illustrates a comparison of the mean peak storey acceleration (PFA) and displacement (D) response in each principal building direction for the Chevron building versus the 1973 archetype. The results indicate that the mean response of the 1973 archetype is consistent with that measured in the Chevron building. Inspection following the earthquake did not reveal any damage (Anderson and Bertero 1998). These observations are consistent with the analysis results of the 1973 archetype, whose response under the Loma Prieta ground motion is linear elastic.

Table 4-11: Mean peak storey acceleration (PFA) and displacement (D) comparison between the instrumented Chevron building and the 1973 archetype building during Loma Prieta earthquake.
Source: Molina Hutt et al. (2017).

Storey	Chevron Building		1973 Archetype		Min/Max Ratio	
	PFA (g)	D (m)	PFA (g)	D (m)	PFA (-)	D(-)
Base	0.12	0.0	0.12	0.0	1.0	1.0
25	0.19	0.084	0.14	0.086	0.74	0.98
30	0.17	0.071	0.16	0.110	0.94	0.65
42	0.18	0.105	0.20	0.125	0.90	0.84

4.2.6 Collapse simulation

While the response of the 1973 archetype building during Loma Prieta is consistent with the measured response of an existing tall building in downtown San Francisco, no data is available to validate the behaviour of the 1973 archetype building at high earthquake ground motion

intensities. At high return period events, some simulations of the 1973 archetype building may predict collapse. To ensure that the numerical simulations accurately capture expected collapse mechanisms, the response of a simulation triggering collapse is presented here. In this study, only sidesway collapse is considered, where structural collapse is assumed to occur when the lateral displacement of a storey or number of storeys, due to p-delta effects and component deterioration, causes dynamic instability. This dynamic instability is caused when the lateral displacement of the structure increases without bounds. Figure 4-23 illustrates a sample collapse mechanism near the top of the building, including a contour of the rotation performance levels of beams and columns throughout the frame, as defined per ASCE 41 (ASCE 2012) and the sample hysteretic response of beams and columns in the storeys in which the collapse mechanism is observed. The results shown in Figure 4-23 indicate that, in this collapse realization, a large concentration of deformation takes place in the top of the building with a non-uniform distribution of ductility, as the remainder of the structure shows significantly lower levels of rotation demand. Similar concentrations of deformation in a small number of storeys are observed in other collapse realizations. These concentrations of deformation in a small number of storeys are also observed at different locations, e.g. near the base or mid-height, depending on the ground motion input.

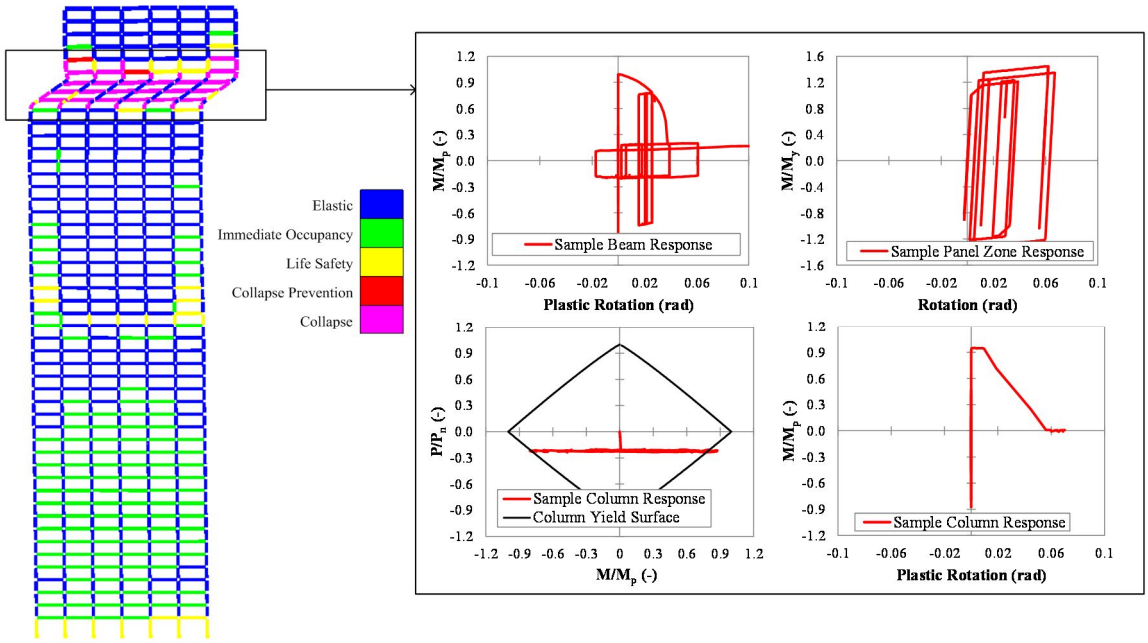

Figure 4-23: Collapse realization results including contour plot illustrating ASCE 41 rotation performance levels as well as sample hysteretic response of a sample beam, panel zone and column in the storeys in which a collapse mechanism is observed.
Source: Molina Hutt et al. (2017).

While no experimental or observed data is available to validate the collapse of a 50-storey steel MRF building such as the one considered in this study, other studies, such as Lignos et al. (2011), have analytically predicted collapse of a steel framed-structure reproducing the results of shake table tests, demonstrating that collapse can be predicted fairly well.

4.2.7 Adjustments for 40- and 20-storey archetypes

The 40- and 20-storey analysis models differ from those of the 50-storey building in that they are 3D as previously shown in Figure 4-17. In these 3D models, in addition to the structural components previously described, concrete slabs are also modelled as elastic cracked concrete 2D shell elements to represent a flexible floor diaphragm. The approach to model columns is as previously described and interaction between bi-axial bending moment and axial force is captured. Similarly, the modelling of the panel zones follows a consistent approach and their behaviour in orthogonal directions is assumed to be de-coupled. The key difference in these simulations is that the beams, which are also modelled as lumped plasticity elements, take a slightly different approach to incorporate the occurrence of fracture in the connections. The beam modelling includes a random fracture model in which the plastic rotation at which fracture occurs is a random variable characterized by a truncated normal distribution as shown in Figure 4-24.

The random fracture model is in accordance with the methodology proposed by Maison and Bonowitz (1999) where the plastic rotation capacity is modelled as a random variable, represented by a truncated lognormal distribution with a mean of 0.006 radians and a standard deviation of 0.004 radians. The truncated tail at zero plastic rotation denotes fracture prior to yield, which is supported by data from the SAC studies (SAC 2000). When fracture prior to yield occurs, fracture is set at 70% of the moment capacity of the beam. The residual moment capacity after fracture is set at 25% of the beam capacity. For each of the analysis runs, subject to a unique earthquake record, a different value of plastic rotation at fracture is assigned for each of the moment connections in the building model by sampling from the probability distribution. Therefore, all analysis runs with these models have a unique distribution of plastic rotation capacities throughout the structure. The benefit of the random fracture model is the simplicity with which the random performance in pre-Northridge moment connections is captured. The benefit of the ASCE 41 approach is that the plastic rotation at fracture is dependent on the beam depth (deeper sections have less plastic rotation capacity), an observation from experimental tests and field observations that the random fracture model fails to capture.

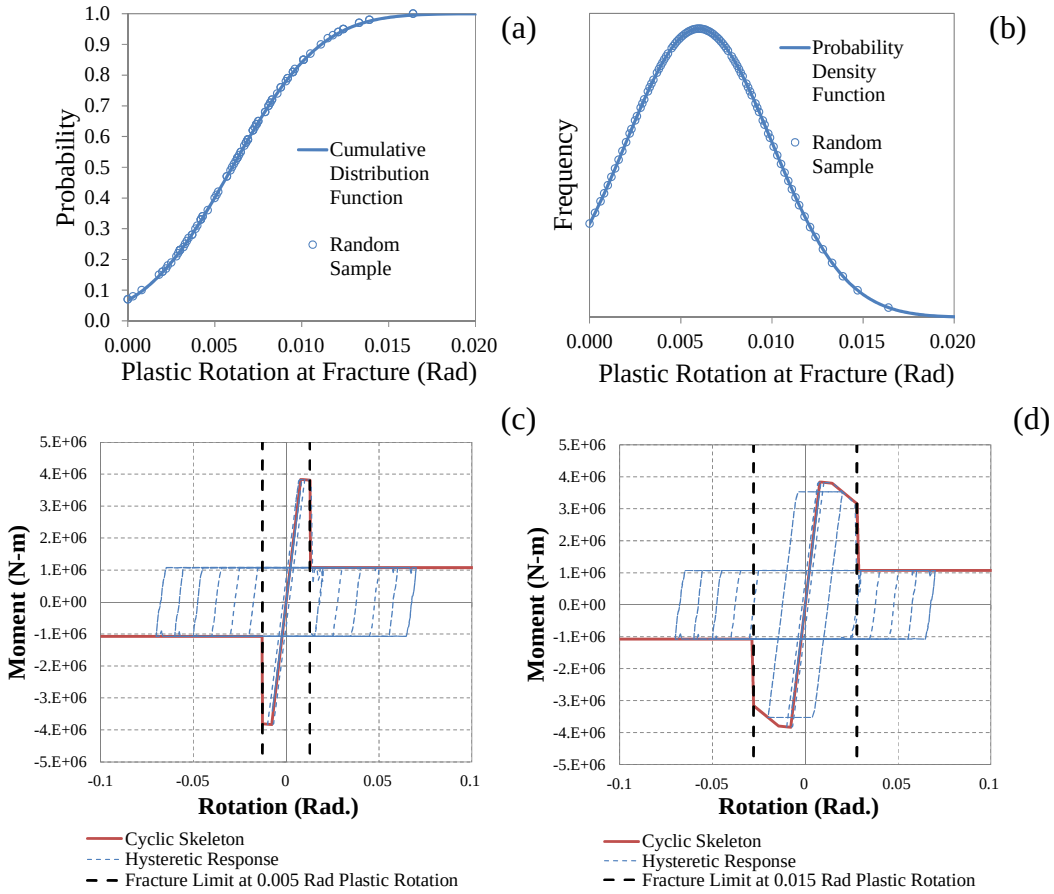

Figure 4-24: Probability distributions CDF (a) and PDF (b), and sample hysteretic response of moment rotation in beam to column moment connections under different levels of plastic rotation at fracture: 0.005 rad (c) and 0.015 (d).

4.3 Building performance model

Communicating performance as the probable consequences in terms of direct economic losses to repair earthquake damage can influence decision making. Financial institutions use quantitative statements of probable building repair cost expressed as a percentage of building replacement value. This metric is used in this work, where the costs are expressed in present dollars. Losses are expressed as a percentage of repair cost, i.e. the cost required to restore a building to its pre-earthquake condition, over total building cost, i.e. the cost required to rebuild with a new structure of similar construction. In this study, total replacement cost includes replacement of basic building structure, exterior enclosure; MEP infrastructure and fitouts. Demolition and site clearance are not included in the total replacement cost. Based on a Class 5 rough order-of-magnitude cost estimate based on the Association for the Advancement of Cost Engineering (AACE), the most likely estimated cost for the archetype buildings in San Francisco in present dollars is \$3,550/m^2 (\$330/ft^2) with an accuracy range of -5 to +30%.

While seismic loss estimates associated with direct economic losses enable discussions with building owners and investors about how individual retrofit interventions can move buildings in the direction of becoming more resilient, they do not provide a quantitative measure of resilience. In addition to direct economic losses, there is great vulnerability to indirect economic losses due to downtime, defined as the time required to achieve a recovery state after an earthquake. SEAONC defines three recovery states: re-occupancy of the building, pre-earthquake functionality and full recovery (Bonowitz 2011). Re-occupancy occurs when the building is deemed safe enough to be used for shelter, though functionality may not be restored. Functional recovery occurs when the building regains its primary function, i.e. it is operational. Lastly, full recovery occurs when the building is restored to its pre-earthquake condition, it follows from functional recovery once additional repairs for aesthetic purposes have been completed. Downtime to re-occupancy and functional recovery are considered in this work. In this study, the building performance model is defined as a model to assess the probability of earthquake losses and downtime. The methodology followed for the loss and downtime assessment is summarized in Figure 4-25. In addition to providing best estimates of downtime to achieve a certain recovery state, this work proposes a method to develop recovery curves that provide an indication of the re-occupancy and functionality ratio of a building over time.

4.3.1 Loss assessment methodology

As illustrated in Figure 4-25, EDPs, including maximum IDRs and PFAs, are obtained from the NLRHA at every storey in the building under consideration. These parameters are used as input demands to the building performance model, which contains structural and non-structural components at each storey level for all components in the building that are susceptible to earthquake damage. Structural component quantities are based on the structural design of the archetype buildings. Non-structural component quantities are estimated based on typical quantities found in buildings of similar occupancy by use of the Normative Quantity Estimation Tool (FEMA 2012). Normative quantities are an estimate of the quantity of components and contents likely to be present in a building of a specific occupancy based on gross square footage. FEMA (2012) developed these quantities based on a detailed analysis of approximately 3,000 buildings across typical occupancies. This study assumes estimates of quantities at the 50^{th} percentile level. For this study, the components and quantities estimated by the Normative Quantity Estimation Tool were verified with registered engineers to confirm the validity and relevance of such components to a tall building designed in the mid-1970s, and adjusted where necessary.

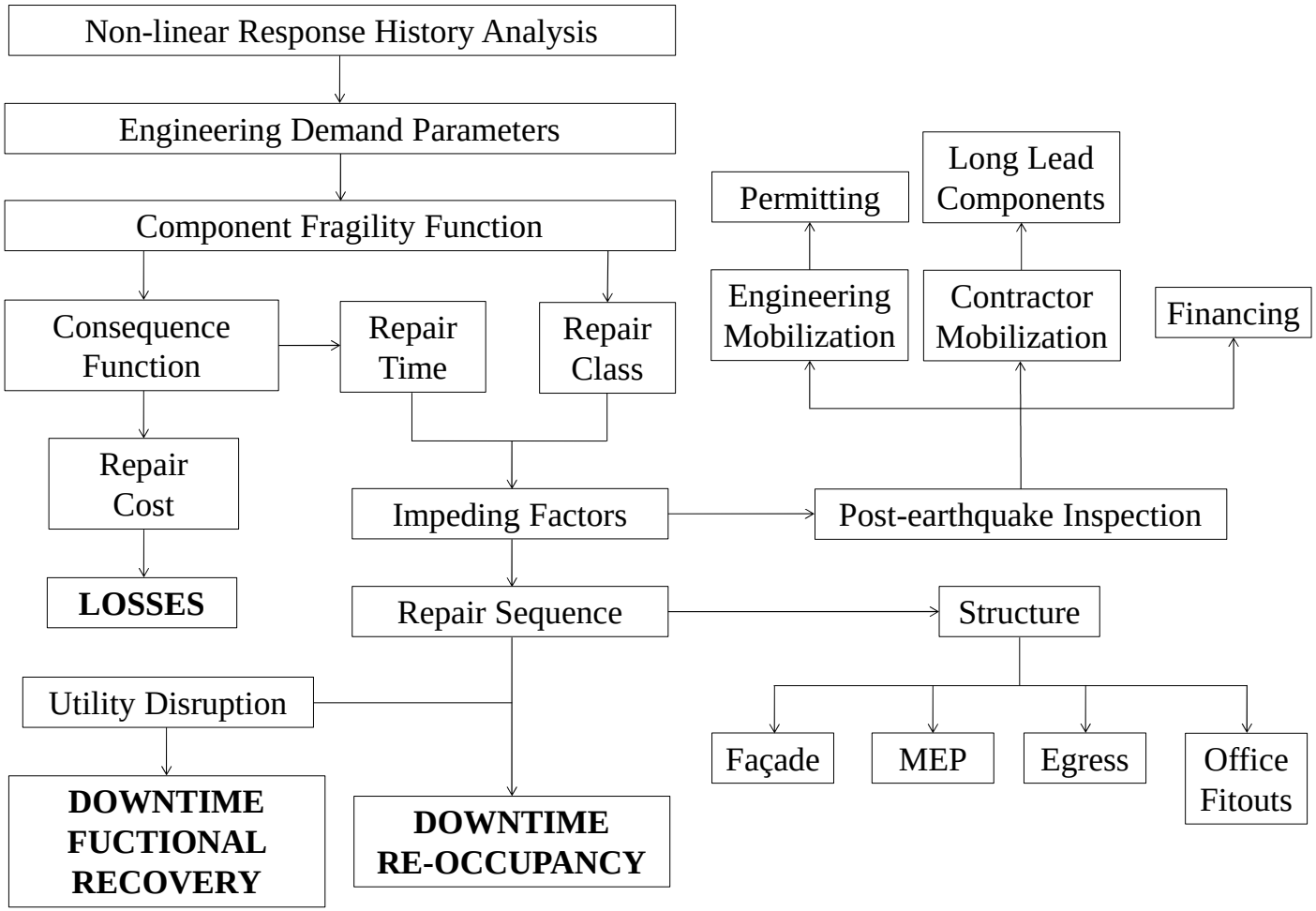

Figure 4-25: Loss and downtime assessment methodology.
Source: Molina Hutt et al. (2015).

Table 4-12 provides fragility numbers, category, description and source for a sample of components included in the 50-storey 1973 archetype building performance model. A component's fragility number is a unique classification code based on building specifications, cost estimating and cost analysis standards (NIST 1999). The component category is a general description for grouping of components with a similar function, e.g. structural elements, fitouts, MEP components, etc. The description provides an overview each individual component, e.g. within structural elements you may find column base plates, splices, beam-to-column connections, etc. The sources provide a reference to authors whose work was used to develop relevant component fragilities within the FEMA P58 project. A detailed list of all components included in the building performance models for all archetype buildings considered in this work is included in Appendix C.

Each one of these structural and non-structural building components has a component fragility function. A component fragility function is a statistical distribution that indicates the conditional probability of incurring damage at a given value of demand. The fragility function is typically assumed to be a cumulative lognormal distribution. Component fragility functions are defined for each damage state in the component. For instance, standard partition walls, designated in Table 4-12 by fragility C1011.001a, have 3 possible damage states (DS): DS1 consists on minor cracking of the wall board, DS2 consists on moderate cracking or crushing of the wall boards typically around corners, and DS3 consists on significant cracking or crushing of the wall boards and buckling of studs (FEMA 2012), as illustrated in Figure 4-26. Each damage state has an associated consequence function, from which the repair cost and repair time associated with the level of damage in the component is estimated. Within the FEMA P58 fragility database, professional construction cost estimators developed relevant consequence data. These estimates were also checked by independent reviews of the resulting cost and repair data (FEMA 2012).

In addition to the information presented in Table 4-12, the information in Appendix C provides a more comprehensive description of each component, as well as additional parameters including EDPs, Quantity (Qty.), Units, Distribution, Number of Damage States (NDS), Median (μ), Dispersion (β), Mean Repair Cost (MRC) and Mean Repair Time (MRT) for all Damage States (DS_i). The 'EDP' denotes the demand parameters that are used to predict damage in each component. The 'Qty.' term indicates the total amount of fragility units considered within each building performance model, e.g. if a particular component fragility represents 1000 linear feet of partition wall and there are 20000 ft of partition walls in the building, the 'Qty.' for that particular component is 20. The 'Units' describe the measure of

each component, e.g. 1000 linear feet in the previous example. The ‘Distribution’ describes how the total ‘Qty.’ of each component is distributed throughout the building, e.g. large MEP components are generally distributed within the MEP floors of a building. The ‘NDS’ column indicates the number of possible damage states for each component. The ‘μ’ and ‘β’ terms denote the median and dispersion associated with the cumulative probability distribution that defines each damage state within the fragility function. The tabulated fragilities are dimensionless for components whose EDP is IDR or residual IDR, and units of g for components whose EDP is peak floor acceleration (PFA). The ‘MRC’ and ‘MRT’ terms describe the mean repair cost and time associated with the corresponding damage state in the component, in units of USD and worker-days, respectively.

The components employed in the building performance model for the archetype 50-storey building designed per IBC 2012 are consistent to those of the 50-storey 1973 archetype building, but fragilities are adjusted to account for modern seismic design requirements of structural and non-structural components. This adjustment is possible because the fragility library developed for the FEMA P58 project includes variations of the same component adjusted for different seismic design categories. For the IBC 2012 archetype building, seismic design category D (as discussed in Section 4.1.1) is selected for relevant non-structural components. For the UBC 1973 archetype building, non-seismically rated components are selected as there was no consideration of seismic design of non-structural components in the 1970s building codes. The library also includes a variety of component types for certain elements, e.g. beam-to-column connections, to account for important changes in design and construction practice, i.e. pre- and post-Northridge moment connection detailing.

Table 4-12: Fragility numbers, category, description and source for a sample of components included in the 50-storey 1973 archetype building performance model.

Fragility Number	Category	Description	Source
B1031.011c	Structure	Steel Column Base Plates	Deierlein and Victorsson (2008)
B1031.021c	Structure	Welded Column Splices	Deierlein and Victorsson (2008)
B1035.042	Structure	Pre-Northridge Beam-Column Joint	Deierlein and Victorsson (2008)
C1011.001a	Fitouts	Wall Partition	Miranda and Mosqueda (2011)
C3027.001	Fitouts	Raised Access Floor	Eidinger (2009)
C3032.001c	Fitouts	Suspended Ceiling	Bachman (2011)
C3034.001	Fitouts	Independent Pendant Lighting	Eidinger (2009)
C2011.001b	Egress	Prefabricated Steel Stair	Higgings (2011)
D2021.011a	MEP	Cold or Hot Potable Piping	Bachman (2012)
D2022.021a	MEP	Heating Hot Water Piping	Bachman (2012)
D3052.011d	MEP	Air Handling Unit	Porter (2011)
D5012.013a	MEP	Motor Control Centre	Porter (2011)
D2031.021a	MEP	Sanitary Waste Piping	Bachman (2012)
D3041.012a	MEP	HVAC Ducting	Bachman (2012)
D4011.021a	MEP	Fire Sprinkler Water Piping	Bachman (2012)
D3041.031a	MEP	HVAC Drops / Diffusers	Bachman (2012)
D4011.031a	MEP	Fire Sprinkler Drop	Bachman (2012)
D3041.041a	MEP	Variable Air Volume (VAV) Box	Bachman (2012)
D3031.011d	MEP	Chiller	Porter (2011)
D3031.021d	MEP	Cooling Tower	Porter (2011)
D5012.021a	MEP	Low Voltage Switchgear	Porter (2011)
B2011.201a	Façade	Precast Concrete Panels	FEMA (2012)
D1014.014	Egress	Vertical Transportation System	(Ibbi Almufti, personal communication 2012)

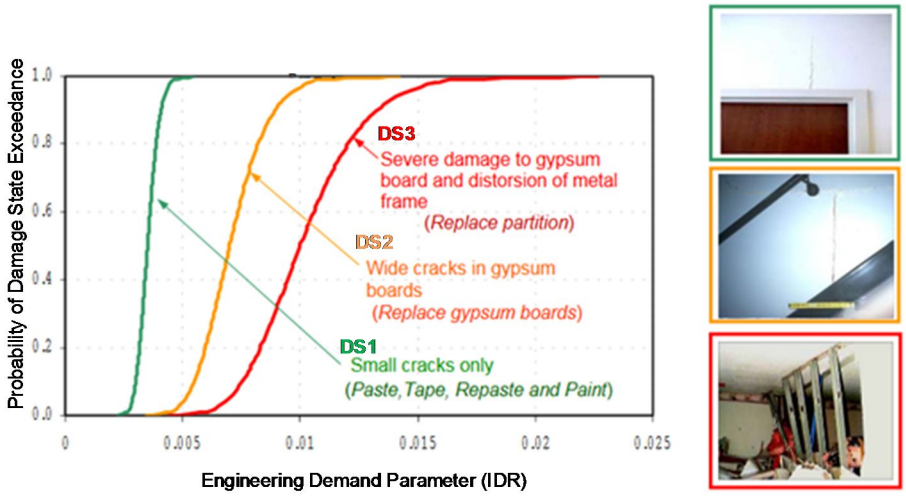

Figure 4-26: Fragility function (and repair consequence) for a standard partition wall. Source: Adapted from FEMA (2012b).

Since there are many factors that can affect performance, such as intensity of ground shaking, building construction quality, building response, or vulnerability of contents among others, there is significant uncertainty in the predicted performance of the building. This uncertainty can be accounted for by means of Monte Carlo simulation, where hundreds of performance realizations are carried out. Each realization represents one possible performance outcome for the building considering a single combination of possible values of each variable considered. Therefore, losses can be expressed as a performance function, i.e. probability of losses of a specified amount or smaller incurred as a result of an earthquake. This methodology to conduct the loss estimates, which can be implemented in tools such as PACT (2012) or SP3 (2017), is used for this study, where each performance assessment consists of 1000 realizations. For each realization, the calculations are as follows: (i) the occurrence of EDPs is estimated from the results of NLRHA; (ii) fragility functions are used in conjunction with EDPs to determine a DS for each component; (iii) consequence functions are then used to translate damage states into repair costs and times (FEMA 2012). The direct economic losses for each realization are then estimated by conducting this calculation for every component at every storey throughout the building.

When estimating losses, residual IDRs are also an important consideration, as they enable accounting for scenarios in which the building is damaged beyond repair. Typical building repair fragility as a function of residual IDR is a lognormal distribution with a median value of 1% and a dispersion of 0.3 (FEMA 2012). In this work, residual IDRs are obtained from NLRHA and checked against published recommendations to derive residual IDRs as a function of peak transient response and yield drifts (FEMA 2012). For each realization, the

analysis uses the maximum residual storey drift together with the building repair fragility to determine if the building is deemed irreparable. If irreparable, repair cost and repair time are taken as the building replacement values. A similar approach is followed to consider collapse contribution to losses by means of a collapse fragility, also developed from the results of NLRHA.

4.3.2 Downtime assessment methodology

In order to provide a more direct measure of resilience, the downtime to achieve building re-occupancy and functional recovery is assessed in this study. These estimates follow the Resilience-based Earthquake Design initiative (REDi) guidelines (Almufti and Willford 2013). These guidelines provide a detailed downtime assessment methodology for individual buildings, and identify the likely causes of downtime such that these can be mitigated to achieve a more resilient design. The methodology identifies the extent of damage and criticality of building components that may hinder achieving a recovery state. It provides a logical approach for labour allocation and repair sequencing including structural, interior, exterior, mechanical, electrical, elevator and stair repairs on a floor per floor basis. Furthermore, the methodology includes delay estimates associated with impeding factors, defined as those factors which may impede the initiation of repairs such as post-earthquake inspection, engineering mobilization for review or re-design, financing, contractor mobilization, permitting and procurement of long lead items. Lastly, utility disruptions are also considered when estimating downtime for functional recovery.

The methodology identifies the extent of damage and criticality of building components that may hinder achieving a recovery state through the introduction of repair classes. Repair classes are assigned to the each damage state for each building component. A repair class with a value of 3 indicates that damage in the component hinders building re-occupancy. A repair class with a value of 2 indicates that damage in the component hinders functional recovery. Lastly, a repair class with a value of 1 indicates that damage in the component hinders full recovery. The repair classes for each damage state in all components included in the building performance models are included in Appendix C. If the damage in any component hinders achieving a certain recovery state, the component needs to be repaired before such recovery state can be achieved.

Following an earthquake, a building owner is expected to submit an inspection request if the structural integrity of the building is in question. Furthermore, the jurisdiction, tenants or

insurance companies may also request an inspection regardless of the extent of damage. Following such post-earthquake inspections, as illustrated in Figure 4-25, there are three distinct sequences of delays due to impeding factors, the longest of which is assumed to be the controlling factor and is used in the downtime estimate. The first sequence of delays is related to engineering mobilization, review or re-design, and permitting. This accounts for the time required to engage an engineer for structural assessment if there is structural damage to the building, perform relevant structural calculations, as well as re-design and issue drawings depending on the level of damage to the structure. The second sequence of delays concerns contractor mobilization. The time required to mobilize a contractor is dependent on a number of factors such as the severity of damage, bidding or building height among others. Furthermore, the mobilization of a contractor to conduct repair work on tall buildings is dependent on the availability of tower cranes. In addition to contractor mobilization, long lead components are a key consideration of downtime. These components are not readily available in normal circumstances or are custom made. The repair schedule can be significantly impacted by long lead components as these items cannot be replaced until they have arrived on site. Long lead delays for relevant components are included in Appendix C. The last sequence of delays is related to financing. The lack of financing to fund repair work can result in significant delays. If the losses associated with earthquake damage exceed the funds available to fund repair work, additional sources of funding need to be sought out. The delays associated with securing such funds are dependent on the method of financing, e.g. private loan versus insurance. A summary of the assumed delays associated with each of the impeding factors is shown in Table 4-13.

Following any delays associated with impeding factors, repair work can commence. A logical approach for labour allocation and repair sequencing of structural and non-structural components on a floor per floor basis is used in this work. The repair sequence defines the order in which repairs take place. As illustrated in Figure 4-25, structural repairs need to be conducted at any given floor before repairs to other building components at that level (or above) can commence. Non-structural repairs are divided into the following categories: egress (stairs and elevators), façade (exterior partitions and cladding), MEP and office fitouts (HVAC systems, partitions and ceiling tiles). Once structural repairs at any given floor are complete, repair of non-structural components can commence, following a rational approach, e.g. repair of interior partition walls cannot commence until HVAC ducts have been repaired. The repair sequence associated with each component in the building performance model is included in Appendix C. Overall repair time is estimated from the fragility function consequence data, which expresses repair time in number of days for a single worker to complete the work

(worker days), and the labour allocation for each floor in the building. Table 4-14 illustrates the labour allocation parameters employed in the repair work estimates. To account for subcontractor resource limitations, the number of workers repairing a certain type of component is limited. Such limit is also included in Table 4-14. Furthermore, the total number of workers in the building is also limited by the number of workers allocated to a project. Following discussions with contractors and cost estimators, the REDi guidelines define the total number of workers on the project as a function of the square footage of the building, which for the 50-storey archetype building corresponds to 114 workers. Work across multiple floors can take place simultaneously as long as the above constraints are met.

Lastly, utility disruption is also considered when estimating downtime for functional recovery. Disruption to the water, gas and electrical systems is considered. The time required for achieving a 50% recovery of the system is assumed as 21, 42 and 3 days for water, gas and electrical systems, respectively. Acknowledging the difficulty in performing accurate predictions of utility disruption, the REDi guidelines present a best estimate of recovery based on an assessment of performance of these systems in past earthquakes. In the present study, utility disruption does not control over other impeding factors in the overall downtime assessment and therefore do not have a direct impact on the downtime estimates. Equation 4-13 illustrates the overall downtime calculation by subdividing delays into the following categories: utility disruption, impeding factors and repair work.

$$\text{Downtime} = \text{MAX}\left\{\begin{array}{l}\text{Utility Disruption}^{*}\\ \text{Impeding Factor Delays}\end{array}\right\} + \text{Repair Work}^{**} \qquad \text{Equation 4-13}$$

**For Full recovery and Functional Recovery only*
***Including delays associated with long lead time components*

Table 4-13: Assumed delays associated with impeding factors.
Source: Molina Hutt et al. (2015).

Impeding Factor	Other Conditions	Mean	Dispersion
Post-Earthquake Inspection	-	5 days	0.54
Engineering Mobilization	Damage to structural components hinders full recovery [Repair Class=1]	6 weeks	0.40
	Damage to structural components hinders functional recovery or re-occupancy [Repair Class ≥2]	12 weeks	0.40
Contractor Mobilization	Damage to any component hinders full recovery [Repair Class =1]	28 weeks	0.30
	Damage to any component hinders functional recovery or re-occupancy [Repair Class ≥2]	40 weeks	0.31
Financing	Private Loans	15 weeks	0.68
Permitting	Damage to structural components hinders full recovery [Repair Class =1]	1 week	0.90
	Damage to structural components hinders functional recovery or re-occupancy [Repair Class ≥2]	8 weeks	0.32

Table 4-14: Assumed labour allocation parameters for repair time estimates.
Source: Molina Hutt et al. (2015).

Component Category	Number of Workers	Maximum Number of Workers
Structure	1 per 500 ft^2	20
Façade	1 per 1000 ft^2	45
Office Fitouts	1 per 1000 ft^2	45
Egress	2 per Damaged Unit	27
MEP	3 per Damaged Unit	18

4.3.3 Recovery functions

Providing best estimates of downtime to achieve a certain recovery state following a damaging earthquake is a step towards the quantification of resilience. However, the loss and downtime assessment methods outlined in Sections 4.3.1 and 4.3.2 fall short of providing an understanding of recovery with time, which is an important consideration for emergency planning and informing post-earthquake recovery efforts, e.g. understanding the ability of residents to shelter in place can help inform temporary shelter needs. Due to the large number of uncertainties associated with the calculation of different recovery paths, a method is proposed here to enable the development of recovery functions probabilistically, by integrating the REDi's downtime assessment methodology (as described in Section 4.3.2) with FEMA P58's framework for assessing damage, losses and repair time (as described in Section 4.3.1). The method is developed to calculate recovery functions to achieve two recovery states: (a) re-occupancy and (b) functional recovery. A schematic of a sample recovery function produced following this method is outlined in Figure 4-27.

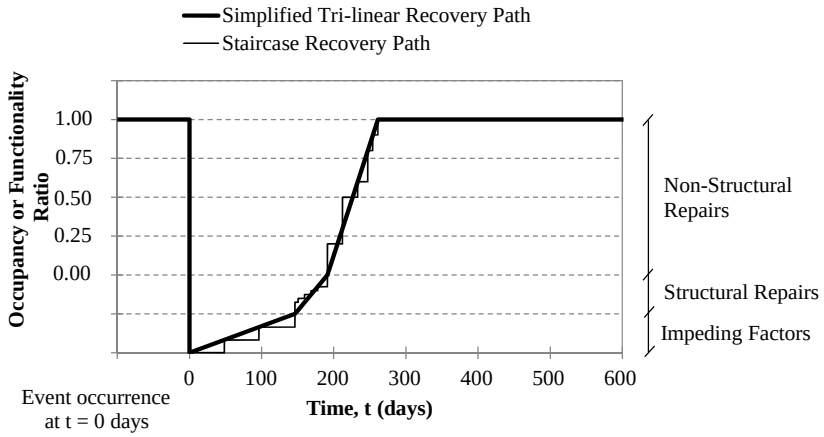

Figure 4-27: Simplified tri-linear recovery path to re-occupancy or functional-recovery.

The recovery path is simplified as a tri-linear function with three distinct recovery phases: (a) impeding factor delays, (b) structural repairs, and (c) non-structural repairs. The tri-linear function is a simplification of the stepping (staircase) function that would more accurately represent each of the different recovery phases as illustrated in Figure 4-27. The initial phase of the recovery path accounts for impeding factors, which delay the initiation of repairs as described in Section 4.3.2. The staircase function for this initial phase would consist of two or three steps, depending on the critical path, as earlier illustrated in Figure 4-25. At the start and the end of this phase, the occupancy or functionality ratio of the building is zero. Even though the change in the vertical axis associated with this phase does not represent a variation in the occupancy or functionality ratios (as reflected in Figure 4-27), a change in the start and end

ordinates is included in the recovery curve in order to provide a visual illustration of the time without occupancy or functionality associated with this phase.

The second phase of the recovery path is associated with structural repairs. The proposed method assumes that structural repairs throughout the building need to be completed before non-structural repairs can take place. This approach is intended to ensure the safety of workers engaging in non-structural repairs. This assumption differs from that presented in REDi (Almufti and Willford 2013), as discussed in Section 4.3.2, which indicates that non-structural repairs on any floor can commence once structural repairs on that floor are complete. In this phase of the recovery, the steps in the staircase recovery curve shown in Figure 4-27 indicate the progressive completion of structural repairs on each storey throughout the building height. Similar to the first phase, the change in the vertical axis does not represent a variation in the occupancy or functionality ratios, as both values are zero at the start and end of the phase. However, as with the impeding factor phase, a change in the start and end ordinates is also included for a visual illustration of the time without occupancy or functionality associated with this phase.

The last phase of the recovery path accounts for non-structural repairs. The departure of this phase occurs at an occupancy or functionality ratio of zero, as seen in Figure 4-27, and gradually escalates as non-structural repairs are completed incrementally up the building height, reaching unity once all non-structural repairs are complete. In this last phase, the vertical axis indicates the proportion of storeys in the building where repairs of damaged components that hindered achieving a recovery state are complete, e.g. an occupancy or functionality ratio of 0.5 indicates that the 25 storeys in a 50-storey building have completed repairs to those components that hindered re-occupancy or functional recovery.

The construction of the proposed recovery curves requires the development of a number of matrices or datasets, using output produced by PACT (2012) or SP3 (2017), which enable the calculation of the recovery function. The required datasets are illustrated in Figures 4-28 through 4-31, and the calculations associated with the three distinct phases of the recovery curve are described next. These calculations were coded in MATLAB (2015) to enable the calculation of probabilistic recovery functions, calculated for each of the loss realizations previously discussed. The results are later illustrated in Chapter 7. If a realization results in collapse or residual drift rendering the building irreparable, the resulting recovery curve is assumed to be a step function where full recovery is only achieved at a time equal to the building replacement time.

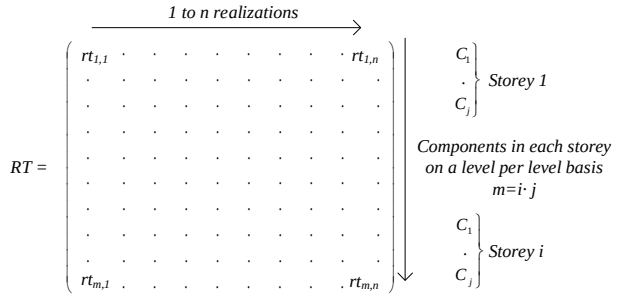

Figure 4-28: Illustration of the Repair Time (RT) matrix or dataset to enable the development of recovery functions.

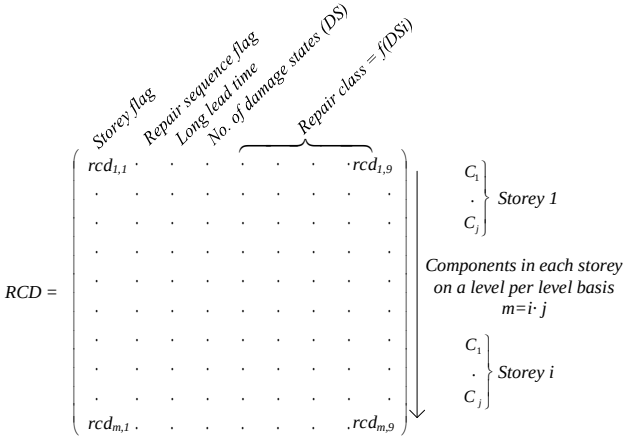

Figure 4-29: Illustration of the Repair Class Database (RCD) matrix or dataset to enable the development of recovery functions.

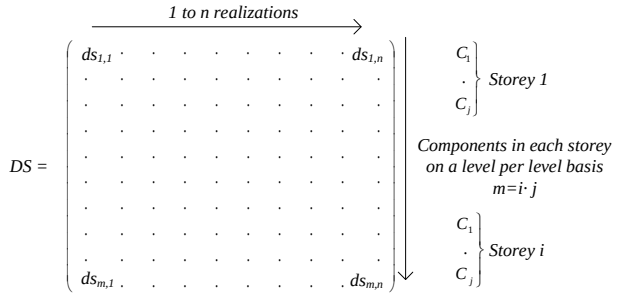

Figure 4-30: Illustration of the Damage State (DS) matrix or dataset to enable the development of recovery functions.

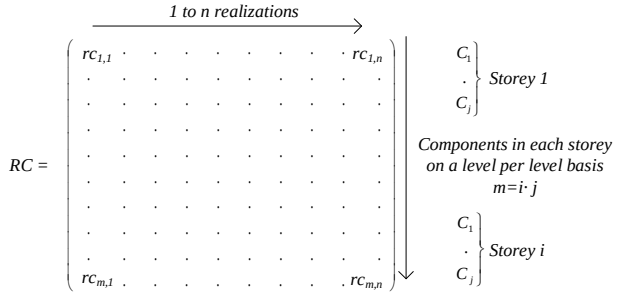

Figure 4-31: Illustration of the Repair Class (RC) matrix or dataset to enable the development of recovery functions.

- Repair Time Matrix

The repair time (RT) matrix can be constructed using direct outputs from PACT or SP3. It consists of a summary of the repair time associated with damage to each component in each floor for each realization conducted in the analysis. The matrix has m rows by n columns, as seen in Figure 4-28, where m is the number of components in each storey in the building performance model ordered on an incremental storey basis, and n is the number of realizations for which building performance is computed.

Compiling the RT matrix may require re-ordering and sorting through the output data from PACT or SP3. For instance, if a drift sensitive component is present in both building directions, the repair times for the component under consideration in each building direction must be considered in each storey where the component is present. The data in the required format can be easily compiled through the use of pivot tables for the sum of repair times per component per floor in each realization.

- Repair Class Database Matrix

Different damage levels in different components hinder achieving a certain recovery state, i.e. re-occupancy, functional recovery or full recovery. The recovery state hindered due to damage in a specific component is summarized in the Repair Class Database (RCD) matrix. In order to automate the downtime calculation associated with different recovery phases, each component must also be linked with a unique repair sequence. Furthermore, if the replacement of the component is a long lead item, the expected delays associated with sourcing this component must also be flagged.

The RCD matrix consists of m rows by p columns, as illustrated in Figure 4-29, where m is the number of components in each storey in the building performance model ordered on an incremental storey basis, and p is an array consisting of a storey flag, repair sequence flag, long lead times, if applicable, the number of possible damage states in each components, and the recovery state hindered by each damage state in each component, expressed through the repair classes introduced in Section 4.3.2.

- Damage State Matrix

The damage state (DS) matrix can be constructed using direct outputs from PACT. It consists of a summary of the expected damage states in each component in each floor for each realization conducted in the analysis. The matrix has m rows by n columns, as illustrated in Figure 4-30, where m is the number of components in each storey in the building performance

model ordered on an incremental storey basis, and n is the number of realizations for which building performance is computed.

As with the RT matrix, compiling the DS matrix may require re-ordering and sorting through the output data. When using SP3 to develop recovery functions, this step is not required as SP3 can directly output the repair class associated with damage to each component in each floor for each realization. This enables understanding whether damage hinders the achievement of a certain recovery state. This information is assembled in the Repair Class (RC) matrix explained next.

- Repair Class Matrix

The repair class (RC) matrix can be constructed by evaluating the results of the DS matrix against the RCD matrix by assessing the damage state in each component, in each floor for each realization against the repair class associated with each damage state. The resulting RC matrix has the same dimensions as the DS matrix, but contains the repair class associated with each component in each storey for each realization, as illustrated in Figure 4-31.

As explained earlier, because SP3 enables the user to input different repair classes associated with each damage state in each component, the RC matrix can be obtained directly from SP3. At the time of writing, these outputs are not accessible within the software interface, but can be requested from the SP3 team as they are produced as an intermediary step in the analysis.

- Calculations associated with structural and non-structural repairs

Once the RT, RCD, DS (if applicable), and RC matrices have been compiled, the calculations associated with the recovery function development can be carried out. As a first step, the RT matrix needs to be filtered such that only the repair time for components with damage that hinders a certain recovery state are considered in the recovery function. This calculation can be easily carried out by means of the RC matrix. For instance, to develop a recovery function to re-occupancy, the RT matrix will be filtered such that repair times are only considered for components with a repair class of 3. For components with lower repair classes, the entries in the filtered RT matrix take a value of zero, i.e. if a component suffers damage that hinders functional recovery, represented through a repair class equal to 2, it does not need to be considered when evaluating recovery to re-occupancy. Similarly, when developing a recovery function to functional recovery, if a component suffers damage that hinders full recovery, represented through a repair class equal to 1, it does not need to be considered when evaluating recovery to functional recovery.

The second step in the calculation is to calculate the repair times per repair sequence, excluding long lead items. Following completion of structural repairs, different repair sequences can be carried out in parallel. Therefore, the repair time associated with each repair sequences needs to be computed. Because the RCD matrix contains a flag for the repair sequence associated with each component in each floor, the repair time associated with each repair sequence can be summed up across each floor in each realization.

The next step is to evaluate the repair times accounting for labour allocation limitations associated with the maximum number of workers in each storey and in each repair sequence. The proposed method assumes recovery for each repair sequence is carried out on a storey per storey basis. The controlling labour allocation limit is the smallest of the maximum number of workers per floor (calculated as a function of gross square footage) and the maximum number of workers per repair sequence (due to contractor constraints). By dividing the repair time for each repair sequence in each storey, by the labour limitations associated with each repair sequence, the actual repair time associated with each repair sequence is obtained. The actual repair times associated with each repair sequence in each storey are then summed for all storeys, providing the total repair time associated for each repair sequence throughout the building. If long lead components require repair to achieve re-occupancy or functional recovery, these delays, as summarized in the RCD matrix, are also added to the relevant repair sequence.

- Calculations associated with impeding factors

In addition to estimating repair times, for each realization considered in the assessment, the proposed method samples different impeding factors to report expected delays before the initiation of repairs can commence. This is different from the impeding factor calculation proposed by REDi because distributions associated with (i) inspection, (ii) engineering and permitting, (iii) financing and (iv) contractor mobilization are sampled in each realization accounting for the uncertainty associated with each one of these external factors. In the method described in Section 4.3.2, delays associated impeding factors are not sampled, but simply use the expected value of each distribution. In each realization, delays associated with impeding factors are taken as the longest sequence shown in Figure 4-25. The criteria and distributions sampled when estimating delays associated with different impeding factors for the archetype buildings are summarized next.

i. If the repair class in all components is less than 1, delays associated with impeding factors are assumed to be zero. If the maximum repair class in any component is greater than 1, which indicates damage that hinders full recovery, the distribution

shown in Table 4-13 is sampled. This assumes that visible damage to any component, even if minor, may trigger requests from building occupants for inspection.

ii. Different distributions associated with engineering and permitting delays are sampled as a function of the maximum repair class in structural components only. If the maximum repair class in all structural components is less than 1, delays associated with engineering and permitting are taken to be zero. Otherwise, the distributions sampled for engineering mobilization and for permitting depend on whether the maximum repair class in any structural component hinders re-occupancy, functional recovery or full recovery, as noted in Table 4-13.

iii. If the expected loss ratio associated with each realization is less than 10% of the building replacement cost, no delays associated with financing are assumed. If the loss ratio is greater than 10%, a distribution is sampled for delays associated with financing via private loans as illustrated in Table 4-13.

iv. Lastly, delays associated with contractor mobilization are sampled depending on the maximum repair class in components in all repair sequences. If the maximum repair class in all repair sequences is zero, delays associated with contractor mobilization are assumed to be zero. Otherwise, the distributions sampled depend on whether the maximum repair class in any repair sequence hinders re-occupancy, functional recovery or full recovery, as noted in Table 4-13. The resulting delays are weighted as a function of the repair class observations in each repair sequence in each storey, i.e. if the maximum repair class in each repair sequence is only observed in half of the floors in the building, then the sample is scaled by 0.50.

As this method is developed to calculate recovery functions for existing tall buildings, due to extensive delays associated with structural and non-structural repairs, utility disruption is assumed not to control over other delays when developing recovery functions for functional recovery.

Chapter 5

BSPE: Scenario-based Assessment

The Working Group on California Earthquake Probabilities (WGCEP) calculates that there is a 33% likelihood of a large (M_w 6.7 or greater) earthquake occurring on the Hayward Fault in the next few decades (Aagaard et al. 2017). In recognition of this considerable threat from potentially damaging earthquakes, USGS is currently working on the HayWired scenario, a M_w 7.0 earthquake on the Hayward fault, developed to study impacts on the San Francisco Bay area (USGS 2016). As part of this work, USGS identified the need to address the following question about tall building performance: "How will an existing tall steel moment frame office building (1970s era) that is representative of a significant portion of the building stock in downtown San Francisco perform in an earthquake such as the HayWired scenario mainshock?" This question was raised in RFP – Reference Number G16PS00702 (USGS HayWired Scenario – Tall Building Performance), which requested developing a defensible analysis of tall building performance and estimates of damage levels, repair costs and downtime for the HayWired earthquake scenario in San Francisco and Oakland.

As part of the USGS HayWired Scenario – Tall Building Performance project, Molina Hutt (2016) carries out non-linear dynamic analysis of a 40-storey and a 20-storey 1970s archetype steel MRF office buildings, as described in Chapter 4, subjected to ground motions developed by USGS. The ground motions are generated by a 3D physics-based simulation (Aagaard et al. 2017) for a M_w 7.0 earthquake on the Hayward fault. The shakemap associated with this scenario is illustrated in Figure 5-1. A single scenario, such as HayWired, is insufficient for probabilistic design, but it enables realistic estimates of the ground shaking to help determine and understand the impacts of expected future large earthquakes (Harris 2017). The 3D physics-based simulation of strong ground shaking caused by the HayWired main shock is an improvement over those based solely on ground-motion prediction equations, as the latter do not include the details of how the geology of the San Francisco Bay region affects earthquakes (Harris 2017). Therefore, the 3D physics-based simulations can produce a more realistic estimate of damage and loss at both the local scale and in the aggregate.

Arup (2017) utilizes the non-linear dynamic analysis results from Molina Hutt (2016) to develop damage, economic loss and downtime estimates associated with the performance of the archetype buildings considered. Within the Arup (2017) report, in addition to the non-

linear dynamic analysis results, the author also provided key inputs to the building performance models, as described in Chapter 4. However, the loss and downtime calculations were carried out by Arup. This chapter provides a summary of the work carried out by Molina Hutt (2016). A summary of the loss and downtime results from Arup (2017) is also included, as it provides a reference point for similar data presented in Chapters 6 and 7, where intensity- and time-based assessments are carried out for similar archetypes. A comparison of the HayWired scenario results versus more comprehensive assessments can help appraise the suitability of a single earthquake scenario for the purpose of evaluating impacts to the built environment and the community. As part of the USGS HayWired Scenario – Tall Building Performance, the USGS requested the development of the 20-storey archetype steel MRF building, as described in Chapter 4, in order to better represent the existing tall building stock in Oakland.

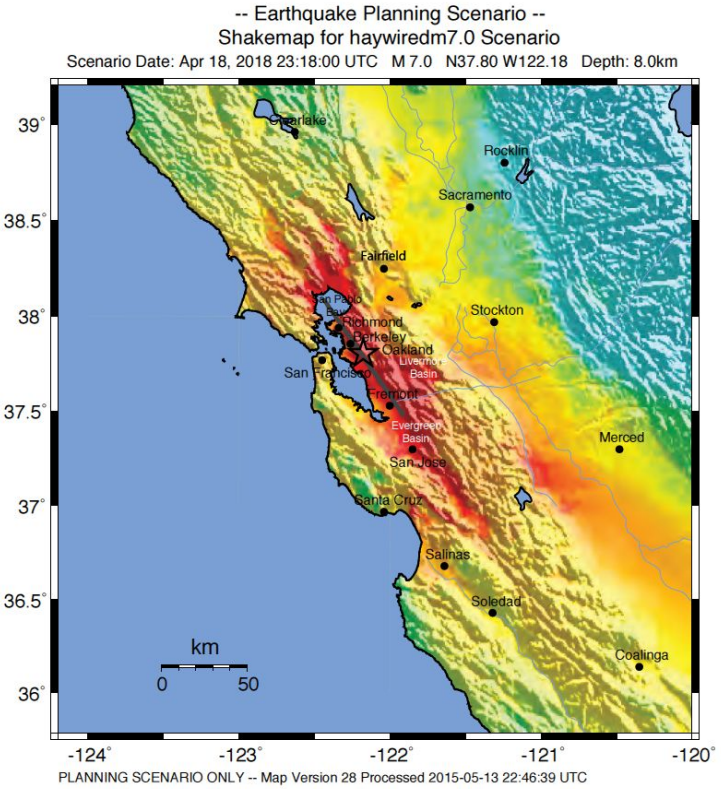

PERCEIVED SHAKING	Not felt	Weak	Light	Moderate	Strong	Very Strong	Severe	Violent	Extreme
POTENTIAL DAMAGE	none	none	none	Very light	Light	Moderate	Mod./Heavy	Heavy	Very Heavy
PEAK ACC.(%g)	<0.05	0.3	2.8	6.2	12	22	40	75	>139
PEAK VEL.(cm/s)	<0.02	0.1	1.4	4.7	9.6	20	41	86	>178
INSTRUMENTAL INTENSITY	I	II-III	IV	V	VI	VII	VIII	IX	X+

Figure 5-1: USGS shakemap of the San Francisco bay area under the HayWired earthquake scenario, a M_w 7.0 earthquake on the Hayward fault.
Source: Aagaard et al. (2017).

5.1 HayWired scenario ground motions

The performance of the archetype buildings is assessed at two locations for which ground motion records are provided by USGS: downtown San Francisco (37.793° N, 122.413° W) and downtown Oakland (37.804° N, 122.270° W). Figure 5-2 illustrates these locations within a map of the San Francisco bay area. Figures 5-3 and 5-4 illustrate the acceleration, velocity and displacement time histories of the ground motions at the downtown San Francisco site and the downtown Oakland site, respectively.

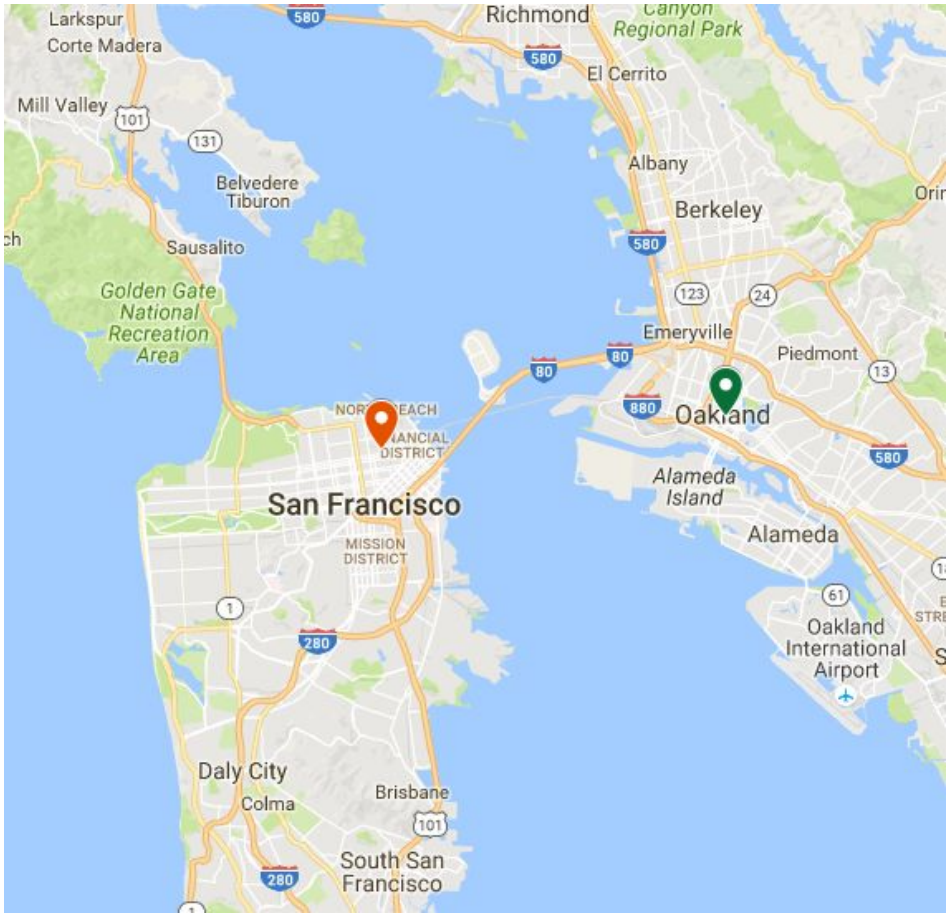

Figure 5-2: HayWired earthquake scenario assessment locations in downtown San Francisco (red pin) and downtown Oakland (green pin).
Source: GoogleMaps (2016)

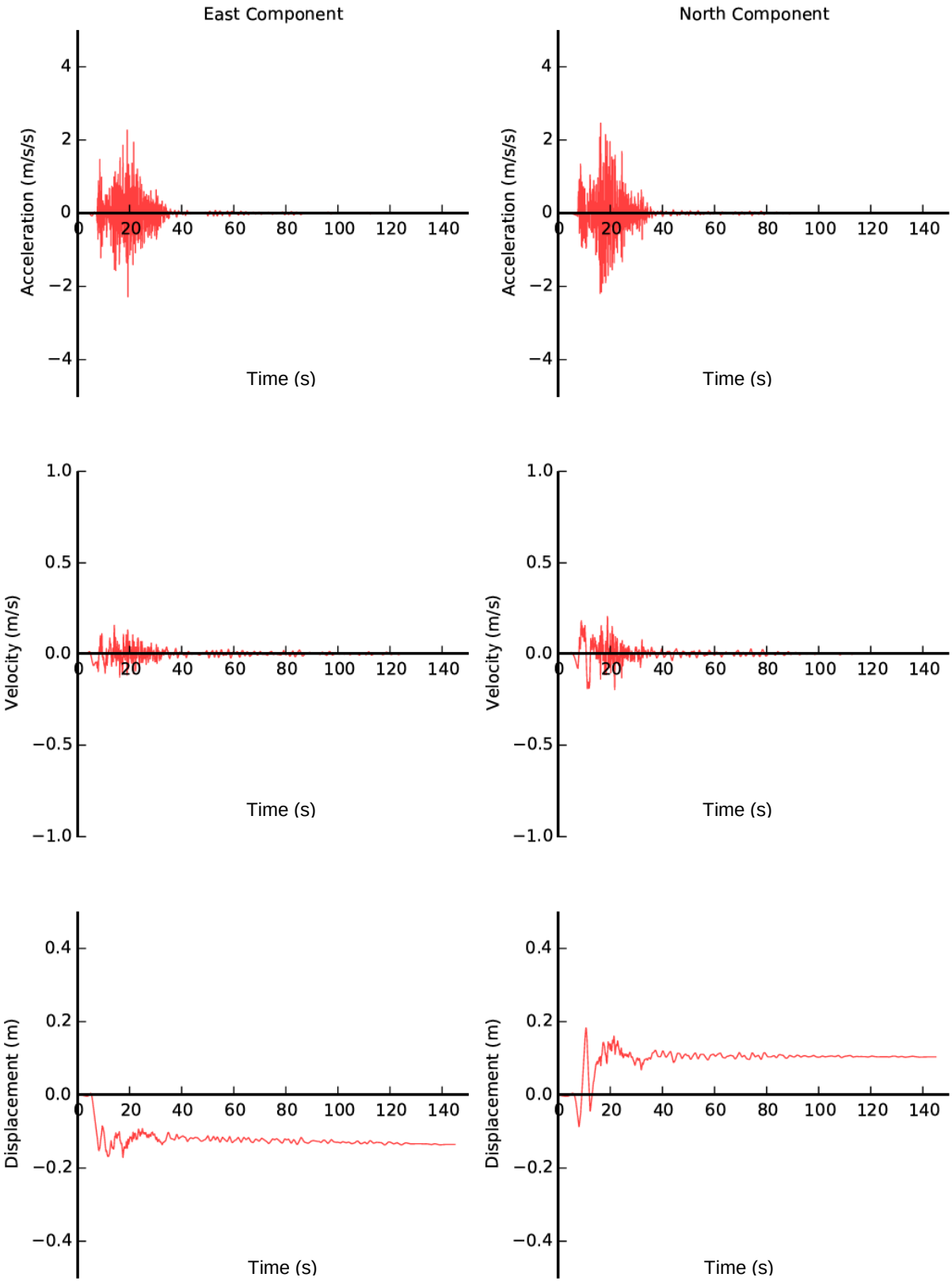

Figure 5-3 Acceleration, velocity and displacement time histories of the east-west and north-south components of the HayWired scenario earthquake in San Francisco.
Source: USGS (2016).

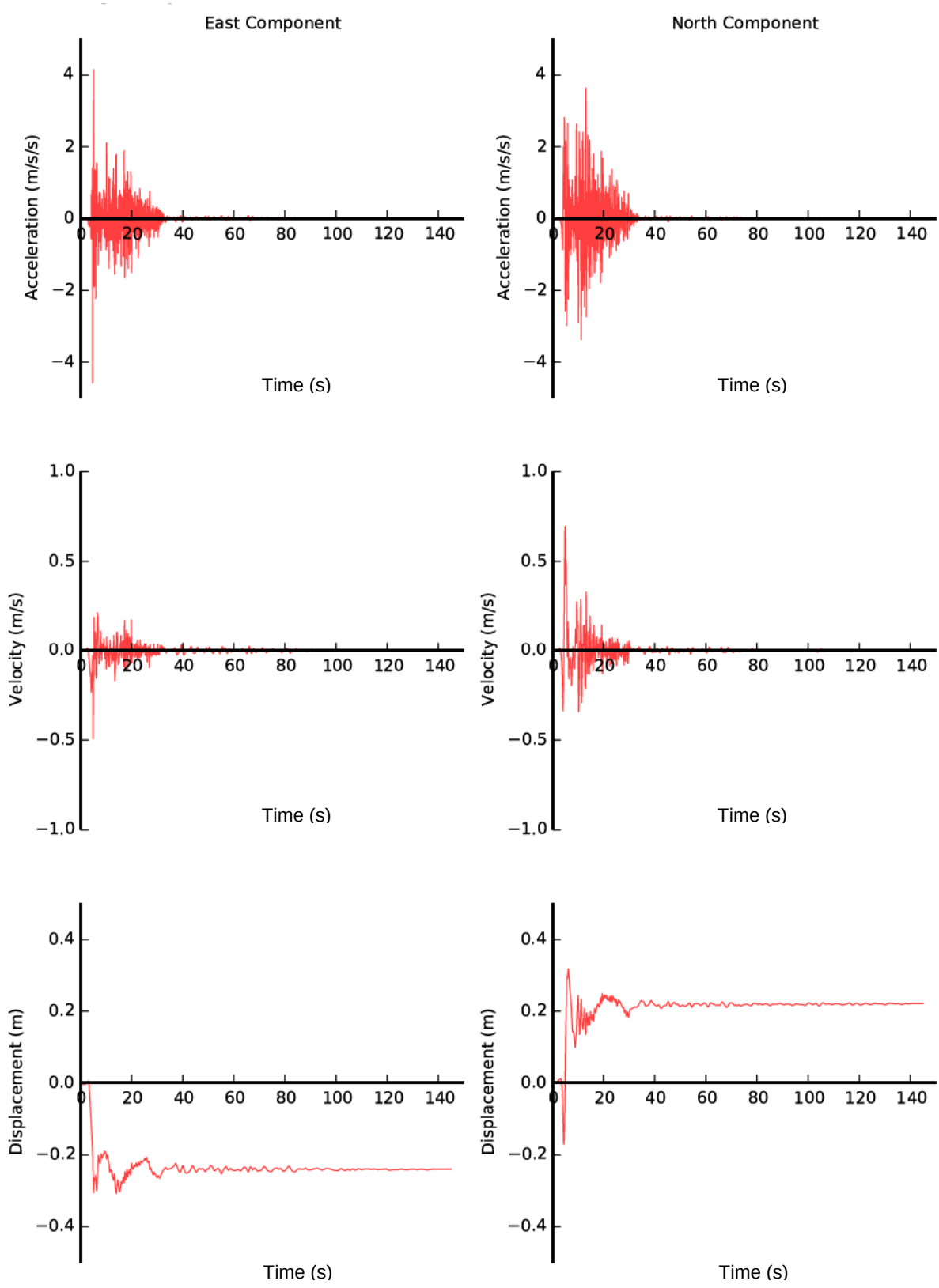

Figure 5-4: Acceleration, velocity and displacement time histories of the east-west and north-south components of HayWired scenario earthquake in Oakland.
Source: USGS (2016).

In order to compare the spectra of the ground motions generated as part of the HayWired scenario against the seismic hazard in the San Francisco bay area, a representative site (37.789° N, 122.402° W) is selected in close proximity to most of the existing tall buildings in downtown San Francisco. This site has soil properties consistent with ASCE 7 Site Class D (ASCE 2010). Seismic hazard data is obtained using the USGS hazard curve calculation tool (USGS 2015) with a 2% probability of exceedance in 50 years (2475 year return period). Seismic hazard data beyond a 5 second period is not available from this USGS tool. Therefore, in order to construct the UHS, hazard data beyond 5 seconds is obtained from OpenSHA (Field et al. 2003). As discussed in Section 2.2.2, in a UHS, by definition, all ordinates have the same annual frequency of exceedance. Hence, the spectral shape is not representative of the source, magnitude and distance combinations that control the hazard at any return period. In order to address these limitations, the CS was introduced (Lin and Baker 2015). The CS is a response spectrum that specifies the probability distribution of spectral accelerations over a range of periods, conditioned on spectral acceleration at a conditioning period of interest. The CS utilizes de-aggregated results (magnitude, distance and epsilon) and correlations between spectral accelerations at different periods to compute the expected response spectrum and additionally accounts for the variability of the response spectra. For comparison with the HayWired ground motion spectra, a CS conditioned at a 5 second period (due to close proximity to the fundamental period of the 40-storey archetype building), is developed for a 2475 year return period using USGS de-aggregation data. A ground motion suite is also selected to collectively match the entire distribution of the CS, by using a computationally efficient algorithm developed by Baker (2016). At the conditioning period of 5 seconds, the spectral acceleration of the CS mean, CS variance, CS ground motion suite record spectra and UHS are coincident.

Figure 5-5 illustrates the spectra of the north-south and east-west components of the HayWired ground motions at both locations (San Francisco and Oakland) against the UHS at the representative site for a 2475 year return period, the CS mean and variance as well as the spectra for a ground motion suite consistent with the CS. Seismic de-aggregation data used to compute the CS is also noted in the figure (top right corner). It can be observed that the HayWired ground motion spectra up to a 1 second period is consistent with the CS, yet at periods greater than 1 second, the spectra is well below that of the CS. At all periods, the HayWired ground motion spectra are well below that of the UHS, particularly at periods in excess of 1 second. The HayWired ground motion spectra selected for assessment has fairly low spectral accelerations at long periods (in close proximity to the fundamental period of the structures considered), though significant structural demands can be induced from higher

mode effects. The north-south component of the HayWired ground motions is significantly larger than the east-west component. Therefore, larger demands are expected in the direction of the building subjected to the north-south component.

For comparison purposes, Figure 5-5 includes the geomean spectra of the ground motion recorded at the base of the Chevron Building in downtown San Francisco during the 1989 Loma Prieta earthquake. The Loma Prieta geomean spectrum is fairly consistent with the HayWired ground motion spectra at periods ranging from 0.7 to 2 seconds, yet significantly lower at other periods.

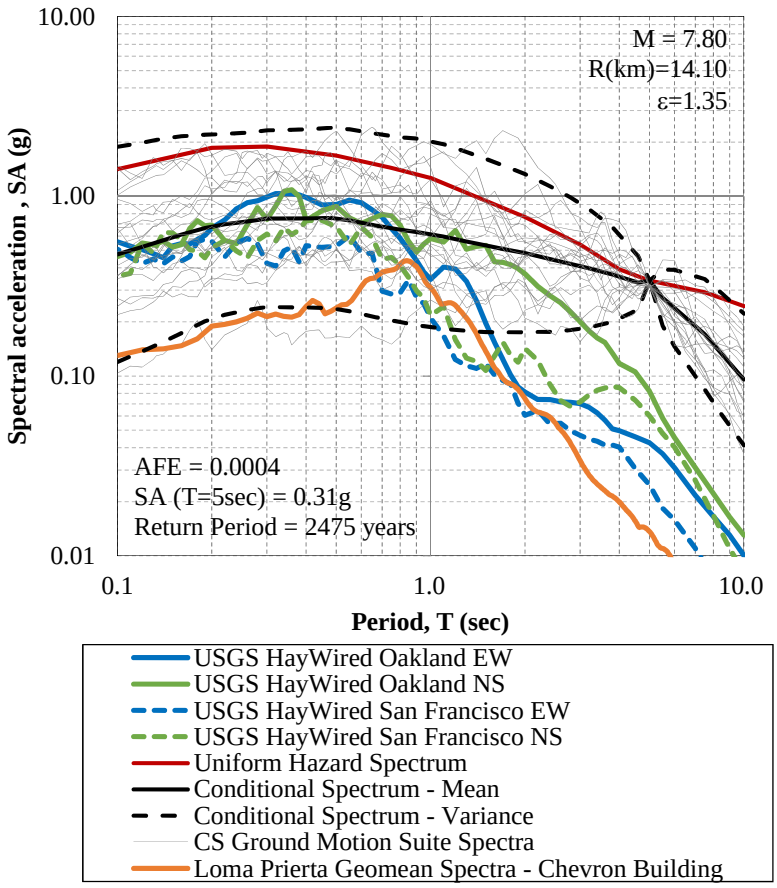

Figure 5-5: Uniform hazard spectrum and conditional spectra (mean, variance and ground motion suite) at a representative site in downtown San Francisco versus ground motion spectra from earthquake scenarios: HayWired (at San Francisco and Oakland sites) and 1989 Loma Prieta (Chevron Building, San Francisco).
Source: Molina Hutt (2016).

5.2 Non-linear dynamic analysis results

This section evaluates non-linear dynamic analysis results with a focus on storey drifts and accelerations, which are proxies for damage to structural and non-structural components in the building, as discussed in Section 2.2.3. Drift and acceleration results are presented for every level in the 40-storey and the 20-storey buildings in each principal direction (see Figure 4-14 for a building plan illustrating x and y, short and long building directions, respectively). Peak transient interstorey drift ratios (IDRs) are the absolute maximum change in horizontal displacement between two adjacent storeys over the storey height. Peak damageable IDRs are indicative of the generalized shear deformation of each storey. The peak damageable IDR is different from the peak transient IDR in that it neglects the rigid body rotation from the drift calculation to predict harmful drifts (Zhou et al. 2015). This calculation is illustrated in Figure 5-6, where h_i is the storey height and l_{ij} is the width of the storey or panel considered and all other terms are as defined in the figure. For frame structures, the displacement induced by floor rotation is typically much smaller than translational displacement. Due the considerable building height of the archetype buildings considered, this phenomenon is evaluated in this chapter. Nevertheless, the results indicate that for the buildings considered, the peak transient and peak damageable IDRs are essentially identical.

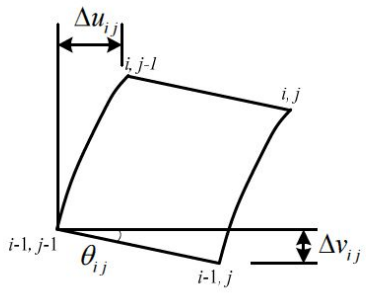

$$\gamma_{ij} = \frac{\Delta u_{ij}}{h_i} - \frac{\Delta v_{ij}}{l_{ij}}$$

$$\theta_{ij} = \frac{\Delta v_{ij}}{l_{ij}}$$

Figure 5-6: Illustration of damageable drift calculation.
Source: Zhou et al. (2015).
See List of Symbols for additional variable definitions.

Residual IDRs represent the permanent change in horizontal displacement between two adjacent storeys over the storey height. PFA is the absolute maximum value of acceleration in the storey. Figure 5-7 through 5-10 illustrate the IDRs (transient, damageable and residual) and PFAs for the 40-storey and the 20-storey buildings in each principal building direction for the Oakland and San Francisco simulations.

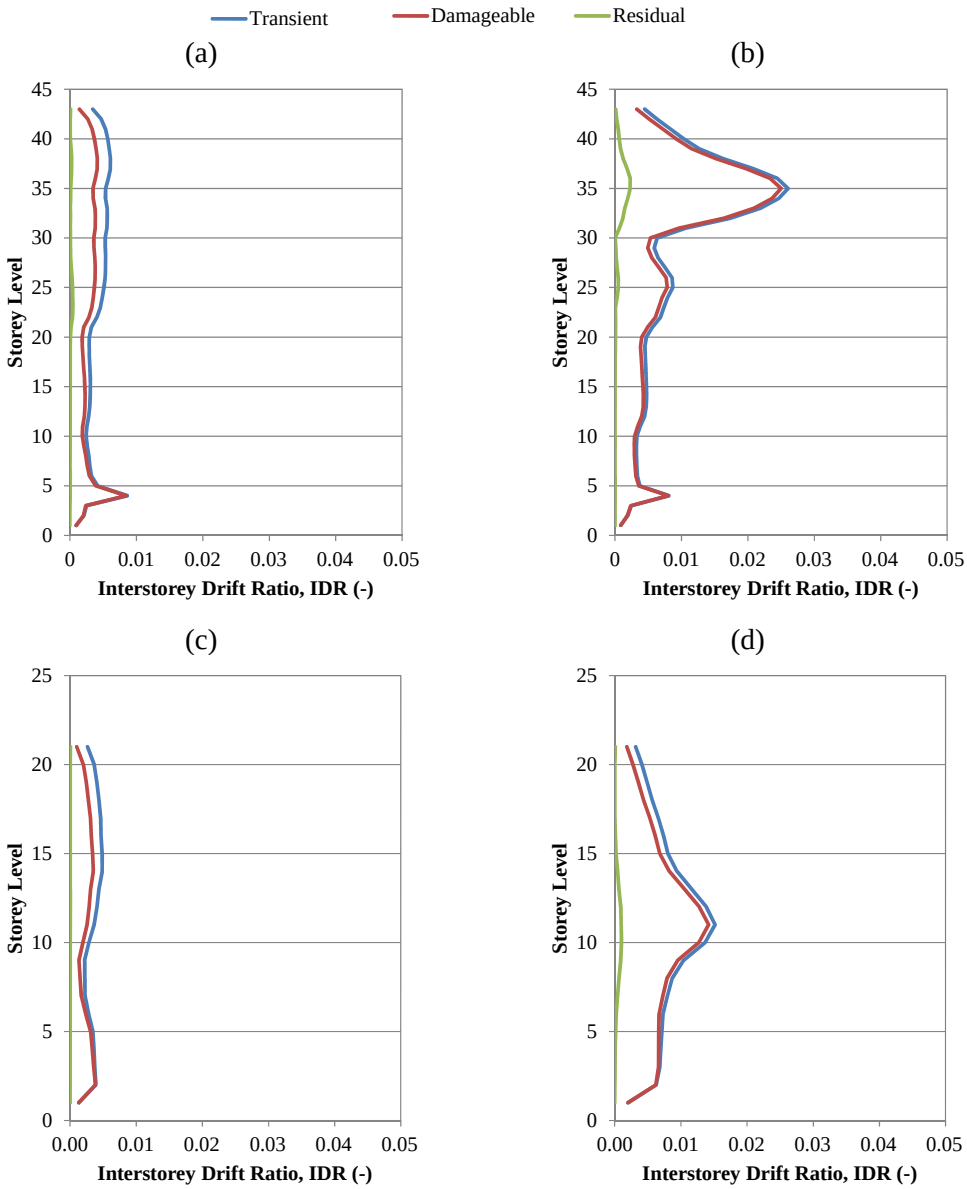

Figure 5-7: Archetype 40-storey (a, b) and 20-storey (c, d) building interstorey drift ratio (IDR) in the short (a, c) and long (b, d) building directions in Oakland.
Source: Molina Hutt (2016).

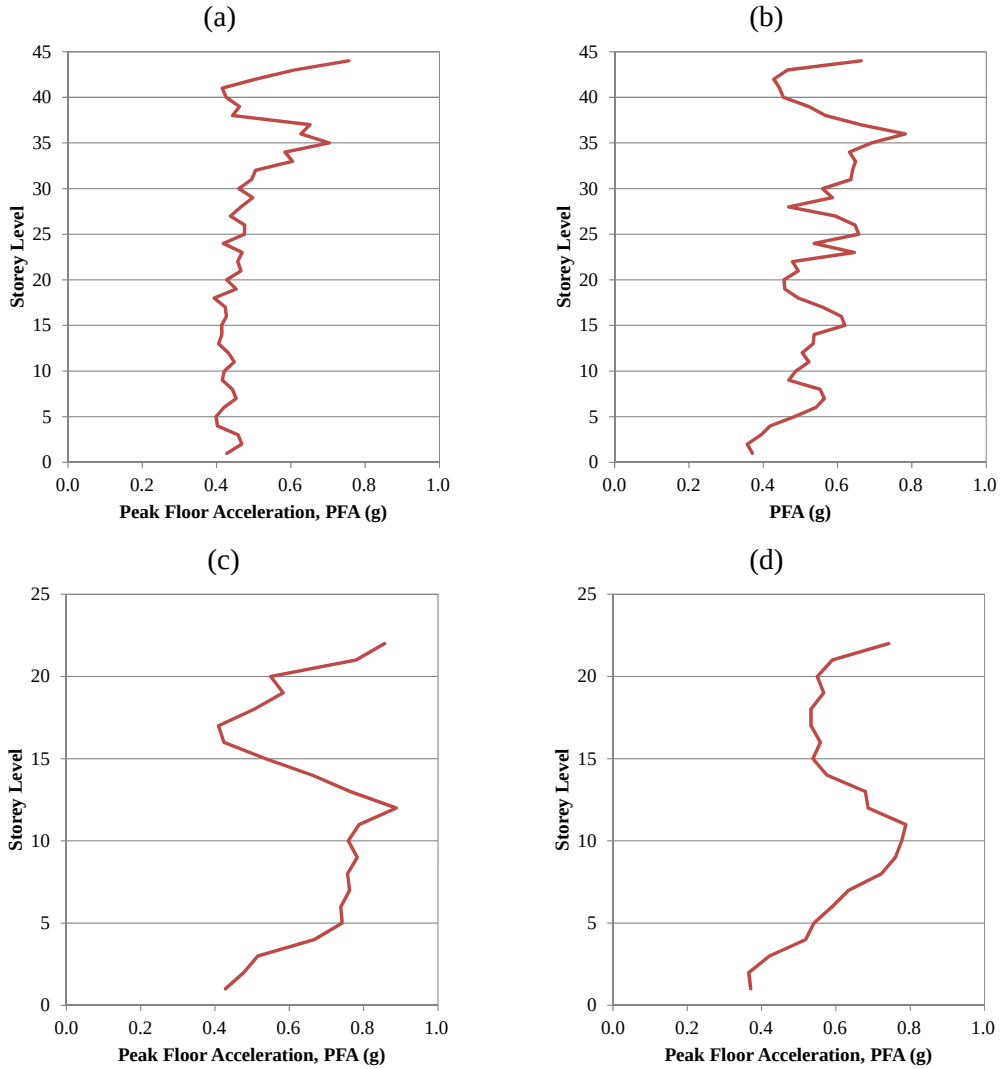

Figure 5-8: Archetype 40-storey (a, b) and 20-storey (c, d) building peak floor acceleration (PFA) in the short (a, c) and long (b, d) building directions in Oakland.
Source: Molina Hutt (2016).

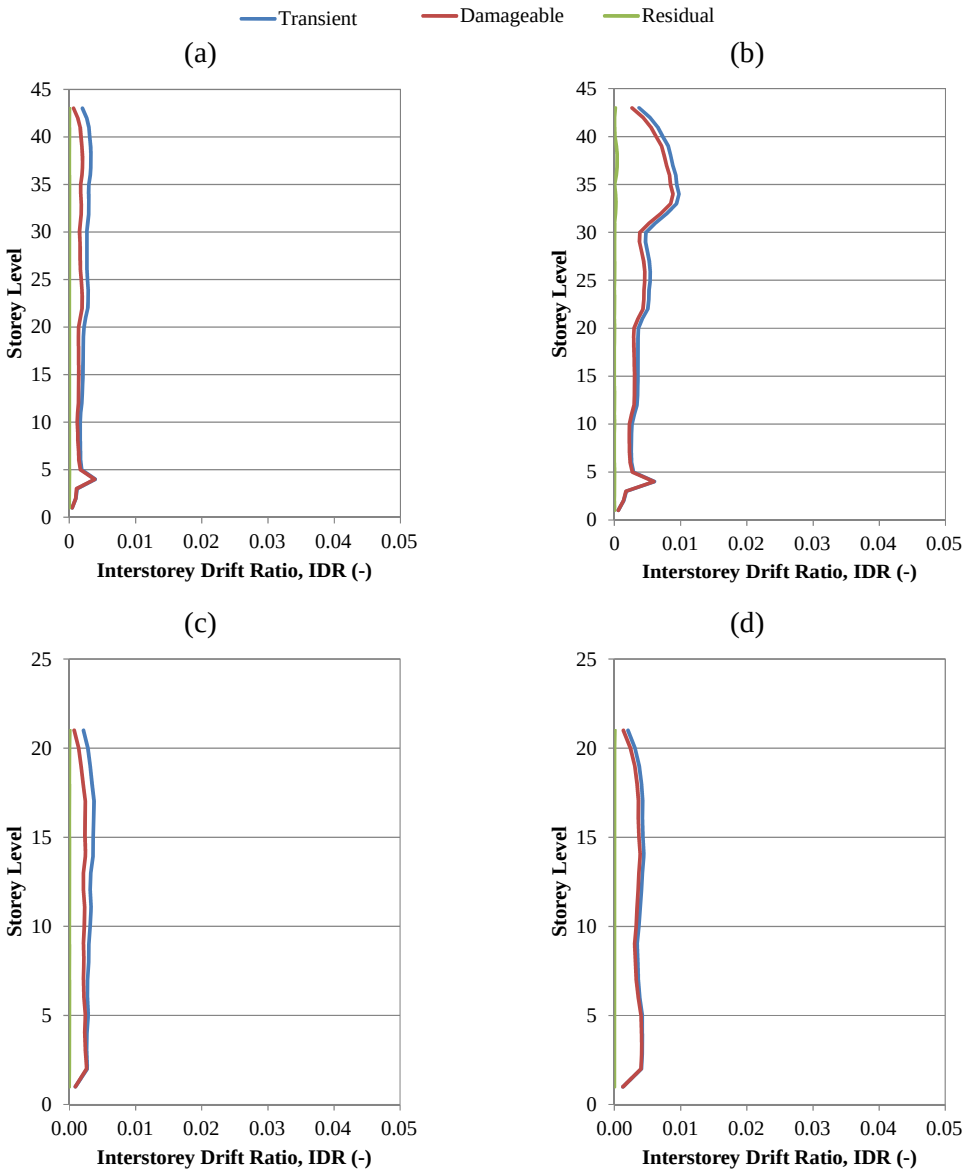

Figure 5-9: Archetype 40-storey (a, b) and 20-storey (c, d) building interstorey drift ratio (IDR) in the short (a, c) and long (b, d) building directions in San Francisco. Source: Molina Hutt (2016).

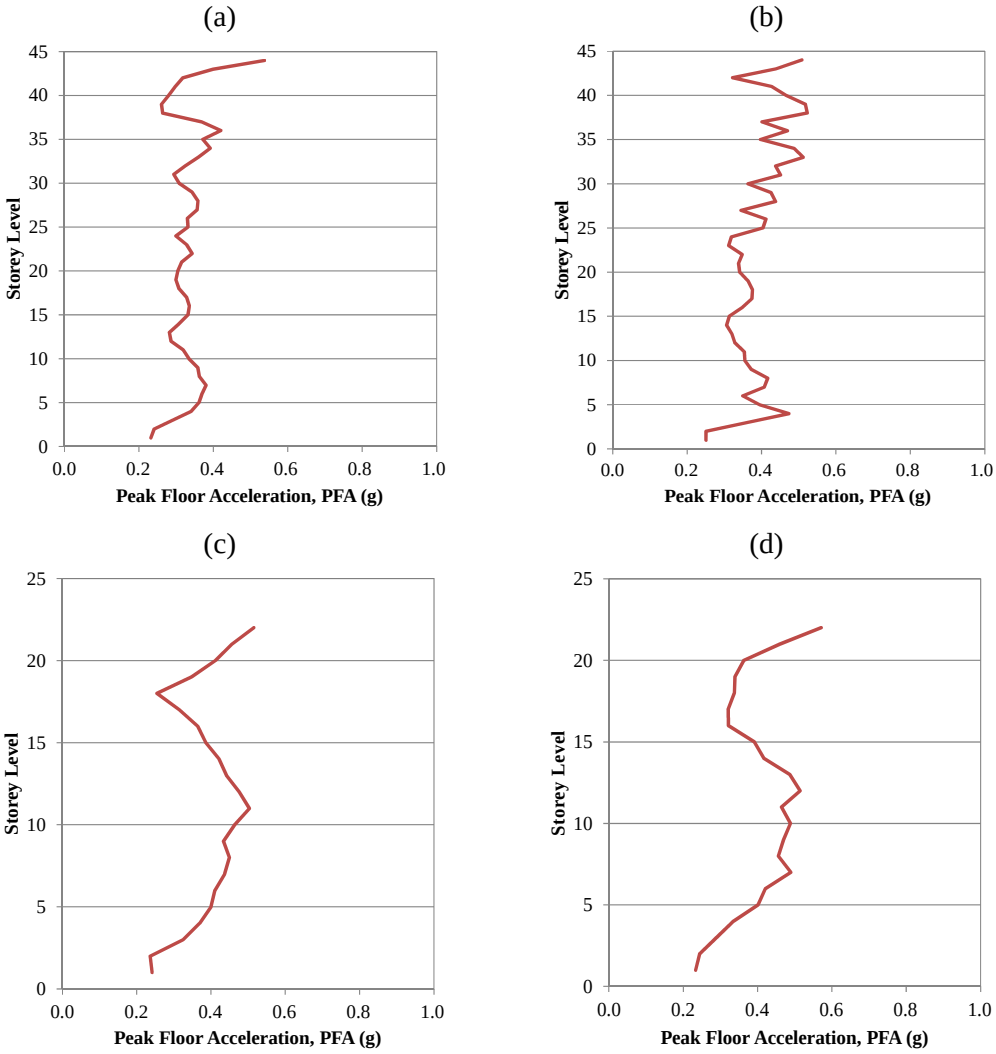

Figure 5-10: Archetype 40-storey (a, b) and 20-storey (c, d) building peak floor acceleration (PFA) in the short (a, c) and long (b, d) building directions in San Francisco.
Source: Molina Hutt (2016).

In order to classify beam performance, as shown in Figures 5-11 and 5-12, the following thresholds, calculated as a function of maximum plastic rotation, are introduced: elastic, yielded and fractured. Elastic denotes, beam demands are within the linear elastic range. Yielded denotes that the beam has yielded, but plastic rotations are below the fracture threshold. Fractured denotes the beam-to-column connection has fractured. Figures 5-11 and 5-12 illustrate the beam performance in two perimeter frame elevations for the 40-storey and 20-storey archetype buildings in Oakland and San Francisco, respectively.

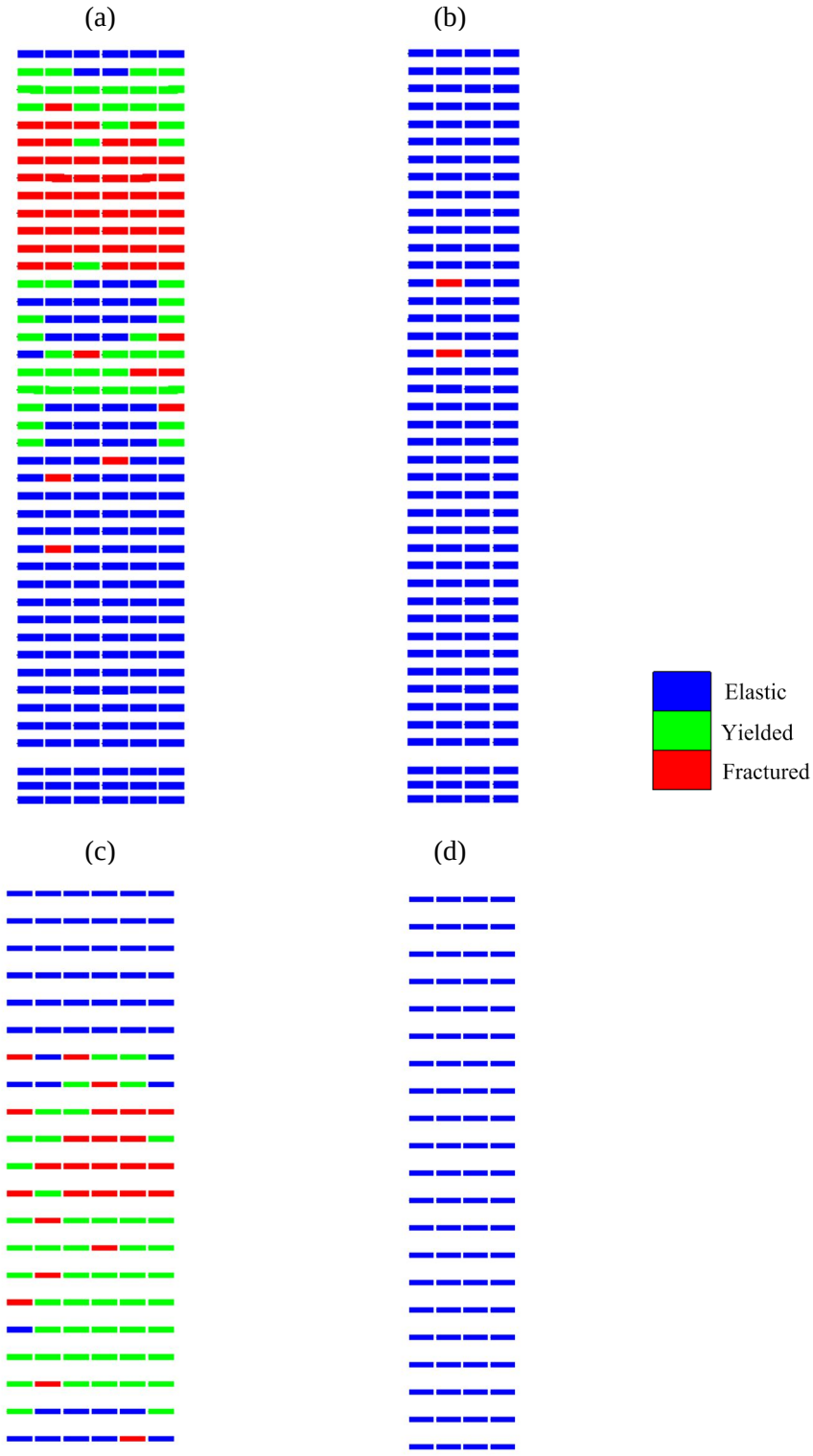

Figure 5-11: Archetype 40-storey (a, b) and 20-storey (c, d) building beam performance for sample long (a, c) and short (b, d) building elevations in Oakland.
Source: Molina Hutt (2016).

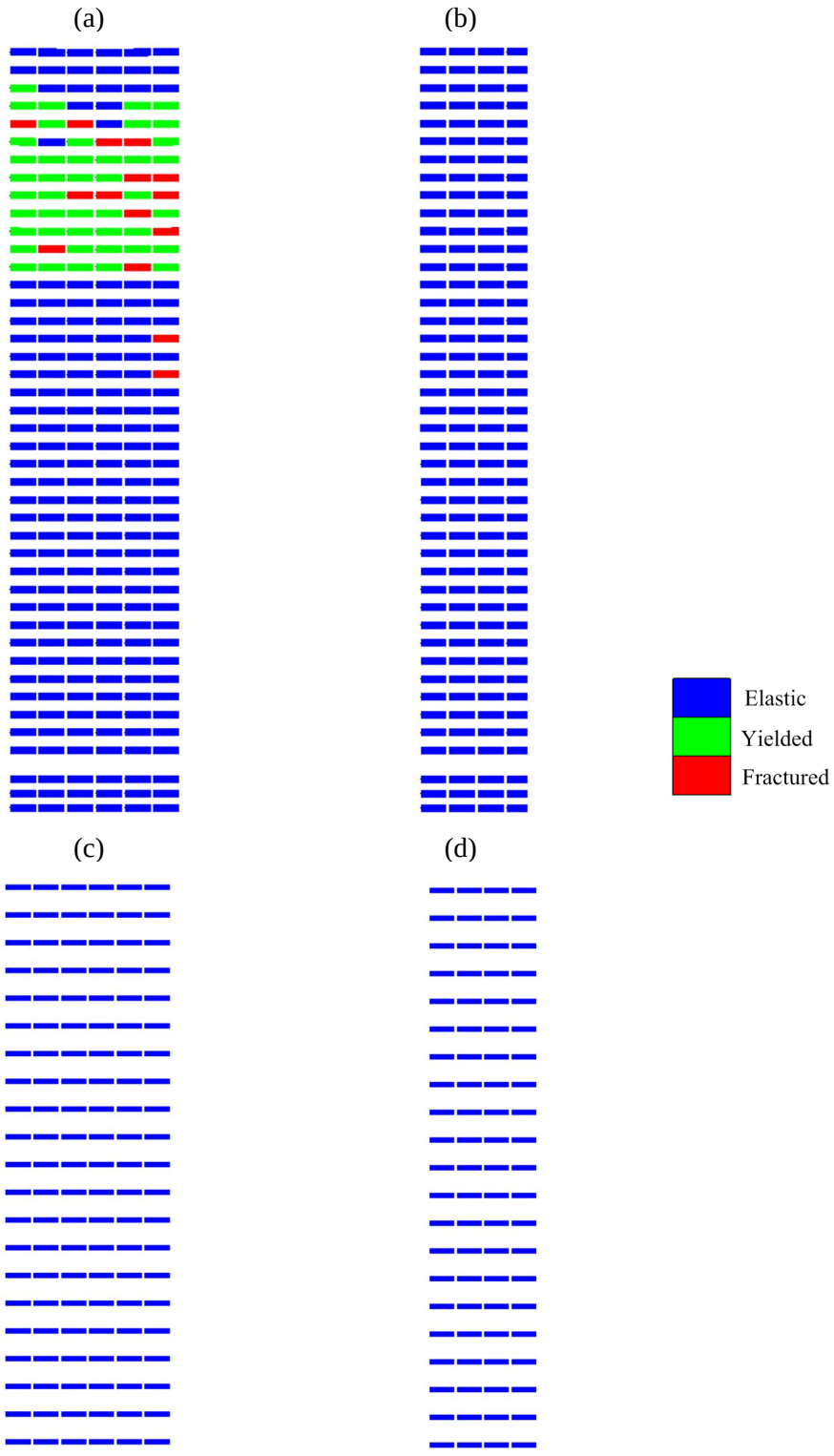

Figure 5-12: Archetype 40-storey (a, b) and 20-storey (c, d) building beam performance for sample long (a, c) and short (b, d) building elevations in San Francisco.
Source: Molina Hutt (2016).

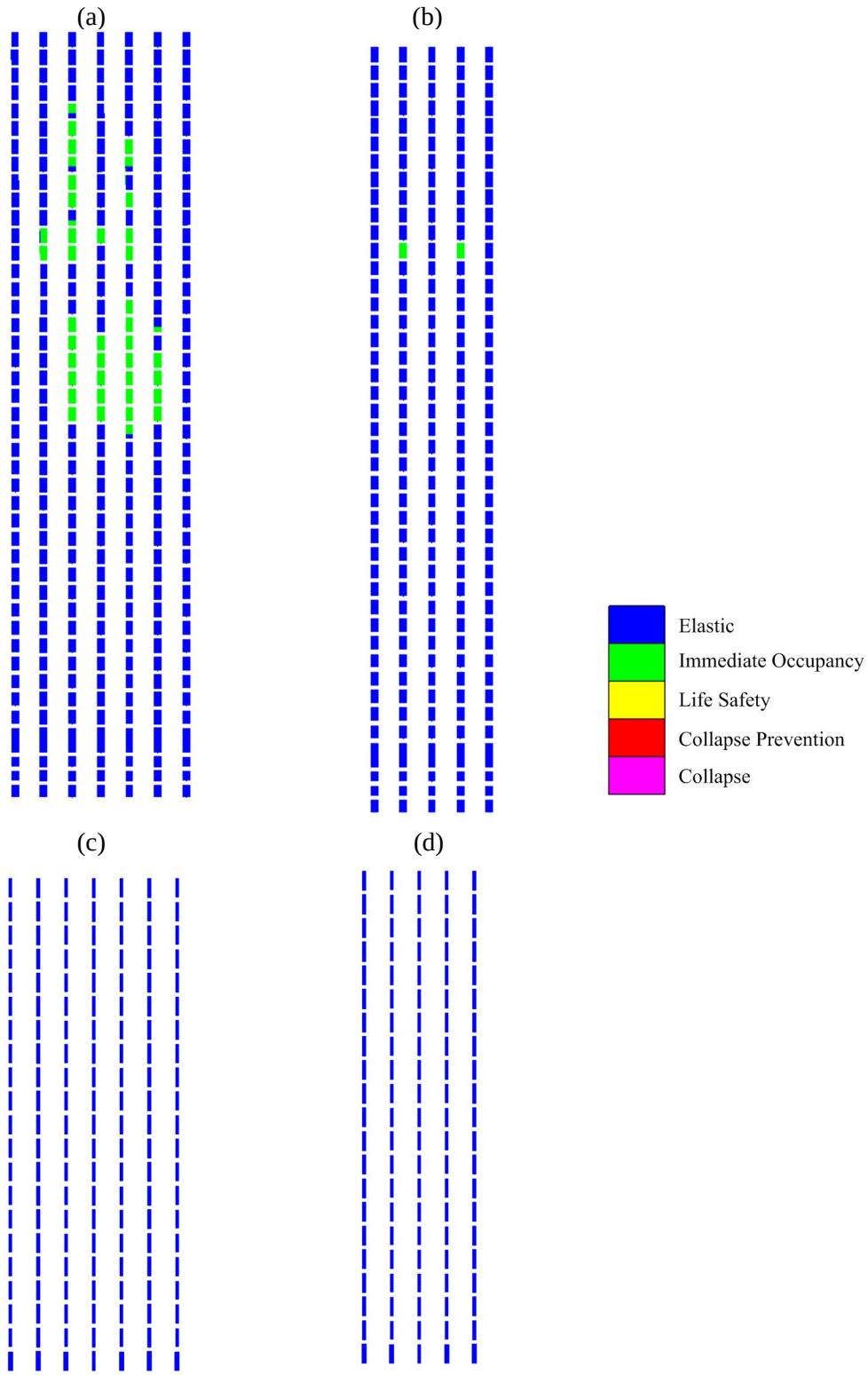

Figure 5-13: Archetype 40-storey (a, b) and 20-storey (c, d) building column performance (ASCE 41 thresholds) for sample long (a, c) and short (b, d) building elevations in Oakland. Source: Molina Hutt (2016).

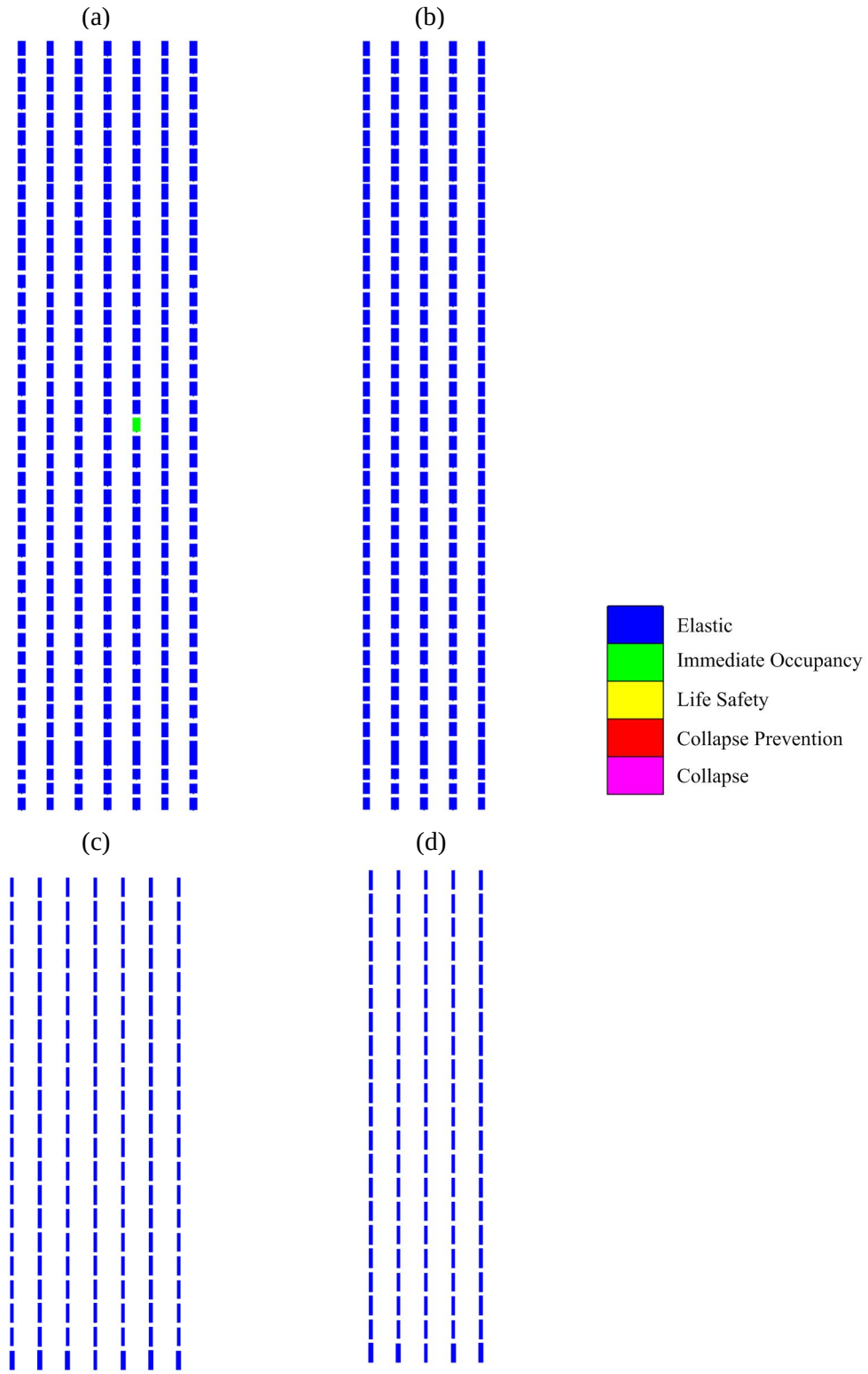

Figure 5-14: Archetype 40-storey (a, b) and 20-storey (c, d) building column performance (ASCE 41 thresholds) for sample long (a, c) and short (b, d) building elevations in San Francisco.
Source: Molina Hutt (2016).

In all analysis runs considered, column splices remain elastic (demands do not exceed nominal capacities). Panel zones remain elastic or undergo small plastic deformation. Similarly, columns throughout the building remain elastic or undergo small plastic deformation, as can be seen in Figures 5-13 and 5-14 by evaluating the column response against ASCE 41 thresholds (ASCE 2013).

The results illustrate considerably higher demands in the Oakland site than the San Francisco site, with peak values observed in the building direction aligned with the north-south component of the HayWired ground motions (long building direction). As illustrated in Figures 5-7 to 5-10, peak transient, damageable and residual IDRs for the 40-storey building are respectively 2.6%, 2.5% and 0.23% in Oakland, versus 0.98%, 0.88% and 0.04% in San Francisco. Maximum PFAs are 0.78g in Oakland and 0.54g in San Francisco. The percentage of fractured connections in Oakland is 11% versus 2% in San Francisco. Peak transient, damageable and residual IDRs for the 20-storey building are 1.52%, 1.42% and 0.1% in Oakland, versus 0.44%, 0.41% and 0.01% in San Francisco. Maximum PFAs for the 20-stroey building are 0.89g in Oakland and 0.57g in San Francisco. The percentage of fractured connections in Oakland is 7% versus none in San Francisco.

The large concentrations of deformation atop the 40-storey building in the 1973 archetype can be traced back to the design procedure of the time. As discussed in Section 4.1.1, UBC 1973 seismic design forces are distributed up the building height based on the first mode translational response of the structure, neglecting contributions to the dynamic response of higher modes, which can result in upper storeys being under-designed. The concentration of deformation in upper storeys is also observed in the analysis results of the Chevron building of Anderson and Bertero (1998), and have also been reported in other studies, as described in Section 2.1.4.

5.2.1 Impact of fracture distribution

In order to assess the impact of the random fracture distribution on the seismic performance, an additional set of analysis simulations are performed for identical models, except for the value of plastic rotation at fracture assigned to each connection in the building. While the value of plastic rotation at fracture for a given beam connection is different from the baseline model, all values of plastic rotation at fracture fit the distribution presented in Figure 4-24 , as discussed in Chapter 4. These results indicate that while the randomness in the plastic rotation at fracture has a direct impact on the distribution of fractured beams throughout the building,

overall it has little impact on the global results of the structure. A comparison of the IDRs, PFAs and beam performance between the two cases (baseline and revised fracture distribution) is included in Appendix F.

In the baseline case, the 40-storey building in Oakland has 80.2% of beams that remain elastic, 8.6% that yield and 11.2% that fracture, whereas 80.5% of beams remain elastic, 7.9% yield and 11.6% fracture in the analysis with the alternate fracture distribution. Similarly, the results of the 40-storey building in San Francisco indicates that 91.8% of beams remain elastic, 6.0% yield and 2.2% fracture in the baseline case, whereas 91.5% of beams remain elastic, 6.3% yield and 2.2% fracture with the alternate fracture distribution. In the baseline case for the 20-storey building in Oakland, 77.8% of beams remain elastic, 15.3% yield and 6.8% fracture, whereas 75.9% of beams remain elastic, 14.1% yield and 10.1% fracture with the alternate fracture distribution. For the 20-storey building in San Francisco, both in the baseline case and the alternate fracture distribution analyses, all beams remain elastic.

5.2.2 Impact of building orientation

As noted in Section 5.1, the north-south component of the HayWired ground motion records selected for this study is significantly larger than the east-west component. In order to assess the impact of the ground motion directionality on the overall performance of the buildings, an additional set of analysis simulations is carried out, in which the input ground motion components are rotated. In the baseline case, the strongest component of the ground motion (north-south) is applied in the long building direction. In this alternate case, the north-south component is applied in the short building direction. The results illustrate that peak values are observed in the building direction that is subject to the largest component of the HayWired ground motions. Tables 5-1 through 5-4 provide a summary of peak IDRs and PFAs for the baseline case and the rotated case for the 40-storey and the 20-storey archetype buildings in Oakland and San Francisco. When considering the average values of peak demand in each building direction, transient IDR results in the baseline case are up to 31% higher than in the rotated case, whereas maximum PFA results are within a 20% range. Appendix F provides a direct comparison of IDR and PFA results up the building height for the baseline and rotated cases, illustrating that the overall distribution of demand throughout the building height is dependent on the ground motion directionality.

Table 5-1: Impact of ground motion directionality on 40-storey archetype peak interstorey drift ratios (IDRs) and peak floor accelerations (PFAs) in Oakland.
Source: Molina Hutt (2016).

Ground Motion Component	Baseline			Rotated		
Building Direction	Short	Long	Average	Short	Long	Average
Transient IDR	0.86%	2.60%	1.73%	1.69%	0.95%	1.32%
Damageable IDR	0.85%	2.50%	1.67%	1.66%	0.88%	1.27%
Residual IDR	0.04%	0.23%	0.14%	0.08%	0.27%	0.17%
PFA	0.76g	0.78g	0.77g	0.88g	0.60g	0.74g

Table 5-2: Impact of ground motion directionality on 20-storey archetype peak interstorey drift ratios (IDRs) and peak floor accelerations (PFAs) in Oakland.
Source: Molina Hutt (2016).

Ground Motion Component	Baseline			Rotated		
Building Direction	Short	Long	Average	Short	Long	Average
Transient IDR	0.49%	1.52%	1.01%	1.00%	0.55%	0.78%
Damageable IDR	0.38%	1.42%	0.90%	0.72%	0.49%	0.61%
Residual IDR	0.00%	0.10%	0.05%	0.01%	0.01%	0.01%
PFA	0.89g	0.79g	0.84g	1.03g	0.73g	0.88g

Table 5-3 Impact of ground motion directionality on 40-storey archetype peak interstorey drift ratios (IDRs) and peak floor accelerations (PFAs) in San Francisco.
Source: Molina Hutt (2016).

Ground Motion Component	Baseline			Rotated		
Building Direction	Short	Long	Average	Short	Long	Average
Transient IDR	0.39%	0.98%	0.68%	0.69%	0.50%	0.59%
Damageable IDR	0.38%	0.88%	0.63%	0.67%	0.45%	0.56%
Residual IDR	0.00%	0.04%	0.02%	0.01%	0.01%	0.01%
PFA	0.54g	0.52g	0.53g	0.47g	0.41g	0.44g

Table 5-4: Impact of ground motion directionality on 20-storey archetype peak interstorey drift ratios (IDRs) and peak floor accelerations (PFAs) in Oakland.
Source: Molina Hutt (2016).

Ground Motion Component	Baseline			Rotated		
Building Direction	Short	Long	Average	Short	Long	Average
Transient IDR	0.37%	0.44%	0.41%	0.37%	0.51%	0.44%
Damageable IDR	0.26%	0.41%	0.34%	0.36%	0.45%	0.41%
Residual IDR	0.00%	0.01%	0.01%	0.00%	0.01%	0.01%
PFA	0.52g	0.57g	0.54g	0.58g	0.60g	0.59g

5.3 Expected direct economic losses and downtime

Arup (2017) utilizes the results presented in Section 5.2 to estimate direct economic losses and downtime to re-occupancy and functional recovery associated with the performance of the archetype buildings. These metrics are developed using building performance models consistent with those presented in Chapter 4. The results are evaluated for the 40-storey archetype building in San Francisco and for the 20-storey building in both San Francisco and Oakland. Results are evaluated for both the baseline and the rotated orientations. Table 5-5 outlines the abbreviation associated with each building case study. Table 5-6 presents the 50^{th} (median) and 90^{th} percentile estimates of the direct economic losses. Table 5-7 summarizes the 50^{th} (median) and 90^{th} percentile of the downtime to re-occupancy and functional recovery for the archetypes considered. Median loss estimates range from 7.4 to 17.5% of building replacement cost. Median estimates of downtime to re-occupancy range from 186 to 250 days, whereas estimates of downtime to functional recovery range from 242 to 288 days. The loss and downtime results for the 40-storey archetype building in Oakland are not evaluated as this archetype building is not believed to be representative of the existing tall building stock in Oakland. This observation is in agreement with the data presented earlier in Figure 4-16.

Table 5-5: Abbreviation for case study buildings for which estimates of direct economic losses and downtime are conducted.
Source: Arup (2017)

Building Case Study	Abbreviation
40-Storey Steel Building in San Francisco, Baseline Orientation	SF-40-Baseline
40-Storey Steel Building in San Francisco, Rotated Orientation	SF-40-Rotated
20-Storey Steel Building in San Francisco, Baseline Orientation	SF-20-Baseline
20-Storey Steel Building in San Francisco, Rotated Orientation	SF-20-Rotated
20-Storey Steel Building in Oakland, Baseline Orientation	OK-20-Baseline
20-Storey Steel Building in Oakland, Rotated Orientation	OK-20-Rotated

Table 5-6: Direct economic loss estimates (50th and 90th percentile) expressed USD and percentage of replacement cost for the case study buildings considered.
Source: Arup (2017)

Case	Total Repair Costs			
	50th Percentile		90th Percentile	
SF-40-Baseline	$15M	10.8%	$17.1M	12.3%
SF-40-Rotated	$13M	9.7%	$15.7M	11.3%
SF-20-Baseline	$5.1M	7.4%	$6.6M	9.5%
SF-20-Rotated	$5.7M	8.2%	$7.3M	10.4%
OK-20-Baseline	$12.2M	17.5%	$14.4M	20.7%
OK-20-Rotated	$11.5M	16.5%	$13M	18.7%

Table 5-7: Downtime estimates to re-occupancy and functional (50th and 90th percentile) for the case study buildings considered.
Source: Arup (2017)

Case	Downtime (days)			
	Re-occupancy		Functional Recovery	
	50th Percentile	90th Percentile	50th Percentile	90th Percentile
SF-40-Baseline	248	288	375	388
SF-40-Rotated	250	288	364	390
SF-20-Baseline	189	242	316	364
SF-20-Rotated	186	251	304	361
OK-20-Baseline	231	273	344	385
OK-20-Rotated	224	269	333	371

5.4 Summary and conclusions

This chapter presents the non-linear dynamic analysis results of a 40-storey and 20-storey 1970s archetype steel MRFs office building subjected to ground motions developed by USGS as part of the HayWired earthquake scenario event. The performance of the archetype building is assessed at two locations for which ground motion records have been provided: downtown San Francisco (37.793° N, 122.413° W) and downtown Oakland (37.804° N, 122.270° W). This chapter presents a summary of the analysis results that describe overall building performance at the global and component level. Sensitivity checks are carried out to assess the impact of the randomness in plastic rotation at fracture of the beams as well as the impact of the ground motion directionality on global results. Overall, results indicate that demands are significantly larger in Oakland than San Francisco, due to smaller epicentral distance. Maximum demands are observed in the building direction oriented with the north-south component of the HayWired ground motions.

Peak transient, damageable and residual IDR for the 40-storey building are 2.6%, 2.5% and 0.23% in Oakland, versus 0.98%, 0.88% and 0.04% in San Francisco. Maximum PFAs are 0.78g in Oakland and 0.54g in San Francisco. The percentage of fractured connections in Oakland is 11% versus 2% in San Francisco. In both locations, the results indicate a concentration of deformation in the upper storeys, which can be traced back to a design process that neglected contribution from higher mode effects to the dynamic response of the building. Peak transient, damageable and residual IDR for the 20-storey building are 1.52%, 1.42% and 0.1% in Oakland, versus 0.44%, 0.41% and 0.01% in San Francisco. Maximum PFAs are 0.89g in Oakland and 0.57g in San Francisco. The percentage of fractured connections in Oakland is 7% versus none in San Francisco.

Based on FEMA (2012) relations between peak transient IDR and damage, the 40-storey archetype building in Oakland is expected to reach a damage state in which some minor realignment of the structural frame may be required as well as related structural and non-structural repairs. The 40-storey archetype building in San Francisco is expected to reach damage levels in which no structural realignment is necessary for structural stability, but the building may require adjustment and repairs to non-structural and mechanical components. Similarly, the 20-storey archetype building in Oakland is expected to reach damage levels in which no structural realignment is necessary for structural stability, but the building may require adjustment and repairs to non-structural and mechanical components, whereas the 20-storey archetype building in San Francisco is expected to remain elastic.

Arup (2017) utilizes the results presented in this chapter to carry out direct estimates of direct economic losses and downtime estimates to re-occupancy and functional recovery associated with the performance of the 40-storey archetype building in San Francisco and the 20-storey archetype building in Oakland and San Francisco. Median loss estimates range from 7.4 to 17.5% of building replacement cost. Median estimates of downtime to re-occupancy range from 186 to 250 days, whereas estimates of downtime to functional recovery range from 242 to 288 days.

Overall results indicate that under the HayWired earthquake scenario, existing tall steel MRF buildings are expected to guarantee the life-safety of occupants. However, the buildings may experience considerable financial losses associated damage to structural and non-structural components. The most remarkable results are the expected delays associated with restoring building occupancy and functionality, which could severely compromise the resilience of the community under the expected earthquake scenario considered.

Chapter 6

BSPE: Intensity-based Assessment

This chapter presents an assessment of the seismic performance of an existing 40-storey archetype building in downtown San Francisco, representative of the state of design and construction practice from the mid-1970s to the mid-1980s. Non-Linear Response History Analyses (NLRHA) are conducted with ground motions consistent with the design earthquake hazard level defined in current building codes and with explicit consideration of near-fault directivity effects. The building performance is reported in terms of several engineering demand parameters, the expected direct economic losses and downtime. A number of strategies are proposed to achieve increased levels of resilience. These include improvements to the structural and non-structural systems as well as mitigation measures to minimize impeding factors. For details on the selection and development of the archetype building, NLRHA simulations, and building performance modelling for loss and downtime estimates, refer to Chapter 4. The results presented in this chapter have been published in Molina Hutt et al. (2015). The author was the key contributor to the referenced journal paper. They key differentiator of this paper is that it explicitly considers downtime and recovery in the assessment methodology. This work goes beyond damage and direct losses to consider repair and recovery times.

Overall, the main contribution of this chapter is that it benchmarks the performance of an archetype tall building considering damage, direct losses (due to repair or replacement), impact on building function and recovery of building function. Furthermore, it evaluates ways of improving resilience by reducing damage and taking measures to improve recovery. Previous studies have assessed the performance of existing steel moment frame buildings (Muto and Krishnan 2011, Gupta and Krawinkler 1999), but these studies were limited to 20 storeys in height and focused on structural performance assessment alone. Other studies have assessed the performance of new tall steel moment frame buildings up to 40 storeys (Jayaram and Shome 2012) and estimated economic losses associated with building performance (Shome et al. 2013), but employed simplified single bay two-dimensional structural models that neglect torsional and biaxial effects and do not enable the study of detailed retrofit schemes for enhanced performance. This work draws a comparison of the direct economic loss estimate results for the archetype building and those presented in Shome et al. (2013) for a similar building typology designed to modern standards.

This work also enables a comparison between the information that can be inferred from an intensity-based seismic performance assessment and more rigorous time-based assessments, as discussed in Section 3.2. Intensity-based assessments are frequent in design practice, where design decisions are often based on a pre-defined earthquake ground motion intensity: DBE or MCE. In design practice, more comprehensive risk-based assessments, in which performance is assessed at an array of ground motion shaking intensities, from levels which cause no damage up to levels that trigger collapse (as outlined in Chapter 7), are rarely used.

6.1 Seismic hazard and ground motions

The majority of tall buildings in San Francisco are clustered in the downtown area, located approximately 14 km from the San Andreas Fault and 16 km from the Hayward Fault. The selected design earthquake hazard level defined in current building codes (ASCE 2010), if expressed in probabilistic terms has a 10% chance of occurring over a 50 year period. A probabilistic seismic hazard analysis (PSHA) is conducted at a representative site, near the San Francisco Transbay Transit Centre development, with subsurface ground conditions consistent with Site Class D as defined in ASCE 7 (2010) for the 10% in 50 year hazard. The selected intensity level is also representative of the "expected earthquake" defined by the San Francisco Planning and Urban Research Association (SPUR) for the purpose of defining resilience. This "expected earthquake" corresponds to a 7.2 earthquake scenario, which is an event that can be expected conservatively to occur within the lifetime of a structure (SPUR 2012). Reference to such scenario earthquake is important as it is a concept easier to grasp than probabilistic measures and therefore effective for communicating risk to policymakers and the public. Related scenario-based assessments are also presented in Chapters 5 and 8.

Directivity effects are known to cause pulse-like ground motions at near-fault sites. Pulse-like ground motions place extreme demands on structures and are known to have caused extensive damage in previous earthquakes (Shahi and Baker 2011). Due to the site's close proximity to active faults, near-fault directivity effects are expected to significantly contribute to the hazard. Therefore, the methodology proposed by Almufti et al. (2013), which is an extension of the method proposed by Shahi and Baker (2011), is utilized to incorporate velocity pulses in the selection of the design level ground motions for this study. This methodology uses de-aggregation data from the PSHA to construct a suite of target spectra used for matching an appropriate proportion of pulse-like motions with characteristics (pulse amplitude and pulse period) representative of a desired hazard intensity level. This methodology has been

successfully implemented in the development of ground motions of a peer-reviewed high rise building project in San Francisco (Almufti et al. 2013).

A CMS approach is used to characterize short and long-period ground motions separately (Baker 2011). Two suites of bedrock motions are developed to cover the entire period range of interest from $0.2T_1$ to $1.5T_1$ as defined in ASCE 7 (2010), where T_1 is the fundamental period of the structure. Each suite consists of 11 bidirectional motions each, well in excess of the 3 to 7 ground motion records required per ASCE 7 Section 16.1.3 (ASCE 2010). The short-period suite covers the range of periods from 0.5 to 4 seconds and the long-period suite covers the range of periods from 4 to 10 seconds. The archetype building has a fundamental period of approximately 5 seconds (refer to Chapter 4) and therefore the period range of interest, 1 to 7.5 seconds, is bounded by the two suites of motions. A pulse-included PSHA at bedrock is conducted at two conditioning periods, 0.75 seconds and 7.5 seconds, which are selected to cover the period range of interest accounting for potential elongation of the fundamental period due to non-linearity of the archetype building and the structural retrofit schemes considered. The de-aggregation of the pulse-included PSHA at the two conditioning periods reveals that approximately 20% of the short-period ground motions (2 out of 11 ground motions) contributing to the hazard are pulse-like, while approximately 80% of long-period ground motions (8 out of 11 ground motions) contributing to the hazard are pulse-like. Arup's in house software SISMIC (2012) is used to conduct the pulse-included PSHA.

For each pulse-like motion, a unique pulse-included CMS is developed as the target spectrum for the pulse component of the ground motion using the method of Shahi and Baker (2011). For non-pulse-like motions, seed ground motions are selected based on de-aggregation results, linearly scaled to the target at the conditioning period, and then spectrally matched to the conventional CMS. In this case, the CMS is developed using epsilon correlations by Baker and Jayaram (2008). Once the bedrock ground motions are developed, a non-linear site response analysis is conducted using LS-DYNA (2013) in order to characterize soil shaking and obtain input motions for the structural analysis. The soil profile and non-linear soil properties that define the shear modulus reduction curves utilized in the site response are obtained from soil testing (Almufti et al. 2013) at the representative site.

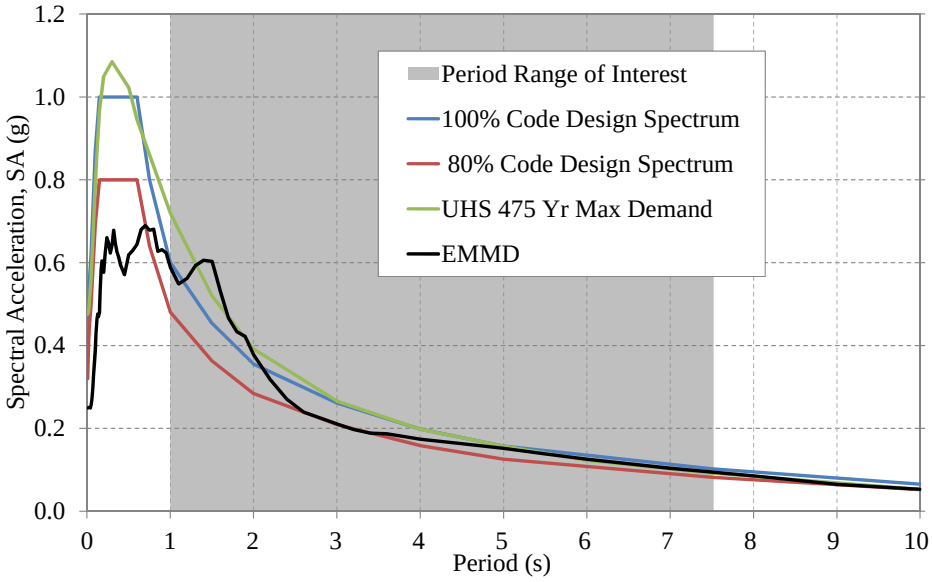

Figure 6-1: Compliance with ASCE 7 for site-specific ground motions.
Source: Molina Hutt et al. (2015).

ASCE 7 (2010) requires that for site-specific ground motions the design level response spectra is no less than 80% of the code prescribed design level spectrum. Figure 6-1 illustrates compliance with this criterion as the Envelope of the Mean of the Maximum Demand (EMMD) surface response spectra for the short and the long-period motions is no less than 80% of design level spectrum over the period range of interest of the structure (shaded in grey) from 1 to 7.5 seconds. In order to meet this requirement, the scale factors applied to the short and long-period suite of motions are 1.0 and 1.6, respectively. Figure 6-1 shows that the EMMD is close to the 475 year probabilistic estimate of the hazard.

The maximum and minimum demand surface response spectra for each suite of motions are shown in Figure 6-2. These ground motions are utilized to conduct the intensity-based performance assessment of the archetype building. A detailed summary of the ground motions suites can be found in Appendix D. The pulse components of the pulse-like ground motions are applied evenly to each of the principal directions of the building, i.e. out of 8 pulse-like motions, 4 are oriented in one direction while the other 4 are oriented orthogonal to that direction. For non-pulse-like motions, the maximum demand orientation is random relative to the principal axes of the structure.

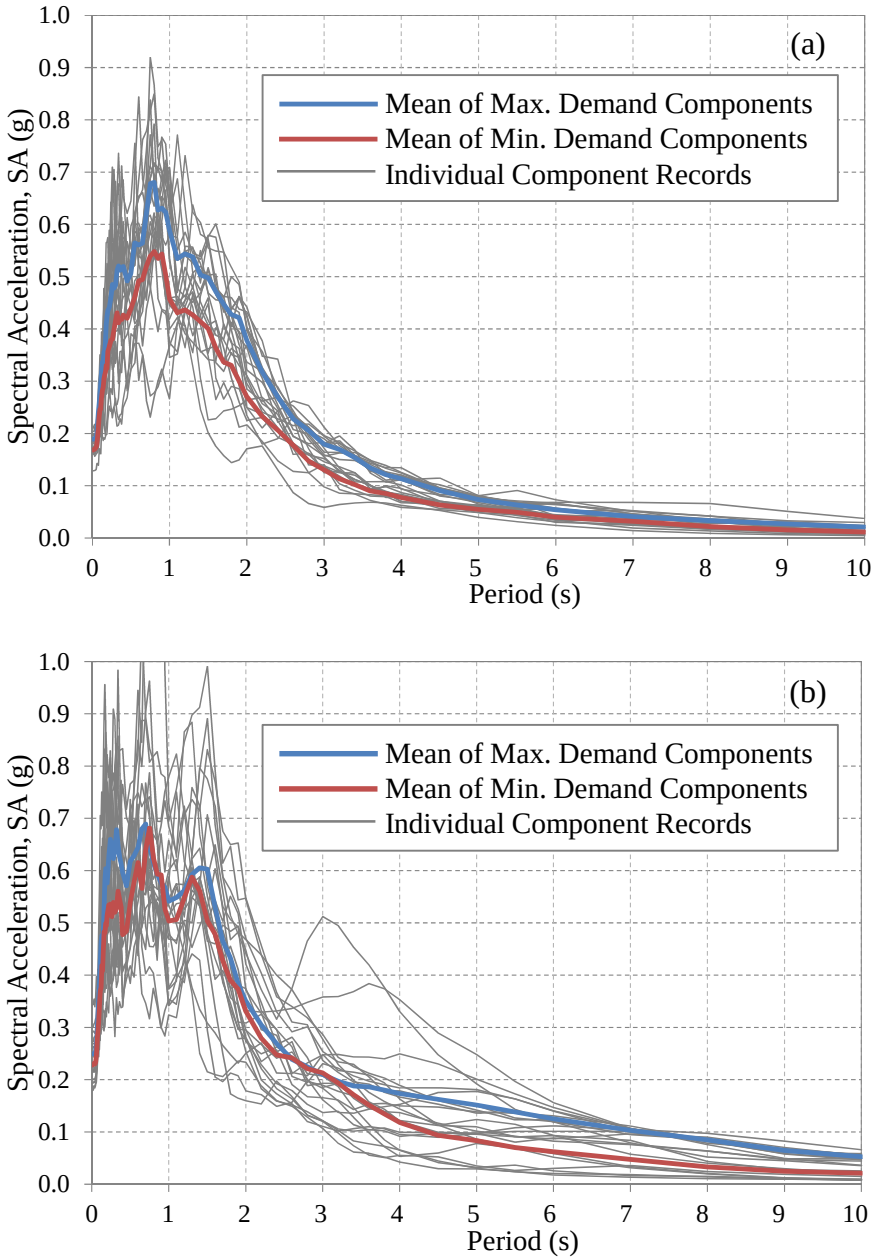

Figure 6-2: Mean of maximum and minimum demand response spectra and individual components for the short period (a) and long period (b) suites of ground motions. Source: Molina Hutt et al. (2015)

6.2 40-storey archetype building and strategies for increased resilience

In order to communicate building performance in terms of direct economic losses and downtime, EDP outputs from NLRHA are used as inputs to the building performance model. Here, transient and residual peak IDRs and maximum PFAs in each storey and each principal building direction are used as the EDPs. These results, summarized in Figure 6-3, indicate that the maximum of the mean of the peak transient IDRs from all ground motion simulations in all storeys is 1% in the X direction and 1.14% in the Y direction. The maximum of the mean of the peak residual IDRs from all ground motion simulations in all storeys is 0.23% in the X direction and 0.20% in the Y direction. The maximum of the mean PFA from all ground motion simulations in all storeys is 0.81g in the X direction and 0.61g in the Y direction. The overall maximum peak transient IDR is 4.45% in the X direction and 3.67% in the Y direction. The overall maximum PFA is 1.59g in the X direction and 1.53g in the Y direction. The absolute maximum results are outliers associated with two pulse-like ground motions that result in large spectral acceleration demands in a period range from 2 to 5 seconds as seen in Figure 6-2b.

For reference, these results can be compared with the global acceptance criteria under the MCE specified by PEER (2010a), i.e. mean peak transient IDR from all ground motion simulations less than 3%, absolute maximum transient IDR less than 4.5% or maximum residual IDR less than 1%. While these limits are met, the implications of the response in overall losses and downtime are rather staggering. The expected losses for the archetype building are in the order of $46M (34% of building cost). Losses are dominated by damage to the elevator system, façade and office fitouts. The expected downtime is 504 days for re-occupancy and 609 days for functional recovery. Downtime is dominated by impeding factors delaying the initiation of repairs, and repair work associated with expected damage levels. In order to enhance the seismic performance of the 40-storey archetype building, a reduction in transient and residual deformations, as well as storey accelerations is required. This objective can be achieved by adding stiffness, damping or a combination of these to the structure. Two conceptual structural retrofit schemes are considered in this study. The first scheme consists of the introduction of an elastic spine with steel bracing in the building core. The second scheme consists of the introduction of base isolation at ground level. Both retrofit schemes are conceived for progressive implementation in the building without loss of functionality or occupancy during construction.

The introduction of an elastic spine is intended to reduce transient and residual IDRs and ensure a more uniform distribution of ductility demand up the building height. This concept has been

implemented in a number of retrofit projects in Japan and has been explored in studies such as Günay et al. (2009) by means of introducing a rocking wall. In this case, the elastic spine is achieved through the introduction of bracing elements in the building core. Bracing elements are designed to remain linear elastic under the design earthquake hazard level. Strength demands are estimated via response spectrum analysis, using the code design spectrum illustrated in Figure 6-1. Braces are assumed to be pinned at their ends to ensure they only carry axial forces (no moment restraints at the ends of the brace). The implementation of the elastic spine retrofit scheme is envisaged to occur progressively up the building core. Steel bracing elements are introduced primarily around staircase and elevator enclosures. While these activities may require demolition and re-construction of certain non-structural elements, the areas affected would be limited and the work could be carried out without major disruptions to the building.

Figure 6-4 summarizes the NLRHA results for the elastic spine retrofit scheme used as inputs to the building performance model. It can be observed that the introduction of the elastic spine throughout the building core enables a more uniform distribution of IDRs up the building height, e.g. the concentration of demands in the upper storeys visible in the IDR-Y plot in Figure 6-3 is eliminated in the corresponding plot for the elastic spine retrofit in Figure 6-4. While the concentrations of deformation in a small number of storeys is eliminated, the overall distribution of demands, in terms of IDRs and PFAs, is fairly consistent between the baseline case and the elastic spine retrofit.

A second retrofit scheme consists of the introduction of base isolation at ground level, and is intended to significantly reduce the seismic demands to the structure. This technique has been implemented in a number of retrofit projects in Japan (Kani and Katsuta 2009). In this work, the goal of base isolation is not for period elongation of the fundamental period, but rather to reduce seismic demands associated with higher mode effects. Triple Pendulum bearing isolators are used, as they are particularly effective at adding damping and reducing storey drifts for tall buildings. Using multi-stage frictions minimizes exciting the higher modes, which dominate the seismic shears and damage.

The isolator properties used in this conceptual retrofit scheme are as recommended by Earthquake Protection System (EPS) for the 40-storey archetype building under consideration (EPS, personal communication 2012). The isolators are implemented at ground level in each column line. Isolators are modelled through a series of non-linear seismic isolator elements that represent each sliding surface within the Triple Pendulum bearing. The properties of each

seismic isolator element in the model are calibrated using an internal Arup tool (Arup, personal communication 2012) based on the overall properties of each sliding surface within the Triple Pendulum bearing (plate radius, curvature and surface friction). The isolator properties properties recommended by EPS are consistent with those utilized by Arup in past projects, expect for the axial stiffness of the isolator elements, which were verified with EPS (EPS, personal communication 2012) to ensure its feasibility for such retrofit application.

The construction sequence of the base isolation scheme is envisaged to be carried out on a column per column basis at ground level. Each column is to be propped and cut, then the base isolator is introduced and the props are slowly released after installation. This process would take place column by column for all column elements at ground level. This scheme would also require re-framing (stiffening) at the level where base isolation is introduced. In practice, this would entail the loss of basement level 1 (used for parking in the archetype building) such that stiff elements (deep beams or trusses) can be introduced in line with the isolators. Disruption during construction would be limited to ground level and basement level 1. While this scheme has been applied to a number of retrofit projects in the past, due to the scale of the building, work would be expected to be carried out at times when the building is not in use (nights and weekends). The greatest cost associated with this scheme is probably related to the contractor fees, which would be considerably higher than more conventional retrofit projects due to the difficulty and risk of the proposed scheme and construction sequence.

Figure 6-5 summarizes the NLRHA results for the base isolation retrofit scheme. The results illustrated in Figure 6-5 for the base isolation retrofit scheme are drastically different than those for the baseline case, as illustrated in Figure 6-4. The results for the base isolation retrofit scheme illustrate a significant reduction in demands up the building height, and a near uniform distribution of EDPs and PFAs up the building height.

While a rough cost estimate of the retrofit schemes considered could evaluate material quantities (total added steel tonnage and/or cost of base isolators), such estimates would fail to account for the greatest cost: contractor fees associated with complex retrofit work in a tall building while it remains operational. If these schemes were to be fully implemented, the design processes and construction sequences here described, envisaged to have minimal impact on the building function during construction, would need to be vetted by practising designers and contractors. A detailed cost estimate could then be carried out to enable a realistic cost-benefit analysis that would not only consider the reduction in expected seismic losses, but also the initial investment required to implement such retrofit schemes.

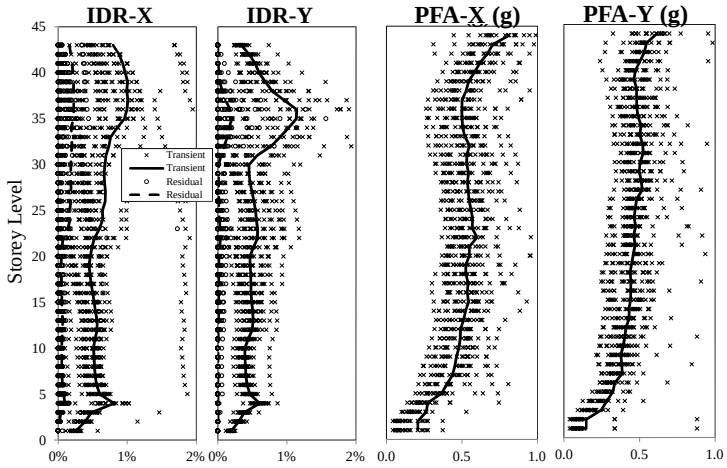

Figure 6-3: Demand parameters for the archetype building: transient and residual drifts (i.e. IDR) and accelerations (i.e. PFA) at each storey in each building direction. Adapted from Molina Hutt et al. (2015).

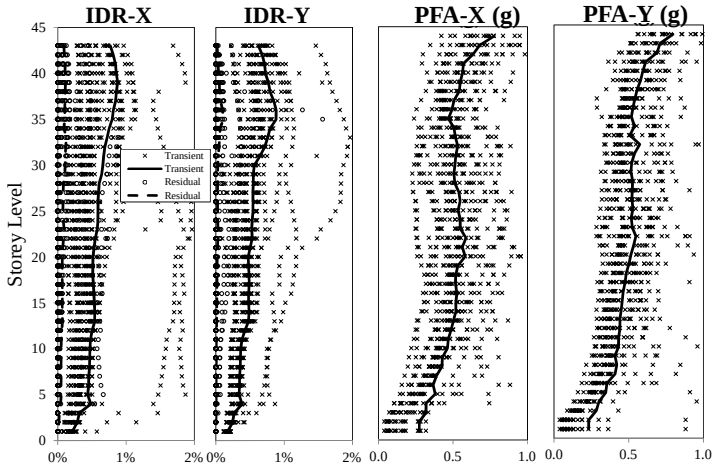

Figure 6-4: Demand parameters for the elastic spine retrofit: transient and residual drifts (i.e. IDR) and accelerations (i.e. PFA) at each storey in each building direction. Adapted from Molina Hutt et al. (2015).

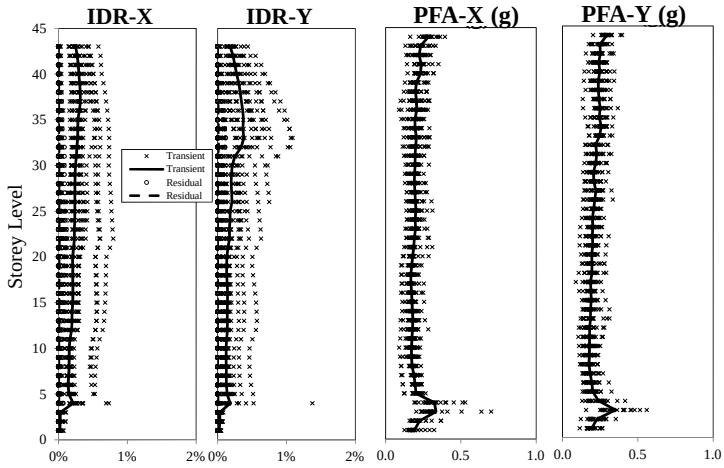

Figure 6-5: Demand parameters for the base isolation retrofit: transient and residual drifts (i.e. IDR) and accelerations (i.e. PFA) at each storey in each building direction. Adapted from Molina Hutt et al. (2015).

In addition to structural retrofit strategies, schemes for enhanced non-structural performance are also adopted in this study. These consist of employing non-structural components that are more resilient to earthquake damage. For instance, the component fragility function for standard partition walls is designated in Table 4-12 by fragility C1011.001a, which has a median value of 0.2% for the IDR associated with damage state 1 (DS1). In the case of the partition walls, where standard components are characterized by little deformation capacity and undergo damage at low storey drift ratios, enhanced partition walls can enable a shift of approximately 1% storey drift before the initiation of damage, as illustrated in Figure 6-6. This is achieved through a simple sliding/frictional connection detail that isolates the partition from lateral deformations while at the same time providing some resistance to in-plane and out-of-plane inertia forces, as described in Araya-Letelier and Miranda (2012). This illustrates that enhanced non-structural components can withstand significantly larger deformations before reaching the same damage state. The resulting fragility functions for the standard and enhanced partition wall are illustrated in Figure 6-6. In this study, the impact of using enhanced non-structural components is evaluated in all three structural schemes considered. When baseline non-structural components are used, these are referred to as standard non-structural components. When non-structural components that are more resilient to earthquake damage are used, there are referred to as enhanced non-structural components. A detailed list of all enhanced components included in the building performance models is included in Appendix C.

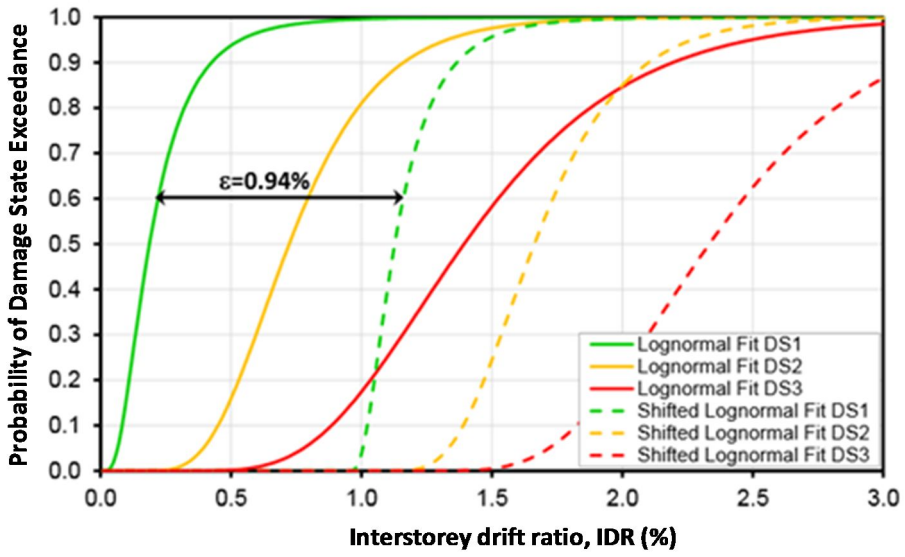

Figure 6-6: Fragility functions for standard (solid line) versus enhanced (dashed line) partitions walls.
Source: Adapted from Araya-Letelier and Miranda (2012).

In order to minimize downtime, a number of mitigation measures are also adopted. As illustrated in Equation 4-13, downtime to achieve re-occupancy is attributed to impeding factors and the time required to repair damaged structural and non-structural components. Downtime to achieve functional recovery is attributed to these same factors, but additionally considers utility disruption. The mitigation measures considered in this study in order to minimize delays associated with impeding factors are illustrated in Table 6-1. For instance, delays associated with post-earthquake inspection can be minimized by joining the City and County of San Francisco's Building Occupancy Resumption Program (BORP) to pre-certify a private post-earthquake inspection rather than waiting for a city appointed inspector. Similarly, delays associated with engineering and contractor mobilization can be minimized by arranging contractual agreements with engineers and contractors to guarantee their services immediately after an earthquake. For instance, as illustrated in Table 6-1, if damage to structural components hinders re-occupancy, expected delays associated with engineering mobilization are 12 weeks. However, these delays can be reduced to 4 weeks by having an engineer on contract. Similarly, for the same level of structural damage, expected delays associated with contractor mobilization are 40 weeks, but these can be reduced to 7 weeks by having a pre-arranged contract with a general contractor. Similar measures can be put in place to minimize other impeding factors.

Table 6-1: Assumed delays associated with impeding factors.
Source: Molina Hutt et al. (2015).

Impeding Factor	Mitigation Measure	Other Conditions	Mean	Dispersion
Post-Earthquake Inspection	None	-	5 days	0.54
	BORP Program	-	1 day	0.54
Engineering Mobilization	None	Damage to structural components hinders full recovery [Repair Class=1]	6 weeks	0.40
		Damage to structural components hinders functional recovery or re-occupancy [Repair Class ≥2]	12 weeks	0.40
	Engineer on Contract	Damage to structural components hinders full recovery [Repair Class=1]	2 weeks	0.30
		Damage to structural components hinders functional recovery or re-occupancy [Repair Class ≥2]	4 weeks	0.50
Contractor Mobilization	None	Damage to any component hinders full recovery [Repair Class =1]	28 weeks	0.30
		Damage to any component hinders functional recovery or re-occupancy [Repair Class ≥2]	40 weeks	0.31
	General Contractor on Contract	Damage to any component hinders full recovery [Repair Class =1]	3 weeks	0.70
		Damage to any component hinders functional recovery or re-occupancy [Repair Class ≥2]	7 weeks	0.40
Financing	None	Private Loans	15 weeks	0.68
	Pre-arranged Credit	-	1 week	0.50
Permitting	None	Damage to structural components hinders functional recovery or re-occupancy [Repair Class ≥2]	8 week	0.32
	Minimize Structural Damage	Damage to structural components hinders full recovery [Repair Class =1]	1 weeks	0.90

A structural only retrofit scheme, which consists of the introduction of an elastic spine with steel bracing in the building core, enables a reduction in expected losses of roughly 25% to $34M (25% of building cost). The structural response demand parameters associated with this retrofit scheme are illustrated in Figure 6-4. An alternate structural only retrofit scheme, which consists of the introduction base isolation at ground level, enables a reduction in expected losses of roughly 80%, to $9M (7% of building cost). The structural response demand parameters associated with this retrofit scheme are illustrated in Figure 6-5. A non-structural only intervention scheme, which consists of the introduction of components that are more resilient to earthquake damage, enables a reduction in expected losses of roughly 32%, to $31M (23% of building cost). When these non-structural enhancements are used in conjunction with the elastic spine structural retrofit scheme, a 56% reduction in expected losses, to $20M (15% of building cost) is attained. Lastly, when these non-structural enhancements are used in conjunction with the base isolation structural retrofit scheme, a 92% reduction in expected losses, to $4M (3% of building cost) is achieved. These results explicitly consider the impact of residual drifts and are summarized in Table 6-2. If the impact of residual drifts is neglected, the reduction in expected losses is as reported in Table 6-3. These results can also be visualized in Figure 6-7 by fitting all realizations in each performance assessment to a lognormal cumulative distribution. Since the engineering demand parameters used as inputs to the building performance model are in line with current code requirements, it is no surprise that expected losses in new tall buildings are not drastically different than those of older tall buildings. The expected losses for an archetype 40-storey building in the Los Angeles area designed per modern buildings codes under an equivalent intensity level are 23% of building cost (Shome et al. 2013).

Figure 6-8 illustrates the contribution of different building components to the total expected losses. Building components are grouped into five main categories: egress, façade, MEP, office fitouts and structure. The performance groups associated with each one of these categories are shown in Tables 4-12 as well as Appendix C. There are similarities in the distribution of building components contributing to the losses between the archetype building and the elastic spine structural retrofit scheme with either standard or enhanced non-structural components. This can be attributed to the similarity in the demand parameter distribution throughout the height for both schemes, as shown in Figure 6-3 and Figure 6-4. The distribution of building components contributing to the losses for the base isolated scheme is distinct due to the unique distribution in demand parameters throughout the building height when compared to the other structural schemes. The use of enhanced non-structural building components enables a significant reduction in losses attributed to damage to the façade (up to 93% for the elastic spine

scheme), office fitouts (up to 94% for the base isolated scheme) and MEP components (up to 97% for the base isolated scheme). Structural losses are largely due to damage to fracture prone pre-Northridge moment connections (70% to 90% depending on the structural scheme). However, these losses vary in absolute value from $5M for the archetype building to $2M for the base isolated scheme. Absolute losses attributed to egress are a result of direct damage to elevators, which require repair costs ranging from $9M for the archetype building to $0.5M for the base isolated scheme.

Table 6-2: Expected loss estimates for the baseline building and enhanced performance schemes with consideration of residual drifts.
Adapted from Molina Hutt et al. (2015).

		Non-structural	
		Standard	Enhanced
Structural	Archetype (Baseline)	$46M (34%)	$31M (23%)
	Elastic Spine	$34M (25%)	$20M (15%)
	Base Isolation	$9M (7%)	$4M (3%)

Table 6-3: Expected loss estimates for the baseline building and enhanced performance schemes without consideration of residual drifts.
Adapted from Molina Hutt et al. (2015).

		Non-structural	
		Standard	Enhanced
Structural	Archetype (Baseline)	$35M (25%)	$19M (14%)
	Elastic Spine	$29M (21%)	$13M (10%)
	Base Isolation	$9M (7%)	$4M (3%)

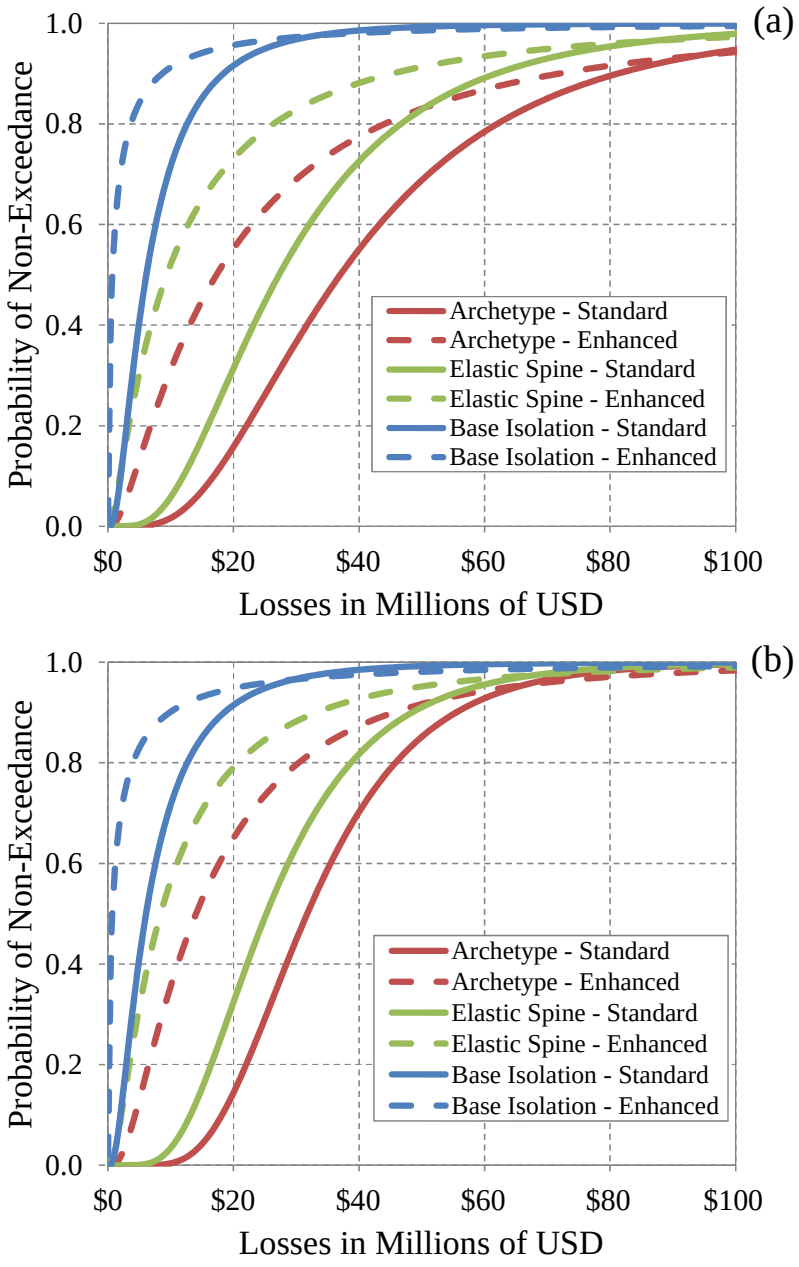

Figure 6-7: Loss estimates for archetype building (baseline), elastic spine, and base isolation retrofit schemes with standard and enhanced non-structural components: (a) with consideration of residual drifts; (b) without consideration of residual drifts. Source: Molina Hutt et al. (2015).

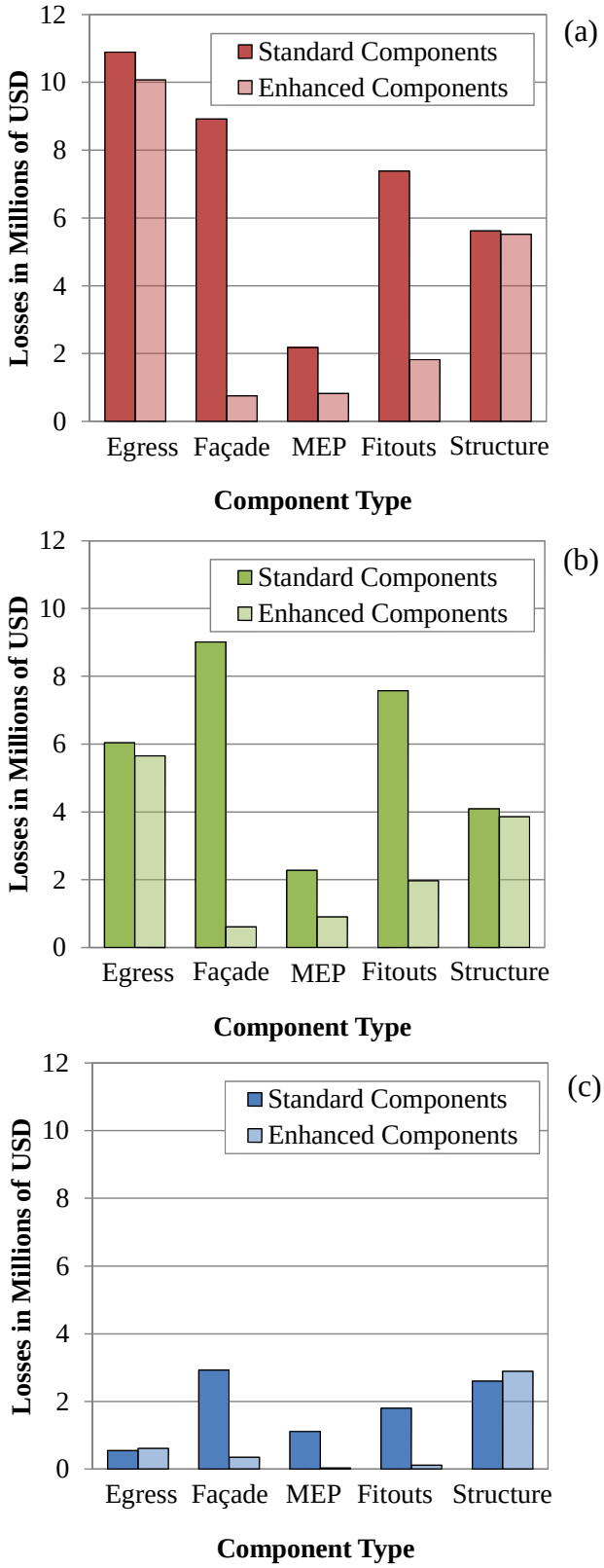

Figure 6-8: Contribution to losses of building components for the following: (a) archetype building (baseline); (b) elastic spine retrofit scheme; (c) base isolation retrofit scheme with standard and enhanced non-structural components.
Source: Molina Hutt et al. (2015).

The discrepancies in the results with and without consideration of residual drifts can be observed in Figure 6-7 by an increase in the median losses as well as in the dispersion of the lognormal distributions. For the 40-storey archetype building with standard non-structural components, the dispersion is 0.44 when residual drifts are neglected and 0.61 when residual drifts are considered. Similarly, for the elastic spine scheme with standard non-structural components, the dispersion has a value of 0.51 when residual drifts are neglected and 0.64 when considered. Lastly, for the base isolated case, the dispersion remains effectively constant at approximately 0.86. A similar trend is observed for the schemes considered when enhanced non-structural components are used. These observations highlight that the increase in variability throughout the set of realizations (i.e. the increase in dispersion) when residual drifts are considered decreases with the introduction of different retrofit interventions.

Even though consideration of residual drifts generally increases the uncertainty in the building performance functions, as illustrated in Figure 6-7, their consideration is critical in the loss estimate methodology since a building may be deemed irreparable if large residual drifts are present. Furthermore, residual drifts are an important consideration in judging the post-earthquake safety of a building. Field manuals for post-earthquake safety evaluation, such as ATC 20-1 (2005), indicate that when any storey in a building has noticeable leaning the building should be posted with an ‘Unsafe’ placard, which categorizes the building as unsafe for occupancy or entry. The REDi downtime assessment methodology assumes that residual drifts are small and therefore the building is repairable. Consideration of residual drifts on the downtime estimate results presented in Table 6-4 and Table 6-5 would increase expected values because for large residual drifts, where the building is deemed unrepairable, total downtime is that of complete re-design and reconstruction. FEMA (2012) proposes 4 damage states associated with residual drift: DS1 requires no structural realignment, though repairs may be required for non-structural components; DS2 requires realignment of the structural frame and related structural repairs; DS3 requires major structural realignment to restore margin of safety for lateral stability though the level of repair may not be economically feasible; lastly, DS4 implies that the structure is in danger of collapse from aftershocks. Figure 6-9 illustrates probability distribution of residual drifts for the archetype (baseline) building, elastic spine and base isolated retrofit schemes against the above-mentioned damage states. The expected peak residual storey drift for the baseline building is 0.44%, consistent with DS2. The expected peak residual storey drift for the elastic spine retrofit scheme is 0.23%, just beyond the threshold of DS1. The expected peak residual storey drift for the base isolated scheme is 0.07%, consistent with DS1 and well below the maximum out-of-plumb tolerance permitted in new construction.

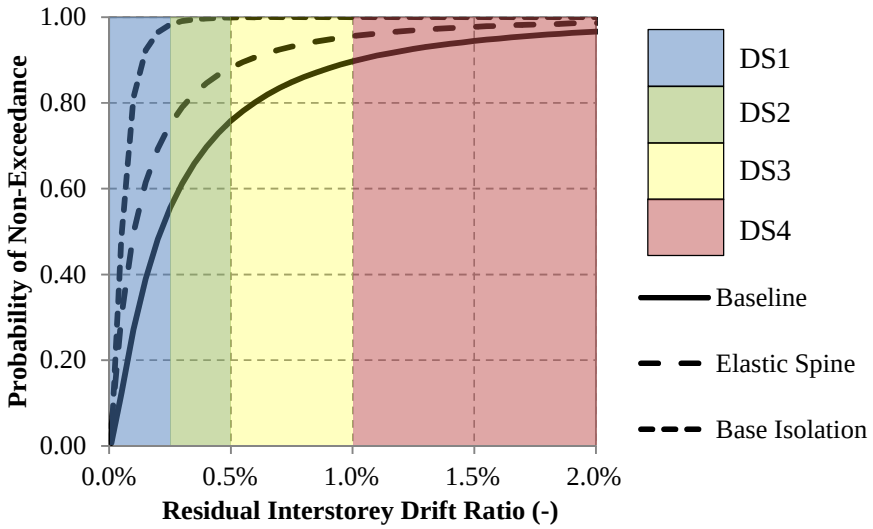

Figure 6-9: Probability distribution of residual drifts for archetype building (baseline), elastic spine, and base isolation retrofit schemes and associated FEMA damage states.
Source: Molina Hutt et al. (2015).

Table 6-4: Downtime estimates for the baseline building and enhanced performance schemes for re-occupancy.
Adapted from Molina Hutt et al. (2015).

		Non-structural	
		Standard	Enhanced
Structural	Archetype (Baseline)	504 days	98 days
	Elastic Spine	504 days	98 days
	Base Isolation	371 days	1 day

Table 6-5: Downtime estimates for the baseline building and enhanced performance schemes for functional recovery.
Adapted from Molina Hutt et al. (2015).

		Non-structural	
		Standard	Enhanced
Structural	Archetype (Baseline)	609 days	224 days
	Elastic Spine	504 days	140 days
	Base Isolation	413 days	1 day

In order to provide a more direct measure of resilience, the downtime to achieve building re-occupancy and functional recovery for the archetype building and retrofit schemes considered is presented in Table 6-4 and Table 6-5, respectively. These results illustrate that while structural retrofits may enable significant reductions in losses, as seen in Table 6-2 and Table 6-3, these measures alone do not ensure a building is resilient. An illustration of the impact of using enhanced non-structural components as well as mitigation measures to minimize delays associated with impeding factors is illustrated in Figure 6-10, where a breakdown of the different downtime contributors as well as de-aggregation of the impeding factors for the archetype building is shown. For the same structural scheme, it can be observed that using enhanced non-structural components and adopting mitigation measures can have a significant impact on downtime.

Downtime for re-occupancy, for all structural schemes with standard non-structural components, is largely driven by delays associated with building inspection, contractor mobilization and long lead components that require replacement. In addition to these delays, which are equal for all schemes, repair times range from 224 days for the baseline and elastic spine schemes to 84 days for the base isolation scheme. Downtime for functional recovery for structural schemes with standard non-structural components vary: 609, 504 and 413 days for the baseline, elastic spine and base isolation schemes, respectively. Utility disruption does not control overall downtime estimates for functional recovery because delays associated with impeding factors exceed those associated with utility disruption (see Equation 4-13). While delays are consistent with those for re-occupancy, repair times are as follows: 322, 217 and 126 days for the baseline, elastic spine and base isolation schemes, respectively. Repair times for re-occupancy are consistent between the baseline scheme and the elastic spine because, while the elastic spine scheme reduces damage and losses to certain components, it does not prevent damage to those components that hinder re-occupancy. However, repair times for functional recovery for the elastic spine scheme are significantly lower than for the baseline scheme because lower residual IDRs reduce damage to elevators. When enhanced non-structural components are adopted in addition to measures to mitigate delays, downtime for re-occupancy can be drastically reduced to 98 days for the baseline and elastic spine schemes, and a day or less for the base isolated scheme. Furthermore, downtime for functional recovery can be reduced to 224 days for the baseline case, 140 days for the elastic spine scheme, and a day or less for the base isolation scheme.

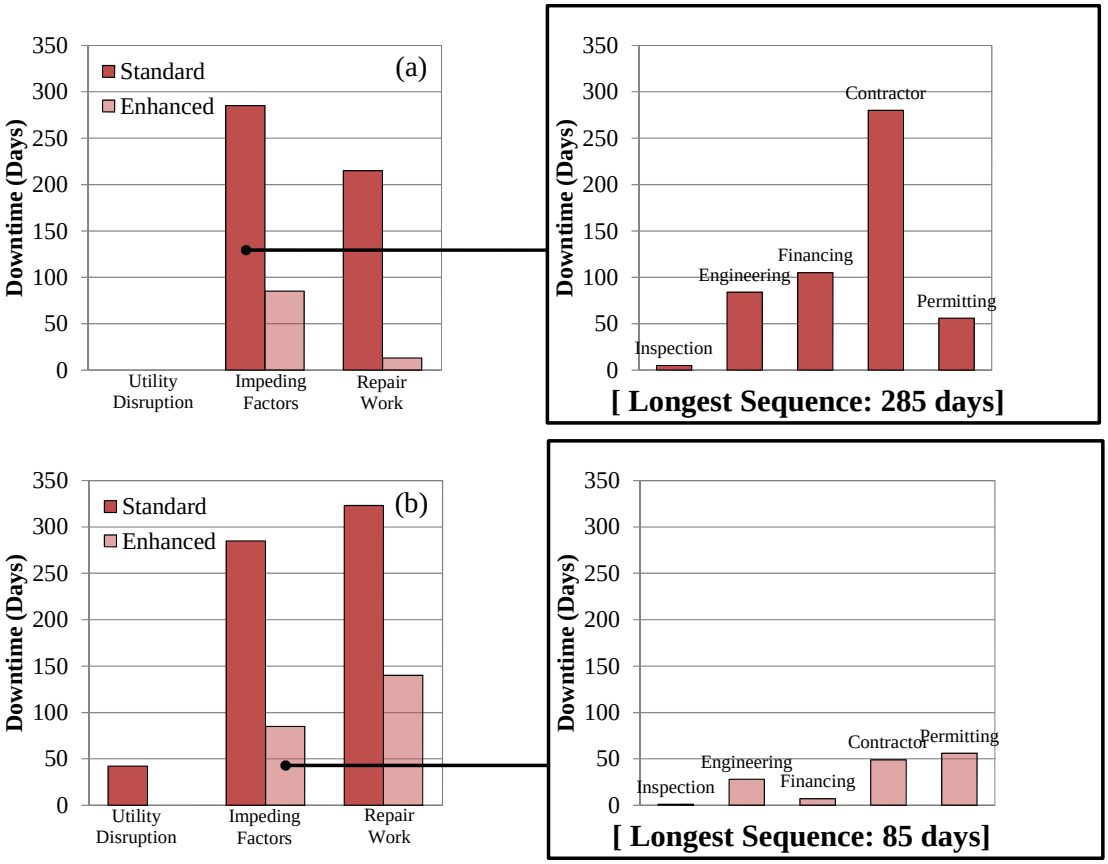

Figure 6-10: Downtime contributors for re-occupancy (a) and functional recovery (b) and sample de-aggregation of impeding factors for the archetype building (baseline) using standard non-structural components and no mitigation measures to minimize impeding factors versus enhanced non-structural components and mitigation measures to minimize impeding factors.
Source: Molina Hutt et al. (2015).

6.3 Summary and conclusions

A seismic performance assessment of existing tall steel-framed buildings from the mid-1970s to the mid-1980s has been presented for a case study city, San Francisco, by means of an archetype 40-storey tall building designed based on an inventory of the existing tall building stock. In order to influence decision making, performance is reported as the expected consequences in terms of direct economic losses and downtime. A number of strategies including structural retrofits, non-structural enhancements and mitigation measures are proposed in order to achieve increased resilience. Expected direct economic losses for the archetype building are in the order of 34% of building cost and the adoption of structural retrofit schemes, enhanced non-structural components and mitigation measures to minimize impeding factors enable up to a 92% reduction in losses. The adoption of non-structural enhancements can enable significant reduction in losses associated with the performance of the façade, office fitouts and MEP components, though overall loss reduction is maximized when adopting both

structural and non-structural enhancements. Downtime for re-occupancy and functional recovery of the archetype building is estimated at 497 and 609 days, respectively. When mitigation measures to reduce delays are used in conjunction with both structural and non-structural enhancements, minimal downtime for both re-occupancy and functional recovery can be achieved. The impact of residual drifts in seismic loss estimates for the 40-storey archetype building and retrofit schemes under consideration is quantified. Consideration of residual drifts in the loss assessment yields an increase in expected losses as well as an increase in the dispersions of the resulting performance functions. Building performance is categorized as a function expected residual drifts, which indicate that the archetype building requires structural realignment of the frame under a design level earthquake, whereas the retrofit schemes presented reduce damage to levels requiring very minor or no structural realignment.

While the response of the structure, in terms of storey drifts, is in line with global acceptance criteria to guarantee life-safety of building occupants, the implications of performance on overall losses and downtime indicates that these buildings are not seismically resilient and would experience a slow and costly recovery when subject to ground motions consistent with a design earthquake hazard level.

This page is intentionally left blank.

Chapter 7

BSPE: Time-based Assessment

In order to benchmark the performance of older existing tall buildings against modern designs, this chapter presents the results of a time-based seismic performance assessment of two archetype tall buildings in San Francisco, CA: a 50-storey steel MRF office building designed following the requirements of UBC 1973, hereinafter referred to as the 1973 50-storey archetype, and a 50-storey steel MRF office building designed following IBC 2012, hereinafter referred to as the 2012 50-storey archetype. The 1973 50-storey archetype is designed to be representative of design and construction practice from the mid-1970-s to the mid-1980s, based on an inventory of existing tall buildings in San Francisco. The 2012 50-storey archetype is a building of the same geometry and occupancy as the 1973 50-storey archetype, but designed following modern building code requirements. As discussed in Chapter 2, PBSD, by definition, implies that pre-defined seismic performance objectives are met at different intensities of ground motion shaking. Rather than adopting a PBSD approach for the modern archetype and verifying pre-defined performance objectives, a modern code-based design is adopted. This approach enables verifying compliance with the life-safety objective of modern codes under MCE shaking and provides an understanding of expected performance at other earthquake intensities. For details on the selection and development of the archetype buildings, NLRHA simulations, and building performance modelling for loss, downtime and recovery estimates, please refer to Chapter 4. This work has been compiled in Molina Hutt et al. (2017) as referenced throughout the chapter. The author was the key contributor to the referenced journal papers. At the time of writing, Molina Hutt et al. (2017) is under review.

7.1 Methodology

A time-based assessment consists of the evaluation of a number of intensity-based performance assessments (as illustrated in Chapter 6) under a range of ground motion intensity levels which are then combined with the ground motion hazard curve to provide the annual rates of exceedance of a performance measure, e.g. storey drift (NEHRP 2011). The technical basis of the methodology used to conduct the time-based seismic performance assessment presented here was developed by PEER, and applies the total probability theorem to predict earthquake consequences in terms of the probability of incurring a particular value of a performance measure (Moehle and Deierlein 2004). Under this framework, performance is

computed through multiple integrations: the probability of incurring an earthquake of different intensities over all possible intensities; the probability of incurring a certain building response (drift, acceleration, etc.) given an intensity of ground shaking; and the probability of incurring certain damage and consequences given a value of building response (FEMA 2012).

The performance assessment of the archetype buildings under consideration follows a Multiple Stripe Analysis (MSA) approach, in which performance is assessed at eight different intensity levels representing different seismic hazard levels. NLRHA are conducted with ground motion suites representative of each intensity level considered. The results of the NLRHA are used as inputs to the building performance model to estimate damage, losses, and downtime. The essence of this time-based approach is that these results are then linked back to probabilistic seismic hazard analysis data, which enables calculating a range of risk metrics, e.g. collapse risk. This notion of 'stripes' is observed in Figures 7-12a, 7-14a, 7-15a or 7-16a, where each stripe represents a set of results at a particular earthquake ground motion shaking intensity level, i.e. SA(T=5sec). Hence, the results from multiple intensity levels results in multiple stripes.

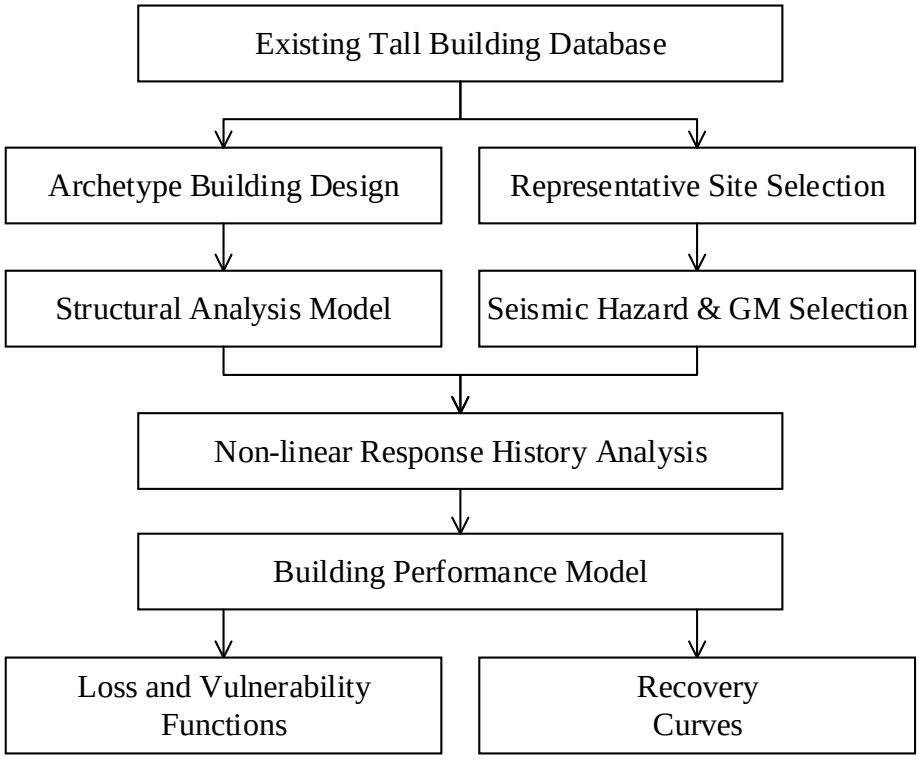

Figure 7-1: Methodology adopted in the time-based assessment of the 1973 and 2012 50-storey archetype buildings.
Source: Molina Hutt et al. (2017).

The methodology for assessing the performance of the 1973 and 2012 50-storey archetype buildings can be split into the following steps: i) design of the archetype buildings based on a

database of the existing tall building stock and selection of a representative site in the case study city; ii) quantification of the seismic hazard at the representative site and selection of ground motions consistent with the hazard; iii) development of non-linear numerical models that capture all elements that contribute significantly to the strength and stiffness of the structure; iv) conducing NLRHA at an array of earthquake ground motion intensities; v) estimation of damage, losses, downtime and recovery; vi) development of performance functions and risk metrics to describe anticipated building performance. This methodology, illustrated in Figure 7-1, is consistent with the approach followed in Chapters 5 and 6. However, this time-based evaluation is more comprehensive than the scenario- and intensity-based assessments because performance is measured at a wide range of shaking intensity levels, which enable the development of advanced risk metrics that cannot be inferred from the results presented in previous chapters.

7.2 Seismic hazard and ground motions

PSHA enables the calculation of hazard curves, which express the annual rate of exceeding of ground motion parameters, such as the spectral acceleration at a selected period, at a particular site, considering the risk from all possible seismic sources. In a MSA, structural assessments are performed at a series of ground motion intensities spanning from low to high probability of occurrence. The upper and lower bound intensity levels considered should result in a range of damage to the structure, from negligible to complete loss. In this study, the minimum and maximum annual frequencies of exceedance (AFE) and corresponding spectral accelerations (SA) are selected, initially, based on the recommendation of FEMA (2012) as follows: Maximum AFE = 0.04 and corresponding minimum spectral acceleration bound (SA_{MIN}), Minimum AFE = 0.0002 and corresponding maximum spectral acceleration bound (SA_{MAX}). These bounds are applied to the seismic hazard curve at the representative site, as shown in Figure 7-2. The hazard curve is obtained using the USGS hazard curve calculation tool (USGS 2015). A seismic hazard curve for a 5 second period is selected as it is in close proximity to fundamental period of the archetype buildings considered, as discussed in Chapter 4, and is the longest period for which USGS provides seismic hazard data.

The lower bound SA (SA_{MIN}) should correspond to a ground motion intensity level that does not result in significant damage to structural components, whereas the upper bound SA (SA_{MAX}) should correspond to a ground motion intensity beyond the level that triggers collapse. Once the bounds of spectral accelerations are determined, the range is split into a number of equal intervals for assessment. Eight intensity level intervals are selected to capture

a wide range of responses. The midpoint SA of each one of these intervals is then computed along with its corresponding AFE. This process is graphically illustrated in Figure 7-2, where the earthquake ground motion intensity intervals and the assessment points are denoted by Δe_i and e_i, respectively. As building performance is not known prior to conducting the analyses, recommended bounds and intervals are initially adopted and later verified to ensure the intensity levels considered capture the intended range of performance from low damage to collapse.

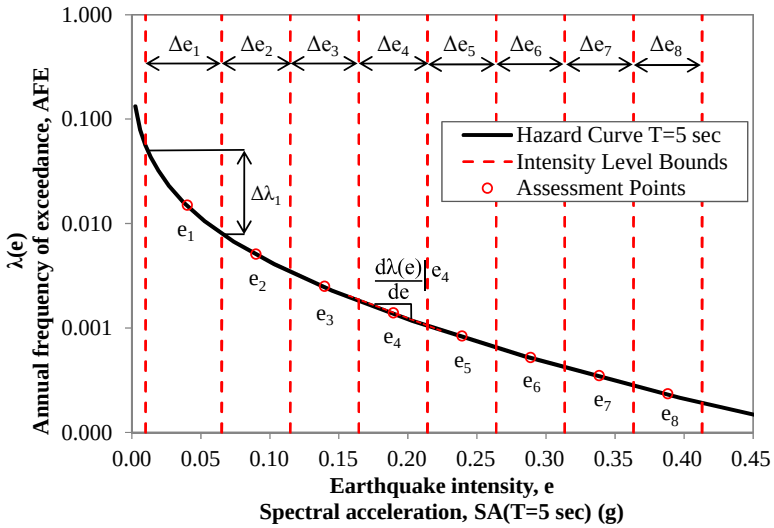

Figure 7-2: Seismic hazard curve at the representative site in downtown San Francisco (V_{s30}=260m/s, T=5sec.) illustrating the earthquake ground motion intensities (e_i) considered in the time-based assessment.
Source: Molina Hutt et al. (2017).

As the rates of exceedance identified consider all possible seismic sources, the resulting intensity is not associated with any particular earthquake magnitude or distance. However, through de-aggregation it is possible to determine the magnitude, distance and epsilon combinations that contribute the most to a particular intensity level. Epsilon is an indicator of spectral shape and it provides a measure of the difference between the computed spectral acceleration at a particular probability of exceedance and the spectral acceleration associated with the controlling magnitude and distance (Baker and Cornell 2006). Table 7-1 summarizes the AFE, SA, magnitude (M), distance (R) and epsilon (ε) associated with each earthquake ground motion intensity level considered in the assessment. Key parameters are also summarized in Figure 7-3. PSHA de-aggregation results for all intensity levels considered are included in Appendix E.

Table 7-1: SAs at a 5 second period, AFEs, return periods and magnitude (M), distance (R) and epsilon (ε) de-aggregation results for the ground motion intensities considered in the time-based assessment.
Source: Molina Hutt et al. (2017).

Earthquake Ground Motion Intensity	SA (g)	AFE (-)	Return Period (years)	M (-)	R (km)	ε (-)
e_1	0.042	0.014	72	7.25	29.50	-0.10
e_2	0.089	0.005	199	7.50	19.90	0.30
e_3	0.140	0.0024	409	7.63	16.80	0.62
e_4	0.185	0.0014	712	7.70	15.60	0.85
e_5	0.220	0.00096	1039	7.73	15.10	1.01
e_6	0.284	0.00053	1898	7.78	14.40	1.25
e_7	0.314	0.00040	2475	7.80	14.10	1.35
e_8	0.370	0.00026	3899	7.82	13.80	1.51

In order to select ground motion records for use in the dynamic analysis, a target spectrum needs to be identified. As discussed in Section 2.2.2, in a UHS, by definition, all ordinates have the same annual frequency of exceedance. Scaling ground motion records to a target UHS over a period range of interest is convenient for seismic design purposes. However, the spectral shape of the records selected is not representative of the source, magnitude and distance combinations that control the hazard at any return period. Furthermore, it is a conservative estimate of the hazard because when the geomean spectral ordinate of a ground motion matches the UHS at a particular period, the spectral ordinates are typically less at other periods. As discussed in Section 5.1, in order to address these limitations, Baker and Cornell (2006) introduce the CS. The CS is a response spectrum that specifies the probability distribution of spectral accelerations over a range of periods, conditioned on spectral acceleration at a conditioning period of interest. The conditional spectrum utilizes de-aggregation results (M, R and ε) and correlations between spectral accelerations at different periods to compute the expected response spectrum and additionally accounts for the variability of the response spectra. The CS can be used as a target response spectrum for site- and structure-specific ground motion selection and provides the link between seismic hazard and structural response (Lin and Baker 2015). For this study, a CS conditioned at a 5 second period is selected as the target spectrum for each of the intensity levels considered in the assessment, using USGS de-aggregation data at each earthquake ground motion intensity considered. Suites of ground motions are selected to collectively match the entire distribution of the CS using a computationally efficient algorithm developed by Baker and Lee (2017). The resulting ground motion suites are summarized in Appendix D.

The target conditional spectrum mean and variance as well as the ground motion records obtained for assessment are checked against the corresponding UHS obtained from the USGS hazard data. It is noted that hazard data beyond a 5 second period is not available from USGS. Therefore, in order to construct relevant UHS, hazard data beyond 5 seconds are obtained

from OpenSHA (Field et al. 2003). Figure 7-3 illustrates the target conditional spectrum mean and variance, as well as the ground motions selected for assessment at all intensity levels considered. At the conditioning period of 5 seconds, the spectral acceleration of the mean, variance, ground motion record spectra and UHS are coincident. Figure 7-3 highlights a sample collapse realization in earthquake ground motion intensity e_8 and the geomean of the Loma Prieta ground motion recorded at the base of the Chevron building in San Francisco in earthquake ground motion intensity e_1. The structural response of the 1973 50-storey archetype building subject to these two ground motion records (collapse realization and Loma Prieta) is discussed in detail in Sections 4.2.5 and 4.2.6, respectively.

At each earthquake ground motion intensity, 20 records are selected to match the conditional spectrum (mean and variance). Records are selected from the PEER NGA West 2 database (PEER 2013). A maximum scale factor of five is used in the record selection process. Only records with earthquake magnitudes greater than five and source to site distances of up to 50 km are considered. No additional criteria are set for record selection concerning shear wave velocity profiles, pulses or other parameters. The effect of pulse-like ground motions is not explicitly considered in the ground motion selection process. However, because record selection is consistent with M, R and ε hazard de-aggregation data, records with pulses are present in most ground motion suites, particularly at high earthquake ground motion intensities. The proportion of pulse-like ground motions in the resulting suites is consistent with those derived in Chapter 6, where pulse-like ground motions are explicitly considered in the ground motion selection process. In Chapter 6, 45% of the ground motions selected had velocity pulses. The return period considered in Chapter 6 (~475 years) sits in between ground motion intensities e_3 and e_4, which have a 40% and 50% proportion of pulse-like motions in their respective suites. The selected ground motions are input at the base of the structural model, which is assumed to have a rigid support at the base. Soil-structure interaction is not explicitly considered in the analyses.

The CS is computed on the basis of a specified conditioning period of 5 seconds. Tall buildings generally have responses that are sensitive to excitation at a range of periods, both shorter (higher mode effects contributions to the response) and longer (lengthened periods due to non-linear behaviour). As a result, questions arise regarding the appropriate choice of the conditioning period when using the CS as the target spectrum for ground motion selection. Lin et al. (2013) investigated the effect of the conditioning period on time-based structural response assessments, such as the one conducted in this study. The study demonstrated that such assessments are relatively insensitive to the choice of conditioning period when ground

motions are selected to ensure hazard consistency. These observations result from the fact that, when CS-based ground motion selection is used, the distributions of response spectra of the selected ground motions are consistent with the site ground motion hazard curves at all relevant periods, and this consistency with the site hazard curves is independent of the conditioning period (Lin et al. 2013).

The NLRHA results from the earthquake intensities originally considered indicated the need to consider additional intensity levels in order to capture the intended range of performance from low damage up to levels that trigger collapse for both archetypes. For the 1973 50-storey archetype, additional assessment points are considered at low SA levels. The following additional assessment points are introduced: e_{1A}, e_{2A} and e_{3A} at the mid-point of intervals e_1-e_2, e_2-e_3 and e_3-e_4, respectively. These additional points are introduced to further evaluate performance in the range of ground motion shaking where small increments in intensity, i.e. SA(T=5sec), result in sudden changes in performance, i.e. increased proportion of collapsed simulations. For the 2012 archetype, additional assessment points are considered at higher SA levels. The following assessment points are introduced: e_{8A}, e_{8B} and e_{8C}. The resulting points of assessment for the 1973 and the 2012 50-storey archetype buildings are shown in Figure 7-4. Ground motion suites for these additional assessment points are obtained by linearly scaling the records selected from the closest assessment point to obtain the intended SA at a 5 second period. Table 7-2 summarizes the SA, AFE, return period, baseline assessment point and scale factors for the additional assessment points considered.

Table 7-2: SAs at a 5 second period, AFEs, return periods and magnitude, distance and epsilon de-aggregation results for the ground motion intensities considered in the time-based assessment.

Additional Assessment Point	Archetype	SA (g)	AFE (-)	Return Period (years)	Baseline Assessment Point	Scale Factor
e_{1A}	1973	0.07	0.0082	122	e_1	1.56
e_{2A}	1973	0.11	0.0036	278	e_2	1.29
e_{3A}	1973	0.16	0.0019	526	e_3	1.16
e_{8A}	2012	0.46	0.00016	6342	e_8	1.25
e_{8B}	2012	0.56	0.00007	14276	e_8	1.50
e_{8C}	2012	0.65	0.00005	20577	e_8	1.75

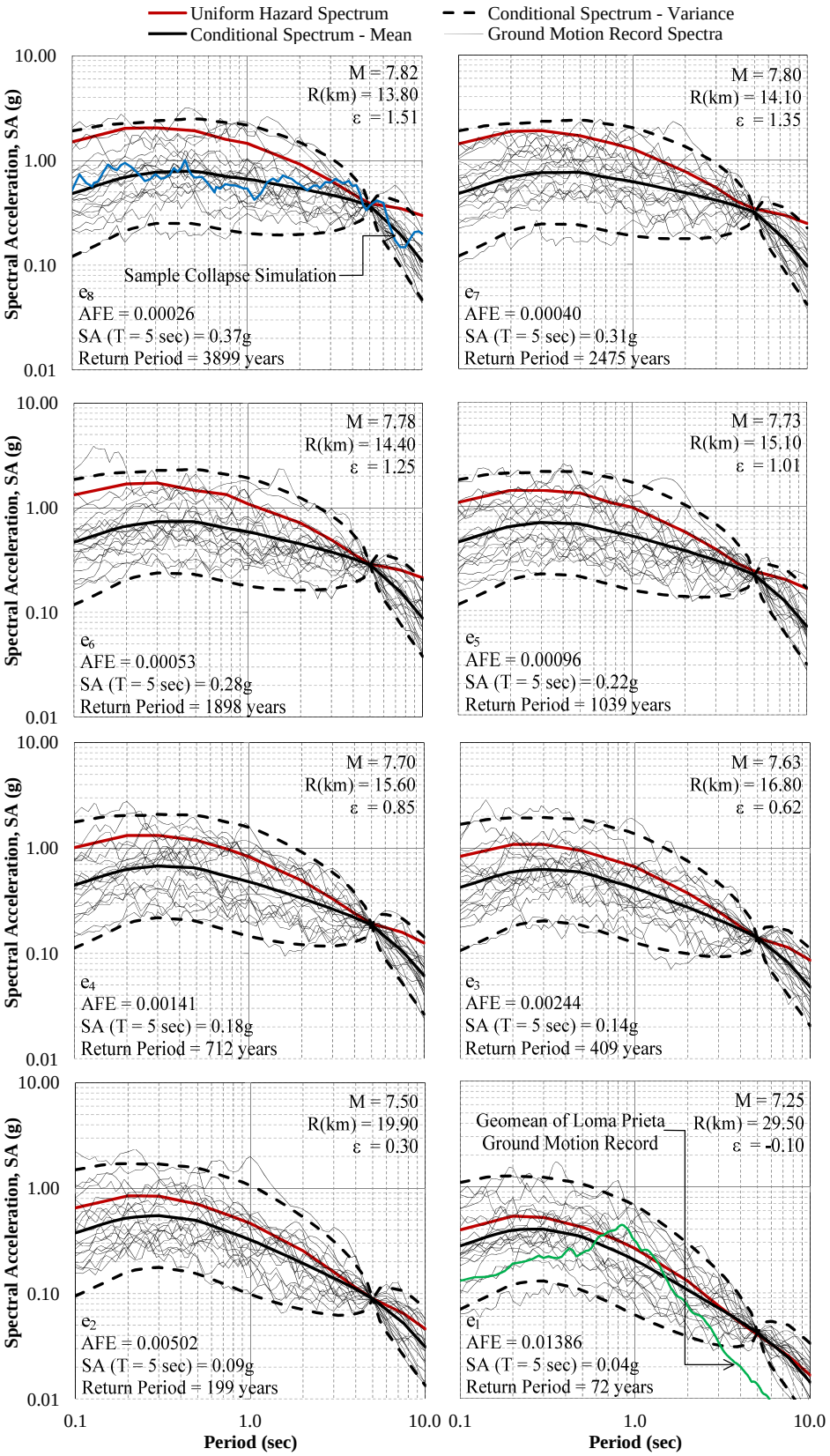

Figure 7-3: Target conditional mean, variance, ground motion records and corresponding the UHS for the intensity levels considered in the time based assessment including SA, AFE, return periods and de-aggregation data (M, R and ε). The geomean spectra of a Loma Prieta ground motion record is also shown for comparison.
Source: Molina Hutt et al. (2017).

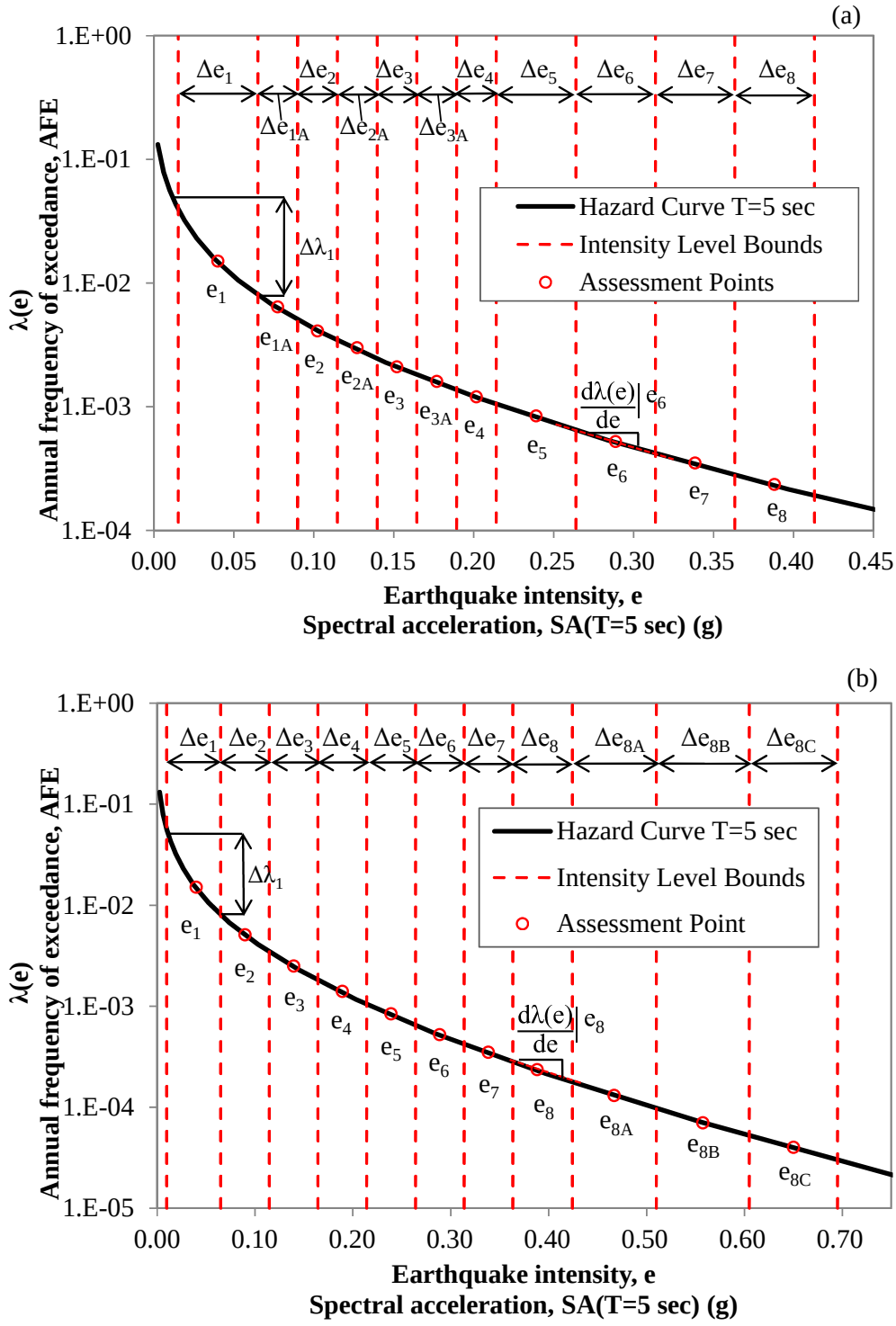

Figure 7-4: Revised earthquake ground motion intensities (e_i) considered in the time-based assessment for (a) the 1973 50-storey archetype building and (b) the 2012 50-storey archetype building.

7.3 Structural performance assessment

In order to evaluate the structural performance of the archetype buildings, this section presents NLRHA results for the earthquake ground motion intensities considered in the assessment. Global performance is reviewed by evaluating maximum IDRs (transient and residual) and PFAs throughout the building height. Component behaviour is reviewed by evaluating maximum rotations in beams, columns and panel zones in all storeys.

The mean and mean plus standard deviation of the peak results in all storeys for all ground motion simulations are illustrated in Figures 7-5 through 7-10 including transient IDRs, residual IDRs, PFAs, beam plastic rotations, column plastic rotations and panel zone rotations, respectively, for each earthquake ground motion intensity level considered. Table 7-3 provides the maximum response parameter values of all simulations and across all storeys in all earthquake ground motion intensities considered (as opposed to the mean values reported in Figures 7-5 through 7-10). The peak results of all simulations in all storeys and all intensities are included in Appendix G. Individual simulation results are omitted from Figures 7-5 through 7-10 for clarity.

The results show the distribution of demands up the building height and highlight fairly uniform deformation demands in the 2012 50-storey archetype building when compared to the 1973 50-storey archetype building, which shows large concentrations of deformation in a small number of storeys. With increasing earthquake ground motion intensities, some analysis runs result in collapse. To reflect the sample size of the dynamic analysis results presented in each figure, the percentage of non-collapsed (PNC) simulations in each ground motion suite for each earthquake intensity is also noted in Figures 7-5 through 7-10. The low values of PNC observed in the 1973 50-storey archetype building at earthquake ground motion intensities e_3 and above are indicative of the high probability of observing collapse, an observation that led to the consideration of additional assessment points in this SA range, as previously discussed in Section 7.2. Results for earthquake intensities e_6 and above are not included for the 1973 50-storey archetype building because all analysis simulations result in collapse.

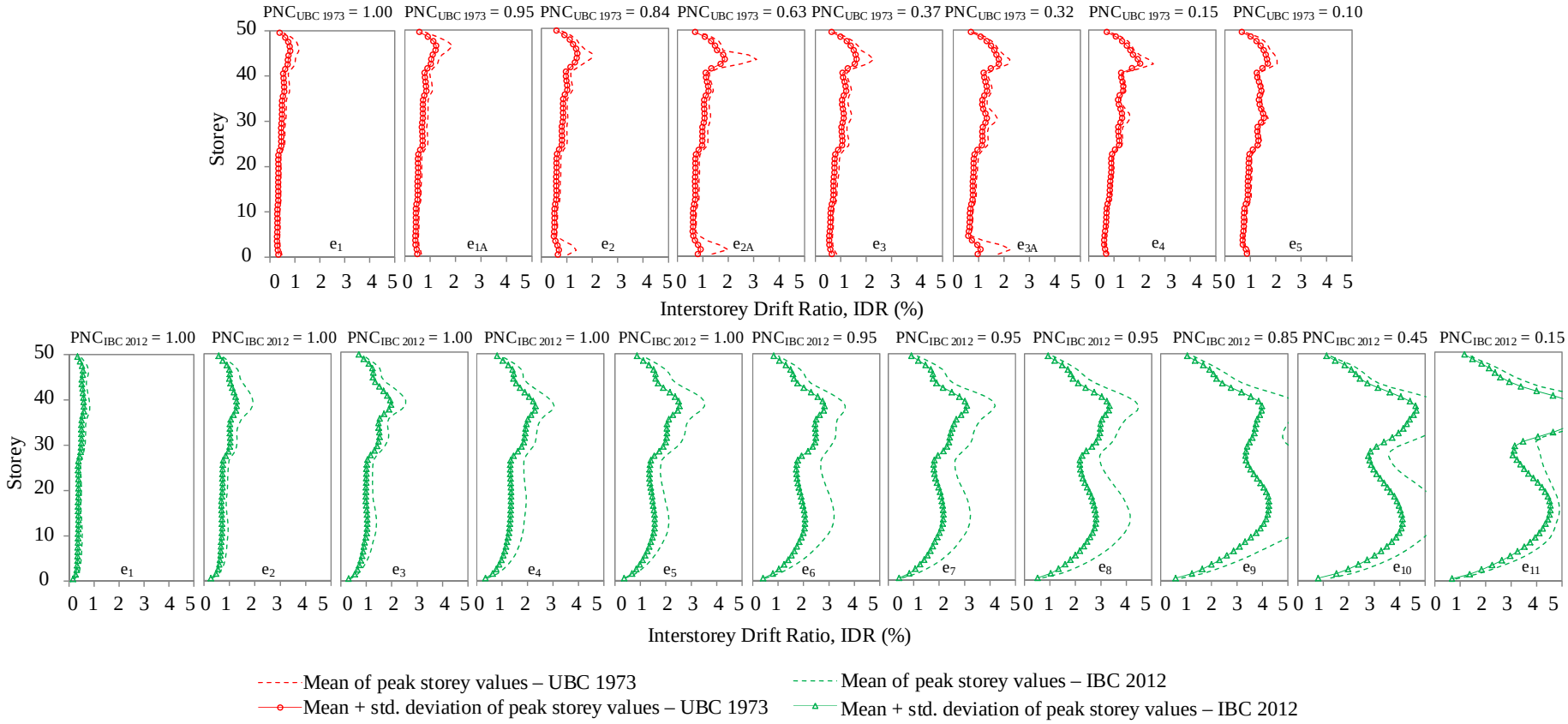

Figure 7-5: Peak transient storey drift results from non-linear dynamic analysis for all intensity levels considered. Probabilities of no collapse at each earthquake intensity specified atop.

Source: Molina Hutt et al. (2017)

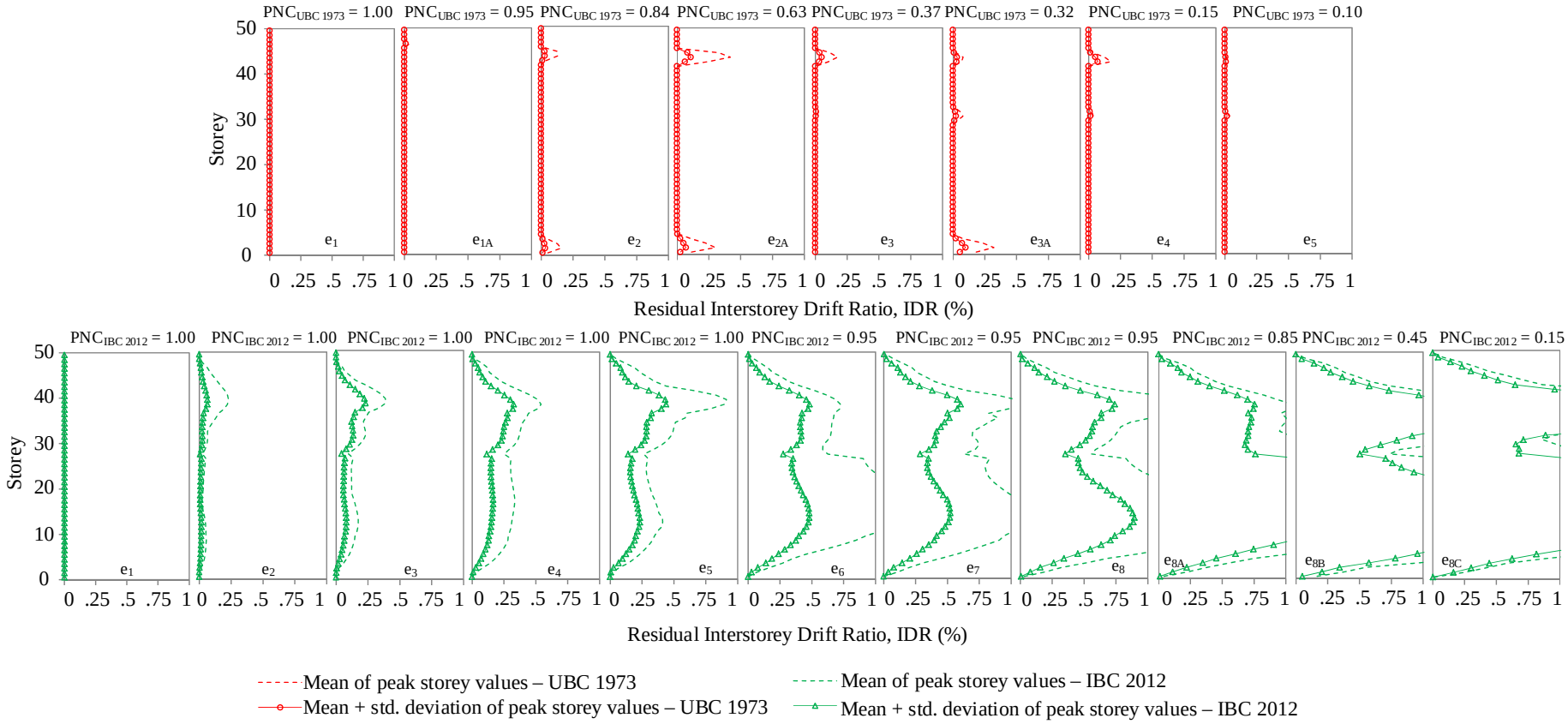

Figure 7-6: Peak residual storey drifts results from non-linear dynamic analysis for all intensity levels considered. Probabilities of no collapse at each earthquake intensity specified atop.
Source: Molina Hutt et al. (2017)

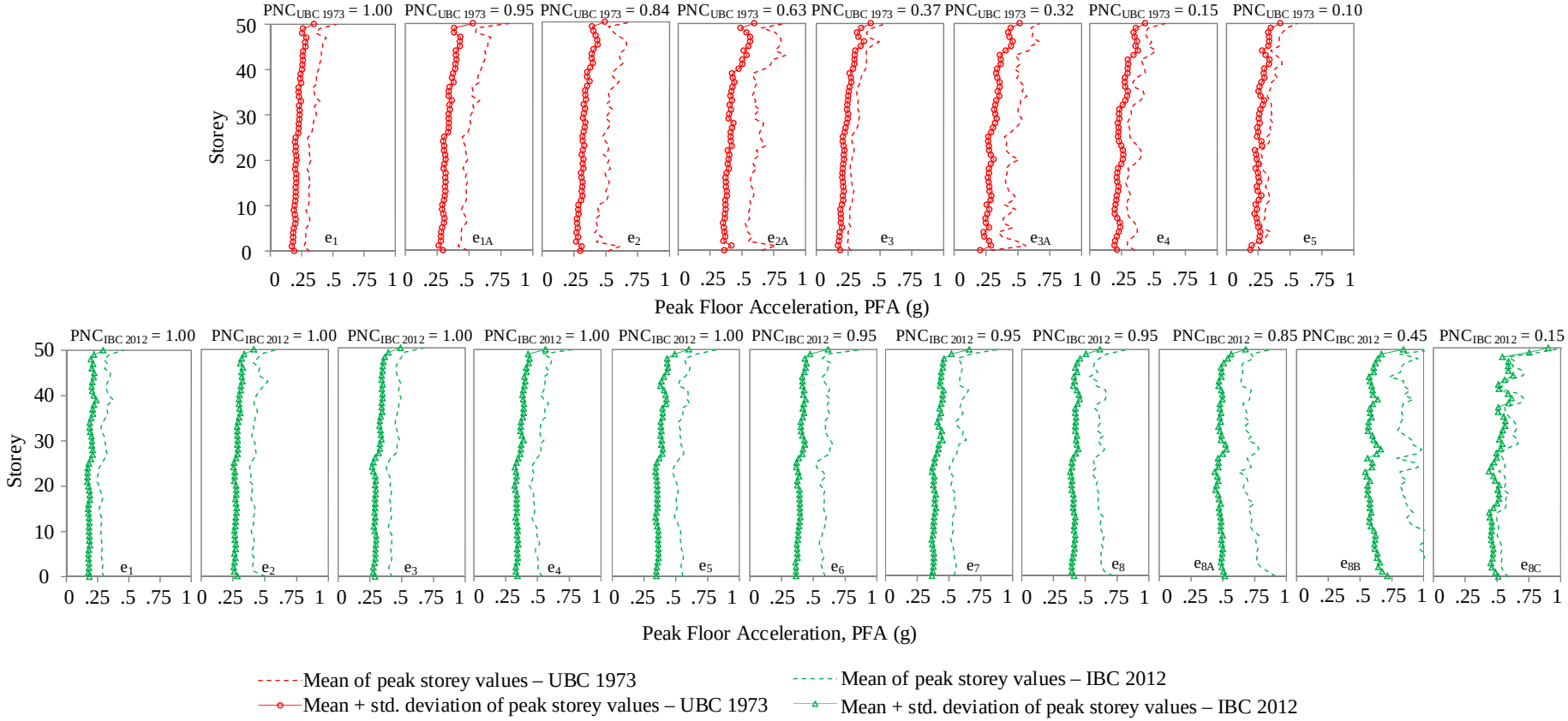

Figure 7-7: Peak floor acceleration results from non-linear dynamic analysis for all intensity levels considered. Probabilities of no collapse at each earthquake intensity specified atop.
Source: Molina Hutt et al. (2017)

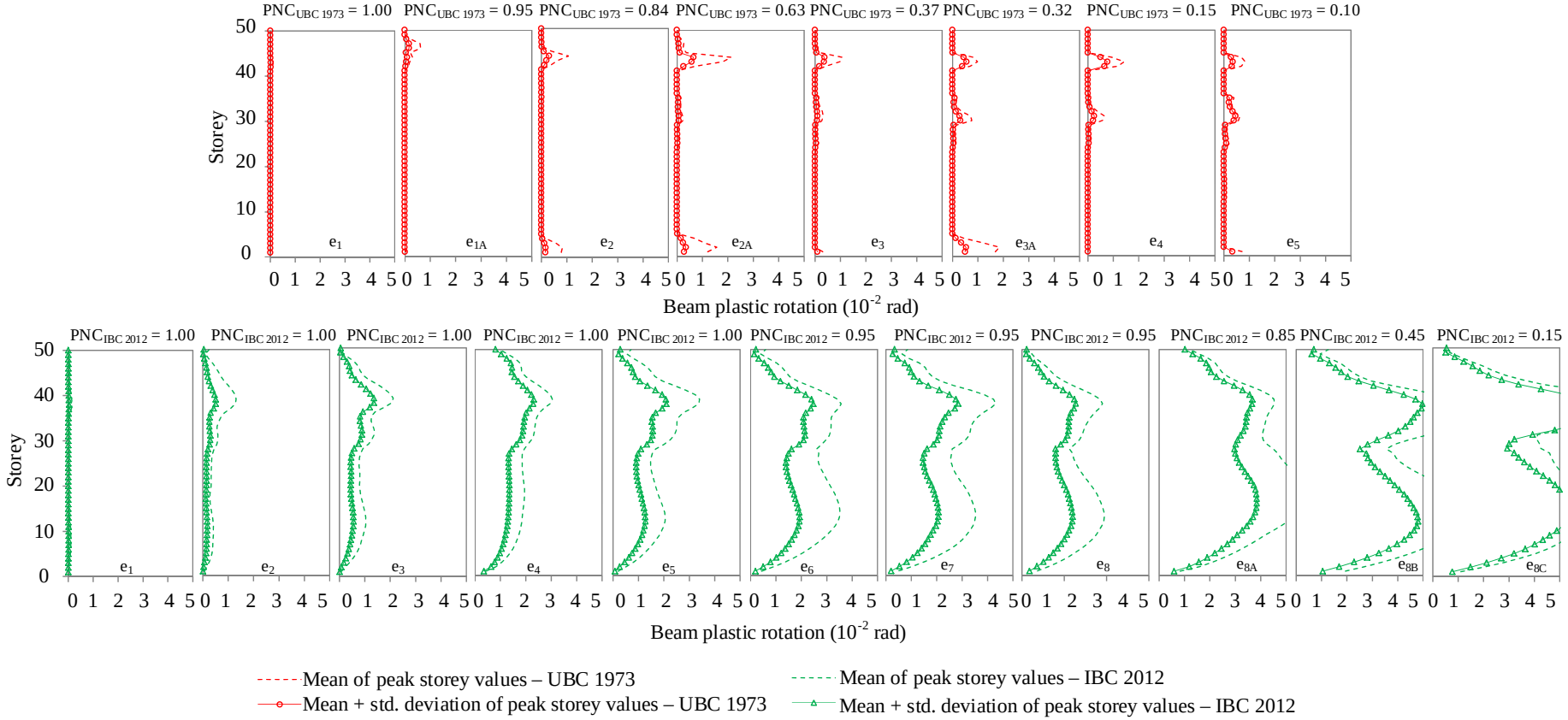

Figure 7-8: Peak beam plastic rotation results from non-linear dynamic analysis for all intensity levels considered. Probabilities of no collapse at each earthquake intensity specified atop.
Source: Molina Hutt et al. (2017)

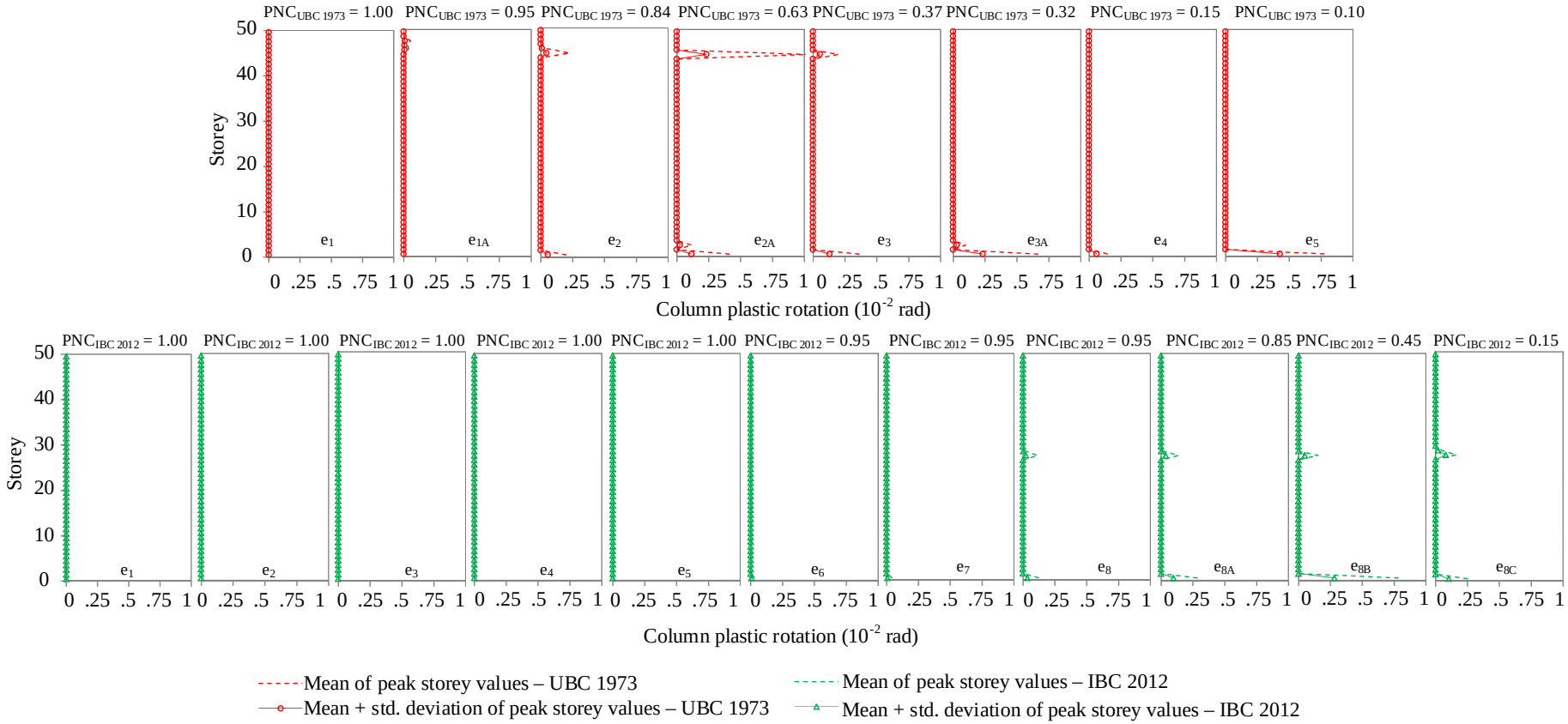

Figure 7-9: Peak column plastic rotation results from non-linear dynamic analysis for all intensity levels considered. Probabilities of no collapse at each earthquake intensity specified atop.
Source: Molina Hutt et al. (2017)

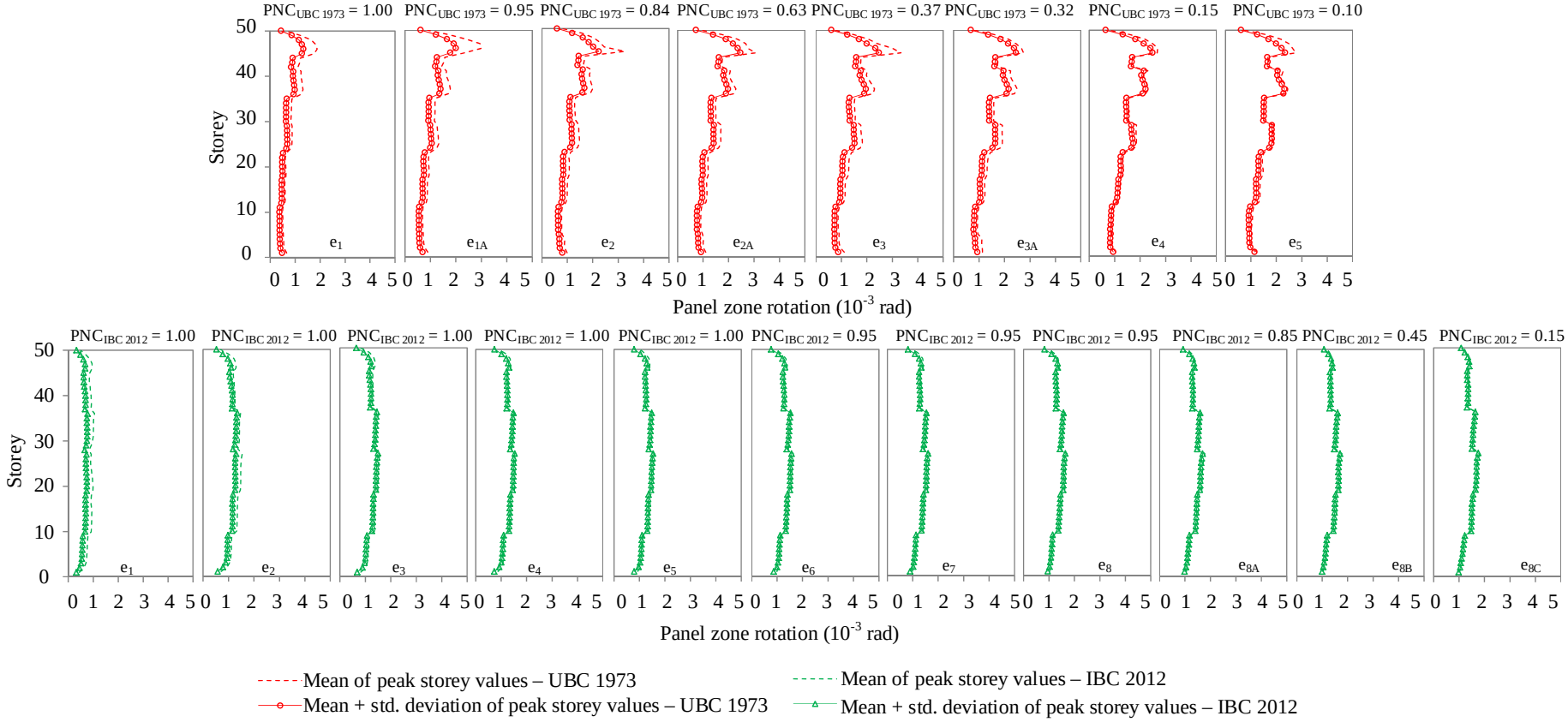

Figure 7-10: Peak panel zone rotation results from non-linear dynamic analysis for all intensity levels considered. Probabilities of no collapse at each earthquake intensity specified atop.
Source: Molina Hutt et al. (2017)

Table 7-3: Maximum of peak storey results from non-linear dynamic analysis: interstorey drift ratio (IDR), residual IDR, peak floor acceleration (PFA), beam plastic rotation, column plastic rotation and panel zone rotations for the 1973 and 2012 50-storey archetype buildings. Source: Molina Hutt et al. (2017)

Earthquake Ground Motion Intensity	Archetype Building	Peak Storey:			Rotation:		
		Transient IDR [%]	Residual IDR [%]	PFA [g]	Beam (Plastic) [rad]	Column (Plastic) [rad]	Panel Zone [rad]
e_1	1973	1.68	0.22	0.74	0.004	0.000	0.0025
	2012	1.29	0.03	0.61	0.005	0.000	0.0014
e_{1A}	1973	2.81	0.47	1.15	0.017	0.002	0.0049
	2012	-	-	-	-	-	-
e_2	1973	3.25	0.98	1.37	0.030	0.007	0.0057
	2012	3.65	0.72	1.05	0.035	0.000	0.0015
e_{2A}	1973	5.64	2.80	1.44	0.052	0.027	0.0041
	2012	-	-	-	-	-	-
e_3	1973	3.07	0.64	0.60	0.019	0.006	0.0043
	2012	2.89	0.50	0.94	0.025	0.000	0.0016
e_{3A}	1973	3.45	1.25	0.88	0.032	0.011	0.0027
	2012	-	-	-	-	-	-
e_4	1973	2.62	0.50	0.61	0.015	0.001	0.0027
	2012	3.75	0.76	1.14	0.037	0.000	0.0017
e_5	1973	1.95	0.33	0.52	0.007	0.007	0.0027
	2012	6.10	2.42	1.09	0.067	0.000	0.0017
e_6	1973	-	-	-	-	-	-
	2012	6.24	3.79	1.50	0.079	0.001	0.0017
e_7	1973	-	-	-	-	-	-
	2012	5.94	2.68	1.05	0.068	0.001	0.0018
e_8	1973	-	-	-	-	-	-
	2012	6.35	3.66	1.49	0.077	0.004	0.0018
e_{8A}	1973	-	-	-	-	-	-
	2012	7.40	4.91	0.82	0.074	0.003	0.0018
e_{8B}	1973	-	-	-	-	-	-
	2012	6.81	4.37	2.23	0.083	0.015	0.0018
e_{8C}	1973	-	-	-	-	-	-
	2012	7.61	3.92	1.04	0.091	0.003	0.0018

The peak IDR results shown in Figure 7-5 illustrate the significant concentration of deformations observed in the 1973 50-storey archetype near the base of the structure and near the top of the building for all the earthquake ground motion intensities considered. In contrast, the 2012 50-storey archetype building illustrates a more uniform distribution of IDR demands up the building height with peak values increasing uniformly with increasing earthquake ground motion intensity. The peak residual IDR results shown in Figure 7-6 follow the patterns observed in Figure 7-5 for the peak transient IDRs. In the 1973 50-storey archetype building, concentrations of residual IDR are only observed in a small number of storeys. In contrast, the 2012 50-storey archetype building illustrates residual IDRs uniformly distributed up the building height. As described in Section 4.3.1, residual IDRs are generally used as an indication

of whether a building is repairable after an earthquake. A threshold of 1% residual IDR is generally used as an indication of whether a building can be repaired (Ramirez and Miranda 2012). Based on this threshold, the residual IDRs observed in the 1973 50-storey archetype building would not generally render the building irreparable. However, the residual IDRs observed for the 2012 50-storey archetype building indicate that the potential for residual IDRs rendering the building irreparable is considerable, particularly at earthquake ground motion intensities e_6 and above. While this observation may seem counterintuitive, it is reasonable if one considers that those simulations which cause large residual IDRs in the 2012 50-storey archetype, and consequently result in an irreparable building, actually cause collapse in the 1973 50-storey archetype, as suggested by the PNC values.

The peak plastic rotations in beams shown in Figure 7-8 follow the patterns observed in Figure 7-5 for the peak transient IDRs. There is effectively no plastic rotation in columns in the 2012 50-storey archetype building at earthquake intensities below e_8, as seen in Figure 7-9. Furthermore, the panel zones are also in the linear elastic range, as seen in Figure 7-10 by comparing panel zone rotations to the yield rotation threshold of 0.0028 radians. Therefore, the deformations of the 2012 50-storey archetype building are effectively dominated by the non-linear response of the beams. Concentration of non-linear deformations in a single element type while the remainder of the structure remains elastic is a direct outcome of the capacity design approach inherent in modern design standards, which is clearly reflected in the results of the 2012 50-storey archetype building. On the other hand, deformations in the 1973 50-storey archetype building are influenced by the non-linear response of beams, columns and panel zones and are always concentrated in small number of storeys. The concentrations of deformations in a small number of storeys observed in the 1973 50-storey archetype building also agree with field observations following Northridge earthquake (Deierlein 1998) and other analytical studies of older steel MRFs (PEER 2015) as discussed in Section 2.1.4. The PFAs shown in Figure 7-7 indicate a fairly uniform distribution of storey accelerations up the building height, with a concentrated increase in accelerations near the roof in both archetype buildings. The concentrated increase in PFA in the upper storeys is in agreement with observations from Taghavi and Miranda (2004), who developed a simplified approach to estimate floor acceleration demands in high rise buildings.

At low earthquake ground motion shaking intensities, the response parameter values illustrated in Figures 7-5 through 7-10, as well as in Table 7-3, are consistently higher for the 1973 50-storey archetype building than those of the 2012 50-storey archetype building. However, with increasing earthquake ground motion shaking intensities, response parameter values in the 2012

50-storey archetype building are higher than those of the 1973 50-storey archetype building. As with previous observations related to higher residual IDRs observed in the 2012 50-storey archetype building, this is explained because the simulations which result in the highest demands in the 2012 50-storey archetype building actually induce collapse in the 1973 50-storey archetype building. Collapse realizations are not considered in the calculation of mean and maximum values reported in Figures 7-5 through 7-10, and Table 7-3, which explains how as the PNC simulations decreases in the 1973 50-storey archetype building, the mean and maximum demand parameters in the 2012 50-storey archetype building appear to be higher. These results are also indicative of the low ductility levels attainable by the 1973 archetype. For instance, the maximum IDR observed in all of the non-collapsed simulations in the 1973 50-storey archetype building is 5.64%, as illustrated in Table 7-3 under earthquake intensity e_{2A}. In contrast the maximum IDR results for the 2012 50-storey archetype building is 7.61%, as illustrated in Table 7-3 under earthquake ground motion intensity e_{8C}. The mean and mean plus standard deviation, for the suite where the maximum IDR is reported for the 1973 50-storey archetype building, are 1.87% and 3.11% respectively, indicating that the maximum IDR is an outlier. In contrast, the mean and mean plus standard deviation, for the suite where the maximum IDR is reported for the 2012 50-storey archetype, are 5.89% and 7.13%, indicating that high ductility levels are consistently achieved in the suite considered.

As previously mentioned in Section 6.2, FEMA (2012) provides a relationship between peak transient IDRs and four DS levels for steel moment resisting frames. DS1 indicates no structural realignment of the structure is required, though there may be some damage to non-structural components. DS2 denotes some structural realignment and subsequent structural repairs will be required. DS3 indicates that major structural realignment is required, though it may not be economically feasible and DS4 is consistent with damage levels triggering collapse. When applying this relationship to the maximum of the mean peak IDRs presented in Figure 7-5, the expected damage state of the 2012 50-storey archetype building corresponds to no damage up to earthquake intensity e_2, DS1 from earthquake intensity e_3 to e_5, DS2 for intensities e_6 to e_8 and DS3 at higher intensities. There are no observations of DS4, which is in agreement with explicit simulation of collapse. In contrast, for the 1973 50-storey archetype building, no damage is expected up earthquake intensity e_2 and DS1 is expected for intensities e_{2A} to e_5. At these intensities, a considerable number of simulations result in collapse, yet based on the maximum mean peak IDR values, no earthquake intensities are associated with DS2 or DS3. These results indicate that this relationship may not be applicable to steel MRF buildings whose ductility is compromised by fracture-prone moment connections.

The large concentrations of deformation near the top of the building in the 1973 archetype 50-storey archetype building can be traced back to the design procedure of the time. UBC 1973 seismic design forces are distributed up the building height based on the first mode translational response of the structure, as discussed in Section 4.1.1, neglecting contributions to the dynamic response of higher modes, which can result upper storeys being under-designed. Figure 7-11 illustrates the storey drifts, shear forces and overturning moments associated with the design requirements of UBC 1973 in comparison to the mean and mean plus standard deviation of the peak storey responses when subject to ground motions representative of a 72-year return period (intensity e_1). Under the UBC 1973 design forces, storey drift response is fairly uniform up the building height. However, even under earthquake ground motions with low return periods, i.e. intensity e_1, there is a high concentration of drifts near the top of the building. This observation highlights the extent to which upper storeys in similar buildings may have been under-designed when following UBC 1973 design requirements and explains the observed concentrations of deformations near the top of the 1973 50-storey archetype building.

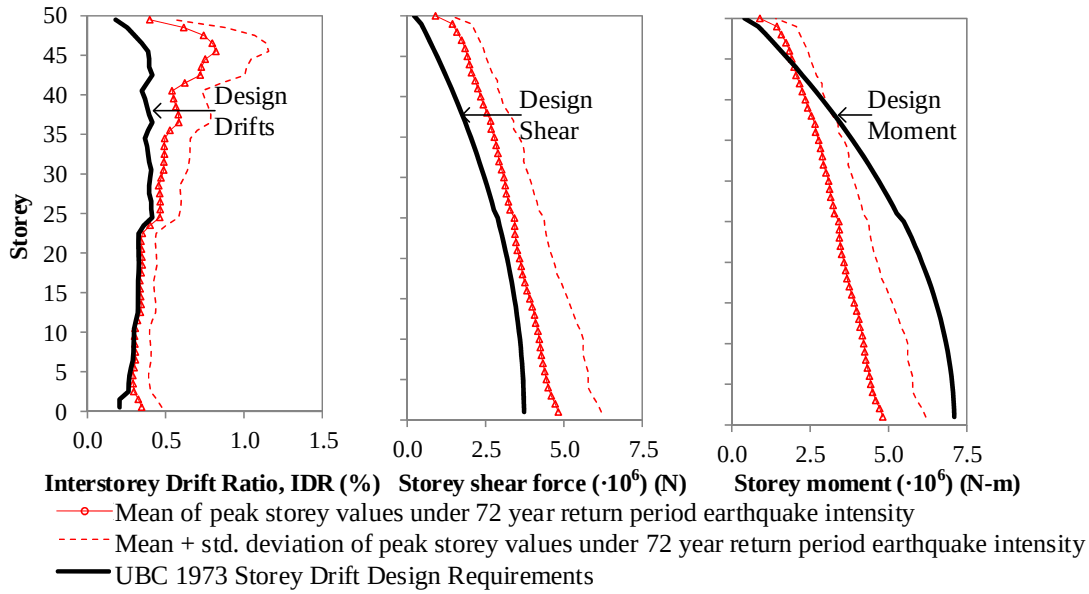

Figure 7-11: UBC 1973 design storey drifts, shear and overturning moment versus peak storey results from non-linear dynamic analysis subject to ground motions consistent with a 72 year return period event.
Source: Molina Hutt et al. (2017)

7.4 Time-based assessment

This section of the time-based assessment is focused on the development of performance functions for peak IDRs (transient and residual) and PFAs. Storey drifts and accelerations are important because they are the most predominant EDPs used in estimating damage, repair cost and repair time for structural and non-structural components, as discussed in Chapter 4. The

collapse risk is also evaluated through the development of the collapse fragility and by estimation of the mean annual rate of collapse, λ_c, for each archetype building. Collapse risk metrics are important not only because collapse prevention is one of the primary goals of earthquake engineering, but additionally because collapse probability also contributes significantly to expected losses.

7.4.1 Collapse risk

Assessing the collapse risk of a structure entails combining information related to the behaviour of the structure with seismic hazard data at the site. The response of the structure is characterized by a collapse fragility, which uses non-linear dynamic analysis results to describe the increasing probability of collapse as a function of the ground motion shaking intensity, typically the SA at the fundamental period of the structure. This study follows a MSA approach in which non-linear dynamic analyses are performed at numerous intensity levels ('stripes') and where hazard consistent ground motions are selected at each intensity level under consideration. At the higher earthquake ground motion shaking intensities, the fraction of ground motions that cause collapse are recorded and used to obtain the collapse fragility for the building, assumed to follow a lognormal cumulative probability distribution. The statistical fitting technique for this data follows the method of maximum likelihood as described by Baker (2015).

The resulting collapse fragility of the 1973 50-storey archetype building has an estimated median of 0.13g and a dispersion of 0.37, while the resulting collapse fragility of the 2012 50-storey archetype building has an estimated median of 0.54g and a dispersion of 0.28, as illustrated in Figure 7-12. The collapse fragility of the modern 50-storey archetype building is in agreement with the design of modern building codes, which is to produce designs with low probability of collapse under MCE level shaking (PEER 2012a). At a period of 5 seconds, the ASCE (2010) MCE spectral ordinate is approximately 0.30g, at which the 2012 archetype building has a negligible (less than 5%) probability of collapse. The results indicate that applying modern code-prescriptive requirements to the design of tall steel moment resisting frames yields collapse performance levels consistent with those targeted by the code.

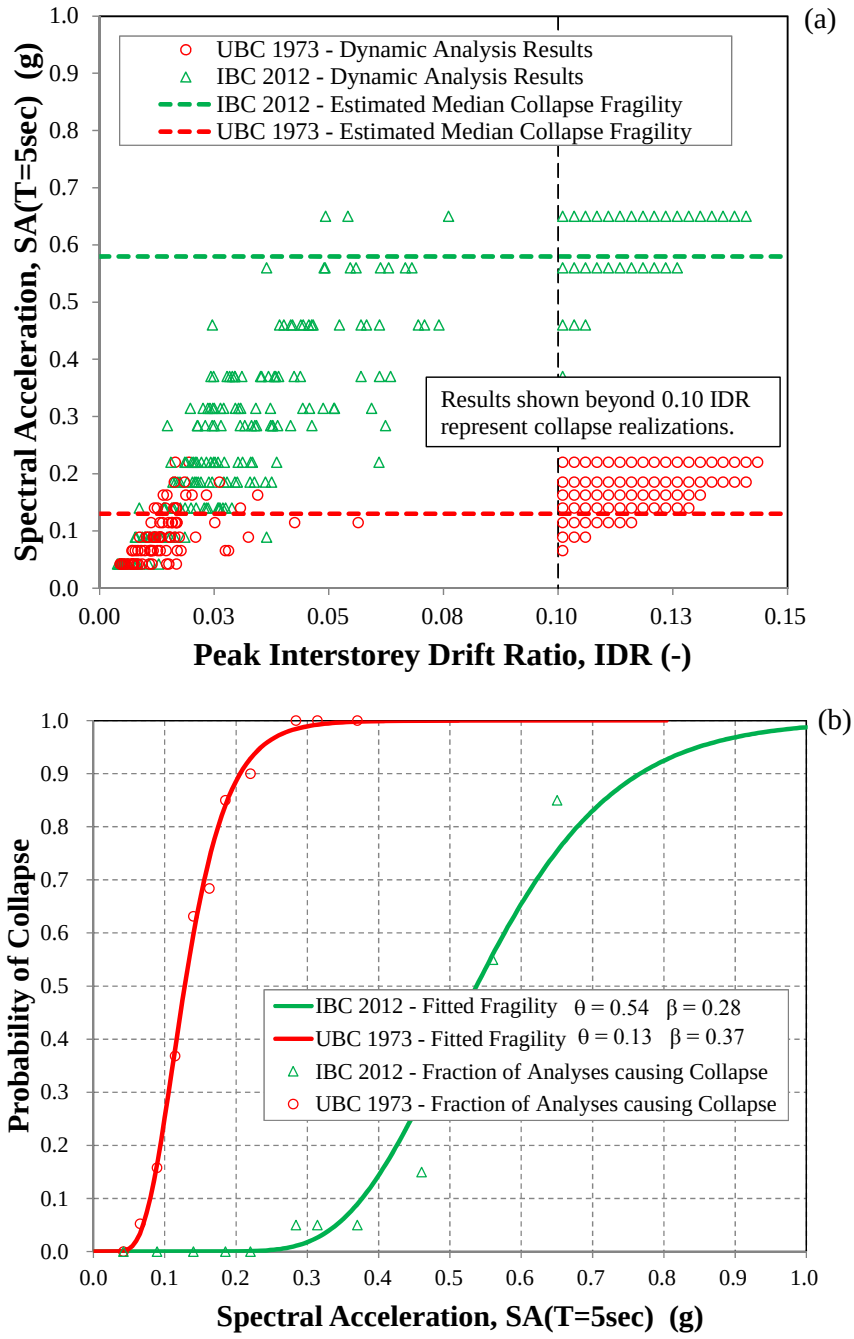

Figure 7-12: Multiple stripe analysis results (a) for collapse fragility derivation (b) of the 1973 and 2012 archetype buildings.
Source: Molina Hutt et al. (2017)

The mean annual frequency of collapse is a powerful risk metric obtained by combining the collapse fragility with seismic hazard data which describes the mean annual frequency of exceeding the ground motion shaking intensity. The collapse risk is estimated by combining the probability of collapse at each ground motion intensity level considered, with seismic hazard data describing how frequently each intensity level is exceeded at the site. This calculation is illustrated in Equation 7-1.

$$\lambda_c = \int_0^\infty P(C|e) \cdot |d\lambda(e)| = \int_0^\infty P(C|e) \cdot \left|\frac{d\lambda(e)}{de}\right| \cdot de = \sum_{i=1}^{n} P(C|e_i) \cdot \left|\frac{d\lambda(e_i)}{de}\right| \cdot \Delta e_i$$

Equation 7-1

Where λ_c is the mean annual frequency of collapse, P(C|e) is the probability of collapse when subjected to an earthquake with a ground motion intensity e, and $\lambda(e)$ is the mean annual frequency of exceedance of the ground motion intensity e, which is an output of PSHA. As there is no closed-form solution to the integral in Equation 7-1, the solution is typically obtained using numerical integration by multiplying the probability of collapse $P(C|e_i)$ and the slope of the seismic hazard curve at each intensity level, $|d\lambda(e_i)/de_i|$, then multiplying the result by the range of Δe_i (representing each intensity level), and adding the results for the number of intensity levels, n, considered in the assessment. This method of computing the collapse risk is outlined in more detail in Eads (2013) and is graphically illustrated in Figure 7-13. Following this calculation, λ_c is computed for the 1973 50-storey archetype building as $28 \cdot 10^{-4}$ versus $1 \cdot 10^{-4}$ for the 2012 50-storey archetype building. The computed rate of collapse of the 50-storey 1973 archetype building, which is is 28 times greater than for an equivalanet modern code-conforming building, should be seen as exceeding acceptable limits, particularly if one considers the catastrophic consequences associated with the collapse of a 50-storey building.

The results for the modern 50-storey archetype building are consistent with the λ_c calculated by Haselton and Deierlein (2007) for modern, code-conforming RC moment frames, which is estimate to range from $0.7 \cdot 10^{-4}$ to $7 \cdot 10^{-4}$. Although these buildings are constructed of different materials, modern codes should achieve similar levels of risk across all structure types, which this comparison seems to support. The risk targeted MCE seismic design parameters, or MCE_R, introduced in Section 4.1.1 were obtained by integrating a site's ground motion seismic hazard information with a generic collapse fragility curve to yield a uniform target collapse risk across the USA of 1% in 50 years (Krawinkler and Deierlein 2014). The collapse risk of the 1973 50-storey archetype building is 13 times greater than the 1% change of collapse in 50 years inherent in modern design standards.

A de-aggregation of λ_c by intensity provides a useful measure for identifying the contribution of different levels of ground motion shaking intensity to the total collapse risk. This calculation is similar to that of de-aggregation by magnitude, distance and epsilon used in PSHA to determine the seismic sources primarily contributing to the hazard. The area under the de-aggregation curve is equal to λ_c, and ground motions intensities with higher ordinates in the de-aggregation curve indicate higher contributions to λ_c, as illustrated in Figure 7-13. De-

aggregation of λ_c reveals that the largest contributors to collapse in the 1973 50-storey archetype building are earthquake intensities e_4 (712 year return period). In contrast, the largest contribution to collapse of the 2012 50-storey archetype building is provided by intensities of shaking above e_8 (3899 year return period), beyond the MCE level generally defined in modern building codes.

While the mean annual frequency of collapse λ_c is a useful metric, it is often easier to communicate these results as the probability of collapse over a period of time. Following the common assumption in earthquake engineering that collapse occurrence follows a Poisson process, the probability of collapse over a period of time can be calculated per Equation 7-2 (Baker 2015, Ibarra and Krawinkler 2005, Medina and Krawinkler 2003).

$$P_{collapse} = 1 - e^{-\lambda_c \cdot t} \qquad \text{Equation 7-2}$$

Table 7-4 illustrates the probability of collapse over different periods of time for the 1973 and the 2012 50-storey archetype buildings, as well as for modern code-conforming RC moment frame structures as estimated by Haselton et al. (2007), for comparison. As an additional reference point, as previously discussed, ASCE (2010) targets a 1% probability of collapse in 50 years when determining spectral values for use in design (Eads 2013).

Table 7-4: Probabilities of collapse over different periods of time for a range of codes and structural systems.
Source: Molina Hutt et al. (2017)

Time (years)	UBC 1973 Steel MF	IBC 2012 Steel MF	IBC 2012 RC MF
25	6.76%	0.25%	0.17-1.73%
50	13.1%	0.50%	0.35-3.44%
75	18.9%	0.75%	0.52-5.11%
100	24.4%	1.00%	0.70-6.76%

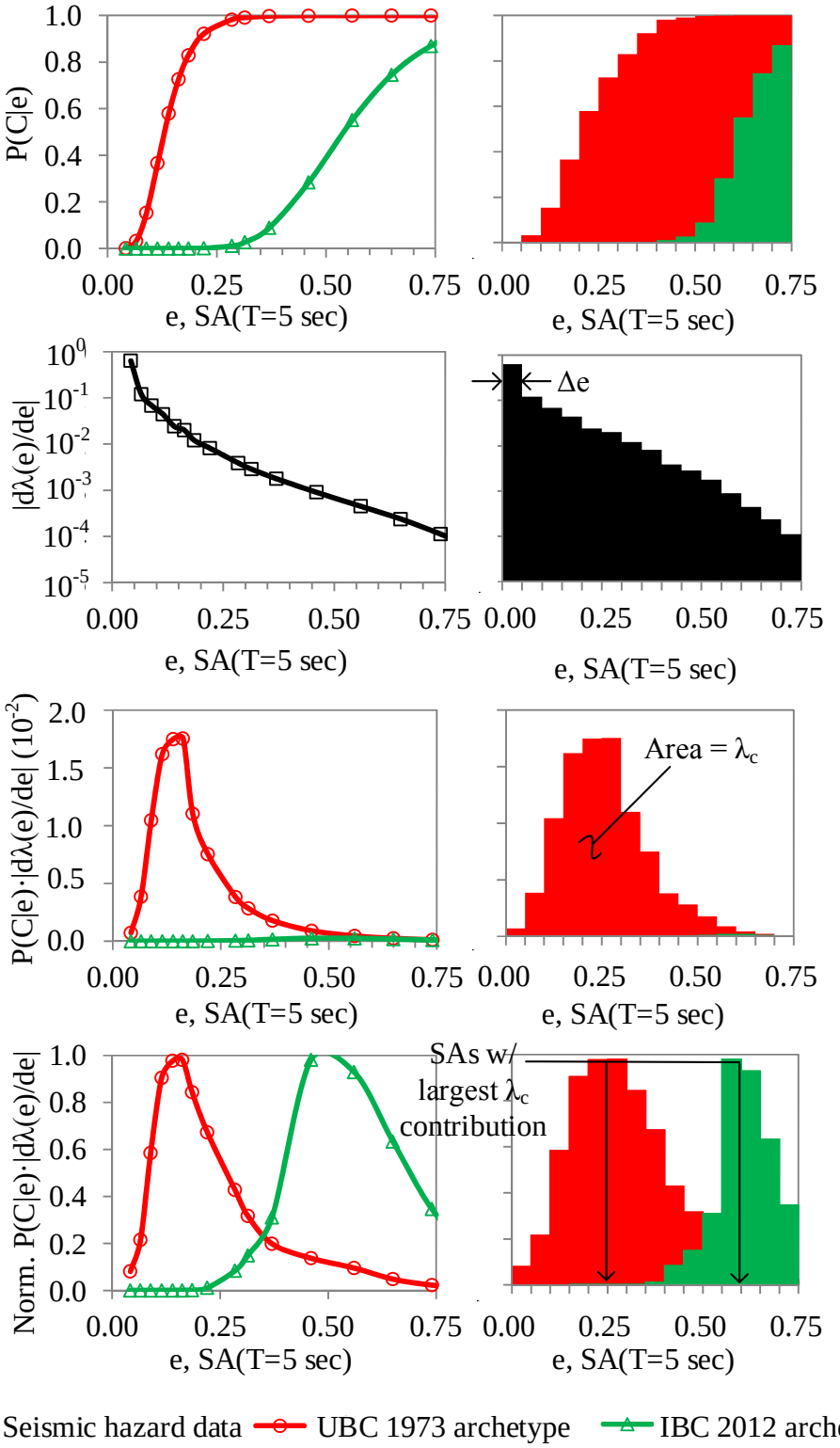

Figure 7-13: Graphical illustration of mean annual frequency of collapse calculation and collapse de-aggregation for the 1973 and 2012 archetype buildings.
Source: Molina Hutt et al. (2017)

7.4.2 Performance functions

Time-based assessments enable the calculation of performance functions, which express the frequency that an engineering demand parameter will be exceeded in a period of time, usually assumed to be one year, although easily converted to other time periods. The probability of exceeding a certain value of demand is computed by considering all possible intensities of shaking that might be experienced by the building within the specified time frame, and by then weighting the outcome of each intensity times the probability that such shaking will occur (FEMA 2012). The approach followed to obtain a performance function is similar to that illustrated for the computation of the mean annual frequency of collapse. The hazard curve is subdivided into a number of intensity levels as shown in Figure 7-2. For each intensity level an intensity-based assessment is performed, which computes the probability distribution associated with a specific demand parameter, e.g. IDR, PFA, etc.

Figures 7-14a, 7-15a and 7-16a illustrate the maximum (transient) IDR, residual IDR and PFA obtained in each ground motion simulation at each intensity level considered in the assessment. As illustrated in the figures, the distribution of response can be defined by a log-normal probability distribution. These distributions allow us to calculate the probability of exceeding a certain value of a given demand parameter at each intensity of shaking. In a similar fashion to how the probability of collapse at each intensity of ground motion shaking is computed, the probability of exceeding a certain value of demand parameter, e.g. 1% peak storey drift, can also be computed. Combining the probability of exceeding a particular value of the demand parameter and then integrating the results with the hazard curve, yields the mean annual rate of exceeding the pre-defined value of demand parameter. This would correspond to a single data point, but when repeated for a wide range of engineering demand parameters, the complete performance function can be obtained, as shown in Figures 7-14b, 7-15b and 7-16b.

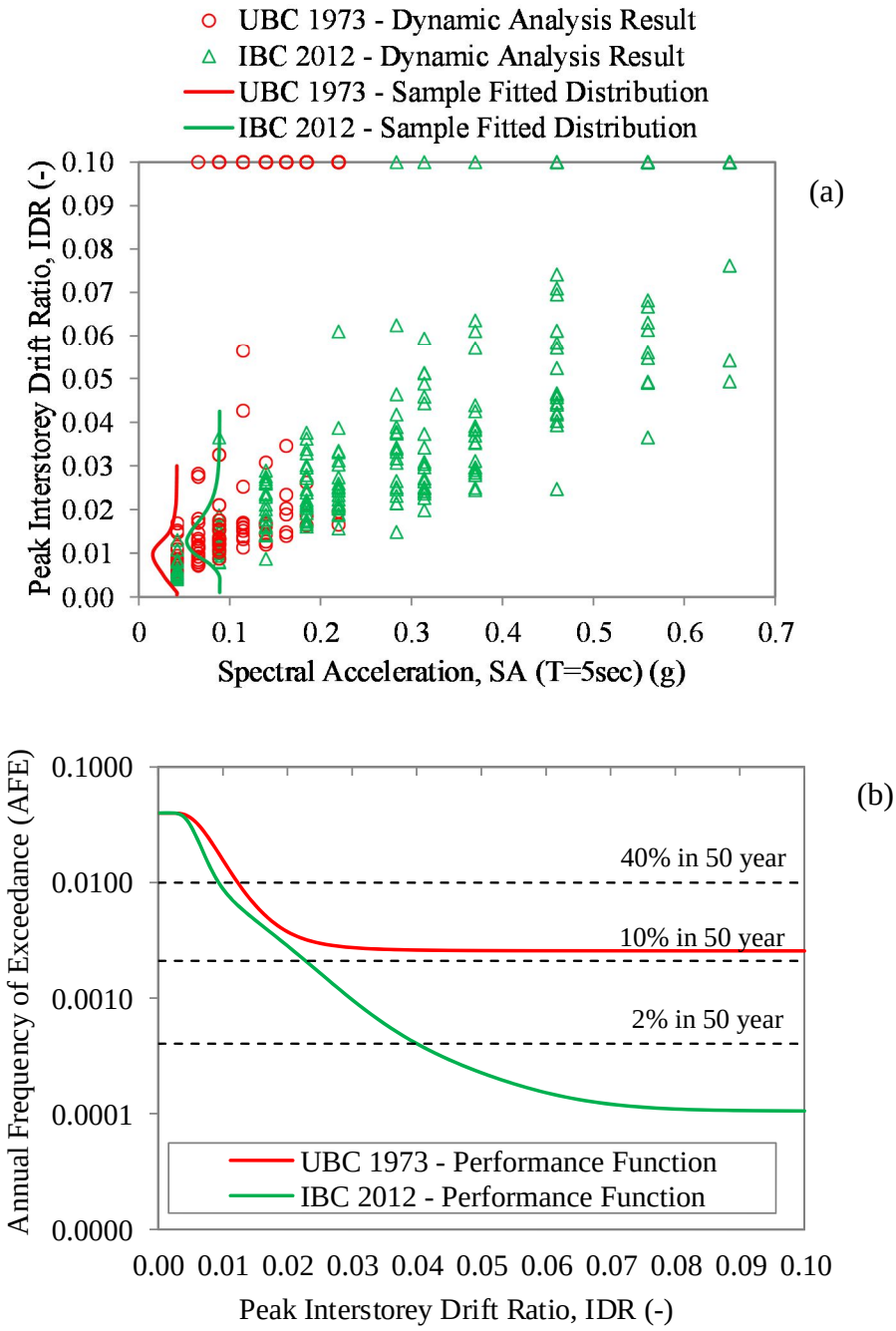

Figure 7-14: Peak Interstorey Drift Ratio (IDR) (a) dynamic analysis results and (b) associated performance functions for 1973 and 2012 50-storey archetype buildings. Source: Molina Hutt et al. (2017)

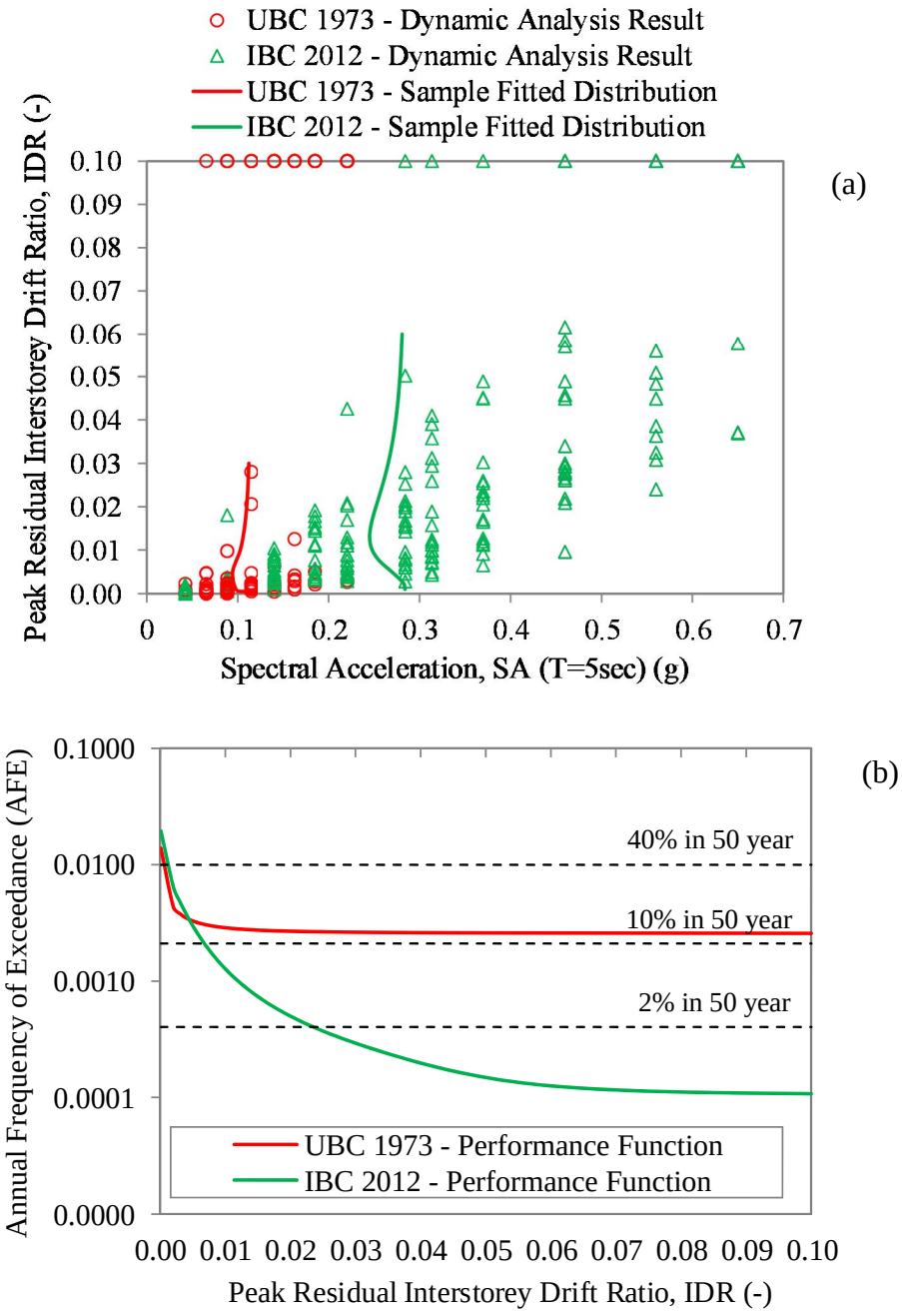

Figure 7-15: Peak Residual Interstorey Drift Ratio (IDR) (a) dynamic analysis results and (b) associated performance functions for 1973 and 2012 50-storey archetype buildings.
Source: Molina Hutt et al. (2017)

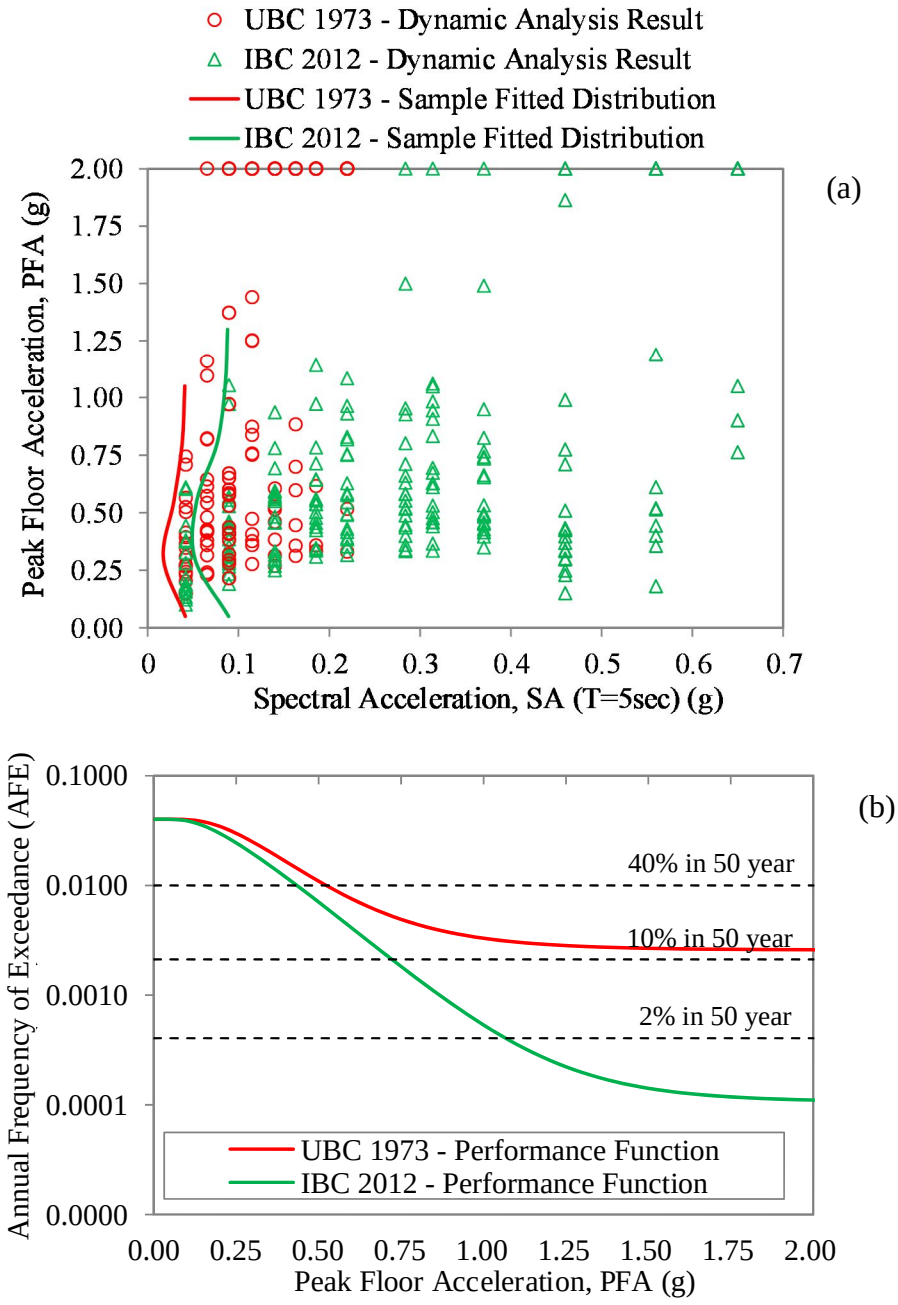

Figure 7-16: Peak floor acceleration (PFA) (a) dynamic analysis results and (b) associated performance functions for 1973 and 2012 50-storey archetype buildings.
Source: Molina Hutt et al. (2017)

Figures 7-14b, 7-15b and 7-16b provide a visual comparison of the annual rates of exceeding peak IDRs up to 10%, peak residual IDRs up to 5% and maximum PFAs up to 2g, respectively. It can be observed from the figures that at high values of IDR and acceleration, the annual frequencies of exceedance converge with the mean annual rates of collapse previously calculated for the 1973 and the 2012 50-storey archetype buildings, respectively. The performance functions allow for the calculation of different performance metrics, including EDPs at different return periods or the annual frequency of exceeding a certain drift or acceleration. Table 7-5 illustrates a range of time-based assessment results for both the 1973 and 2012 50-storey archetype buildings. The results illustrate consistently higher IDRs and PFAs for the 1973 50-storey archetype building compared to the 2012 50-storey archetype building. However, values of peak residual IDRs are higher for the 2012 than the 1973 50-storey archetype building up to the annual frequencies of exceedance at which the 1973 50-storey archetype building curve is dominated by collapse ($28 \cdot 10^{-4}$).

Table 7-5. Time-based performance assessment metrics related to peak IDRs, peak residual IDRs and maximum PFAs for the 1973 and 2012 archetype buildings. CP denotes collapse. Source: Molina Hutt et al. (2017)

Performance Assessment Metrics		UBC 1973	IBC 2012
Annual Rate	PFA > 0.5g	0.0109	0.0070
	IDR > 2%	0.0038	0.0028
	Residual IDR > 1%	0.0029	0.0013
2% 50-year or 0.00404	PFA(g)	CP	1.08
	IDR (%)	CP	4.10
	Residual IDR (%)	CP	2.35
10% 50-year or 0.002105	PFA(g)	CP	0.73
	IDR (%)	CP	2.25
	Residual IDR (%)	CP	0.68
40% 50-year or 0.010218	PFA(g)	0.53	0.42
	IDR (%)	1.20	0.90
	Residual IDR (%)	0.02	0.08

7.5 Loss assessment

In order to estimate the expected direct economic losses under each earthquake ground motion intensity considered in the time-based assessment, the key outputs from NLRHA presented in Section 7.3 are used as inputs to the building performance model described in Section 4.3. As the intensity levels considered in the assessment are intended to capture a range of outcomes from low damage up to levels triggering collapse, in addition to estimating costs associated with repairable damage, the costs associated with peak residual IDRs rendering the building irreparable as well as the potential for collapse are also considered in the assessment. Irreparable damage is considered through a building repair fragility as a function of peak residual IDR represented by a lognormal distribution with a median value of 1% and a dispersion of 0.35 (FEMA 2012). Collapse risk is considered through the use of the collapse fragilities derived in Section 7.4. In the event of collapse or peak residual IDRs rendering the building irreparable, the building is assumed to be a total loss, with a resulting loss ratio, defined as the expected loss over the total building cost (as defined in Section 4.3) equal to 1.

Figures 7-17 and 7-18 illustrate the computed loss realizations and fitted loss curves under the earthquake intensities considered for both the 1973 and the 2012 50-storey archetype buildings. The SAs at each intensity level and the estimated mean and dispersion for each distribution are noted in the figures. These results only represent realizations in which repairable damage is observed. Figure 7-17 and Figure 7-18 illustrate increasing mean loss ratios, associated with repairable damage, with increasing earthquake ground motion intensities. The mean values of loss ratio range from 0.05 to 0.20 for the 1973 50-storey archetype building, and 0.01 to 0.16 for the 2012 50-storey archetype building. The results also indicate that loss realizations resulting in repairable damage in both building archetypes are generally below a loss ratio of 0.50. In addition to considering contributions from repairable damage, the total expected loss ratio must also consider loss contributions associated with residual IDRs rendering the building irreparable or collapse realizations. Because the loss ratio associated with the latter outcomes is equal to 1, and due to low loss ratios associated with repairable damage, at earthquake intensities with large residual IDRs and/or considerable probabilities of collapse, residual drift and collapse are likely to represent a greater contribution to the total expected loss ratio than repairable damage.

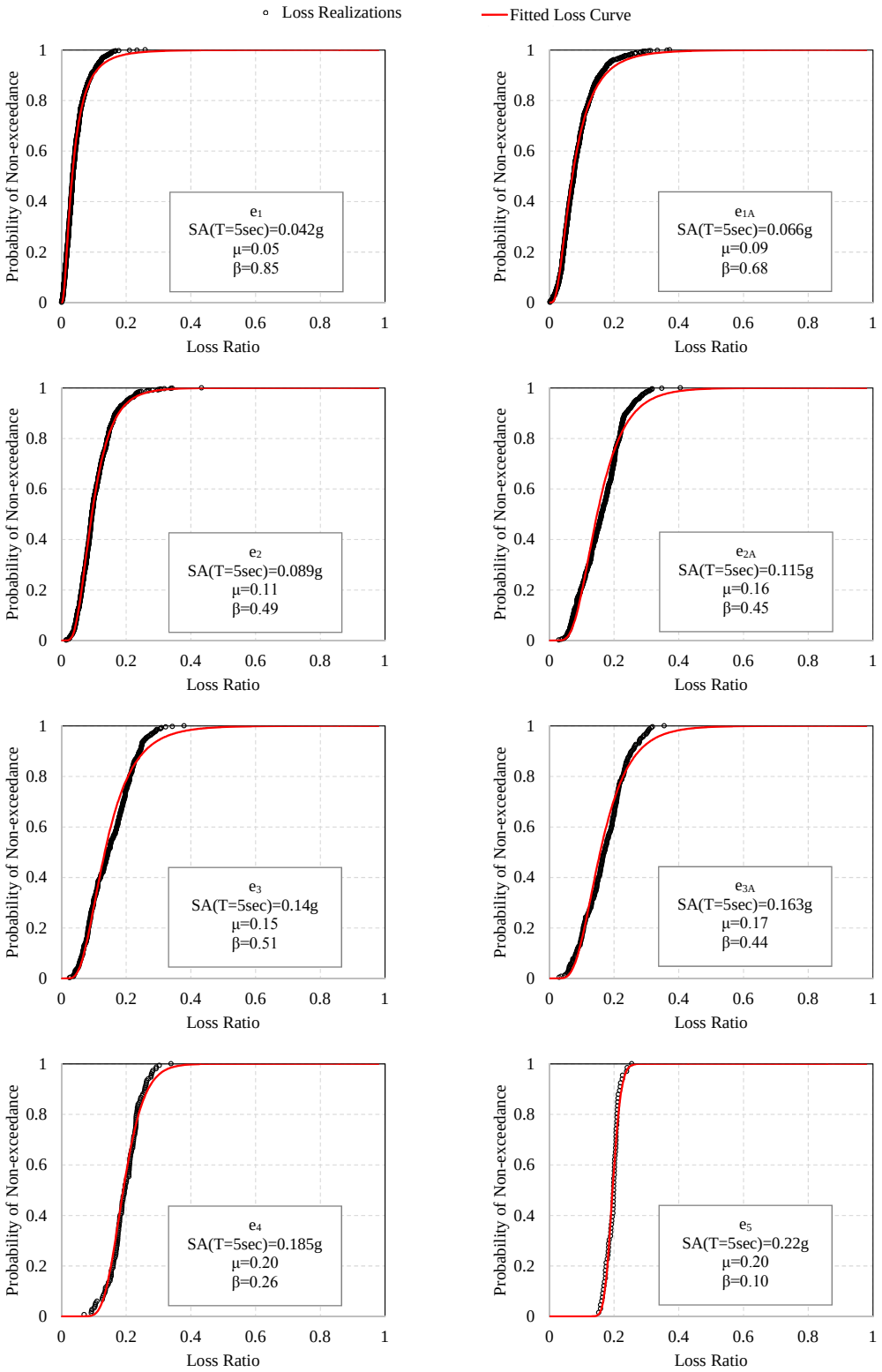

Figure 7-17: Loss realizations and fitted loss curves under earthquake intensities considered in the time-based assessment for the 1973 50-storey archetype building.

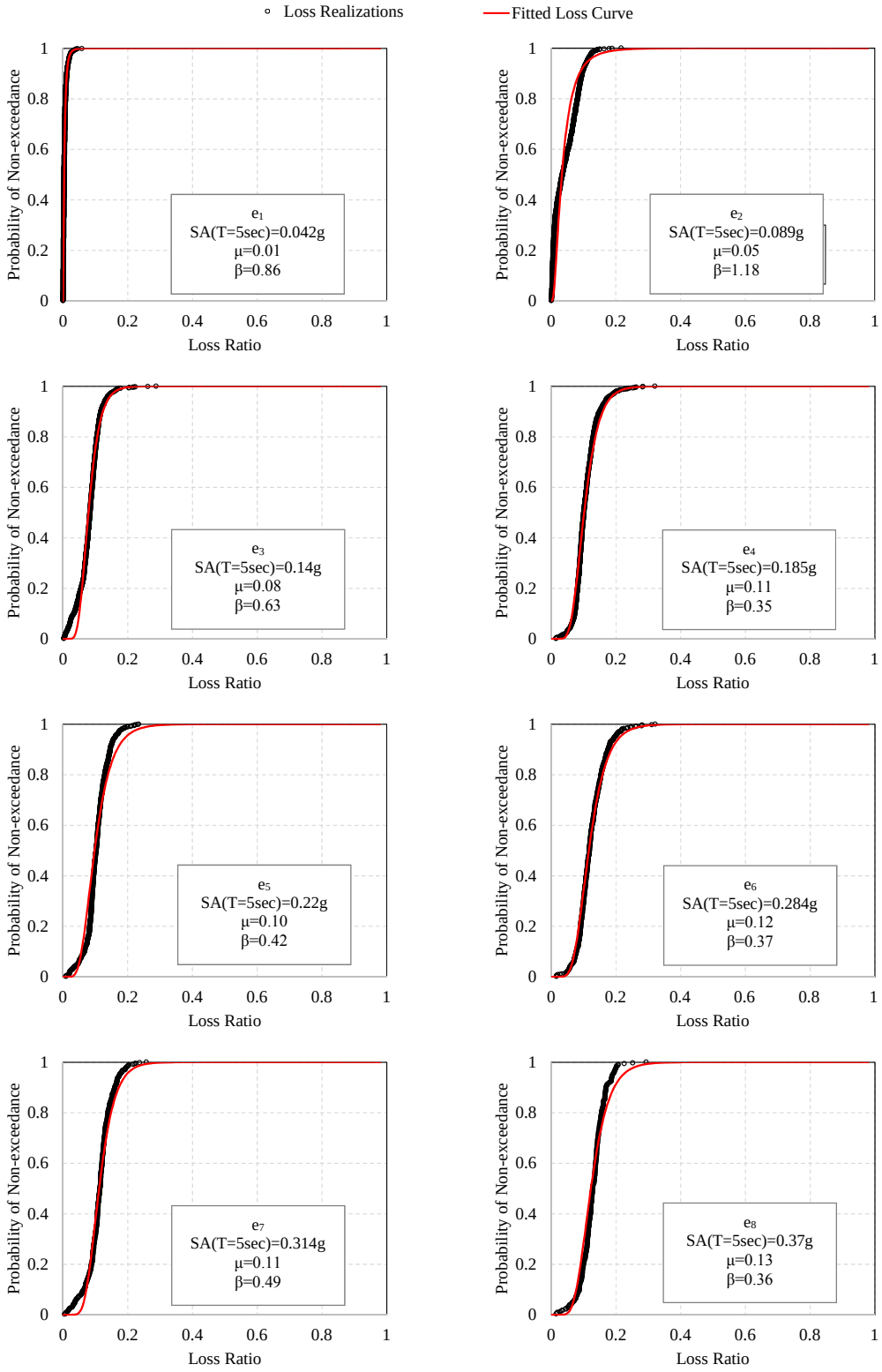

Figure 7-18: Loss realizations and fitted loss curves under earthquake intensities considered in the time-based assessment for the 2012 50-storey archetype building.

De-aggregation of the information presented in Figures 7-17 and 7-18 enables an evaluation of the contribution of drift and acceleration sensitive components to the repairable losses at the earthquake intensities considered. Similarly, the loss contribution of different building components can also be studied. This information is summarized in Figures 7-19 and 7-20, respectively. Figure 7-19 indicates that drift sensitive components dominate losses due to repairable damage in both 50-storey archetype buildings. Therefore, any interventions to enhance the performance of these buildings should focus on minimizing peak transient IDRs. Figure 7-20 illustrates that repairable losses in the 1973 50-storey archetype building are dominated by damage to the façade, whereas in the 2012 50-storey archetype building, these are controlled by damage to office fitouts. Targeted seismic retrofit interventions aimed at minimizing direct economic losses should focus on upgrading of these components.

The information presented in Figures 7-19 and 7-20 can be further subdivided to evaluate contributions to losses on a storey-by-storey basis. For illustration, Figure 7-21 provides the breakdown of acceleration versus drift sensitive components, as well as the contribution of different building components to losses due to repairable damage on a storey-by-storey basis for the 1973 50-storey archetype building under earthquake ground motion intensity e_{2A}. Results are normalized with respect to the expected losses due to repairable damage at the earthquake intensity considered, as illustrated in Figures 7-17 and 7-18. Additional results are provided in Appendix H for both 50-storey archetype buildings and all earthquake ground motion intensities considered in the time-based assessment. The high concentrations of loss at mid-height and at the top of the building correspond to the mechanical rooms where costly MEP components are located, as described in Chapter 4. Most of these components are acceleration sensitive. Consequently, at those storeys, losses due to acceleration sensitive components dominate over those due to drift sensitive components.

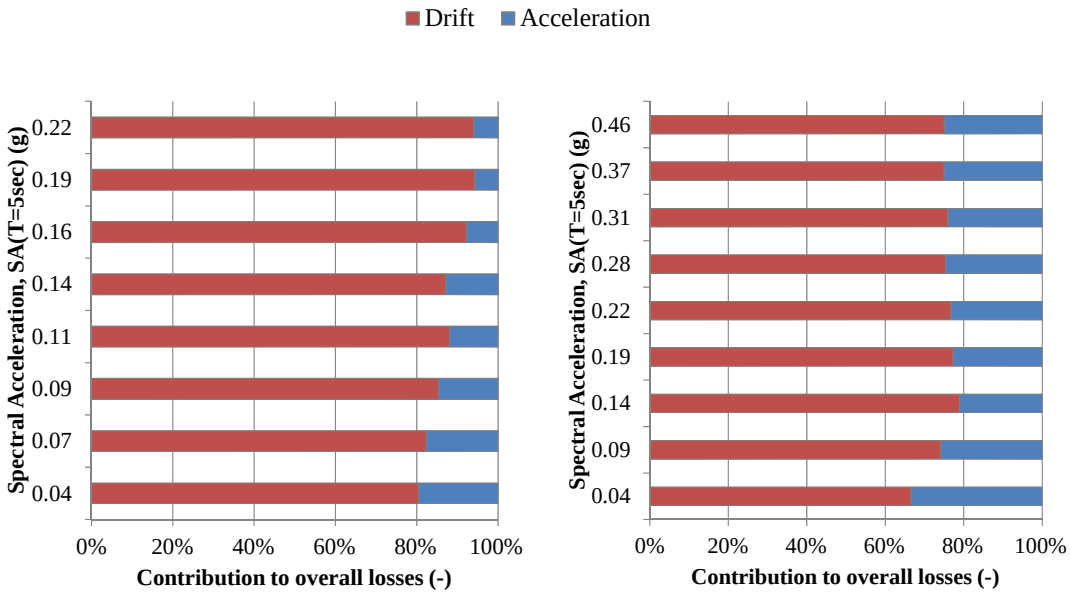

Figure 7-19: Contribution of drift and acceleration sensitive components to repairable damage at different intensities of ground motion shaking for the (a) 1973 and (b) 2012 50-storey archetype buildings.

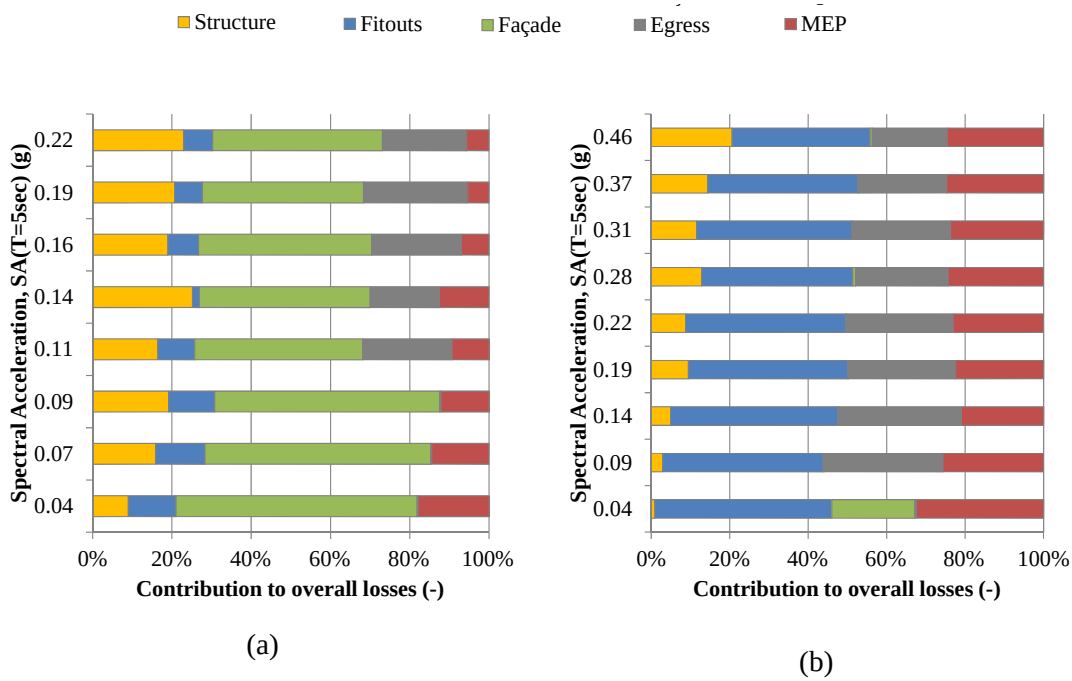

Figure 7-20: Contribution of different building component categories to repairable damage at different intensities of ground motion shaking for the (a) 1973 and (b) 2012 50-storey archetype buildings.

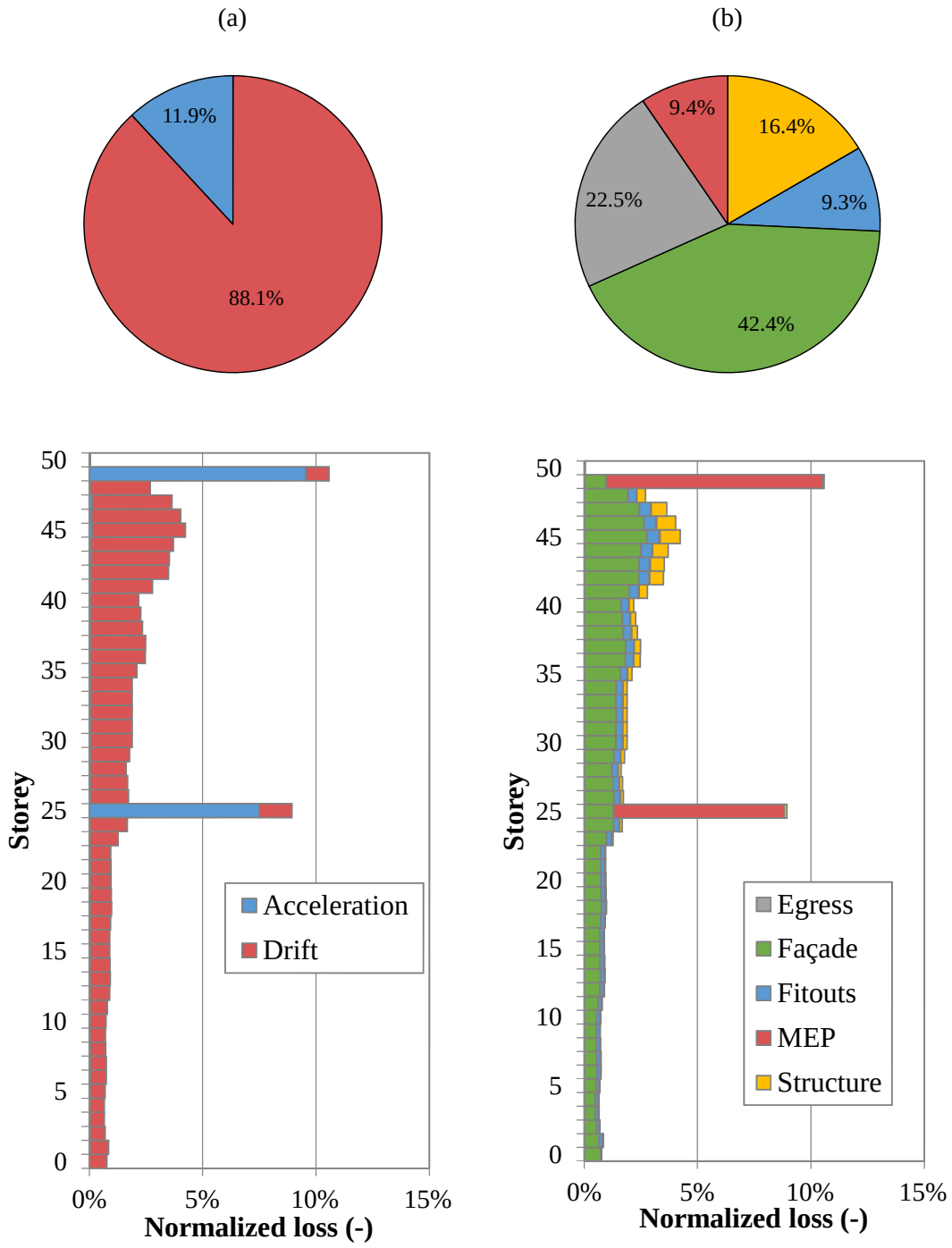

Figure 7-21: Contribution of (a) acceleration versus drift-sensitive and (b) different building component categories to repairable damage under earthquake ground motion intensity e_{2A} for the 1973 archetype.

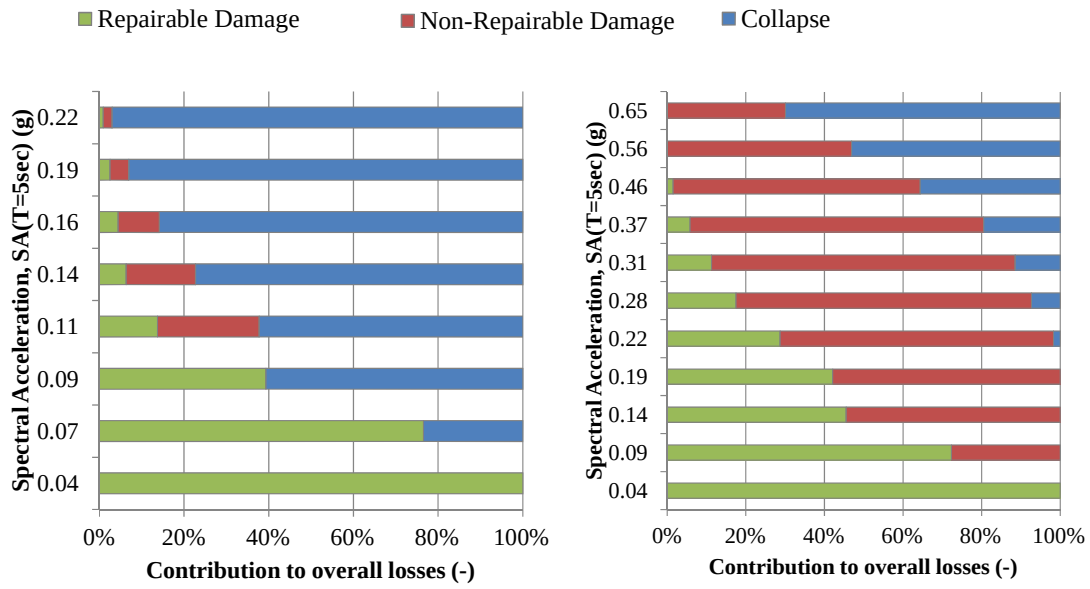

Figure 7-22: Probabilities of observing repairable damage, irreparable damage or collapse at different intensities of ground motion shaking for the (a) 1973 and (b) 2012 50-storey archetype buildings.

Figure 7-22 illustrates the probabilities of observing (i) repairable damage, (ii) residual IDRs rendering the building irreparable or (iii) collapse at each earthquake ground motion intensity considered in the assessment for both 50-storey archetype buildings. Figure 7-22a indicates that collapse potential is the greatest contributor to the expected losses in the 1973 50-storey archetype building. In contrast, residual IDRs are the greatest contributor to the expected loss in the 2012 50-storey archetype building, as illustrated in Figure 7-22b.

7.5.1 Loss function and average annual loss

As with the peak IDR and maximum PFA performance functions presented in Section 7.5.4, the results of the MSA can also be used to develop tools and metrics related to the expected economic losses associated with the performance of the building, such as the loss function or the annualized seismic loss, i.e. AAL. A loss function provides the annual frequency of exceeding a certain value of loss. It provides information in a language that is easier to communicate to building owners and decision makers than the probability of exceeding an EDP. The loss function can be calculated using Equation 7-3 (FEMA 2012, Krawinkler and Miranda 2004, Goulet et al. 2007):

$$P\ (L > x) = \int P(L > x|E = e) \cdot\ |d\lambda(e)| = \sum_{i=1}^{n} P(L > x|e_i) \cdot \left|\frac{d\lambda(e_i)}{de}\right| \cdot\ \Delta e_i$$

Equation 7-3

Where P(L>x | E=e), the probability of exceeding a certain value of loss at a given intensity of ground motion shaking, is integrated with the seismic hazard curve |dλ(e)|. The probability of exceeding a certain value of loss at a given intensity of ground motion shaking can be broken down as the sum of three components as illustrated in Equation 7-4.

$$P(L > x|E = e) = SUM\begin{Bmatrix} P(L > x|C) \cdot P(C|E = e) \\ P(L > x|NC, R) \cdot P(NC|E = e) \cdot P(R|NC, E = e) \\ (L > x|NC, NR) \cdot P(NC|E = e) \cdot P(NR|NC, E = e) \end{Bmatrix}$$

Equation 7-4

Component P(L>x | C) P(C | E=e) denotes the probability of observing a value of loss greater than x, given that collapse has occurred, multiplied by the probability of observing collapse at a given intensity of ground shaking. Component P(L>x | NC,R) P(NC | E=e) ·P(R | NC, E=e) denotes the probability of observing a value of loss greater than x, given that no collapse has occurred and residual drifts deem the building irreparable, multiplied by the probability of observing no collapse at a given intensity of ground motion shaking, multiplied by the probability of residual drifts rendering the building irreparable given that no collapse has occurred. Lastly, component P(L>x | NC,NR) P(NC | E=e) P(NR | NC, E=e) denotes the probability of observing a value of loss greater than x, given that no collapse has occurred and residual drifts do not deem the building irreparable, multiplied by the probability of observing no collapse at a given intensity of ground motion shaking, multiplied by the probability of residual drifts not rendering the building irreparable given that no collapse has occurred. The integral shown in Equation 7-3 can be solved through numerical integration over the number of earthquake ground motion intensities, n, considered in the time-based assessment, where intensity e_i is assumed to represent all earthquake ground motion shaking intensities in the interval Δe_i. Figure 7-23 illustrates the resulting loss curves for the 1973 and 2012 50-storey archetype buildings. The contribution of the different intensities of ground motion shaking considered to the overall loss curves are illustrated in Figures 7-25 and 7-26 for the 1973 and 2012 50-storey archetype buildings, respectively.

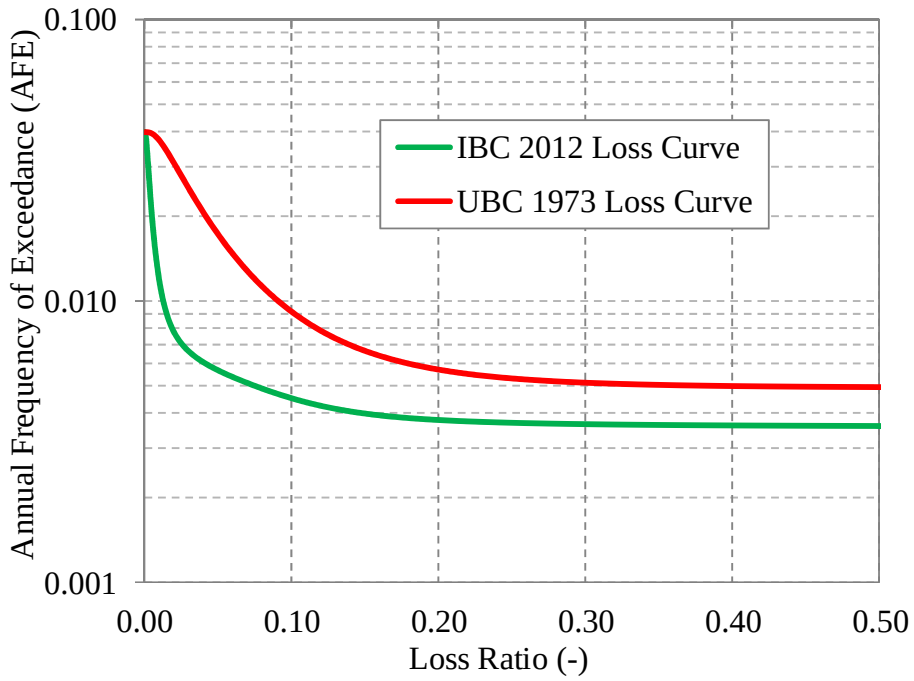

Figure 7-23: Loss curves for the (a) 1973 and (b) 2012 50-storey archetype buildings.

Given the loss function, expected AAL can be calculated per Equation 7-5 (Jayaram et al. 2012). The AAL is a useful metric, which building owners can easily relate to annual insurance payments.

$$AAL = \sum_{i=1}^{n}(L_i \cdot \Delta\lambda_i) \qquad \text{Equation 7-5}$$

Where n is the number of intensity levels considered in the assessment, $\Delta\lambda_i$ is the annual rate of occurrence of intensity level i, denoted in Figure 7-2, and L_i is the expected loss at intensity level i. The AAL for the 1973 50-storey archetype building is estimated at 0.66% of building replacement cost, whereas the AAL for the 2012 50-storey archetype building is estimated at 0.40%. The contribution of repairable damage, irreparable damage and collapse to the AAL is illustrated in Figure 7-24 and coincides with previous observations of collapse and irreparable damage controlling the overall loss in the 1973 and the 2012 50-storey archetype buildings, respectively. As a reference point, Ramirez et al. (2012) evaluated the performance of a set of modern concrete-framed 20-storey buildings to have AALs on the order of 0.4 to 0.7% of building replacement cost. These results are consistent with the results for the 2010 50-storey archetype considered in this study, particularly when considering that, as discussed in Section 2.1.4, normalized seismic losses tend to be lower in tall buildings.

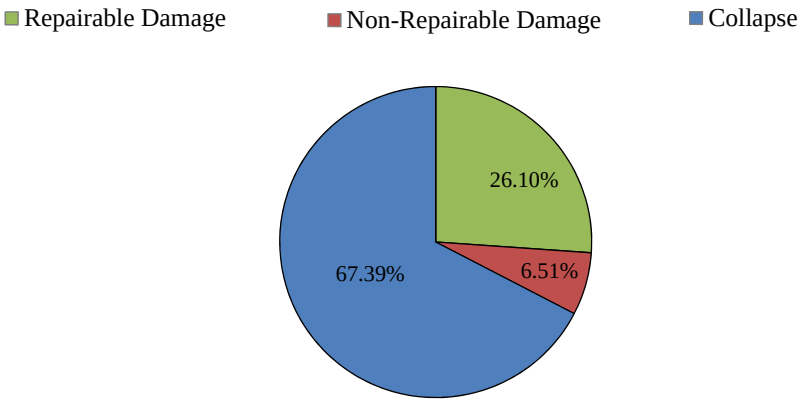

(a)

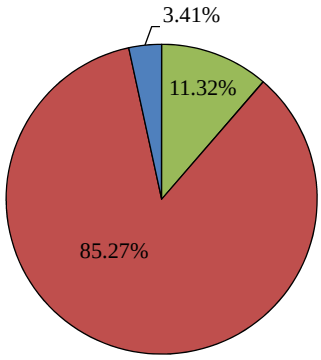

(b)

Figure 7-24: Contribution of repairable damage, irreparable damage and collapse to the average annual loss (AAL) for the (a) 1973 and (b) 2012 50-storey archetype buildings.

The AAL can also be used to conduct cost benefit analyses of adopting structural retrofit or other building enhancements. Cost benefit analyses conduct a comparison between the net present value of the average annual costs that are prevented through enhanced seismic performance. In addition to the AAL, loss exceedance rates can also be computed per Equation 7-6 (Jayaram et al. 2012).

$$ER(x) = 1 - e^{-\sum_{i=1}^{n}(\Delta\lambda_i \cdot P(L>x))} \qquad \text{Equation 7-6}$$

The exceedance rates for 10%, 20% and 40% of building replacement cost are 110, 175 and 201 years for the 1973 50-storey archetype building and 222, 265 and 277 years for the 2012 50-storey archetype building, respectively.

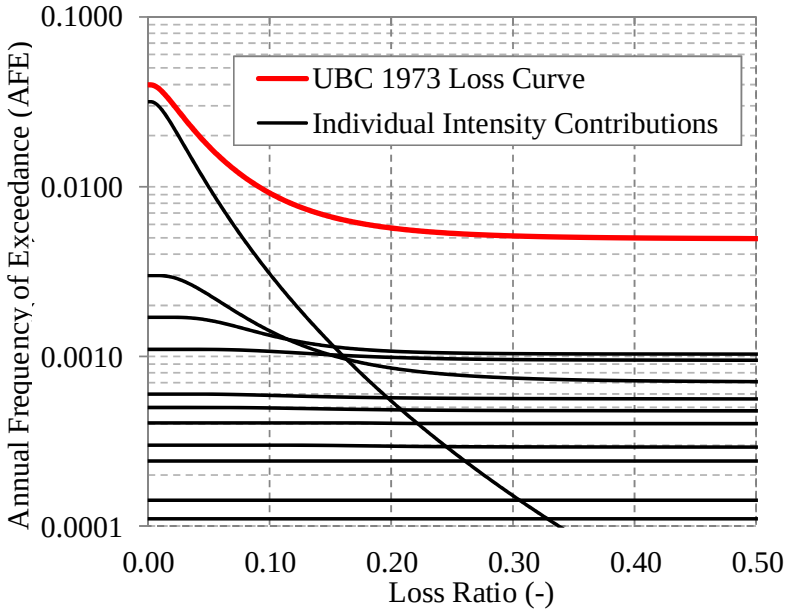

Figure 7-25: Contribution of different earthquake ground motion intensities to the cumulative 1973 50-storey archetype building loss curve.

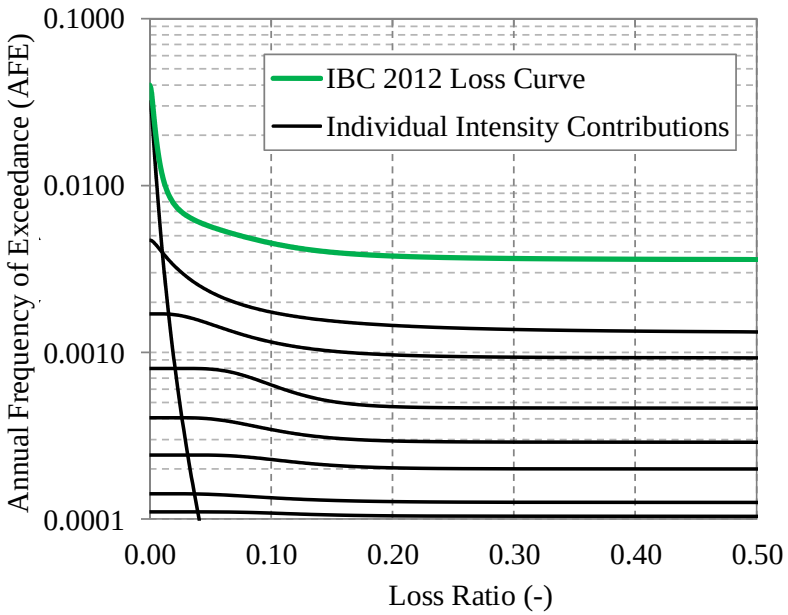

Figure 7-26: Contribution of different earthquake ground motion intensities to the cumulative 2012 50-storey archetype building loss curve.

7.5.2 Seismic vulnerability function

The financial resources needed to recover from seismic damage to tall buildings are generally not trivial amounts, and thus the ability to realistically model losses is important. The results presented in this chapter, have highlighted some of the unique challenges of loss assessment of tall buildings, including the tendency for significant damage to be concentrated in a few storeys rather than distributed throughout the building and the presence of excessive residual IDRs in one or a few storeys resulting in the building being declared a total loss and demolished, even when the levels of damage in the rest of the building are relatively low. The loss function presented in Section 7.5.1 can provide useful metrics related to expected losses of the archetype buildings. However, the results are linked with the seismic hazard at the site. In order to provide a simple tool to enable estimation of expected losses for the archetype buildings at different sites, seismic vulnerability functions can be constructed. A vulnerability function provides the loss ratio, (total loss over total building cost, as defined in Section 4.3), versus spectral acceleration at the fundamental period of the structure and enables rapid estimates of loss. These functions are frequently used in catastrophe modelling to estimate expected seismic losses to portfolios of buildings.

The vulnerability functions for the archetype buildings can be constructed by describing the expected loss ratio against the spectral acceleration at the fundamental period of the structure for each intensity of ground motion shaking considered in the assessment. The loss ratio is computed considering the key contributors to the total loss described earlier: (1) Collapse, (2) Non-collapse, Non-repairable and (3) Non-collapse, Repairable. The resulting vulnerability functions are shown in Figures 7-27a and 7-27b for the 1973 and 2012 50-storey archetype buildings, respectively. As previously noted, collapse is the greatest contributor to the loss of the 1973 50-storey archetype building and residual IDRs rendering the building irreparable are the greatest contributors to the loss in the 2012 50-storey archetype building. The contributions of (1) Collapse, (2) Non-collapse, Non-repairable and (3) Non-collapse, Repairable loss to the overall vulnerability function for the 2012 50-storey archetype building is consistent with the results from Ramirez et al. (2012) for modern concrete-framed buildings.

(a)

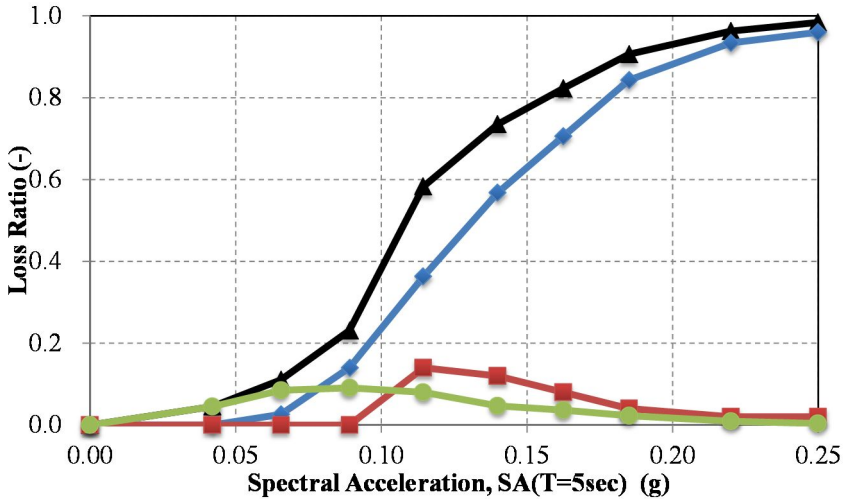

(b)

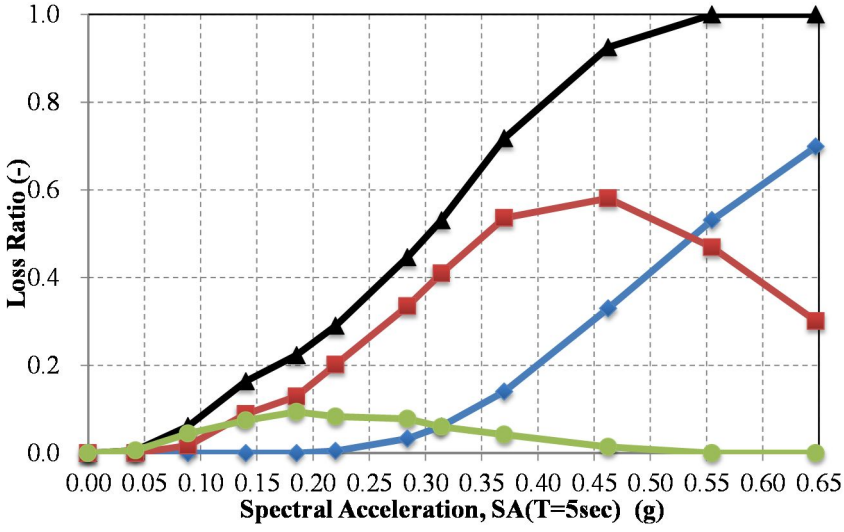

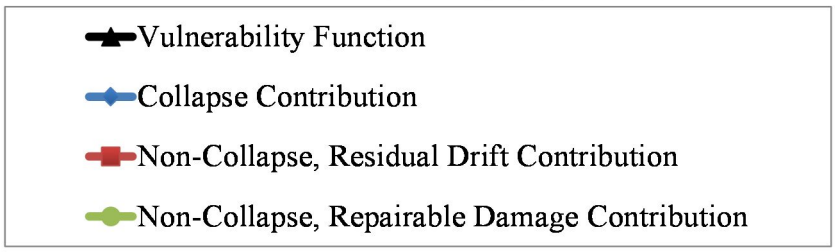

Figure 7-27: Seismic vulnerability functions for the (a) 1973 and the (b) 2012 50-storey archetype buildings illustrating loss contribution from collapse, repairable and irreparable damage.

7.6 Recovery functions

Thus far, the work presented in this chapter provides useful comparative metrics between an archetype 1970s tall building versus a modern code-based design. However, the metrics developed fall short of providing indicators of resilience that can be used to evaluate the impact of seismic performance on the community. This section illustrates an application of the methodology developed in Section 4.3.3 to develop recovery curves to re-occupancy and functional recovery for the 1973 and 2012 50-storey archetype buildings.

Recovery functions are developed probabilistically for 1000 simulations, based on the damage estimates obtained from the loss realizations in the building performance model. Estimates for external or impeding factors are also sampled in each realization to account for the expected variability in external factors which may delay the initiation of repairs, e.g. post-earthquake inspection, engineering mobilization, etc. The sequence of repair estimates carried out in the development of the recovery functions enable understanding the occupancy and functionality ratios of the buildings against time. Figures 7-28 to 7-29 provide re-occupancy recovery curves under the earthquake intensities considered in the time-based assessment for the 1973 and the 2012 50-storey archetype buildings, respectively. Figures 7-30 to 7-31 provide functionality recovery curves under the earthquake intensities considered in the time-based assessment for the 1973 and the 2012 50-storey archetype buildings, respectively. These results only represent realizations in which repairable damage is observed. In the event of collapse or residual deformations rendering the building irreparable, the recovery curves is considered as a step function from 0 to 1 at the estimated building replacement time. In the case of the archetypes considered, building replacement time is estimated as 1000 days. Demolition and re-design is estimated to take 300 days. Reconstruction is assumed to take 700 days (approximately two weeks per storey).

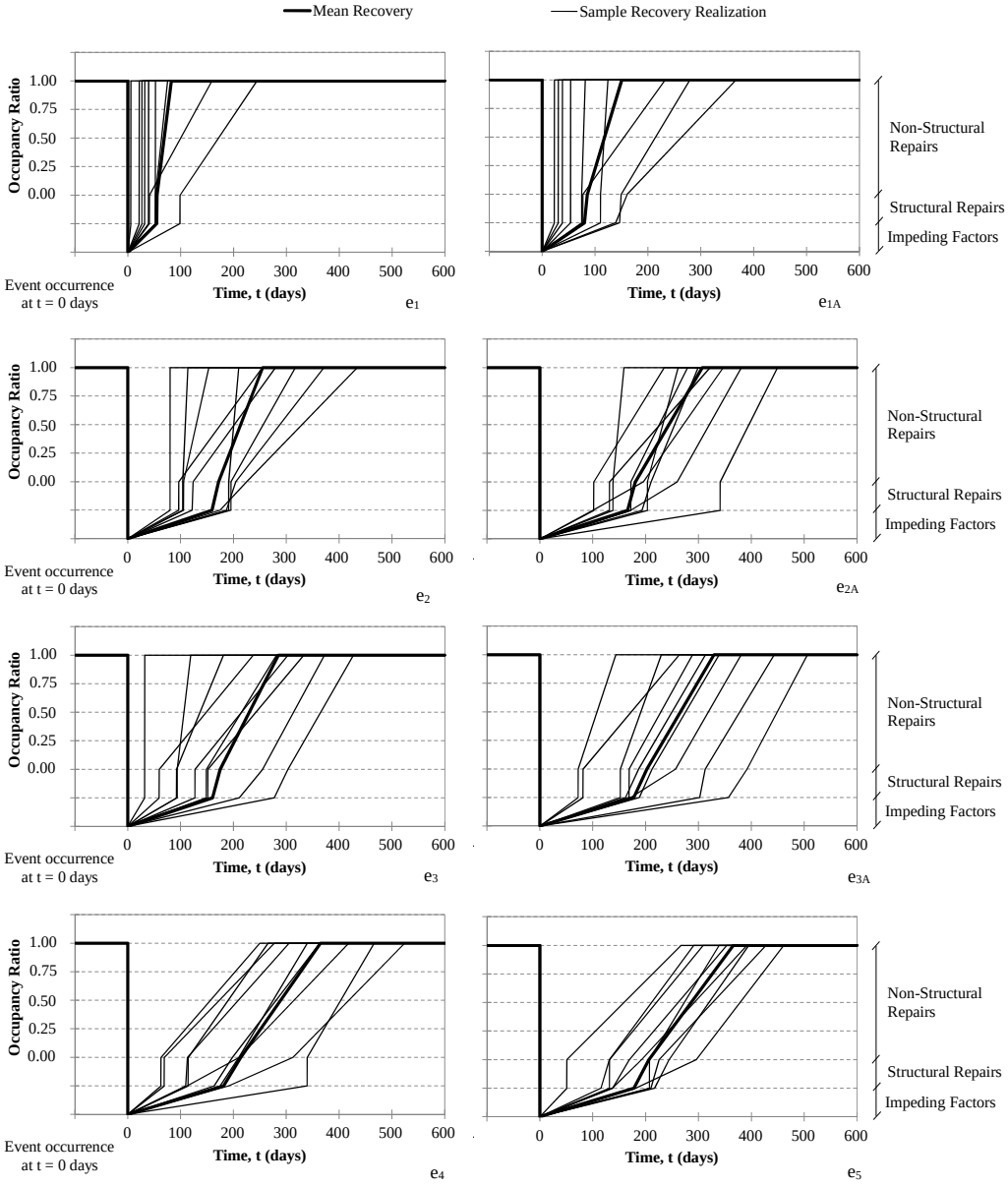

Figure 7-28: Re-occupancy recovery curves under the earthquake intensities considered in the time-based assessment for the 1973 50-storey archetype building showing mean and sample realizations (10^{th}, 20^{th} 30^{th}, 40^{th}, 50^{th}, 60^{th}, 70^{th}, 80^{th}, 90^{th} percentile estimates) for realizations where damage is repairable.

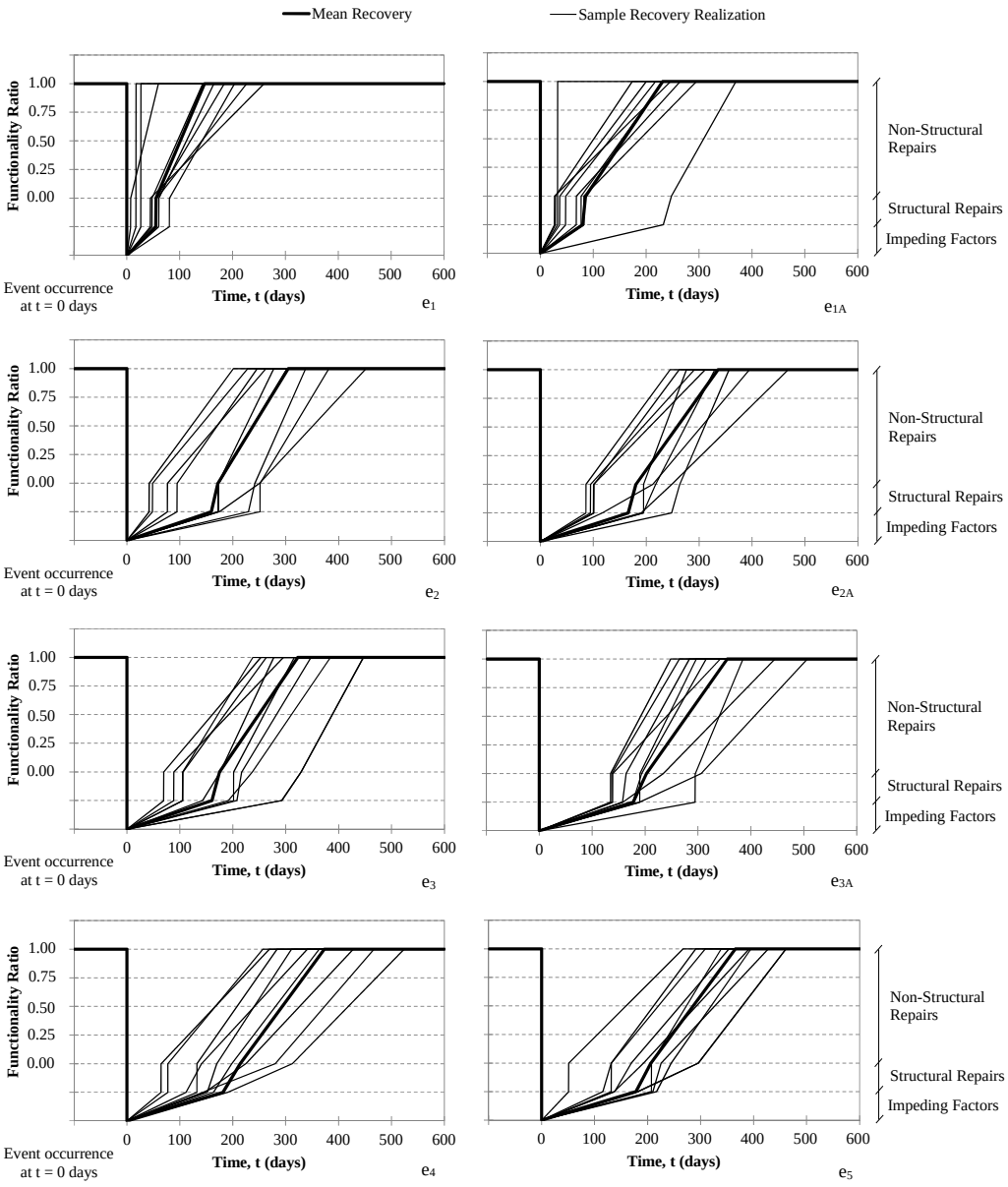

Figure 7-29: Functionality recovery curves under the earthquake intensities considered in the time-based assessment for the 1973 50-storey archetype building showing mean and sample realizations (10^{th}, 20^{th} 30^{th}, 40^{th}, 50^{th}, 60^{th}, 70^{th}, 80^{th}, 90^{th} percentile estimates) for realizations where damage is repairable.

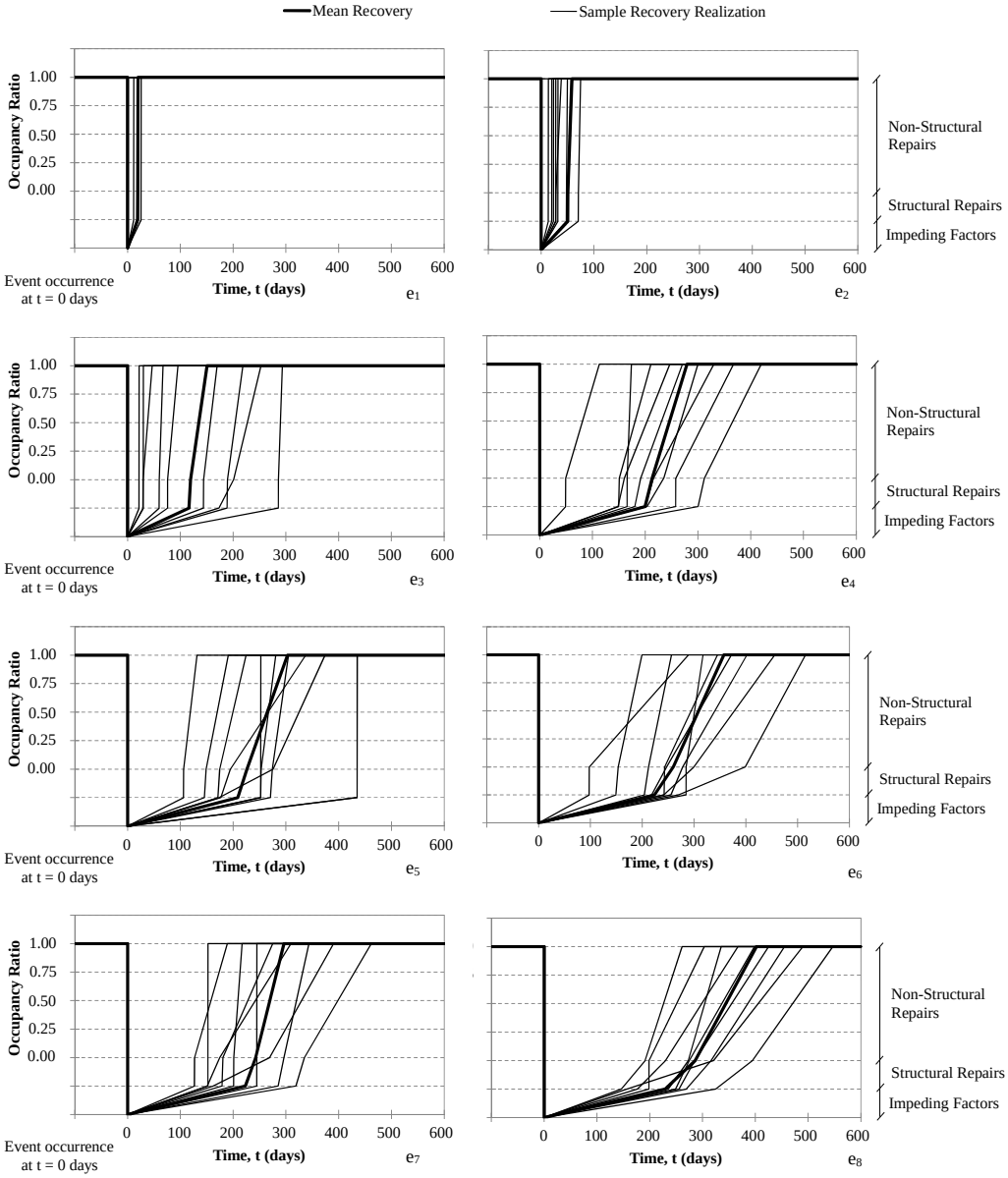

Figure 7-30: Re-occupancy recovery curves under the earthquake intensities considered in the time-based assessment for the 2012 50-storey archetype building showing mean and sample realizations (10^{th}, 20^{th} 30^{th}, 40^{th}, 50^{th}, 60^{th}, 70^{th}, 80^{th}, 90^{th} percentile estimates) for realizations where damage is repairable.

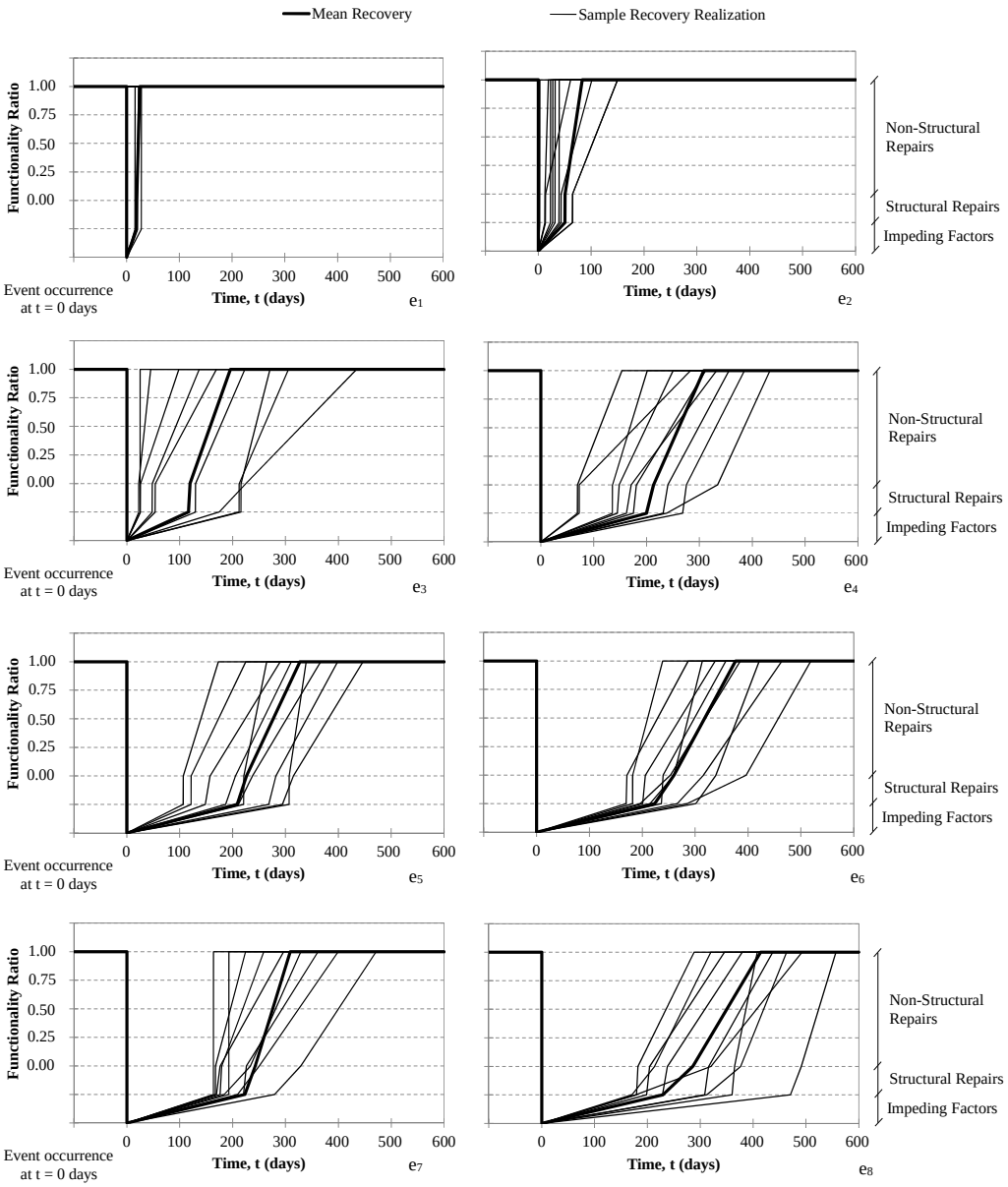

Figure 7-31: Functionality recovery curves under the earthquake intensities considered in the time-based assessment for the 2012 50-storey archetype building showing mean and sample realizations (10^{th}, 20^{th} 30^{th}, 40^{th}, 50^{th}, 60^{th}, 70^{th}, 80^{th}, 90^{th} percentile estimates) for realizations where damage is repairable.

The mean and dispersion associated with each phase of the recovery curve (impeding factors, structural repairs and non-structural repairs) from figures 7-28 to 7-31 are summarized in Tables 7-6 and 7-7 for re-occupancy and functional recovery, respectively. The results illustrate that even in the best of circumstances, where no collapse or residual drifts are observed and losses to the building are limited, delays associated with re-occupancy and functional recovery in both archetypes are significant, even under low earthquake ground motion intensities.

Table 7-6: Median (μ) and dispersion (β) of time to re-occupancy estimates in key recovery phases for the 1973 and 2012 50-storey archetype building.

Earthquake Ground Motion Intensity	Archetype Building	Time to Re-occupancy (days)					
		Impeding Factors		Structural Repairs		Non-Structural Repairs	
		μ_{IF}	β_{IF}	μ_{Struct}	β_{Struct}	$\mu_{Non\text{-}Struct}$	$\beta_{Non\text{-}Struct}$
e_1	1973	55	0.82	1	1.07	27	1.63
	2012	19	0.96	0	0.00	1	0.99
e_{1A}	1973	80	0.83	5	1.21	65	1.40
	2012	-	-	-	-	-	-
e_2	1973	159	0.54	12	1.32	84	1.11
	2012	51	0.95	0	0.00	8	1.07
e_{2A}	1973	166	0.51	15	1.12	127	0.79
	2012	-	-	-	-	-	-
e_3	1973	161	0.54	14	1.10	111	0.77
	2012	117	1.06	3	1.15	31	0.97
e_{3A}	1973	178	0.48	25	1.12	127	0.66
	2012	-	-	-	-	-	-
e_4	1973	181	0.53	33	1.16	151	0.47
	2012	200	0.49	14	1.29	66	0.77
e_5	1973	178	0.41	28	0.97	160	0.21
	2012	209	0.49	17	1.36	77	0.74
e_6	1973	-	-	-	-	-	-
	2012	224	0.41	36	1.36	98	0.67
e_7	1973	-	-	-	-	-	-
	2012	223	0.42	19	1.39	54	0.63
e_8	1973	-	-	-	-	-	-
	2012	229	0.33	57	1.25	116	0.46
e_{8A}	1973	-	-	-	-	-	-
	2012	242	0.32	110	0.74	142	0.26

Table 7-7: Median (μ) and dispersion (β) of time to functional recovery in key recovery phases for the 1973 and 2012 50-storey archetype buildings.

Earthquake Ground Motion Intensity	Archetype Building	Time to Functional Recovery (days)					
		Impeding Factors		Structural Repairs		Non-Structural Repairs	
		μ_{IF}	β_{IF}	μ_{Struct}	β_{Struct}	$\mu_{Non\text{-}Struct}$	$\beta_{Non\text{-}Struct}$
e_1	1973	55	0.82	1	1.07	92	0.54
	2012	19	0.96	0	0.00	6	1.53
e_{1A}	1973	80	0.83	5	1.21	145	0.59
	2012	-	-	-	-	-	-
e_2	1973	159	0.54	12	1.32	133	0.50
	2012	51	0.95	0	0.00	33	1.21
e_{2A}	1973	166	0.51	15	1.12	155	0.32
	2012	-	-	-	-	-	-
e_3	1973	161	0.54	14	1.10	148	0.32
	2012	117	1.06	3	1.15	76	0.71
e_{3A}	1973	178	0.48	25	1.12	153	0.29
	2012	-	-	-	-	-	-
e_4	1973	181	0.53	33	1.16	159	0.31
	2012	200	0.49	14	1.29	95	0.55
e_5	1973	178	0.41	28	0.97	160	0.21
	2012	209	0.49	17	1.36	101	0.56
e_6	1973	-	-	-	-	-	-
	2012	224	0.41	36	1.36	117	0.55
e_7	1973	-	-	-	-	-	-
	2012	223	0.42	19	1.39	66	0.41
e_8	1973	-	-	-	-	-	-
	2012	229	0.33	57	1.25	128	0.30
e_{8A}	1973	-	-	-	-	-	-
	2012	242	0.32	110	0.74	144	0.24

The results presented in Tables 7-6 and 7-7 enable the development of downtime curves to re-occupancy and functional recovery, equivalent to the loss curves computed in Section 7.5, or the other performance functions computed in Section 7.4 that express the mean annual rates of exceeding a performance measure. The resulting downtime curves to re-occupancy and functional recovery for both archetype buildings are illustrated in Figures 7-32 and 7-33, respectively.

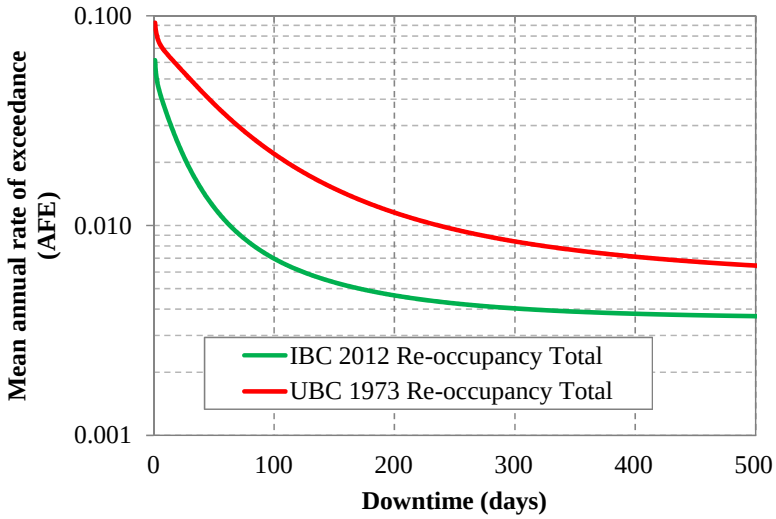

Figure 7-32: Downtime curves to re-occupancy for the 1973 and 2012 50-storey archetype buildings.

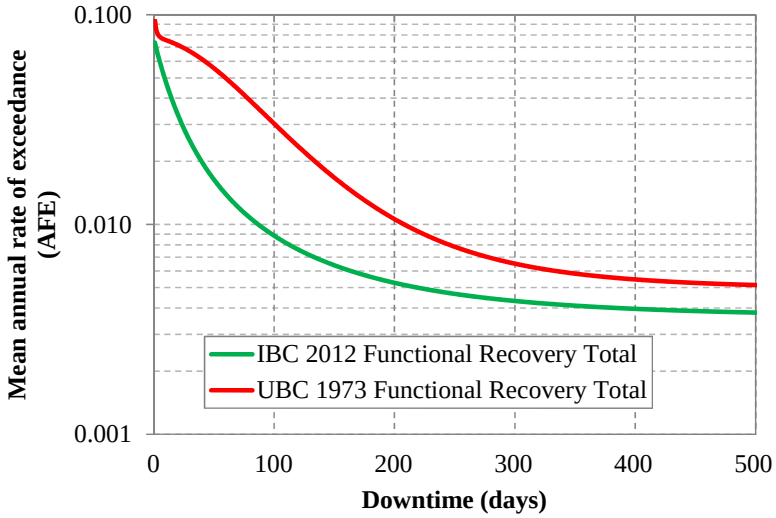

Figure 7-33: Downtime curves to functional recovery for the 1973 and 2012 50-storey archetype buildings.

The total downtime curves illustrated in Figures 7-32 and 7-33 are constructed by evaluating the different contributions to total downtime from impeding factors, structural repairs, non-structural repairs, residual IDRs rendering the building irreparable, and collapse. The contributions of these components to the total downtime to re-occupancy and functional recovery are illustrated in Figures 7-34 and 7-35 for the 1973 and 2012 50-storey archetype buildings, respectively.

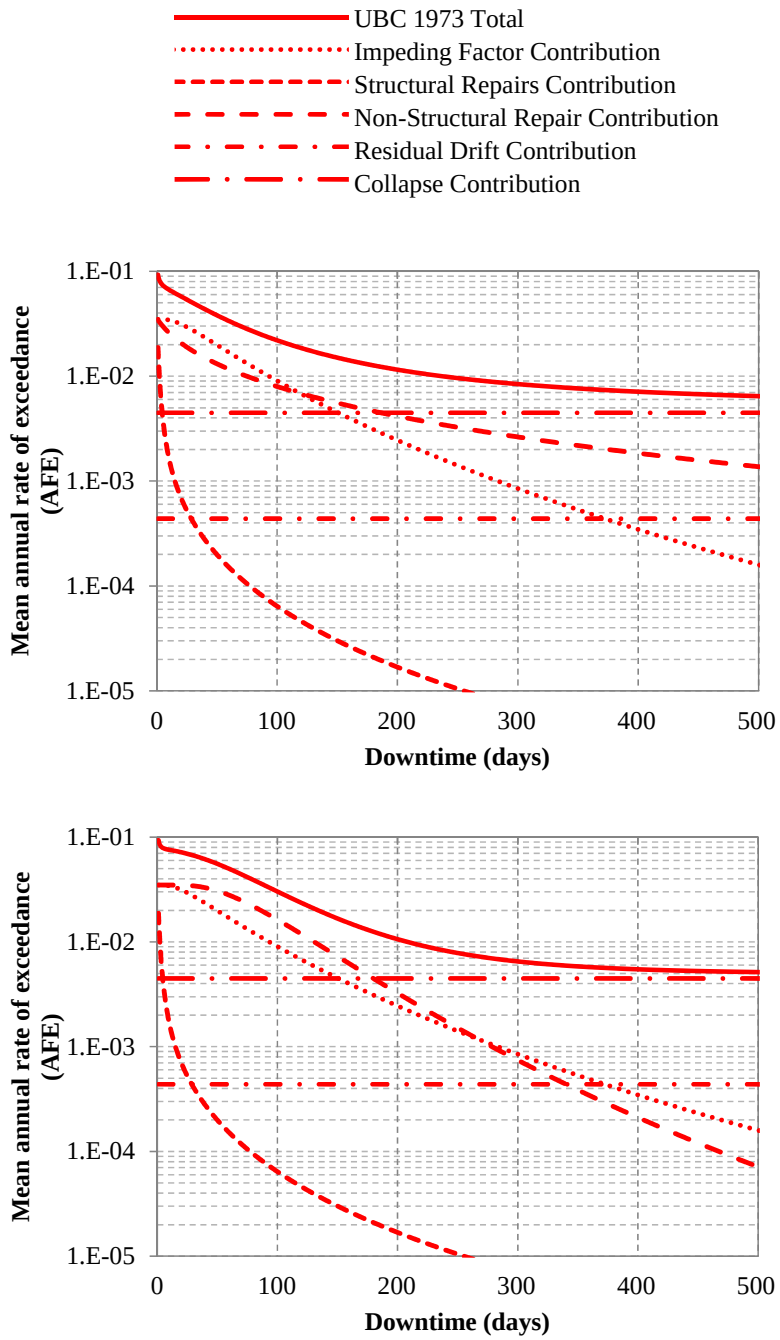

Figure 7-34: Impeding factors, structural repairs, non-structural repairs, residual drift and collapse contribution to the 1973 50-storey archetype building's downtime curve to (a) re-occupancy and (b) functional recovery.

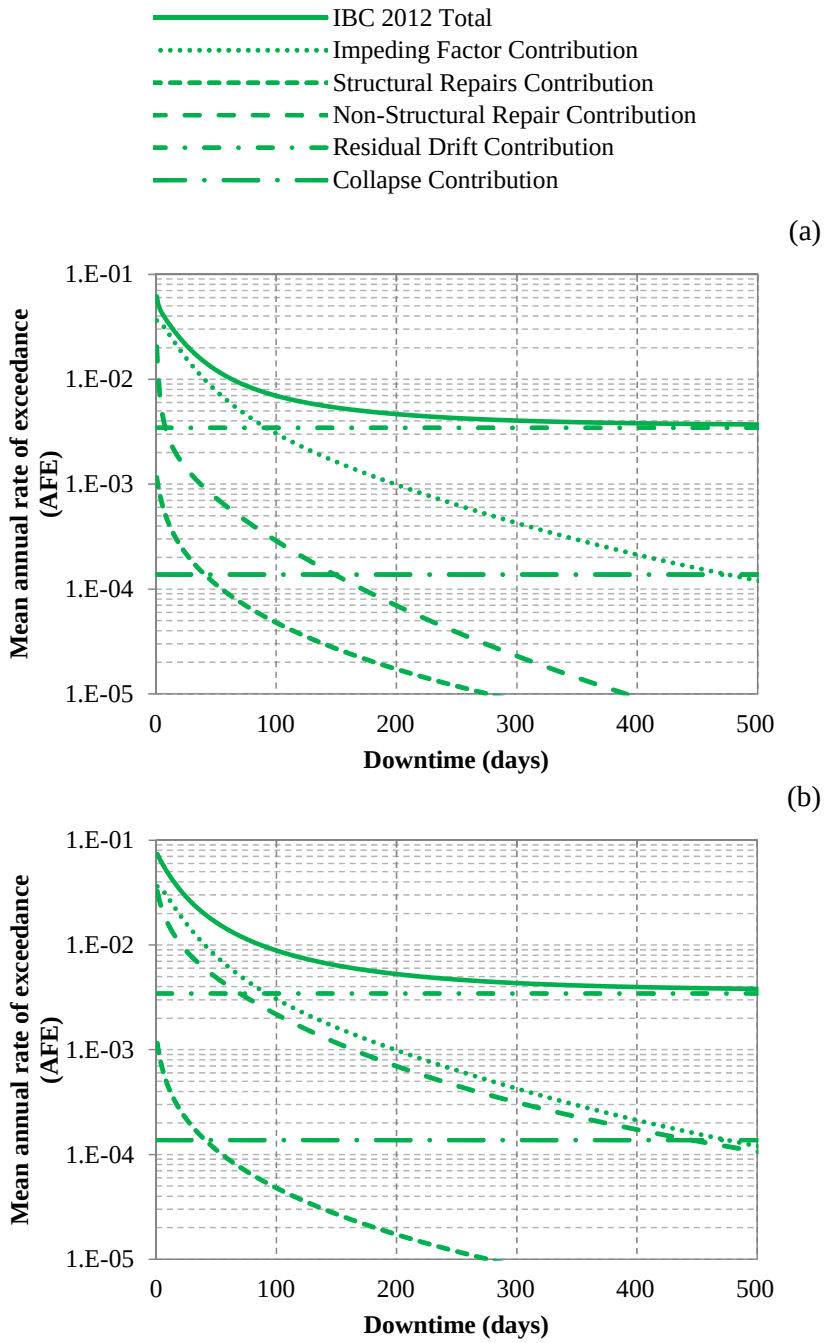

Figure 7-35: Impeding factors, structural repairs, non-structural repairs, residual drift and collapse contribution to the 2012 50-storey archetype building's downtime curve to (a) re-occupancy and (b) functional recovery.

These results indicate that at low annual frequencies of exceedance, the greatest contributor to downtime is collapse risk in the 1973 50-storey archetype building and potential for residual IDRs rendering the building irreparable in the 2012 50-storey archetype building. The difference in the downtime curves for re-occupancy and functional recovery is driven by the magnitude of repairs to non-structural components. The considerable time associated with repairs of non-structural components to achieve functional recovery in the 1973 50-storey archetype building at high annual frequencies of exceedance leads to the 'belly shaped' curve, illustrated in Figure 7-33b, when compared to the 2012 50-storey archetype building downtime curve in the same figure. Contributions to downtime from impeding factors, structural repairs, residual IDRs and collapse are consistent in each archetype whether re-occupancy or functional recovery are evaluated, as illustrated in Figures 7-34 and 7-35.

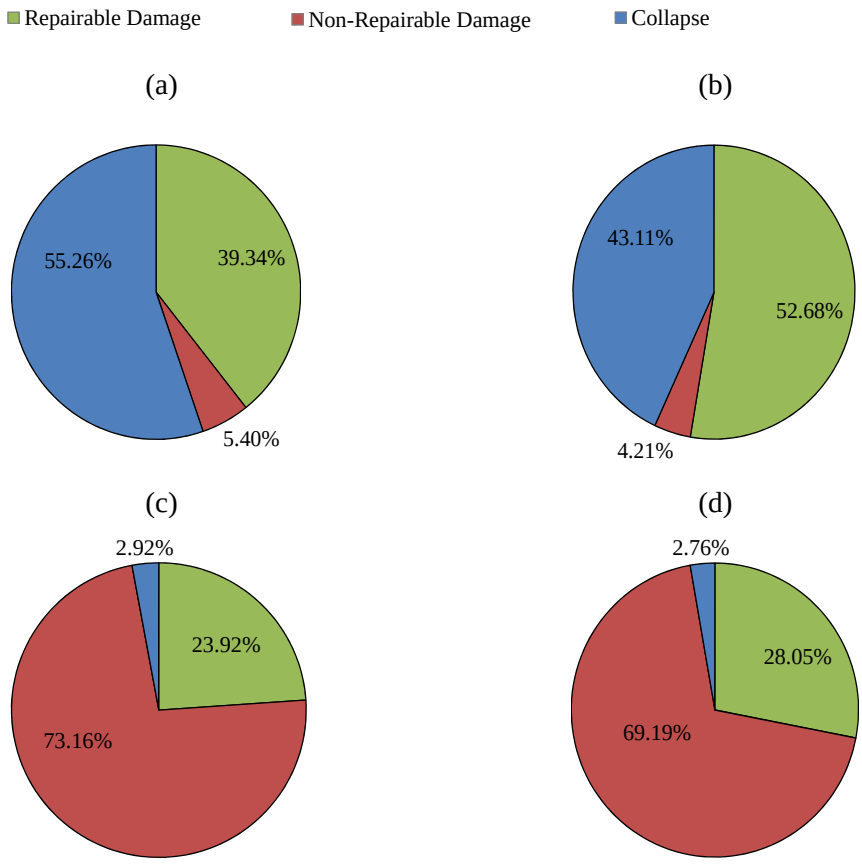

Figure 7-36: Contribution of repairable damage, irreparable damage from residual IDRs and collapse to the average annual downtime (AAD) to (a, c) re-occupancy and (b, d) functional recovery for the (a, b) 1973 and (c, d) 2012 50-storey archetype buildings.

As with the loss curve, enabling the calculation of the AAL, the downtime curve enables the calculation of the annualized downtime, i.e. AAD, which can be a useful tool for estimating business disruption and other indirect losses associated with building closures due to seismic damage. The AAD to re-occupancy for the 1973 50-storey archetype building is estimated at 8.1 days, whereas for the 2012 50-storey archetype building, it is estimated at 4.7 days. The AAD to functional recovery for the 1973 50-storey archetype building is estimated at 10.4 days, whereas for the 2012 50-storey archetype building, it is estimated at 5.0 days. The contribution of repairable damage, irreparable damage and collapse to the AAL is illustrated in Figure 7-36 and coincides with previous observations of collapse and irreparable damage controlling the overall loss in the 1973 and the 2012 50-storey archetype buildings, respectively.

7.7 Implications of results on deaths and injuries

This section provides a brief description of the challenges associated with seismic casualty risk estimation and a qualitative discussion of the implications of the results of this work for death and injury estimates. As discussed in Section 2.2.4, while the FEMA P58 project has made significant progress in utilizing direct economic losses as a decision variable, evaluation of casualty risks as a decision variable is more complex and not as far advanced as modelling of repair costs (Deierlein 2004). The prediction of casualty rates is problematic, due in large part to the lack of verifiable data (Krawinkler 2004).

Building collapse is the principal cause of earthquake casualties. In order to develop casualty estimates, the FEMA P58 project introduces building population models, which define the number of people per gross square footage, and as a function of building occupancy. Population models generally define the peak population and the expected fractions at different times of the day, e.g. peak population for a commercial office is 4 people per 1000 ft^2 around mid-morning and mid-afternoon (FEMA 2012). Casualties caused by building collapse are based on collapse risk, as discussed in Section 7.4.1, and estimates of building occupancy based on populations models. While this calculation may seem straightforward, further considerations are required to account for different collapse modes, as the casualties associated with a partially collapsed building can be drastically lower than those of a fully collapse building. Krawinkler (2004) suggests that fatality rates expressed as a percentage of expected building occupancy are on the order of 1% to 1.5% for partially collapsed buildings and 10% to 20% for fully collapsed buildings.

In addition to building collapse, some damage states associated with individual building components can result in casualties, e.g. due to falling debris. Within the FEMA P58 project, to facilitate casualty estimation from damage to building components, consequence functions define: (i) the potential life safety hazards associated with each damage state, (ii) the affected area associated with the life safety hazard, and (iii) the percentage of individuals that, if located within the affected area, are likely to be injured by the component. Even though this method enables quantification of casualties associated with component damage, these values are judgmentally determined (FEMA 2012).

Even though consideration of injuries and fatalities may be of greater relevance for policy planning than other decision variables, there is generally great difficulty in adopting such metrics for decision making. Building owners generally prefer seismic performance to be reported in terms of direct economic losses than in terms of casualty rates (personal communication with Building Owners and Managers Association of San Francisco, 2012). The seismic performance assessments presented in this chapter focus on response parameters, direct economic losses, downtime and recovery. Nevertheless, even if the casualties associated with the seismic performance of the archetype buildings evaluated are not explicitly considered, a qualitative evaluation of the implications of the results on death and injury estimates is relevant, particularly due to the large occupancies associated with tall buildings.

If considering the 1973 and the 2012 50-storey archetype buildings evaluated in this chapter, the casualty implications of collapse versus the building being damaged beyond repair will be very different. Peak occupancy, based on FEMA P58 population models, is expected to be in the thousands of occupants. Collapse at a time of peak occupancy could result in hundreds, if not thousands, of casualties. In contrast, if the building were damaged beyond repair, some occupants may be injured, but the majority would ultimately be able to safely exit the damaged building after the earthquake. If only considering direct economic losses as a decision variable, the consequence of either outcome (collapse or irreparable damage) is the same: expected losses equal the total building replacement cost. As reported in Section 7.5.1, the AAL of the 1973 50-storey archetype building is only 65% higher than that of the 2012 50-storey archetype building. However, because the greatest contributor to the losses in the 1973 archetype building is collapse risk (67% of AAL) versus irreparable damage in the 2012 archetype building (85% of AAL), behind these relatively consistent loss metrics lies a drastically greater seismic safety margin provided by the 2012 versus the 1973 archetype building.

7.8 Summary and conclusions

The assessment presented in this chapter follows a MSA approach, in which performance is assessed at an array of earthquake ground motion intensities spanning from frequent to very rare events. NLRHA are conducted with ground motion suites representative of each intensity level considered. The results of the NLRHA are used as inputs to the building performance model to estimate damage, losses, downtime and recovery. The essence of this time-based approach is that these results are then linked back to probabilistic seismic hazard analysis data, which enables calculating a range of risk metrics including (i) the collapse fragility and mean annual rate of collapse, λ_c (ii) performance functions for peak IDRs (transient and residual) and PFAs (iii) loss curves and expected AAL, (iv) seismic vulnerability functions, (v) downtime curves and expected AAD, and (vi) recovery curves for re-occupancy and functional recovery.

Dynamic analysis results, illustrate large concentrations of deformation in a small number of storeys in the 1973 50-storey archetype building due to inelastic deformations in the beams, columns and panel zones. In contrast, the response of the 2012 50-storey archetype building illustrates a more uniform distribution of deformation demands up the building height where non-linear behaviour of components is limited to that of the beams.

The fitted collapse fragilities have a mean 5-second SA of 0.13g and 0.54g for the 1973 and the 2012 50-storey archetype buildings, respectively. Integrating the collapse fragility with seismic hazard data results in a mean annual frequency of collapse 28 times greater for the 1973 versus the 2012 50-storey archetype building (28·10-4 versus 1·10-4), or approximately 13% versus 0.5% probability of collapse in 50 years.

Performance functions for peak IDRs and maximum PFAs illustrate that the annual frequencies of exceedance are consistently larger for the 1973 than the 2012 50-storey archetype building, e.g. annual rate of peak storey accelerations greater than 0.5g are 0.0109 versus 0.007, or annual rates of peak storey drifts greater than 2% of 0.0038 versus 0.0028. However, performance functions for residual peak inter-storey drifts indicate that the 2012 building has higher annual frequencies of exceedance up to 0.5% residual drifts.

The loss curves indicate that at low loss ratios, the annual frequencies of exceedance are drastically higher for the 1973 than the 2012 50-storey archetype building, e.g. a loss ratio of 0.05 has a mean annual rate of exceedance of 0.005 in the 2012 building versus 0.017 in the 1973 building. The expected AAL is 65% higher for the 1973 than the 2012 50-storey archetype

building (0.66% versus 0.40%). The greatest contributor to AAL in the 1973 archetype building is collapse risk (67% of AAL). The greatest contributor to AAL in the 2012 archetype building is irreparable damage due to residual IDRs (85% of AAL). The resulting vulnerability functions for both 50-storey archetype buildings also highlight these large contributions to the overall loss.

Downtime curves to re-occupancy and functional recovery for both archetype buildings illustrate similar trends to those of the loss curves. The AAD to re-occupancy for the 1973 archetype building is 72% greater than that of the 2012 archetype building (8.1 vs 4.7 days). The AAD to functional recovery for the 1973 archetype building is twice that of the 2012 archetype building (10.4 vs 5.0 days).

Recovery curves indicate that even at the lowest earthquake ground motion shaking intensity considered in the assessment, delays associated with external factors, structural and non-structural repairs result in a median time to re-occupancy and functional recovery of 35 days and 145 days respectively for the 1973 50-storey archetype building. The 2012 50-storey archetype building illustrates faster recovery at the lowest earthquake ground motion intensities considered with median delays to re-occupancy and functional recovery less than 50 and 120 days, respectively, for intensities e_3 and below, yet considerably longer delays at higher intensities, e.g. time to re-occupancy and functional recovery of 270 days and 310 days at earthquake intensity e_4.

Overall, the results of this study indicate that tall steel MRFs designed according to modern building code requirements result in designs that comply with the implicit objective of the code of providing damage control at low earthquake ground motion intensities and overall collapse safety. In contrast, existing tall steel MRF buildings consistent with the 1973 50-storey archetype building are far from complying with modern design requirements, not only in terms of collapse safety, but in terms of damage control. Estimated recovery time to re-occupancy and functional recovery in both buildings indicate seismic performance that lacks the ability to swiftly recover from earthquakes.

Chapter 8

Beyond Individual Building Evaluations

8.1 Overview

The scenario-based, intensity-based and time-based assessments described earlier are building specific evaluations of expected seismic performance. These evaluations consider individual buildings in isolation and neglect the impact of damage to these buildings on neighbouring buildings and overall community resilience. To address these limitations, this chapter aims to develop a framework to assess earthquake risk of existing tall buildings, considering implications for both individual buildings and their impact on surrounding areas and the community. This chapter describes the proposed method and illustrates it through a simple case study intended to demonstrate the feasibility and usefulness of this technique.

8.2 Methodology

The proposed methodology aims to integrate PBEE tools and seismic risk assessment methodologies into a GIS framework that enables analysis and visualization of the seismic performance assessment of building clusters. This tool can help highlight critical risk hotspots, e.g. where building damage is most likely to have disproportionate impacts on the urban community, and the broader socio-economic factors that affect resilience (e.g. services provided in the affected buildings to the community). The proposed framework, introduced in Section 3.3, is a direct extension of the methods applied in previous chapters, to assess the earthquake risk of individual existing tall buildings, in order to additionally enable evaluating their impact on surrounding areas and the urban community. As shown in Figure 3-4, different research components are integrated through a modular framework that facilitates evaluation of alternative buildings, building retrofit interventions, and community resilience outcomes to inform policy decisions. The modular format facilitates models that combine varying levels of refinement for various buildings and systems in the urban community.

Chapter 7 illustrates a detailed evaluation of index buildings following a time-based approach. Extensions to the framework implemented in Chapter 7 are proposed here to enable estimating the impact of building closures on the community. It is proposed that this extension is achieved through the development of vulnerability curves for resilience-based evaluations, which describe the impact of building damage on recovery and potential for barricades or cordons

around damaged buildings that would prevent access to surrounding areas. These curves can be derived systematically utilizing the results of a time-based evaluation of individual building archetypes, as discussed in Section 8.2.1.

8.2.1 Vulnerability curves for resilience-based evaluations

In order to link structural performance, loss and downtime estimates to impact to the urban community and surrounding areas, this section describes a method to develop vulnerability curves for resilience-based evaluations. These vulnerability curves are different from those introduced in Section 7.5.2, which summarize expected loss ratio against the spectral acceleration at the fundamental period of the structure. The goal of the vulnerability curves for resilience-based evaluations is to enable estimating the impact of building damage on recovery and closure of surrounding areas under a given ground motion shaking intensity. The following limit states are defined within the proposed vulnerability curves for resilience-based evaluations: (i) no-damage, (ii) hindered re-occupancy, (iii) hindered functional recovery, (iv) irreparable damage and (v) collapse. No-damage implies that no damage to structural or non-structural components hinders inspection or repair work. Hindered re-occupancy indicates that damage to certain components in the building, whether structural or non-structural, hinder re-occupancy and require repair before the building can be re-occupied. Hindered functional recovery implies that damage to certain components in the building, whether structural or non-structural, hinder functionality and require repair before functionality is fully restored. Irreparable damage indicates that permanent residual deformations in the building render it irreparable and the building must be demolished and re-built. Collapse implies that total or partial collapse has occurred and demolition and re-building is required. The vulnerability functions for resilience-based evaluations can be constructed systematically by drawing on the results presented in Chapter 7. As part of the results presented in Section 7.6, data is recorded to indicate whether the results of each realization, at each intensity of ground motion shaking, induce damage corresponding to the limit states previously defined. Tables 8-1 and 8-2 illustrate the number of realizations at each intensity of ground motion shaking, from the time-based assessment results of the 1973 and 2012 50-storey archetype buildings evaluated in Chapter 7, that result in each of the limit states previously defined. These results enable calculating the probabilities of observing each of the limit states considered by following function fitting techniques such as those implemented in section 7.4.1 for the development of the collapse fragility function. The resulting vulnerability curves for resilience-based evaluation are illustrated in Figures 8-1 and 8-2 for the 1973 and the 2012 50-storey archetypes, respectively.

Table 8-1: Summary of time-based assessment results for the 1973 50-storey archetype building that enable the development of vulnerability curves for resilience-based evaluations (number of realizations or probability of observing each limit state).

Earthquake Ground Motion Intensity	SA(g)	Hindered Functional Recovery	Hindered Re-occupancy	Irreparable Damage	Collapse
e_1	0.042	295	486	0	0
e_{1A}	0.0655	228	669	0	26
e_2	0.089	138	680	0	140
e_{2A}	0.1145	7	490	140	363
e_3	0.14	19	293	120	568
e_{3A}	0.1625	10	204	80	706
e_4	0.185	1	116	40	843
e_5	0.22	0	46	20	934

Table 8-2: Summary of time-based assessment results for the 2012 50-storey archetype building that enable the development of vulnerability curves for resilience-based evaluations (number of realizations or probability of observing each limit state).

Earthquake Ground Motion Intensity	SA(g)	Hindered Functional Recovery	Hindered Re-occupancy	Irreparable Damage	Collapse
e_1	0.042	102	134	0	0
e_2	0.089	162	420	17	0
e_3	0.14	70	709	89	0
e_4	0.185	42	798	129	0
e_5	0.22	20	751	202	5
e_6	0.284	10	619	335	33
e_7	0.314	7	515	410	61
e_8	0.37	1	322	536	140
e_{8A}	0.4625	0	89	581	330
e_{8B}	0.555	0	0	469	530
e_{8C}	0.6475	0	0	300	700

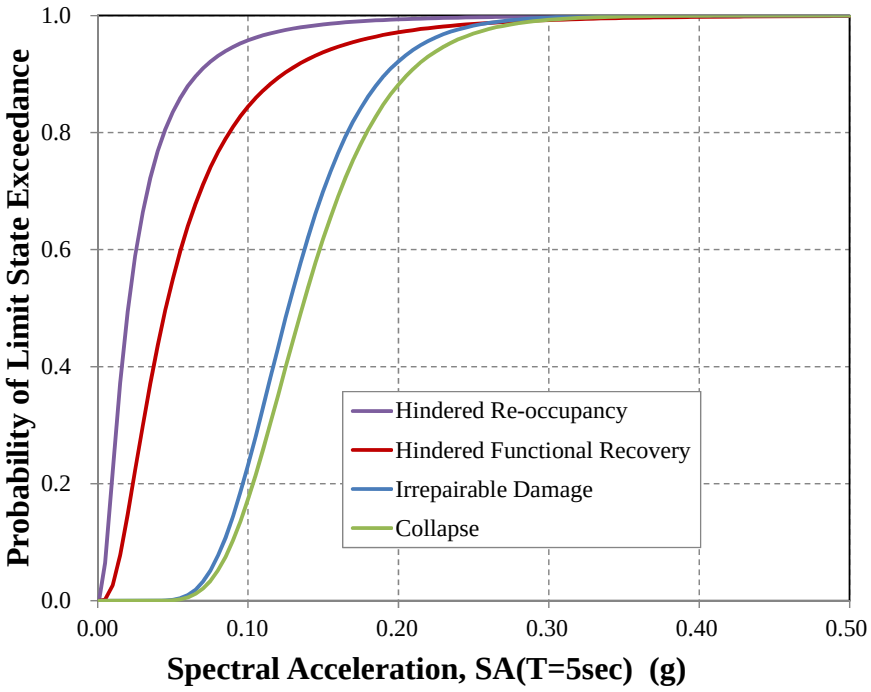

Figure 8-1: 1973 50-storey archetype building vulnerability curves for resilience-based evaluations.

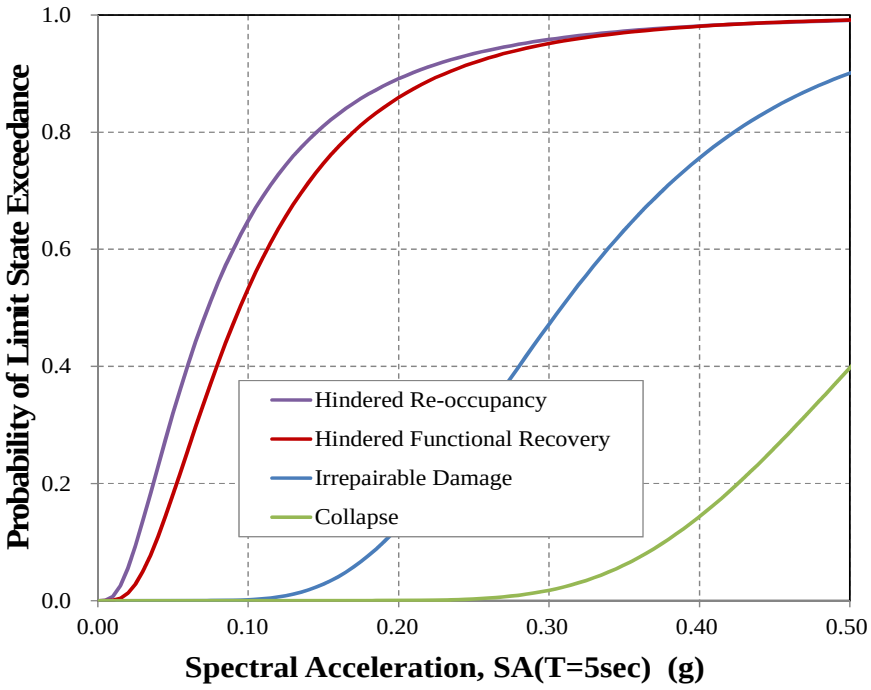

Figure 8-2: 2012 50-storey archetype building vulnerability curves for resilience-based evaluations.

The vulnerability curves for resilience-based evaluation enable estimating the probability of observing different limit states as a function of ground motion shaking intensity. The impact of each limit state on surrounding buildings and the urban community is introduced through consequence functions associated with each limit state. The consequence functions provide estimates of recovery with time and the potential for closure of surrounding areas conditioned on a particular limit state and range of ground motion shaking intensity. For the hindered re-occupancy and hindered functional recovery limit states, it is assumed that no closures of areas surrounding the building are anticipated. However, it is noted that this assumption neglects that damage to exterior components at height, such as the façade, could trigger the closure of a small area around the building. By evaluating the recovery functions developed probabilistically in Section 7.6, the median and dispersion associated with each phase of the recovery path can be estimated for the hindered re-occupancy and hindered functionality limit states for each earthquake ground motion shaking intensity level considered in the time-based assessment.

As described in Section 4.3.3 and illustrated in Section 7.6, the different phases of the recovery path include those in which the recovery (building re-occupancy or functionality) ratio is zero (due to impeding factors and structural repairs), and those in which the recovery ratio increases with time (due to non-structural repairs), which enables estimating the time to partial recovery. The recovery path associated with the irreparable damage and collapse limit states, as described in Section 7.6, is represented by a step function where full recovery is achieved after demolition and reconstruction. Because these limit states represent considerable damage levels to the structure, including permanent residual deformations, which may compromise the structural stability, and/or total or partial collapse, a cordon around the building that would prevent access to surrounding areas is modelled for these limit states. The cordon is assumed to be circular in shape and its radius is represented by a lognormal distribution with a median equal to the building height and a dispersion equal to 0.3. The median value is based on post-earthquake safety evaluation guidelines, which suggest that when permanent deformations are present in a building, an area around the building with a radius equal to the building height or even up to 1.5 times the building height should be enforced (ATC 2005). As mentioned in Chapter 1, these recommendations are consistent with observations following the Canterbury earthquake in New Zealand in 2011, where damage to the 26-storey Hotel Grand Chancellor prompted authorities to cordon off an area with a radius that was roughly equal to its height (NZPA 2011). Tables 8-3 and 8-4 provide the consequence data for the 1973 and the 2012 50-storey archetype buildings, respectively, as derived from the results presented in Section 7.6, which summarize expected recovery paths as well as potential closure of surrounding areas for the limit states considered. Because these values are highly uncertain, they are represented through

probabilistic distributions, hence the results report the expected value and the variability associated with each phase of the recovery at different earthquake ground motion shaking intensities. The bulk of the data presented in Tables 8-3 and 8-4 is consistent with the results shown in Tables 7-6 and 7-7, but re-arranged to depict the consequence data associated with each of the limit states within the vulnerability curves for resilience-based evaluations here introduced.

8.3 Comprehensive scenario-based assessments

For the purposes of quantifying resilience and developing mitigation policies, San Francisco's Community Action Plan for Seismic Safety (CAPSS) utilizes different scenario earthquakes, which can be expected conservatively, but reasonably during the design life of a building. ATC-52 (2010), as part of "*Here Today – Here Tomorrow: The Road to Earthquake Resilience in San Francisco*," studies four events: a M6.5, M7.2 and M7.9 earthquakes on the San Andreas fault, and a M6.9 earthquake on the Hayward fault. The choice of realistic earthquake scenarios is intended to serve for planning and emergency response, as the agencies involved conduct training based on realistic earthquake situations. In this instance, earthquake scenarios are not intended to predict the exact size and location of a theoretical future earthquake, but rather to make a reasonable prediction of its effects (ATC 2010).

Chapter 5 presents the results of a scenario-based evaluation intended to provide an indication of the expected performance of existing tall steel MFRs from the 1970s in an earthquake such as the HayWired scenario main shock. The HayWired scenario is a M7.0 earthquake on the Hayward fault, developed by USGS to study impacts on the San Francisco Bay area (Detweiler and Wein 2017). While the results of such assessment are informative, because they are conditioned on a single main shock ground motion simulation, they fail to capture the uncertainty in ground motion shaking associated with such a scenario event, and do not provide metrics that are as informative as those presented in Chapters 6 and 7, which are derived from intensity-based and time-based evaluations. In this section, vulnerability curves for resilience-based evaluations are used to estimate the response of the 1973 and 2012 50-storey archetype steel MRF buildings under an array of earthquake scenarios. The choice of the earthquake magnitude range and causative fault are based on a review of the seismic hazard de-aggregation data for the range of ground motion intensities considered in Chapter 7. As illustrated in Appendix E, the controlling earthquake magnitudes range from of M7 to M8 and originate on the San Andreas fault. This magnitude range and causative fault is consistent with that used by CAPSS in the ATC-52 project.

GMPEs generally take the form illustrated in Equation 8-1. Where Y_{ij} represents the ground motion parameter of interest, such as the SA at the fundamental period of the structure under consideration, at site i during earthquake scenario j; $\overline{Y}_{ij}$ represents the ground motion model median prediction as a function of parameters such as the magnitude, distance, period or local soil conditions; ε_{ij} represents the intra-event residual, which is a normal random variable with zero mean and standard deviation, σ_{ij}; and η_{ij} represents the inter-event residual, which is a normal random variable zero mean and standard deviation τ_{ij}. The variables, σ_{ij} and τ_{ij} are estimated as part of the ground-motion model.

$$\ln(Y_{ij}) = \ln(\bar{Y}_{ij}) + \sigma_{ij}\varepsilon_{ij} + \tau_{ij}\eta_{ij} \qquad \text{Equation 8-1}$$

During an earthquake, the inter-event residual computed at any particular period is constant across all sites. As discussed in Han et al. (2012), for a particular earthquake, the prediction model can be used to simulate varying ground-motion intensities at a site of interest. This is achieved by first using the GMPE to obtain the median ground motion $\overline{Y}_{ij}$ and the standard deviations of the inter-event and intra-event residuals (σ_{ij} and τ_{ij}). Then, the normalized inter-event and intra-event residuals are sampled from the normal distributions in order to obtain a vector of ground motions Y_{ij}. For this study, the Boore-Atkinson (2008) GMPE is used to obtain 1000 sampled spectral intensities at a 5 second period (due close proximity to the fundamental period of the structures under consideration), for a representative building site in downtown San Francisco at a distance of 13.3km (source to site distance based on the seismic hazard de-aggregation results shown in Appendix E) and soil conditions consistent with site class D (V_{s30}=260 m/s), per the soil properties downtown San Francisco (USGS 2017a) where the majority of tall buildings are located. The resulting median response spectrum for all magnitudes considered is shown in Figure 8-3. The sampled spectral intensities at a 5 second period for the range of magnitude earthquakes considered are shown in Figure 8-4. The variation in sampled spectral intensities for any given magnitude earthquake is an indication of the variability in ground motion intensities that the study conducted in Chapter 5 fails to capture. Therefore, the scenario-based evaluations carried out in this chapter are referred to as comprehensive scenario-based evaluations to distinguish them from those in Chapter 5.

Table 8-3: UBC 1973 limit state consequence data as a function of earthquake ground motion intensity.

		Hindered Re-occupancy						Hindered Functional Recovery						Irreparable Damage / Collapse			
		Impeding Factors (days)		Structural Repairs (days)		Non-Structural Repairs (days)		Impeding Factors (days)		Structural Repairs (days)		Non-Structural Repairs (days)		Replacement Time (days)		External Closures (m)	
Earthquake Ground Motion Intensity	SA (g)	μ	β	μ	β	μ	β	μ	β	μ	β	μ	β	μ	β	μ	β
e_1	0.040	55	0.82	1	1.07	27	1.63	55	0.82	1	1.07	92	0.54	1000	0.3	192.8	0.3
e_{1A}	0.077	80	0.83	5	1.21	65	1.4	80	0.83	5	1.21	145	0.59				
e_2	0.102	159	0.54	12	1.32	84	1.11	159	0.54	12	1.32	133	0.5				
e_{2A}	0.127	166	0.51	15	1.12	127	0.79	166	0.51	15	1.12	155	0.32				
e_3	0.152	161	0.54	14	1.1	111	0.77	161	0.54	14	1.1	148	0.32				
e_{3A}	0.177	178	0.48	25	1.12	127	0.66	178	0.48	25	1.12	153	0.29				
e_4	0.202	181	0.53	33	1.16	151	0.47	181	0.53	33	1.16	159	0.31				
e_5	0.239	178	0.41	28	0.97	160	0.21	178	0.41	28	0.97	160	0.21				

Table 8-4: IBC 2012 limit state consequence data as a function of earthquake ground motion intensity.

		Hindered Re-occupancy						Hindered Functional Recovery						Irreparable Damage / Collapse			
		Impeding Factors (days)		Structural Repairs (days)		Non-Structural Repairs (days)		Impeding Factors (days)		Structural Repairs (days)		Non-Structural Repairs (days)		Replacement Time (days)		External Closures (m)	
Earthquake Ground Motion Intensity	SA (g)	μ	β	μ	β	μ	β	μ	β	μ	β	μ	β	μ	β	μ	β
e_1	0.042	19	0.96	0	0	1	0.99	19	0.96	0	0	6	1.53				
e_2	0.089	51	0.95	0	0	8	1.07	51	0.95	0	0	33	1.21				
e_3	0.140	117	1.06	3	1.15	31	0.97	117	1.06	3	1.15	76	0.71				
e_4	0.185	200	0.49	14	1.29	66	0.77	200	0.49	14	1.29	95	0.55				
e_5	0.220	209	0.49	17	1.36	77	0.74	209	0.49	17	1.36	101	0.56	1000	0.3	192.8	0.3
e_6	0.284	224	0.41	36	1.36	98	0.67	224	0.41	36	1.36	117	0.55				
e_7	0.314	223	0.42	19	1.39	54	0.63	223	0.42	19	1.39	66	0.41				
e_8	0.370	229	0.33	57	1.25	116	0.46	229	0.33	57	1.25	128	0.3				
e_{8A}	0.463	242	0.32	110	0.74	142	0.26	242	0.32	110	0.74	144	0.24				

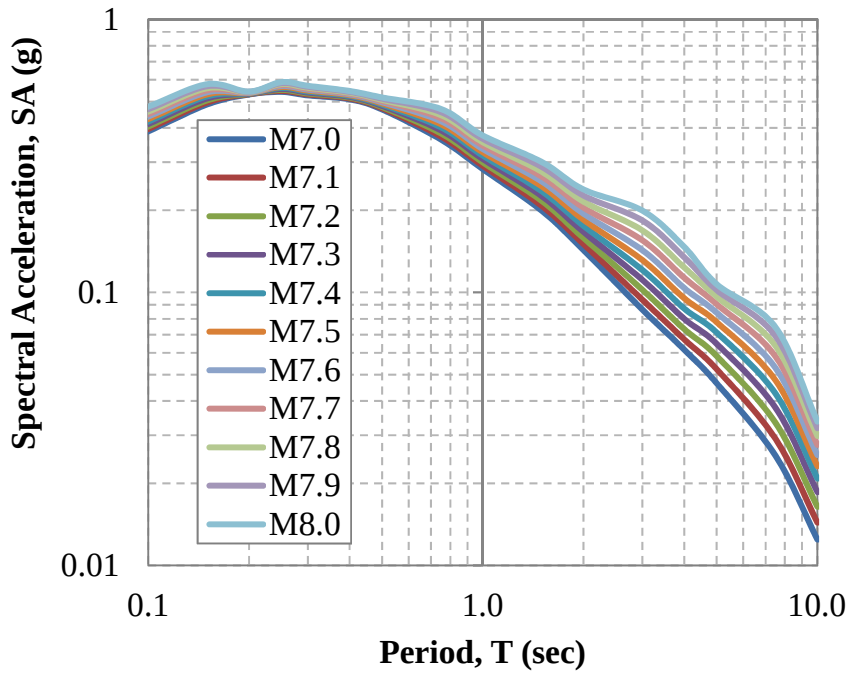

Figure 8-3: Median spectra for earthquake scenarios ranging from M7 to M8.

For all 1000 sampled spectral intensities at each earthquake magnitude considered, the expected recovery path to re-occupancy and functional recovery, as well as the potential cordon around the damaged building is calculated. These calculations account for the probabilities of different limit states being observed at all sampled spectral intensities. The probabilities of different limits states being observed are derived from the vulnerability functions for resilience-based evaluations for the 1973 and 2012 50-storey archetype buildings, as illustrated earlier in Figures 8-1 and 8-2. The mean recovery paths to re-occupancy and functional recovery, from all 1000 simulations, as well as the mean cordon radius and duration is shown in Figures 8-5 and 8-6 for the 1973 and 2012 buildings, respectively.

In Figures 8-5 and 8-6, the mean recovery paths for certain earthquake magnitude simulations do not return to an occupancy or functionality ratio of 1 within the time extent shown in the plots. As discussed earlier, for the irreparable and collapse limit states, the recovery path is represented by a step function, where full recovery is achieved after demolition and reconstruction. As denoted in Tables 8-3 and 8-4, in such limit states, the mean replacement time is estimated at 1000 days. Therefore, the mean recovery curves in Figures 8-5 and 8-6 do ultimately return to 1, but this occurs beyond the time extents shown in the figures.

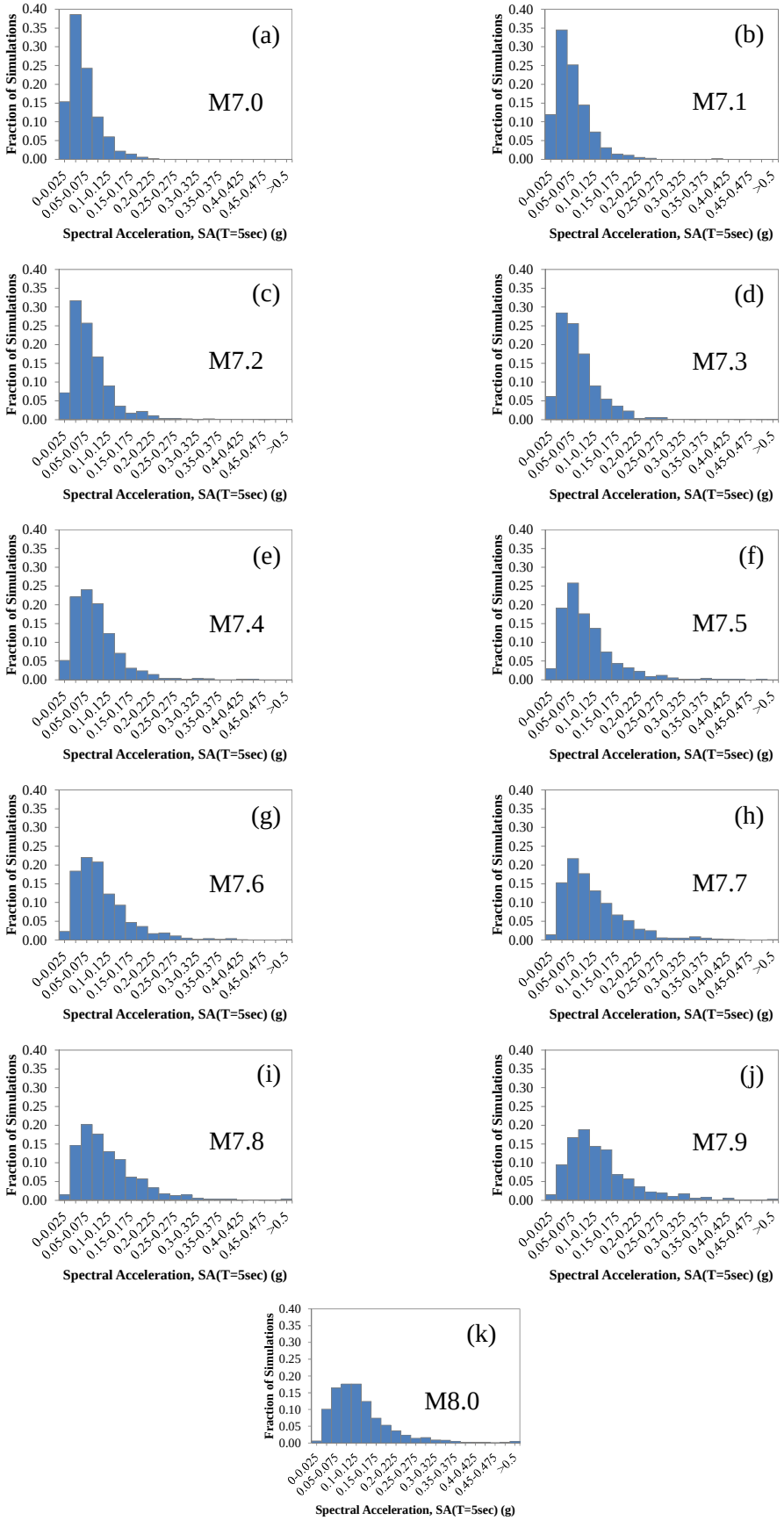

Figure 8-4: Distribution of sampled spectral intensities at a 5 second period for earthquake scenarios ranging from M7 to M8 at the site of interest.

(a)

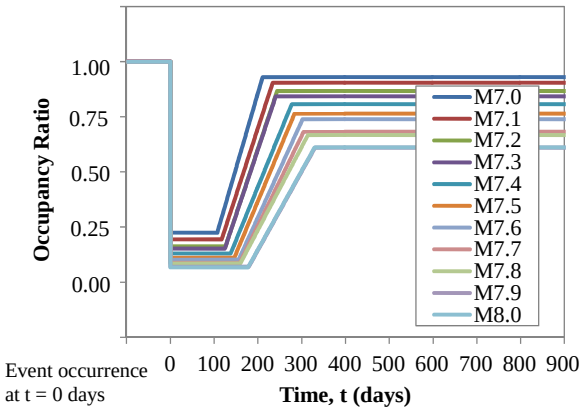

(b)

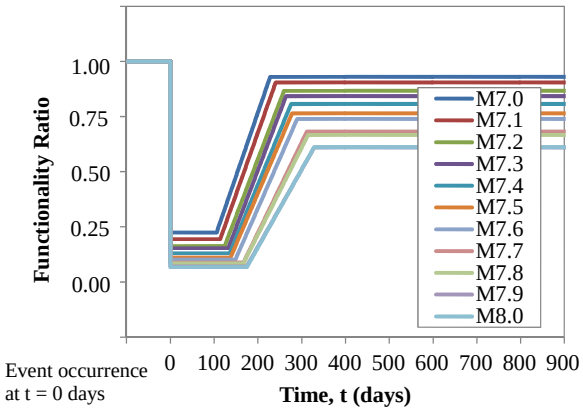

(c)

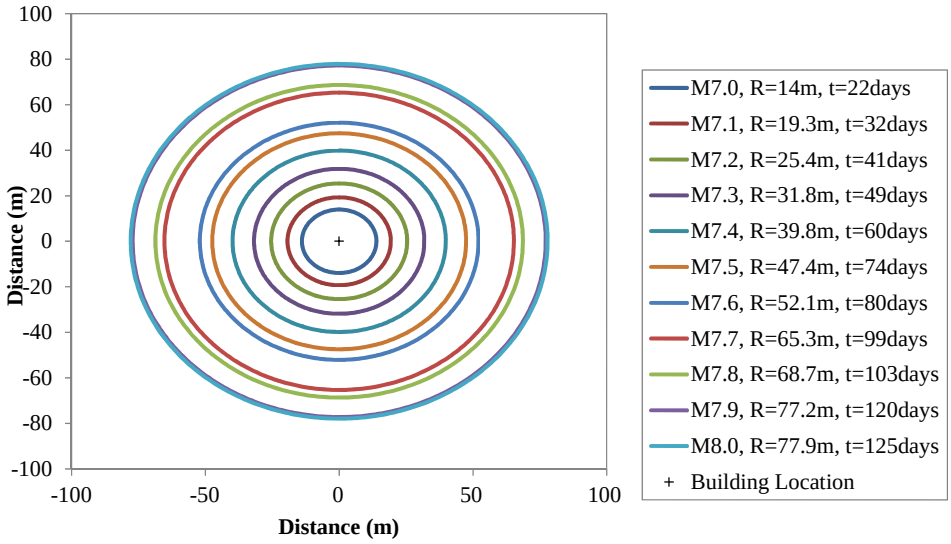

Figure 8-5: UBC 1973 mean recovery curves to (a) re-occupancy and (b) functional recovery, as well as expected cordon radius and duration (c) for earthquake scenarios ranging from M7 to M8.

(a)

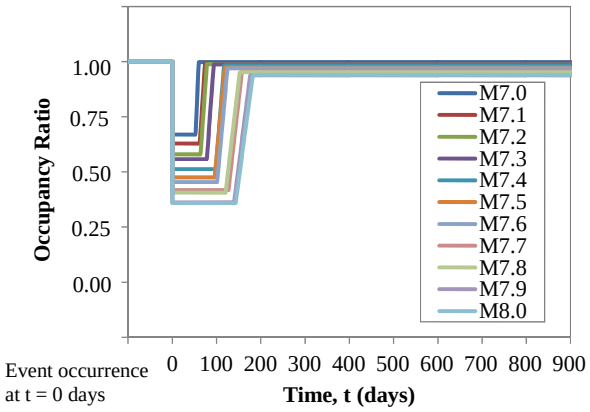

(b)

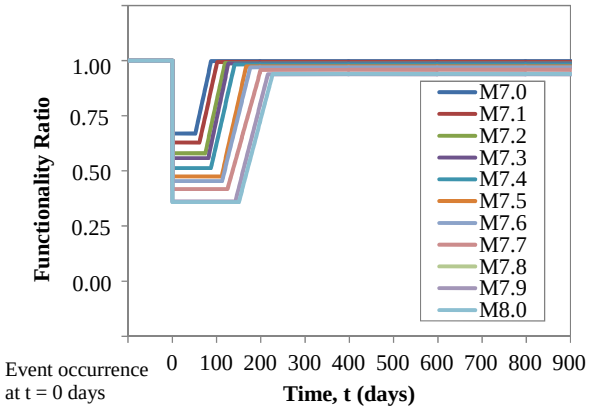

(c)

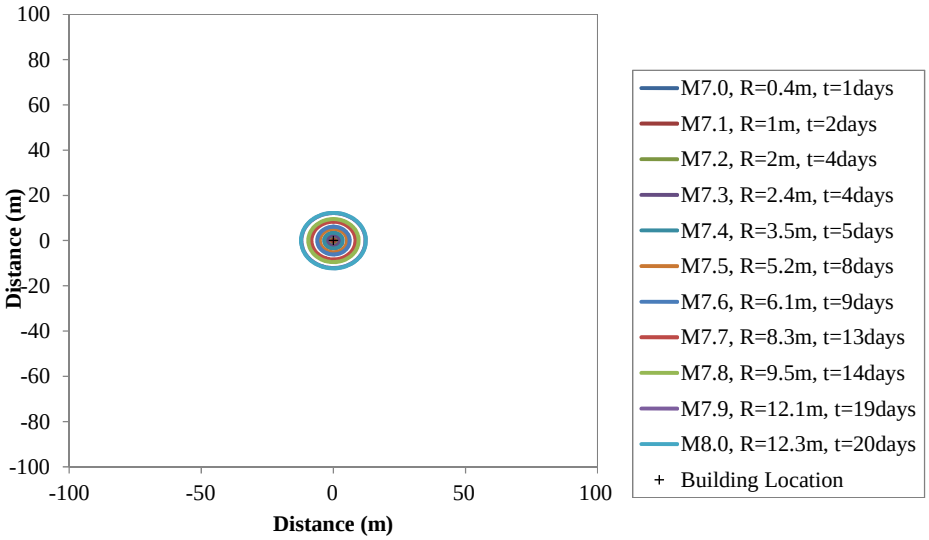

Figure 8-6: IBC 2012 mean recovery curves to (a) re-occupancy and (b) functional recovery, as well as expected cordon radius and duration (c) for earthquake scenarios ranging from M7 to M8.

The immediate post-earthquake occupancy and functionality ratios in the IBC 2012 50-storey archetype building take values ranging from 0.57 for the M7.0 scenario down to 0.36 for the M8.0 scenario. Instead, for the UBC 1973 50-storey archetype building these ratios are as low as 0.22 for the M7.0 scenario and 0.07 for the M8.0 scenario. The time to achieve a recovery ratio of 0.75 in the IBC 2012 archetype ranges from 55 days for the M7.0 scenario to 170 days for the M8.0 scenario. Expected delays to achieve a 0.75 functional recovery ratio in the IBC 2012 archetype are 61 and 202 days for the M7.0 and M8.0 scenarios, respectively. In the UBC 1973 50-storey archetype building, time to achieve 0.75 re-occupancy and functionality ratios are 185 and 197 days, respectively, for the M7.0 scenario. However, such high ratios of re-occupancy and functional recovery are only achieved for the M8.0 scenario by means of building replacement, with mean estimates in excess of 1000 days.

Table 8-5: Probabilities of observing a building cordon with an average radius equal to the building height and a time equal to the demolition time (R=192.8 m, t = 300 days) for the IBC 2012 and UBC 1973 archetypes under different scenarios.

Earthquake Scenario Magnitude	Archetype Building	
	IBC 2012	UBC 1973
M7.0	0.2%	7.0%
M7.1	0.5%	9.5%
M7.2	1.1%	13.2%
M7.3	1.2%	15.7%
M7.4	1.7%	19.2%
M7.5	2.6%	23.5%
M7.6	3.0%	26.0%
M7.7	4.2%	31.7%
M7.8	4.8%	33.3%
M7.9	6.2%	39.0%
M8.0	6.2%	40.0%

The differences in expected (mean) cordon radius and duration between the IBC 2012 and the UBC 1973 archetype buildings are significant. For the IBC 2012 archetype building the mean cordon radius ranges from less than 1 meter up to 12 meters for the M7.0 and M8.0 earthquake scenarios, respectively. In contrast, the mean cordon radius for the UBC 1973 archetype building ranges from 14 meters up to 78 meters for the M7.0 and M8.0 earthquake scenarios, respectively. Low mean cordon radii, e.g. 1 meter cordon, are not indicative of a physical 1 meter cordon being placed around the building, but rather, they highlight that only a small number of the 1000 realizations trigger a cordon. For the purpose of measuring impact on the surrounding area, these results can also be expressed as the probability of observing a cordon with a mean radius equal to the building height in place for a time equal to the length of

demolition works (as illustrated previously in Tables 8-3 and 8-4). These results are summarized in Table 8-5 for the archetype buildings and all earthquake magnitudes considered.

8.4 Building cluster assessment

The comprehensive scenario-based assessments illustrated in section 8.3 are used here to evaluate the impact of a building typology on the urban community. The building typology is represented through a cluster of buildings in a study area, whose performance is assessed under an expected earthquake scenario. This simple case study is intended to demonstrate the feasibility and usefulness of this approach. The vulnerability functions for resilience-based evaluations developed in section 8.2.1 are based on the results presented in Chapter 7 for a 50-storey steel MRF archetype building. In order to make use of these functions, five buildings are selected from the San Francisco existing tall building database presented in Chapter 4 and Appendix B. The buildings are steel MRFs with construction dates ranging from 1969 to 1985 and storey counts ranging from 46 to 52 storeys. The earthquake scenario selected for this case study is a M7.5 earthquake on the San Andreas fault, with an epicentre located at coordinates N37.75 and W122.55, consistent with those of the 1906 San Francisco earthquake (USGS 2017b). Table 8-6 illustrates the site labels, coordinates, distance to the assumed epicentre, and Cartesian coordinates used to plot the results, with the reference point taken as building site A. The location of these buildings in downtown San Francisco is shown in Figure 8-7. Two assessments are carried out, one assuming all buildings are consistent with the UBC 1973 archetype, and another assuming all buildings are consistent with the UBC 2012 archetype. Even though this comparison does not explicitly study the impact of retrofit interventions, these evaluations provide an understanding of the potential benefit or impact of retrofitting these buildings to meet the requirements of modern design standards.

Table 8-6: Site labels, coordinates and distances to epicentre for the buildings selected to evaluate impact on the urban community.

Building Site	Latitude (degrees)	Longitude (degrees)	Distance to Epicentre (m)	X Coordinate (m)	Y Coordinate (m)
A	N37.79205	W122.40371	13706	0	0
B	N37.79511	W122.40278	13901	81.9	339.6
C	N37.78568	W122.41047	12915	-595.4	-707
D	N 37.79283	W122.39792	14216	510	86.6
E	N37.79257	W122.40053	13989	280.1	57.7

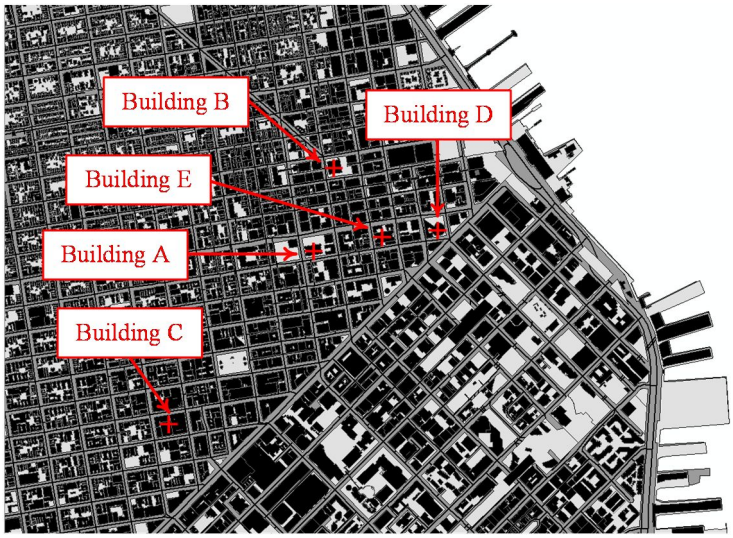

Figure 8-7: Location of buildings sites in downtown San Francisco.

In order to simulate ground motion parameters at the sites of interest for the earthquake scenario under consideration, an approach similar to that presented in section 8.3 is followed. The key difference is that for this case study, the objective is to simulate ground motion parameters at different sites. For each site under consideration, the Boore-Atkinson (2008) GMPE is used to obtain median predictions, $\overline{Y}_{ij,}$ of 5 second spectral intensities for the same magnitude (M7.5) and local soil conditions (V_{s30}=260 m/s), consistent with the soil properties downtown San Francisco (USGS 2017a) where the majority of tall buildings are located, and unique source-to-site distances, as reported in Table 8-6. The normalized inter-event residual term, $\eta_{ij,}$ is then sampled for each simulation. As discussed earlier, for each simulation, this sample is constant for all sites considered. Then the intra-event residual, ε_{ij}, is sampled for all sites. In this case, correlation between sites is accounted for by means of the correlation model for spatially distributed ground motion intensities outlined in Jayaram and Baker (2009). The sampled correlated spectral intensities at a 5 second period for all the sites considered when subjected to a M7.5 earthquake scenario is illustrated in Figure 8-8. For all 1000 correlated spectral intensities sampled at each building site under a M7.5 earthquake scenario, the vulnerability functions for resilience-based evaluations for the UBC 1973 and the IBC 2012 archetype buildings, as illustrated earlier in Figures 8-1 and 8-2, are employed to estimate the recovery path to re-occupancy and functional recovery, as well as the potential cordon around the damaged building. The expected individual building and cumulative building cluster recovery paths to re-occupancy and functional, accounting for the probabilities of different limit states being observed at all sampled spectral intensities, is shown in Figures 8-9 and 8-10 for the 1973 and 2012 archetype buildings, respectively. The expected cordon radius and duration is illustrated in Figure 8-11.

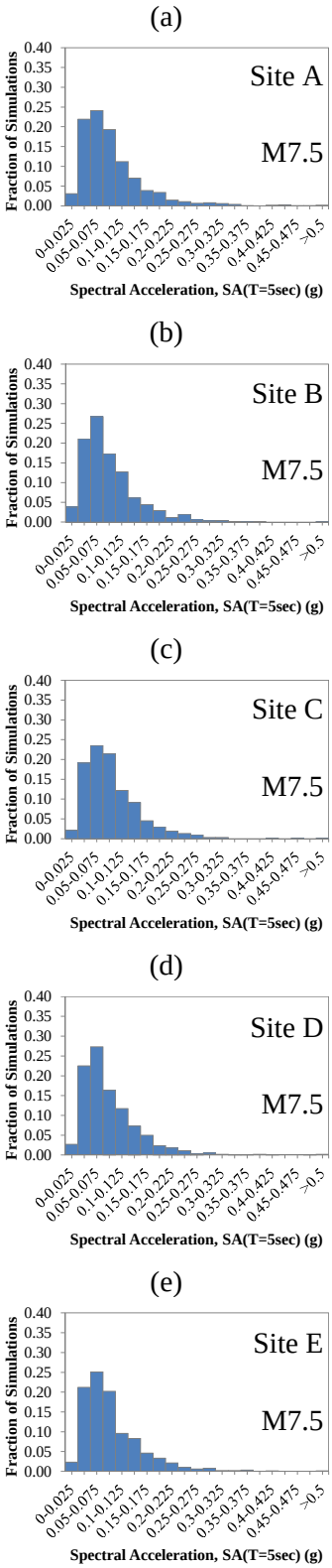

Figure 8-8: Distribution of spectral intensities for earthquake scenario with M7.5 at buildings sites A through E considered in the building cluster assessment.

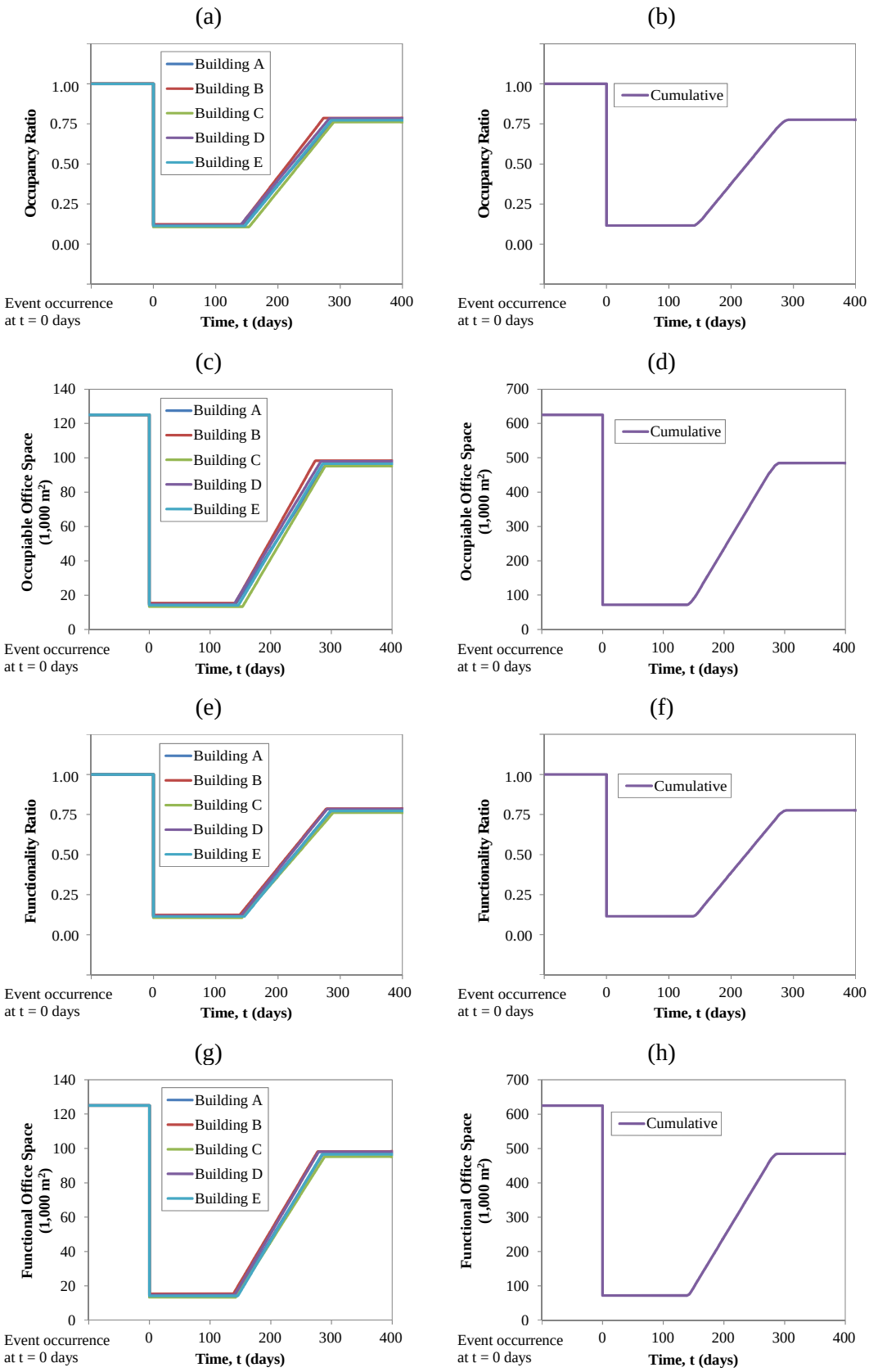

Figure 8-9: Mean recovery curves to (a to d) re-occupancy and (e to h) functional recovery, (a, b, e, f) normalized and (c, d, g, h) in absolute terms, for (a, c, e, g) individual buildings and (b, d, f, h) the overall cluster under a M7.5 earthquake scenario assuming UBC 1973 archetypes.

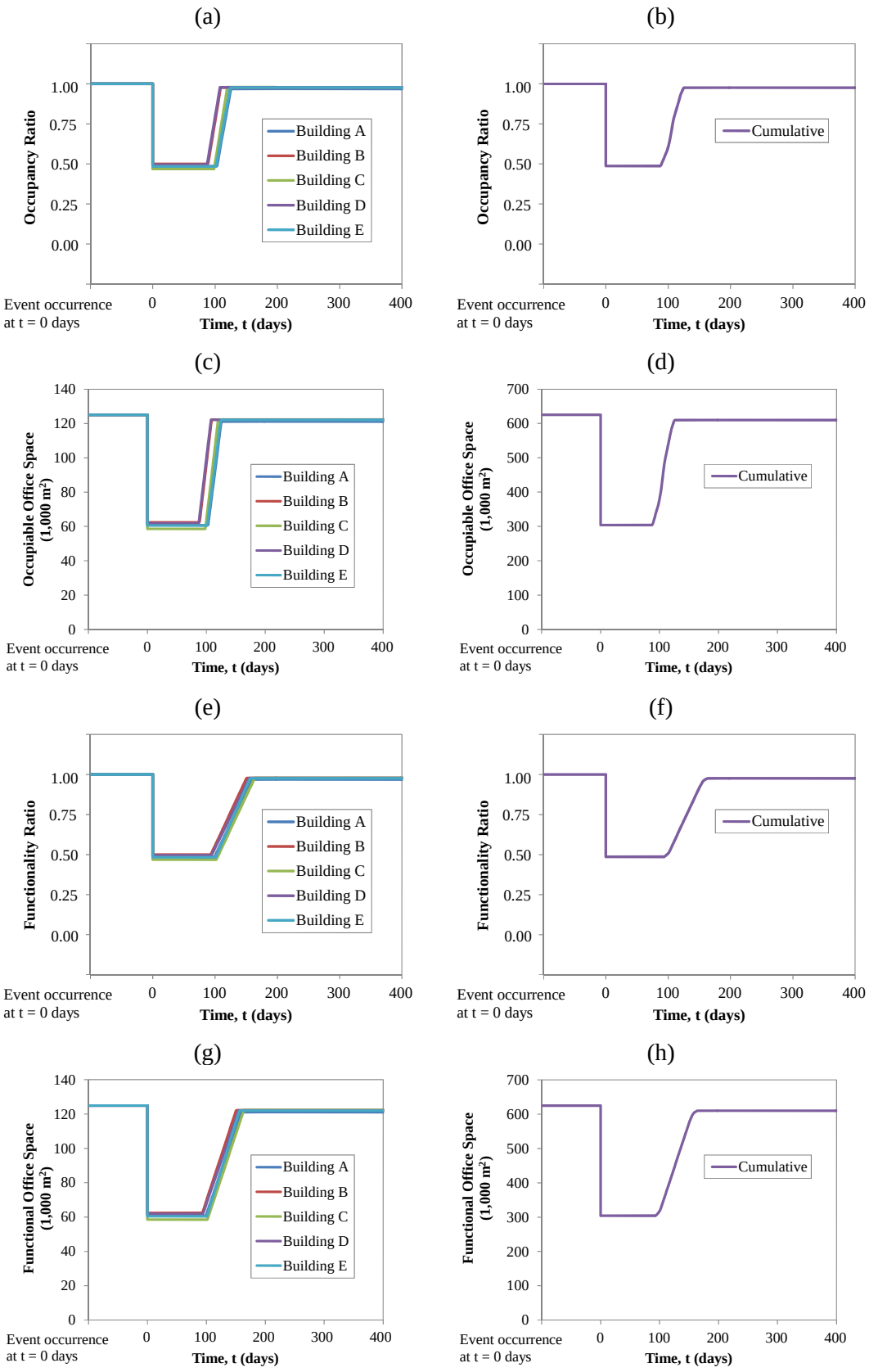

Figure 8-10: Mean recovery curves to (a to d) re-occupancy and (e to h) functional recovery, (a, b, e, f) normalized and (c, d, g, h) in absolute terms, for (a, c, e, g) individual buildings and (b, d, f, h) the overall cluster under a M7.5 earthquake scenario assuming IBC 2012 archetypes.

(a)

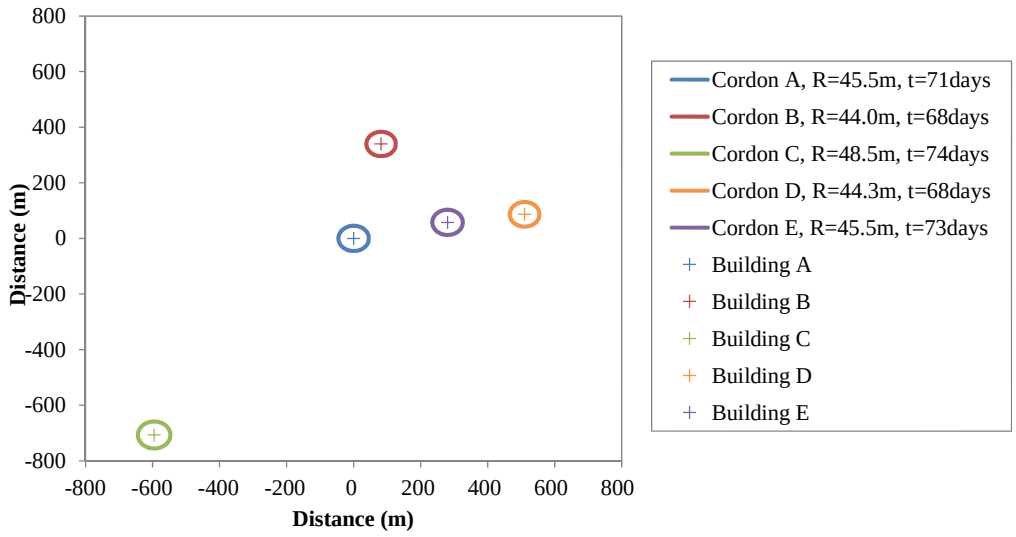

(b)

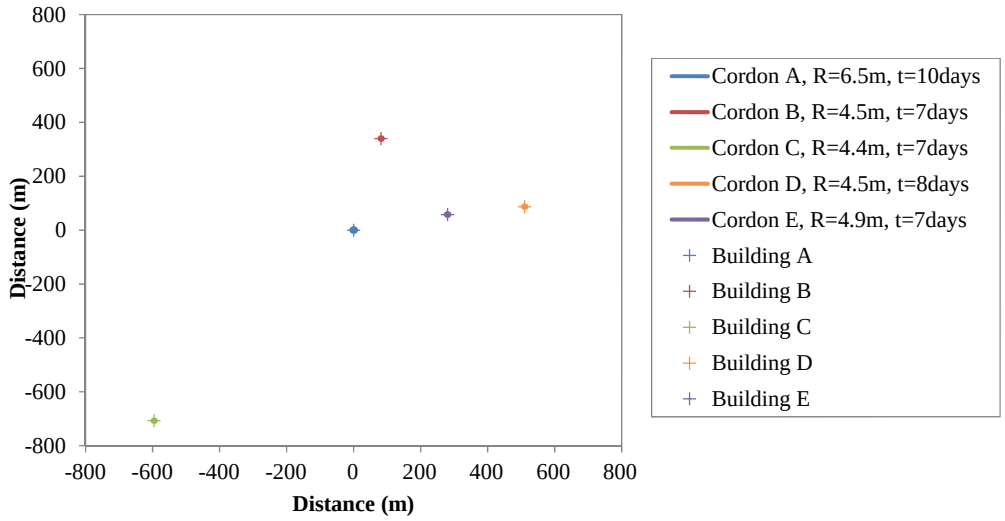

Figure 8-11: Mean cordon preventing access to surrounding areas under a M7.5 earthquake scenario assuming (a) UBC 1973 and (b) IBC 2012 archetypes.

Due to the close proximity of the building sites considered in the assessment, the simulated ground motion intensities are highly correlated (as evidenced by the distributions illustrated in Figure 8-8). Additionally, because all five buildings considered in the cluster are represented by the same set of vulnerability functions for resilience based evaluations, whether assuming they are all consistent with the UBC 1973 or IBC 2012 archetypes, the expected recovery paths for individual buildings are very similar. These results would be considerably different if extending the evaluation to consider buildings with distinct fundamental periods, which would result in greater differences in the sampled ground motion intensities at each site, and unique vulnerability functions for resilience-based evaluations, which would result in further differences in the recovery paths.

The archetype buildings studied are commercial office buildings. Therefore, the impact on the urban community is measured in terms of lost or unavailable office space as a result of seismic damage to the buildings considered. As described in Chapter 4, these buildings provide a considerable amount of office space, with a gross surface area per floor of 2600 m^2 or 125000 m^2 total area throughout the building (two out of 50 storeys are mechanical floors). The cumulative office area provided by the five archetype buildings is roughly 625000 m^2. The expected immediate loss of office space assuming the buildings considered are represented by the UBC 1973 archetype is 553000 m^2 or 88.5% of the office space provided by these buildings. The expected delays to recover 50% of the total office space, or 312500 m^2, are 220 and 227 days both for re-occupancy and functional recovery. The times to recover 75% of the total office space, or 468750 m^2, are 280 and 288 days both for re-occupancy and functional recovery. The expected immediate loss of office space assuming the buildings considered are represented by the IBC 2012 archetype is 321000 m^2 or 51.4% of the office space provided by these buildings. The expected delays to recover 50% of the total office space, or 312500 m^2, are 90 and 98 days both for re-occupancy and functional recovery. The times to recover 75% of the total office space, or 468750 m^2, are 107 and 130 days for re-occupancy and functional recovery, respectively. While achieving re-occupancy is of greater relevance to the evaluation of residential buildings, as it enables occupants to shelter in place, it is also relevant to commercial buildings as it implies businesses re-gain access to contents that may be required to help resume their activity. From personal experience, while working in New York when hurricane Sandy affected the area in 2012, I returned to my downtown office building, which had been affected by the event before the building had achieved a functional recovery state (no heating, water or other basic services were operable yet some employees were returning to work).

The mean cordon radius in the IBC 2012 archetype building at the building sites considered ranges from 4.4 to 6.5 meters for the M7.5 earthquake scenario. In contrast, the mean cordon radius in the UBC 1973 archetype at the building sites ranges from 44 to 48.5 meters. As described earlier, low mean cordon radii, e.g. 5 meters, are not indicative of a physical 5 meter cordon being placed around the building, but rather, they highlight that only a small number of the 1000 realizations trigger a cordon. For the purpose of measuring impact on the surrounding area, these results can also be expressed as the probability of observing a cordon with a mean radius equal to the building height in place for a time equal to the length of demolition works. Figures 8-12 and 8-13 illustrate the probabilities of observing such cordoned areas for the UBC 1973 and the IBC 2012 archetype building clusters respectively. The potential loss of access to areas surrounding the damaged buildings can inform emergency planning, particularly if essential facilities, roads or infrastructure fall within the expected cordons. The results in Figure 8-12 and 8-13 indicate that the potential for observing large cordons around the building clusters considered is roughly 10 times greater for the 1973 versus the 2012 archetype buildings.

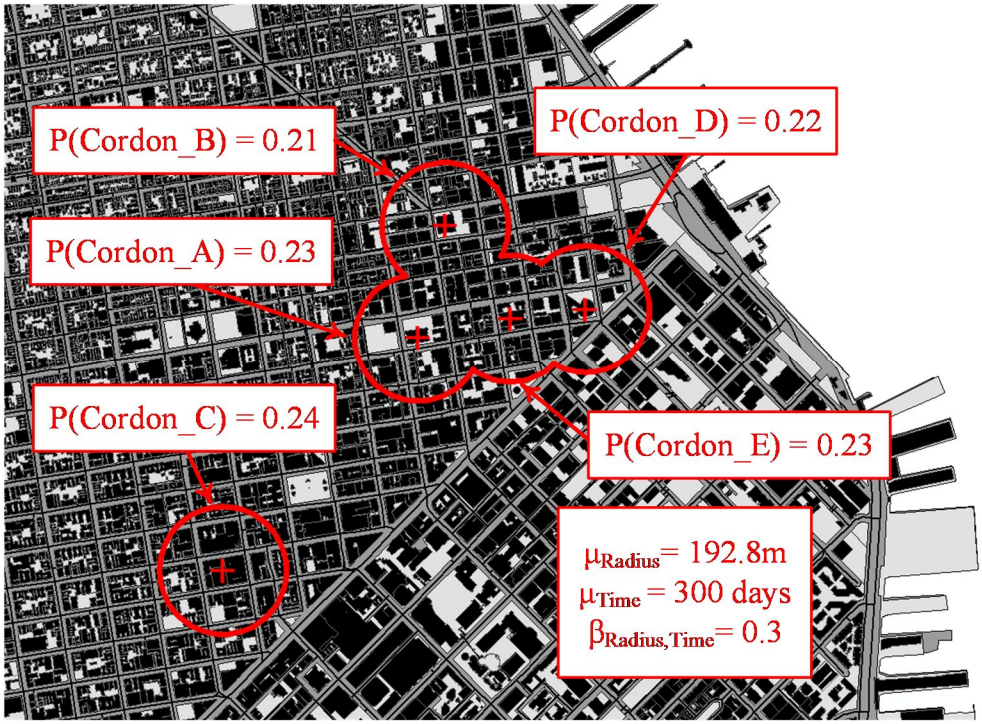

Figure 8-12: Probability of cordon with a mean radius equal to the building height and duration equal to the building demolition time under a M7.5 earthquake scenario assuming UBC 1973 archetypes integrated with GIS map.

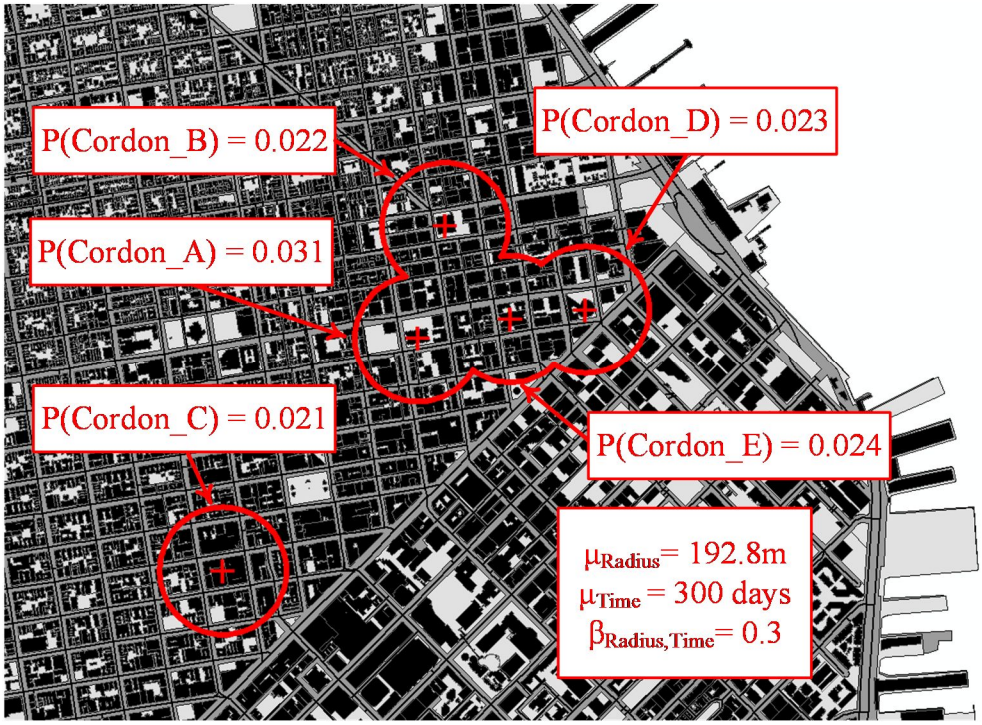

Figure 8-13: Probability of cordon with a mean radius equal to the building height and duration equal to the building demolition time under a M7.5 earthquake scenario assuming IBC 2012 archetypes integrated with GIS map.

8.5 Conclusions

This chapter proposes a methodology to assess earthquake risk of existing tall buildings, considering implications for individual buildings and their impact on surrounding areas. The method is an extension of PBEE, which, through the introduction of vulnerability functions for resilience-based evaluations, enables the estimating the impact of building damage on the recovery, and closure of surrounding areas for a given ground motion shaking intensity. In order to support ongoing efforts of the San Francisco's Earthquake Safety Implementation Program (CAPSS 2011), the expected response two 50-storey archetype steel MRF buildings, designed per UBC 1973 and IBC 2012, is simulated following a comprehensive-scenario based assessment for a range of expected magnitude earthquakes, based on seismic hazard de-aggregation data and other studies aimed at increasing the seismic resilience of San Francisco.

The results highlight the enhanced resilience of the modern archetype when compared to the 1970s archetype. Furthermore, a simple case study is presented to demonstrate the feasibility and usefulness of this technique to evaluate the impact of different building typologies, represented through building clusters, on the urban community. The case study evaluates a cluster of five existing 50-storey steel MRF buildings in downtown San Francisco versus five modern 50-storey steel MRF buildings. The results illustrate the potential loss in commercial office space associated with a M7.5 scenario earthquake, the delays associated with the recovery of occupancy and function, as well as the potential closure of areas surrounding these buildings. The case study highlights the drastic enhancement associated with upgrading existing tall buildings, represented through the UBC 1973 building archetype, to achieve performance levels consistent with with modern designs, represented through the IBC 2012 building archetype.

The assessments carried out in this chapter have shifted back to the evaluation of scenario earthquakes. However, the study now utilizes results from comprehensive risk-based evaluations, such as the time-based assessment presented in Chapter 7, within a comprehensive scenario-based evaluation framework. The case study presented suggest that while comprehensive scenario-based evaluations are best suited for planning and emergency response, when these are used in conjunction with comprehensive risk-based assessments, the results are most informative.

Chapter 9

Summary and Conclusions

9.1 Overview

This thesis addresses the risks posed by the older seismically deficient steel buildings, which constitute a significant proportion of existing tall buildings in San Francisco, Los Angeles and other west coast US cities with high seismic hazard. These include many steel MRF buildings, constructed during the late 1960's through mid-1990's, with the type of welded connections that experienced sudden brittle fractures during the 1994 Northridge earthquake. Buildings of that era were designed following a prescriptive force-based approach that does not provide an explicit understanding of seismic performance, and without capacity design principles to protect against storey mechanisms, without seismic drift limits, and with lower base shear strengths than those specified in modern codes. Furthermore, new seismological data indicates that earthquake ground motion hazards at long periods, which can affect tall buildings, may be larger than previously thought. This research applies PBEE tools to this potential seismic safety problem and proposes new methodological approaches to assess the seismic risk of these existing tall steel buildings and their implications on urban resilience.

To this end, Chapter 2 provides an overview of seismic design evolution of building codes in the US and a review of PBEE including aspects related to seismic hazard estimation and ground motion selection, non-linear response simulation, and methods for estimating seismic damage and associated consequences, including direct economic losses and downtime to achieve different recovery states.

Chapter 3 outlines the approach to evaluate the seismic risk of existing tall steel MRF buildings with assessment approaches of increasing complexity, namely scenario-based, intensity-based and time-based assessments, as well as city-level evaluations. San Francisco is selected as the case study city in order to permit engagement and support of ongoing efforts of the city’s Earthquake Safety Implementation Program (CAPSS 2011). Expected seismic performance is evaluated through the development of archetype buildings representative of the existing tall building stock. The key characteristics of the archetype buildings as well as the numerical models developed to evaluate seismic performance are outlined in Chapter 4.

9.2 Summary of findings and conclusions

9.2.1 BSPE: Scenario-based evaluation

Chapter 5 evaluates the performance of a 40-storey and a 20-storey 1970s steel MRF archetype buildings when subjected to an earthquake scenario, with a specific magnitude and location. The HayWired scenario (USGS 2016) is used in this study, a M_w 7.0 earthquake on the Hayward fault, developed to study impacts on the San Francisco Bay area. The key contribution of this chapter is that it provides an understanding of the expected performance of tall steel MRF buildings in San Francisco and Oakland under a realistic earthquake scenario main shock, highlighting the likely impacts on the built environment such that steps can be taken to change negative outcomes and reduce future risk.

Overall, results indicate that demands are significantly larger in Oakland than San Francisco, due to the smaller fault distance. Results also highlight that maximum demands are sensitive to the orientation of the buildings with regards to the largest component of the HayWired ground motions. An evaluation of the HayWired ground motion spectra highlights fairly low spectral accelerations at long periods (in close proximity to the fundamental period of the structures considered), suggesting that the scenario main shock considered, while relevant for emergency planning, is not the most likely to cause greatest impacts on the existing tall building stock.

Results in both archetype buildings highlight concentrations of deformation in a small number of stories: around mid-height for the 20-storey building and at the top of the building for the 40-storey archetype building. Results indicate that in the 40-storey building, 11% of beam-to-column connections are expected to fracture in Oakland versus 2% in San Francisco, whereas in the 20-storey archetype building, 7% of connections are expected to fracture in Oakland and none in San Francisco. The 40-storey archetype in Oakland is expected to reach a damage state in which some minor realignment of the structural frame may be required in addition to structural and non-structural repairs. The 40-storey archetype building in San Francisco and the 20-storey archetype building in Oakland are expected to reach damage levels where no structural realignment is necessary, but the building may require some repairs to non-structural and mechanical components. The 20-storey archetype building in San Francisco is expected to remain elastic. Direct economic losses associated with the performance of the archetype buildings range from 7.4 to 17.5% of building replacement cost. Downtime estimates to re-occupancy range from 186 to 250 days, and downtime estimates to functional recovery range from 242 to 288 days.

Overall the results indicate that under the HayWired earthquake scenario, existing tall steel MRF buildings are expected to guarantee the life-safety of occupants. However, considerable financial losses may result from damage to structural and non-structural components. The most notable results are the expected delays associated with restoring building occupancy and functionality, which can result in considerable indirect losses.

9.2.2 BSPE: Intensity-based evaluation

Chapter 6 presents an intensity-based seismic performance assessment of a 1970s 40-storey steel MRF archetype building in San Francisco. Building performance is evaluated under a specified earthquake shaking intensity consistent with DBE level shaking in modern building codes. This chapter advances the work presented in Chapter 5, as it (i) extends the analysis from a scenario-based to an intensity-based evaluation, and it (ii) investigates options for reducing direct economic losses and downtime. As opposed to Chapter 5, which focused the discussion on expected EDPs and associated performance, the focus of Chapter 6 is on the loss and downtime evaluation. It also explores ways of improving resilience by reducing damage and taking other measures to improve recovery. The results of the intensity-based evaluation provide a performance reference point for design practitioners, who often utilize design-level earthquake shaking for performance assessments.

Expected direct economic losses for the archetype building are in the order of 34% of the building cost and the adoption of structural retrofit schemes, enhanced non-structural components and mitigation measures to minimize impeding factors enable up to a 92% reduction in losses. The adoption of non-structural enhancements can enable significant reduction in losses associated with the performance of the façade, office fitouts and MEP components, though overall loss reduction is maximized when adopting both structural and non-structural enhancements. Downtime for re-occupancy and functional recovery of the archetype building is estimated at 497 and 609 days, respectively. When mitigation measures to reduce delays are used in conjunction with both structural and non-structural enhancements, minimal downtime for both re-occupancy and functional recovery can be achieved. The impact of residual IDRs in seismic loss estimates for the archetype building and retrofit schemes under consideration is quantified. Consideration of peak residual IDRs in the loss assessment yields an increase both in expected losses and in the dispersion in the performance functions. Furthermore, based on peak residual IDRs under a design level earthquake shaking, the archetype 40-storey building is expected to reach damage levels where structural

realignment of the frame is required, whereas the retrofit schemes presented reduce damage to levels where very minor or no structural realignment is needed.

While the response of existing tall steel MRFs, in terms of IDRs, is in line with global acceptance criteria to guarantee life-safety of building occupants and collapse prevention, its seismic performance does not guarantee a level of damage control consistent with ensuring the seismic resilience of the community. Overall loss and downtime estimates indicate that these buildings are not seismically resilient and would experience a slow and costly recovery when subject to ground motions consistent with a design earthquake hazard level.

9.2.3 BSPE: Time-based evaluation

Chapter 7 presents the results of a comparative time-based seismic performance assessment of a 1970s 50-storey steel MRF archetype building and an equivalent 50-storey steel MRF building designed to modern code requirements. The key contribution of this chapter is that it benchmarks the performance of older existing tall steel MRF buildings against modern designs. Furthermore, it contributes evidence towards verification of the compliance with the life-safety objective of modern codes under extreme events. As performance is evaluated at an array of earthquake intensities from levels that cause no damage up to levels that trigger collapse, in addition to the results obtained under a scenario-based or intensity-based assessment, more advanced risk metrics such as the annual rate of collapse (λ_c), annualized losses (AAL), or annualized downtime (AAD) can be calculated.

As in the scenario-based and intensity-based assessments, dynamic analysis results illustrate large concentrations of deformation in a small number of stories in the 1970s archetype building due to inelastic deformations in the beams, columns and panel zones. In contrast, the response of the modern archetype building illustrates a more uniform distribution of deformation demands up the building height, with non-linear behaviour of components being limited to the beams.

The mean annual frequency of collapse of the 1970s archetype building is 28 times greater than for the modern archetype building ($28 \cdot 10^{-4}$ versus $1 \cdot 10^{-4}$). The probabilities of collapse in the design life of the buildings (50 years) are 13% and 0.5% for the 1970s and the modern building, respectively. These results indicate that the collapse risk of the 1970s archetype is well in excess of the 1% chance of collapse in 50 years intended in modern design standards.

Performance functions for peak IDR and maximum PFA illustrate that the annual frequencies of exceedance are consistently larger for the 1973 archetype building than for its modern counterpart, e.g. the annual rate of PFA greater than 0.5g is 0.0109 versus 0.007, and the annual rate of peak IDR greater than 2% is 0.0038 versus 0.0028. Despite the latter, performance functions for peak residual IDR indicate that the modern archetype building has higher annual frequencies of exceedance than its older counterpart for values up to 0.5%.

The expected AAL is 65% higher for the 1970s archetype building than the modern archetype building (0.66% versus 0.40%). The greatest contributor to AAL in the 1970s archetype building is the collapse risk (67%). The greatest contributor to AAL in the modern archetype building is irreparable damage due to residual IDRs (85%). The resulting vulnerability functions for both archetypes also highlight these large contributions to the overall loss. The expected AAD to re-occupancy and functional recovery illustrates similar trends to those of the AAL. The expected AAD to re-occupancy for the 1970s archetype building is 72% greater than for its modern counterpart (8.1 vs 4.7 days). The AAD to functional recovery for the 1970s archetype building is twice that of its modern counterpart (10.4 vs 5.0 days).

Recovery curves indicate that even at the lowest earthquake ground motion intensity considered in the assessment, delays associated with external factors, structural and non-structural repairs result in a median time to re-occupancy and functional recovery of 35 days and 145 days, respectively, for the 1970s archetype building. The modern archetype building illustrates faster recovery at the lowest earthquake ground motion intensities considered, with median delays to re-occupancy and functional recovery less than 50 and 120 days, respectively, for return periods less than 400 years. However, considerably longer delays are seen at higher intensities, e.g. time to re-occupancy and functional recovery of 270 days and 310 days for events with a 700 year return period.

Overall, the results of this study indicate that tall steel MRF designed according to modern building code requirements result in designs that comply with the intent of the code to provide damage control at low earthquake ground motion intensities and overall collapse safety. In contrast, existing tall steel MRF buildings consistent with the 1970s archetype building are far from complying with modern design requirements, not only in terms of collapse safety, but also in terms of damage control. Estimated recovery time to re-occupancy and functional recovery in both archetypes indicates building designs that lack the ability to swiftly recover from earthquakes.

9.2.4 Beyond individual building evaluations

Chapter 8 proposes a methodology to assess earthquake risk of existing tall buildings, considering implications for individual buildings and their impact on surrounding areas. The method is an extension of PBEE, which, through the introduction of vulnerability functions for resilience-based evaluations, enables the estimating the impact of building damage on the recovery (loss of function or occupancy), and closure of surrounding areas for a given ground motion shaking intensity.

The expected response of the 50-storey steel MRF archetype buildings studied in Chapter 7 is simulated for a range of expected magnitude earthquakes. The archetype buildings studied are commercial office buildings. Therefore, the impact on the urban community is measured in terms of lost or unavailable office space as a result of seismic damage to the buildings considered. The potential cordon areas are also evaluated because they can inform emergency planning, particularly if essential facilities, roads or infrastructure fall within the closed off areas. A simple case study is presented to demonstrate the feasibility and usefulness of this technique to evaluate the impact of different building typologies, represented through building clusters, on the urban community. The case study evaluates a cluster of five 1970s 50-storey steel MRF buildings in downtown San Francisco versus five modern 50-storey steel MRF buildings.

The results indicate that under a M7.5 scenario earthquake, the expected immediate loss of office space assuming the building cluster is composed of five 1970s archetype buildings is 88.5% of the office space. The expected delays to recover 50% of the total office space are 220 and 227 days both for re-occupancy and functional recovery. In contrast, the expected immediate loss of office space assuming the building cluster is composed by the modern archetype buildings is 51.4% of the office space. The expected delays to recover 50% of the total office space are 90 and 98 days both for re-occupancy and functional recovery. The potential for observing large cordons around the building clusters, with a cordon radius around each building equal to the building height, is roughly 10 times greater for the 1970s archetypes than for its modern counterparts.

9.3 Reflections on transferability

The work presented in this thesis is intended to inform the debate over the expected seismic performance of older tall steel MRF buildings. While a modern steel MRF building design is also developed in Chapter 7 to provide a benchmark for comparison, in reality, modern tall

steel MRF buildings are extremely rare due the flexibility of the structural system. In modern high rise construction, coupled RC wall systems are more common due to their superior strength and stiffness over other systems. However, even though modern coupled RC wall systems are believed to behave well in terms of life safety, post-earthquake repair can be costly and time consuming due to considerable seismic damage levels in RC coupling beams. Ji et al. (2016) evaluate the expected seismic performance of a modern RC coupled wall system through a number of intensity-based assessments. Furthermore, the impact of incorporating innovative structural components, such as RSCBs, which concentrate seismic damage in easily replaceable elements, allowing for a swift recovery after earthquakes, is also evaluated in the study. Ji et al. (2016) follow a similar method to that presented in Chapter 5. However, rather than assessing and benchmarking performance of older buildings and retrofit strategies, the purpose of the evaluation is to incentivize the use of novel structural systems that enable enhanced seismic performance over conventional construction methods. The study uses a case study building in Beijing, China where the proposed system was implemented in a recently completed project. This study, which the author of this thesis co-authored, enables a reflection on the transferability of the methods used in this thesis to evaluate existing tall steel MRF buildings in San Francisco, to different structural systems and geographical areas. The reflections on transferability focus on three key aspects: seismic hazard data, dynamic analysis simulations and building performance modelling for losses and downtime.

With regards to the availability of seismic hazard data, a change in geographical area from San Francisco, CA to Beijing, China implies a change from a data-rich context to one where only limited seismic hazard data is available. Seismic hazard analysis tools are readily available in California and other parts of the US through open access tools, e.g. USGS (2008) or OpenSHA (2003). These tools enable obtaining site-specific seismic hazard curves at multiple periods, which, in turn, enable the development of different target spectra, i.e. UHS. Furthermore, alternative target spectra, such as the CS developed by Lin and Baker (2015), can be implemented by utilizing seismic hazard de-aggregation results from PSHA. In contrast, in the Ji et al. (2016) study, seismic hazard data is limited to that of the building code. As part of the latter study, four intensities of ground motion shaking are evaluated: service-level earthquake (SLE), DBE, MCE and very rare earthquake (VRE). Even though these evaluations appear to provide extensive seismic hazard information, in reality these are anchored in a single intensity level defined by the Chinese code: DBE. The additional intensity levels considered, namely SLE, MCE and VRE, are obtained by linearly scaling the DBE target spectrum. Such evaluations imply that results are conditioned on code-defined shaking intensity levels. Even though the Chinese code associates each one of these intensity levels to

a particular probability of exceedance, additional evaluations at return periods different than those suggested by the code are difficult to carry out. Furthermore, the selection of hazard consistent ground motions or other target spectra, e.g. UHS or CS, are difficult to develop without the necessary PSHA tools. Advanced metrics, such as those obtained through the time-based assessment presented in Chapter 7, require extensive seismic hazard data at a wide range of ground motion intensities. Efforts to extend the Ji et al. (2016) study to provide more advanced risk metrics, e.g. collapse risk, are hindered by the lack of detailed and readily available seismic hazard data.

With regards to dynamic analysis simulations, the key difference in the Ji et al. (2016) study to that developed in this thesis is the change in structural system. Ji et al. (2016) evaluate RC coupled wall (with conventional RC coupling beams and innovative RSCBs) as opposed to the evaluation of steel MRF structures. Despite the evaluation of different structural systems, guidelines for the analytical simulation of the different structural components considered are readily available in the literature. Furthermore, experimental test data to validate the analytical simulations, as done in both studies, is also readily available. In these two studies, there are few challenges related to NLRHA simulations. However, if a similar method is implemented to evaluate unconventional structural systems that have not been extensively researched, such studies would require experimental programs and analytical studies to enable the necessary numerical simulations.

One of the greatest challenges associated with the transferability of the method is that related to building performance modelling, in particular regarding loss and downtime estimates. To infer repair costs and times from NLRHA results, damage prediction is a necessary step. As discussed in Section 4.3.1, this can be achieved through fragility functions. Generally, if recommendations for NLRHA modelling are available for a particular structural component, experimental or analytical models associated with such guidelines can enable the development of fragility functions. For instance, Ji et al. (2016) evaluate the use of novel RSCBs. Since fragility functions for these components are not readily available, as part of the study, fragility functions for this novel structural component are developed. These functions are developed by compiling and analysing a database of RSCB laboratory experiments. While the FEMA P58 methodology enables the development and incorporation of user-defined fragility functions, the greatest challenge is in the need to adjust or develop consequence data, i.e. repair cost and repair time. This can be particularly challenging if the existing fragility database is to be adapted for use outside of the US. As a result, studies that intend to evaluate losses following this method need to either (i) utilize US-based consequence data and use the

results strictly for comparison studies between different systems, or, alternatively (ii) must develop consequence data consistent with construction practices and costs for the country or region under consideration. This aspect is also important when considering downtime estimates, particularly in regions of the world where the construction industry is less regulated and therefore many of the constraints considered in the downtime assessment methodology, as discussed in Chapter 4, would not apply, e.g. maximum number of workers per square footage, number of hours in a worker's shift, etc.

In essence, while the methods employed in this thesis can provide useful metrics related to the expected seismic performance of buildings, there are significant challenges associated with the transferability of the method to different geographical contexts. This reflection highlights some of these challenges, which studies such as Ji et al. (2016) are helping address.

9.4 Limitations and future research

There a number of limitations associated with the work presented in this thesis. These limitations can help inform future research on the subject. A number of possible research avenues are proposed in this section:

- Building Inventory and Archetype Building Development

A significant limitation of this work is that it attempts to understand the seismic performance of existing tall steel MRF buildings by means of archetype buildings. While the archetype buildings considered in this work are selected based on a database of the existing tall building stock in San Francisco, unrestricted access to existing building drawings would enable a more realistic evaluation of expected seismic performance. Additionally, the archetypes considered in this work are designed to comply with the requirements of UBC 1973. While the archetypes selected are a representation of design practice from the mid-1970s to the mid-1980s, consideration of designs to earlier and later standards would provide insightful information about the expected variability in seismic performance associated with buildings designed to different versions of the Uniform Building Code.

- Building Irregularities and other Sensitivity Analyses

The archetypes considered in this work are regular buildings. Many existing tall buildings have vertical and horizontal irregularities up the building height. The presence of vertical and horizontal irregularities can have a negative impact on the seismic performance of buildings. The implication of building irregularities on the seismic performance assessment results

warrants further study. An interesting observation from a sidewalk survey of the buildings in San Francisco included within the existing tall building database in Appendix B, is that many buildings lacked corner columns. The impact of this design feature on expected seismic performance has not been considered in this work.

Additionally, as part of this work, no sensitivity analyses are carried out to account for variability of element dimensions (section sizes, beam spans, storey heights, etc.) and construction material properties in the archetype buildings considered. While archetype buildings of different heights are assessed within this thesis, this research has not been designed to enable a parametric analysis of the effect of building height on structural performance. This is an area that could be investigated in the future.

- Improvements to NLRHA Models

In order to conduct non-linear dynamic analysis of the archetype buildings, analytical models capable of capturing the response of all structural elements that significantly contribute to the strength and stiffness of the system are developed. Component models to represent the response of non-linear beams, columns and panel zones are calibrated, where possible, against available experimental test data for validation. Additionally, as a sanity check of the global behaviour of the archetype buildings considered, their response is compared with that of similar buildings instrumented in past earthquakes. Despite these checks, several modelling assumptions warrant further study: i) the impact of composite action on the hysteretic response of beams that form part of the gravity and lateral resisting system as opposed to those assuming bare frame properties; ii) degradation parameters in the moment-rotation response of columns based on varying levels of axial demand throughout the time history record as opposed to calibrated based on expected levels of axial demand, assumed to remain constant throughout the analysis; iii) consideration of additional levels of plastic rotation capacities for different pre-Northridge moment connection details; iv) consideration of coupled shear force-deformation response of panel zones in 3D models.

- Detailed Design of Retrofit Schemes

Only two structural retrofit schemes are considered in this work, namely the introduction of an elastic spine to ensure a more uniform distribution of ductility demands up the building height and the introduction of base isolation at ground level, aimed at minimizing excitation of higher modes. These retrofit schemes, outlined in Chapter 6, are only conceptually designed. In order to better understand possible retrofit solutions to enhance the seismic performance of existing tall steel MRF buildings, additional retrofit schemes should be

considered, e.g. introduction of supplemental damping devices. Furthermore, retrofit schemes should be vetted by design practitioners and the construction industry to ensure their feasibility from a constructability perspective. Additionally, while the impact of incorporating these retrofits, and other building enhancements, has been evaluated in terms of the resulting seismic losses, the costs associated with these schemes have not been explored in this work. In order to carry out true cost-benefit analyses for different retrofit schemes, the associated construction costs of each retrofit scheme must be considered.

- Improvements to Building Performance Models

Within the building performance model, non-structural component quantities are estimated based on typical quantities found in buildings of similar occupancy by use of the Normative Quantity Estimation Tool (FEMA 2012). Normative quantities are an estimate of the quantity of components and contents likely to be present in a building of a specific occupancy based on gross square footage. FEMA (2012) developed these quantities based on a detailed analysis of approximately 3000 buildings across typical occupancies. In this study, non-structural components in the 1970s archetype buildings are assumed to be consistent with components in the FEMA (2012) fragility database that neglect seismic action in their design. Detailed surveys of existing tall buildings can help provide better estimates of non-structural performance quantities specific to the building typology considered. Such surveys can also inform which, if any, components have been upgraded with changes of tenancy/occupancy. Additionally, there are a number of fragilities that warrant further study, in particular those related to pre-cast façade panels and elevators.

FEMA (2012) provides consequence data for pre-cast façade panel components, but it does not specify fragility data. Therefore, fragility parameters for these components is developed following FEMA (2012) recommendations: *"Non-structural components for which displacement based fragilities can be developed include exterior wall systems, such as precast cladding […],generally constructed with a gap to accommodate horizontal drift. Using geometric relationships, the size of the gap can be expressed as a storey drift ratio that the wall panel system can accommodate before contact with adjacent panels occurs (usually at corners and column covers). If drawings depicting the gap system are available, users should determine if actual drift tolerance can be determined from these drawings. A dispersion of 0.5 is recommended for storey drift related fragilities."* Based on drawings depicting such gap, the fragilities are developed based assuming 20 mm (~0.75 in.) between one-storey high panels. The validity of this assumption warrants further study.

Regarding elevators systems, FEMA (2012) elevator fragilities were originally developed as a function of PGA from data for shorter buildings. The fragility ignores the location and distribution of elevators within a building. To account for these shortcomings, in this study, elevator fragilities are developed in consultation with design practitioners (personal communication with Arup, 2013) as a function of residual drifts up the building height, which are believed to compromise the functionality of vertical transportation systems. The median residual drifts expected to cause damage to the elevator system is taken as 0.2%. The validity of this assumption to different elevator systems warrants further study.

- Injury and Fatality Estimation

The seismic performance assessments presented in this work are focused on response parameters, direct economic losses, downtime and recovery. Injuries and fatalities associated with the seismic performance of the archetypes evaluated are not considered. Tall buildings can house many occupants; hence consideration of injuries and fatalities may be of greater relevance for policy planning than some of the results presented in this body of work. Communicating the annual mortality rates as opposed to the annual rate of collapse could influence the interpretation of results.

- Evaluation of Indirect Economic Losses

A significant limitation of this study is that, while efforts have been made to simulate different recovery paths to re-occupancy and functional recovery, the indirect costs associated with loss of occupancy and functionality have not been explored, e.g. business interruption, temporary housing costs, etc. Similarly, despite evaluating the potential for cordoning off areas around severely damaged tall buildings, the impact of these cordons, in terms of indirect costs, have not been studied. These studies would be of great interest, yet difficult to generalize, as they are location specific. The evaluation of cordons is also conditioned on accurate estimates of residual IDRs, which are sensitive to numerous modeling assumptions and warrant further study.

- Time-based Assessments using Conditional Spectra

The time-based assessment results presented in Chapter 7 are computed on the basis of a specified conditioning period of 5 seconds, which forms the basis of the CS mean, variance and ground motions suites selected for evaluation. Tall buildings generally have responses that are sensitive to excitation at a range of periods, both shorter (higher mode effect contributions to the response) and longer (lengthened periods due to non-linear behaviour). As a result, questions arise regarding the appropriate choice of the conditioning period when

using the CS as the target spectrum for ground motion selection. While, as discussed in Chapter 7, Lin et al. (2013) investigated the effect of the conditioning period on time-based structural response assessments, such as the one conducted in this work, their study only empirically demonstrated that such assessments are relatively insensitive to the choice of conditioning period when ground motions are selected to ensure hazard consistency. Further studies should evaluate the impact of conditioning period selection on the results here presented.

9.5 Concluding remarks

The results of this piece of research serve to inform the debate over the expected seismic performance of existing 1970s tall steel MRF buildings. This work provides an array of results from different types of assessment that can be informative to different parties including design practitioners, building owners, policy makers and the insurance sector. Results are communicated not only in terms of structural response, but also in terms of direct economic losses, downtime and recovery, which are more accessible to decision makers. Methods are proposed to develop re-occupancy and functionality ratios against time as well as a framework to evaluate performance of clusters of buildings and how they may impact the resilience of the community, going beyond individual building performance towards more holistic seismic performance evaluations.

This page is intentionally left blank.

References

Aagaard B., Boatwright J., Jones J., MacDonald T., Porter K. and Wein A. (2017) "HayWired Scenario Mainshock Ground Motions." In USGS Scientific Investigations Report 2017–5013, Edited by Detweiler S. and Wein A., United States Geological Survey, Menlo Park, CA, USA.

AISC (2010a). "Specification for Structural Steel Buildings." ANSI/AISC 360-10, American Institute of Steel Construction, Chicago, IL, USA.

AISC (2010b). "Seismic Provisions for Structural Steel Buildings." ANSI/AISC 341-10, American Institute of Steel Construction, Chicago, IL, USA.

Almufti I. and Willford M. (2013). "Resilience-based Earthquake Design Initiative (REDi) for the Next Generation of Buildings." Arup, San Francisco, CA, USA.

Almufti I., Motamed R., Grant D. and Willford M. (2013). "Incorporation of velocity pulses in design ground motions for response history analysis using a probabilistic framework." Earthquake Spectra, 31(3): 1647-1666.

Anderson J. and Bertero V. (1998). "Seismic response of a 42-story steel building." United States Geological Survey, Washington, D.C., USA.

Araya-Letelier G. and Miranda E. (2012). "Novel Sliding/Frictional Connections for Improved Seismic Performance of Gypsum Wallboard Partitions." Proc., 15th World Conference of Earthquake Engineering, Lisbon, Portugal.

Arup (2017). "USGS HayWired Scenario Study – Tall Building Performance. Tall Buildings Analytical Results and Loss Assessment." Arup, San Francisco, CA, USA.

ASCE (2003). "ASCE-31: Seismic Evaluation of Existing Buildings." American Society of Civil Engineers, Reston, VA, USA.

ASCE (2006). "ASCE-41: Seismic Evaluation and Retrofit of Existing Buildings." ASCE/Structural Engineering Institute (SEI) 41-13, Reston, VA, USA.

ASCE (2010). "Minimum design loads for buildings and other structures." ASCE/Structural Engineering Institute (SEI) 7-10, Reston, VA, USA.

ASCE (2013). "ASCE-41: Seismic Evaluation and Retrofit of Existing Buildings." ASCE/Structural Engineering Institute (SEI) 41-13, Reston, VA, USA.

Aslani H. and Miranda E. (2005). "Probabilistic Earthquake Loss Estimation and Loss Disaggregation in Buildings." John A. Blume Earthquake Engineering Center, Technical Report 157, Stanford, CA, USA.

ATC (1978). "Tentative Provisions for the Development of Seismic Regulations for Buildings." Applied Technology Council, Redwood City, CA, USA.

ATC (1987). "ATC-14: Evaluating the Seismic Resistance of Existing Buildings." Applied Technology Council, Redwood City, CA, USA.

ATC (2005). “Field manual: postearthquake safety evaluation of buildings (2nd edition)”. ATC-20-1, Applied Technology Council, Redwood City, CA, USA.

ATC (2010). “ATC-52-2: Here today-Here Tomorrow: The Road to Earthquake Resilience in San Francsico. A Community Action plan for Seismic Safety.” Applied Technology Council, Redwood City, CA, USA.

Bachman R. (2011). “Development of Seismic Fragilities for Acoustical Tile or Lay-in Panel Suspended Ceilings.” Prepared for FEMA as part of the ATC 58 Project. FEMA P-58/BD-3.9.4.

Bachman R. (2012). “Development of Seismic Fragilities for MEP Distribution Systems for the ATC-58 Project.” Prepared for FEMA as part of the ATC 58 Project. FEMA P-58/BD-3.9.11.

Baker J. (2008). "An Introduction to Probabilistic Seismic Hazard Analysis (PSHA)." White Paper. [Online] Available at: web.stanford.edu/~bakerjw/publications.html [Last accessed: September 2017]

Baker J. (2011). "Conditional Mean Spectrum: Tool for ground motion selection." Journal of Structural Engineering, 137(3): 322-331.

Baker J. (2015). “Efficient analytical fragility function fitting using dynamic structural analysis,” Earthquake Spectra, 31(1): 579-599.

Baker, J. and Cornell, A. (2006). “Spectral shape, epsilon and record selection.” Earthquake Engineering and Structural Dynamics, 35: 1077-1095.

Baker J. and Jayaram N. (2008). “Correlations of spectral acceleration values from NGA ground motion models.” Earthquake Spectra, 23(1): 299-317.

Baker J. and Lee C. (2017). “An Improved Algorithm for Selecting Ground Motions to Match a Conditional Spectrum.” Journal of Earthquake Engineering, (in press).

Bayer K. (2012). “Quake city landmark will soon be rubble.” The New Zealand Herald. [Online] Available at: www.nzherald.co.nz/nz/news/article.cfm?c_id=1&objectid=10808303 [Last accessed: September 2017]

Bonowitz D. (2009). “The dilemma of existing buildings: private property, public risk.” San Francisco Planning and Urban Research Association, San Francisco, CA, USA.

Bonowitz D. (2011). “Resilience Criteria for Seismic Evaluation of Existing Buildings.” A 2008 Special Projects Initiative Report to Structural Engineers Association of Northern California, San Francisco, CA, USA.

Boore D. and Atkinson G. (2008). “Ground-motion prediction equations for the average horizontal component of PGA, PGV and 5% damped SA at spectral periods between 0.1 s and 10.0 s.” Earthquake Spectra, 24(1): 99-138.

Bruneau M. and Mahin S. (1990). “Ultimate behavior of heavy steel section welded splices and design implications.” Journal of Structural Engineering, 116(8): 2214-2235.

Bruneau M. and Reinhorn A. (2004). “Seismic resilience of communities – conceptualization and operationalization.” In “Performance-based seismic design-concepts and implementations.” Edited by Fajfar P. and Krawinkler H. Proc. of the International Workshop on Performance-Based Seismic Design, Bled, Slovenia, PEER report 2004/05, University of California at Berkeley, 161-172.

Bruneau M. and Reinhorn A. (2006). “Overview of the Resilience Concept.” Proc., 8th U.S. National Conference on Earthquake Engineering, San Francisco, CA, USA.

Bruneau M. and Reinhorn A. (2007). “Exploring the concept of seismic resilience for acute care facilities.” Earthquake Spectra, 23(1): 41-62.

Bruneau M., Chang S., Eguchi T., Lee G., O’Rourke T., Reinhorn A., Shinozuka M., Tierney K., Wallace W. and Winterfeldt D. (2003). “A Framework to Quantitatively Assess and Enhance the Seismic Resilience of Communities.” Earthquake Spectra, 19(4): 733-752.

Buchanan C. and Partners (2008). “The economic impact of high density development and tall buildings in central business districts”. A report for the British Property Federation, London, UK.

Burton H., Deierlein G., Lallemant D., and Lin T. (2015). “Framework for Incorporating Probabilistic Building Performance in the Assessment of Community Seismic Resilience.” Journal of Structural Engineering, 142(8): C4015007.

CAPSS (2011). “CAPSS Earthquake Safety Implementation Program: Workplan 2012-2042.” Community Action Plan for Seismic Safety, The City and County of San Francisco, CA, USA.

CERC (2012). “Christchurch, the city and approach to this inquiry.” Canterbury Earthquakes Royal Commission, Final Report, Volume 5, Canterbury, New Zealand.

CESMD (2007). “Center of Engineering Strong Motion Data.” [Online]. Available at: www.strongmotioncenter.org [Last accessed: September 2017].

Cimellaro G., Reinhorn A. and Bruneau M. (2006). “Quantification of Seismic Resilience.” Proc., 8th U.S. National Conference on Earthquake Engineering, San Francisco, CA, USA.

Cimellaro G., Reinhorn A. and Bruneau M. (2010). “Framework for analytical quantification of disaster resilience.” Engineering Structures, 32 (2010): 3639-3649.

Cimellaro G., Villa O. and Bruneau M. (2014). “Resilience-Based Design of Natural Gas Distribution Networks.” Journal of Infrastructure Systems, 21(1): 05014005.

Comartin C. (2004). “Applications of Performance-based earthquake engineering to risk-management decisions.” In “Performance-based seismic design-concepts and implementations.” Edited by Fajfar P. and Krawinkler H. Proc. of the International Workshop on Performance-Based Seismic Design, Bled, Slovenia, PEER report 2004/05, University of California at Berkeley, 101-112.

Comerio M. (2006). “Estimating Downtime in Loss Modeling.” Earthquake Spectra, 22(2): 349-365.

Cornell A. (1968). “Engineering Seismic Risk Analysis.” Bulletin of the Seismological Society of America, 58(5): 1583-1606.

Cornell A. and Krawinkler H. (2000). “Progress and challenges in seismic performance assessment.” PEER Center News 3(2): 1–3.

CTBUH (2010). “Recommendations for the Sismic Design of High-rise Buildings.” Council of Tall Buildings and Urban Habitat, Chicago, IL, USA.

Cutter S., Burton C., and Emrich C. (2010). “Disaster resilience indicators for benchmarking baseline conditions.” Journal of Homeland Security and Emergency Management, 7(1): 51.

Deierlein G. (2004). “Overview of a Comprehensive Framework for Earthquake Performance Assessment.” Performance-based Seismic Design – Concepts and Implementation.” PEER Special Publication, Pacific Earthquake Engineering Research Center, University of California, Berkeley, CA, USA.

Deierlein G., Reinhorn A. and Willford M. (2010). “Nonlinear Structural Analysis for Seismic Design. A Guide for Practicing Engineers.” NIST GCR 10-917-5, NEHRP Seismic Design Technical Brief No. 4 prepared for the National Institute of Standards and Technology, Gaithersburg, MD, USA.

Deierlein G. and Victorsson V. (2008). “Fragility Curves for Components of Steel SMF Systems.” Prepared for FEMA as part of the ATC 58 Project. FEMA P-58/BD-3.8.3.

Detweiler S. and Wein A. (2017). “The HayWired earthquake scenario.” USGS Scientific Investigations Report 2017–5013, United States Geological Survey, Menlo Park, CA, USA.

Eads L. (2013). “Seismic collapse risk assessment of buildings: effects of intensity measure selection and computational approach.” John A. Blume Earthquake Engineering Center, Technical Report 184, Stanford, CA, USA.

Eads L., Molina Hutt C. and Menun C. (2017). "Loss assessment of tall buildings from a vulnerability perspective." Proc., 16th World Conference of Earthquake Engineering, Santiago, Chile.

Eberhard M., Mookerjee A. and Parrish M. (2001). “Uncertainties in Performance Estimates for RC Columns.” PEER Special Publication, Pacific Earthquake Engineering Research Center, University of California, Berkeley, CA, USA.

EEFIT (1994). “The Northridge, California Earthquake of 17 January 1994 – A field report by EEFIT.” Institution of Structural Engineers, London, UK.

EERI (1994). “Preliminary Report -Northridge, California, Earthquake of January 17, 1994.” Earthquake Engineering Research Institute, Oakland, CA, USA.

Eidinger J. (2009). “Fragility of Non-Structural Components” Prepared for FEMA as part of the ATC 58 Project. FEMA P-58/BD-3.9.12.

Emporis (2000). “The global provider of building data.” [Online]. Available at: www.emporis.com [Last accessed: September 2017].

Farokhnia K. and Porter K. (2012). “Estimating the Non-Structural Seismic Vulnerability of Building Categories.” Proc., 15th World Conference of Earthquake Engineering, Lisbon, Portugal.

FEMA (1997). “NEHRP Guidelines for Seismic Rehabilitation of Buildings.” Report No. FEMA-273, Federal Emergency Management Agency, Washington, D.C., USA.

FEMA (2000a). “State of the Art Report on Systems Performance of Steel Moment Frames Subject to Earthquake Ground Shaking.” FEMA 355-C, Federal Emergency Management Agency, Washington, D.C., USA.

FEMA (2000b). “State of the Art Report on Past Performance of Steel Moment-Frame Buildings in Earthquakes.” FEMA 355-E, Federal Emergency Management Agency, Washington, D.C., USA.

FEMA (2000c). “Recommended postearthquake evaluation and repair criteria for welded steel moment-frame buildings. Program to reduce the hazards of steel moment frame structures.” FEMA 352, Federal Emergency Management Agency, Washington, D.C., USA.

FEMA (2012). “Seismic performance assessment of buildings.” FEMA P-58 prepared by the Applied Technology Council for the Federal Emergency Management Agency, Washington, D.C., USA.

Field E., Jordan T. and Cornell C. (2003). “OpenSHA: A Developing Community-Modeling Environment for Seismic Hazard Analysis,” Seismological Research Letters, 4(74): 406-419.

Freeman S. (2007). “Response Spectra as a Useful Design and Analysis Tool for Practicing Structural Engineers.” Journal of Earthquake Technology, 475(44): 25-37.

Gerges R., Benuska K. and Kumabe C. (2012). “Performance-Based Seismic Design of Tall Buildings.” Structure magazine, National Council of Structural Engineers Associations (NCSEA), Chicago, IL, USA.

GSA (2012). [Computer software]. Oasys General Structural Analysis, Arup, London, UK.

Günay S., Korolyk M., Mar D., Mosalam K.M. and Rodgers J. (2009). “Infill walls as a spine to enhance the seismic performance of non-ductile reinforced concrete frames.” Proc., Applied Technology Council and the Structural Engineering Institute 2009 Conference on Improving the Seismic, Performance of Existing Buildings and Other Structures, San Francisco, CA, USA.

Gupta A. and Krawinkler H. (1999). “Seismic Demands for Performance Evaluation of Steel Moment Resisting Frame Structures.” John A. Blume Earthquake Engineering Center, Technical Report 132, Stanford, CA, USA.

Hamburger R. (2004). “Development of Next-Generation Performance-based Seismic Design Guidelines.” Performance-based Seismic Design – Concepts and Implementation, PEER Special Publication, Pacific Earthquake Engineering Research Center, University of California, Berkeley, CA, USA.

Hamburger R. (2009). “Performance-based Seismic Upgrade of Building Structural Systems. A 2020 Vision.” Proc., Applied Technology Council and the Structural Engineering Institute 2009 Conference on Improving the Seismic, Performance of Existing Buildings and Other Structures, San Francisco, CA, USA.

Han Y. and Davidson R. (2012). “Probabilistic seismic hazard analysis for spatially distributed infrastructure. Earthquake Engineering & Structural Dynamics, 41(15): 2141-2158.

Harris R. (2017) “Overview of the HayWired Scenario Earthquake.” In USGS Scientific Investigations Report 2017–5013, Edited by Detweiler S. and Wein A., United States Geological Survey, Menlo Park, CA, USA.

Haselton C. and Deierlein G. (2007). “Assessing Seismic Collapse Safety of Modern Reinforced Concrete Frame Buildings.,” PEER Report 2007/08, Pacific Earthquake Engineering Research Center, University of California, Berkeley, CA, USA.

Haselton C., Liel A., Deierlein G., Dean B. and Chou J. (2011). “Seismic Collapse Safety of Reinforced Concrete Buildings: I. Assessment of Ductile Moment Frames,” Journal of Structural Engineering, 137(4): 481-491.

HAZUS (2014). “Earthquake Advanced Engineering Building Module.” HAZUS Multi-hazard Loss Estimation Methodology, Federal Emergency Management Agency, Washington, D.C., USA.

HAZUS (2017). [Computer software]. HAZUS Software, Federal Emergency Management Agency, Washington, D.C., USA.

Higgins C. (2011). “Seismic Fragility of Standard Building Stairs.” Prepared for FEMA as part of the ATC 58 Project. FEMA P-58/BD-3.9.6.

Holmes W. (2009). “Progress of Seismic Rehabilitation of Buildings in the U. S.” Proc., Applied Technology Council and the Structural Engineering Institute 2009 Conference on Improving the Seismic, Performance of Existing Buildings and Other Structures, San Francisco, CA, USA.

Hoover C. (1992). “Seismic Retrofit Policies: An Evaluation of Local Practices in Zone 4 and their Application to Zone 3.” Earthquake Engineering Research Institute, Oakland, CA, USA.

Hudnut K., Wein A., Cox D., Perry S., Porter K., Johnson L. and Strauss J. (2017) “The HayWired Scenario—How Can the San Francisco Bay Region Bounce Back from or Avert an Earthquake Disaster in an Interconnected World?” In USGS Scientific Investigations Report 2017–5013, Edited by Detweiler S. and Wein A., United States Geological Survey, Menlo Park, CA, USA.

Hutchinson T. and Chaudhuri S. (2004). “Seismic Fragility of Small Equipment and Contents.” In “Performance-based seismic design-concepts and implementations.” Edited by Fajfar P. and Krawinkler H. Proc. of the International Workshop on Performance-Based Seismic Design, Bled, Slovenia, PEER report 2004/05, University of California at Berkeley, 197-208.

Hwang S. and Lignos D. (2017). “Earthquake-induced loss assessment of steel frame buildings with special moment frames designed in highly seismic regions.” Earthquake Engineering and Structural Dynamics, 46: 2141-2162.

IBC (2012). “2012 International Building Code.” IBC 2012, International Code Council, Country Club Hills, IL, USA.

Jayaram N. and Baker J. (2009). "Correlation model for spatially-distributed ground-motion intensities," Earthquake Engineering and Structural Dynamics, 38(15): 1687-1708.

Jayaram N. and Shome N. (2012). “A Statistital Analysis of the Response of Tall Buildings to Recorded and Simulated Ground Motions.” Proc., 15th World Conference of Earthquake Engineering, Lisbon, Portugal.

Jayaram N., Lin T., and Baker J. (2011). “A computationally efficient ground-motion selection algorithm for matching a target response spectrum mean and variance.” Earthquake Spectra, 27(3), 797-815.

Jayaram N., Shome N. and Rahnama M. (2012). “Development of earthquake vulnerability functions for tall buildings.” Journal of Earthquake Engineering and Structural Dynamics, 41(11): 1495-1514.

Jin J. and El-Tawil S. (2005). “Evaluation of FEMA-350 Seismic Provisions for Steel Panel Zones.” Journal of Structural Engineering, 131(2), 250-258.

Kani N. and Katsuta S. (2009). “Seismic Isolation Retrofit for Existing Buildings in Japan.” Proc., Applied Technology Council and the Structural Engineering Institute 2009 Conference on Improving the Seismic, Performance of Existing Buildings and Other Structures, San Francisco, CA, USA.

Khater M., Scawthron C. and Johnson J. (2002). “Loss Estimation.” Earthquake Engineering Handbook, Chapter 31, CRC Press, Boca Raton, FL, USA.

Kim K. and Engelhart M. (1995). “Development of Analytical Models for Earthquake Analysis of Steel Moment Frames.” Report No. PMFSEL 95-2, Dept. of Civil Eng., Univ. of Texas at Austin, TX, USA.

Krawinkler H. (1978). “Shear in beam–column joints in seismic design of steel frames.” Engineering Journal, AISC, 3, 82–91.

Krawinkler H. (1999). “Challenges and Progress in Performance-based Earthquake Engineering”. International Seminar on Seismic Engineering for Tomorrow – In Honor of Professor Hiroshi Akiyama, Tokyo, Japan.

Krawinkler H. (2004). “Van Nuys Hotel Building Testbed Report: Exercising Seismic Performance Assessment.” PEER Report 2005/11, Pacific Earthquake Engineering Research Center, University of California, Berkeley, CA, USA.

Krawinkler H. (2006). “Importance of Good Nonlinear Analysis.” The Structural Design of Tall and Special Buildings, 15: 515-531.

Krawinkler H. and Deierlein G. (2014). “Challenges Towards Achieving Earthquake Resilience Through Performance-Based Earthquake Engineering.” In: Performance-Based Seismic Engineering: Vision for an Earthquake Resilient Society, Edited by Matej Fischinger, Chapter 1.

Krawinkler H. and Miranda E. (2004). “Performance-Based Earthquake Engineering.” In: Earthquake Engineering: From Engineering Seismology to Performance-Based Engineering, Edited by Bozorgnia Y. and Bertero V., CRC Press, Chapter 9.

Krishnan S., Ji C. and Komatitsch D. (2006). “Performance of Two 18-Story Steel Moment-Frame Buildings in Southern California during Two Large Simulated San Andreas Earthquakes”, Earthquake Spectra, 22(4): 1035–1061.

Kurata M., Suita K. and Nakashima M. (2005). “Test on large cyclic deformation of steel tube columns having fixed column bases.” Journal of Structural and Construction Engineering, 598:149-154.

LATBSDC. (2011). “An Alternative Procedure for Seismic Analysis and Design of Tall Buildings Located in the Los Angeles Region.” Los Angeles Tall Buildings Structural Design Council, Los Angeles, CA, USA.

Lavan O. (2010). “Seismic design procedure for total accelerations and inter-story drifts reduction of existing and new buildings with protective systems.” Structures Congress, American Society of Civil Engineering, Reston, VA, USA.

Lee K. and Foutch D. (2000). “Performance prediction and evaluation of steel special moment frames for seismic loads.” SAC Steel Project, Report No. SAC/BD-00/25, Richmond, CA, USA.

Lignos D. (2013). “Web-Based Interactive Tools for Performance-Based Earthquake Engineering.” [Online]. Available at: dimitrios-lignos.research.mcgill.ca/databases/ [Last accesed: September 2017]

Lignos D. and Krawinkler H. (2010). “A steel database for component deteriorration of tubular hollow square steel columns under varying axial load for collapse assessment of steel structures under earthquakes”. Joint Conference Proc., 7th Internation Conference on Urban Earthquake Engineering & 5th International Conference on Earthquake Engineering, Tokyo Institute of Technology, Tokyo, Japan.

Lignos D. and Krawinkler H. (2011). “Deterioration Modeling of Steel Components in Support of Collapse Prediction of Steel Moment Frames under Earthquake Loading”. Journal of Structural Engineering, 131(11): 1291-1302.

Lignos D., Chung Y., Nagae T. and Nakashima M. (2011). “Numerical and Experimental Evaluation of Seismic Capacity of High-Rise Steel Buildings Subjected to Long Duration Earthquakes,” Journal of Computers and Structures, 89(11-12): 959-967.

Lignos D., Krawinkler H. and Whittaker A. (2010). “Prediction and validation of sidesway collapse of two scale models of a 4-story steel moment frame.” Earthquake Engineering and Structural Dynamics, 40(7): 807-825.

Liel A., Haselton C. and Deierlein G. (2011). “Seismic Collapse Safety of Reinforced Concrete Buildings. II: Comparative Assessment of Nonductile and Ductile Moment Frames.” Journal of Structural Engineering, 137(4): 492-502.

Lin T. and Baker J. (2015). “Conditional Spectra.” Encyclopedia of Earthquake Engineering, Edited by Beer M., Kougioumtzoglou, I., Patelli E. and Au S., 461-472.

Lin T., Haselton C. and Baker J. (2013). “Conditional-Spectrum-based ground motion selection. Part I: Hazard consistency for risk-based assessments.” Earthquake Engineering & Structural Dynamics, 42(12): 1847-1865.

LSTC (2011). [Computer software]. LS-DYNA, Livermore Software Technology Corporation, Livermore, CA, USA.

Maison F. and Bonowitz D. (1999). “How safe are pre-Northridge WSMFs? A case study of the SAC Los Angeles nine-story building.” Earthquake Spectra, 15(4): 765-789.

MATLAB (2015). [Computer software]. The MathWorks, Inc., Natick, MA, USA.

May P. (2001). “Organizational and Societal Considerations for Performance-Based Earthquake Engineering.” PEER Report. 2001/04, Pacific Earthquake Engineering Research Center, University of California, Berkeley, CA, USA.

Medina R. and Krawinkler H. (2005). “Evaluation of Drift Demands for the Seismic Performance Assessment of Frames.” Journal of Structural Engineering, 131(7): 1003-1013.

Mieler M., Stojadinovic B., Budnitz R., Comerio M., and Mahin S. (2014). “A framework for linking community-resilience goals to specific performance targets for the built environment.” Earthquake Spectra, 31(3): 1267-1283.

Miles S., and Chang S. (2011). “ResilUS: A community based disaster resilience model.” Cartography and Geographic Information Science, 38(1): 36–51.

Miranda E. and Aslani H. (2003). “Probabilistic Response Assessment for Building-Specific Loss Estimation.” PEER Report 2003/03, Pacific Earthquake Engineering Research Center, University of California, Berkeley, CA, USA.

Miranda E. and Mosqueda G. (2011). “Seismic Fragility of Building Interior Cold-Formed Steel Framed Gypsum Partition Walls.” Prepared for FEMA as part of the ATC 58 Project. FEMA P-58/ BD-3.9.2.

Miranda E., Aslani H., and Taghavi S. (2004). “Assessment of seismic performance in terms of economic losses.” In “Performance-based seismic design-concepts and implementations.” Edited by Fajfar P. and Krawinkler H. Proc. of the International Workshop on Performance-Based Seismic Design, Bled, Slovenia, PEER report 2004/05, University of California at Berkeley, 149-160.

Mitrani-Reiser J. (2007). “An ounce of prevention: probabilistic loss estimation for performance-based earthquake engineering. Dissertation (Ph.D.), California Institute of Technology, Pasadena, CA, USA.

Moehle J. (2000). “State of Research on Seismic Retrofit of Concrete Building Structures in the US.” US-Japan Symposium and Workshop on Seismic Retrofit of Concrete Structures - State of Research and Practice, Japan Concrete Institute, Tokyo, Japan.

Moehle J. and Deierlein G. (2004). “A framework methodology for performance-based earthquake engineering.” in Proc., 13th World Conference of Earthquake Engineering, Tokyo, Japan.

Molina Hutt C. (2016). “USGS Tall Building Study – Haywired Scenario. Nonlinear Dynamic Analysis Results of 1970s Tall Stele Moment Resisting Frame buildings. ” Independent Consultant, London, UK.

Molina Hutt C., Almufti I., Willford M., Deierlein G. (2015). “Seismic loss and downtime assessment of existing tall steel-framed buildings and strategies for increased resilience.” Journal of Structural Engineering, 142(8): C4015005.

Molina Hutt C., Rossetto, T. and Deierlein G. (2017). “Comparative risk-based seismic performance assessment of 1970s vs modern tall steel moment resisting frames.” (In preparation).

Muto M. and Krishnan S. (2011). “Hope for the Best, Prepare for the Worst: Response of Tall Steel Buildings to the ShakeOut Scenario Earthquake.” Earthquake Spectra, 27(2): 375-398.

NEHRP (2011). “Selecting and scaling earthquake ground motions for performing response-history analyses.” NIST GCR 11-917-15 prepared by NEHRP Consultants Joint Venture for the National Institute of Standards and Technology, Gaithersburg, MD, USA.

NIST (1999) “UNIFORMAT II Elemental Classification for Building Specifications, Cost Estimating and Cost Analysis.” NISTIR 6389 Report, National Institute of Standards and Technology, Gaithersburg, MS, USA.

NZPA (2011). “Christchurch earthquake: Cordon around Grand Chancellor narrows.” New Zealand Press Association. [Online] Available at: www.stuff.co.nz/national/christchurch-earthquake/4716748/Christchurch-earthquake-Cordon-around-Grand-Chancellor-narrows [Last accessed: September 2017]

Pagni C. and Lowes L. (2006). “Fragility Functions for Older Reinforced Concrete Beam-Column Joints.” Earthquake Spectra: 22(1): 215-238.

PEER (2010a). “Tall buildings initiative: guidelines for performance-based seismic design of tall buildings.” PEER Report 2010/05, Pacific Earthquake Engineering Research Center, University of California, Berkeley, CA, USA.

PEER (2010b). “Modeling and acceptance criteria for seismic design and analysis of tall buildings.” PEER Report 2010/111 also published as PEER/ATC-72-1, Pacific Earthquake Engineering Research Center, University of California, Berkeley, CA, USA.

PEER (2013). “NGA-West2 Database.” PEER Report 2013/03, Pacific Earthquake Engineering Research Center, University of California, Berkeley, CA, USA.

Pekelnicky R. and Poland C. (2012). “ASCE 41-13: Seismic Evaluation and Retrofit of Existing Buildings.” Proc., 2012 SEAOC-SEANM Convention, Santa Fe, NM, USA.

Poland C. (2009). “The Resilient City: Defining what San Francisco needs from its seismic mitigation policies.” San Francisco Planning and Urban Research Association, San Francisco, CA, USA.

Porter K. (2011). “Fragility of Mechanical, Electrical, and Plumbing Equipment Considering Installation Conditions.” Prepared for FEMA as part of the ATC 58 Project. FEMA P-58/BD-3.9.10.

Porter K. and Kiremidjian A. (2001). “Assembly-Based Vulnerability of Buildings and Its Uses in Seismic Performance Evaluation and Risk Management Decision-Making.” John A. Blume Earthquake Engineering Center, Technical Report 139, Stanford, CA, USA.

Porter K., Johnson G., Sheppard R. and Bachman R. (2011). “Response to discussions of fragility of mechanical, electrical and plumbing equipment.” Earthquake Spectra, 27 (1): 229-233

Ramirez M. and Miranda E. (2012). “Significance of residual drifts in building earthquake loss estimation.” Earthquake Engineering & Structural Dynamics, 41: 1477–1493.

Ramirez M., Liel A., Mitrani-Reiser J., Haselton C., Spear A., Steiner J., Deierlein G. and Miranda E. (2012). “Expected earthquake damage and repair costs in reinforced concrete frame buildings.” Earthquake Engineering & Structural Dynamics, 41 (11): 1455-1475.

Roger Y. and Jirsa J. (1998). “Nonlinear Analyses of an Instrumented Structure Damaged in the 1994 Northridge Earthquake.” Earthquake Spectra, 14(2): 265-283.

SAC (2000). “Performance prediction and evaluation of steel special moment frames for seismic loads.” SAC Steel Project, Report No. SAC/BD-00/25, Richmond, CA, USA.

Siamak S. and Liel A. (2016). “Seismic Performance of Nonductile Reinforced Concrete Frames with Masonry Infill Walls—II: Collapse Assessment.” Earthquake Spectra: 32(2): 819-842.

SEAOC (1959). “Recommended lateral force requirements and commentary.” Seismology Committee, Structural Engineers Association of California, Sacramento, CA, USA.

SEAOC (1973). “Recommended lateral force requirements and commentary.” Seismology Committee, Structural Engineers Association of California, Sacramento, CA, USA.

SEAOC (1995). “Vision 2000: Performance-Based Seismic Engineering of Buildings.” Structural Engineers Association of California, Sacramento, CA, USA.

SEAONC (2007). “Recommended Administrative Bulletin on the Seismic Design and Review of Tall Buildings Using Non-Prescriptive Procedures.” Structural Engineers Association of Northern California, San Francisco, CA, USA.

SEAONC (2009). “Report Cards for Buildings: A Proposed Rating System for Earthquake Performance.” Proc., Applied Technology Council and the Structural Engineering Institute 2009 Conference on Improving the Seismic, Performance of Existing Buildings and Other Structures, San Francisco, CA, USA.

Yun S., Hamburger R., Cornell A. and Foutch D. (2002). “Seismic Performance Evaluation for Steel Moment Frames.” Journal of Structural Engineering, 128(4): 534-545.

Seung-Yul Y., Hamburger R., Cornell A. and Foutch D. (2002). “Seismic Performance Evaluation for Steel Moment Frames.” Journal of Structural Engineering, 128(4): 534-545.

SFPIM (2000). “San Francisco Property Information Map.” San Francsico Planning Department [Online]. Available at: propertymap.sfplanning.org [Last accessed: September 2017].

Shahi S. and Baker J. (2011). “An empirically calibrated framework for including the effects of near-fault directivity in probabilistic seismic hazard analysis.” Bulletin of the Seismological Society of America, 101(2): 742–755.

Shome N., Jayaram N. and Rahnama M. (2013). “Development of Earthquake Vulnerability Functions for Tall Buildings.” Proc., 11th International Conference on Structural Safety and Reliability, New York, NY, USA.

Shome N., Jayaram N., Krawinkler H., Rahnama M. (2015): Loss estimation of tall buildings designed for the PEER Tall Building Initiative Project. Earthquake Spectra, 31(3): 1309-1336.

SISMIC (2012). [Computer software]. Oasys Sismic, Probabilistic Seismic Hazard Program, Arup, London, UK.

SPUR (2012). “Safe enough to stay.” San Francisco Planning and Urban Research Association, San Francisco, CA, USA.

SP3 (2017). [Computer software]. Seismic Performance Prediction Program, Haselton Baker Risk Group, Chico, CA, USA.

PACT (2012). [Computer software]. Performance Assessment Calculation Tool, Federal Emergency Management Agency, Washington, D.C., USA.

Taghavi S. and Miranda E. (2003). “Response assessment of nonstructural building elements.” PEER Report 2003/05, Pacific Earthquake Engineering Research Center, University of California, Berkeley, CA, USA.

Tsai K. and Popov E. (1988). “Steel Beam-Column Joints in Seismic Moment Resisting Frames.” Report UCB/EERC-88/19, Earthquake Engineering Research Center, Richmond, CA, USA.

Twigg J. (2009). “Characteristics of a disaster-resilient community: A guidance note.” 2nd Ed., Disaster Risk Reduction Interagency Coordination Group, London, UK.

UBC (1973). “Uniform building code 1973 edition.” UBC 73, International Conference of Building Officials, Whittier, CA, USA.

USGS (2008). “United States Geological Survey hazard curve calculation tool.” [Online]. Available at: geohazards.usgs.gov/hazardtool/ [Last accessed: September 2016].

USGS (2016). “United States Geological Survey HayWired Scenario.” [Online]. Available at: geography.wr.usgs.gov/science/mhdp/haywired.html [Last accessed: September 2017].

USGS (2017a). “Soil Type and Shaking Hazard in the San Francisco Bay. Area Interactive Map.” [Online]. Available at: https://earthquake.usgs.gov/hazards/urban/sfbay/soiltype/map [Last accessed: September 2017].

USGS (2017b). “The Northern California Earthquake, April 18, 1906.” [Online]. Available at:earthquake.usgs.gov/earthquakes/events/1906calif/virtualtour/earthquake.php [Last accessed: September 2017].

Walsh K., Henry R., Simkin G., Brooke N., Davidson B. and Ingham J. (2016). “Testing of reinforced concrete frames extracted from a building damaged during the Canterbury Earthquakes.” ACI Structural Journal, 113 (2): 349-362.

Wang C. and Blackmore J. (2009). “Resilience Concepts for Water Resource Systems.” Journal of Water Resources Planning and Management, 135(6): 528-536.

Wang S., Lai J., Schoettler M. and Mahin S. (2017). “Seismic assessment of existing tall buildings: A case study of a 35-story steel building with pre-Northridge connection.” Engineering Structures, 141: 624-633.

Whittaker A., Hamburger R., Huang Y. (2007). “Building Specific Loss Assessment.” Australian Earthquake Engineering Society 2007 Conference, Australia.

Youssef N., Bonowitz D. and Gross J. (1995). “A Survey of Steel Moment-Resisting Frame Buildings Affected by the 1994 Northridge Earthquake.” National Institute of Standards and Technology, Gaithersburg, MD, USA.

Zhou J., Bu G. and Li K. (2015). “Calculation Methods for Inter-Story Drifts of Building Structures.” Proc., 15th World Conf. of Earthquake Engineering, International Association for Earthquake Engineering, Lisbon, Portugal.

Zimmerman R. and Holmes W. (2012). “Seismic performance investigation draft report of Clarendon Tower.” Rutherford & Chekene, San Francisco, CA, USA.

This page is intentionally left blank.

Appendix A

Appendix A is subdivided into Appendix A1, A2 and A3. Each sub-section includes a journal publication as outlined below:

A1. Molina Hutt C., Almufti I., Willford M. and Deierlein G. (2015). "Seismic loss and downtime assessment of existing tall steel-framed buildings and strategies for increased resilience." American Society of Civil Engineers, Journal of Structural Engineering, Special Issue Resilience-Based Analysis and Design of Structures and Infrastructure Systems. Available at: (http://dx.doi.org/10.1061/(ASCE)ST.1943-541X.0001314).

A2. Ji X., Liu D., Ya S. and Molina Hutt C. (2016). "Seismic performance assessment of a hybrid coupled wall system with replaceable steel coupling beams versus traditional RC coupling beams." Journal of Earthquake Engineering and Structural Dynamics. Available at: (http://dx.doi.org/10.1002/eqe.2801).

A3. Goretti A., Molina Hutt C. and Hedelung L. (2017). "Post-earthquake safety evaluation of buildings in Portoviejo, Manabí following the M7.8 coastal Ecuador earthquake of 16 April 2016." International Journal of Disaster Risk Reduction. Available at: (https://doi.org/10.1016/j.ijdrr.2017.06.011)

This appendix, which includes copyright material, has been omitted from the electronic version of the thesis. The journal publications above referenced were originally included in print version to provide examiners with easy access to peer-reviewed publications that resulted from the work discussed in the main body of the thesis.

This page is intentionally left blank.

Appendix B

Appendix B provides details of the existing tall building database discussed in Chapter 4. The database includes buildings in San Francisco above 50 m in height tabulated by name, address (number and street), height, number of stories, year completed, material and lateral resisting system (when known), as well as links to external sources of data such as EMPORIS (www.emporis.com) or the SFPIM (propertymap.sfplanning.org) from the City and County of San Francisco's Planning Department. Building profile pages in EMPORIS can be accessed by clicking on the hyperlinks provided or by searching for the building name and address followed by 'San Francisco' within the EMPORIS website search bar. Relevant building parcel data can be found by searching within the SFPIM database using the SFPIM code provided for each building. Links to external data were last accessed on October 10, 2017.

This page is intentionally left blank.

Building Name	Number	Street	Height (m)	Stories	Year Completed	Material (MAT), Lateral Resisting System (LRS) & External Links (SFPIM & Emporis)
Ritz-Carlton Club and Residences	690	Market	95	24	1889	MAT: Steel; SFPIM: 0311016; Emporis
Mills Building	220	Montgomery	52	10	1892	MAT: Steel; LRS: MF; SFPIM: 0268008; Emporis
Ferry Building	1	Ferry Building	75	12	1898	MAT: Steel; SFPIM: 9900274; Emporis
Central Tower	703	Market	91	21	1898	MAT: Steel; SFPIM: 3706001; Emporis
One Kearny Street Building	1	Kearny	54	12	1902	MAT: Concrete; SFPIM: 0312031; Emporis
The Merchants Exchange	465	California	69	15	1904	MAT: Unknown; SFPIM: 0260015; Emporis
The Westin St. Francis	335	Powell	60	13	1904	MAT: Steel; SFPIM: 0307001; Emporis
Whittel Building	166	Geary	60	16	1907	MAT: Steel; SFPIM: 0309038; Emporis
One Sixth Street	1	6th	57	15	1908	MAT: Steel; SFPIM: 3704078; Emporis
Maxwell Hotel	386	Geary	51	12	1908	MAT: Concrete; SFPIM: 0307007; Emporis
Humbolt Bank Building	785	Market	85	19	1908	MAT: Unknown; SFPIM: 3706048; Emporis
Adam Grant Building	114	Sansome	64	14	1908	MAT: Steel; SFPIM: 0267010; Emporis
209 Post Building	209	Post	55	13	1909	MAT: Steel; SFPIM: 0309001; Emporis
Campton Place Hotel	340	Stockton	53	16	1913	MAT: Concrete; SFPIM: 0294013; Emporis

Building Name	Number	Street	Height (m)	Stories	Year Completed	Material (MAT), Lateral Resisting System (LRS) & External Links (SFPIM & Emporis)
Hobart Building	582	Market	87	21	1914	MAT: Steel; SFPIM: 0291006; Emporis
The Chancellor Hotel	433	Powell	59	15	1914	MAT: Steel; SFPIM: 0296005; Emporis
San Francisco City Hall	1	Carlton B Goodlett	94	4	1915	MAT: Unknown; SFPIM: 0787001; Emporis
115 Sansome Street	115	Sansome	61	13	1915	MAT: Steel; SFPIM: 0268002; Emporis
Southern Pacific Building	1	Market	65	12	1916	MAT: Steel; SFPIM: 3713007; Emporis
300 Montgomery	300	Montgomery	65	12	1917	MAT: Steel; SFPIM: 0260010; Emporis
JH Dollar Building	351	California	73	16	1920	MAT: Steel; SFPIM: 0261010A; Emporis
Commercial Union Assurance Building	315	Montgomery	94	16	1921	MAT: Steel; SFPIM: 0259029; Emporis
Alexander Building	155	Montgomery	60	15	1921	MAT: Steel; SFPIM: 0288001; Emporis
225 Bush Street	225	Bush	100	22	1922	MAT: Steel; LRS: MF; SFPIM: 0289007; Emporis
605 Market Street	605	Market	61	15	1922	MAT: Steel; SFPIM: 3707001; Emporis
Huntington Hotel	1075	California	52	12	1924	MAT: Steel; SFPIM: 0254024; Emporis
PG&E Headquarters	245	Market	78	18	1924	MAT: Steel; LRS: MF; SFPIM: 3711018; Emporis
Kensington Park Hotel	450	Post	62	14	1924	MAT: Unknown; SFPIM: 0296009; Emporis

Building Name	Number	Street	Height (m)	Stories	Year Completed	Material (MAT), Lateral Resisting System (LRS) & External Links (SFPIM & Emporis)
Bank of the Orient Building	233	Sansome	53	13	1924	MAT: Unknown; SFPIM: 0260002; Emporis
Pac Bell Building	140	New Montgomery	133	26	1925	MAT: Steel; LRS: MF; SFPIM: 3722080; Emporis
Serrano Hotel	405	Taylor	56	16	1925	MAT: Steel; SFPIM: 0317003; Emporis
The Mark Hopkins Hotel	999	California	93	20	1926	MAT: Steel; SFPIM: 0255002; Emporis
Omni San Francisco Hotel	500	California	66	15	1926	MAT: Steel; SFPIM: 0240003; Emporis
Clift Hotel	491 to 499	Geary	64	15	1926	MAT: Steel; SFPIM: 0316013; Emporis
Marines' Memorial Club & Hotel	609	Sutter	66	12	1926	MAT: Steel; SFPIM: 0297001 ; Emporis
Crown Tower Apartments	666	Post	55	16	1926	MAT: Steel/RC; SFPIM: 0298C001; Emporis
220 Sansome Street	220	Sansome	66	16	1926	MAT: Steel; SFPIM: 0261007; Emporis
Hunter-Dulin Building	111	Sutter	94	22	1926	MAT: Steel; SFPIM: 0292001; Emporis
1090 Chestnut Co-Op	1090	Chestnut	53	13	1927	MAT: Steel/RC; SFPIM: 0047C001; Emporis
945 Green Street	945	Green	53	14	1927	MAT: Steel/RC; SFPIM: 0127C101; Emporis
Clay-Jones Apartments	1250	Jones	70	21	1927	MAT: Steel; SFPIM: 0221044; Emporis
Russ Building	235	Montgomery	133	32	1927	MAT: Steel/RC; SFPIM: 0269001; Emporis

Building Name	Number	Street	Height (m)	Stories	Year Completed	Material (MAT), Lateral Resisting System (LRS) & External Links (SFPIM & Emporis)
Medico Dental Building	490	Post	64	16	1928	MAT: Steel; SFPIM: 0296015; Emporis
Sir Francis Drake Hotel	450	Powell	96	22	1928	MAT: Steel; SFPIM: 0295008; Emporis
Shell Building	100	Bush	115	29	1929	MAT: Steel; SFPIM: 0267004; Emporis
McAllister Tower Apartments	100	McAllister	94	28	1929	MAT: Unknown; SFPIM: 0348006; Emporis
Hamilton Apartments	631	O'Farrell	64	18	1929	MAT: Steel; SFPIM: 0322A198; Emporis
450 Sutter	450	Sutter	105	26	1929	MAT: Steel; SFPIM: 0285006; Emporis
Cathedral Apartments	1201	California	74	19	1930	MAT: Unknown; SFPIM: 0252C001; Emporis
Bellaire Tower	1101	Green	77	20	1930	MAT: Steel/RC; SFPIM: 0125026; Emporis
Pacific National Bank	333 to 341	Montgomery	93	18	1930	MAT: Steel; Emporis; (Recently Demolished)
Clarion Hotel Cosmo	761	Post	60	16	1930	MAT: Steel; SFPIM: 0304015; Emporis
Pacific Coast Stock Exchange Tower	155	Sansome	60	13	1930	MAT: Steel; SFPIM: 0268001A; Emporis
Mills Tower	220	Bush	92	22	1931	MAT: Steel/RC; SFPIM: 0268006; Emporis
Bureau of Citizenship and Immigration	444	Washington	67	16	1944	MAT: Steel; SFPIM: 0206013; Emporis
1000 Green Apartments	1000	Green	51	16	1950	MAT: Steel; SFPIM: 0121004; Emporis

Building Name	Number	Street	Height (m)	Stories	Year Completed	Material (MAT), Lateral Resisting System (LRS) & External Links (SFPIM & Emporis)
UCSF Medical Center Parnassus	505	Parnassus	77	18	1954	MAT: Unknown; SFPIM: 1757035 ; Emporis
Medical Sciences Building	513	Parnassus	70	17	1954	MAT: Unknown; SFPIM: 1756001 ; Emporis
Equitable Life	120	Montgomery	108	25	1955	MAT: Steel; LRS: MF; SFPIM: 0289005; Emporis
One Bush Plaza	1	Bush	94	20	1959	MAT: Steel; LRS: CBF/EBF & MF; SFPIM: 0290011; Emporis
Industrial Indemnity Building	255	California	70	17	1959	MAT: RC; SFPIM: 0262013; Emporis
Philip Burton Federal Building	450	Golden Gate	95	21	1959	MAT: Unknown; SFPIM: 0764023; Emporis
Bethlehem Steel Company HQ	100	California	52	13	1960	MAT: Steel; SFPIM: 0236017; Emporis
International Building	601	California	107	22	1961	MAT: Steel; SFPIM: 0258032; Emporis
Green Hill Tower	1070	Green	65	21	1961	MAT: Steel; SFPIM: 0121A001; Emporis
The Comstock	1333	Jones	55	16	1961	MAT: Unknown; SFPIM: 0215C001; Emporis
Fairmont Hotel Tower	950	Mason	99	29	1962	MAT: Unknown; SFPIM: 244001; Emporis
Grosvenor Suites	899	Pine	70	20	1962	MAT: Unknown; SFPIM: 0273013; Emporis
66 Cleary Court	66	Cleary	61	18	1963	MAT: RC; SFPIM: 0712115; Emporis
10 Miller	10	Miller	70	22	1963	MAT: RC; SFPIM: 0224034; Emporis

Building Name	Number	Street	Height (m)	Stories	Year Completed	Material (MAT), Lateral Resisting System (LRS) & External Links (SFPIM & Emporis)
Nob Hill Community Apartments	1170	Sacramento	61	19	1963	MAT: Unknown; SFPIM: 0222A001; Emporis
Hartford Building	650	California	142	34	1964	MAT: Steel; LRS: MF; SFPIM: 0241025; Emporis
One Maritime Plaza	300	Clay	121	27	1964	MAT: Steel; LRS: CBF/EBF & MF; SFPIM: 0204021; Emporis
Carillon Tower	1100	Gough	66		1964	MAT: RC; SFPIM: 0720037; Emporis
555 Market Street	555	Market	95	22	1964	MAT: Unknown; SFPIM: 3708057; Emporis
Pacific Heights Towers	2200	Sacramento	65	20	1964	MAT: Steel; SFPIM: 0627A001; Emporis
Macondray House	405	Davis	80	25	1965	MAT: RC/Steel; LRS: Wall/MF; SFPIM: 0199022; Emporis
Golden Gateway Center 4	440	Davis	67	22	1965	MAT: RC; SFPIM: 0200014; Emporis
Cathedral Hill Tower	1200	Gough	91	27	1965	MAT: Unknown; SFPIM: 0713035; Emporis
The Summit	999	Green	96	32	1965	MAT: RC; SFPIM: 0127029; Emporis
Buckelew House	155	Jackson	80	25	1965	MAT: RC; SFPIM: 0199022; Emporis
111 Pine Street	111	Pine	76	19	1965	MAT: RC; LRS: Wall; SFPIM: 0266001; Emporis
Royal Towers	1750	Taylor	101	29	1965	MAT: Unknown; SFPIM: 0128C001; Emporis
Archstone Fox Plaza	1390	Market	108	29	1966	MAT: Unknown; SFPIM: 0813008; Emporis

Building Name	Number	Street	Height (m)	Stories	Year Completed	Material (MAT), Lateral Resisting System (LRS) & External Links (SFPIM & Emporis)
Beal Bank Building	180	Sansome	76	17	1966	MAT: Steel; LRS: MF; SFPIM: 0267016; Emporis
Golden Gateway Center 1	550	Battery	67	22	1967	MAT: RC; SFPIM: 0198008; Emporis
Bechtel Building	50	Beale	100	23	1967	MAT: Steel; LRS: MF; SFPIM: 3710018; Emporis
Bank of California Building	400	California	95	22	1967	MAT: Steel; SFPIM: 0239003; Emporis
44 Montgomery	44	Montgomery	172	43	1967	MAT: Steel; LRS: MF; SFPIM: 0291012; Emporis
Fontana West	1050	North Point	80	18	1967	MAT: Unknown; SFPIM: 0451133; Emporis
Fontana East	1000	North Point	80	18	1967	MAT: Unknown; SFPIM: 0451007; Emporis
PacBell - Pine Street Building	555	Pine	88	16	1967	MAT: RC; LRS: Wall; SFPIM: 0270039; Emporis
Insurance Center Building	450	Sansome	93	19	1967	MAT: Steel; SFPIM: 0229018; Emporis
425 California Street	425	California	109	26	1968	MAT: Steel; LRS: MF; SFPIM: 0260001; Emporis
555 California Street	555	California	237	52	1969	MAT: Steel; LRS: MF; SFPIM: 0259026; Emporis
One California	1	California	134	32	1969	MAT: Steel; SFPIM: 0264004; Emporis
The Sequoias	1400	Geary	80	25	1969	MAT: Unknown; SFPIM: 0697039; Emporis
McKesson Plaza	1	Post	161	38	1969	MAT: Steel; LRS: MF; SFPIM: 0311015; Emporis

Building Name	Number	Street	Height (m)	Stories	Year Completed	Material (MAT), Lateral Resisting System (LRS) & External Links (SFPIM & Emporis)
Donatello Hotel	501	Post	54	15	1969	MAT: Unknown; SFPIM: 0306026; Emporis
Pacific Gas & Electric Building	77	Beale	150	34	1971	MAT: Steel; LRS: MF; SFPIM: 3711010; Emporis
One Embarcadero Center	355	Clay	173	45	1971	MAT: Steel; LRS: MF; SFPIM: 0230028; Emporis
Hilton Financial District	750	Kearny	111	30	1971	MAT: RC; SFPIM: 0208024; Emporis
Hilton San Francisco	333	O'Farrell	150	46	1971	MAT: Steel; LRS: MF; SFPIM: 0325031; Emporis
475 Sansome Street	475	Sansome	86	21	1971	MAT: Steel; LRS: Wall; SFPIM: 0228039; Emporis
50 California Street	50	California	148	37	1972	MAT: Steel; SFPIM: 0235022; Emporis
Transamerica Pyramid	600	Montgomery	260	48	1972	MAT: Steel; LRS: Wall; SFPIM: 0207032; Emporis
100 Pine Center	100	Pine	145	33	1972	MAT: Steel; LRS: Wall; SFPIM: 0262020; Emporis
The Westin St. Francis	335	Powell	120	32	1972	MAT: Steel; SFPIM: 0307001; Emporis
Grand Hyatt San Francisco	345	Stockton	108	35	1972	MAT: RC; SFPIM: 0295016; Emporis
San Francisco Marriott Union Square	480	Sutter	95	29	1972	MAT: Unknown; SFPIM: 0285020; Emporis
Holiday Inn/Golden Gateway Hotel	1500	Van Ness	88	26	1972	MAT: Unknown; SFPIM: 0646016; Emporis
Hyatt Regency	5	Embarcadero	85	20	1973	MAT: Unknown; SFPIM: 0234017; Emporis

Building Name	Number	Street	Height (m)	Stories	Year Completed	Material (MAT), Lateral Resisting System (LRS) & External Links (SFPIM & Emporis)
211 Main Street	211	Main	67	17	1973	MAT: Steel; LRS: MF; SFPIM: 3740033; Emporis
First Market Tower	525	Market	161	39	1973	MAT: Steel; LRS: MF; SFPIM: 3708056; Emporis
425 Market Street	425	Market	160	38	1973	MAT: Steel; LRS: MF; SFPIM: 3709014; Emporis
Twelve Hundred California	1200	California	88	27	1974	MAT: Unknown; SFPIM: 0247C002; Emporis
Two Embarcadero Center	255	Clay	126	30	1974	MAT: Steel; LRS: MF; SFPIM: 0231023; Emporis
221 Main Street	221	Main	64	16	1974	MAT: Steel; LRS: MF; SFPIM: 3740034; Emporis
California Automobile Association	100	Van Ness	122	29	1974	MAT: Steel; LRS: MF; SFPIM: 0814020; Emporis
Chevron Tower	575	Market	175	40	1975	MAT: Steel; LRS: MF; SFPIM: 3708058; Emporis
Hinode Tower	1615	Sutter	55	15	1975	MAT: RC; SFPIM: 0687036; Emporis
Spear Tower	1	Market	172	43	1976	MAT: Steel; LRS: MF; SFPIM: 3713007; Emporis
Steuart Tower	1	Market	111	27	1976	MAT: Steel; LRS: MF; SFPIM: 3713007; Emporis
California Building	350	California	99	23	1977	MAT: Unknown; SFPIM: 0238008; Emporis
Three Embarcadero Center	155	Clay	126	31	1977	MAT: Steel; LRS: MF; SFPIM: 0232016; Emporis
Bank of America Computer Center	1455	Market	88	21	1977	MAT: Unknown; SFPIM: 3507040; Emporis

Building Name	Number	Street	Height (m)	Stories	Year Completed	Material (MAT), Lateral Resisting System (LRS) & External Links (SFPIM & Emporis)
1275 Market Street	1275	Market	81	17	1977	MAT: Unknown; SFPIM: 3701065; Emporis
Gramercy Towers	1177	California	61	17	1978	MAT: RC; SFPIM: 0253A001; Emporis
45 Fremont Center	45	Fremont	145	34	1978	MAT: Steel; LRS: MF; SFPIM: 3710019; Emporis
601 Montgomery Street	601	Montgomery	77	20	1978	MAT: RC; SFPIM: 0208026; Emporis
Shaklee Terraces	444	Market	164	38	1979	MAT: Steel; LRS: MF; SFPIM: 0266009; Emporis
333 Market Street	333	Market	144	33	1979	MAT: Steel; LRS: MF; SFPIM: 3710020; Emporis
595 Market Street	595	Market	125	30	1979	MAT: Steel; LRS: MF; SFPIM: 3708059; Emporis
180 Montgomery Street	180	Montgomery	98	24	1979	MAT: Unknown; SFPIM: 0289009; Emporis
The Pacific Center	22	4th	67	17	1980	MAT: Unknown; SFPIM: 3705Z003; Emporis
201 California	201	California	72	17	1980	MAT: Steel; LRS: MF; SFPIM: 0262021; Emporis
Two Transamerica Center	505	Sansome	80	20	1980	MAT: Steel; LRS: MF; SFPIM: 0207037; Emporis
Providian Financial Building	201	Mission	127	30	1981	MAT: RC/Steel; LRS: Wall/MF; SFPIM: 3718026; Emporis
101 California Street	101	California	183	48	1982	MAT: Steel; LRS: MF; SFPIM: 0263011; Emporis
Four Embarcadero Center	55	Clay	174	45	1982	MAT: RC/Steel; LRS: Wall/MF; SFPIM: 0233/044; Emporis

Building Name	Number	Street	Height (m)	Stories	Year Completed	Material (MAT), Lateral Resisting System (LRS) & External Links (SFPIM & Emporis)
Telesis Tower	1	Montgomery	152	38	1982	MAT: Steel; LRS: MF; SFPIM: 0292002; Emporis
353 Sacramento	353	Sacramento	95	23	1982	MAT: Unknown; SFPIM: 0237014; Emporis
150 Spear	150	Spear	79	18	1982	MAT: Unknown; SFPIM: 3717021; Emporis
1 Ecker Square	1	Ecker	85	18	1983	MAT: Steel; LRS: MF; SFPIM: 3708097; Emporis
Montgomery Washington Tower	655	Montgomery	91	26	1983	MAT: Unknown; SFPIM: 0208028; Emporis
100 Spear Street	100	Spear	83	22	1983	MAT: Steel; LRS: MF; SFPIM: 3717001; Emporis
Westin San Francisco	50	3rd	114	34	1984	MAT: Unknown; SFPIM: 3706074; Emporis
Renaissance Parc 55 Hotel	55	Cyril Magnin	107	32	1984	MAT: RC; SFPIM: 0330026; Emporis
101 Montgomery	101	Montgomery	123	28	1984	MAT: Steel; LRS: MF; SFPIM: 0288031; Emporis
Bank of Canton	555	Montgomery	86	18	1984	MAT: Unknown; SFPIM: 0227048; Emporis
One Sansome Street	1	Sansome	168	43	1984	MAT: Steel; LRS: MF; SFPIM: 0289004; Emporis
50 Fremont Center	50	Fremont	183	43	1985	MAT: Steel; LRS: MF; SFPIM: 3709019; Emporis
456 Montgomery Street	456	Montgomery	115	26	1985	MAT: Unknown; SFPIM: 0239013; Emporis
160 Spear	160	Spear	78	19	1985	MAT: Steel; SFPIM: 3717010; Emporis

Building Name	Number	Street	Height (m)	Stories	Year Completed	Material (MAT), Lateral Resisting System (LRS) & External Links (SFPIM & Emporis)
Spear Street Terrace	201	Spear	75	18	1985	MAT: Unknown; SFPIM: 3741032; Emporis
333 Bush Street	333	Bush	151	43	1986	MAT: Steel; LRS: MF; SFPIM: 0288033; Emporis
345 California Center	345	California	212	48	1986	MAT: Steel; LRS: MF; SFPIM: 0261019; Emporis
301 Howard Street	301	Howard	92	23	1986	MAT: Steel; LRS: MF; SFPIM: 3738011; Emporis
88 Kearny Street	88	Kearny	94	22	1986	MAT: RC; SFPIM: 0311009; Emporis
135 Main Street	135	Main	90	23	1986	MAT: Steel; SFPIM: 3717012; Emporis
123 Mission Street	123	Mission	124	29	1986	MAT: Unknown; SFPIM: 3717022; Emporis
Continental Center	250	Montgomery	69	17	1986	MAT: Unknown; SFPIM: 0268017; Emporis
33 New Montgomery	33	New Montgomery	65	20	1986	MAT: RC/Steel; LRS: Wall/MF; SFPIM: 3707062; Emporis
90 New Montgomery	90	New Montgomery	65	15	1986	MAT: Unknown; SFPIM: 3707016; Emporis
580 California	580	California	107	23	1987	MAT: RC/Steel; LRS: Wall/MF; SFPIM: 0240007; Emporis
Hawthorne Plaza	75	Hawthorne	85	20	1987	MAT: Unknown; SFPIM: 3735062; Emporis
Central Plaza	455	Market	97	23	1987	MAT: Steel; SFPIM: 3709012; Emporis
388 Market	388	Market	94	24	1987	MAT: Steel; SFPIM: 0265003; Emporis

Building Name	Number	Street	Height (m)	Stories	Year Completed	Material (MAT), Lateral Resisting System (LRS) & External Links (SFPIM & Emporis)
Hotel Nikko	222	Mason	90	28	1987	MAT: Unknown; SFPIM: 0326011; Emporis
JW Marriott Hotel	500	Post	70	20	1987	MAT: Unknown; SFPIM: 0297028; Emporis
Stevenson Place	71	Stevenson	103	28	1987	MAT: Unknown; SFPIM: 3708028; Emporis
Le Meridien San Francisco	333	Battery	80	25	1988	MAT: Steel; SFPIM: 0229020; Emporis
100 First Plaza	100	First	136	27	1988	MAT: Unknown; SFPIM: 3721001; Emporis
505 Montgomery	505	Montgomery	100	24	1988	MAT: Steel; SFPIM: 0227007; Emporis
49 Stevenson Street	49	Stevenson	61	15	1988	MAT: RC; SFPIM: 3708040; Emporis
San Francisco Marriott	55	4th	133	39	1989	MAT: Steel; LRS: MF; SFPIM: 3706096; Emporis
Embarcadero West	275	Battery	123	34	1989	MAT: Steel; LRS: MF; SFPIM: 0238001; Emporis
One Daniel Burnham Court West	1	Daniel Burnham	62	18	1989	MAT: RC/Steel; LRS: Wall/MF; SFPIM: 0690037; Emporis
88 Howard Street	88	Howard	95	24	1989	MAT: Unknown; SFPIM: 3716021; Emporis
Fillmore Center Towe 1	1755	O'farrell	64	20	1989	MAT: Unknown; SFPIM: 0726/021; Emporis
101 Spear Street	101	Spear	95	24	1989	MAT: Unknown; SFPIM: 3716021; Emporis
Hills Plaza	345	Spear	75	19	1989	MAT: Steel/RC; SFPIM: 3744003; Emporis

Building Name	Number	Street	Height (m)	Stories	Year Completed	Material (MAT), Lateral Resisting System (LRS) & External Links (SFPIM & Emporis)
235 Pine Street	235	Pine	110	26	1990	MAT: Unknown; SFPIM: 0267015; Emporis
600 California Street	600	California	85	22	1992	MAT: Steel; SFPIM: 0241027; Emporis
Post International	1377	Post	60	14	1993	MAT: Unknown; SFPIM: 0696025; Emporis
PacBell Central	611	Folsom	80	20	1995	MAT: Steel; LRS: MF; SFPIM: 3750087; Emporis
San Francisco Towers	1661	Pine	53	13	1997	MAT: Unknown; SFPIM: 0666030; Emporis
101 Second Street	101	2nd	108	26	1999	MAT: Steel; SFPIM: 3721089; Emporis
Second Street Towers	246	2nd	58	17	1999	MAT: RC; LRS: Wall/MF SFPIM: 3735065; Emporis
W Hotel	181	3rd	96	33	1999	MAT: RC; SFPIM: 3722081; Emporis
Avalon Towers North	388	Beale	76	20	1999	MAT: RC; LRS: Wall/MF SFPIM: 3747092; Emporis
Avalon Towers South	388	Beale	76	20	1999	MAT: RC; LRS: Wall/MF SFPIM: 3747092; Emporis
150 California	150	California	101	24	2000	MAT: Steel; LRS: CBF/EBF & MF; SFPIM: 0236019; Emporis
199 Fremont Street	199	Fremont	111	27	2000	MAT: Steel; LRS: CBF/EBF & MF; SFPIM: 3719018; Emporis
Hiram W. Johnson Building	455	Golden Gate	58	14	2000	MAT: Unknown; SFPIM: 0765003; Emporis
Courtyard San Francisco Downtown	299	2nd	62	18	2001	MAT: RC; LRS: Wall; SFPIM: 3736029; Emporis

Building Name	Number	Street	Height (m)	Stories	Year Completed	Material (MAT), Lateral Resisting System (LRS) & External Links (SFPIM & Emporis)
The Brannan, Tower 1	229	Brannan	65	18	2001	MAT: RC; LRS: MF; SFPIM: 3789518; Emporis
The Brannan, Tower 2	219	Brannan	65	18	2001	MAT: RC; LRS: MF; SFPIM: 3789518; Emporis
Gap Building	2	Folsom	84	14	2001	MAT: RC/Steel; LRS: Wall/MF; SFPIM: 3741035; Emporis
Four Seasons Hotel	757 or 735	Market	121	40	2001	MAT: Steel; LRS: CBF/EBF & MF; SFPIM: 3706096; Emporis
55 Second Street	55	2nd	101	25	2002	MAT: Steel; LRS: MF; SFPIM: 3708096; Emporis
BridgeView	400	Beale	87	26	2002	MAT: RC; LRS: Wall/MF; SFPIM: 3766012; Emporis
The Brannan, Tower 3	239	Brannan	66	18	2002	MAT: RC; LRS: MF; SFPIM: 3789518; Emporis
JPMorgan Chase Building	560	Mission	128	31	2002	MAT: Steel; SFPIM: 3708095; Emporis
The Paramount	680	Mission	128	40	2002	MAT: Pre-cast RC; SFPIM: 3707063; Emporis
The Beacon West	260	King	57	16	2003	MAT: RC; LRS: Wall/MF; SFPIM: 8702011; Emporis
Avalon at Mission Bay	255	King	58	17	2003	MAT: RC; LRS: Wall; SFPIM: 8702011; Emporis
The Metropolitan I	355	1st	81	26	2004	MAT: Unknown; SFPIM: 3748033; Emporis
The Metropolitan II	333	1st	66	21	2004	MAT: Unknown; SFPIM: 3748033; Emporis
St. Regis San Francisco	125	3rd	148	42	2005	MAT: RC; SFPIM: 3722257; Emporis

Building Name	Number	Street	Height (m)	Stories	Year Completed	Material (MAT), Lateral Resisting System (LRS) & External Links (SFPIM & Emporis)
International Hotel and St. Mary Catholic Center	848	Kearny	59	15	2005	MAT: RC; SFPIM: 0195019; Emporis
The Watermark	501	Beale	73	22	2006	MAT: RC; SFPIM: 3771004; Emporis
Avalon at Mission Bay, Phase 2, Bldg A	301	King	58	17	2006	MAT: RC; LRS: Wall; SFPIM: 8705011; Emporis
San Francisco Federal Building	90	7th	71	18	2007	MAT: Unknown; SFPIM: 3702055; Emporis
SoMa Grand	1160	Mission	71	23	2007	MAT: RC; SFPIM: 3702058; Emporis
One Rincon Hill, South	425	1st	184	54	2008	MAT: RC; LRS: Wall; SFPIM: 3765023; Emporis
Arterra	300	Berry	55	16	2008	MAT: RC; SFPIM: 8704008; Emporis
InterContinental San Francisco	868	Howard	104	32	2008	MAT: RC; SFPIM: 3724/072; Emporis
555 Mission Street	555	Mission	140	33	2008	MAT: Steel; LRS: MF; SFPIM: 3721120; Emporis
Argenta	1	Polk	68	20	2008	MAT: RC; LRS: Wall; SFPIM: 0814022; Emporis
The Infinity, Phase 1	301	Main Street	107	37	2008	MAT: Unknown; SFPIM: 3745012; Emporis
Millennium Tower	301	Mission	197	58	2009	MAT: RC; LRS: Wall/MF; SFPIM: 3719020; Emporis
The Infinity, Phase II	300	Spear	137	41	2009	MAT: RC; LRS: Wall; SFPIM: 3745012; Emporis
Health Sciences West	513	Parnassus	64	16	N/A	MAT: RC; LRS: Wall; SFPIM: 1757035; Emporis

Building Name	Number	Street	Height (m)	Stories	Year Completed	Material (MAT), Lateral Resisting System (LRS) & External Links (SFPIM & Emporis)
Health Sciences East	513	Parnassus	64	16	N/A	MAT: Unknown; SFPIM: 1757035; Emporis
Fillmore Center, Tower 2	1510	Eddy	55	18	N/A	MAT: Unknown; SFPIM: 0731018; Emporis
680 Folsom	680	Folsom	52	13	N/A	MAT: Steel; LRS: MF; SFPIM: 3735013; Emporis
Crede Ambulatory Care	400	Parnassus	62	16	N/A	MAT: Unknown; SFPIM: 1756001; Emporis

RC: Reinforced Concrete
MF: Moment Frame
EBF: Eccentrically Braced Frame
CBF: Concentrically Braced Frame

This page is intentionally left blank.

Appendix C

Appendix C provides a breakdown of the components included in the building performance models utilized throughout this thesis as described in Chapter 4. Components are tabulated for the building performance models listed below in sub-sections C1 to C5. The assumed building cost, based on gross square footage, as described in Section 4.3, is noted below in parenthesis for each archetype building, where M denotes millions of USD.

C1. 20-storey UBC 1973 Archetype Building ($70M)
C2. 40-storey UBC 1973 Archetype Building ($140M)
C3. 40-storey UBC 1973 Archetype Building (Enhanced Components) ($140M)
C4. 50-storey UBC 1973 Archetype Building ($465M)
C5. 50-storey IBC 2012 Archetype Building ($465M)

The information presented in these tables is easiest to interpret after revisiting section 4.3 of this thesis. The tables provided summarize the following information: Tracking, Fragility Number, Category, Description, Source, Engineering Demand Parameter (EDP), Quantity (Qty.), Units and Distribution on one side of each page; and Tracking, Fragility Number, Number of Damage States (NDS), Damage State Sequences (including sequential 'Seq' and/or mutually exclusive 'MutEx' damages states) + Damage State data for all damage states (DS_i) in each component, including Median (μ), Dispersion (β), Mean Repair Cost (MRC), Mean Repair Time (MRT), Long lead time (LL) and Repair Sequence on the reverse side of the page. The 'Tracking' column is intended for easy cross referencing and reading of the tables as they list components within each building performance model considered. The 'Fragility Number' column provides a unique code for each component type as outlined in FEMA (2012). The 'Category' column classifies components into different groups. The 'Description' column provides a summary of each component. The 'Source' column provides the authors whose worked was used to develop each component. The 'EDP' column denotes the demand parameters that are used to predict damage in each component. The 'Qty.' column indicates the total amount of fragility units considered within each building performance model, e.g. if a particular fragility represents 1000 linear feet of partition wall and there are 20000 ft of partition walls in the building, the 'Qty.' for that particular component is 20. The 'Units' column describes the measure of each component, e.g. 1000 linear feet in the previous example. The 'Distribution' column describes how the total 'Qty.' of each component is distributed throughout the building, e.g. large MEP components are distributed within the MEP floors of a building. The 'NDS' column indicates the number of possible damage states for each component. The 'DS Sequence +

DSi' column provide the sequence of component damage with increasing EDP, and relevant damage state data for each damage state including: μ, β, MRC, MRT, RC. The 'μ' and 'β' terms denote the median and dispersion associated with the cumulative probability distribution that defines each fragility. The tabulated fragilities are dimensionless for components whose EDP is IDR or residual IDR, and units of g for components whose EDP PFA. The 'MRC' and 'MRT' terms denote the mean repair cost and time associated with the corresponding damage state in the component in units of USD and worker days, respectively. The 'RC' term denotes the repair class associated with each damage state for each component. The 'LL' column indicates long lead delays associated with the replacement of the component in days. The 'Repair Sequence' column indicates the sequence of repairs that each component contributes to within the downtime calculation.

For the 40- and 20-storey buildings, the quantity of drift sensitive components in each storey level is subdivided in the X and Y directions proportionally to the overall building length in each direction with respect to the overall perimeter (rectangular floor plan). For the 50-storey buildings, the quantity of drift sensitive components in each storey level is split equally in the X and Y directions (square floor plan).

For components in the building performance model for the 40-storey UBC 1973 archetype building with enhanced components, those components considered as enhanced with respect to the baseline building are shown underlined in the 'Fragility Number' column.

Tracking	Fragility Number	Category	Description	Source	EDP	Qty.	Units	Distribution
20-storey UBC-1	B1031.011c	Structure	Steel Column Base Plates, Column W > 300 plf	Deierlein and Victorsson (2008)	IDR	26	Each	Per Structural Configuration
20-storey UBC-2	B1031.021b	Structure	Welded column splices, Column 150 plf < W < 300 plf	Deierlein and Victorsson (2008)	IDR	56	Each	Per Structural Configuration
20-storey UBC-3	B1031.021c	Structure	Welded column splices, Column W > 300 plf	Deierlein and Victorsson (2008)	IDR	113	Each	Per Structural Configuration
20-storey UBC-4	B1035.041	Structure	Pre-Northridge WUF-B beam-column joint, beam one side of column, beam depth <= W27	Deierlein and Victorsson (2008)	IDR	120	Each	Per Structural Configuration
20-storey UBC-5	B1035.042	Structure	Pre-Northridge WUF-B beam-column joint, beam one side of column, beam depth >= W30	Deierlein and Victorsson (2008)	IDR	258	Each	Per Structural Configuration
20-storey UBC-6	B1035.051	Structure	Pre-Northridge WUF-B beam-column joint, beam both sides of column, beam depth <= W27	Deierlein and Victorsson (2008)	IDR	440	Each	Per Structural Configuration
20-storey UBC-7	B1035.052	Structure	Pre-Northridge WUF-B beam-column joint, beam both sides of column, beam depth >= W30	Deierlein and Victorsson (2008)	IDR	736	Each	Per Structural Configuration
20-storey UBC-8	C1011.001a	Fitout	Wall Partition, Type: Gypsum with metal studs, Full Height, Fixed Below, Fixed Above	Miranda and Mosqueda (2011)	IDR	183	13'x100' Panels	Office Levels
20-storey UBC-9	C3011.001a	Fitout	Wall Partition, Type: Gypsum + Wallpaper, Full Height, Fixed Below, Fixed Above	Miranda and Mosqueda (2011)	IDR	14	9'x100' Panels	Office Levels
20-storey UBC-10	C3027.001	Fitout	Raised Access Floor, non-seismically rated.	Eidinger (2009)	PFA	1368	100 SF	Office Levels
20-storey UBC-11	C3032.001b	Fitout	Suspended Ceiling, SDC A,B,C, Area (A): 250 < A < 1000, Vert support only	Bachman (2011)	PFA	274	600 SF	Office Levels

See reverse.

Tracking	Fragility Number	NDS	DS Sequence + DSi (μ, β, MRC, MRT, RC)	LL	Repair Sequence
20-storey UBC-1	B1031.011c	4	Seq(MutEx(DS1,DS2),DS3,DS4) + DS1(0.04, 0.4, 0, 0, 3) + DS2(0.04, 0.4, 21363, 14, 3) + DS3(0.07, 0.4, 32566, 21, 3) + DS4(0.1, 0.4, 41889, 27, 3)		Structure
20-storey UBC-2	B1031.021b	3	Seq(MutEx(DS1,DS2),DS3) + DS1(0.02, 0.4, 0, 0, 3) + DS2(0.02, 0.4, 10245, 7, 3) + DS3(0.05, 0.4, 13012, 9, 3)		Structure
20-storey UBC-3	B1031.021c	3	Seq(MutEx(DS1,DS2),DS3) + DS1(0.02, 0.4, 0, 0, 3) + DS2(0.02, 0.4, 11445, 7, 3) + DS3(0.05, 0.4, 14812, 10, 3)		Structure
20-storey UBC-4	B1035.041	5	Seq(MutEx(DS1,DS2),MutEx(DS3,DS4),DS5) + DS1(0.017, 0.4, 11979, 7, 3) + DS2(0.017, 0.4, 13646, 8, 3) + DS3(0.025, 0.4, 16860, 10, 3) + DS4(0.025, 0.4, 17676, 10, 3) + DS5(0.03, 0.4, 14260, 8, 3)		Structure
20-storey UBC-5	B1035.042	5	Seq(MutEx(DS1,DS2),MutEx(DS3,DS4),DS5) + DS1(0.017, 0.4, 12313, 7, 3) + DS2(0.017, 0.4, 14313, 8, 3) + DS3(0.025, 0.4, 17646, 10, 3) + DS4(0.025, 0.4, 17676, 10, 3) + DS5(0.03, 0.4, 14260, 8, 3)		Structure
20-storey UBC-6	B1035.051	5	Seq(MutEx(DS1,DS2),MutEx(DS3,DS4),DS5) + DS1(0.017, 0.4, 16653, 10, 3) + DS2(0.017, 0.4, 18319, 11, 3) + DS3(0.025, 0.4, 23353, 14, 3) + DS4(0.025, 0.4, 23559, 14, 3) + DS5(0.03, 0.4, 18286, 11, 3)		Structure
20-storey UBC-7	B1035.052	5	Seq(MutEx(DS1,DS2),MutEx(DS3,DS4),DS5) + DS1(0.017, 0.4, 16653, 10, 3) + DS2(0.017, 0.4, 18319, 11, 3) + DS3(0.025, 0.4, 22019, 12, 3) + DS4(0.025, 0.4, 24226, 14.18, 3) + DS5(0.03, 0.4, 19826, 14, 3)		Structure
20-storey UBC-8	C1011.001a	3	Seq(DS1,DS2,DS3) + DS1(0.005, 0.4, 1966, 2, 1) + DS2(0.01, 0.3, 4297, 3, 1) + DS3(0.021, 0.2, 8990, 7, 3)		A
20-storey UBC-9	C3011.001a	1	Seq(DS1) + DS1(0.0021, 0.6, 2828, 2, 1)		A
20-storey UBC-10	C3027.001	1	Seq(DS1) + DS1(0.5, 0.5, 121, 0.1, 2)		A
20-storey UBC-11	C3032.001b	3	Seq(DS1,DS2,DS3) + DS1(1.01, 0.25, 849, 0.8, 1) + DS2(1.45, 0.25, 6631, 6, 3) + DS3(1.69, 0.25, 14322, 13, 3)		A

Continues on next page.

Tracking	Fragility Number	Category	Description	Source	EDP	Qty.	Units	Distribution
20-storey UBC-12	C3034.001	Fitout	Independent Pendant Lighting - non seismic	Eidinger (2009)	PFA	3096	Each	Office Levels
20-storey UBC-13	D2022.011a	MEP	Heating hot Water Piping - Small Diameter Threaded Steel - (2.5 inches in diameter or less), SDC A or B, PIPING FRAGILITY	Bachman (2012)	PFA	19	1000 ft Segments	All Levels
20-storey UBC-14	D2021.011a	MEP	Cold or Hot Potable - Small Diameter Threaded Steel - (2.5 inches in diameter or less), SDC A or B, PIPING FRAGILITY	Bachman (2012)	PFA	3	1000 ft Segments	All Levels
20-storey UBC-15	D2022.011b	MEP	Heating hot Water Piping - Small Diameter Threaded Steel - (2.5 inches in diameter or less), SDC A or B, BRACING FRAGILITY	Bachman (2012)	PFA	19	1000 ft Segments	All Levels
20-storey UBC-16	D2022.021a	MEP	Heating hot Water Piping - Large Diameter Welded Steel - (greater than 2.5 inches in diameter), SDC A or B, PIPING FRAGILITY	Bachman (2012)	PFA	7	1000 ft Segments	All Levels
20-storey UBC-17	D2031.021a	MEP	Sanitary Waste Piping - Cast Iron w/bell and spigot couplings, SDC A,B, PIPING FRAGILITY	Bachman (2012)	PFA	12	1000 ft Segments	All Levels
20-storey UBC-18	D2031.021b	MEP	Sanitary Waste Piping - Cast Iron w/bell and spigot couplings, SDC A,B, BRACING FRAGILITY	Bachman (2012)	PFA	12	1000 ft Segments	All Levels
20-storey UBC-19	D3041.011a	MEP	HVAC Galvanized Sheet Metal Ducting less than 6 sq. ft in cross sectional area, SDC A or B	Bachman (2012)	PFA	16	1000 ft Segments	All Levels

See reverse.

Tracking	Fragility Number	NDS	DS Sequence + DSi (μ, β, MRC, MRT, RC)	LL	Repair Sequence
20-storey UBC-12	C3034.001	1	Seq(DS1) + DS1(0.6, 0.4, 483, 0.001, 3)		A
20-storey UBC-13	D2022.011a	2	Seq(DS1,DS2) + DS1(0.55, 0.4, 278, 0.3, 2) + DS2(1.1, 0.4, 2596, 0.3, 3)		A
20-storey UBC-14	D2021.011a	2	Seq(DS1,DS2) + DS1(1.5, 0.4, 278, 0.3, 2) + DS2(2.6, 0.4, 2596, 0.3, 3)		A
20-storey UBC-15	D2022.011b	2	Seq(DS1,DS2) + DS1(1.2, 0.4, 382, 0.4, 3) + DS2(2.4, 0.4, 3873, 0.4, 3)		A
20-storey UBC-16	D2022.021a	2	Seq(DS1,DS2) + DS1(1.5, 0.4, 348, 0.4, 2) + DS2(2.6, 0.4, 3212, 3, 3)		A
20-storey UBC-17	D2031.021a	1	Seq(DS1) + DS1(2.25, 0.4, 3166, 3.5, 2)		A
20-storey UBC-18	D2031.021b	2	Seq(DS1,DS2) + DS1(1.2, 0.4, 423, 0.4, 3) + DS2(2.4, 0.4, 3499, 4.6, 3)		A
20-storey UBC-19	D3041.011a	2	Seq(DS1,DS2) + DS1(1.5, 0.4, 680, 0.8, 3) + DS2(2.25, 0.4, 6464, 2, 3)		A

Continues on next page.

Tracking	Fragility Number	Category	Description	Source	EDP	Qty.	Units	Distribution
20-storey UBC-20	D3041.012a	MEP	HVAC Galvanized Sheet Metal Ducting - 6 sq. ft cross sectional area or greater, SDC A or B	Bachman (2012)	PFA	4	1000 ft Segments	All Levels
20-storey UBC-21	D3041.031a	MEP	HVAC Drops / Diffusers in suspended ceilings - No independent safety wires, SDC A or B	Bachman (2012)	PFA	186	10 Units	All Levels
20-storey UBC-22	D3041.041a	MEP	Variable Air Volume (VAV) box with in-line coil, SDC A or B	Bachman (2012)	PFA	145	10 Units	All Levels
20-storey UBC-23	D4011.021a	MEP	Fire Sprinkler Water Piping - Horizontal Mains and Branches - Old Style Victaulic - Thin Wall Steel - No bracing, SDC A or B, PIPING FRAGILITY	Bachman (2012)	PFA	42	1000 ft Segments	All Levels
20-storey UBC-24	D4011.031a	MEP	Fire Sprinkler Drop Standard Threaded Steel - Dropping into unbraced lay-in tile SOFT ceiling - 6 ft. long drop maximum, SDC A or B	Bachman (2012)	PFA	19	100 Units	All Levels
20-storey UBC-25	C2011.001b	Egress	Prefabricated steel stair with steel treads and landings with no seismic joint.	Higgings (2011)	IDR	22	Each	All Levels
20-storey UBC-26	D5012.021a	MEP	Low Voltage Switchgear - Capacity: 100 to <350 Amp - Unanchored equipment that is not vibration isolated - Equipment fragility only	Porter (2011)	PFA	22	Each (225 Amp Unit)	All Levels
20-storey UBC-27	D3031.011c	MEP	Chiller - Capacity: 350 to <750 Ton - Unanchored equipment that is not vibration isolated - Equipment fragility only	Porter (2011)	PFA	1	Each (500 Ton Unit)	MEP Levels

See reverse.

Tracking	Fragility Number	NDS	DS Sequence + DSi (μ, β, MRC, MRT, RC)	LL	Repair Sequence
20-storey UBC-20	D3041.012a	2	Seq(DS1,DS2) + DS1(1.5, 0.4, 996, 1.1, 3) + DS2(2.25, 0.4, 8004, 2.8, 3)		A
20-storey UBC-21	D3041.031a	1	Seq(DS1) + DS1(1.3, 0.4, 2833, 3, 3)		A
20-storey UBC-22	D3041.041a	1	Seq(DS1) + DS1(1.9, 0.4, 14795, 17, 2)		A
20-storey UBC-23	D4011.021a	2	Seq(DS1,DS2) + DS1(1.1, 0.4, 348, 0.4, 2) + DS2(2.4, 0.5, 2596, 0.6, 3)		A
20-storey UBC-24	D4011.031a	2	Seq(DS1,DS2) + DS1(0.75, 0.4, 526, 0.2, 2) + DS2(0.95, 0.4, 526, 0.6, 3)		A
20-storey UBC-25	C2011.001b	3	Seq(DS1,DS2,DS3) + DS1(0.005, 0.6, 393, 0.4, 1) + DS2(0.017, 0.6, 2710, 3, 3) + DS3(0.028, 0.45, 20016, 22, 3)		F
20-storey UBC-26	D5012.021a	1	Seq(DS1) + DS1(1.28, 0.4, 9706, 2, 2)		D
20-storey UBC-27	D3031.011c	1	Seq(DS1) + DS1(0.2, 0.4, 263966, 26, 2)	42	C

Continues on next page.

Tracking	Fragility Number	Category	Description	Source	EDP	Qty.	Units	Distribution
20-storey UBC-28	D3031.021c	MEP	Cooling Tower - Capacity: 350 to <750 Ton - Unanchored equipment that is not vibration isolated - Equipment fragility only	Porter (2011)	PFA	1	Each (500 Ton Unit)	MEP Levels
20-storey UBC-29	D3052.011d	MEP	Air Handling Unit - Capacity: 25000 to <40000 CFM - Unanchored equipment that is not vibration isolated - Equipment fragility only	Porter (2011)	PFA	7	Each (30000 CFM Unit)	MEP Levels
20-storey UBC-30	D5012.013a	MEP	Motor Control Center - Capacity: all - Unanchored equipment that is not vibration isolated - Equipment fragility only	Porter (2011)	PFA	9	Each	MEP Levels
20-storey UBC-31	B2011.201a	Façade	Precast Concrete Panels 4.5 inches thick - in plane deformation	FEMA (2012)	IDR	267	13'x30' Panels	Per Level
20-storey UBC-32	D1014.014	Egress	Vertical Transportation System (Elevators)	(Ibbi Almufti, personal communication 2012)	Residual IDR	6	Each	All Levels

See reverse.

Tracking	Fragility Number	NDS	DS Sequence + DSi (μ, β, MRC, MRT, RC)		
20-storey UBC-28	D3031.021c	1	Seq(DS1) + DS1(0.5, 0.4, 134657, 15, 2)	42	C
20-storey UBC-29	D3052.011d	2	MutEx(DS1,DS2) + DS1(0.25, 0.4, 2066, 2, 2) + DS2(0.25, 0.4, 192163, 15, 2)	42	C
20-storey UBC-30	D5012.013a	1	Seq(DS1) + DS1(0.73, 0.45, 4166, 1, 2)		C
20-storey UBC-31	B2011.201a	2	MutEx(DS1,DS2) + DS1(0.005, 0.5, 11728, 2, 3) + DS2(0.01, 0.5, 58643, 9, 3)	84	B
20-storey UBC-32	D1014.014	1	Seq(DS1) + DS1(0.002, 0.3, 1M, 7.5, 2)	42	E

Table C1 ends here.

Tracking	Fragility Number	Category	Description	Source	EDP	Qty.	Units	Distribution
40-storey UBC-1	B1031.011c	Structure	Steel Column Base Plates, Column W > 300 plf	Deierlein and Victorsson (2008)	IDR	26	Each	Per Structural Configuration
40-storey UBC-2	B1031.021b	Structure	Welded column splices, Column 150 plf < W < 300 plf	Deierlein and Victorsson (2008)	IDR	112	Each	Per Structural Configuration
40-storey UBC-3	B1031.021c	Structure	Welded column splices, Column W > 300 plf	Deierlein and Victorsson (2008)	IDR	226	Each	Per Structural Configuration
40-storey UBC-4	B1035.041	Structure	Pre-Northridge WUF-B beam-column joint, beam one side of column, beam depth <= W27	Deierlein and Victorsson (2008)	IDR	456	Each	Per Structural Configuration
40-storey UBC-5	B1035.042	Structure	Pre-Northridge WUF-B beam-column joint, beam one side of column, beam depth >= W30	Deierlein and Victorsson (2008)	IDR	318	Each	Per Structural Configuration
40-storey UBC-6	B1035.051	Structure	Pre-Northridge WUF-B beam-column joint, beam both sides of column, beam depth <= W27	Deierlein and Victorsson (2008)	IDR	1552	Each	Per Structural Configuration
40-storey UBC-7	B1035.052	Structure	Pre-Northridge WUF-B beam-column joint, beam both sides of column, beam depth >= W30	Deierlein and Victorsson (2008)	IDR	856	Each	Per Structural Configuration
40-storey UBC-8	C1011.001a	Fitout	Wall Partition, Type: Gypsum with metal studs, Full Height, Fixed Below, Fixed Above	Deierlein and Victorsson (2008)	IDR	365	13'x100' Panels	Office Levels
40-storey UBC-9	C3011.001a	Fitout	Wall Partition, Type: Gypsum + Wallpaper, Full Height, Fixed Below, Fixed Above	Deierlein and Victorsson (2008)	IDR	28	9'x100' Panels	Office Levels
40-storey UBC-10	C3027.001	Fitout	Raised Access Floor, non seismically rated.	Eidinger (2009)	PFA	2736	100 SF	Office Levels
40-storey UBC-11	C3032.001b	Fitout	Suspended Ceiling, SDC A,B,C, Area (A): 250 < A < 1000, Vert support only	Bachman (2011)	PFA	547	600 SF	Office Levels

See reverse.

Tracking	Fragility Number	NDS	DS Sequence + DSi (μ, β, MRC, MRT, RC)	LL	Repair Sequence
40-storey UBC-1	B1031.011c	4	Seq(MutEx(DS1,DS2),DS3,DS4) + DS1(0.04, 0.4, 0, 0, 3) + DS2(0.04, 0.4, 21363, 14, 3) + DS3(0.07, 0.4, 32566, 21, 3) + DS4(0.1, 0.4, 41889, 27, 3)		Structure
40-storey UBC-2	B1031.021b	3	Seq(MutEx(DS1,DS2),DS3) + DS1(0.02, 0.4, 0, 0, 3) + DS2(0.02, 0.4, 10245, 7, 3) + DS3(0.05, 0.4, 13012, 9, 3)		Structure
40-storey UBC-3	B1031.021c	3	Seq(MutEx(DS1,DS2),DS3) + DS1(0.02, 0.4, 0, 0, 3) + DS2(0.02, 0.4, 11445, 7, 3) + DS3(0.05, 0.4, 14812, 10, 3)		Structure
40-storey UBC-4	B1035.041	5	Seq(MutEx(DS1,DS2),MutEx(DS3,DS4),DS5) + DS1(0.017, 0.4, 11979, 7, 3) + DS2(0.017, 0.4, 13646, 8, 3) + DS3(0.025, 0.4, 16860, 10, 3) + DS4(0.025, 0.4, 17676, 10, 3) + DS5(0.03, 0.4, 14260, 8, 3)		Structure
40-storey UBC-5	B1035.042	5	Seq(MutEx(DS1,DS2),MutEx(DS3,DS4),DS5) + DS1(0.017, 0.4, 12313, 7, 3) + DS2(0.017, 0.4, 14313, 8, 3) + DS3(0.025, 0.4, 17646, 10, 3) + DS4(0.025, 0.4, 17676, 10, 3) + DS5(0.03, 0.4, 14260, 8, 3)		Structure
40-storey UBC-6	B1035.051	5	Seq(MutEx(DS1,DS2),MutEx(DS3,DS4),DS5) + DS1(0.017, 0.4, 16653, 10, 3) + DS2(0.017, 0.4, 18319, 11, 3) + DS3(0.025, 0.4, 23353, 14, 3) + DS4(0.025, 0.4, 23559, 14, 3) + DS5(0.03, 0.4, 18286, 11, 3)		Structure
40-storey UBC-7	B1035.052	5	Seq(MutEx(DS1,DS2),MutEx(DS3,DS4),DS5) + DS1(0.017, 0.4, 16653, 10, 3) + DS2(0.017, 0.4, 18319, 11, 3) + DS3(0.025, 0.4, 22019, 12, 3) + DS4(0.025, 0.4, 24226, 14.18, 3) + DS5(0.03, 0.4, 19826, 14, 3)		Structure
40-storey UBC-8	C1011.001a	3	Seq(DS1,DS2,DS3) + DS1(0.005, 0.4, 1966, 2, 1) + DS2(0.01, 0.3, 4297, 3, 1) + DS3(0.021, 0.2, 8990, 7, 3)		A
40-storey UBC-9	C3011.001a	1	Seq(DS1) + DS1(0.0021, 0.6, 2828, 2, 1)		A
40-storey UBC-10	C3027.001	1	Seq(DS1) + DS1(0.5, 0.5, 121, 0.1, 2)		A
40-storey UBC-11	C3032.001b	3	Seq(DS1,DS2,DS3) + DS1(1.01, 0.25, 849, 0.8, 1) + DS2(1.45, 0.25, 6631, 6, 3) + DS3(1.69, 0.25, 14322, 13, 3)		A

Continues on next page.

Tracking	Fragility Number	Category	Description	Source	EDP	Qty.	Units	Distribution
40-storey UBC-12	C3034.001	Fitout	Independent Pendant Lighting - non seismic	Eidinger (2009)	PFA	6192	Each	Office Levels
40-storey UBC-13	D2022.011a	MEP	Heating hot Water Piping - Small Diameter Threaded Steel - (2.5 inches in diameter or less), SDC A or B, PIPING FRAGILITY	Bachman (2012)	PFA	37	1000 ft Segments	All Levels
40-storey UBC-14	D2021.011a	MEP	Cold or Hot Potable - Small Diameter Threaded Steel - (2.5 inches in diameter or less), SDC A or B, PIPING FRAGILITY	Bachman (2012)	PFA	6	1000 ft Segments	All Levels
40-storey UBC-15	D2022.011b	MEP	Heating hot Water Piping - Small Diameter Threaded Steel - (2.5 inches in diameter or less), SDC A or B, BRACING FRAGILITY	Bachman (2012)	PFA	37	1000 ft Segments	All Levels
40-storey UBC-16	D2022.021a	MEP	Heating hot Water Piping - Large Diameter Welded Steel - (greater than 2.5 inches in diameter), SDC A or B, PIPING FRAGILITY	Bachman (2012)	PFA	14	1000 ft Segments	All Levels
40-storey UBC-17	D2031.021a	MEP	Sanitary Waste Piping - Cast Iron w/bell and spigot couplings, SDC A,B, PIPING FRAGILITY	Bachman (2012)	PFA	24	1000 ft Segments	All Levels
40-storey UBC-18	D2031.021b	MEP	Sanitary Waste Piping - Cast Iron w/bell and spigot couplings, SDC A,B, BRACING FRAGILITY	Bachman (2012)	PFA	24	1000 ft Segments	All Levels
40-storey UBC-19	D3041.011a	MEP	HVAC Galvanized Sheet Metal Ducting less than 6 sq. ft in cross sectional area, SDC A or B	Bachman (2012)	PFA	31	1000 ft Segments	All Levels

See reverse.

Tracking	Fragility Number	NDS	DS Sequence + DSi (μ, β, MRC, MRT, RC)	LL	Repair Sequence
40-storey UBC-12	C3034.001	1	Seq(DS1) + DS1(0.6, 0.4, 483, 0.001, 3)		A
40-storey UBC-13	D2022.011a	2	Seq(DS1,DS2) + DS1(0.55, 0.4, 278, 0.3, 2) + DS2(1.1, 0.4, 2596, 0.3, 3)		A
40-storey UBC-14	D2021.011a	2	Seq(DS1,DS2) + DS1(1.5, 0.4, 278, 0.3, 2) + DS2(2.6, 0.4, 2596, 0.3, 3)		A
40-storey UBC-15	D2022.011b	2	Seq(DS1,DS2) + DS1(1.2, 0.4, 382, 0.4, 3) + DS2(2.4, 0.4, 3873, 0.4, 3)		A
40-storey UBC-16	D2022.021a	2	Seq(DS1,DS2) + DS1(1.5, 0.4, 348, 0.4, 2) + DS2(2.6, 0.4, 3212, 3, 3)		A
40-storey UBC-17	D2031.021a	1	Seq(DS1) + DS1(2.25, 0.4, 3166, 3.5, 2)		A
40-storey UBC-18	D2031.021b	2	Seq(DS1,DS2) + DS1(1.2, 0.4, 423, 0.4, 3) + DS2(2.4, 0.4, 3499, 4.6, 3)		A
40-storey UBC-19	D3041.011a	2	Seq(DS1,DS2) + DS1(1.5, 0.4, 680, 0.8, 3) + DS2(2.25, 0.4, 6464, 2, 3)		A

Continues on next page.

Tracking	Fragility Number	Category	Description	Source	EDP	Qty.	Units	Distribution
40-storey UBC-20	D3041.012a	MEP	HVAC Galvanized Sheet Metal Ducting - 6 sq. ft cross sectional area or greater, SDC A or B	Bachman (2012)	PFA	8	1000 ft Segments	All Levels
40-storey UBC-21	D3041.031a	MEP	HVAC Drops / Diffusers in suspended ceilings - No independent safety wires, SDC A or B	Bachman (2012)	PFA	372	10 Units	All Levels
40-storey UBC-22	D3041.041a	MEP	Variable Air Volume (VAV) box with in-line coil, SDC A or B	Bachman (2012)	PFA	289	10 Units	All Levels
40-storey UBC-23	D4011.021a	MEP	Fire Sprinkler Water Piping - Horizontal Mains and Branches - Old Style Victaulic - Thin Wall Steel - No bracing, SDC A or B, PIPING FRAGILITY	Bachman (2012)	PFA	83	1000 ft Segments	All Levels
40-storey UBC-24	D4011.031a	MEP	Fire Sprinkler Drop Standard Threaded Steel - Dropping into unbraced lay-in tile SOFT ceiling - 6 ft. long drop maximum, SDC A or B	Bachman (2012)	PFA	37	100 Units	All Levels
40-storey UBC-25	C2011.001b	Egress	Prefabricated steel stair with steel treads and landings with no seismic joint.	Higgings (2011)	IDR	43	Each	All Levels
40-storey UBC-26	D5012.021a	MEP	Low Voltage Switchgear - Capacity: 100 to <350 Amp - Unanchored equipment that is not vibration isolated - Equipment fragility only	Porter (2011)	PFA	43	Each (225 Amp Unit)	All Levels
40-storey UBC-27	D3031.011c	MEP	Chiller - Capacity: 350 to <750 Ton - Unanchored equipment that is not vibration isolated - Equipment fragility only	Porter (2011)	PFA	2	Each (500 Ton Unit)	MEP Levels

See reverse.

Tracking	Fragility Number	NDS	DS Sequence + DSi (μ, β, MRC, MRT, RC)	LL	Repair Sequence
40-storey UBC-20	D3041.012a	2	Seq(DS1,DS2) + DS1(1.5, 0.4, 996, 1.1, 3) + DS2(2.25, 0.4, 8004, 2.8, 3)		A
40-storey UBC-21	D3041.031a	1	Seq(DS1) + DS1(1.3, 0.4, 2833, 3, 3)		A
40-storey UBC-22	D3041.041a	1	Seq(DS1) + DS1(1.9, 0.4, 14795, 17, 2)		A
40-storey UBC-23	D4011.021a	2	Seq(DS1,DS2) + DS1(1.1, 0.4, 348, 0.4, 2) + DS2(2.4, 0.5, 2596, 0.6, 3)		A
40-storey UBC-24	D4011.031a	2	Seq(DS1,DS2) + DS1(0.75, 0.4, 526, 0.2, 2) + DS2(0.95, 0.4, 526, 0.6, 3)		A
40-storey UBC-25	C2011.001b	3	Seq(DS1,DS2,DS3) + DS1(0.005, 0.6, 393, 0.4, 1) + DS2(0.017, 0.6, 2710, 3, 3) + DS3(0.028, 0.45, 20016, 22, 3)		F
40-storey UBC-26	D5012.021a	1	Seq(DS1) + DS1(1.28, 0.4, 9706, 2, 2)		D
40-storey UBC-27	D3031.011c	1	Seq(DS1) + DS1(0.2, 0.4, 263966, 26, 2)	42	C

Continues on next page.

Tracking	Fragility Number	Category	Description	Source	EDP	Qty.	Units	Distribution
40-storey UBC-28	D3031.021c	MEP	Cooling Tower - Capacity: 350 to <750 Ton - Unanchored equipment that is not vibration isolated - Equipment fragility only	Porter (2011)	PFA	2	Each (500 Ton Unit)	MEP Levels
40-storey UBC-29	D3052.011d	MEP	Air Handling Unit - Capacity: 25000 to <40000 CFM - Unanchored equipment that is not vibration isolated - Equipment fragility only	Porter (2011)	PFA	13	Each (30000 CFM Unit)	MEP Levels
40-storey UBC-30	D5012.013a	MEP	Motor Control Center - Capacity: all - Unanchored equipment that is not vibration isolated - Equipment fragility only	Porter (2011)	PFA	17	Each	MEP Levels
40-storey UBC-31	B2011.201a	Façade	Precast Concrete Panels 4.5 inches thick - in plane deformation	FEMA (2012)	IDR	533	13'x30' Panels	Per Level
40-storey UBC-32	D1014.014	Egress	Vertical Transportation System (Elevators)	(Ibbi Almufti, personal communication 2012)	Residual IDR	12	Each	All Levels

See reverse.

Tracking	Fragility Number	NDS	DS Sequence + DSi (μ, β, MRC, MRT, RC)	LL	Repair Sequence
40-storey UBC-28	D3031.021c	1	Seq(DS1) + DS1(0.5, 0.4, 134657, 15, 2)	42	C
40-storey UBC-29	D3052.011d	2	MutEx(DS1,DS2) + DS1(0.25, 0.4, 2066, 2, 2) + DS2(0.25, 0.4, 192163, 15, 2)	42	C
40-storey UBC-30	D5012.013a	1	Seq(DS1) + DS1(0.73, 0.45, 4166, 1, 2)		C
40-storey UBC-31	B2011.201a	2	MutEx(DS1,DS2) + DS1(0.005, 0.5, 11728, 2, 3) + DS2(0.01, 0.5, 58643, 9, 3)	84	B
40-storey UBC-32	D1014.014	1	Seq(DS1) + DS1(0.002, 0.3, 1M, 7.5, 2)	42	E

Table C2 ends here.

Tracking	Fragility Number	Category	Description	Source	EDP	Qty.	Units	Distribution
40-storey UBC-R-1	B1031.011c	Structure	Steel Column Base Plates, Column W > 300 plf	Deierlein and Victorsson (2008)	IDR	26	Each	Per Structural Configuration
40-storey UBC-R-2	B1031.021b	Structure	Welded column splices, Column 150 plf < W < 300 plf	Deierlein and Victorsson (2008)	IDR	112	Each	Per Structural Configuration
40-storey UBC-R-3	B1031.021c	Structure	Welded column splices, Column W > 300 plf	Deierlein and Victorsson (2008)	IDR	226	Each	Per Structural Configuration
40-storey UBC-R-4	B1035.041	Structure	Pre-Northridge WUF-B beam-column joint, beam one side of column, beam depth <= W27	Deierlein and Victorsson (2008)	IDR	456	Each	Per Structural Configuration
40-storey UBC-R-5	B1035.042	Structure	Pre-Northridge WUF-B beam-column joint, beam one side of column, beam depth >= W30	Deierlein and Victorsson (2008)	IDR	318	Each	Per Structural Configuration
40-storey UBC-R-6	B1035.051	Structure	Pre-Northridge WUF-B beam-column joint, beam both sides of column, beam depth <= W27	Deierlein and Victorsson (2008)	IDR	1552	Each	Per Structural Configuration
40-storey UBC-R-7	B1035.052	Structure	Pre-Northridge WUF-B beam-column joint, beam both sides of column, beam depth >= W30	Deierlein and Victorsson (2008)	IDR	856	Each	Per Structural Configuration
40-storey UBC-R-8	C1011.001d	Fitout	Wall Partition, Type: Gypsum with metal studs, Full Height, Fixed Below, Slip Track Above w/o returns (friction connections)	Araya-Letelier and Miranda (2012)	IDR	365	13'x100' Panels	Office Levels
40-storey UBC-R-9	C3011.001d	Fitout	Wall Partition, Type: Gypsum + Wallpaper, Full Height, Fixed Below, Slip Track Above w/o returns (friction connection)	Araya-Letelier and Miranda (2012)	IDR	28	9'x100' Panels	Office Levels
40-storey UBC-R-10	C3027.002	Fitout	Raised Access Floor, seismically rated.	Eidinger (2009)	PFA	2736	100 SF	Office Levels

See reverse.

Tracking	Fragility Number	NDS	DS Sequence + DSi (μ, β, MRC, MRT, RC)	LL	Repair Sequence
40-storey UBC-R-1	B1031.011c	4	Seq(MutEx(DS1,DS2),DS3,DS4) + DS1(0.04, 0.4, 0, 0, 3) + DS2(0.04, 0.4, 21363, 14, 3) + DS3(0.07, 0.4, 32566, 21, 3) + DS4(0.1, 0.4, 41889, 27, 3)		Structure
40-storey UBC-R-2	B1031.021b	3	Seq(MutEx(DS1,DS2),DS3) + DS1(0.02, 0.4, 0, 0, 3) + DS2(0.02, 0.4, 10245, 7, 3) + DS3(0.05, 0.4, 13012, 9, 3)		Structure
40-storey UBC-R-3	B1031.021c	3	Seq(MutEx(DS1,DS2),DS3) + DS1(0.02, 0.4, 0, 0, 3) + DS2(0.02, 0.4, 11445, 7, 3) + DS3(0.05, 0.4, 14812, 10, 3)		Structure
40-storey UBC-R-4	B1035.041	5	Seq(MutEx(DS1,DS2),MutEx(DS3,DS4),DS5) + DS1(0.017, 0.4, 11979, 7, 3) + DS2(0.017, 0.4, 13646, 8, 3) + DS3(0.025, 0.4, 16860, 10, 3) + DS4(0.025, 0.4, 17676, 10, 3) + DS5(0.03, 0.4, 14260, 8, 3)		Structure
40-storey UBC-R-5	B1035.042	5	Seq(MutEx(DS1,DS2),MutEx(DS3,DS4),DS5) + DS1(0.017, 0.4, 12313, 7, 3) + DS2(0.017, 0.4, 14313, 8, 3) + DS3(0.025, 0.4, 17646, 10, 3) + DS4(0.025, 0.4, 17676, 10, 3) + DS5(0.03, 0.4, 14260, 8, 3)		Structure
40-storey UBC-R-6	B1035.051	5	Seq(MutEx(DS1,DS2),MutEx(DS3,DS4),DS5) + DS1(0.017, 0.4, 16653, 10, 3) + DS2(0.017, 0.4, 18319, 11, 3) + DS3(0.025, 0.4, 23353, 14, 3) + DS4(0.025, 0.4, 23559, 14, 3) + DS5(0.03, 0.4, 18286, 11, 3)		Structure
40-storey UBC-R-7	B1035.052	5	Seq(MutEx(DS1,DS2),MutEx(DS3,DS4),DS5) + DS1(0.017, 0.4, 16653, 10, 3) + DS2(0.017, 0.4, 18319, 11, 3) + DS3(0.025, 0.4, 22019, 12, 3) + DS4(0.025, 0.4, 24226, 14.18, 3) + DS5(0.03, 0.4, 19826, 14, 3)		Structure
40-storey UBC-R-8	C1011.001d	2	Seq(DS1,DS2) + DS1(0.017, 0.6, 983, 0.9, 1) + DS2(0.024, 0.45, 2148, 2, 1)		A
40-storey UBC-R-9	C3011.001d	1	Seq(DS1) + DS1(0.017, 0.6, 2828, 2, 1)		A
40-storey UBC-R-10	C3027.002	1	Seq(DS1) + DS1(1.5, 0.4, 121, 0.1, 2)		A

Continues on next page.

Tracking	Fragility Number	Category	Description	Source	EDP	Qty.	Units	Distribution
40-storey UBC-R-11	C3032.004b	Fitout	Suspended Ceiling, SDC D,E,F (Ip=1.5), Area (A): 250 < A < 1000, Vert & Lat support	Bachman (2011)	PFA	547	600 SF	Office Levels
40-storey UBC-R-12	C3034.002	Fitout	Independent Pendant Lighting - seismically rated	Eidinger (2009)	PFA	6192	Each	Office Levels
40-storey UBC-R-13	D2022.014a	MEP	Heating hot Water Piping - Small Diameter Threaded Steel - (2.5 inches in diameter or less), SDC D, E, or F (OSHPD or sim), PIPING FRAGILITY	Bachman (2012)	PFA	37	1000 ft Segments	All Levels
40-storey UBC-R-14	D2021.014a	MEP	Cold or Hot Potable - Small Diameter Threaded Steel - (2.5 inches in diameter or less), SDC D, E, or F (OSHPD or sim), PIPING FRAGILITY	Bachman (2012)	PFA	6	1000 ft Segments	All Levels
40-storey UBC-R-15	D2021.014b	MEP	Cold or Hot Potable - Small Diameter Threaded Steel - (2.5 inches in diameter or less), SDC D, E, or F (OSHPD or sim), BRACING FRAGILITY	Bachman (2012)	PFA	6	1000 ft Segments	All Levels
40-storey UBC-R-16	D2022.014b	MEP	Heating hot Water Piping - Small Diameter Threaded Steel - (2.5 inches in diameter or less), SDC D, E, or F (OSHPD or sim), BRACING FRAGILITY	Bachman (2012)	PFA	37	1000 ft Segments	All Levels
40-storey UBC-R-17	D2022.024a	MEP	Heating hot Water Piping - Large Diameter Welded Steel - (greater than 2.5 inches in diameter), SDC D, E, or F (OSHPD or sim), PIPING FRAGILITY	Bachman (2012)	PFA	14	1000 ft Segments	All Levels

See reverse.

Tracking	Fragility Number	NDS	DS Sequence + DSi (μ, β, MRC, MRT, RC)	LL	Repair Sequence
40-storey UBC-R-11	C3032.004b	3	Seq(DS1,DS2,DS3) + DS1(1.76, 0.3, 849, 0.8, 1) + DS2(2.26, 0.3, 6631, 6, 3) + DS3(2.44, 0.3, 14322, 13, 3)		A
40-storey UBC-R-12	C3034.002	1	Seq(DS1) + DS1(1.5, 0.4, 483, 0.5, 3)		A
40-storey UBC-R-13	D2022.014a	2	Seq(DS1,DS2) + DS1(0.55, 0.4, 278, 0.3, 2) + DS2(1.1, 0.4, 2596, 3, 3)		A
40-storey UBC-R-14	D2021.014a	2	Seq(DS1,DS2) + DS1(2.25, 0.4, 278, 0.3, 2) + DS2(4.1, 0.4, 2596, 3, 3)		A
40-storey UBC-R-15	D2021.014b	1	Seq(DS1) + DS1(1.5, 0.4, 382, 0.4, 2)		A
40-storey UBC-R-16	D2022.014b	1	Seq(DS1) + DS1(3, 0.4, 382, 0.4, 3)		A
40-storey UBC-R-17	D2022.024a	2	Seq(DS1,DS2) + DS1(2.25, 0.4, 348, 0.4, 3) + DS2(4.1, 0.4, 3212, 3, 3)		A

Continues on next page.

Tracking	Fragility Number	Category	Description	Source	EDP	Qty.	Units	Distribution
40-storey UBC-R-18	D2022.024b	MEP	Heating hot Water Piping - Large Diameter Welded Steel - (greater than 2.5 inches in diameter), SDC D, E, or F (OSHPD or sim), BRACING FRAGILITY	Bachman (2012)	PFA	14	1000 ft Segments	All Levels
40-storey UBC-R-19	D2031.024a	MEP	Sanitary Waste Piping - Cast Iron w/bell and spigot couplings, SDC D,E,F (OSHPD or sim), PIPING FRAGILITY	Bachman (2012)	PFA	24	1000 ft Segments	All Levels
40-storey UBC-R-20	D2031.024b	MEP	Sanitary Waste Piping - Cast Iron w/bell and spigot couplings, SDC D,E,F (OSHPD or sim), BRACING FRAGILITY	Bachman (2012)	PFA	24	1000 ft Segments	All Levels
40-storey UBC-R-21	D3041.011d	MEP	HVAC Galvanized Sheet Metal Ducting less than 6 sq. ft in cross sectional area, SDC D, E, or F (OSHPD or sim)	Bachman (2012)	PFA	31	1000 ft Segments	All Levels
40-storey UBC-R-22	D3041.012d	MEP	HVAC Galvanized Sheet Metal Ducting - 6 sq. ft cross sectional area or greater, SDC D, E, or F (OSHPD or sim)	Bachman (2012)	PFA	8	1000 ft Segments	All Levels
40-storey UBC-R-23	D3041.032d	MEP	HVAC Drops / Diffusers without ceilings - supported by ducting only - No independent safety wires, SDC D, E, or F (OSHPD or sim)	Bachman (2012)	PFA	372	10 Units	All Levels
40-storey UBC-R-24	D3041.041b	MEP	Variable Air Volume (VAV) box with in-line coil, SDC C	Bachman (2012)	PFA	289	10 Units	All Levels
40-storey UBC-R-25	D4011.024a	MEP	Fire Sprinkler Water Piping - Horizontal Mains and Branches - Old Style Victaulic - Thin Wall Steel - with designed bracing, SDC D, E, or F (OSHPD or sim), PIPING FRAGILITY	Bachman (2012)	PFA	83	1000 ft Segments	All Levels

See reverse.

Tracking	Fragility Number	NDS	DS Sequence + DSi (μ, β, MRC, MRT, RC)	LL	Repair Sequence
40-storey UBC-R-18	D2022.024b	2	Seq(DS1,DS2) + DS1(1.5, 0.4, 348, 0.4, 2) + DS2(2.25, 0.4, 348, 0.4, 3)		A
40-storey UBC-R-19	D2031.024a	1	Seq(DS1) + DS1(3, 0.4, 3166, 3, 3)		A
40-storey UBC-R-20	D2031.024b	1	Seq(DS1) + DS1(2.25, 0.4, 423, 0.4, 3)		A
40-storey UBC-R-21	D3041.011d	2	Seq(DS1,DS2) + DS1(1.5, 0.4, 680, 0.7, 3) + DS2(2.25, 0.4, 6464, 2.2, 3)		A
40-storey UBC-R-22	D3041.012d	2	Seq(DS1,DS2) + DS1(3.75, 0.4, 996, 1, 3) + DS2(4.5, 0.4, 8004, 3, 3)		A
40-storey UBC-R-23	D3041.032d	1	Seq(DS1) + DS1(1.5, 0.4, 2833, 3, 3)		A
40-storey UBC-R-24	D3041.041b	1	Seq(DS1) + DS1(1.9, 0.4, 14795, 17, 2)		A
40-storey UBC-R-25	D4011.024a	2	Seq(DS1,DS2) + DS1(1.9, 0.4, 348, 0.4, 2) + DS2(3.4, 0.4, 2596, 0.6, 3)		A

Continues on next page.

Tracking	Fragility Number	Category	Description	Source	EDP	Qty.	Units	Distribution
40-storey UBC-R-26	D4011.034a	MEP	Fire Sprinkler Drop Standard Threaded Steel - Dropping into unbraced lay-in tile SOFT ceiling - 6 ft. long drop maximum, SDC D, E, or F (OSHPD or sim)	Bachman (2012)	PFA	37	100 Units	All Levels
40-storey UBC-R-27	C2011.001a	Egress	Prefabricated steel stair with steel treads and landings with seismic joints that accommodate drift.	Higgings (2011)	IDR	43	Each	All Levels
40-storey UBC-R-28	D5012.023b	MEP	Low Voltage Switchgear - Capacity: 100 to <350 Amp - Equipment that is either hard anchored or is vibration isolated with seismic snubbers/restraints - Equipment fragility only	Porter (2011)	PFA	43	Each (225 Amp Unit)	All Levels
40-storey UBC-R-29	D3031.013h	MEP	Chiller - Capacity: 350 to <750 Ton - Equipment that is either hard anchored or is vibration isolated with seismic snubbers/restraints - Equipment fragility only	Porter (2011)	PFA	2	Each (500 Ton Unit)	MEP Levels
40-storey UBC-R-30	D3031.023h	MEP	Cooling Tower - Capacity: 350 to <750 Ton - Equipment that is either hard anchored or is vibration isolated with seismic snubbers/restraints - Equipment fragility only	Porter (2011)	PFA	2	Each (500 Ton Unit)	MEP Levels
40-storey UBC-R-31	D3052.013k	MEP	Air Handling Unit - Capacity: 25000 to <40000 CFM - Equipment that is either hard anchored or is vibration isolated with seismic snubbers/restraints - Equipment fragility only	Porter (2011)	PFA	13	Each (30000 CFM Unit)	MEP Levels

See reverse.

Tracking	Fragility Number	NDS	DS Sequence + DSi (μ, β, MRC, MRT, RC)	LL	Repair Sequence
40-storey UBC-R-26	D4011.034a	1	Seq(DS1) + DS1(1.3, 0.4, 526, 0.6, 2)		A
40-storey UBC-R-27	C2011.001a	3	Seq(DS1,DS2,DS3) + DS1(0.015, 0.6, 393, 0.4, 1) + DS2(0.027, 0.6, 2710, 3, 3) + DS3(0.038, 0.45, 20016, 22, 3)		F
40-storey UBC-R-28	D5012.023b	1	Seq(DS1) + DS1(2.4, 0.4, 9706, 2, 2)		D
40-storey UBC-R-29	D3031.013h	1	Seq(DS1) + DS1(0.72, 0.2, 263966, 30, 2)	42	C
40-storey UBC-R-30	D3031.023h	1	Seq(DS1) + DS1(1.52, 0.4, 134657, 15, 2)	42	C
40-storey UBC-R-31	D3052.013k	2	MutEx(DS1,DS2) + DS1(1.54, 0.6, 2066, 2, 2) + DS2(1.54, 0.6, 192163, 15, 2)	42	C

Continues on next page.

Tracking	Fragility Number	Category	Description	Source	EDP	Qty.	Units	Distribution
40-storey UBC-R-32	D5012.013c	MEP	Motor Control Center - Capacity: all - Equipment that is either hard anchored or is vibration isolated with seismic snubbers/restraints - Equipment fragility only	Porter (2011)	PFA	17	Each	MEP Levels
40-storey UBC-R-33	B2022.002	Façade	Curtain Walls - Generic Midrise Stick-Built Curtain wall, Config: Insulating Glass Units (dual pane), Lamination: Unknown, Glass Type: Unknown, Details: Aspect ratio = 6:5, Other details Unknown	FEMA (2012)	IDR	6933	30 SF	All Levels
40-storey UBC-R-34	D1014.014	Egress	Vertical Transportation System (Elevators)	(Ibbi Almufti, personal communication 2012)	Residual IDR	12	Each	All Levels

See reverse.

Tracking	Fragility Number	NDS	DS Sequence + DSi (μ, β, MRC, MRT, RC)	LL	Repair Sequence
40-storey UBC-R-32	D5012.013c	1	Seq(DS1) + DS1(2.5, 0.4, 4166, 5, 2)		C
40-storey UBC-R-33	B2022.002	2	Seq(DS1,DS2) + DS1(0.02, 0.45, 2162, 0.87, 2) + DS2(0.024, 0.45, 2162, 0.87, 3)	84	B
40-storey UBC-R-34	D1014.014	1	Seq(DS1) + DS1(0.002, 0.3, 1M, 7.5, 2)	42	E

Table C3 ends here.

Tracking	Fragility Number	Category	Description	Source	EDP	Qty.	Units	Distribution
50-storey UBC-1	B1031.011c	Structure	Steel Column Base Plates, Column W > 300 plf	Deierlein and Victorsson (2008)	IDR	49	Each	Per Structural Configuration
50-storey UBC-2	B1031.021b	Structure	Welded column splices, Column 150 plf < W < 300 plf	Deierlein and Victorsson (2008)	IDR	196	Each	Per Structural Configuration
50-storey UBC-3	B1031.021c	Structure	Welded column splices, Column W > 300 plf	Deierlein and Victorsson (2008)	IDR	588	Each	Per Structural Configuration
50-storey UBC-4	B1035.041	Structure	Pre-Northridge WUF-B beam-column joint, beam one side of column, beam depth <= W27	Deierlein and Victorsson (2008)	IDR	420	Each	Per Structural Configuration
50-storey UBC-5	B1035.042	Structure	Pre-Northridge WUF-B beam-column joint, beam one side of column, beam depth >= W30	Deierlein and Victorsson (2008)	IDR	980	Each	Per Structural Configuration
50-storey UBC-6	B1035.051	Structure	Pre-Northridge WUF-B beam-column joint, beam both sides of column, beam depth <= W27	Deierlein and Victorsson (2008)	IDR	1050	Each	Per Structural Configuration
50-storey UBC-7	B1035.052	Structure	Pre-Northridge WUF-B beam-column joint, beam both sides of column, beam depth >= W30	Deierlein and Victorsson (2008)	IDR	2450	Each	Per Structural Configuration
50-storey UBC-8	C1011.001a	Fitouts	Wall Partition, Type: Gypsum with metal studs, Full Height, Fixed Below, Fixed Above	Miranda and Mosqueda (2011)	IDR	1592	13'x100' Panels	Office Levels
50-storey UBC-9	C3011.001a	Fitouts	Wall Partition, Type: Gypsum + Wallpaper, Full Height, Fixed Below, Fixed Above	Miranda and Mosqueda (2011)	IDR	250	9'x100' Panels	Office Levels
50-storey UBC-10	C3027.001	Fitouts	Raised Access Floor, non seismically rated.	Eidinger (2009)	PFA	11940	100 SF	Office Levels

See reverse.

Tracking	Fragility Number	NDS	DS Sequence + DSi (μ, β, MRC, MRT, RC)	LL	Repair Sequence
50-storey UBC-1	B1031.011c	4	Seq(MutEx(DS1,DS2),DS3,DS4) + DS1(0.04, 0.4, 0, 0, 3) + DS2(0.04, 0.4, 21363, 14, 3) + DS3(0.07, 0.4, 32566, 21, 3) + DS4(0.1, 0.4, 41889, 27, 3)		Structure
50-storey UBC-2	B1031.021b	3	Seq(MutEx(DS1,DS2),DS3) + DS1(0.02, 0.4, 0, 0, 3) + DS2(0.02, 0.4, 10245, 7, 3) + DS3(0.05, 0.4, 13012, 9, 3)		Structure
50-storey UBC-3	B1031.021c	3	Seq(MutEx(DS1,DS2),DS3) + DS1(0.02, 0.4, 0, 0, 3) + DS2(0.02, 0.4, 11445, 7, 3) + DS3(0.05, 0.4, 14812, 10, 3)		Structure
50-storey UBC-4	B1035.041	5	Seq(MutEx(DS1,DS2),MutEx(DS3,DS4),DS5) + DS1(0.017, 0.4, 11979, 7, 3) + DS2(0.017, 0.4, 13646, 8, 3) + DS3(0.025, 0.4, 16860, 10, 3) + DS4(0.025, 0.4, 17676, 10, 3) + DS5(0.03, 0.4, 14260, 8, 3)		Structure
50-storey UBC-5	B1035.042	5	Seq(MutEx(DS1,DS2),MutEx(DS3,DS4),DS5) + DS1(0.017, 0.4, 12313, 7, 3) + DS2(0.017, 0.4, 14313, 8, 3) + DS3(0.025, 0.4, 17646, 10, 3) + DS4(0.025, 0.4, 17676, 10, 3) + DS5(0.03, 0.4, 14260, 8, 3)		Structure
50-storey UBC-6	B1035.051	5	Seq(MutEx(DS1,DS2),MutEx(DS3,DS4),DS5) + DS1(0.017, 0.4, 16653, 10, 3) + DS2(0.017, 0.4, 18319, 11, 3) + DS3(0.025, 0.4, 23353, 14, 3) + DS4(0.025, 0.4, 23559, 14, 3) + DS5(0.03, 0.4, 18286, 11, 3)		Structure
50-storey UBC-7	B1035.052	5	Seq(MutEx(DS1,DS2),MutEx(DS3,DS4),DS5) + DS1(0.017, 0.4, 16653, 10, 3) + DS2(0.017, 0.4, 18319, 11, 3) + DS3(0.025, 0.4, 22019, 12, 3) + DS4(0.025, 0.4, 24226, 14.18, 3) + DS5(0.03, 0.4, 19826, 14, 3)		Structure
50-storey UBC-8	C1011.001a	3	Seq(DS1,DS2,DS3) + DS1(0.005, 0.4, 1966, 2, 1) + DS2(0.01, 0.3, 4297, 3, 1) + DS3(0.021, 0.2, 8990, 7, 3)		A
50-storey UBC-9	C3011.001a	1	Seq(DS1) + DS1(0.0021, 0.6, 2828, 2, 1)		A
50-storey UBC-10	C3027.001	1	Seq(DS1) + DS1(0.5, 0.5, 121, 0.1, 2)		A

Continues on next page.

Tracking	Fragility Number	Category	Description	Source	EDP	Qty.	Units	Distribution
50-storey UBC-11	C3032.001c	Fitouts	Suspended Ceiling, SDC A,B,C, Area (A): 1000 < A < 2500, Vert support only	Bachman (2011)	PFA	663	1800 SF	Office Levels
50-storey UBC-12	C3034.001	Fitouts	Independent Pendant Lighting - non seismic	Eidinger (2009)	PFA	26464	Each	Office Levels
50-storey UBC-13	C2011.001b	Egress	Prefabricated steel stair with steel treads and landings with no seismic joint.	Higgings (2011)	IDR	204	Each	All Levels
50-storey UBC-14	D2021.011a	MEP	Cold or Hot Potable - Small Diameter Threaded Steel - (2.5 inches in diameter or less), SDC A or B, PIPING FRAGILITY	Bachman (2012)	PFA	28	1000 ft Segments	All Levels
50-storey UBC-15	D2022.021a	MEP	Heating hot Water Piping - Large Diameter Welded Steel - (greater than 2.5 inches in diameter), SDC A or B, PIPING FRAGILITY	Bachman (2012)	PFA	71	1000 ft Segments	All Levels
50-storey UBC-16	D3052.011d	MEP	Air Handling Unit - Capacity: 25000 to <40000 CFM - Unanchored equipment that is not vibration isolated - Equipment fragility only	Porter (2011)	PFA	43	Each (30000 CFM Unit)	MEP Levels
50-storey UBC-17	D5012.013a	MEP	Motor Control Center - Capacity: all - Unanchored equipment that is not vibration isolated - Equipment fragility only	Porter (2011)	PFA	99	Each	MEP Levels
50-storey UBC-18	D2022.011a	MEP	Heating hot Water Piping - Small Diameter Threaded Steel - (2.5 inches in diameter or less), SDC A or B, PIPING FRAGILITY	Bachman (2012)	PFA	308	1000 ft Segments	All Levels
50-storey UBC-19	D2031.021a	MEP	Sanitary Waste Piping - Cast Iron w/bell and spigot couplings, SDC A,B, PIPING FRAGILITY	Bachman (2012)	PFA	175	1000 ft Segments	All Levels

See reverse.

Tracking	Fragility Number	NDS	DS Sequence + DSi (μ, β, MRC, MRT, RC)	LL	Repair Sequence
50-storey UBC-11	C3032.001c	3	Seq(DS1,DS2,DS3) + DS1(0.7, 0.25, 2549, 2, 1) + DS2(1.2, 0.25, 19895, 18, 3) + DS3(1.43, 0.25, 42968, 37, 3)		A
50-storey UBC-12	C3034.001	1	Seq(DS1) + DS1(0.6, 0.4, 483, 0.001, 3)		A
50-storey UBC-13	C2011.001b	3	Seq(DS1,DS2,DS3) + DS1(0.005, 0.6, 393, 0.4, 1) + DS2(0.017, 0.6, 2710, 3, 3) + DS3(0.028, 0.45, 20016, 22, 3)		F
50-storey UBC-14	D2021.011a	2	Seq(DS1,DS2) + DS1(1.5, 0.4, 278, 0.3, 2) + DS2(2.6, 0.4, 2596, 0.3, 3)		A
50-storey UBC-15	D2022.021a	2	Seq(DS1,DS2) + DS1(1.5, 0.4, 348, 0.4, 2) + DS2(2.6, 0.4, 3212, 3, 3)		A
50-storey UBC-16	D3052.011d	2	MutEx(DS1,DS2) + DS1(0.25, 0.4, 2066, 2, 2) + DS2(0.25, 0.4, 192163, 15, 2)	42	C
50-storey UBC-17	D5012.013a	1	Seq(DS1) + DS1(0.73, 0.45, 4166, 1, 2)		C
50-storey UBC-18	D2022.011a	2	Seq(DS1,DS2) + DS1(0.55, 0.4, 278, 0.3, 2) + DS2(1.1, 0.4, 2596, 0.3, 3)		A
50-storey UBC-19	D2031.021a	1	Seq(DS1) + DS1(2.25, 0.4, 3166, 3.5, 2)		A

Continues on next page.

Tracking	Fragility Number	Category	Description	Source	EDP	Qty.	Units	Distribution
50-storey UBC-20	D3041.012a	MEP	HVAC Galvanized Sheet Metal Ducting - 6 sq. ft cross sectional area or greater, SDC A or B	Bachman (2012)	PFA	50	1000 ft Segments	All Levels
50-storey UBC-21	D3041.011a	MEP	HVAC Galvanized Sheet Metal Ducting less than 6 sq. ft in cross sectional area, SDC A or B	Bachman (2012)	PFA	100	1000 ft Segments	All Levels
50-storey UBC-22	D4011.021a	MEP	Fire Sprinkler Water Piping - Horizontal Mains and Branches - Old Style Victaulic - Thin Wall Steel - No bracing, SDC A or B, PIPING FRAGILITY	Bachman (2012)	PFA	300	1000 ft Segments	All Levels
50-storey UBC-23	D3041.031a	MEP	HVAC Drops / Diffusers in suspended ceilings - No independent safety wires, SDC A or B	Bachman (2012)	PFA	2820	10 Units	All Levels
50-storey UBC-24	D4011.031a	MEP	Fire Sprinkler Drop Standard Threaded Steel - Dropping into unbraced lay-in tile SOFT ceiling - 6 ft. long drop maximum, SDC A or B	Bachman (2012)	PFA	150	100 Units	All Levels
50-storey UBC-25	D2031.021b	MEP	Sanitary Waste Piping - Cast Iron w/bell and spigot couplings, SDC A,B, BRACING FRAGILITY	Bachman (2012)	PFA	100	1000 ft Segments	All Levels
50-storey UBC-26	D3041.041a	MEP	Variable Air Volume (VAV) box with in-line coil, SDC A or B	Bachman (2012)	PFA	1412	10 Units	All Levels
50-storey UBC-27	D3031.011d	MEP	Chiller - Capacity: 750 to <1000 Ton - Unanchored equipment that is not vibration isolated - Equipment fragility only	Porter (2011)	PFA	6	Each (850 Ton Unit)	MEP Levels

See reverse.

Tracking	Fragility Number	NDS	DS Sequence + DSi (μ, β, MRC, MRT, RC)	LL	Repair Sequence
50-storey UBC-20	D3041.012a	2	Seq(DS1,DS2) + DS1(1.5, 0.4, 996, 1.1, 3) + DS2(2.25, 0.4, 8004, 2.8, 3)		A
50-storey UBC-21	D3041.011a	2	Seq(DS1,DS2) + DS1(1.5, 0.4, 680, 0.8, 3) + DS2(2.25, 0.4, 6464, 2, 3)		A
50-storey UBC-22	D4011.021a	2	Seq(DS1,DS2) + DS1(1.1, 0.4, 348, 0.4, 2) + DS2(2.4, 0.5, 2596, 0.6, 3)		A
50-storey UBC-23	D3041.031a	1	Seq(DS1) + DS1(1.3, 0.4, 2833, 3, 3)		A
50-storey UBC-24	D4011.031a	2	Seq(DS1,DS2) + DS1(0.75, 0.4, 526, 0.2, 2) + DS2(0.95, 0.4, 526, 0.6, 3)		A
50-storey UBC-25	D2031.021b	2	Seq(DS1,DS2) + DS1(1.2, 0.4, 423, 0.4, 3) + DS2(2.4, 0.4, 3499, 4.6, 3)		A
50-storey UBC-26	D3041.041a	1	Seq(DS1) + DS1(1.9, 0.4, 14795, 17, 2)		A
50-storey UBC-27	D3031.011d	1	Seq(DS1) + DS1(0.2, 0.4, 445291, 31, 2)	42	C

Continues on next page.

Tracking	Fragility Number	Category	Description	Source	EDP	Qty.	Units	Distribution
50-storey UBC-28	D3031.021d	MEP	Cooling Tower - Capacity: 750 to <1000 Ton - Unanchored equipment that is not vibration isolated - Equipment fragility only	Porter (2011)	PFA	6	Each (850 Ton Unit)	MEP Levels
50-storey UBC-29	D5012.021a	MEP	Low Voltage Switchgear - Capacity: 100 to <350 Amp - Unanchored equipment that is not vibration isolated - Equipment fragility only	Porter (2011)	PFA	50	Each (225 Amp Unit)	All Levels
50-storey UBC-30	B2011.201a	Façade	Precast Concrete Panels 4.5 inches thick - in plane deformation	FEMA (2012)	IDR	1100	13'x30' Panels	Per Level
50-storey UBC-31	D1014.014	Egress	Vertical Transportation System (Elevators)	(Ibbi Almufti, personal communication 2012)	Residual IDR	24	Each	All Levels

See reverse.

Tracking	Fragility Number	NDS	DS Sequence + DSi (μ, β, MRC, MRT, RC)	LL	Repair Sequence
50-storey UBC-28	D3031.021d	1	Seq(DS1) + DS1(0.5, 0.4, 225825, 18, 2)	42	C
50-storey UBC-29	D5012.021a	1	Seq(DS1) + DS1(1.28, 0.4, 9706, 2, 2)		D
50-storey UBC-30	B2011.201a	2	MutEx(DS1,DS2) + DS1(0.005, 0.5, 11728, 2, 3) + DS2(0.01, 0.5, 58643, 9, 3)	84	B
50-storey UBC-31	D1014.014	1	Seq(DS1) + DS1(0.002, 0.3, 1M, 7.5, 2)	42	E

Table C4 ends here.

Tracking	Fragility Number	Category	Description	Source	EDP	Qty.	Units	Distribution
50-storey IBC-1	B1031.001	Structure	Bolted shear tab gravity connections	Deierlein and Victorsson (2008)	IDR	6200	Each	Per Structural Configuration
50-storey IBC-2	B1031.011c	Structure	Steel Column Base Plates, Column W > 300 plf	Deierlein and Victorsson (2008)	IDR	49	Each	Per Structural Configuration
50-storey IBC-3	B1031.021b	Structure	Welded column splices, Column 150 plf < W < 300 plf	Deierlein and Victorsson (2008)	IDR	49	Each	Per Structural Configuration
50-storey IBC-4	B1031.021c	Structure	Welded column splices, Column W > 300 plf	Deierlein and Victorsson (2008)	IDR	686	Each	Per Structural Configuration
50-storey IBC-5	B1035.002	Structure	Post-Northridge RBS connection with welded web, beam one side of column only, beam depth >= W30	Deierlein and Victorsson (2008)	IDR	200	Each	Per Structural Configuration
50-storey IBC-6	B1035.012	Structure	Post-Northridge RBS connection with welded web, beams both sides of column, beam depth >= W30	Deierlein and Victorsson (2008)	IDR	1000	Each	Per Structural Configuration
50-storey IBC-7	C1011.001c	Fitouts	Wall Partition, Type: Gypsum with metal studs, Full Height, Fixed Below, Slip Track Above with returns	Miranda and Mosqueda (2011)	IDR	1592	13'x100' Panels	Office Levels
50-storey IBC-8	C3011.001c	Fitouts	Wall Partition, Type: Gypsum + Wallpaper, Full Height, Fixed Below, Slip Track Above w/ returns (friction connection)	Miranda and Mosqueda (2011)	IDR	250	9'x100' Panels	Office Levels
50-storey IBC-9	C3027.002	Fitouts	Raised Access Floor, seismically rated.	Eidinger (2009)	PFA	11940	100 SF	Office Levels
50-storey IBC-10	C3032.003c	Fitouts	Suspended Ceiling, SDC D,E (Ip=1.0), Area (A): 1000 < A < 2500, Vert & Lat support	Bachman (2011)	PFA	663	1800 SF	Office Levels
50-storey IBC-11	C3034.002	Fitouts	Independent Pendant Lighting - seismically rated	Eidinger (2009)	PFA	26464	Each	Office Levels

See reverse.

Tracking	Fragility Number	NDS	DS Sequence + DSi (μ, β, MRC, MRT, RC)	LL	Repair Sequence
50-storey IBC-1	B1031.001	4	Seq(MutEx(DS1,DS2),DS3,DS4) + DS1(0.04, 0.4, 0, 0, 3) + DS2(0.04, 0.4, 12106, 11, 3) + DS3(0.08, 0.4, 12356, 12, 3) + DS4(0.11, 0.4, 12306, 12, 3)		Structure
50-storey IBC-2	B1031.011c	4	Seq(MutEx(DS1,DS2),DS3,DS4) + DS1(0.04, 0.4, 0, 0, 3) + DS2(0.04, 0.4, 21363, 14, 3) + DS3(0.07, 0.4, 32566, 21, 3) + DS4(0.1, 0.4, 41889, 27, 3)		Structure
50-storey IBC-3	B1031.021b	3	Seq(MutEx(DS1,DS2),DS3) + DS1(0.02, 0.4, 0, 0, 3) + DS2(0.02, 0.4, 10245, 7, 3) + DS3(0.05, 0.4, 13012, 9, 3)		Structure
50-storey IBC-4	B1031.021c	3	Seq(MutEx(DS1,DS2),DS3) + DS1(0.02, 0.4, 0, 0, 3) + DS2(0.02, 0.4, 11445, 7, 3) + DS3(0.05, 0.4, 14812, 10, 3)		Structure
50-storey IBC-5	B1035.002	3	Seq(DS1,DS2,DS3) + DS1(0.03, 0.3, 17033, 11, 3) + DS2(0.04, 0.3, 28432, 19, 3) + DS3(0.05, 0.3, 28432, 19, 3)		Structure
50-storey IBC-6	B1035.012	3	Seq(DS1,DS2,DS3) + DS1(0.03, 0.3, 28733, 19, 3) + DS2(0.04, 0.3, 52398, 34, 3) + DS3(0.05, 0.3, 52398, 34, 3)		Structure
50-storey IBC-7	C1011.001c	3	Seq(DS1,DS2,DS3) + DS1(0.004, 0.45, 786, 0.6, 1) + DS2(0.011, 0.35, 1718, 1, 1) + DS3(0.019, 0.25, 3596, 2.73, 3)		A
50-storey IBC-8	C3011.001c	1	Seq(DS1) + DS1(0.002, 0.7, 2828, 2, 1)		A
50-storey IBC-9	C3027.002	1	Seq(DS1) + DS1(1.5, 0.4, 121, 0.1, 2)		A
50-storey IBC-10	C3032.003c	3	Seq(DS1,DS2,DS3) + DS1(1.21, 0.3, 2549, 2, 1) + DS2(1.75, 0.3, 19895, 18, 3) + DS3(1.95, 0.3, 42968, 37, 3)		A
50-storey IBC-11	C3034.002	1	Seq(DS1) + DS1(1.5, 0.4, 483, 0.5, 3)		A

Continues on next page.

Tracking	Fragility Number	Category	Description	Source	EDP	Qty.	Units	Distribution
50-storey IBC-12	D2021.013a	MEP	Cold or Hot Potable - Small Diameter Threaded Steel - (2.5 inches in diameter or less), SDC D, E, or F, PIPING FRAGILITY	Bachman (2012)	PFA	204	1000 ft Segments	All Levels
50-storey IBC-13	D2022.023a	MEP	Heating hot Water Piping - Large Diameter Welded Steel - (greater than 2.5 inches in diameter), SDC D, E, or F, PIPING FRAGILITY	Bachman (2012)	PFA	28	1000 ft Segments	All Levels
50-storey IBC-14	D3052.013k	MEP	Air Handling Unit - Capacity: 25000 to <40000 CFM - Equipment that is either hard anchored or is vibration isolated with seismic snubbers/restraints - Equipment fragility only	Porter (2011)	PFA	71	Each (30000 CFM Unit)	MEP Levels
50-storey IBC-15	D5012.013c	MEP	Motor Control Center - Capacity: all - Equipment that is either hard anchored or is vibration isolated with seismic snubbers/restraints - Equipment fragility only	Porter (2011)	PFA	43	Costing is per unit.	MEP Levels
50-storey IBC-16	D2022.013a	MEP	Heating hot Water Piping - Small Diameter Threaded Steel - (2.5 inches in diameter or less), SDC D, E, or F, PIPING FRAGILITY	Bachman (2012)	PFA	99	1000 ft Segments	All Levels
50-storey IBC-17	D2031.023b	MEP	Sanitary Waste Piping - Cast Iron w/bell and spigot couplings, SDC D,E,F, BRACING FRAGILITY	Bachman (2012)	PFA	308	1000 ft Segments	All Levels
50-storey IBC-18	D3041.012c	MEP	HVAC Galvanized Sheet Metal Ducting - 6 sq. ft cross sectional area or greater, SDC D, E, or F	Bachman (2012)	PFA	175	1000 ft Segments	All Levels

See reverse.

Tracking	Fragility Number	NDS	DS Sequence + DSi (μ, β, MRC, MRT, RC)	LL	Repair Sequence
50-storey IBC-12	D2021.013a	2	Seq(DS1,DS2) + DS1(2.25, 0.4, 278, 0.3, 2) + DS2(4.1, 0.4, 2596, 2.8, 3)		A
50-storey IBC-13	D2022.023a	2	Seq(DS1,DS2) + DS1(2.25, 0.4, 348, 0.4, 2) + DS2(4.1, 0.4, 3213, 3, 3)		A
50-storey IBC-14	D3052.013k	2	MutEx(DS1,DS2) + DS1(1.54, 0.6, 2066, 2, 2) + DS2(1.54, 0.6, 192163, 15, 2)	42	C
50-storey IBC-15	D5012.013c	1	Seq(DS1) + DS1(2.5, 0.4, 4166, 5, 2)		C
50-storey IBC-16	D2022.013a	2	Seq(DS1,DS2) + DS1(0.55, 0.4, 278, 0.3, 2) + DS2(1.1, 0.4, 2596, 3, 3)		A
50-storey IBC-17	D2031.023b	1	Seq(DS1) + DS1(2.25, 0.4, 42, 0.4, 3)		A
50-storey IBC-18	D3041.012c	2	Seq(DS1,DS2) + DS1(3.75, 0.4, 996, 1, 3) + DS2(4.5, 0.4, 8004, 3, 3)		A

Continues on next page.

Tracking	Fragility Number	Category	Description	Source	EDP	Qty.	Units	Distribution
50-storey IBC-19	D3041.011c	MEP	HVAC Galvanized Sheet Metal Ducting less than 6 sq. ft in cross sectional area, SDC D, E, or F	Bachman (2012)	PFA	50	1000 ft Segments	All Levels
50-storey IBC-20	D4011.023a	MEP	Fire Sprinkler Water Piping - Horizontal Mains and Branches - Old Style Victaulic - Thin Wall Steel - Poorly designed bracing, SDC D, E, or F , PIPING FRAGILITY	Bachman (2012)	PFA	100	1000 ft Segments	All Levels
50-storey IBC-21	D3041.032c	MEP	HVAC Drops / Diffusers without ceilings - supported by ducting only - No independent safety wires, SDC D, E, or F	Bachman (2012)	PFA	300	10 Units	All Levels
50-storey IBC-22	D4011.033a	MEP	Fire Sprinkler Drop Standard Threaded Steel - Dropping into unbraced lay-in tile SOFT ceiling - 6 ft. long drop maximum, SDC D, E, or F	Bachman (2012)	PFA	2820	100 Units	All Levels
50-storey IBC-23	D2031.023a	MEP	Sanitary Waste Piping - Cast Iron w/bell and spigot couplings, SDC D,E,F, PIPING FRAGILITY	Bachman (2012)	PFA	150	1000 ft Segments	All Levels
50-storey IBC-24	D3041.041b	MEP	Variable Air Volume (VAV) box with in-line coil, SDC C	Bachman (2012)	PFA	100	10 Units	All Levels
50-storey IBC-25	D3031.012k	MEP	Chiller - Capacity: 750 to <1000 Ton - Vibration isolated equipment that is not snubbed or restrained - Equipment fragility only	Porter (2011)	PFA	1412	Each (850 Ton Unit)	MEP Levels
50-storey IBC-26	D3031.022k	MEP	Cooling Tower - Capacity: 750 to <1000 Ton - Vibration isolated equipment that is not snubbed or restrained - Equipment fragility only	Porter (2011)	PFA	6	Each (850 Ton Unit)	MEP Levels

See reverse.

Tracking	Fragility Number	NDS	DS Sequence + DSi (μ, β, MRC, MRT, RC)	LL	Repair Sequence
50-storey IBC-19	D3041.011c	2	Seq(DS1,DS2) + DS1(1.5, 0.4, 680, 0.7, 3) + DS2(2.25, 0.4, 6464, 2, 3)		A
50-storey IBC-20	D4011.023a	2	Seq(DS1,DS2) + DS1(1.5, 0.4, 348, 0.4, 2) + DS2(2.6, 0.4, 2596, 0.6, 3)		A
50-storey IBC-21	D3041.032c	1	Seq(DS1) + DS1(1.5, 0.4, 2833, 3, 3)		A
50-storey IBC-22	D4011.033a	1	Seq(DS1) + DS1(0.95, 0.4, 526, 0.6, 2)		A
50-storey IBC-23	D2031.023a	1	Seq(DS1) + DS1(3, 0.4, 3166, 3, 2)		A
50-storey IBC-24	D3041.041b	1	Seq(DS1) + DS1(1.9, 0.4, 14795, 17, 2)		A
50-storey IBC-25	D3031.012k	1	Seq(DS1) + DS1(0.43, 0.6, 445291, 31, 2)	42	C
50-storey IBC-26	D3031.022k	1	Seq(DS1) + DS1(0.97, 0.6, 225825, 18, 2)	42	C

Continues on next page.

Tracking	Fragility Number	Category	Description	Source	EDP	Qty.	Units	Distribution
50-storey IBC-27	D5012.023e	MEP	Low Voltage Switchgear - Capacity: 350 to <750 Amp - Equipment that is either hard anchored or is vibration isolated with seismic snubbers/restraints - Equipment fragility only	Porter (2011)	PFA	6	Each (400 Amp Unit)	All Levels
50-storey IBC-28	C2011.001a	Egress	Prefabricated steel stair with steel treads and landings with seismic joints that accommodate drift.	Higgings (2011)	IDR	50	Each	All Levels
50-storey IBC-29	B2011.201a	Façade	Precast Concrete Panels 4.5 inches thick - in plane deformation	FEMA (2012)	IDR	1100	13'x30' Panels	Per Level
50-storey IBC-30	D1014.014	Egress	Vertical Transportation System (Elevators)	(Ibbi Almufti, personal communication 2012)	Residual IDR	24	Each	All Levels

See reverse.

Tracking	Fragility Number	NDS	DS Sequence + DSi (μ, β, MRC, MRT, RC)	LL	Repair Sequence
50-storey IBC-27	D5012.023e	1	Seq(DS1) + DS1(2.4, 0.4, 16433, 3, 2)		D
50-storey IBC-28	C2011.001a	3	Seq(DS1,DS2,DS3) + DS1(0.015, 0.6, 393, 0.4, 1) + DS2(0.027, 0.6, 2710, 3, 3) + DS3(0.038, 0.45, 20016, 22, 3)		F
50-storey IBC-29	B2011.201a	2	MutEx(DS1,DS2) + DS1(0.02, 0.5, 11728, 2, 3) + DS2(0.025, 0.5, 58643, 9, 3)	84	B
50-storey IBC-30	D1014.014	1	Seq(DS1) + DS1(0.002, 0.3, 1M, 7.5, 2)	42	E

Table C5 ends here.

Appendix D

Appendix D provides a breakdown of the ground motion suites utilized throughout the thesis. Appendix D1 includes ground motion data for the short and long period ground motion suites discussed in the BSPE: Intensity-based assessment in Chapter 6. Appendix D2 includes ground motion data for each intensity level considered in the BSPE: Time-based assessment in Chapter 7.

D1. BSPE: Intensity-based Assessment:
Table D1.1: BSPE: Intensity-based Assessment Short Period Ground Motion Suite
Table D1.2: BSPE: Intensity-based Assessment Long Period Ground Motion Suite
D2. BSPE: Intensity-based Assessment:
Table D2.1: BSPE: Time-based Assessment Intensity e_1 (72-year Return Period)
Table D2.2: BSPE: Time-based Assessment Intensity e_2 (199-year Return Period)
Table D2.3: BSPE: Time-based Assessment Intensity e_3 (409-year Return Period)
Table D2.4: BSPE: Time-based Assessment Intensity e_4 (712-year Return Period)
Table D2.5: BSPE: Time-based Assessment Intensity e_5 (1039-year Return Period)
Table D2.6: BSPE: Time-based Assessment Intensity e_6 (1898-year Return Period)
Table D2.7: BSPE: Time-based Assessment Intensity e_7 (2475-year Return Period)
Table D2.8: BSPE: Time-based Assessment Intensity e_8 (3898-year Return Period)

The ground motion records listed in this appendix can be accessed through the "PEER NGA-West2 Database" (PEER 2013) by using the NGA Record Number provided within the tables. References for other ground motion records used in this work, e.g. HayWired earthquake scenario discussed in Chapter 5, are provided within the main body of this thesis.

This page is intentionally left blank.

Table D1.1: BSPE: Intensity-based Assessment Short Period Ground Motion Suite

GM Number	Earthquake	Station	NGA Record	M_w	Fault Type	Closest Distance (km)	V_{S30} (m/s)	Extracted Pulse Period (sec)
1	1999 Chi-Chi Taiwan	CHY019	1190	7.6	Reverse-Oblique	50.5	478	N.A.
2	1999 Duzce, Turkey	Lamont Station 531	1618	7.1	Strike-Slip	8	660	N.A.
3	1999 Hector Mine	Fort Irwin	1783	7.1	Strike-Slip	65.9	345	N.A.
4	1979 Imperial Valley-06	Cerro Prieto	164	6.5	Strike-Slip	15.2	660	N.A.
5	1979 Imperial Valley-06	Delta	169	6.5	Strike-Slip	22	275	N.A.
6	1952 Kern County	LA Hollywood Stor Pe Lot	12	7.36	Reverse	117.8	317	N.A.
7	1999 Kocaeli Turkey	Zeytinburnu	1177	7.5	Strike-Slip	53.9	275	N.A.
8	1992 Landers	Desert Hot Springs	850	7.3	Strike-Slip	21.8	345	N.A.
9	1992 Cape Mendocino	Fortuna-Fortuna Blvd	827	7	Reverse	19.9	457	N.A.
10**	1980 Irpinia Italy-01	Bagnoli Irpinio	285	6.9	Normal	8.2	1000	1.75
11**	1989 Loma Prieta	Gilroy - Historic Bldg.	764	6.93	Reverse-Oblique	11	339	1.39

** Pulse-like ground motions

Table D1.2: BSPE: Intensity-based Assessment Long Period Ground Motion Suite

GM Number	Earthquake	Station	NGA Record	M_w	Fault Type	Closest Distance (km)	V_{S30} (m/s)	Extracted Pulse Period (sec)
1	1999 Kocaeli, Turkey	Yarimca	1176	7.5	Strike-slip	4.8	297	4.9
2	1979 Imperial Valley	El Centro Array#8	183	6.5	Strike-slip	3.9	206	5.82
3	1978 Tabas, Iran	Tabas	143	7.35	Reverse	2	767	6.19
4	1999 Kocaeli, Turkey	Arcelik	1148	7.5	Strike-slip	13.5	523	6.94
5	1992 Landers	Yermo Fire Station	900	7.3	Strike-slip	23.6	354	7.5
6	1999 Chi-Chi, Taiwan	TCU103	1530	7.62	Reverse-oblique	6.1	494	7.82
7	1992 Landers	Barstow	838	7.3	Strike-slip	34.9	371	8.88
8	2010 Darfield New Zealand	RHSC	6960	7	Strike-slip	13.6	270	9.45
9*	1972 Sitka, Alaska	Sitka Observatory	1626	7.68	Strike-slip	34.6	660	N.A.
10*	1999 Chi-Chi, Taiwan	CHY019	1190	7.62	Reverse-oblique	50.5	478	N.A.
11*	1999 Duzce Turkey	Bursa Tofas	1603	7.14	Strike-slip	166.1	275	N.A.

* Seed records for non-pulse-like ground motions.

Table D2.1: BSPE: Time-based Assessment Intensity e_1 (72-year Return Period)

GM Number	NGA Record	SF	Component	Earthquake	M_w	Station	Fault Type	Closest Distance (km)	V_{S30} (m/s)	Extracted Pulse Period (sec)
1	1496	0.3	2	"Chi-Chi_ Taiwan" 1999	7.62	"TCU056"	Reverse Oblique	10.48	403.2	8.939
2	6927	0.69	2	"Darfield_ New Zealand" 2010	7	"LINC"	Strike Slip	5.07	263.2	7.371
3	5829	0.39	1	"Cucapah_ Mexico" 2010	7.2	"RIITO"	Strike Slip	13.7	242.05	-
4	1270	3.17	2	"Chi-Chi_ Taiwan" 1999	7.62	"HWA020"	Reverse Oblique	39.8	626.43	-
5	8597	1.76	2	"Cucapah_ Mexico" 2010	7.2	"Sam W. Stewart"	Strike Slip	31.79	503	-
6	1490	0.51	1	"Chi-Chi_ Taiwan" 1999	7.62	"TCU050"	Reverse Oblique	9.49	542.41	-
7	5798	1.4	2	"Iwate_ Japan" 2008	6.9	"Takanashi Daisen"	Reverse	44.75	217.1	-
8	6890	0.61	1	"Darfield_ New Zealand" 2010	7	"Cashmere High School"	Strike Slip	17.64	204	-
9	6959	0.33	1	"Darfield_ New Zealand" 2010	7	"Christchurch Resthaven "	Strike Slip	19.48	141	12.019
10	6879	1.6	2	"Darfield_ New Zealand" 2010	7	"ADCS"	Strike Slip	28.46	249.28	-
11	163	0.98	1	"Imperial Valley-06" 1979	6.53	"Calipatria Fire Station"	Strike Slip	23.17	205.78	-
12	2462	1.62	2	"Chi-Chi_ Taiwan-03" 1999	6.2	"CHY029"	Reverse	31.08	544.74	-

Continues on reverse.

GM Number	NGA Record	SF	Component	Earthquake	M_w	Station	Fault Type	Closest Distance (km)	V_{S30} (m/s)	Extracted Pulse Period (sec)
13	1549	0.43	1	"Chi-Chi_ Taiwan" 1999	7.62	"TCU129"	Reverse Oblique	1.83	511.18	-
14	8062	2.15	1	"Christchurch_ New Zealand" 2011	6.2	"Canterbury Aero Club"	Reverse Oblique	14.41	280.26	-
15	4853	1.57	1	"Chuetsu-oki_ Japan" 2007	6.8	"Joetsu City"	Reverse	25.68	294.71	-
16	8123	0.53	1	"Christchurch_ New Zealand" 2011	6.2	"Christchurch Resthaven "	Reverse Oblique	5.11	141	1.554
17	6879	1.34	1	"Darfield_ New Zealand" 2010	7	"ADCS"	Strike Slip	28.46	249.28	-
18	850	2.88	1	"Landers" 1992	7.28	"Desert Hot Springs"	Strike Slip	21.78	359	-
19	138	1.47	2	"Tabas_ Iran" 1978	7.35	"Boshrooyeh"	Reverse	24.07	324.57	-

The 20th record in this suite corresponded to NGA Record 4816. However, this record was not available through the PEER NGA-West2 Database.

Table D2.2: BSPE: Time-based Assessment Intensity e_2 (199-year Return Period)

GM Number	NGA Record	SF	Component	Earthquake	M_w	Station	Fault Type	Closest Distance (km)	V_{S30} (m/s)	Extracted Pulse Period (sec)
1	787	3.59	1	"Loma Prieta" 1989	6.93	"Palo Alto - SLAC Lab"	Reverse Oblique	30.62	425.3	-
2	1478	0.73	1	"Chi-Chi_ Taiwan" 1999	7.62	"TCU033"	Reverse Oblique	40.88	423.4	8.974
3	2615	3.69	1	"Chi-Chi_ Taiwan-03" 1999	6.2	"TCU061"	Reverse	39.93	379.64	-
4	1496	1.3	1	"Chi-Chi_ Taiwan" 1999	7.62	"TCU056"	Reverse Oblique	10.48	403.2	8.939
5	2114	0.57	1	"Denali_ Alaska" 2002	7.9	"TAPS Pump Station #10"	Strike Slip	0.18	329.4	3.157
6	1199	2.47	2	"Chi-Chi_ Taiwan" 1999	7.62	"CHY032"	Reverse Oblique	35.43	192.71	-
7	1493	0.87	2	"Chi-Chi_ Taiwan" 1999	7.62	"TCU053"	Reverse Oblique	5.95	454.55	13.118
8	187	2.04	1	"Imperial Valley-06" 1979	6.53	"Parachute Test Site"	Strike Slip	12.69	348.69	-
9	2619	4.85	1	"Chi-Chi_ Taiwan-03" 1999	6.2	"TCU067"	Reverse	27.66	433.63	-
10	170	0.72	2	"Imperial Valley-06" 1979	6.53	"EC County Center FF"	Strike Slip	7.31	192.05	4.417
11	286	1.7	1	"Irpinia_ Italy-01" 1980	6.9	"Bisaccia"	Normal	17.51	496.46	-
12	1182	0.97	2	"Chi-Chi_ Taiwan" 1999	7.62	"CHY006"	Reverse Oblique	9.76	438.19	2.5704

Continues on reverse.

GM Number	NGA Record	SF	Component	Earthquake	M_w	Station	Fault Type	Closest Distance (km)	V_{S30} (m/s)	Extracted Pulse Period (sec)
13	807	2.25	2	"Loma Prieta" 1989	6.93	"Sunol - Forest Fire Station"	Reverse Oblique	47.41	400.62	-
14	5969	1.46	2	"Cucapah_ Mexico" 2010	7.2	"Bonds Corner"	Strike Slip	30.75	223.03	-
15	5745	1.78	1	"Iwate_ Japan" 2008	6.9	"YMT002"	Reverse	36.92	365.59	-
16	4348	3.94	1	"Umbria Marche_ Italy" 1997	6	"Castelnuovo-Assisi"	Normal	17.28	293	-
17	1211	3.78	2	"Chi-Chi_ Taiwan" 1999	7.62	"CHY052"	Reverse Oblique	38.7	573.04	-
18	1199	1.59	1	"Chi-Chi_ Taiwan" 1999	7.62	"CHY032"	Reverse Oblique	35.43	192.71	-
19	6879	2.83	1	"Darfield_ New Zealand" 2010	7	"ADCS"	Strike Slip	28.46	249.28	-

The 20th record in this suite corresponded to NGA Record 4716. However, this record was not available through the PEER NGA-West2 Database.

Table D2.3: BSPE: Time-based Assessment Intensity e_3 (409-year Return Period)

GM Number	NGA Record	SF	Component	Earthquake	M_w	Station	Fault Type	Closest Distance (km)	V_{S30} (m/s)	Extracted Pulse Period (sec)
1	1487	2.2	1	"Chi-Chi_ Taiwan" 1999	7.62	"TCU047"	Reverse Oblique	35	520.37	12.313
2	1476	0.6	2	"Chi-Chi_ Taiwan" 1999	7.62	"TCU029"	Reverse Oblique	28.04	406.53	5.285
3	1551	2.06	1	"Chi-Chi_ Taiwan" 1999	7.62	"TCU138"	Reverse Oblique	9.78	652.85	-
4	721	1.62	2	"Superstition Hills-02" 1987	6.54	"El Centro Imp. Co. Cent"	Strike Slip	18.2	192.05	-
5	1113	4.61	2	"Kobe_ Japan" 1995	6.9	"OSAJ"	Strike Slip	21.35	256	-
6	192	2.92	2	"Imperial Valley-06" 1979	6.53	"Westmorland Fire Sta"	Strike Slip	14.75	193.67	-
7	1527	0.81	2	"Chi-Chi_ Taiwan" 1999	7.62	"TCU100"	Reverse Oblique	11.37	535.13	-
8	1547	1.93	1	"Chi-Chi_ Taiwan" 1999	7.62	"TCU123"	Reverse Oblique	14.91	270.22	-
9	1486	1.74	1	"Chi-Chi_ Taiwan" 1999	7.62	"TCU046"	Reverse Oblique	16.74	465.55	8.043
10	1494	1.54	2	"Chi-Chi_ Taiwan" 1999	7.62	"TCU054"	Reverse Oblique	5.28	460.69	-
11	1496	1	2	"Chi-Chi_ Taiwan" 1999	7.62	"TCU056"	Reverse Oblique	10.48	403.2	8.939
12	1511	1.3	1	"Chi-Chi_ Taiwan" 1999	7.62	"TCU076"	Reverse Oblique	2.74	614.98	4.732

Continues on reverse.

GM Number	NGA Record	SF	Component	Earthquake	M_w	Station	Fault Type	Closest Distance (km)	V_{S30} (m/s)	Extracted Pulse Period (sec)
13	316	1.61	1	"Westmorland" 1981	5.9	"Parachute Test Site"	Strike Slip	16.54	348.69	4.389
14	1183	1.69	2	"Chi-Chi_ Taiwan" 1999	7.62	"CHY008"	Reverse Oblique	40.43	210.73	-
15	173	1.38	1	"Imperial Valley-06" 1979	6.53	"El Centro Array #10"	Strike Slip	8.6	202.85	4.515
16	1541	1.21	1	"Chi-Chi_ Taiwan" 1999	7.62	"TCU116"	Reverse Oblique	12.38	493.09	-
17	1484	0.89	2	"Chi-Chi_ Taiwan" 1999	7.62	"TCU042"	Reverse Oblique	26.31	578.98	-
18	175	3.31	1	"Imperial Valley-06" 1979	6.53	"El Centro Array #12"	Strike Slip	17.94	196.88	-
19	1500	1.32	1	"Chi-Chi_ Taiwan" 1999	7.62	"TCU061"	Reverse Oblique	17.17	379.64	-

The 20th record in this suite corresponded to NGA Record 4798. However, this record was not available through the PEER NGA-West2 Database.

Table D2.4: BSPE: Time-based Assessment Intensity e_4 (712-year Return Period)

GM Number	NGA Record	SF	Component	Earthquake	M_w	Station	Fault Type	Closest Distance (km)	V_{S30} (m/s)	Extracted Pulse Period (sec)
1	1476	0.8	2	"Chi-Chi_ Taiwan" 1999	7.62	"TCU029"	Reverse Oblique	28.04	406.53	5.285
2	8161	2.12	1	"Cucapah_ Mexico" 2010	7.2	"El Centro Array #12"	Strike Slip	9.98	196.88	8.722
3	6969	1.9	2	"Darfield_ New Zealand" 2010	7	"Styx Mill Transfer Station "	Strike Slip	20.86	247.5	9.352
4	2114	1.2	1	"Denali_ Alaska" 2002	7.9	"TAPS Pump Station #10"	Strike Slip	0.18	329.4	3.157
5	5969	4.38	1	"Cucapah_ Mexico" 2010	7.2	"Bonds Corner"	Strike Slip	30.75	223.03	-
6	1496	1.32	2	"Chi-Chi_ Taiwan" 1999	7.62	"TCU056"	Reverse Oblique	10.48	403.2	8.939
7	838	4.53	2	"Landers" 1992	7.28	"Barstow"	Strike Slip	34.86	370.08	9.128
8	827	4.68	2	"Cape Mendocino" 1992	7.01	"Fortuna - Fortuna Blvd"	Reverse	15.97	457.06	-
9	173	1.82	1	"Imperial Valley-06" 1979	6.53	"El Centro Array #10"	Strike Slip	8.6	202.85	4.515
10	1527	1.07	2	"Chi-Chi_ Taiwan" 1999	7.62	"TCU100"	Reverse Oblique	11.37	535.13	-
11	1477	1.3	2	"Chi-Chi_ Taiwan" 1999	7.62	"TCU031"	Reverse Oblique	30.17	489.22	5.929
12	8160	1.84	1	"Cucapah_ Mexico" 2010	7.2	"El Centro Array #4"	Strike Slip	35.08	208.91	-

Continues on reverse.

GM Number	NGA Record	SF	Component	Earthquake	M_w	Station	Fault Type	Closest Distance (km)	V_{S30} (m/s)	Extracted Pulse Period (sec)
13	1497	1.17	2	"Chi-Chi_ Taiwan" 1999	7.62	"TCU057"	Reverse Oblique	11.83	555.23	-
14	1538	1.66	1	"Chi-Chi_ Taiwan" 1999	7.62	"TCU112"	Reverse Oblique	27.48	190.54	-
15	1605	0.73	2	"Duzce_ Turkey" 1999	7.14	"Duzce"	Strike Slip	0	281.86	-
16	1204	3.96	2	"Chi-Chi_ Taiwan" 1999	7.62	"CHY039"	Reverse Oblique	31.87	201.21	-
17	286	3.54	1	"Irpinia_ Italy-01" 1980	6.9	"Bisaccia"	Normal	17.51	496.46	-
18	1531	1.97	1	"Chi-Chi_ Taiwan" 1999	7.62	"TCU104"	Reverse Oblique	12.87	410.45	7.189
19	1204	3.19	1	"Chi-Chi_ Taiwan" 1999	7.62	"CHY039"	Reverse Oblique	31.87	201.21	-
20	1510	0.86	1	"Chi-Chi_ Taiwan" 1999	7.62	"TCU075"	Reverse Oblique	0.89	573.02	4.998

Table D2.5: BSPE: Time-based Assessment Intensity e_5 (1039-year Return Period)

GM Number	NGA Record	SF	Component	Earthquake	M_w	Station	Fault Type	Closest Distance (km)	V_{S30} (m/s)	Extracted Pulse Period (sec)
1	1527	1.27	2	"Chi-Chi_ Taiwan" 1999	7.62	"TCU100"	Reverse Oblique	11.37	535.13	-
2	5823	2.44	1	"Cucapah_ Mexico" 2010	7.2	"Chihuahua"	Strike Slip	18.21	242.05	-
3	2114	1.42	1	"Denali_ Alaska" 2002	7.9	"TAPS Pump Station #10"	Strike Slip	0.18	329.4	3.157
4	1540	1.31	1	"Chi-Chi_ Taiwan" 1999	7.62	"TCU115"	Reverse Oblique	21.76	215.34	-
5	1499	3.32	1	"Chi-Chi_ Taiwan" 1999	7.62	"TCU060"	Reverse Oblique	8.51	375.42	-
6	1502	1.93	1	"Chi-Chi_ Taiwan" 1999	7.62	"TCU064"	Reverse Oblique	16.59	645.72	8.456
7	1539	3.33	2	"Chi-Chi_ Taiwan" 1999	7.62	"TCU113"	Reverse Oblique	31.05	230.3	-
8	1533	1.38	2	"Chi-Chi_ Taiwan" 1999	7.62	"TCU106"	Reverse Oblique	14.97	451.37	-
9	36	4.91	2	"Borrego Mtn" 1968	6.63	"El Centro Array #9"	Strike Slip	45.12	213.44	-
10	1533	2.06	1	"Chi-Chi_ Taiwan" 1999	7.62	"TCU106"	Reverse Oblique	14.97	451.37	-
11	728	4.12	1	"Superstition Hills-02" 1987	6.54	"Westmorland Fire Sta"	Strike Slip	13.03	193.67	-
12	1488	2.07	1	"Chi-Chi_ Taiwan" 1999	7.62	"TCU048"	Reverse Oblique	13.53	551.21	-

Continues on reverse.

GM Number	NGA Record	SF	Component	Earthquake	M_w	Station	Fault Type	Closest Distance (km)	V_{S30} (m/s)	Extracted Pulse Period (sec)
13	6975	1.59	2	"Darfield_ New Zealand" 2010	7	"TPLC"	Strike Slip	6.11	249.28	8.932
14	1545	2.32	1	"Chi-Chi_ Taiwan" 1999	7.62	"TCU120"	Reverse Oblique	7.4	459.34	-
15	6912	2.32	2	"Darfield_ New Zealand" 2010	7	"Hulverstone Drive Pumping Station"	Strike Slip	25.4	206	-
16	1554	2.01	2	"Chi-Chi_ Taiwan" 1999	7.62	"TCU145"	Reverse Oblique	35.32	240.43	-
17	1233	2.31	2	"Chi-Chi_ Taiwan" 1999	7.62	"CHY082"	Reverse Oblique	36.09	193.69	-
18	1496	3.22	1	"Chi-Chi_ Taiwan" 1999	7.62	"TCU056"	Reverse Oblique	10.48	403.2	8.939
19	20	4.73	1	"Northern Calif-03" 1954	6.5	"Ferndale City Hall"	Strike Slip	26.72	219.31	-
20	1477	1.55	2	"Chi-Chi_ Taiwan" 1999	7.62	"TCU031"	Reverse Oblique	30.17	489.22	5.929

Table D2.6: BSPE: Time-based Assessment Intensity e_6 (1898-year Return Period)

GM Number	NGA Record	SF	Component	Earthquake	M_w	Station	Fault Type	Closest Distance (km)	V_{S30} (m/s)	Extracted Pulse Period (sec)
1	1547	3.92	1	"Chi-Chi_ Taiwan" 1999	7.62	"TCU123"	Reverse Oblique	14.91	270.22	-
2	1238	1.46	2	"Chi-Chi_ Taiwan" 1999	7.62	"CHY092"	Reverse Oblique	22.69	253.72	-
3	6890	4.1	1	"Darfield_ New Zealand" 2010	7	"Cashmere High School"	Strike Slip	17.64	204	-
4	1544	4.83	2	"Chi-Chi_ Taiwan" 1999	7.62	"TCU119"	Reverse Oblique	37.93	221.7	-
5	1554	2.6	2	"Chi-Chi_ Taiwan" 1999	7.62	"TCU145"	Reverse Oblique	35.32	240.43	-
6	1552	4.14	1	"Chi-Chi_ Taiwan" 1999	7.62	"TCU140"	Reverse Oblique	32.95	223.6	-
7	1496	4.15	1	"Chi-Chi_ Taiwan" 1999	7.62	"TCU056"	Reverse Oblique	10.48	403.2	8.939
8	1534	2.17	1	"Chi-Chi_ Taiwan" 1999	7.62	"TCU107"	Reverse Oblique	15.99	409	-
9	2114	1.83	1	"Denali_ Alaska" 2002	7.9	"TAPS Pump Station #10"	Strike Slip	0.18	329.4	3.157
10	5825	2.04	2	"Cucapah_ Mexico" 2010	7.2	"CERRO PRIETO GEOTHERMAL"	Strike Slip	8.88	242.05	-
11	1194	1.66	1	"Chi-Chi_ Taiwan" 1999	7.62	"CHY025"	Reverse Oblique	19.07	277.5	-
12	1548	1.76	1	"Chi-Chi_ Taiwan" 1999	7.62	"TCU128"	Reverse Oblique	13.13	599.64	9.023

Continues on reverse.

GM Number	NGA Record	SF	Component	Earthquake	M_w	Station	Fault Type	Closest Distance (km)	V_{S30} (m/s)	Extracted Pulse Period (sec)
13	5836	2.05	1	"Cucapah_ Mexico" 2010	7.2	"El Centro - Meloland Geot. Array"	Strike Slip	28.53	264.57	-
14	1531	1.6	2	"Chi-Chi_ Taiwan" 1999	7.62	"TCU104"	Reverse Oblique	12.87	410.45	7.189
15	2662	3.62	2	"Chi-Chi_ Taiwan-03" 1999	6.2	"TCU140"	Reverse	45.17	223.6	-
16	1233	3.48	1	"Chi-Chi_ Taiwan" 1999	7.62	"CHY082"	Reverse Oblique	36.09	193.69	-
17	1540	2.03	2	"Chi-Chi_ Taiwan" 1999	7.62	"TCU115"	Reverse Oblique	21.76	215.34	-
18	1527	3.06	1	"Chi-Chi_ Taiwan" 1999	7.62	"TCU100"	Reverse Oblique	11.37	535.13	-
19	1550	2.42	1	"Chi-Chi_ Taiwan" 1999	7.62	"TCU136"	Reverse Oblique	8.27	462.1	8.8816
20	1488	2.67	1	"Chi-Chi_ Taiwan" 1999	7.62	"TCU048"	Reverse Oblique	13.53	551.21	-

Table D2.7: BSPE: Time-based Assessment Intensity e_7 (2475-year Return Period)

GM Number	NGA Record	SF	Component	Earthquake	M_w	Station	Fault Type	Closest Distance (km)	V_{S30} (m/s)	Extracted Pulse Period (sec)
1	2459	2.47	2	"Chi-Chi_ Taiwan-03" 1999	6.2	"CHY026"	Reverse	38.3	226.01	-
2	5838	2.38	1	"Cucapah_ Mexico" 2010	7.2	"El Centro - Meloland Geotechnic"	Strike Slip	28.53	186.21	-
3	1531	1.77	2	"Chi-Chi_ Taiwan" 1999	7.62	"TCU104"	Reverse Oblique	12.87	410.45	7.189
4	1477	2.21	2	"Chi-Chi_ Taiwan" 1999	7.62	"TCU031"	Reverse Oblique	30.17	489.22	5.929
5	1542	3.08	2	"Chi-Chi_ Taiwan" 1999	7.62	"TCU117"	Reverse Oblique	25.42	198.58	-
6	1194	1.84	1	"Chi-Chi_ Taiwan" 1999	7.62	"CHY025"	Reverse Oblique	19.07	277.5	-
7	1527	1.81	2	"Chi-Chi_ Taiwan" 1999	7.62	"TCU100"	Reverse Oblique	11.37	535.13	-
8	1534	2.4	1	"Chi-Chi_ Taiwan" 1999	7.62	"TCU107"	Reverse Oblique	15.99	409	-
9	1496	4.59	1	"Chi-Chi_ Taiwan" 1999	7.62	"TCU056"	Reverse Oblique	10.48	403.2	8.939
10	1533	1.97	2	"Chi-Chi_ Taiwan" 1999	7.62	"TCU106"	Reverse Oblique	14.97	451.37	-
11	6952	2.39	2	"Darfield_ New Zealand" 2010	7	"Papanui High School "	Strike Slip	18.73	263.2	-
12	1510	1.46	1	"Chi-Chi_ Taiwan" 1999	7.62	"TCU075"	Reverse Oblique	0.89	573.02	4.998

Continues on reverse.

GM Number	NGA Record	SF	Component	Earthquake	M_w	Station	Fault Type	Closest Distance (km)	V_{S30} (m/s)	Extracted Pulse Period (sec)
13	1542	1.84	1	"Chi-Chi_ Taiwan" 1999	7.62	"TCU117"	Reverse Oblique	25.42	198.58	-
14	1540	1.86	1	"Chi-Chi_ Taiwan" 1999	7.62	"TCU115"	Reverse Oblique	21.76	215.34	-
15	1491	3.63	1	"Chi-Chi_ Taiwan" 1999	7.62	"TCU051"	Reverse Oblique	7.64	350.06	10.381
16	5665	2.49	2	"Iwate_ Japan" 2008	6.9	"MYG006"	Reverse	30.38	146.72	-
17	5831	3.79	2	"Cucapah_ Mexico" 2010	7.2	"EJIDO SALTILLO"	Strike Slip	14.8	242.05	-
18	1527	3.39	1	"Chi-Chi_ Taiwan" 1999	7.62	"TCU100"	Reverse Oblique	11.37	535.13	-
19	1536	3.45	2	"Chi-Chi_ Taiwan" 1999	7.62	"TCU110"	Reverse Oblique	11.58	212.72	-
20	1488	1.67	2	"Chi-Chi_ Taiwan" 1999	7.62	"TCU048"	Reverse Oblique	13.53	551.21	-

Table D2.8: BSPE: Time-based Assessment Intensity e_8 (3898-year Return Period)

GM Number	NGA Record	SF	Component	Earthquake	M_w	Station	Fault Type	Closest Distance (km)	V_{S30} (m/s)	Extracted Pulse Period (sec)
1	2459	2.91	2	"Chi-Chi_ Taiwan-03" 1999	6.2	"CHY026"	Reverse	38.3	226.01	-
2	2114	2.39	1	"Denali_ Alaska" 2002	7.9	"TAPS Pump Station #10"	Strike Slip	0.18	329.4	3.157
3	1488	1.96	2	"Chi-Chi_ Taiwan" 1999	7.62	"TCU048"	Reverse Oblique	13.53	551.21	-
4	1497	2.34	2	"Chi-Chi_ Taiwan" 1999	7.62	"TCU057"	Reverse Oblique	11.83	555.23	-
5	1477	2.35	1	"Chi-Chi_ Taiwan" 1999	7.62	"TCU031"	Reverse Oblique	30.17	489.22	5.929
6	1534	2.82	1	"Chi-Chi_ Taiwan" 1999	7.62	"TCU107"	Reverse Oblique	15.99	409	-
7	1477	2.6	2	"Chi-Chi_ Taiwan" 1999	7.62	"TCU031"	Reverse Oblique	30.17	489.22	5.929
8	1233	4.53	1	"Chi-Chi_ Taiwan" 1999	7.62	"CHY082"	Reverse Oblique	36.09	193.69	-
9	1531	2.09	2	"Chi-Chi_ Taiwan" 1999	7.62	"TCU104"	Reverse Oblique	12.87	410.45	7.189
10	1194	2.16	1	"Chi-Chi_ Taiwan" 1999	7.62	"CHY025"	Reverse Oblique	19.07	277.5	-
11	1530	2.67	1	"Chi-Chi_ Taiwan" 1999	7.62	"TCU103"	Reverse Oblique	6.08	494.1	8.687
12	1527	2.13	2	"Chi-Chi_ Taiwan" 1999	7.62	"TCU100"	Reverse Oblique	11.37	535.13	-

Continues on reverse.

GM Number	NGA Record	SF	Component	Earthquake	M_w	Station	Fault Type	Closest Distance (km)	V_{S30} (m/s)	Extracted Pulse Period (sec)
13	1180	1.82	2	"Chi-Chi_ Taiwan" 1999	7.62	"CHY002"	Reverse Oblique	24.96	235.13	-
14	1538	4.17	2	"Chi-Chi_ Taiwan" 1999	7.62	"TCU112"	Reverse Oblique	27.48	190.54	-
15	1183	4.46	2	"Chi-Chi_ Taiwan" 1999	7.62	"CHY008"	Reverse Oblique	40.43	210.73	-
16	1545	3.9	1	"Chi-Chi_ Taiwan" 1999	7.62	"TCU120"	Reverse Oblique	7.4	459.34	-
17	6906	2.15	2	"Darfield_ New Zealand" 2010	7	"GDLC"	Strike Slip	1.22	344.02	6.23
18	1488	3.48	1	"Chi-Chi_ Taiwan" 1999	7.62	"TCU048"	Reverse Oblique	13.53	551.21	-
19	6969	3.8	2	"Darfield_ New Zealand" 2010	7	"Styx Mill Transfer Station "	Strike Slip	20.86	247.5	9.352
20	1535	1.83	2	"Chi-Chi_ Taiwan" 1999	7.62	"TCU109"	Reverse Oblique	13.06	535.13	-

Appendix E

Appendix E includes probabilistic seismic hazard de-aggregation data and geographical seismic hazard de-aggregation data, as obtained from USGS (2008), for an array earthquake shaking intensities considered in the time-based assessment presented in Chapter 7. This data is summarized in a series of figures as listed below.

E1. Figure E1: Probabilistic seismic hazard de-aggregation at the representative site in downtown San Francisco (V_{s30}=260m/s, T=5sec.) for a return period of 72 years including M, R and ε data (a) and geographical (b) de-aggregation data used in the time-based assessment.

E2. Figure E2: Probabilistic seismic hazard de-aggregation at the representative site in downtown San Francisco (V_{s30}=260m/s, T=5sec.) for a return period of 199 years including M, R and ε data (a) and geographical (b) de-aggregation data used in the time-based assessment.

E3. Figure E3: Probabilistic seismic hazard de-aggregation at the representative site in downtown San Francisco (V_{s30}=260m/s, T=5sec.) for a return period of 409 years including M, R and ε data (a) and geographical (b) de-aggregation data used in the time-based assessment.

E4. Figure E4: Probabilistic seismic hazard de-aggregation at the representative site in downtown San Francisco (V_{s30}=260m/s, T=5sec.) for a return period of 712 years including M, R and ε data (a) and geographical (b) de-aggregation data used in the time-based assessment.

E5. Figure E5: Probabilistic seismic hazard de-aggregation at the representative site in downtown San Francisco (V_{s30}=260m/s, T=5sec.) for a return period of 1039 years including M, R and ε data (a) and geographical (b) de-aggregation data used in the time-based assessment.

E6. Figure E6: Probabilistic seismic hazard de-aggregation at the representative site in downtown San Francisco (V_{s30}=260m/s, T=5sec.) for a return period of 1898 years including M, R and ε data (a) and geographical (b) de-aggregation data used in the time-based assessment.

E7. Figure E7: Probabilistic seismic hazard de-aggregation at the representative site in downtown San Francisco (V_{s30}=260m/s, T=5sec.) for a return period of 2475 years including M, R and ε data (a) and geographical (b) de-aggregation data used in the time-based assessment.

E8. Figure E8: Probabilistic seismic hazard de-aggregation at the representative site in downtown San Francisco (V_{s30}=260m/s, T=5sec.) for a return period of 3898 years including M, R and ε data (a) and geographical (b) de-aggregation data used in the time-based assessment.

This page is intentionally left blank.

(a)

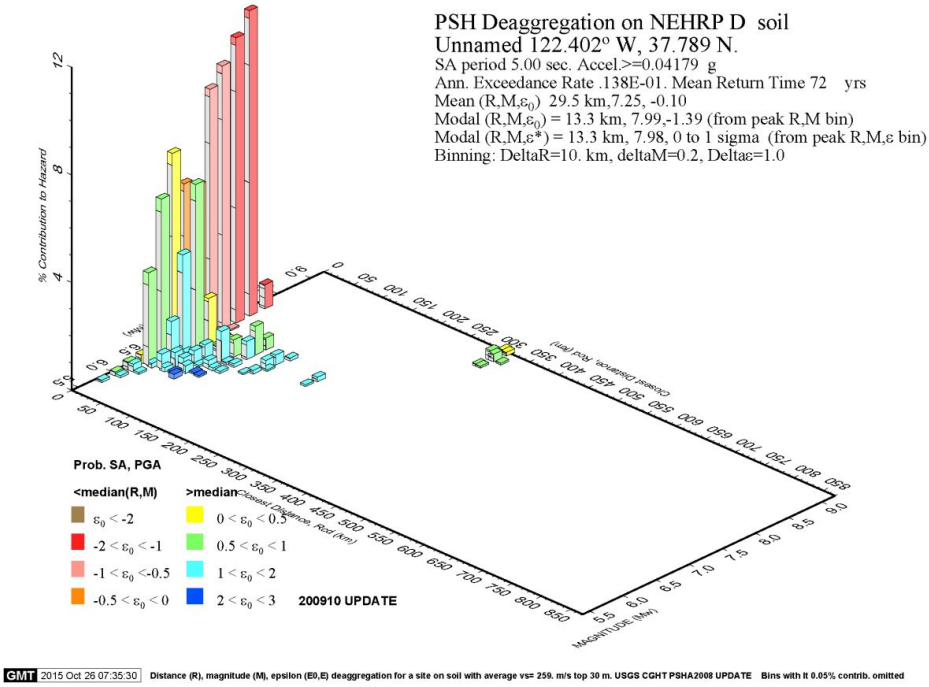

(b)

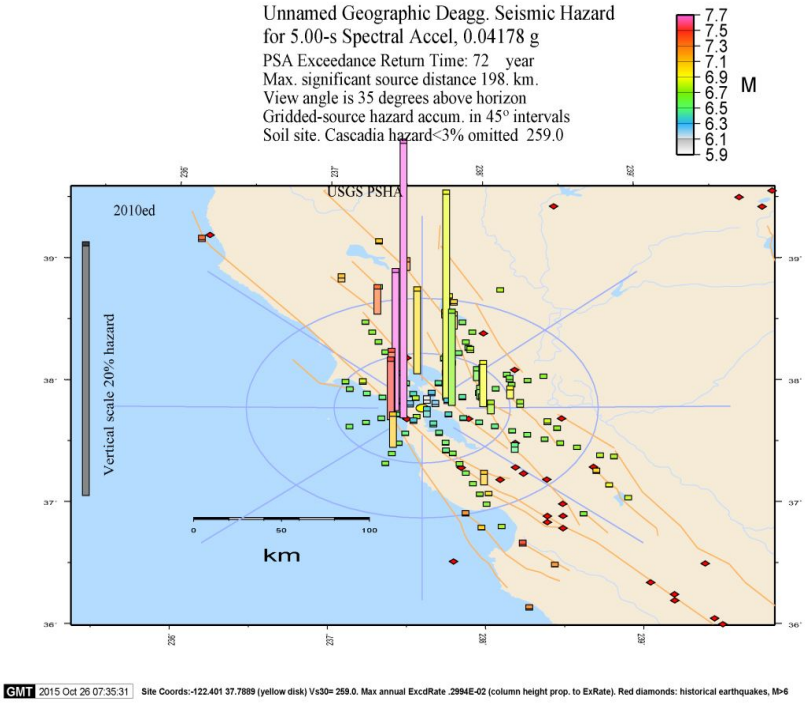

Figure E1: Probabilistic seismic hazard de-aggregation at the representative site in downtown San Francisco (V_{s30}=260m/s, T=5sec.) for a return period of 72 years including M, R and ε data (a) and geographical (b) de-aggregation data used in the time-based assessment.

(a)

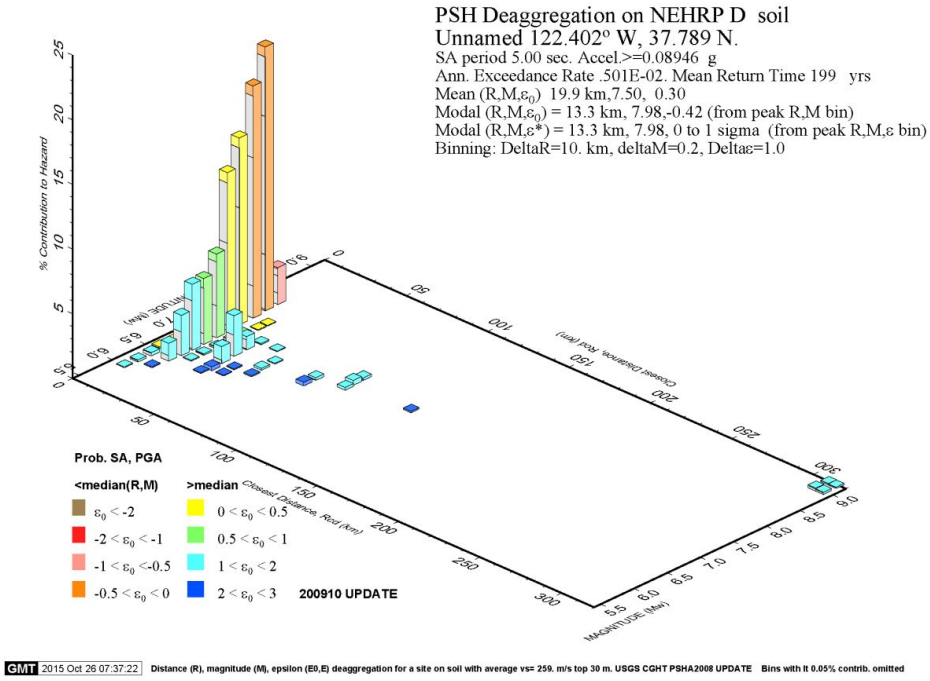

(b)

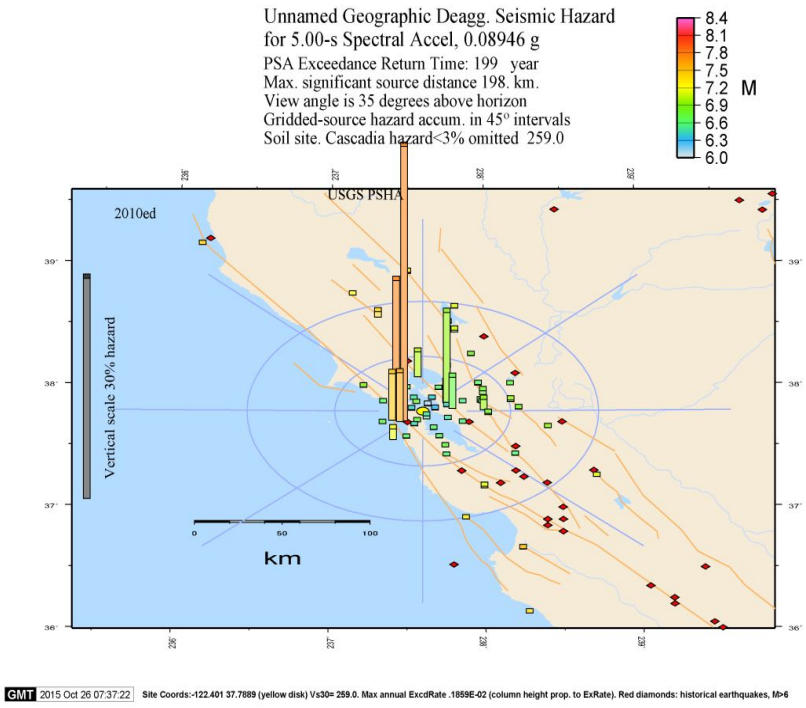

Figure E2: Probabilistic seismic hazard de-aggregation at the representative site in downtown San Francisco (V_{s30}=260m/s, T=5sec.) for a return period of 199 years including M, R and ε data (a) and geographical (b) de-aggregation data used in the time-based assessment.

(a)

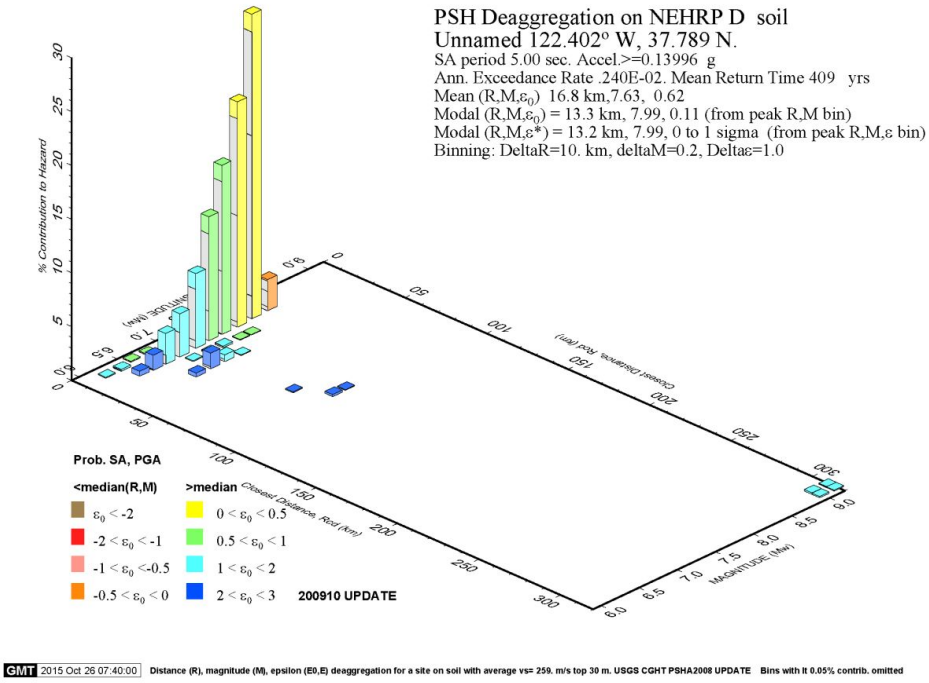

(b)

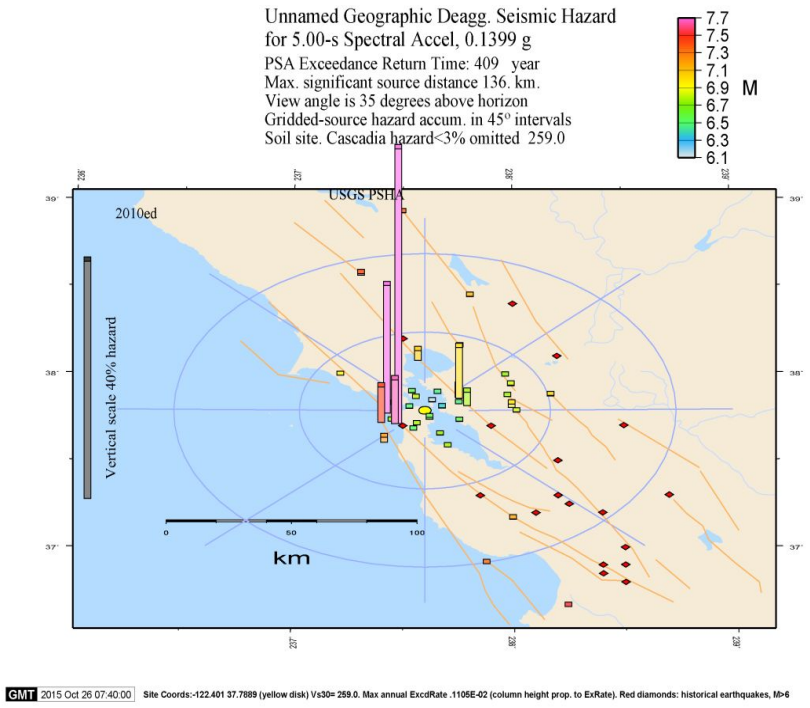

Figure E3: Probabilistic seismic hazard de-aggregation at the representative site in downtown San Francisco (V_{s30}=260m/s, T=5sec.) for a return period of 409 years including M, R and ε data (a) and geographical (b) de-aggregation data used in the time-based assessment.

(a)

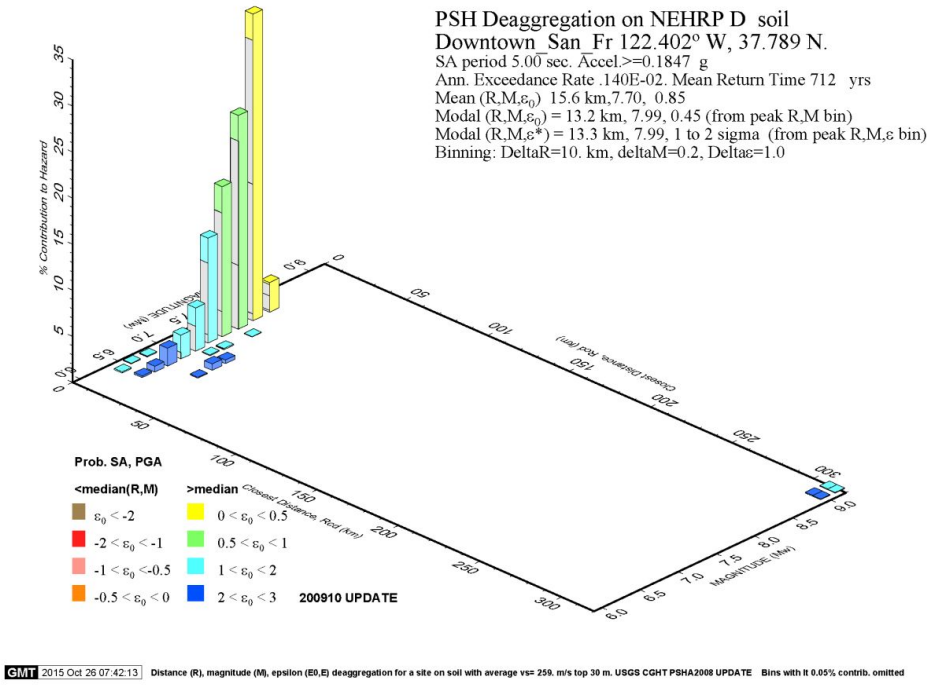

(b)

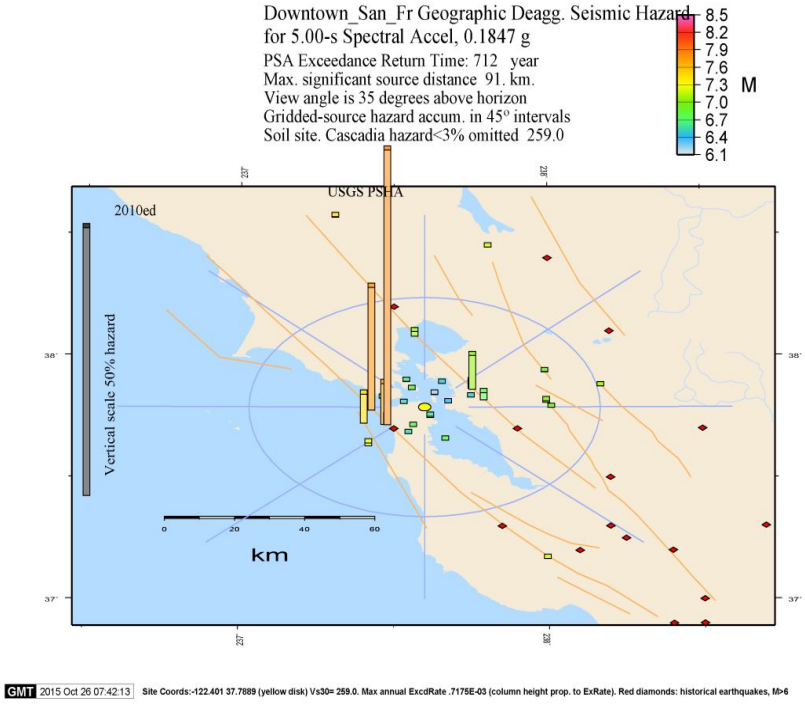

Figure E4: Probabilistic seismic hazard de-aggregation at the representative site in downtown San Francisco (V_{s30}=260m/s, T=5sec.) for a return period of 712 years including M, R and ε data (a) and geographical (b) de-aggregation data used in the time-based assessment.

(a)

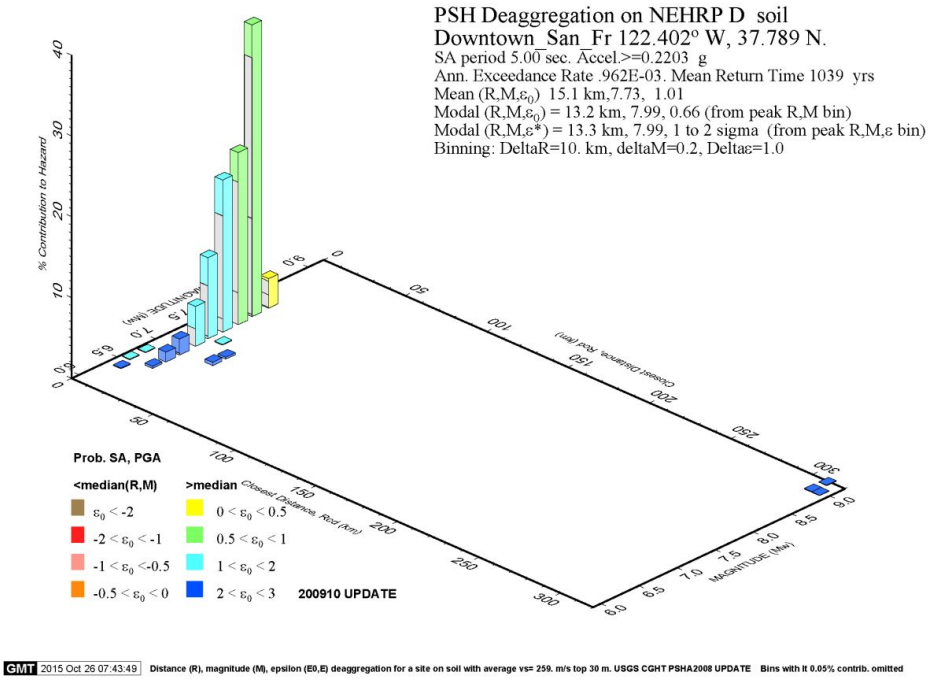

(b)

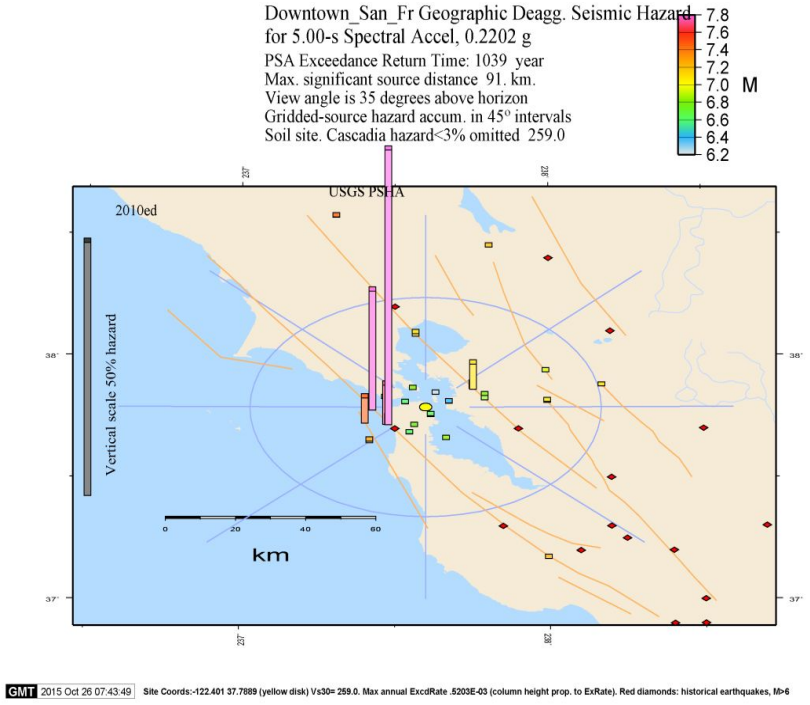

Figure E5: Probabilistic seismic hazard de-aggregation at the representative site in downtown San Francisco (V_{s30}=260m/s, T=5sec.) for a return period of 1039 years including M, R and ε data (a) and geographical (b) de-aggregation data used in the time-based assessment.

(a)

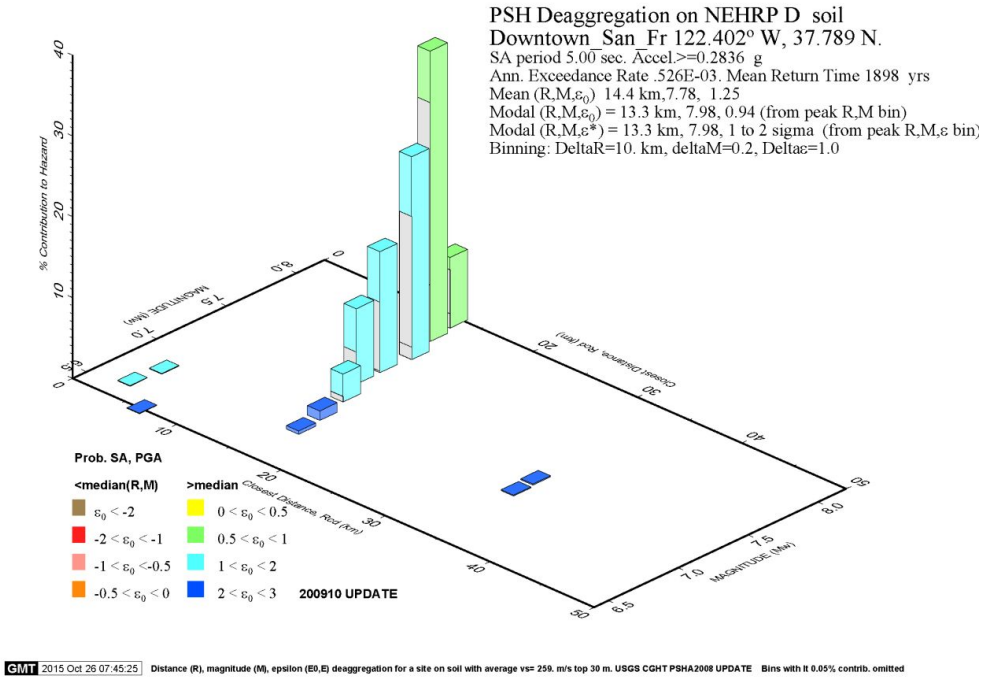

(b)

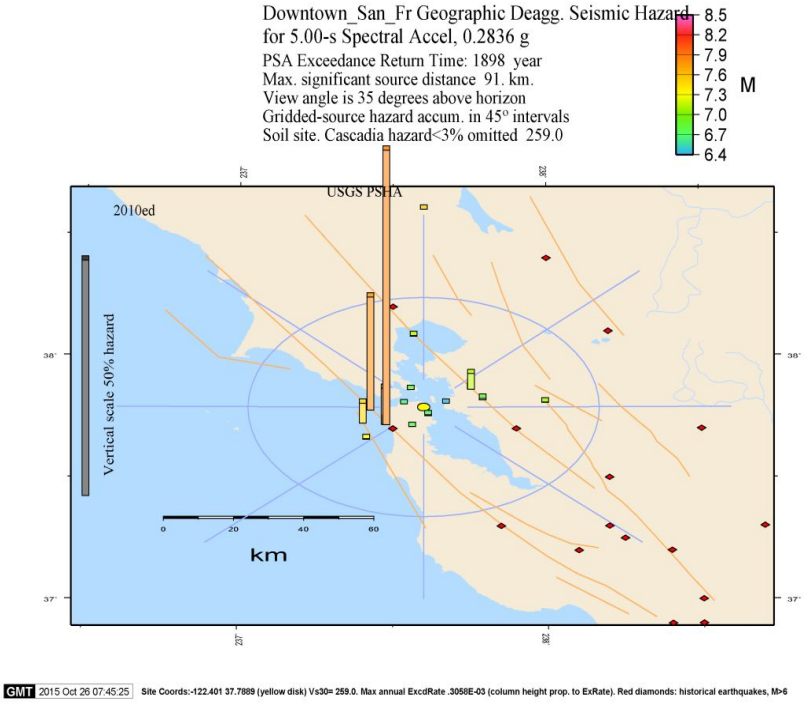

Figure E6: Probabilistic seismic hazard de-aggregation at the representative site in downtown San Francisco (V_{s30}=260m/s, T=5sec.) for a return period of 1898 years including M, R and ε data (a) and geographical (b) de-aggregation data used in the time-based assessment.

(a)

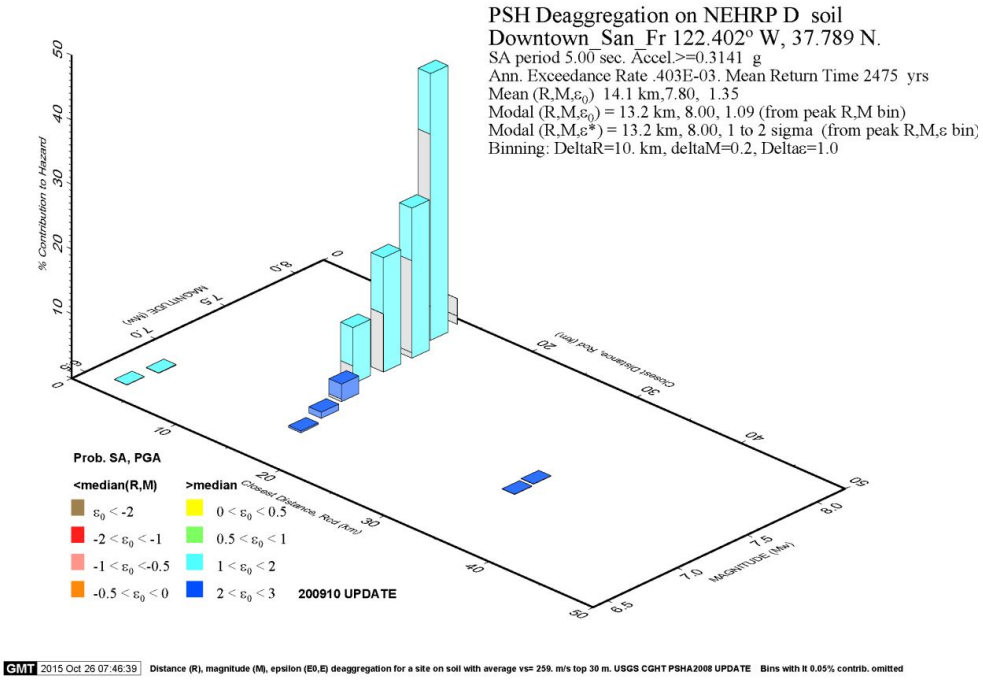

(b)

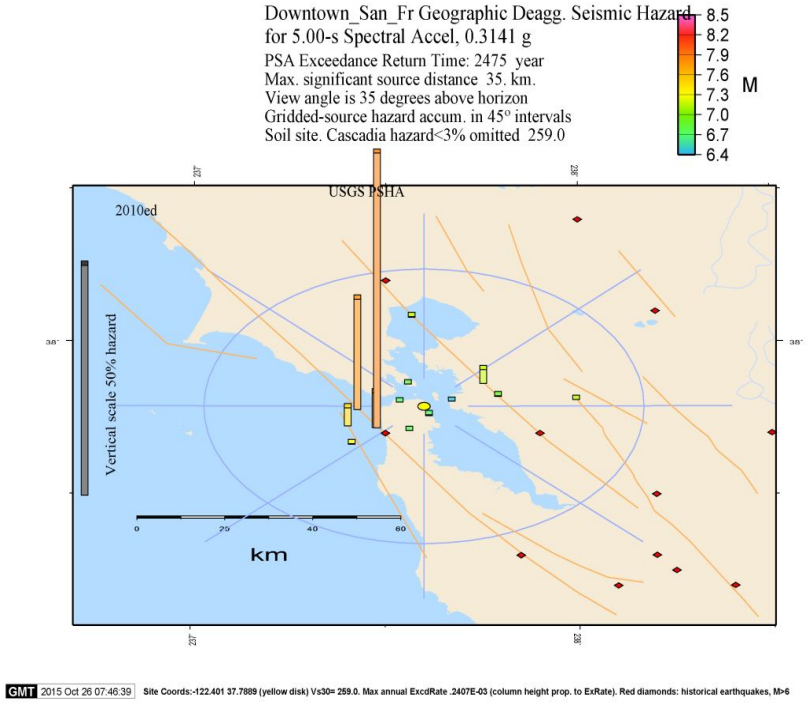

Figure E7: Probabilistic seismic hazard de-aggregation at the representative site in downtown San Francisco (V_{s30}=260m/s, T=5sec.) for a return period of 2475 years including M, R and ε data (a) and geographical (b) de-aggregation data used in the time-based assessment.

(a)

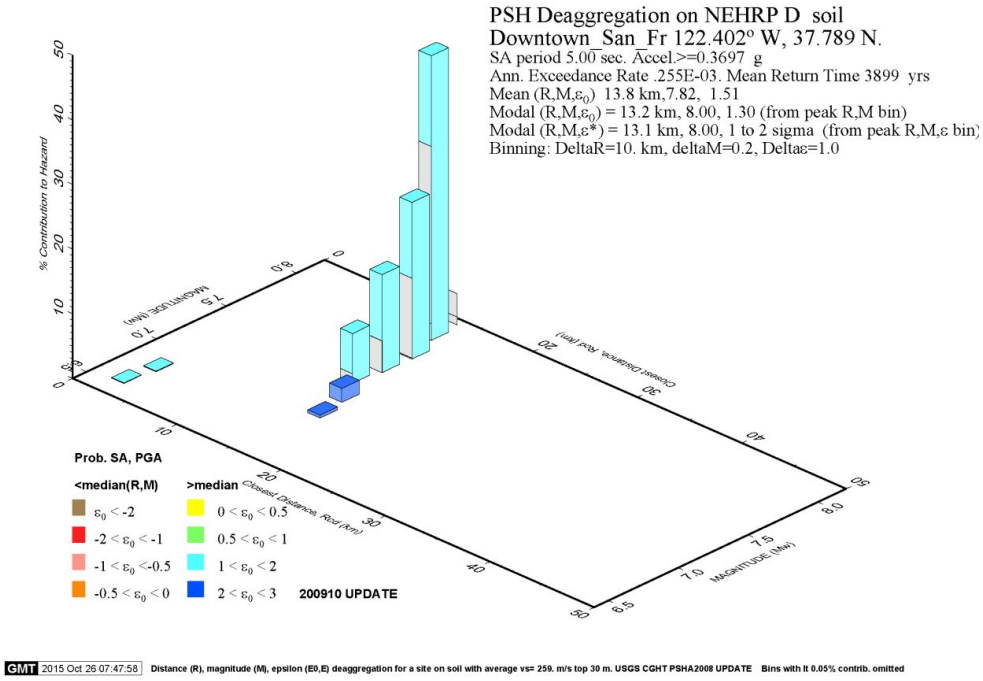

(b)

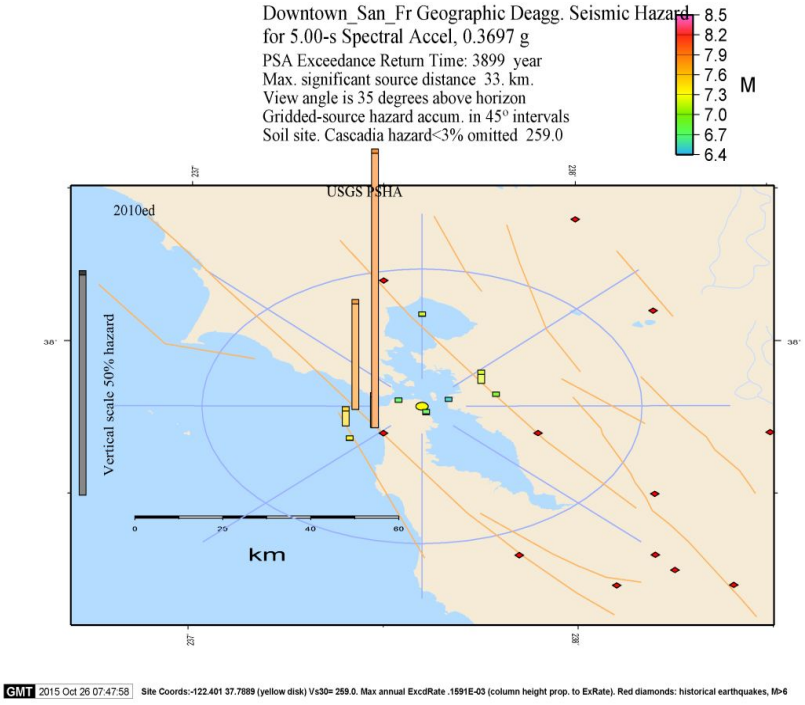

Figure E8: Probabilistic seismic hazard de-aggregation at the representative site in downtown San Francisco (V_{s30}=260m/s, T=5sec.) for a return period of 3898 years including M, R and ε data (a) and geographical (b) de-aggregation data used in the time-based assessment.

Appendix F

Appendix F provides the results of a comparative study that evaluates the impact of beam fracture distribution (Appendix F1) and building orientation (Appendix F2) on the results (IDRs, PFAs and beam performance) presented for the baseline case discussed in Chapter 5. The results are summarized in the following figures included within Appendix F1 and F2.

F1. Figure F1.1: Archetype 40-storey (a, b) and 20-storey (c, d) building interstorey drift ratio (IDR) in the short (a, c) and long (b, d) building directions in Oakland with baseline and revised fracture distributions. Source: Molina Hutt (2016)

Figure F1.2: Archetype 40-storey (a, b) and 20-storey (c, d) building peak floor accelerations (PFA) in the short (a, c) and long (b, d) building directions in Oakland with baseline and revised fracture distributions. Source: Molina Hutt (2016).

Figure F1.3: Archetype 40-storey (a, b) and 20-storey (c, d) building interstorey drift ratio (IDR) in the short (a, c) and long (b, d) building directions in San Francisco with baseline and revised fracture distributions. Source: Molina Hutt (2016).

Figure F1.4: Archetype 40-storey (a, b) and 20-storey (c, d) building peak floor accelerations (PFA) in the short (a, c) and long (b, d) building directions in San Francisco with baseline and revised fracture distributions. Source: Molina Hutt (2016).

Figure F1.5: Archetype 40-storey (a, b) and 20-storey (c, d) building beam performance for sample long (a, c) and short (b, d) building elevations in Oakland with revised fracture distributions. Source: Molina Hutt (2016).

Figure F1.6: Archetype 40-storey (a, b) and 20-storey (c, d) building beam performance for sample long (a, c) and short (b, d) building elevations in San Francisco with revised fracture distributions. Source: Molina Hutt (2016).

F2. Figure F2.1: Archetype 40-storey (a, b) and 20-storey (c, d) building interstorey drift ratio (IDR) in the short (a, c) and long (b, d) building directions in Oakland with baseline and with rotated ground motion inputs. Source: Molina Hutt (2016).

Figure F2.2: Archetype 40-storey (a, b) and 20-storey (c, d) building peak floor accelerations (PFA) in the short (a, c) and long (b, d) building directions in Oakland with baseline and with rotated ground motion inputs. Source: Molina Hutt (2016).

Figure F2.3: Archetype 40-storey (a, b) and 20-storey (c, d) building interstorey drift ratio (IDR) in the short (a, c) and long (b, d) building directions in San Francisco with baseline and with rotated ground motion inputs. Source: Molina Hutt (2016).

Figure F2.4: Archetype 40-storey (a, b) and 20-storey (c, d) building peak floor accelerations (PFA) in the short (a, c) and long (b, d) building directions in San Francisco with baseline and with rotated ground motion inputs. Source: Molina Hutt (2016).

This page is intentionally left blank.

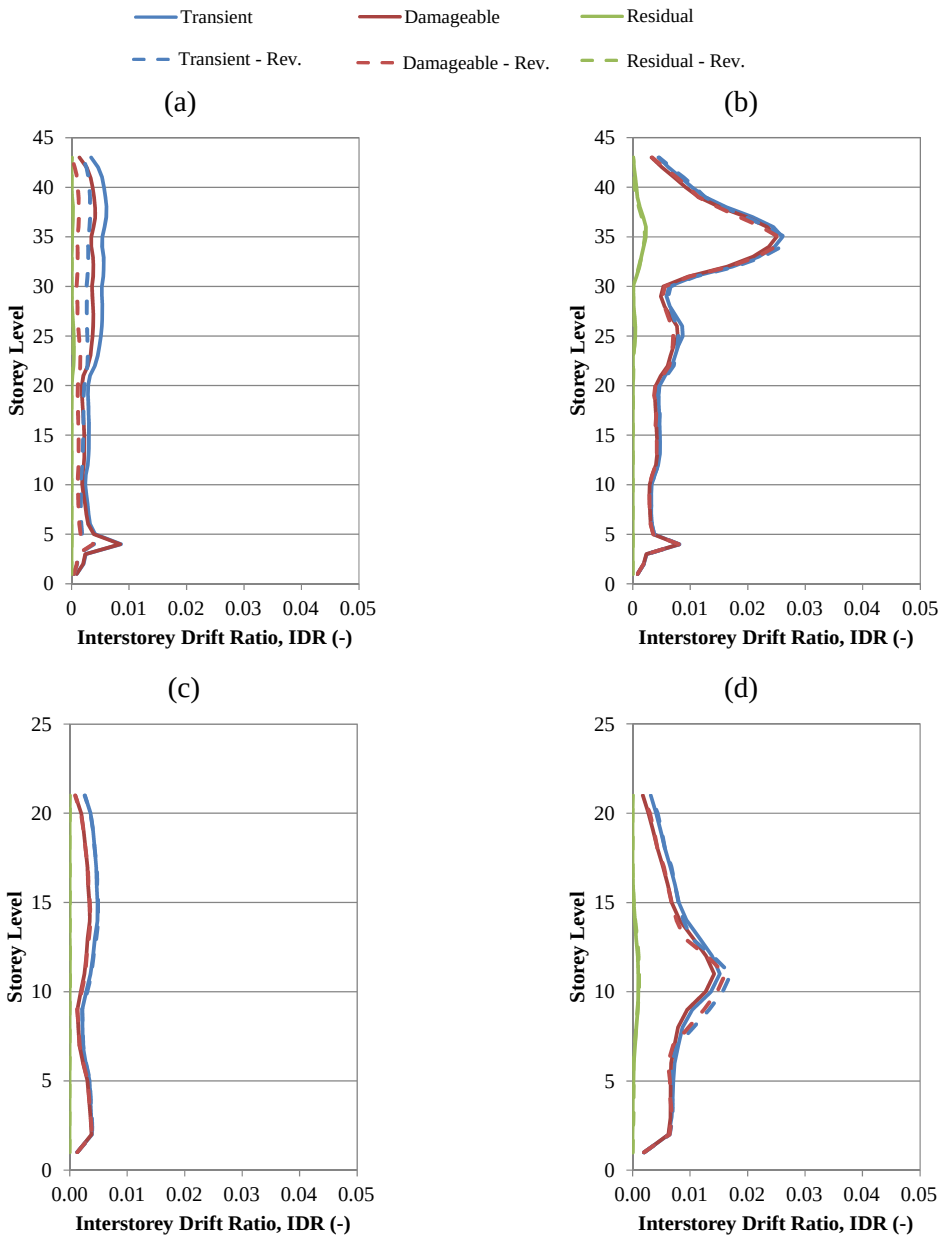

Figure F1.1: Archetype 40-storey (a, b) and 20-storey (c, d) building interstorey drift ratio (IDR) in the short (a, c) and long (b, d) building directions in Oakland with baseline and revised fracture distributions.
Source: Molina Hutt (2016).

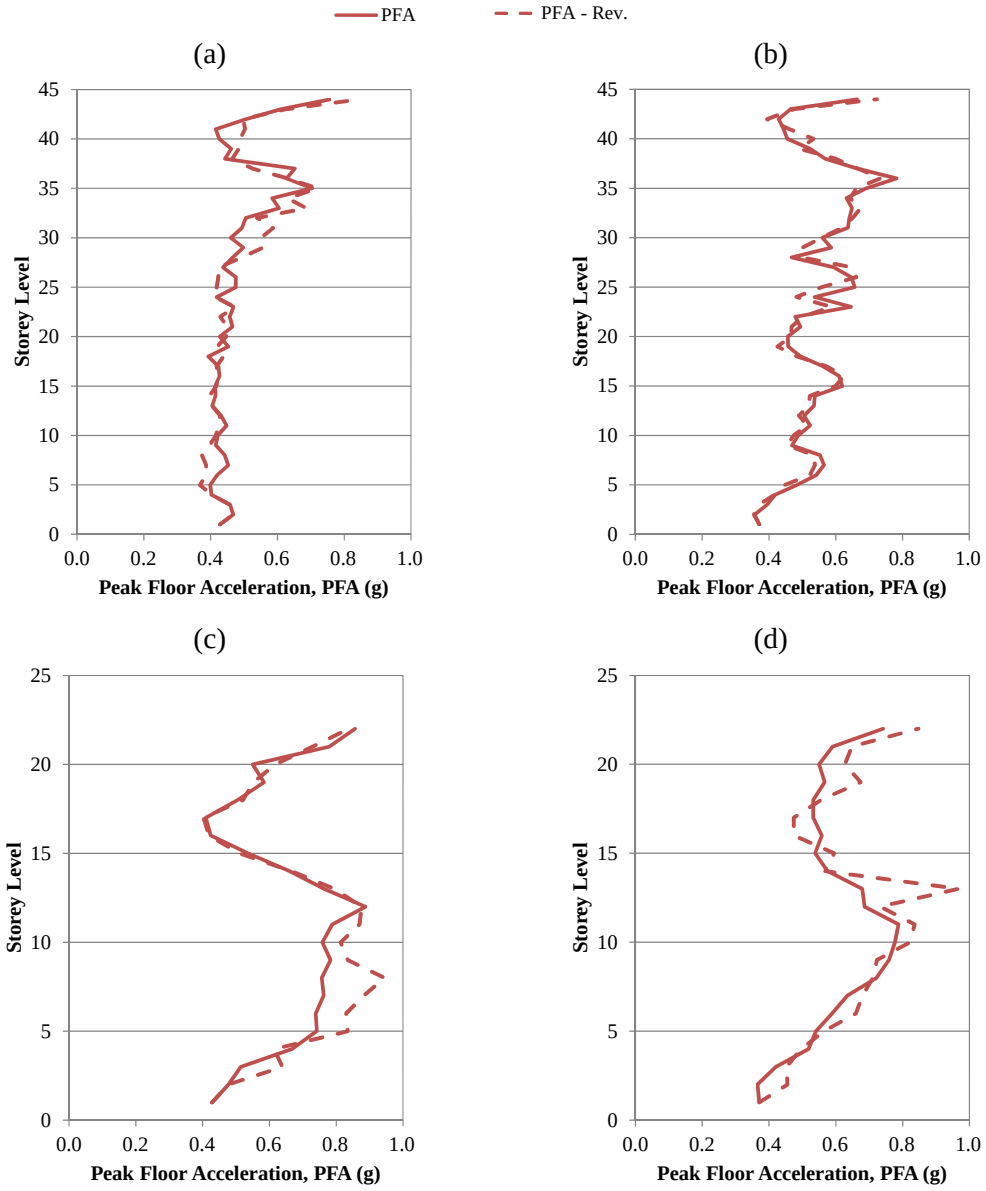

Figure F1.2: Archetype 40-storey (a, b) and 20-storey (c, d) building peak floor accelerations (PFA) in the short (a, c) and long (b, d) building directions in Oakland with baseline and revised fracture distributions.
Source: Molina Hutt (2016).

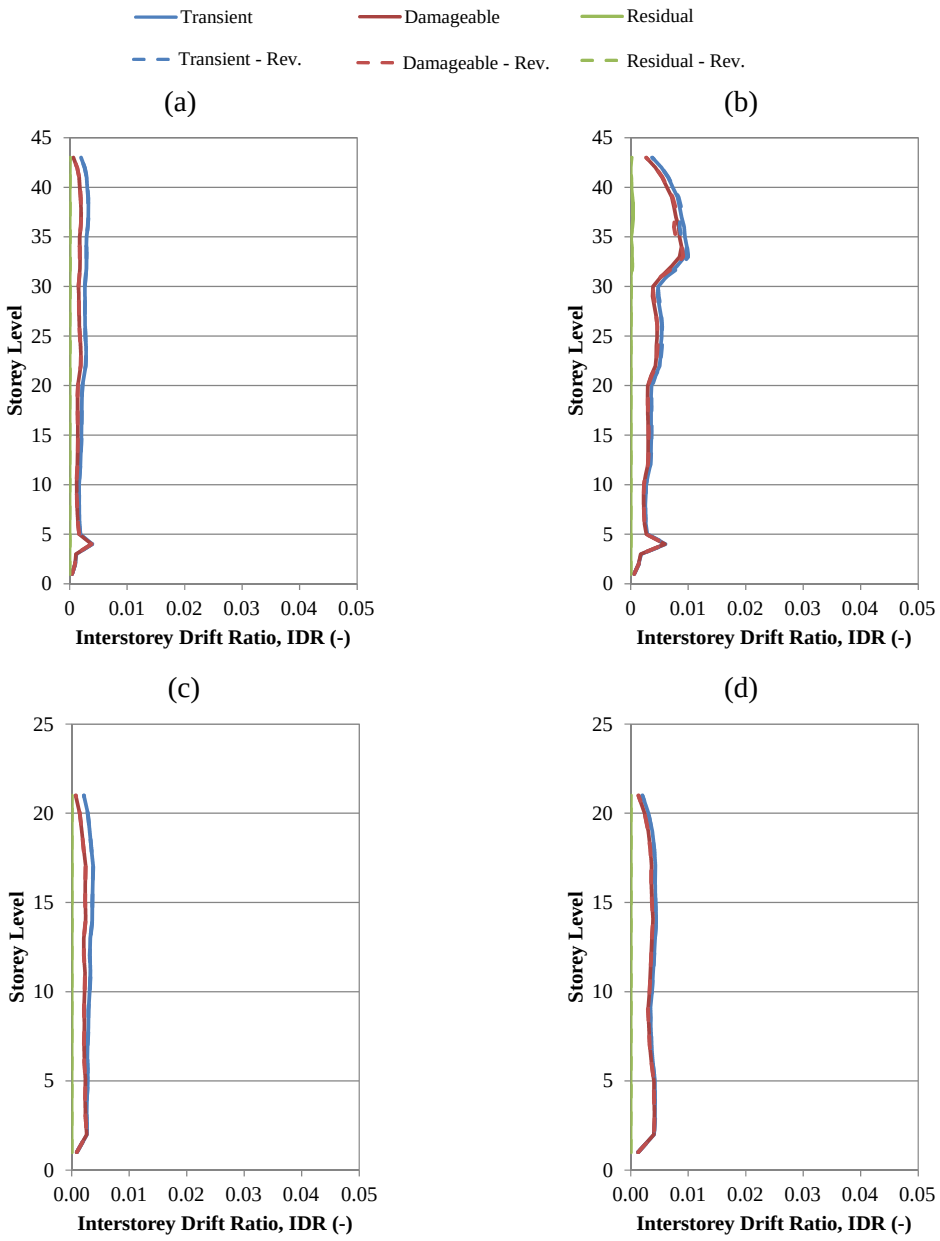

Figure F1.3: Archetype 40-storey (a, b) and 20-storey (c, d) building interstorey drift ratio (IDR) in the short (a, c) and long (b, d) building directions in San Francisco with baseline and revised fracture distributions.
Source: Molina Hutt (2016).

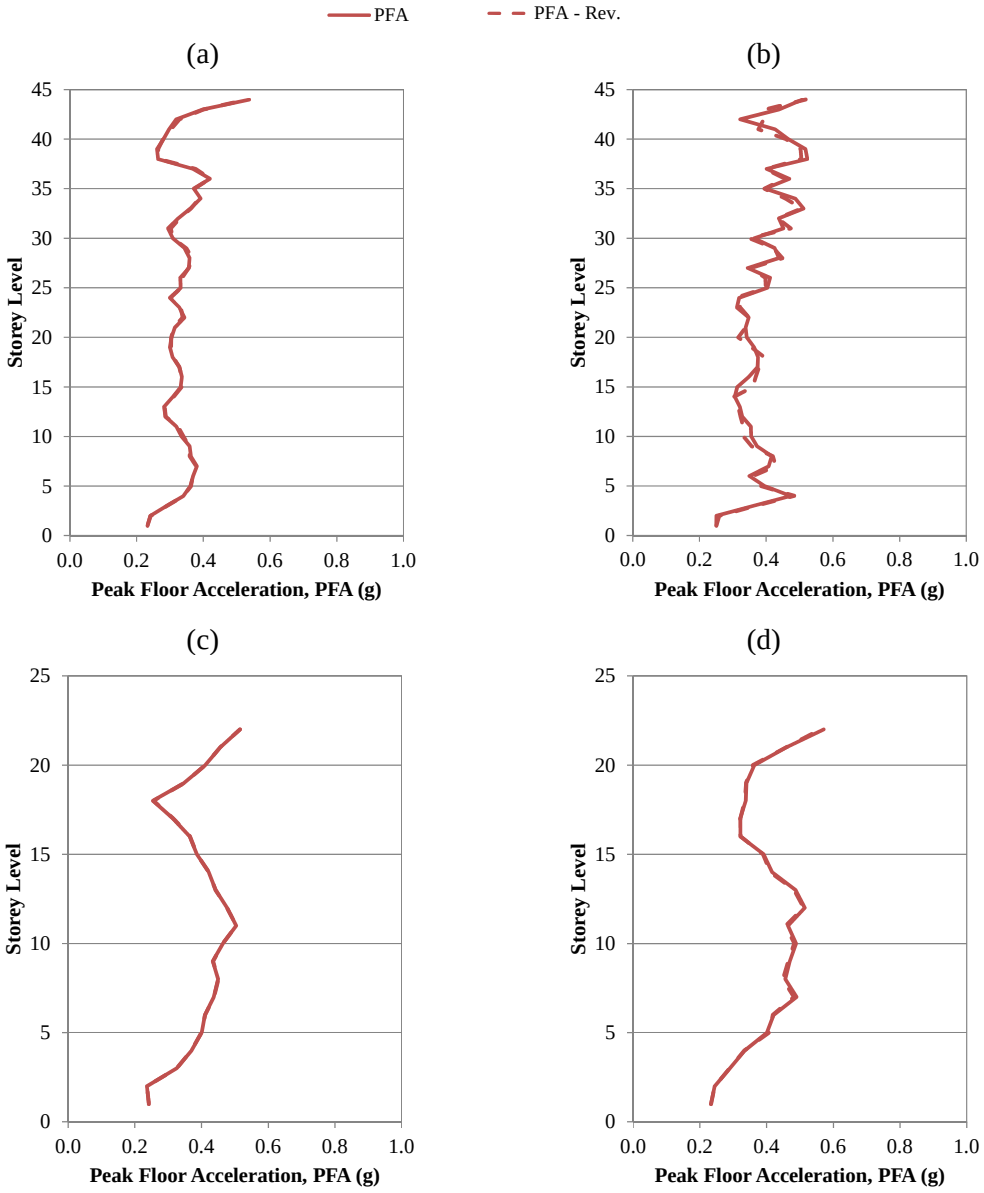

Figure F1.4: Archetype 40-storey (a, b) and 20-storey (c, d) building peak floor accelerations (PFA) in the short (a, c) and long (b, d) building directions in San Francisco with baseline and revised fracture distributions.
Source: Molina Hutt (2016).

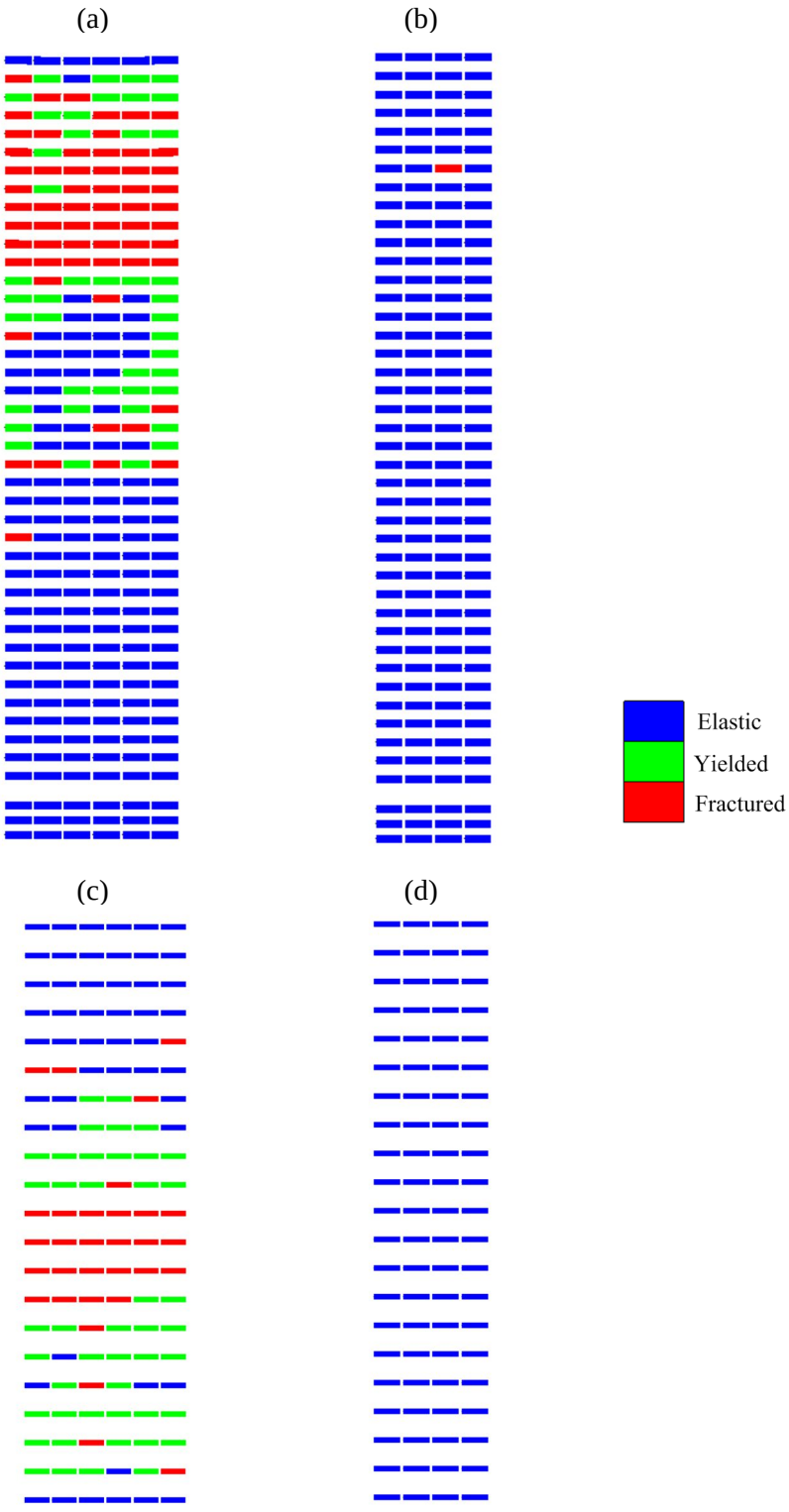

Figure F1.5: Archetype 40-storey (a, b) and 20-storey (c, d) building beam performance for sample long (a, c) and short (b, d) building elevations in Oakland with revised fracture distributions.
Source: Molina Hutt (2016).

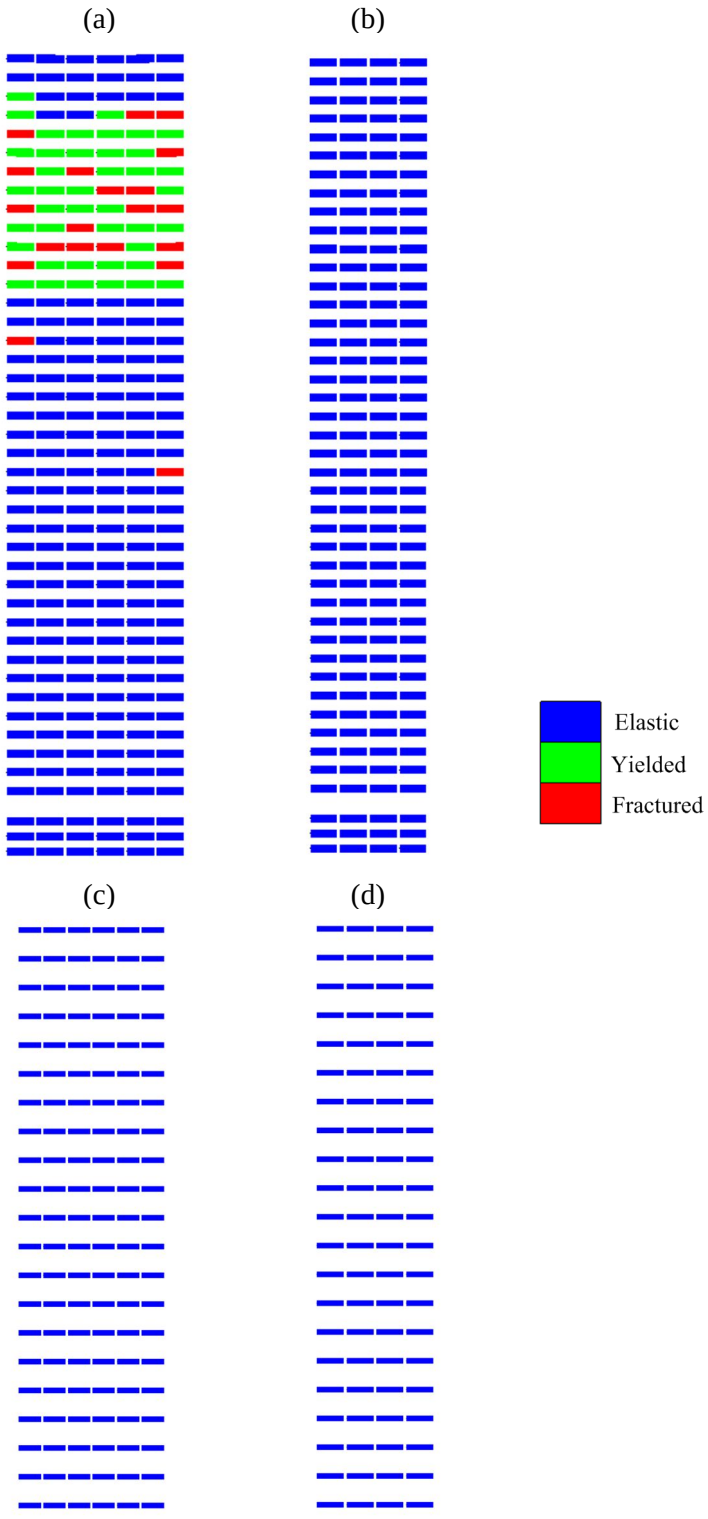

Figure F1.6: Archetype 40-storey (a, b) and 20-storey (c, d) building beam performance for sample long (a, c) and short (b, d) building elevations in San Francisco with revised fracture distributions.
Source: Molina Hutt (2016).

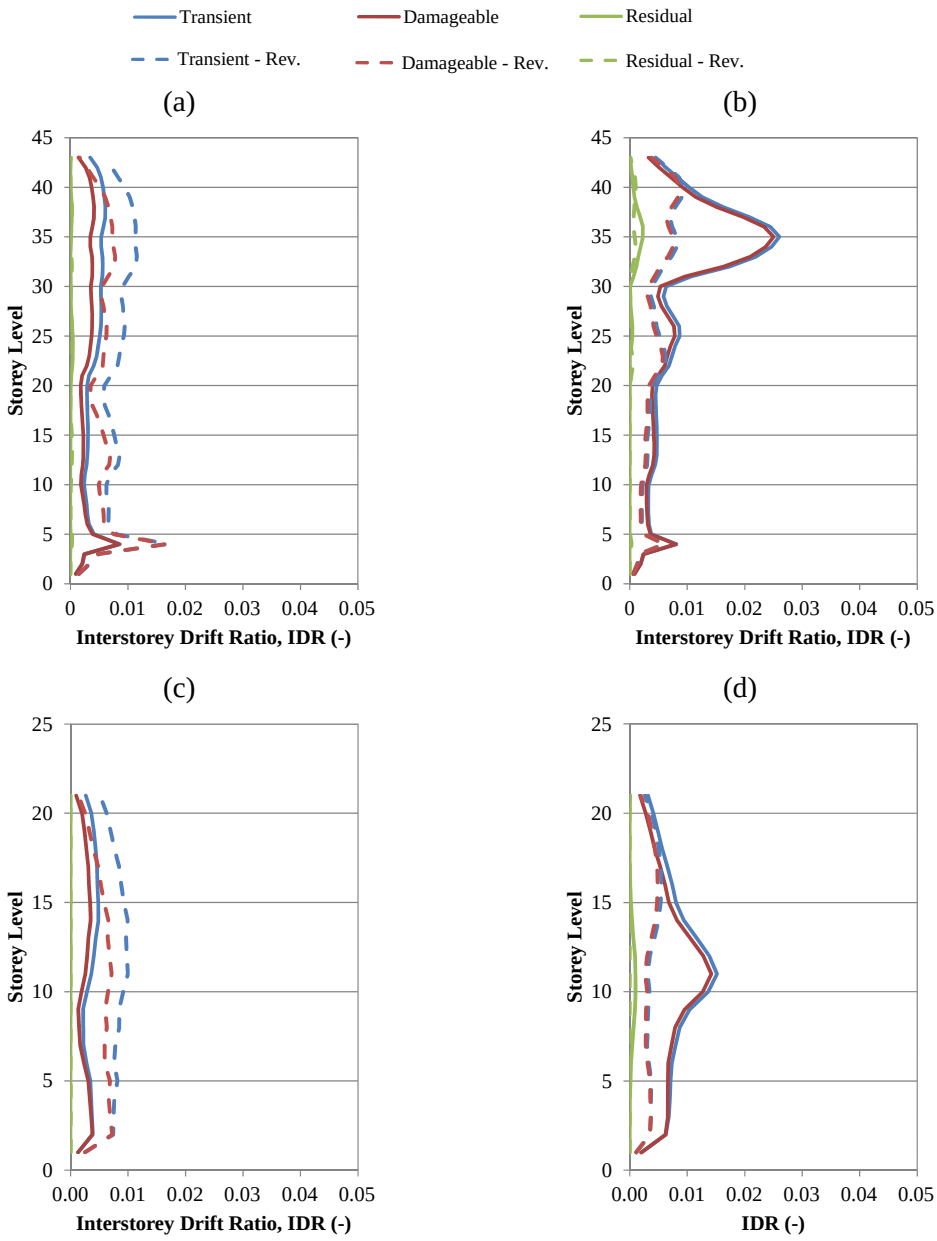

Figure F2.1: Archetype 40-storey (a, b) and 20-storey (c, d) building interstorey drift ratio (IDR) in the short (a, c) and long (b, d) building directions in Oakland with baseline and with rotated ground motion inputs.
Source: Molina Hutt (2016).

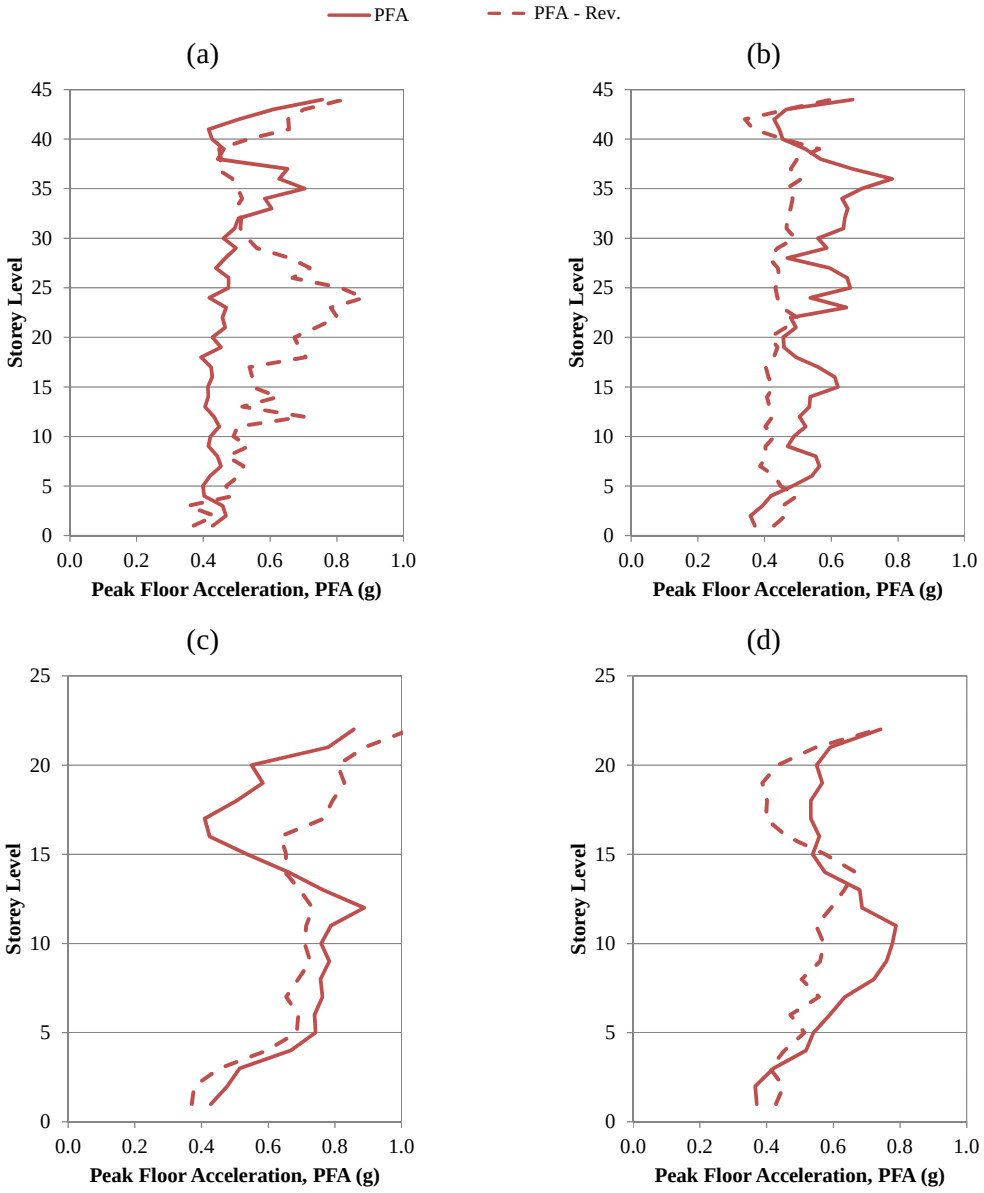

Figure F2.2: Archetype 40-storey (a, b) and 20-storey (c, d) building peak floor accelerations (PFA) in the short (a, c) and long (b, d) building directions in Oakland with baseline and with rotated ground motion inputs.
Source: Molina Hutt (2016).

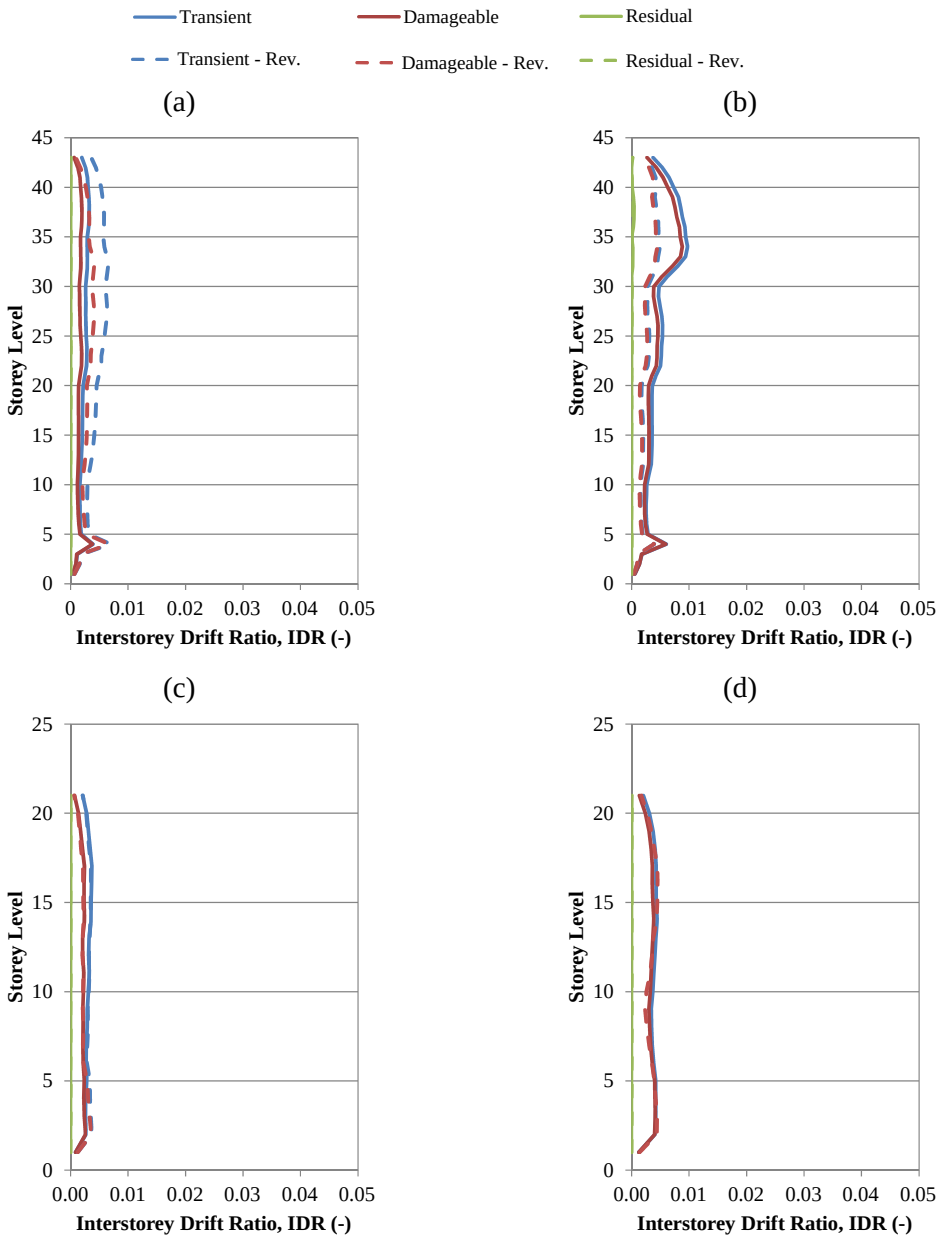

Figure F2.3: Archetype 40-storey (a, b) and 20-storey (c, d) building interstorey drift ratio (IDR) in the short (a, c) and long (b, d) building directions in San Francisco with baseline and with rotated ground motion inputs.
Source: Molina Hutt (2016).

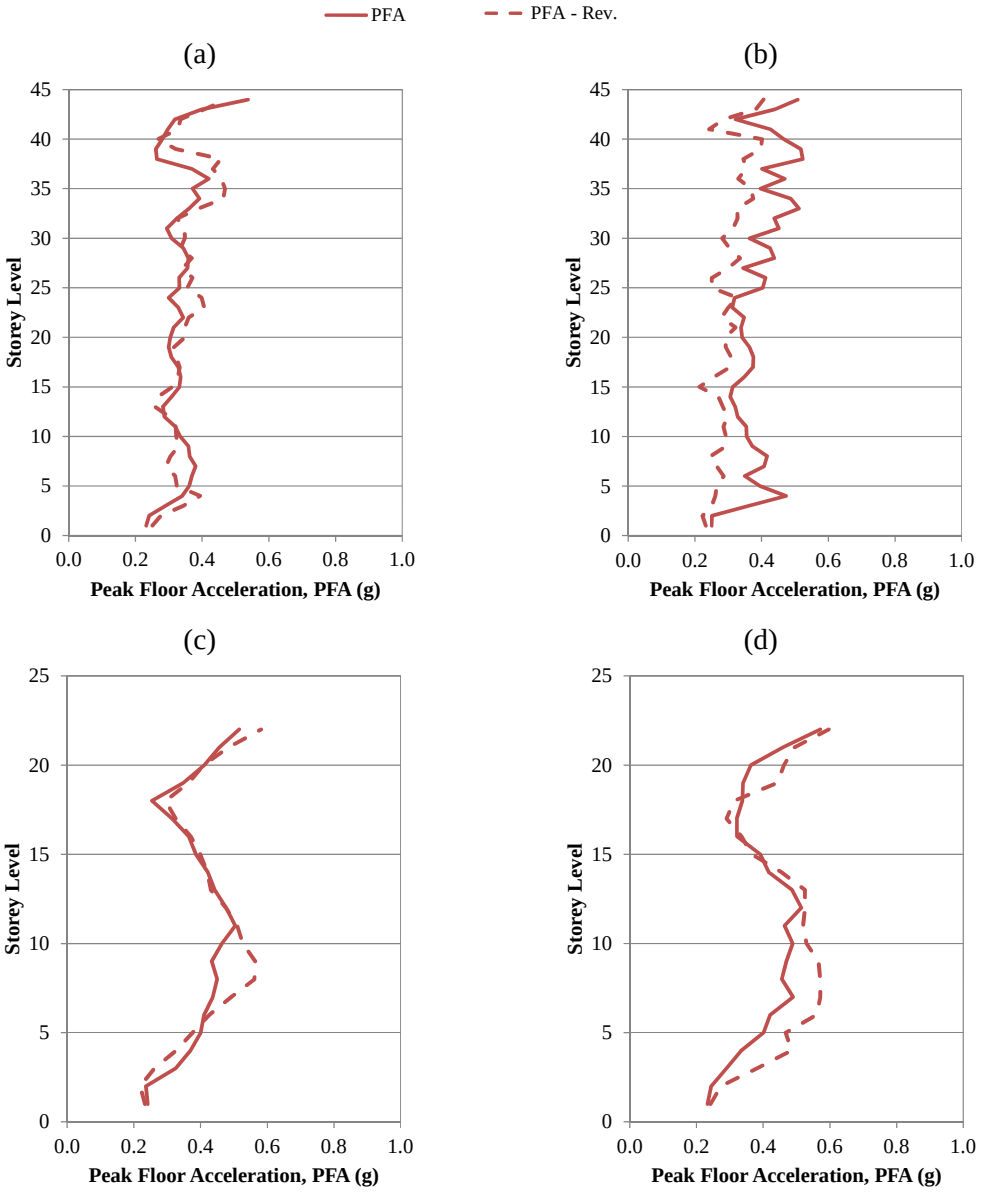

Figure F2.4: Archetype 40-storey (a, b) and 20-storey (c, d) building peak floor accelerations (PFA) in the short (a, c) and long (b, d) building directions in San Francisco with baseline and with rotated ground motion inputs.
Source: Molina Hutt (2016).

Appendix G

Appendix G includes non-linear dynamic analysis results under varying earthquake ground motion intensities for the UBC 1973 and IBC 2012 50-storey archetype buildings evaluated in Chapter 7.

G1. Figure G1: UBC 1973 non-linear dynamic analysis results under earthquake ground motion intensity (e_1), including: peak floor acceleration (a), peak interstorey drift (b), peak residual interstorey drift (c), maximum beam plastic rotation (d), maximum column plastic rotation (d) and maximum panel zone rotation (f).

G2. Figure G2: UBC 1973 non-linear dynamic analysis results under earthquake ground motion intensity (e_{1A}), including: peak floor acceleration (a), peak interstorey drift (b), peak residual interstorey drift (c), maximum beam plastic rotation (d), maximum column plastic rotation (d) and maximum panel zone rotation (f).

G3. Figure G3: UBC 1973 non-linear dynamic analysis results under earthquake ground motion intensity (e_2), including: peak floor acceleration (a), peak interstorey drift (b), peak residual interstorey drift (c), maximum beam plastic rotation (d), maximum column plastic rotation (d) and maximum panel zone rotation (f).

G4. Figure G4: UBC 1973 non-linear dynamic analysis results under earthquake ground motion intensity (e_{2A}), including: peak floor acceleration (a), peak interstorey drift (b), peak residual interstorey drift (c), maximum beam plastic rotation (d), maximum column plastic rotation (d) and maximum panel zone rotation (f).

G5. Figure G5: UBC 1973 non-linear dynamic analysis results under earthquake ground motion intensity (e_3), including: peak floor acceleration (a), peak interstorey drift (b), peak residual interstorey drift (c), maximum beam plastic rotation (d), maximum column plastic rotation (d) and maximum panel zone rotation (f).

G6. Figure G6: UBC 1973 non-linear dynamic analysis results under earthquake ground motion intensity (e_{3A}), including: peak floor acceleration (a), peak interstorey drift (b), peak residual interstorey drift (c), maximum beam plastic rotation (d), maximum column plastic rotation (d) and maximum panel zone rotation (f).

G7. Figure G7: UBC 1973 non-linear dynamic analysis results under earthquake ground motion intensity (e_4), including: peak floor acceleration (a), peak interstorey drift (b), peak residual interstorey drift (c), maximum beam plastic rotation (d), maximum column plastic rotation (d) and maximum panel zone rotation (f).

G8. Figure G8: UBC 1973 non-linear dynamic analysis results under earthquake ground motion intensity (e_5), including: peak floor acceleration (a), peak interstorey drift (b), peak residual interstorey drift (c), maximum beam plastic rotation (d), maximum column plastic rotation (d) and maximum panel zone rotation (f).

G9. Figure G9: IBC 2012 non-linear dynamic analysis results under earthquake ground motion intensity (e_1), including: peak floor acceleration (a), peak interstorey drift (b), peak residual interstorey drift (c), maximum beam plastic rotation (d), maximum column plastic rotation (d) and maximum panel zone rotation (f).

G10. Figure G10: IBC 2012 non-linear dynamic analysis results under earthquake ground motion intensity (e_2), including: peak floor acceleration (a), peak interstorey drift (b), peak residual interstorey drift (c), maximum beam plastic rotation (d), maximum column plastic rotation (d) and maximum panel zone rotation (f).

G11. Figure G11: IBC 2012 non-linear dynamic analysis results under earthquake ground motion intensity (e_3), including: peak floor acceleration (a), peak interstorey drift (b), peak residual interstorey drift (c), maximum beam plastic rotation (d), maximum column plastic rotation (d) and maximum panel zone rotation (f).

G12. Figure G12: IBC 2012 non-linear dynamic analysis results under earthquake ground motion intensity (e_4), including: peak floor acceleration (a), peak interstorey drift (b), peak residual interstorey drift (c), maximum beam plastic rotation (d), maximum column plastic rotation (d) and maximum panel zone rotation (f).

G13. Figure G13: IBC 2012 non-linear dynamic analysis results under earthquake ground motion intensity (e_5), including: peak floor acceleration (a), peak interstorey drift (b), peak residual interstorey drift (c), maximum beam plastic rotation (d), maximum column plastic rotation (d) and maximum panel zone rotation (f).

G14. Figure G14: IBC 2012 non-linear dynamic analysis results under earthquake ground motion intensity (e_6), including: peak floor acceleration (a), peak interstorey drift (b), peak residual interstorey drift (c), maximum beam plastic rotation (d), maximum column plastic rotation (d) and maximum panel zone rotation (f).

G15. Figure G15: IBC 2012 non-linear dynamic analysis results under earthquake ground motion intensity (e_7), including: peak floor acceleration (a), peak interstorey drift (b), peak residual interstorey drift (c), maximum beam plastic rotation (d), maximum column plastic rotation (d) and maximum panel zone rotation (f).

G16. Figure G16: IBC 2012 non-linear dynamic analysis results under earthquake ground motion intensity (e_8), including: peak floor acceleration (a), peak interstorey drift (b), peak residual interstorey drift (c), maximum beam plastic rotation (d), maximum column plastic rotation (d) and maximum panel zone rotation (f).

G17. Figure G17: IBC 2012 non-linear dynamic analysis results under earthquake ground motion intensity (e_{8A}), including: peak floor acceleration (a), peak interstorey drift (b), peak residual interstorey drift (c), maximum beam plastic rotation (d), maximum column plastic rotation (d) and maximum panel zone rotation (f).

G18. Figure G18: IBC 2012 non-linear dynamic analysis results under earthquake ground motion intensity (e_{8B}), including: peak floor acceleration (a), peak interstorey drift (b), peak residual interstorey drift (c), maximum beam plastic rotation (d), maximum column plastic rotation (d) and maximum panel zone rotation (f).

G19. Figure G19: UBC 1973 non-linear dynamic analysis results under earthquake ground motion intensity (e_{8C}), including: peak floor acceleration (a), peak interstorey drift (b), peak residual interstorey drift (c), maximum beam plastic rotation (d), maximum column plastic rotation (d) and maximum panel zone rotation (f).

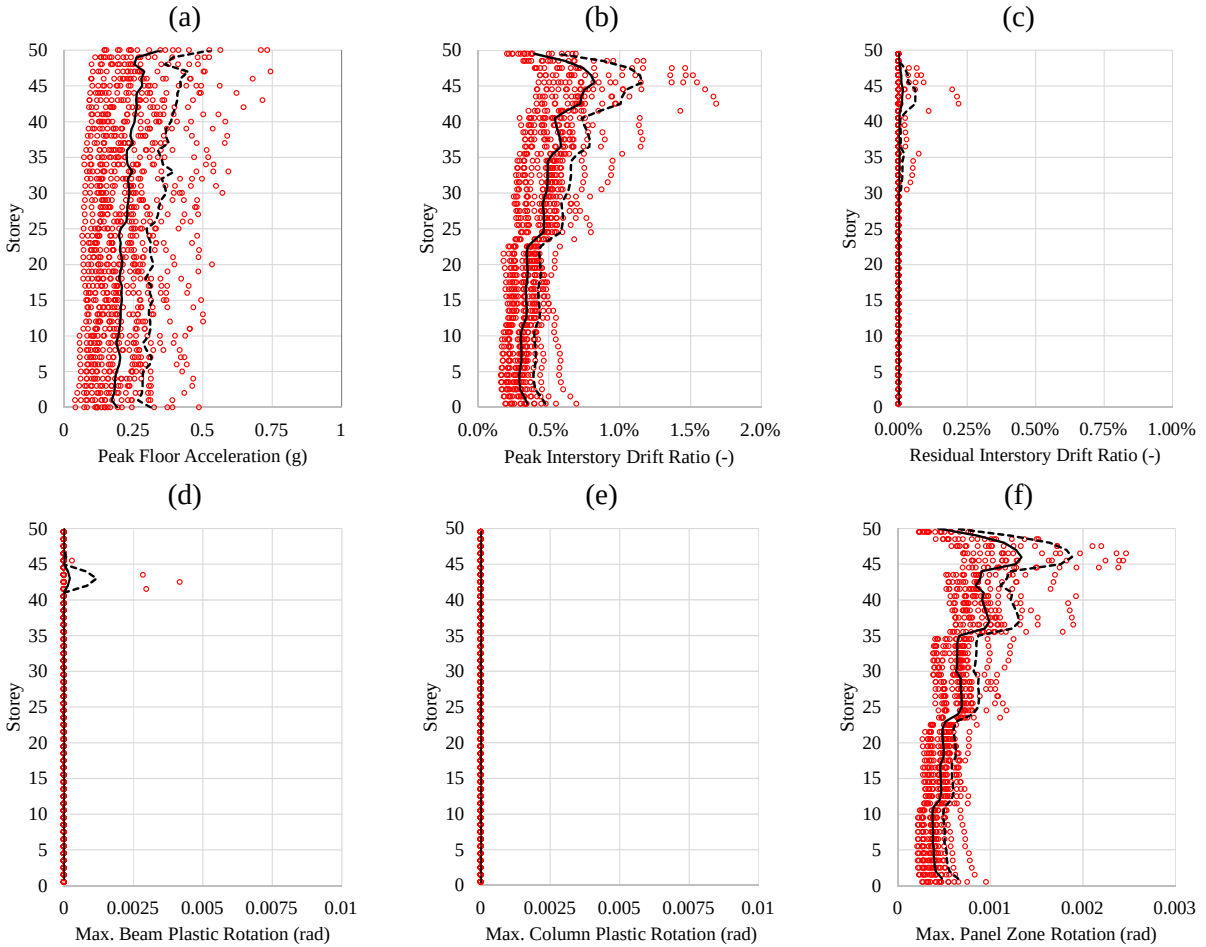

Figure G1: UBC 1973 non-linear dynamic analysis results under earthquake ground motion intensity (e_1), including: peak floor acceleration (a), peak interstorey drift (b), peak residual interstorey drift (c), maximum beam plastic rotation (d), maximum column plastic rotation (d) and maximum panel zone rotation (f).

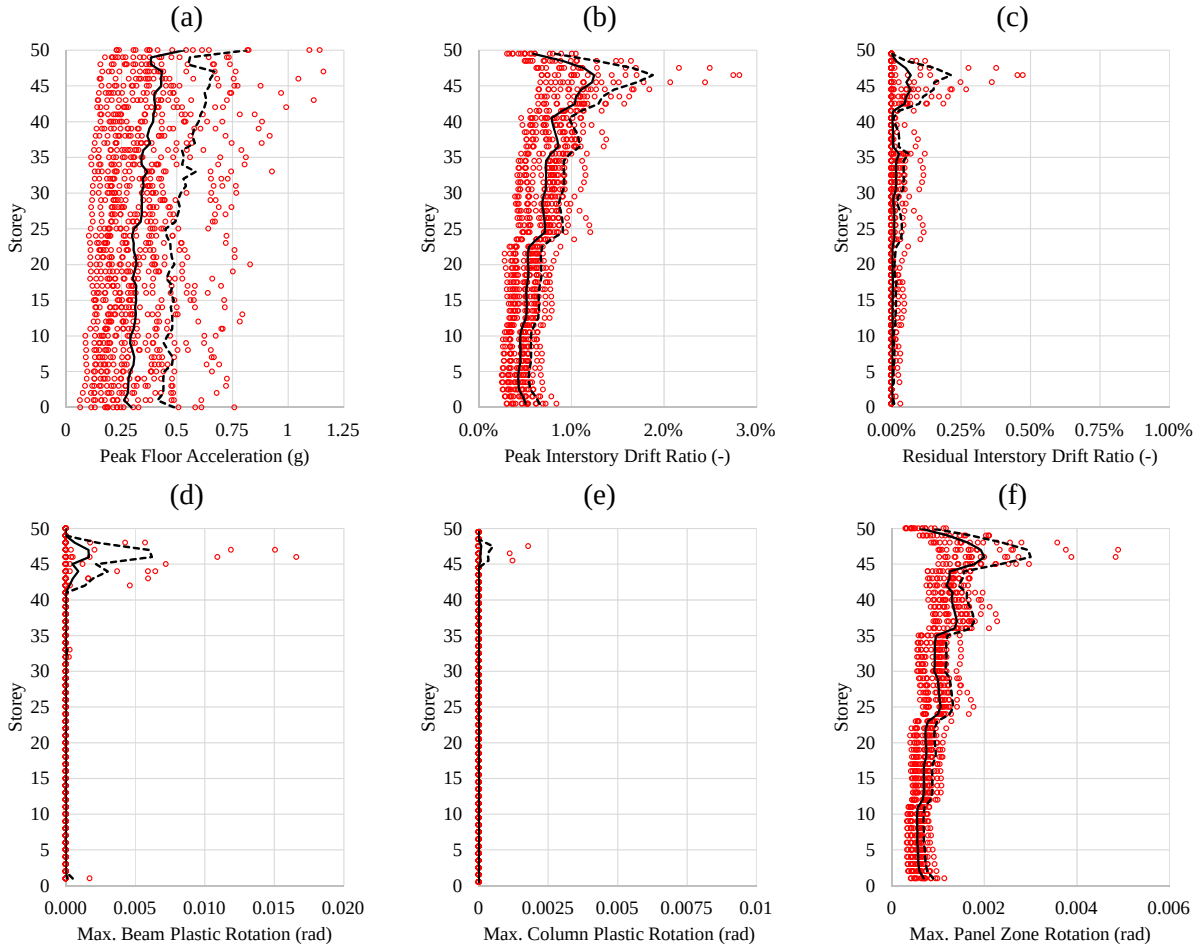

Figure G2: UBC 1973 non-linear dynamic analysis results under earthquake ground motion intensity (e_{1A}), including: peak floor acceleration (a), peak interstorey drift (b), peak residual interstorey drift (c), maximum beam plastic rotation (d), maximum column plastic rotation (d) and maximum panel zone rotation (f).

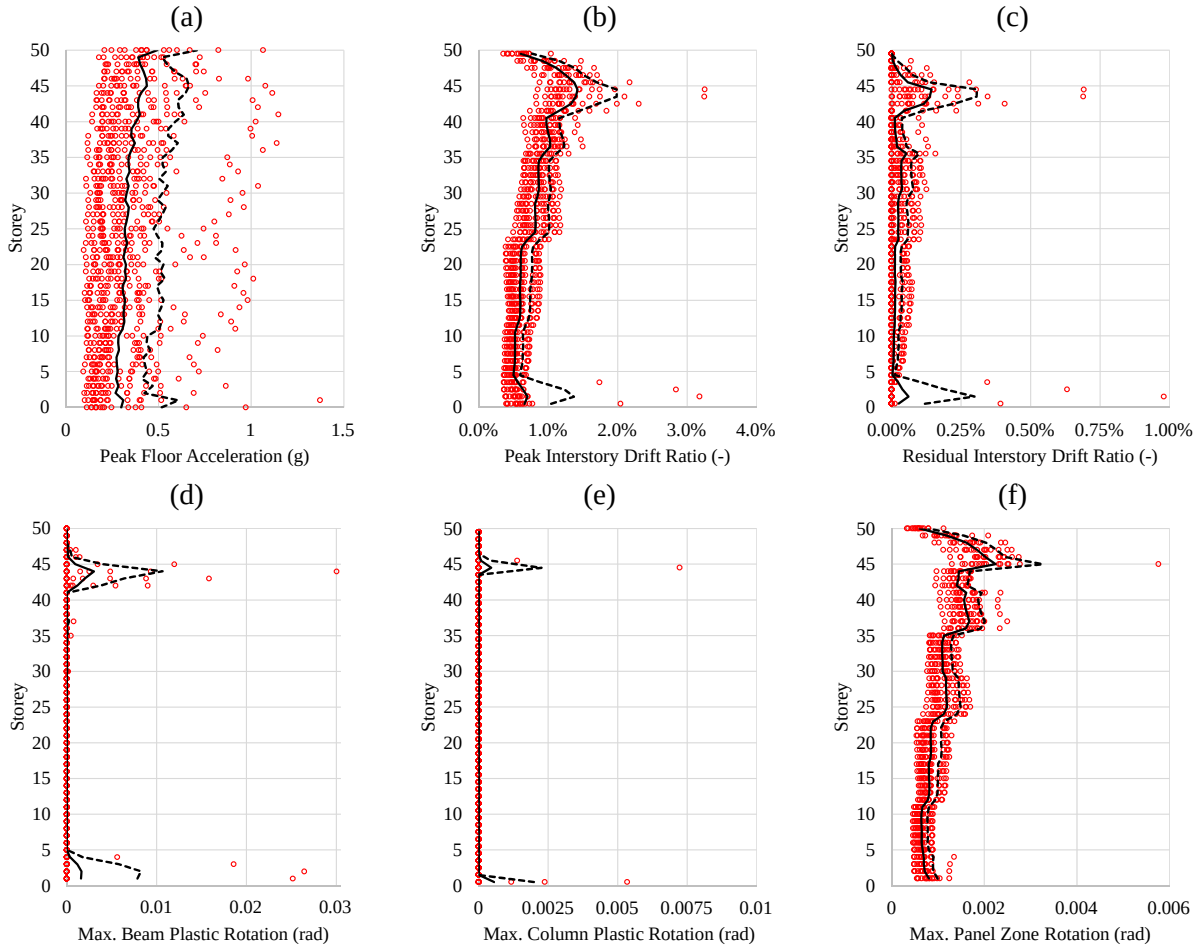

Figure G3: UBC 1973 non-linear dynamic analysis results under earthquake ground motion intensity (e_2), including: peak floor acceleration (a), peak interstorey drift (b), peak residual interstorey drift (c), maximum beam plastic rotation (d), maximum column plastic rotation (d) and maximum panel zone rotation (f).

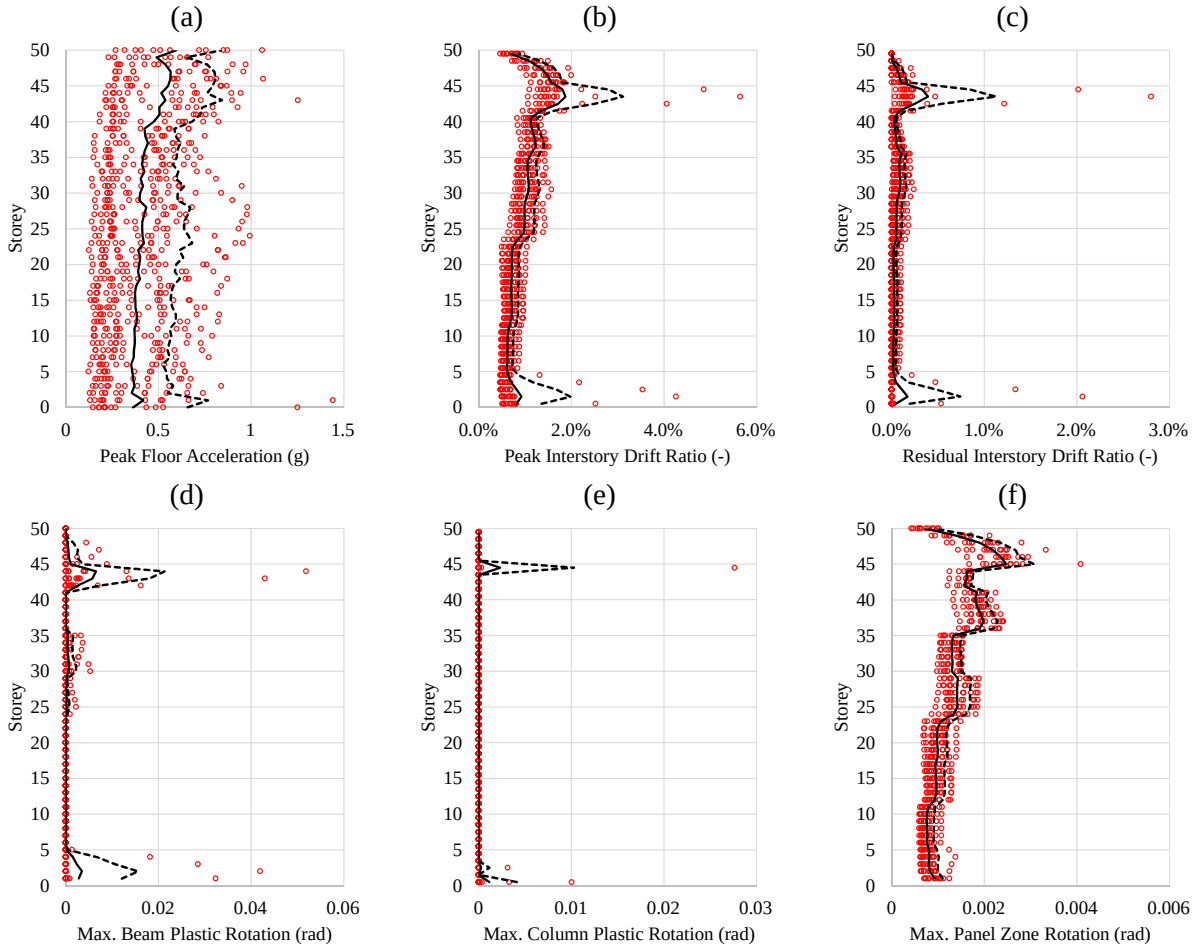

Figure G4: UBC 1973 non-linear dynamic analysis results under earthquake ground motion intensity (e_{2A}), including: peak floor acceleration (a), peak interstorey drift (b), peak residual interstorey drift (c), maximum beam plastic rotation (d), maximum column plastic rotation (d) and maximum panel zone rotation (f).

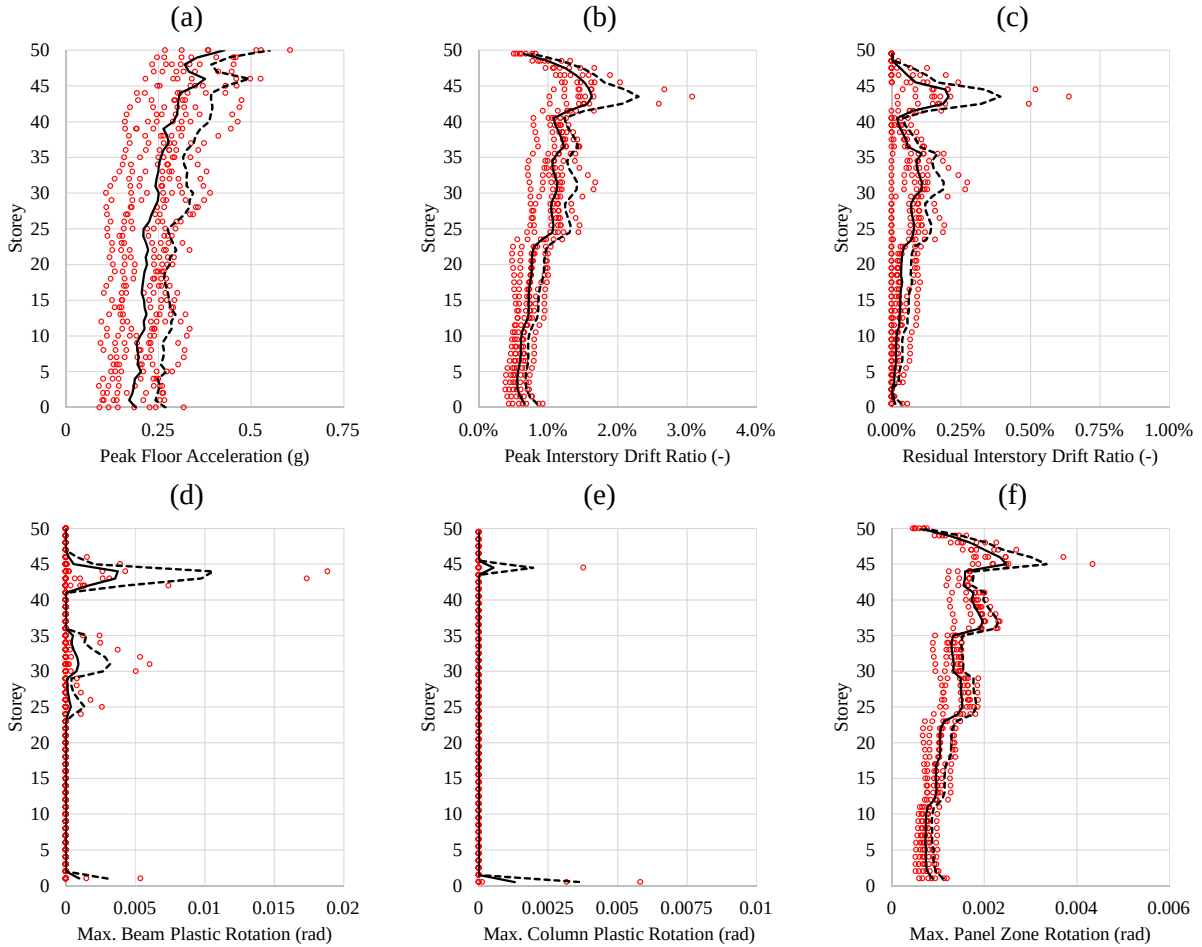

Figure G5: UBC 1973 non-linear dynamic analysis results under earthquake ground motion intensity (e_3), including: peak floor acceleration (a), peak interstorey drift (b), peak residual interstorey drift (c), maximum beam plastic rotation (d), maximum column plastic rotation (d) and maximum panel zone rotation (f).

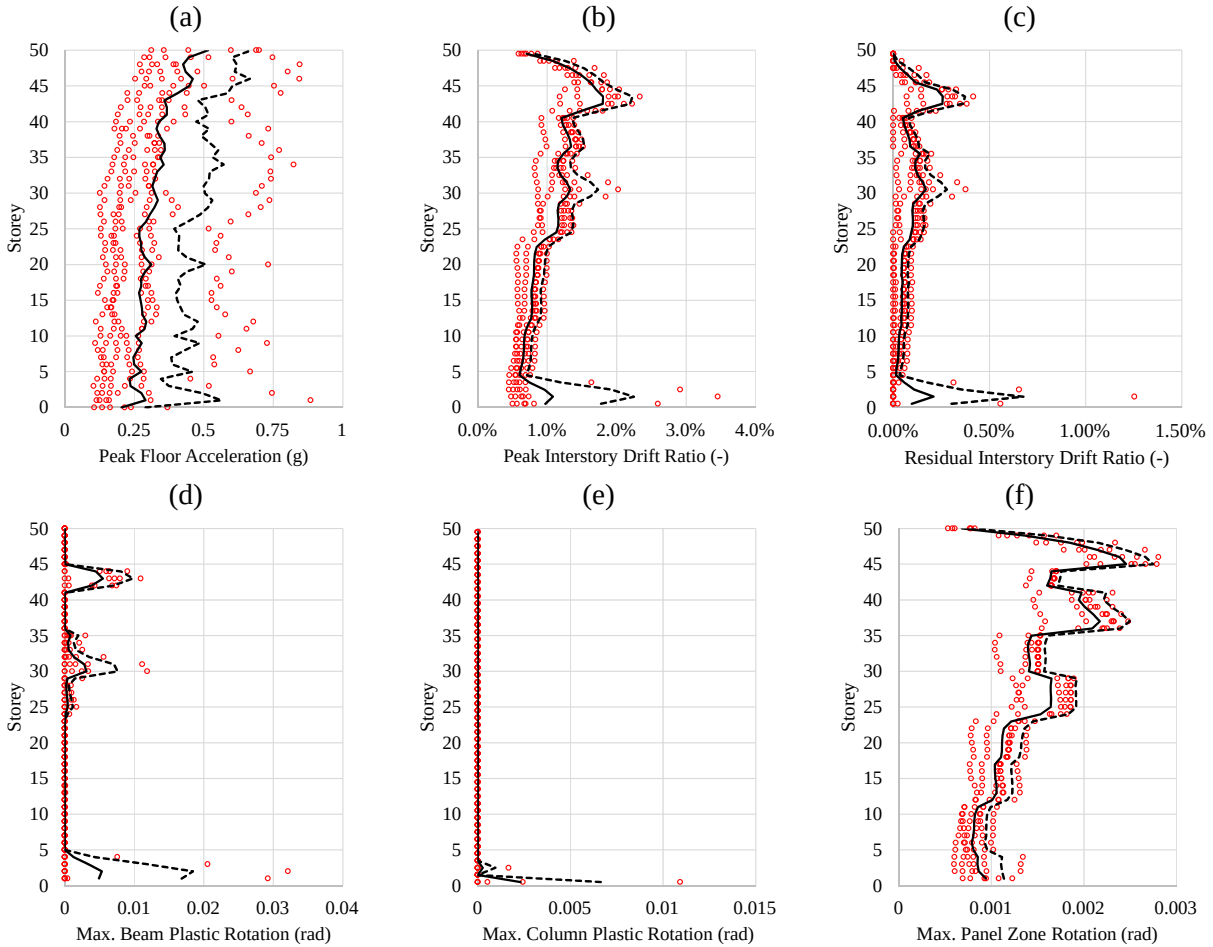

Figure G6: UBC 1973 non-linear dynamic analysis results under earthquake ground motion intensity (e_{3A}), including: peak floor acceleration (a), peak interstorey drift (b), peak residual interstorey drift (c), maximum beam plastic rotation (d), maximum column plastic rotation (d) and maximum panel zone rotation (f).

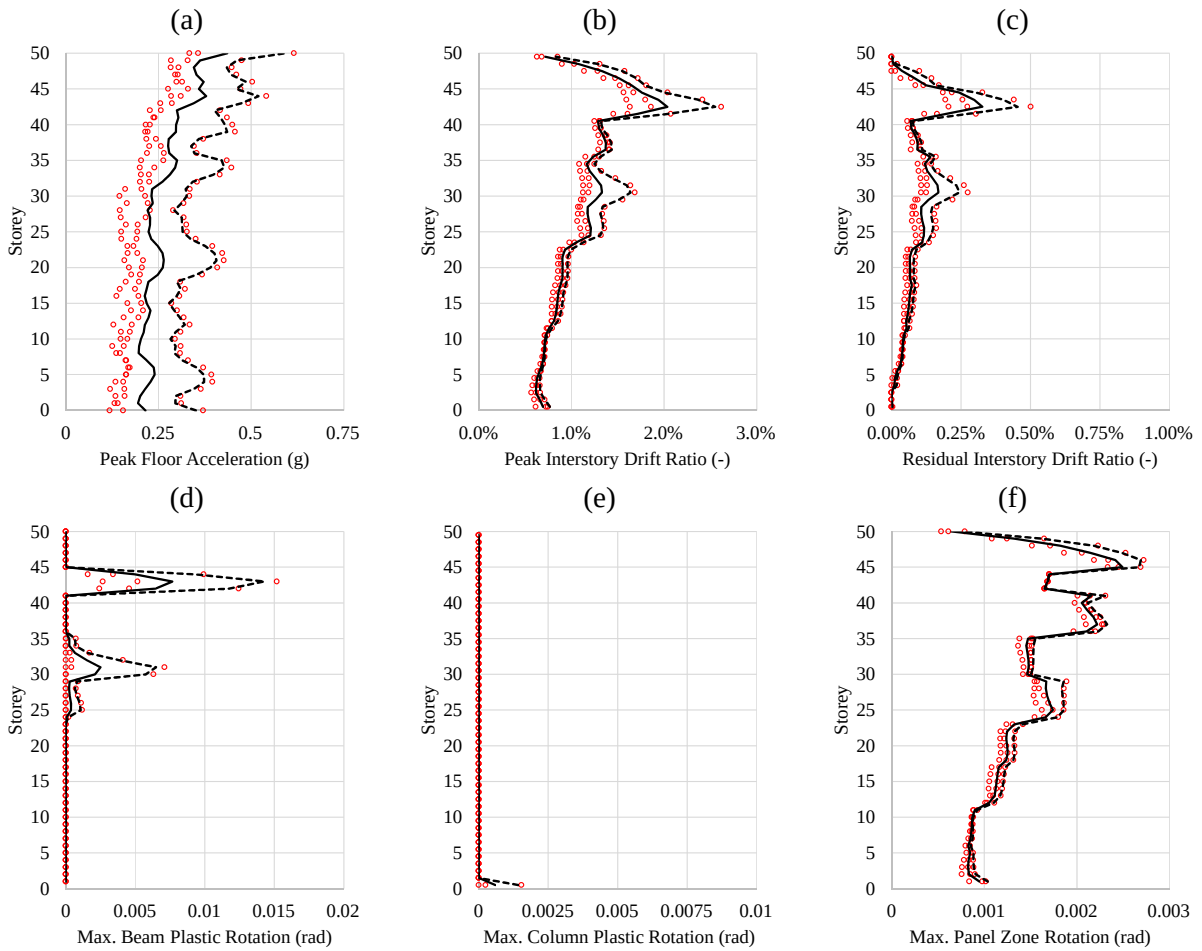

Figure G7: UBC 1973 non-linear dynamic analysis results under earthquake ground motion intensity (e_4), including: peak floor acceleration (a), peak interstorey drift (b), peak residual interstorey drift (c), maximum beam plastic rotation (d), maximum column plastic rotation (d) and maximum panel zone rotation (f).

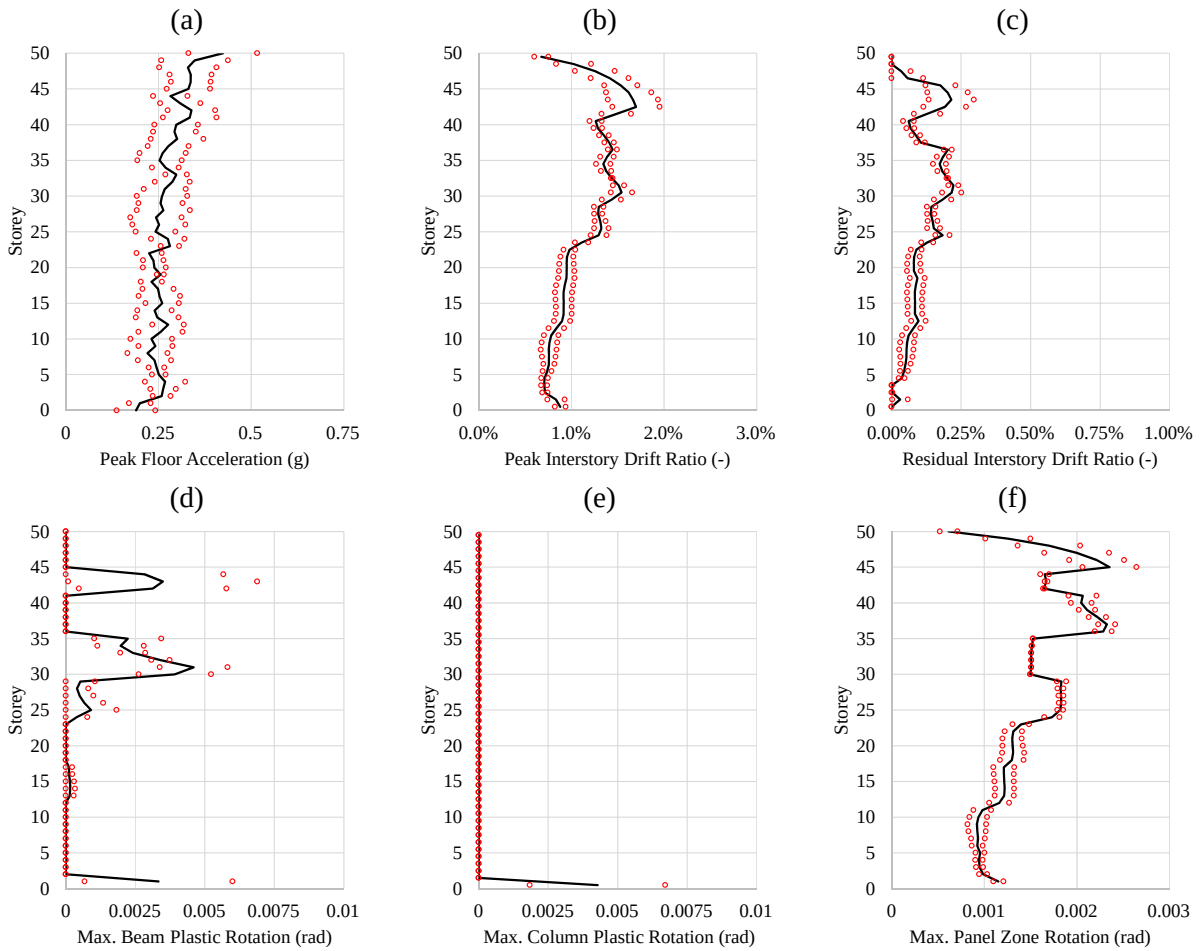

Figure G8: UBC 1973 non-linear dynamic analysis results under earthquake ground motion intensity (e_5), including: peak floor acceleration (a), peak interstorey drift (b), peak residual interstorey drift (c), maximum beam plastic rotation (d), maximum column plastic rotation (d) and maximum panel zone rotation (f).

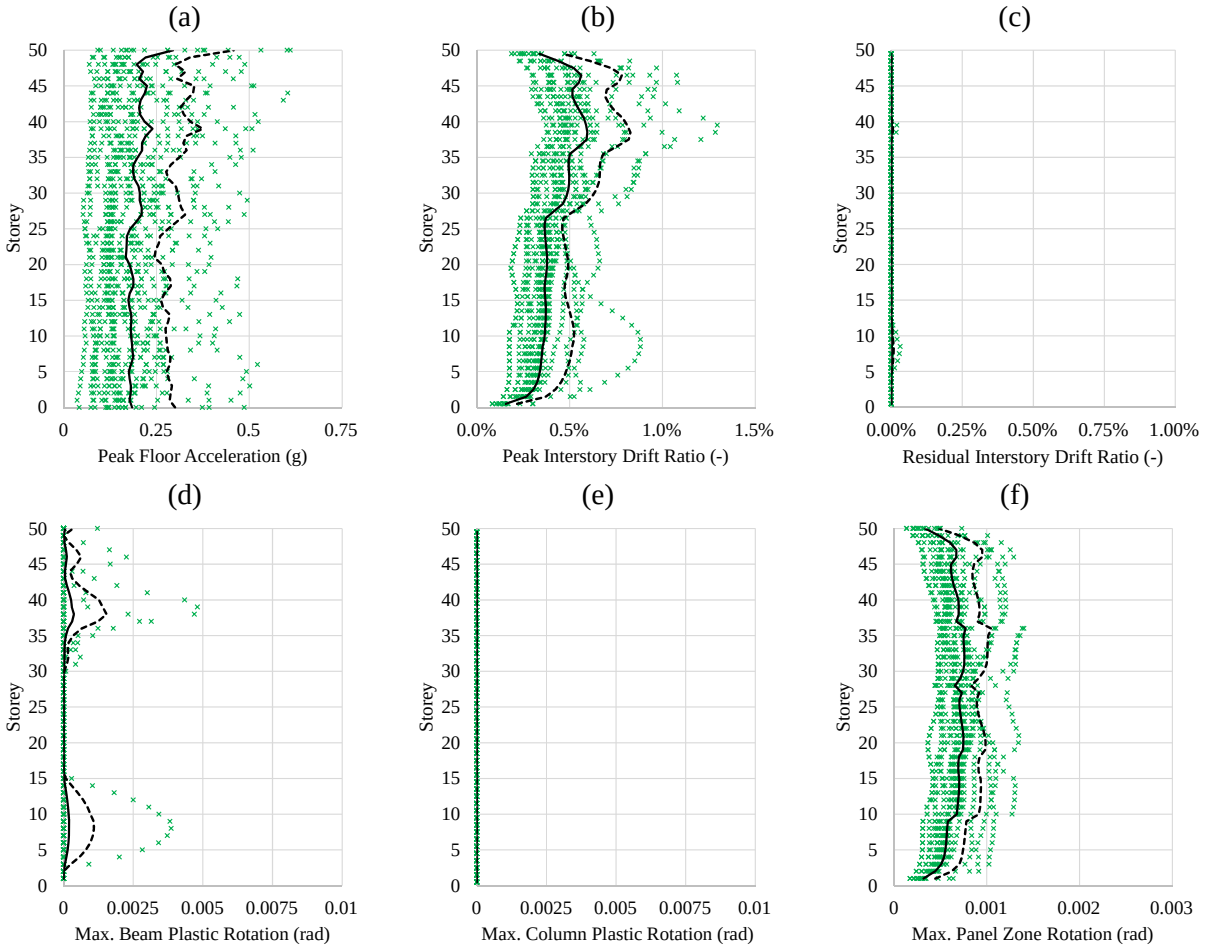

Figure G9: IBC 2012 non-linear dynamic analysis results under earthquake ground motion intensity (e_1), including: peak floor acceleration (a), peak interstorey drift (b), peak residual interstorey drift (c), maximum beam plastic rotation (d), maximum column plastic rotation (d) and maximum panel zone rotation (f).

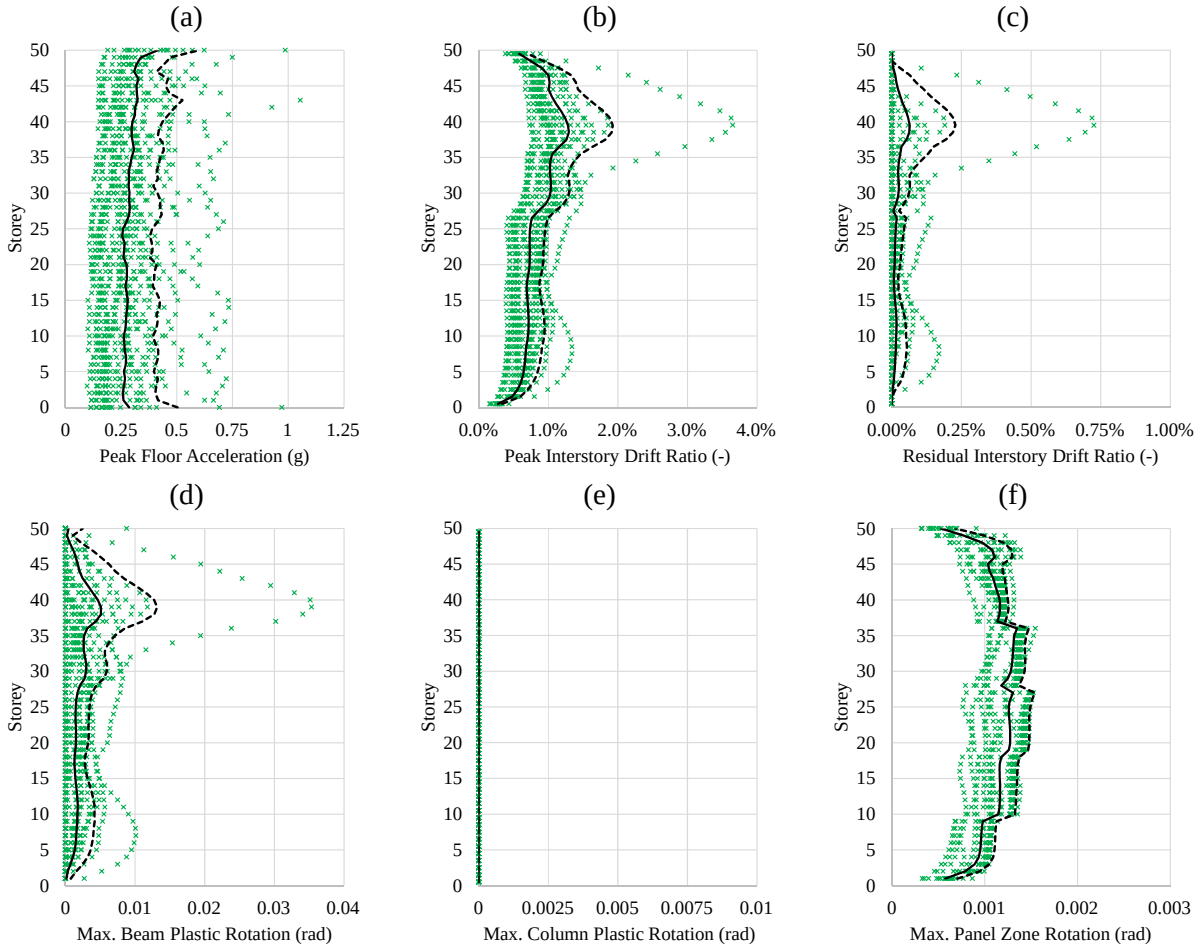

Figure G10: IBC 2012 non-linear dynamic analysis results under earthquake ground motion intensity (e_2), including: peak floor acceleration (a), peak interstorey drift (b), peak residual interstorey drift (c), maximum beam plastic rotation (d), maximum column plastic rotation (d) and maximum panel zone rotation (f).

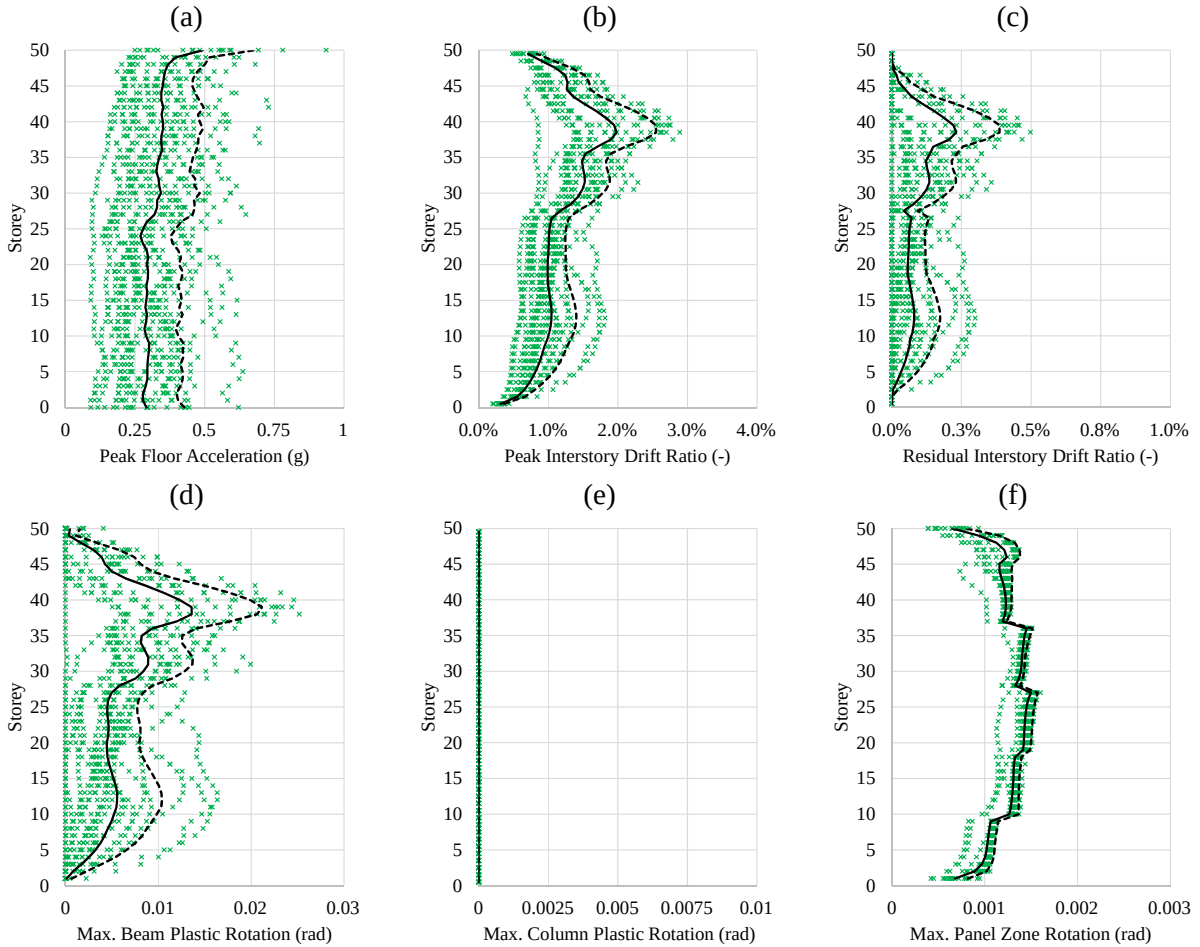

Figure G11: IBC 2012 non-linear dynamic analysis results under earthquake ground motion intensity (e_3), including: peak floor acceleration (a), peak interstorey drift (b), peak residual interstorey drift (c), maximum beam plastic rotation (d), maximum column plastic rotation (d) and maximum panel zone rotation (f).

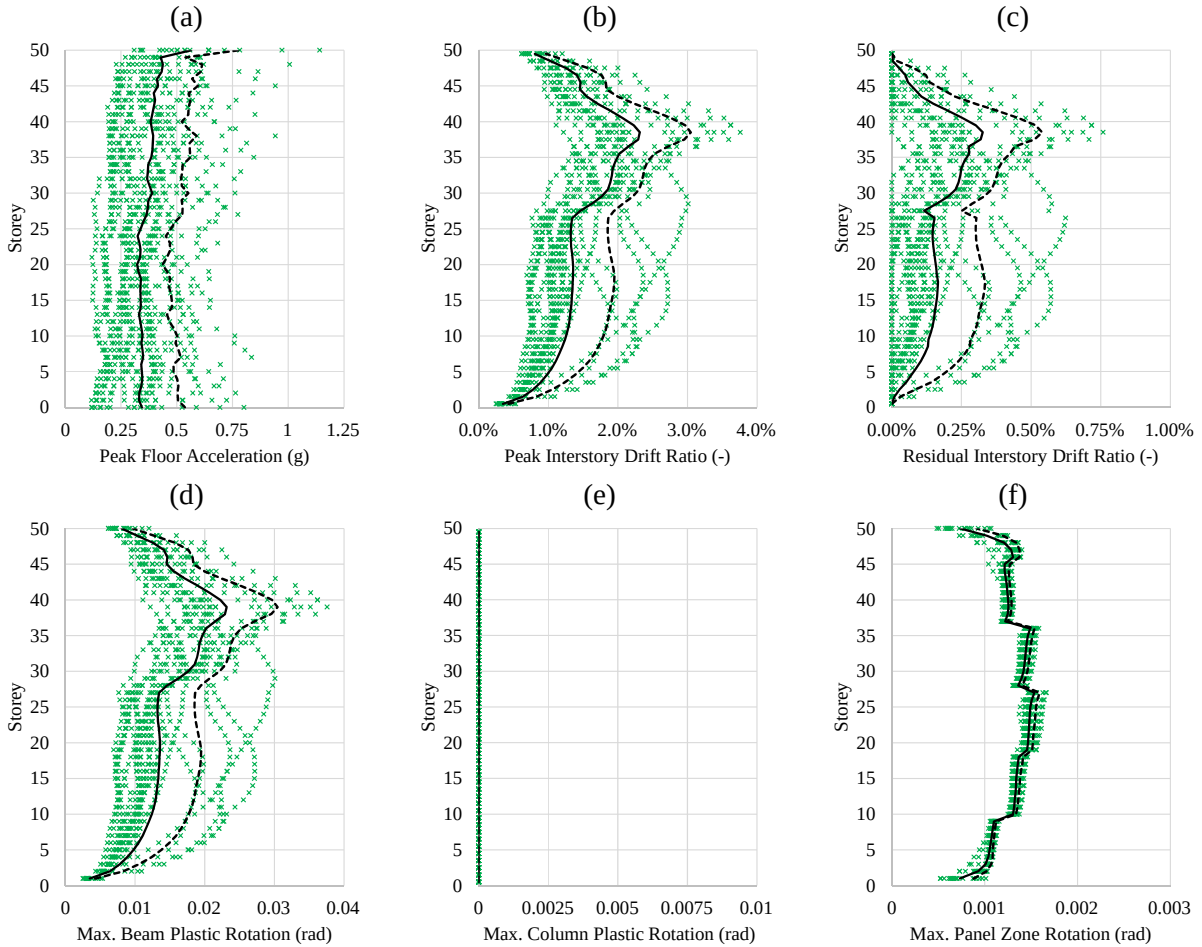

Figure G12: IBC 2012 non-linear dynamic analysis results under earthquake ground motion intensity (e_4), including: peak floor acceleration (a), peak interstorey drift (b), peak residual interstorey drift (c), maximum beam plastic rotation (d), maximum column plastic rotation (d) and maximum panel zone rotation (f).

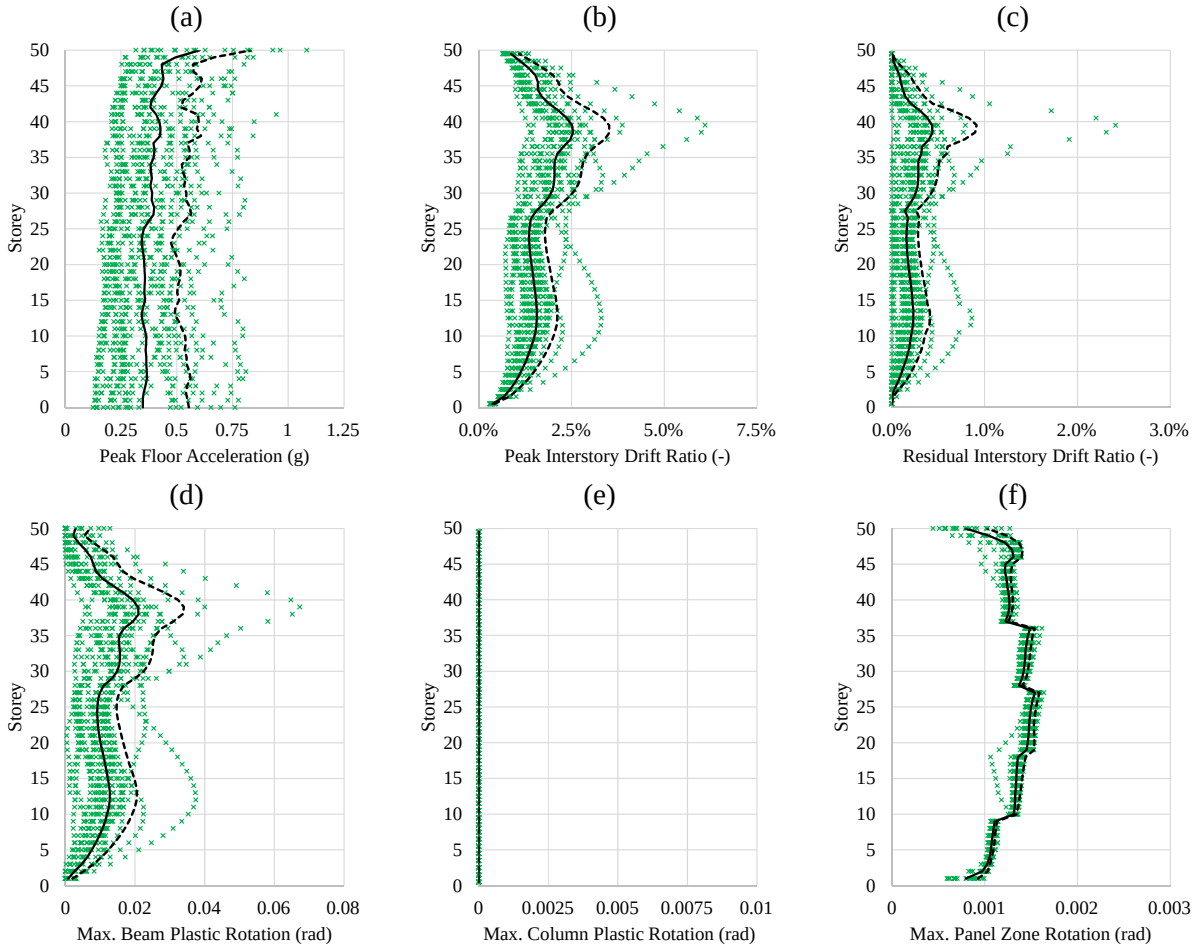

Figure G13: IBC 2012 non-linear dynamic analysis results under earthquake ground motion intensity (e_5), including: peak floor acceleration (a), peak interstorey drift (b), peak residual interstorey drift (c), maximum beam plastic rotation (d), maximum column plastic rotation (d) and maximum panel zone rotation (f).

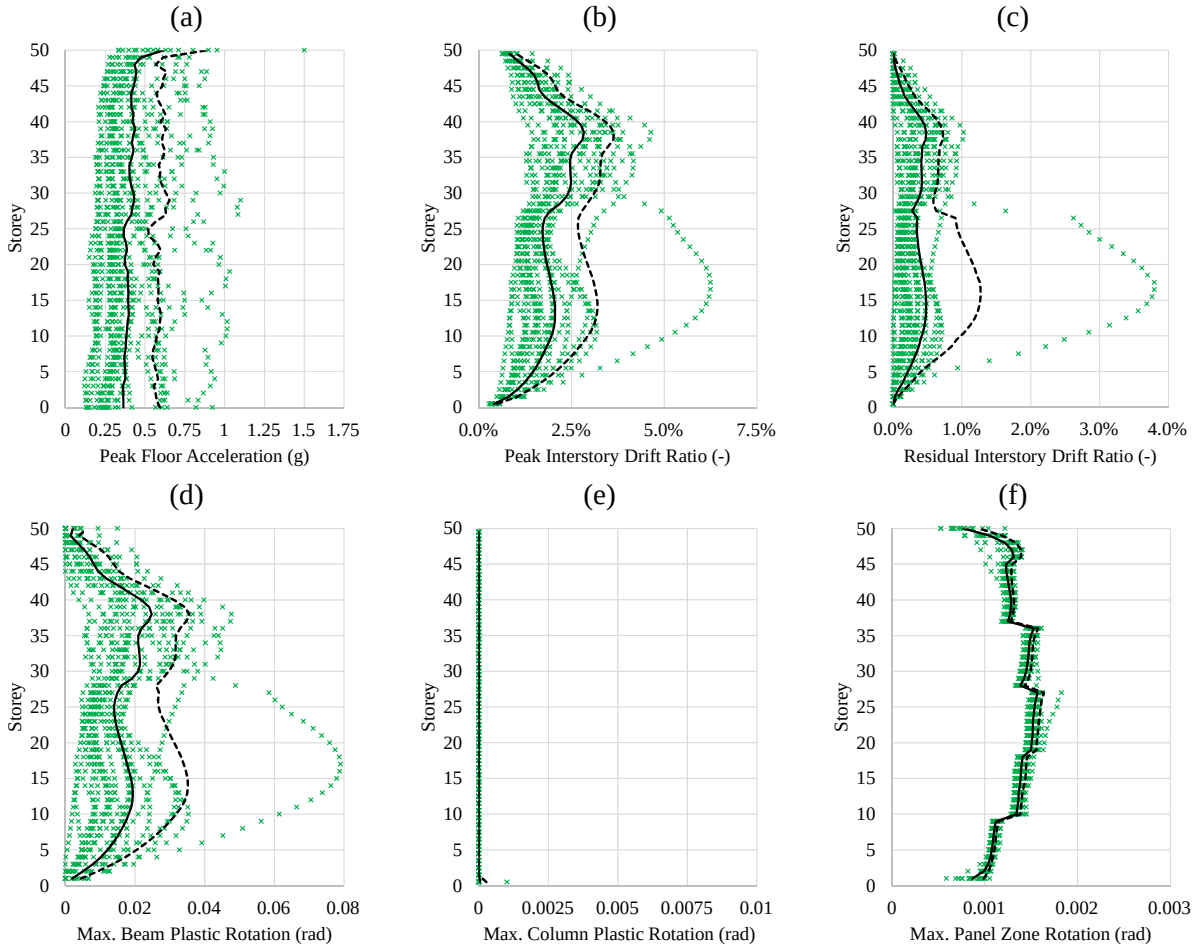

Figure G14: IBC 2012 non-linear dynamic analysis results under earthquake ground motion intensity (e_6), including: peak floor acceleration (a), peak interstorey drift (b), peak residual interstorey drift (c), maximum beam plastic rotation (d), maximum column plastic rotation (d) and maximum panel zone rotation (f).

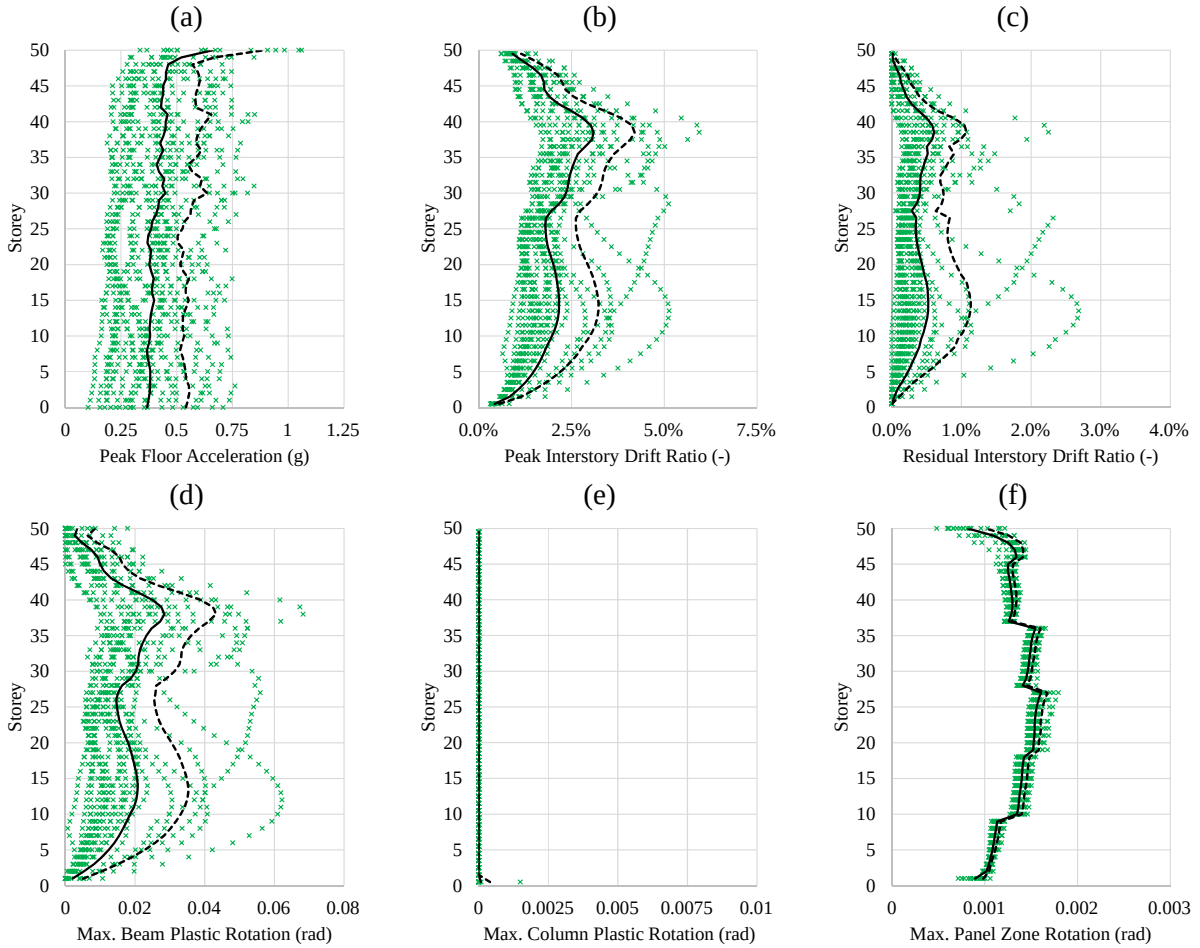

Figure G15: IBC 2012 non-linear dynamic analysis results under earthquake ground motion intensity (e_7), including: peak floor acceleration (a), peak interstorey drift (b), peak residual interstorey drift (c), maximum beam plastic rotation (d), maximum column plastic rotation (d) and maximum panel zone rotation (f).

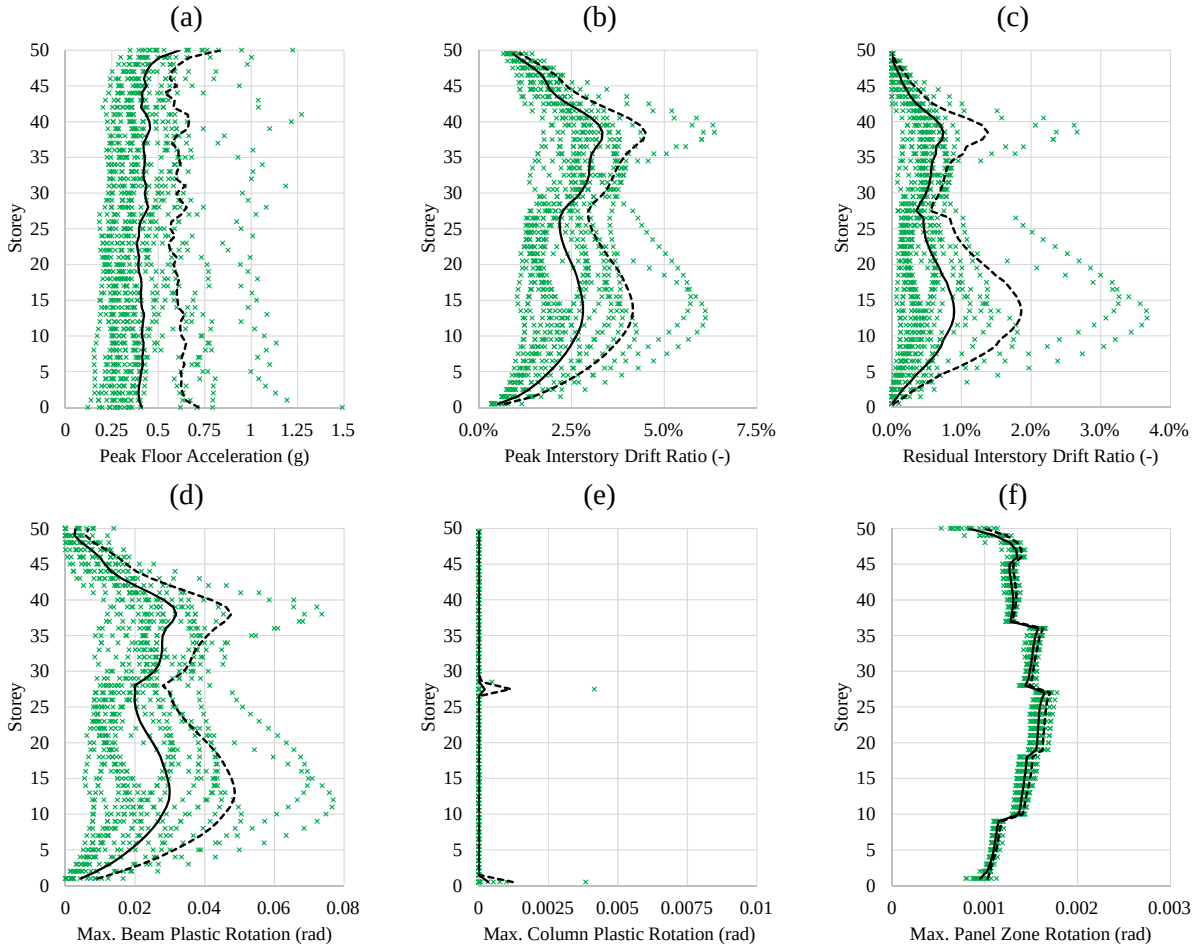

Figure G16: IBC 2012 non-linear dynamic analysis results under earthquake ground motion intensity (e_8), including: peak floor acceleration (a), peak interstorey drift (b), peak residual interstorey drift (c), maximum beam plastic rotation (d), maximum column plastic rotation (d) and maximum panel zone rotation (f).

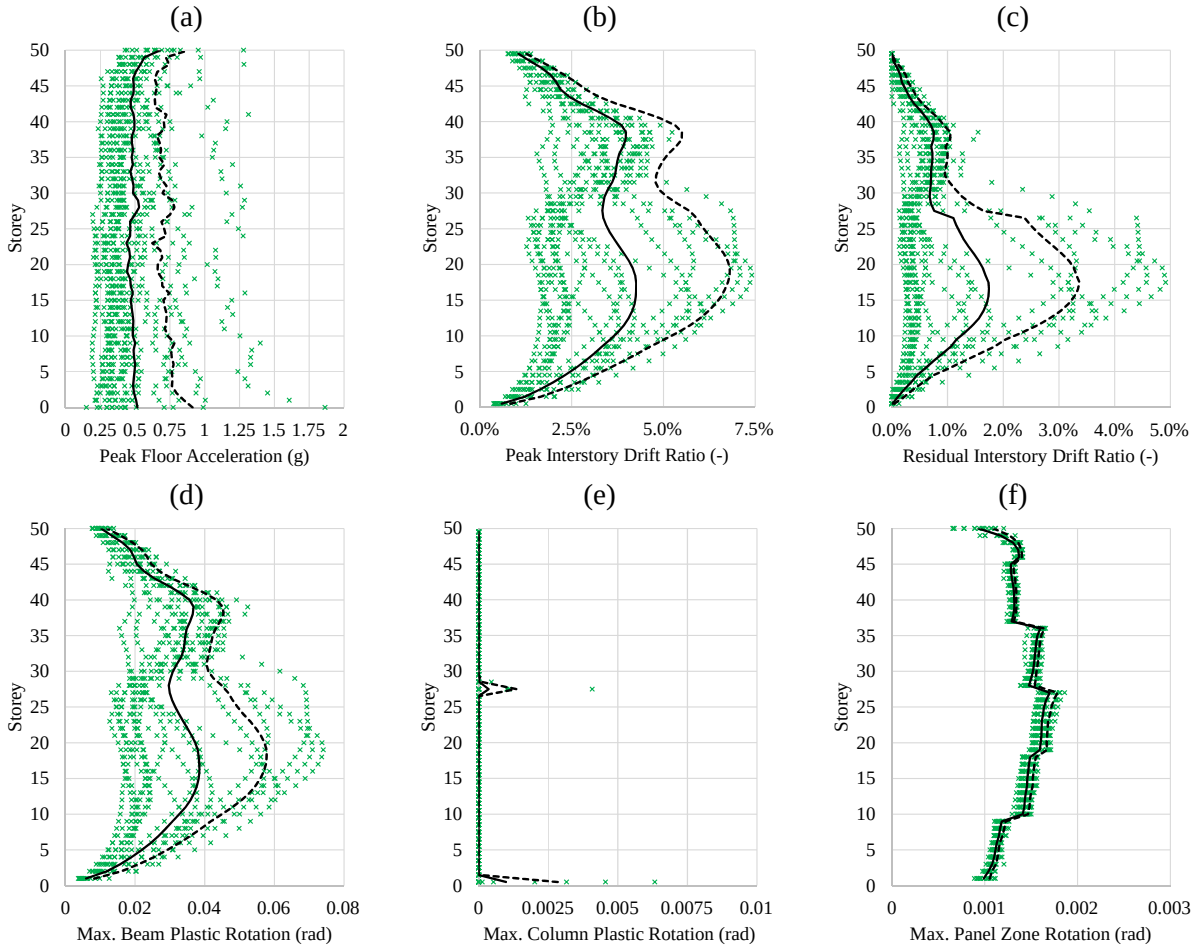

Figure G17: IBC 2012 non-linear dynamic analysis results under earthquake ground motion intensity (e_{8A}), including: peak floor acceleration (a), peak interstorey drift (b), peak residual interstorey drift (c), maximum beam plastic rotation (d), maximum column plastic rotation (d) and maximum panel zone rotation (f).

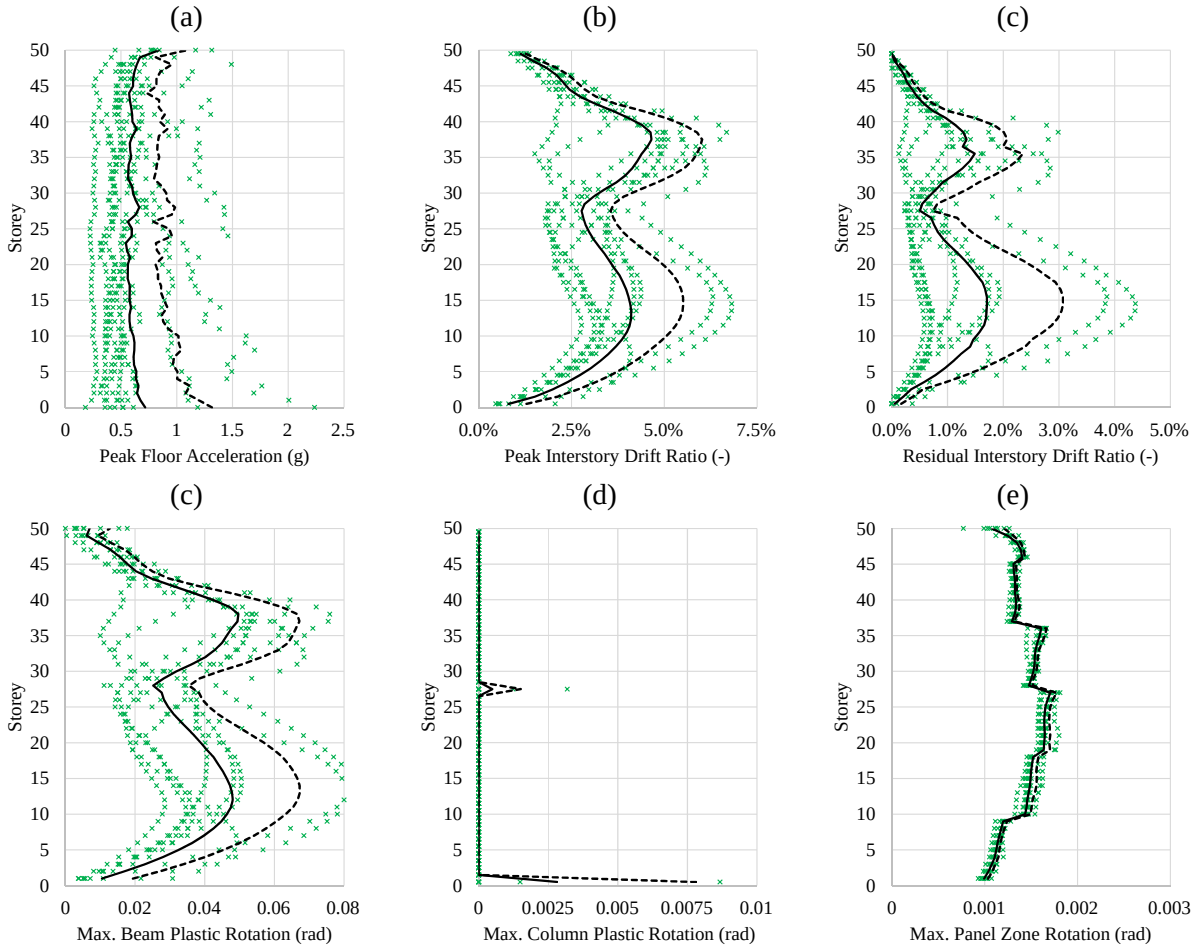

Figure G18: IBC 2012 non-linear dynamic analysis results under earthquake ground motion intensity (e_{8B}), including: peak floor acceleration (a), peak interstorey drift (b), peak residual interstorey drift (c), maximum beam plastic rotation (d), maximum column plastic rotation (d) and maximum panel zone rotation (f).

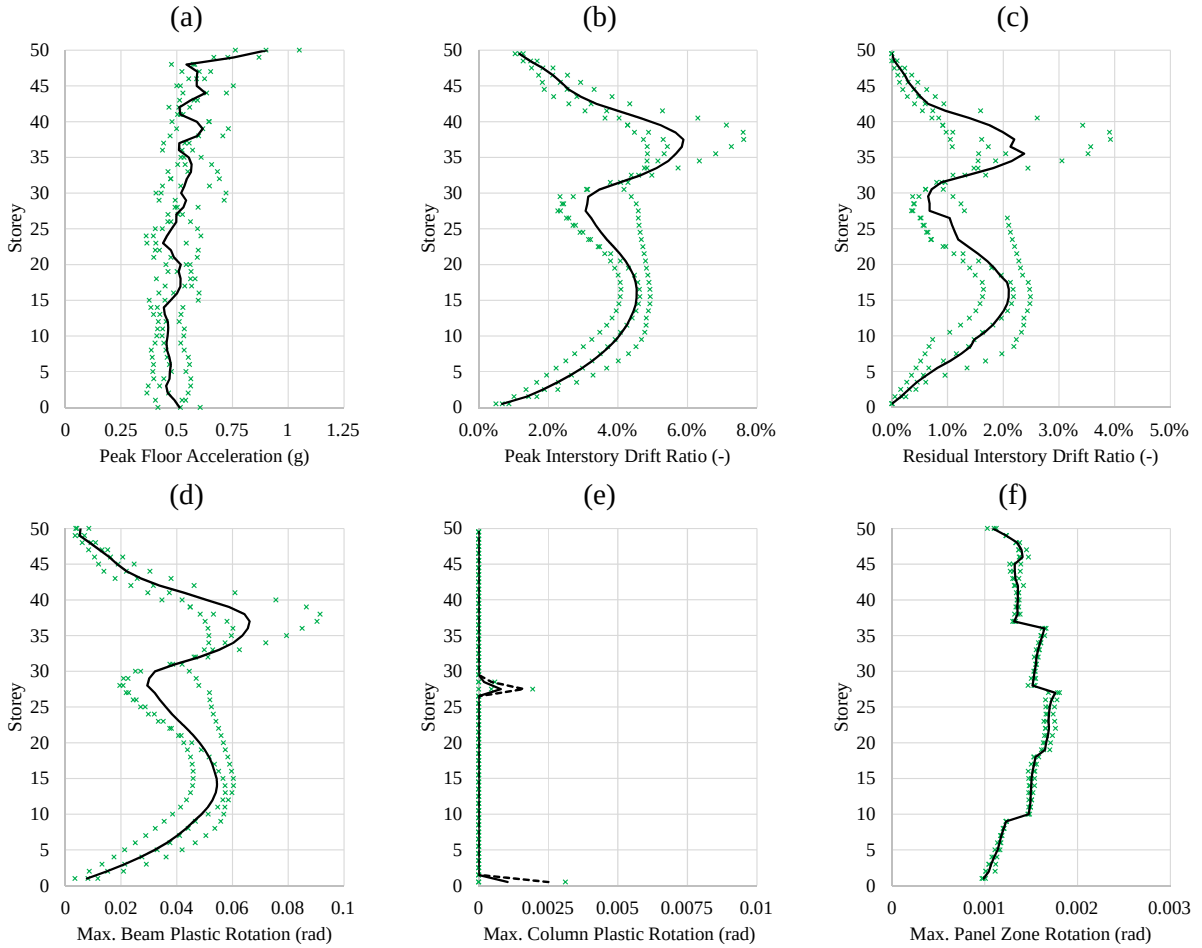

Figure G19: IBC 2012 non-linear dynamic analysis results under earthquake ground motion intensity (e_{8C}), including: peak floor acceleration (a), peak interstorey drift (b), peak residual interstorey drift (c), maximum beam plastic rotation (d), maximum column plastic rotation (d) and maximum panel zone rotation (f).

This page is intentionally left blank.

Appendix H

Appendix H provides a breakdown of different contributions (acceleration vs drift sensitive components; building component categories) to earthquake damage for the 1973 and the 2012 archetype buildings for an array of earthquake ground motion intensities, as discussed in Chapter 7. Note that the results presented in each figure are normalized with respect to the expected loss at each intensity level considered. For relevant loss ratios, refer to Figures 7-17 and 7-18.

H1. Figure H1: Contribution of acceleration versus drift-sensitive (a) and different building component categories (b) to repairable damage under earthquake ground motion intensity e_1 for the 1973 archetype.

H2. Figure H2: Contribution of acceleration versus drift-sensitive (a) and different building component categories (b) to repairable damage under earthquake ground motion intensity e_{1A} for the 1973 archetype.

H3. Figure H3: Contribution of acceleration versus drift-sensitive (a) and different building component categories (b) to repairable damage under earthquake ground motion intensity e_2 for the 1973 archetype.

H4. Figure H4: Contribution of acceleration versus drift-sensitive (a) and different building component categories (b) to repairable damage under earthquake ground motion intensity e_{2A} for the 1973 archetype.

H5. Figure H5: Contribution of acceleration versus drift-sensitive (a) and different building component categories (b) to repairable damage under earthquake ground motion intensity e_3 for the 1973 archetype.

H6. Figure H6: Contribution of acceleration versus drift-sensitive (a) and different building component categories (b) to repairable damage under earthquake ground motion intensity e_{3A} for the 1973 archetype.

H7. Figure H7: Contribution of acceleration versus drift-sensitive (a) and different building component categories (b) to repairable damage under earthquake ground motion intensity e_4 for the 1973 archetype.

H8. Figure H8: Contribution of acceleration versus drift-sensitive (a) and different building component categories (b) to repairable damage under earthquake ground motion intensity e_5 for the 1973 archetype.

H9. Figure H9: Contribution of acceleration versus drift-sensitive (a) and different building component categories (b) to repairable damage under earthquake ground motion intensity e_1 for the 2012 archetype.

H10. Figure H10: Contribution of acceleration versus drift-sensitive (a) and different building component categories (b) to repairable damage under earthquake ground motion intensity e_2 for the 2012 archetype.

H11. Figure H11: Contribution of acceleration versus drift-sensitive (a) and different building component categories (b) to repairable damage under earthquake ground motion intensity e_3 for the 2012 archetype.

H12. Figure H12: Contribution of acceleration versus drift-sensitive (a) and different building component categories (b) to repairable damage under earthquake ground motion intensity e_4 for the 2012 archetype.

H13. Figure H13: Contribution of acceleration versus drift-sensitive (a) and different building component categories (b) to repairable damage under earthquake ground motion intensity e_5 for the 2012 archetype.

H14. Figure H14: Contribution of acceleration versus drift-sensitive (a) and different building component categories (b) to repairable damage under earthquake ground motion intensity e_6 for the 2012 archetype.

H15. Figure H15: Contribution of acceleration versus drift-sensitive (a) and different building component categories (b) to repairable damage under earthquake ground motion intensity e_7 for the 2012 archetype.

H16. Figure H16: Contribution of acceleration versus drift-sensitive (a) and different building component categories (b) to repairable damage under earthquake ground motion intensity e_8 for the 2012 archetype.

H17. Figure H17: Contribution of acceleration versus drift-sensitive (a) and different building component categories (b) to repairable damage under earthquake ground motion intensity e_{8A} for the 2012 archetype.

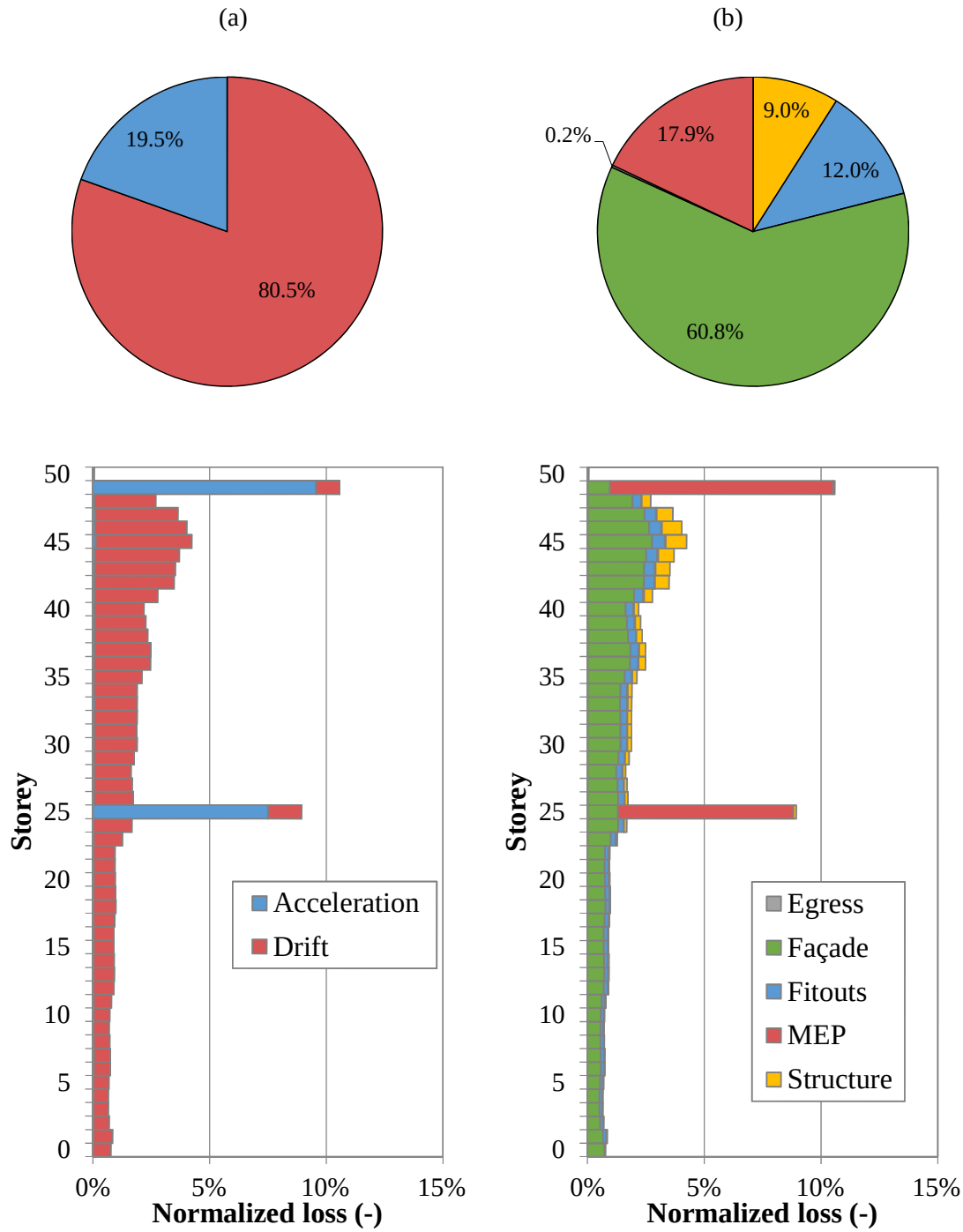

Figure H1: Contribution of acceleration versus drift-sensitive (a) and different building component categories (b) to repairable damage under earthquake ground motion intensity e_1 for the 1973 archetype.

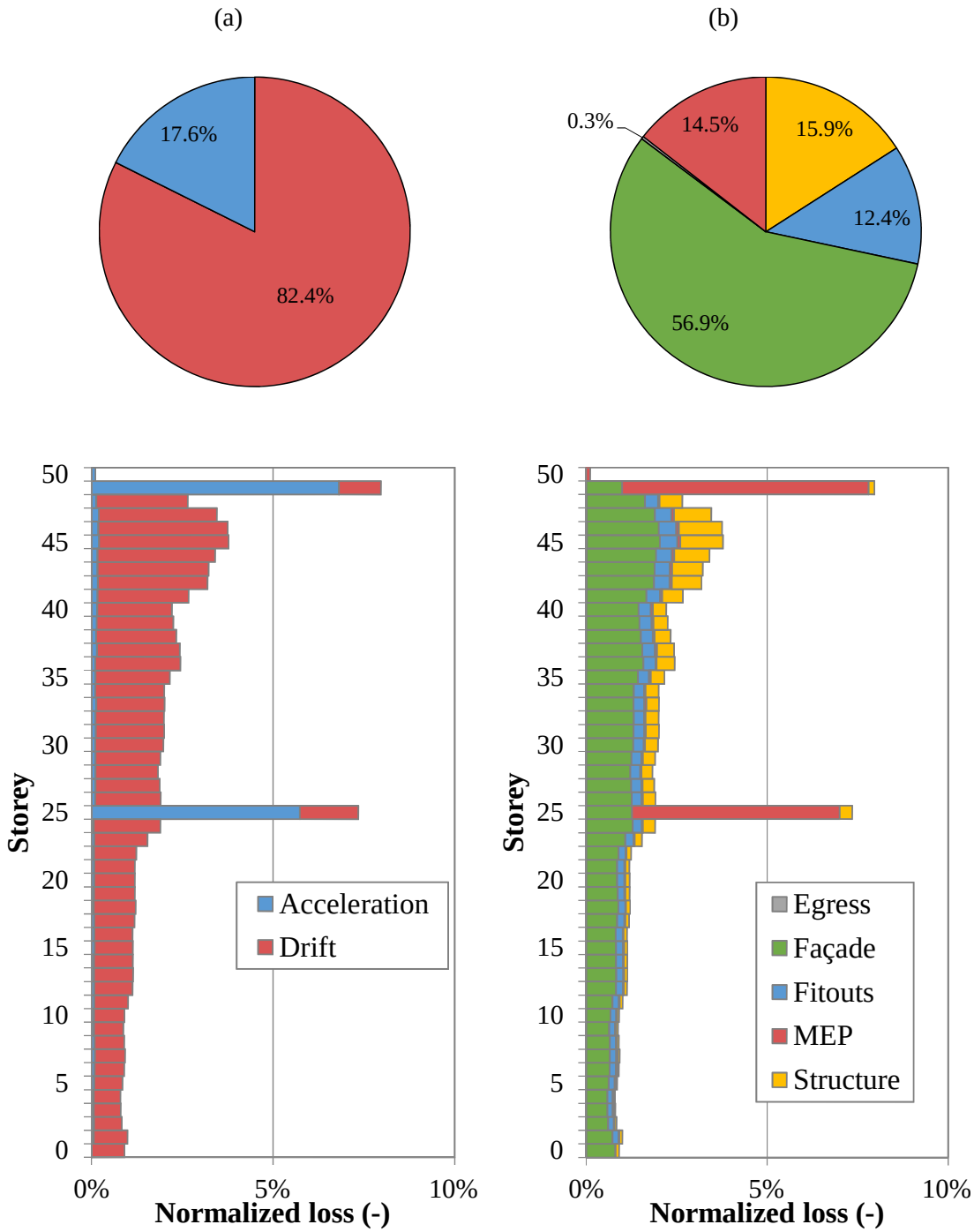

Figure H2: Contribution of acceleration versus drift-sensitive (a) and different building component categories (b) to repairable damage under earthquake ground motion intensity e_{1A} for the 1973 archetype.

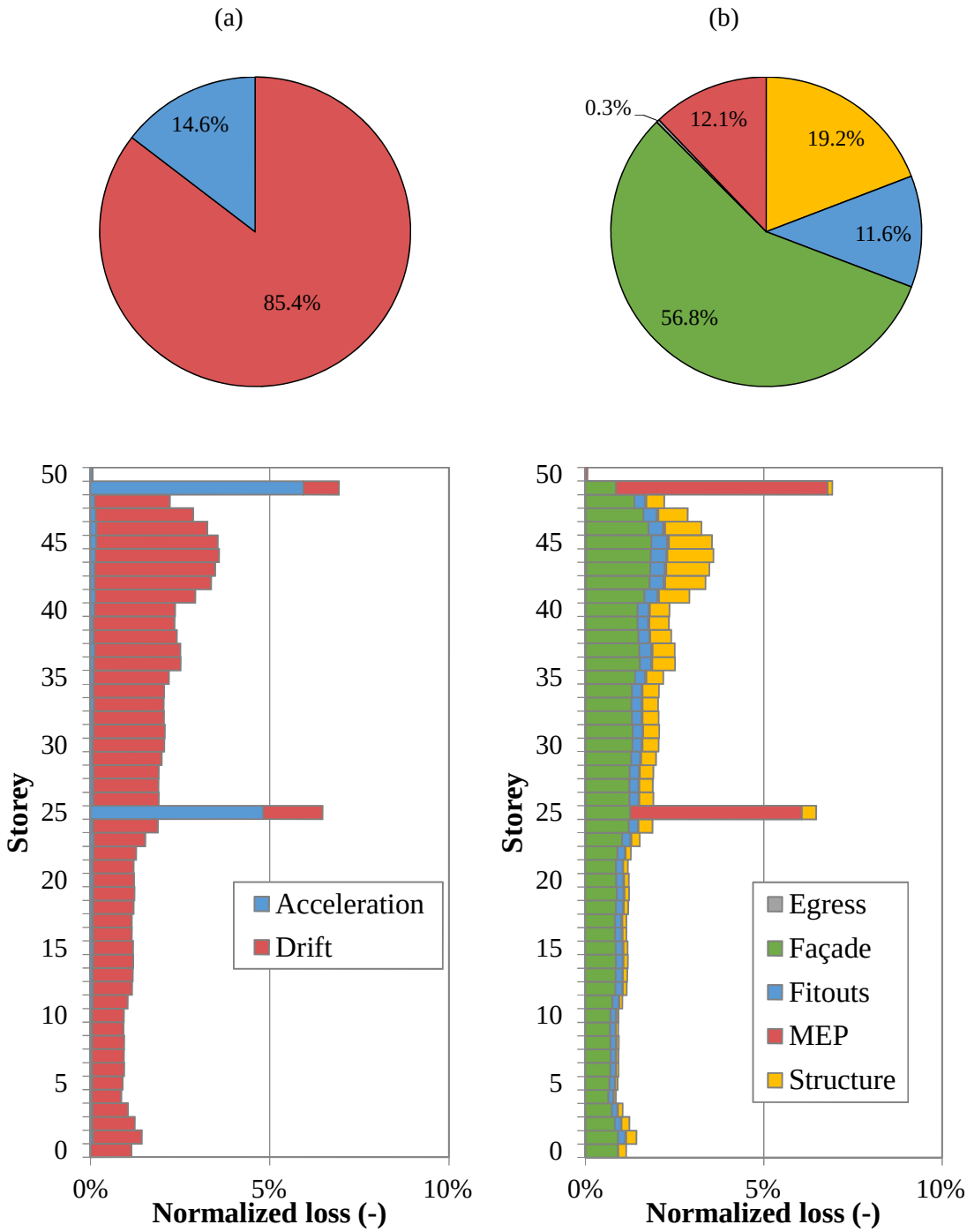

Figure H3: Contribution of acceleration versus drift-sensitive (a) and different building component categories (b) to repairable damage under earthquake ground motion intensity e_2 for the 1973 archetype.

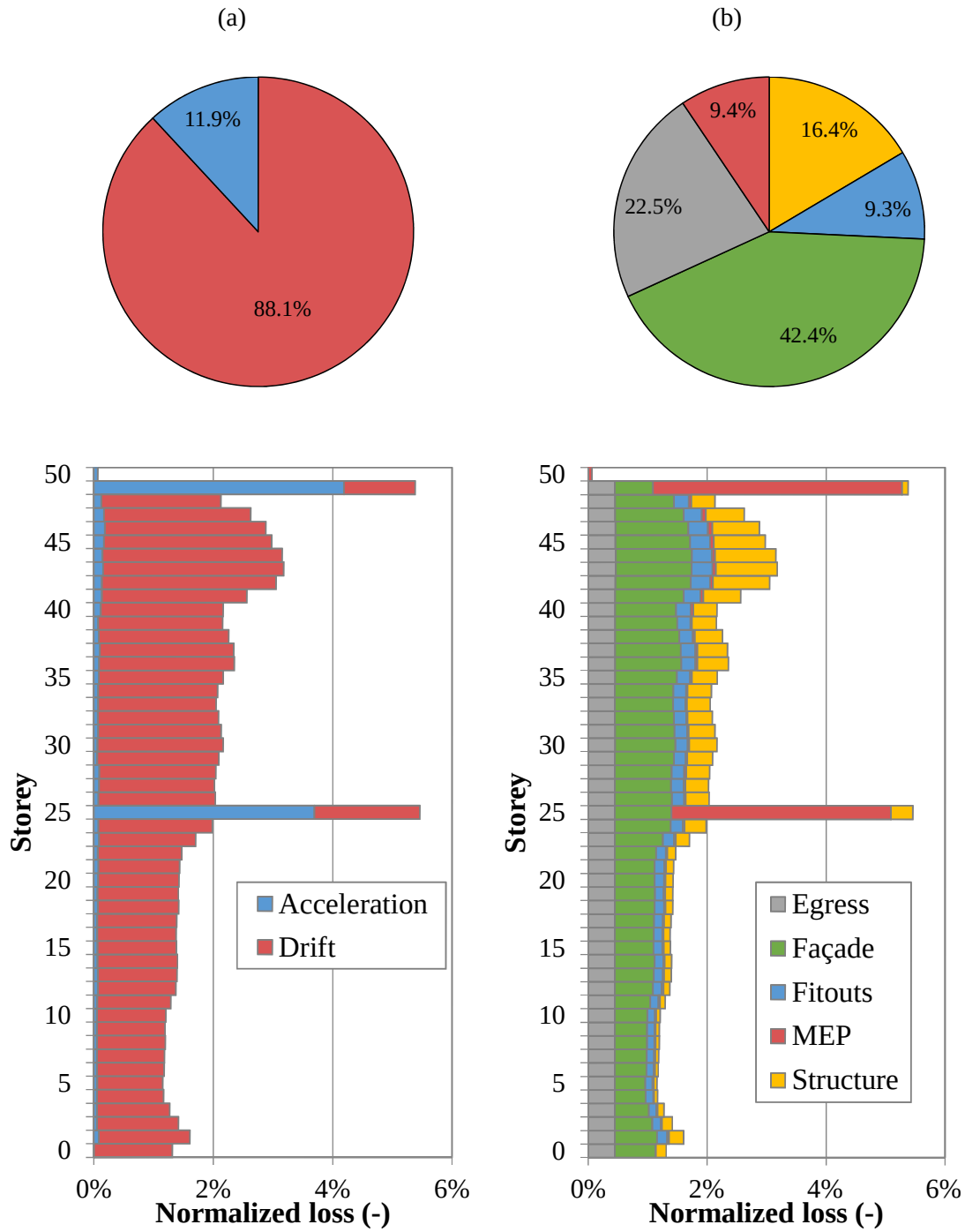

Figure H4: Contribution of acceleration versus drift-sensitive (a) and different building component categories (b) to repairable damage under earthquake ground motion intensity e_{2A} for the 1973 archetype.

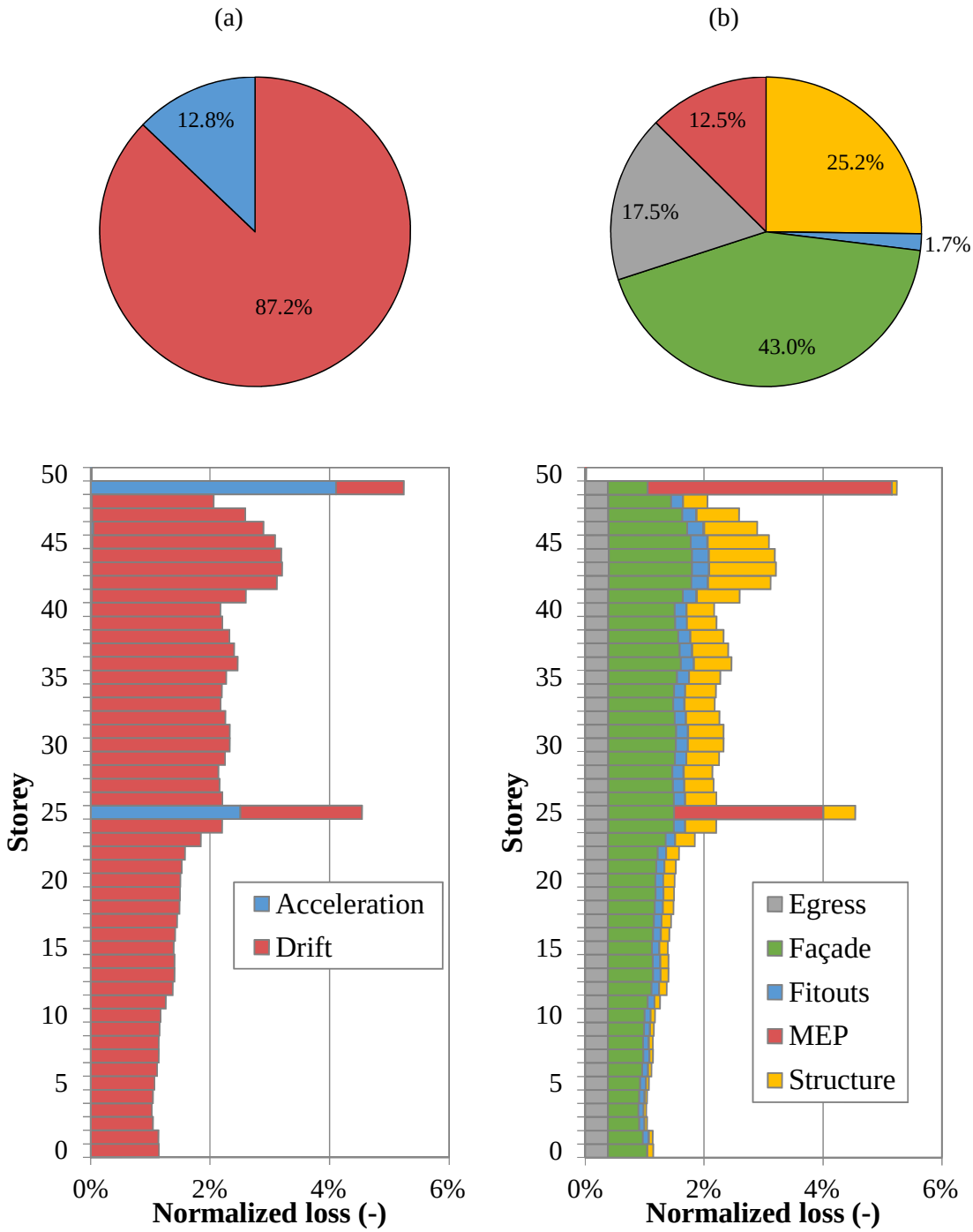

Figure H5: Contribution of acceleration versus drift-sensitive (a) and different building component categories (b) to repairable damage under earthquake ground motion intensity e_3 for the 1973 archetype.

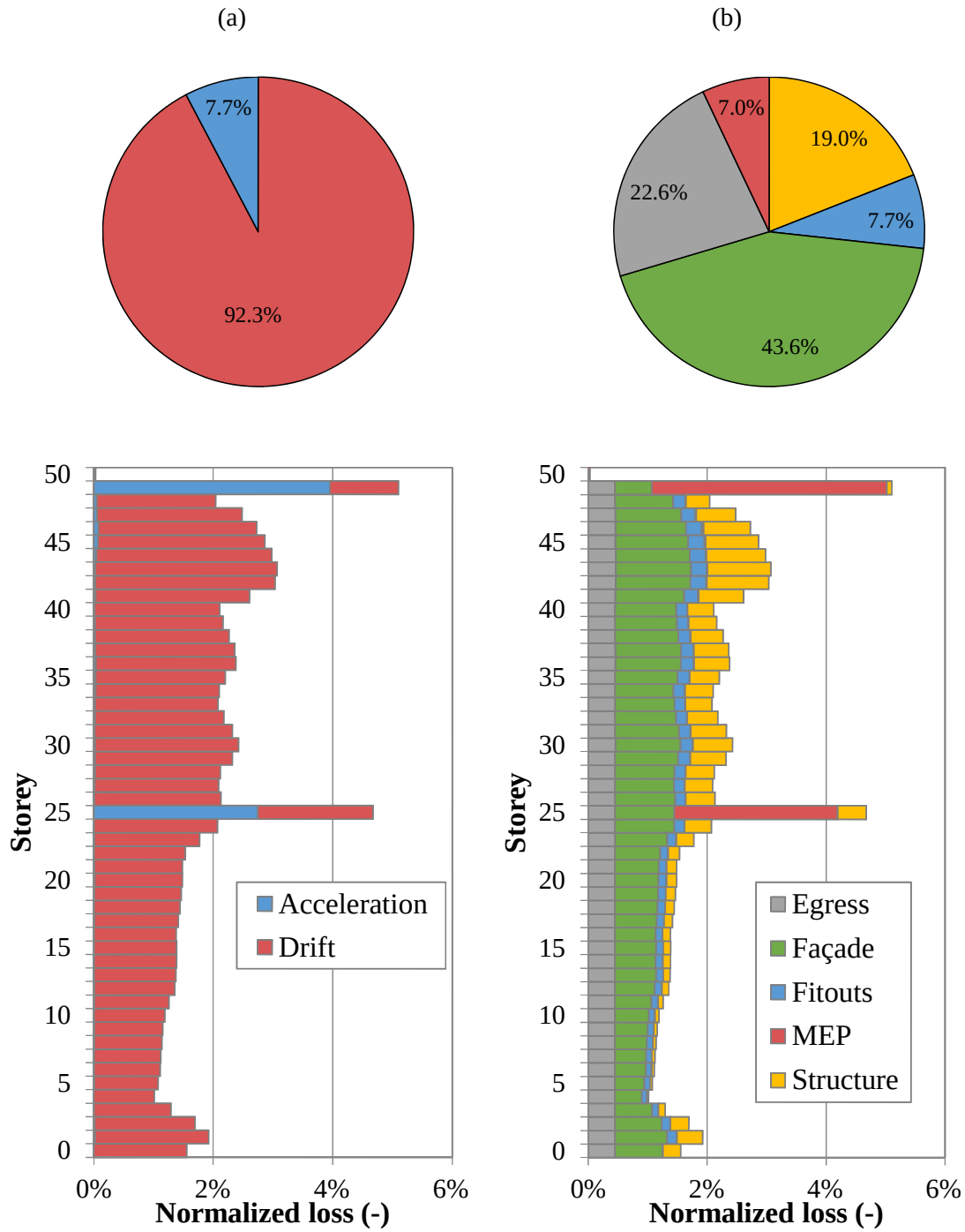

Figure H6: Contribution of acceleration versus drift-sensitive (a) and different building component categories (b) to repairable damage under earthquake ground motion intensity e_{3A} for the 1973 archetype.

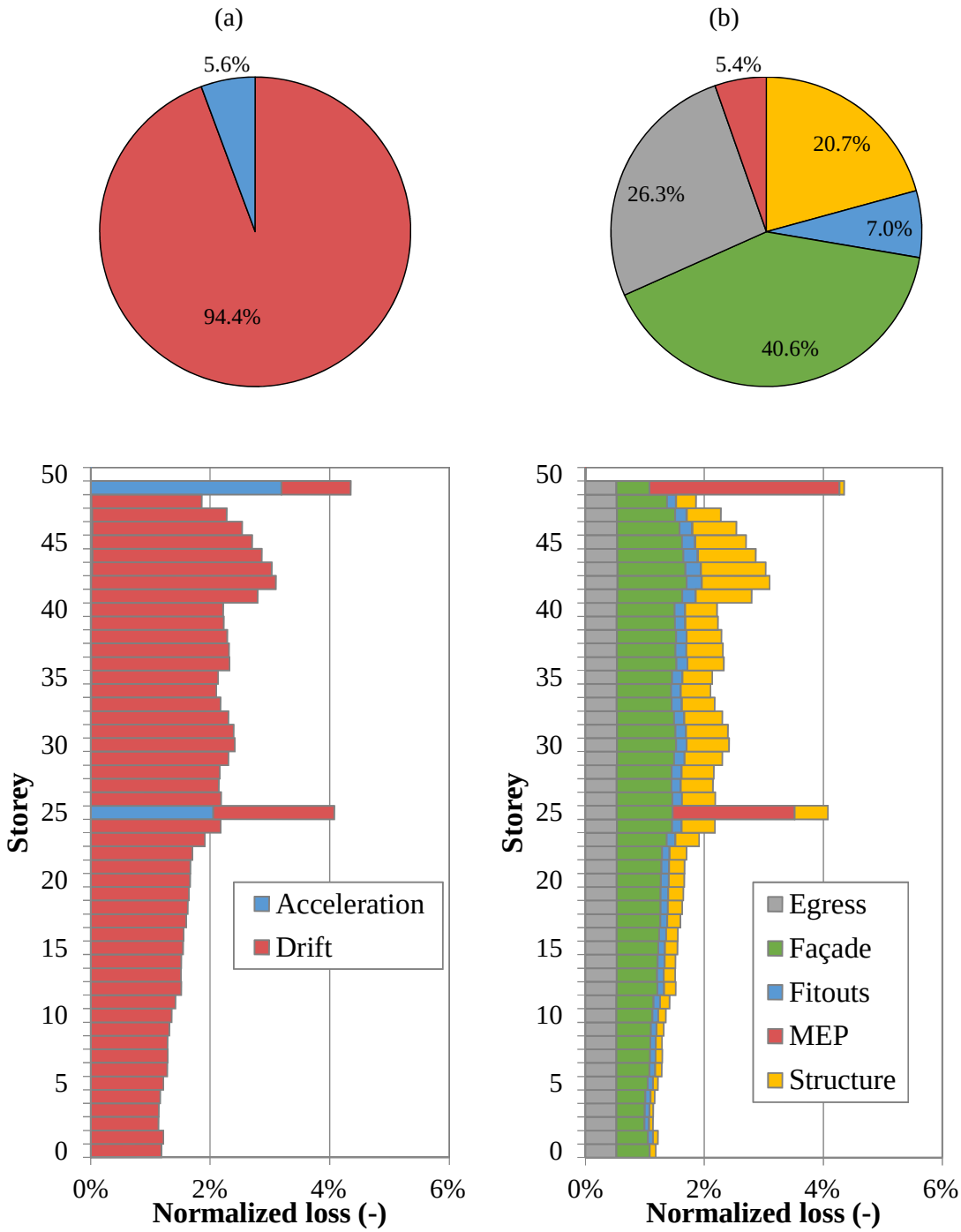

Figure H7: Contribution of acceleration versus drift-sensitive (a) and different building component categories (b) to repairable damage under earthquake ground motion intensity e_4 for the 1973 archetype.

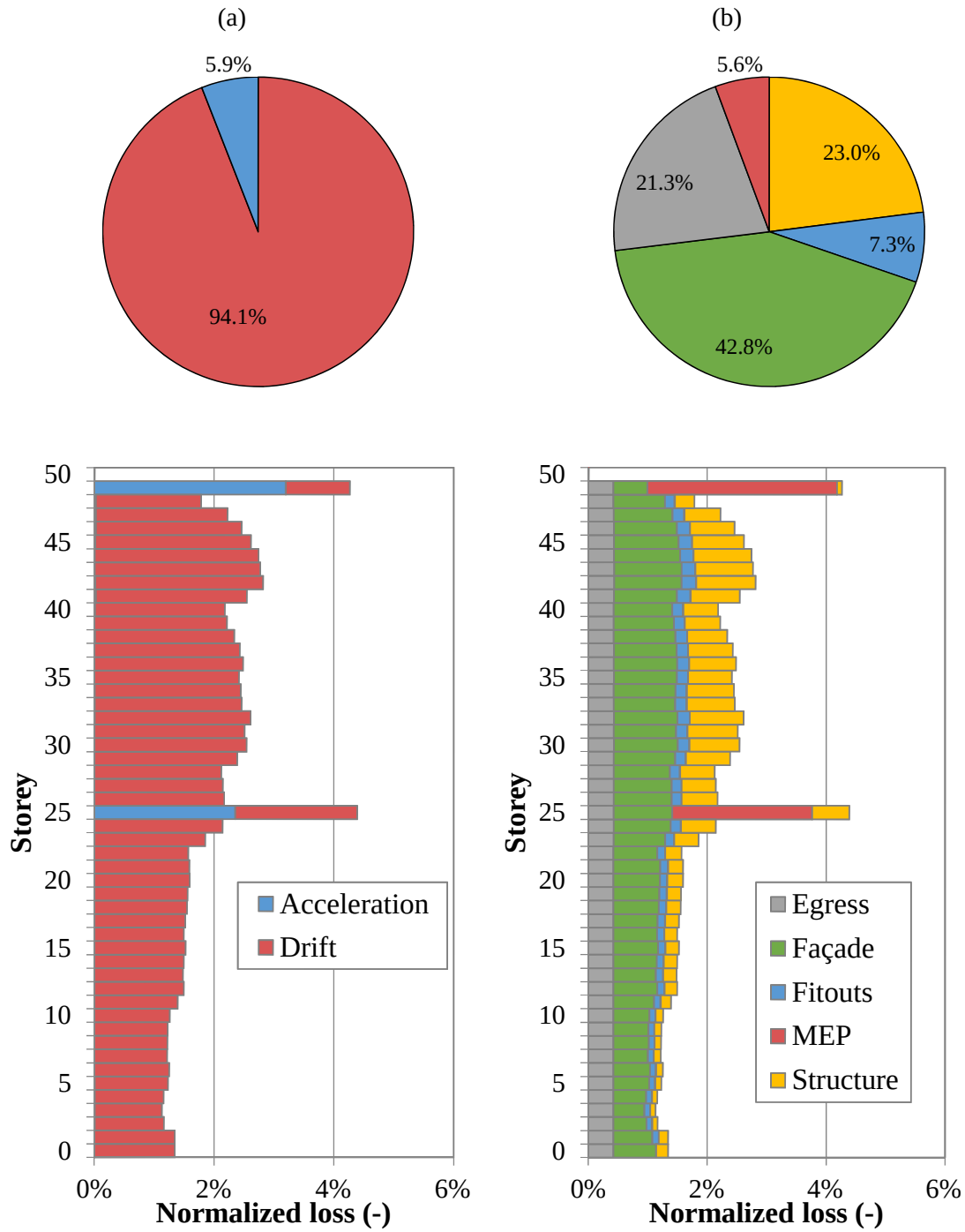

Figure H8: Contribution of acceleration versus drift-sensitive (a) and different building component categories (b) to repairable damage under earthquake ground motion intensity e_5 for the 1973 archetype.

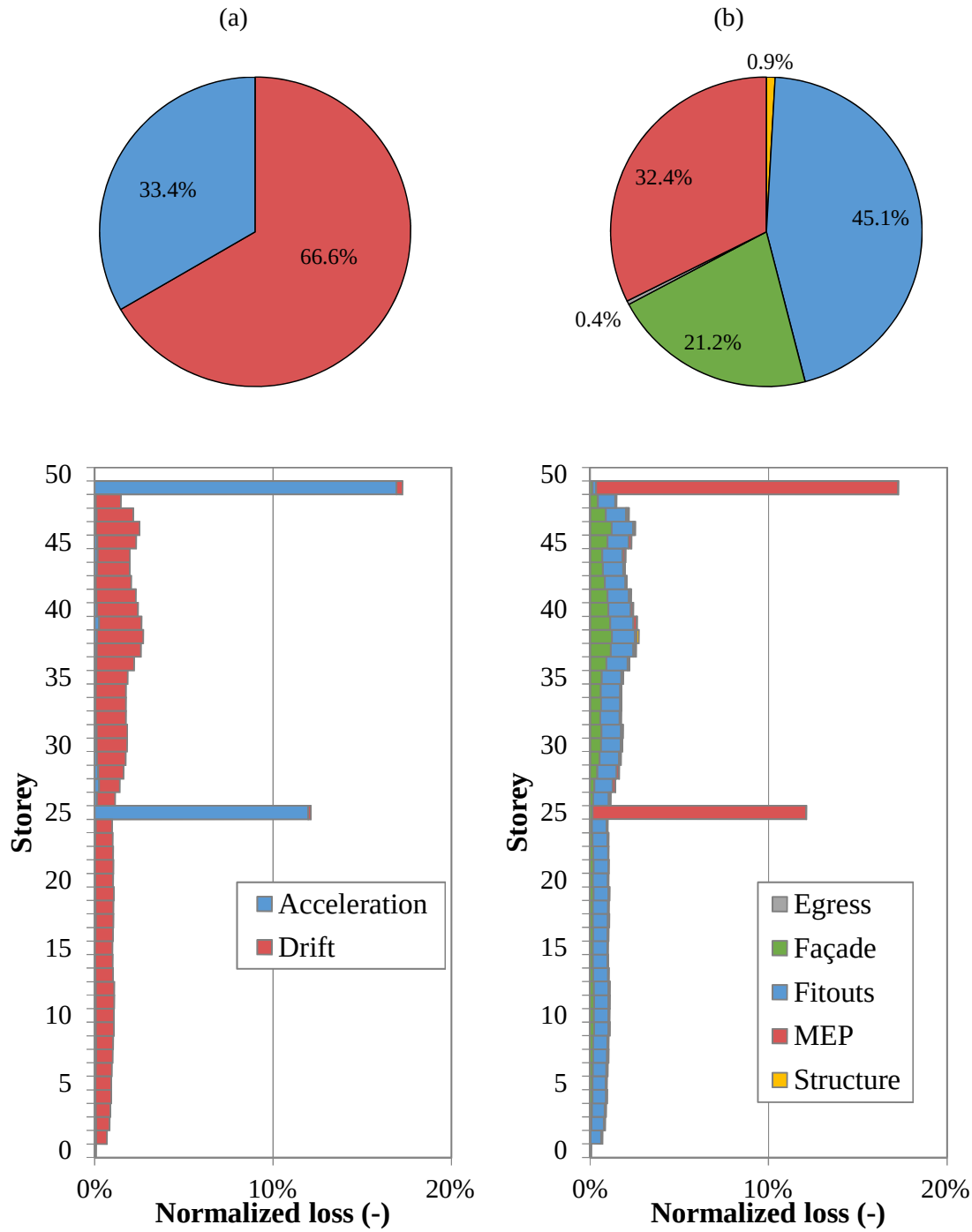

Figure H9: Contribution of acceleration versus drift-sensitive (a) and different building component categories (b) to repairable damage under earthquake ground motion intensity e_1 for the 2012 archetype.

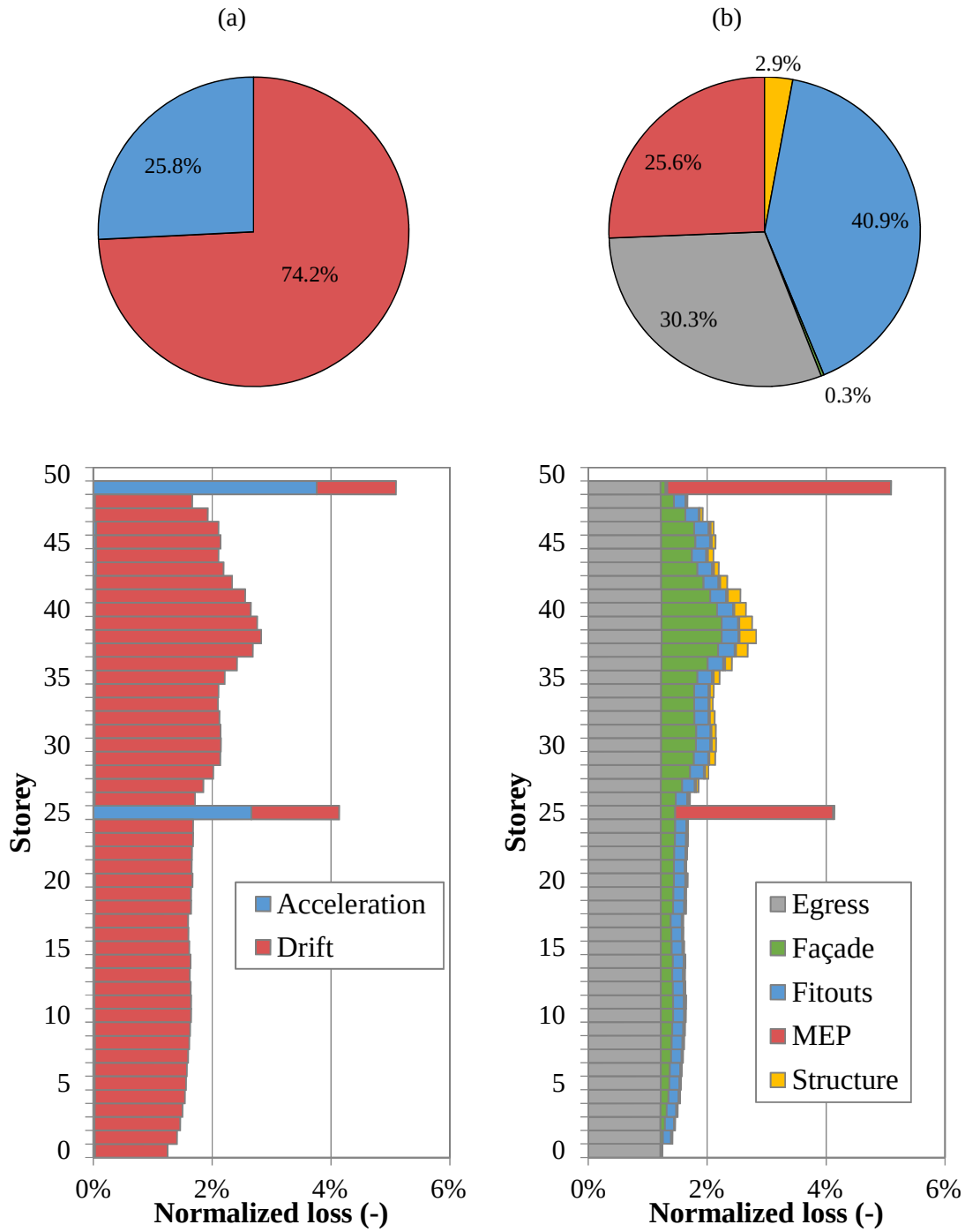

Figure H10: Contribution of acceleration versus drift-sensitive (a) and different building component categories (b) to repairable damage under earthquake ground motion intensity e_2 for the 2012 archetype.

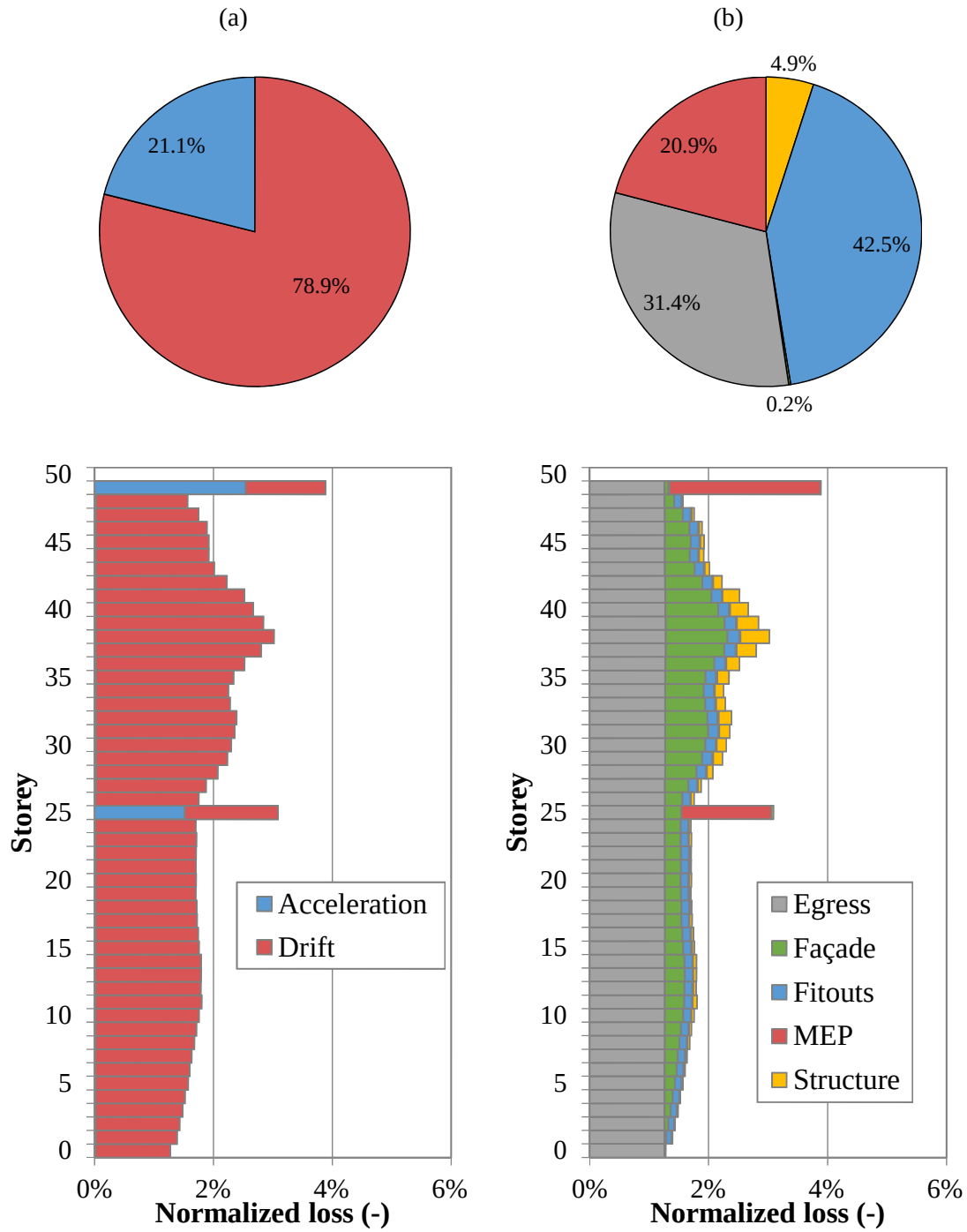

Figure H11: Contribution of acceleration versus drift-sensitive (a) and different building component categories (b) to repairable damage under earthquake ground motion intensity e_3 for the 2012 archetype.

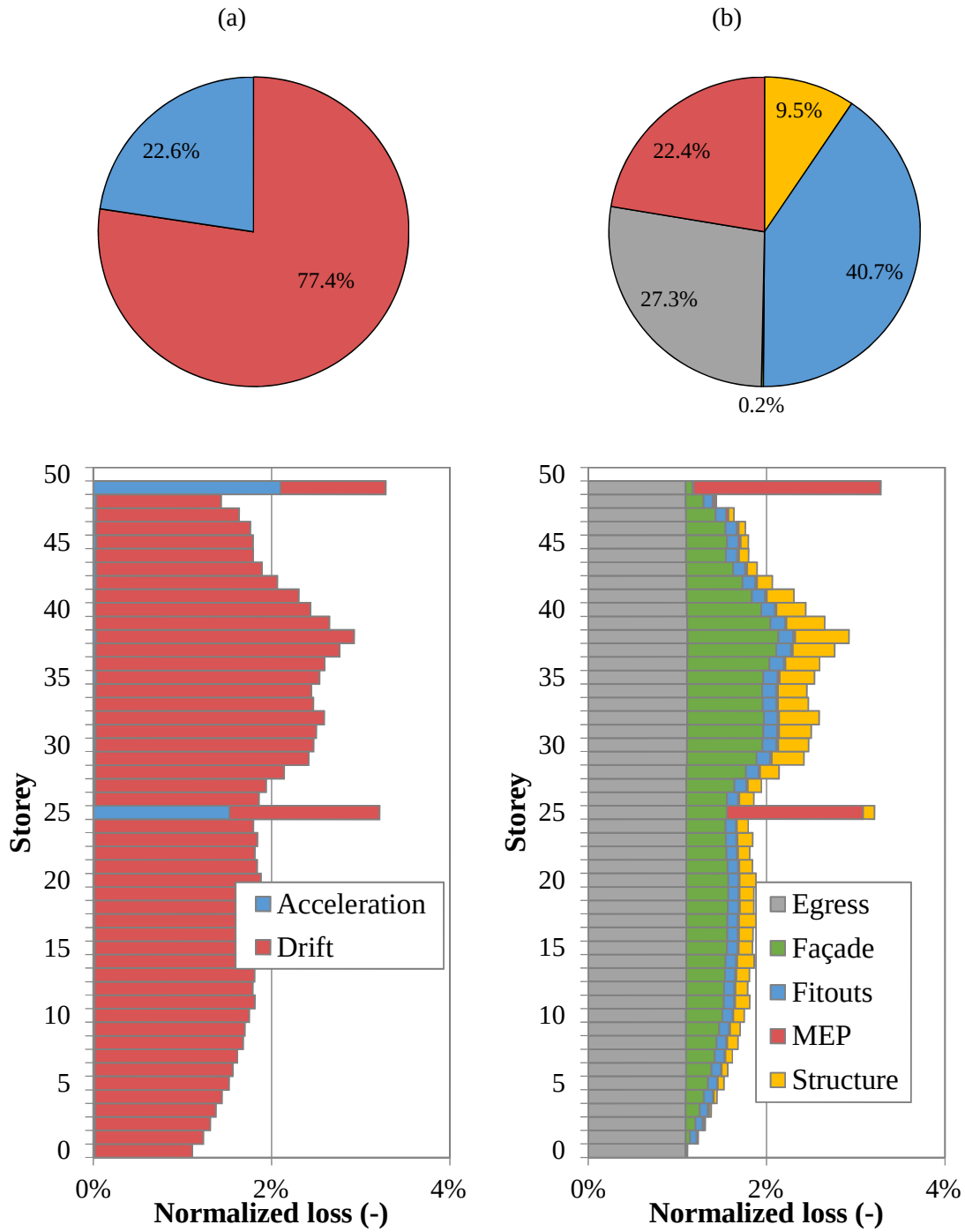

Figure H12: Contribution of acceleration versus drift-sensitive (a) and different building component categories (b) to repairable damage under earthquake ground motion intensity e_4 for the 2012 archetype.

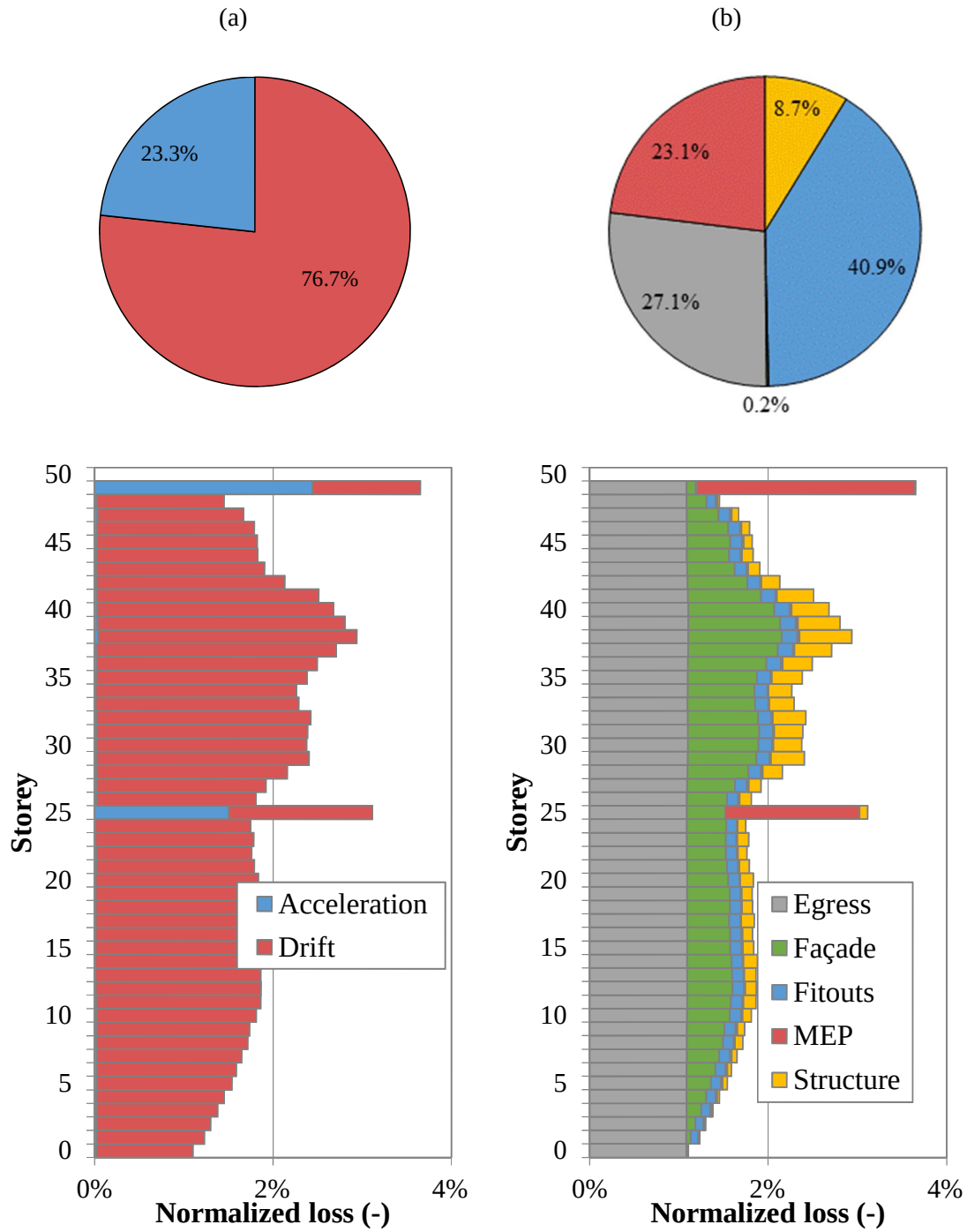

Figure H13: Contribution of acceleration versus drift-sensitive (a) and different building component categories (b) to repairable damage under earthquake ground motion intensity e_5 for the 2012 archetype.

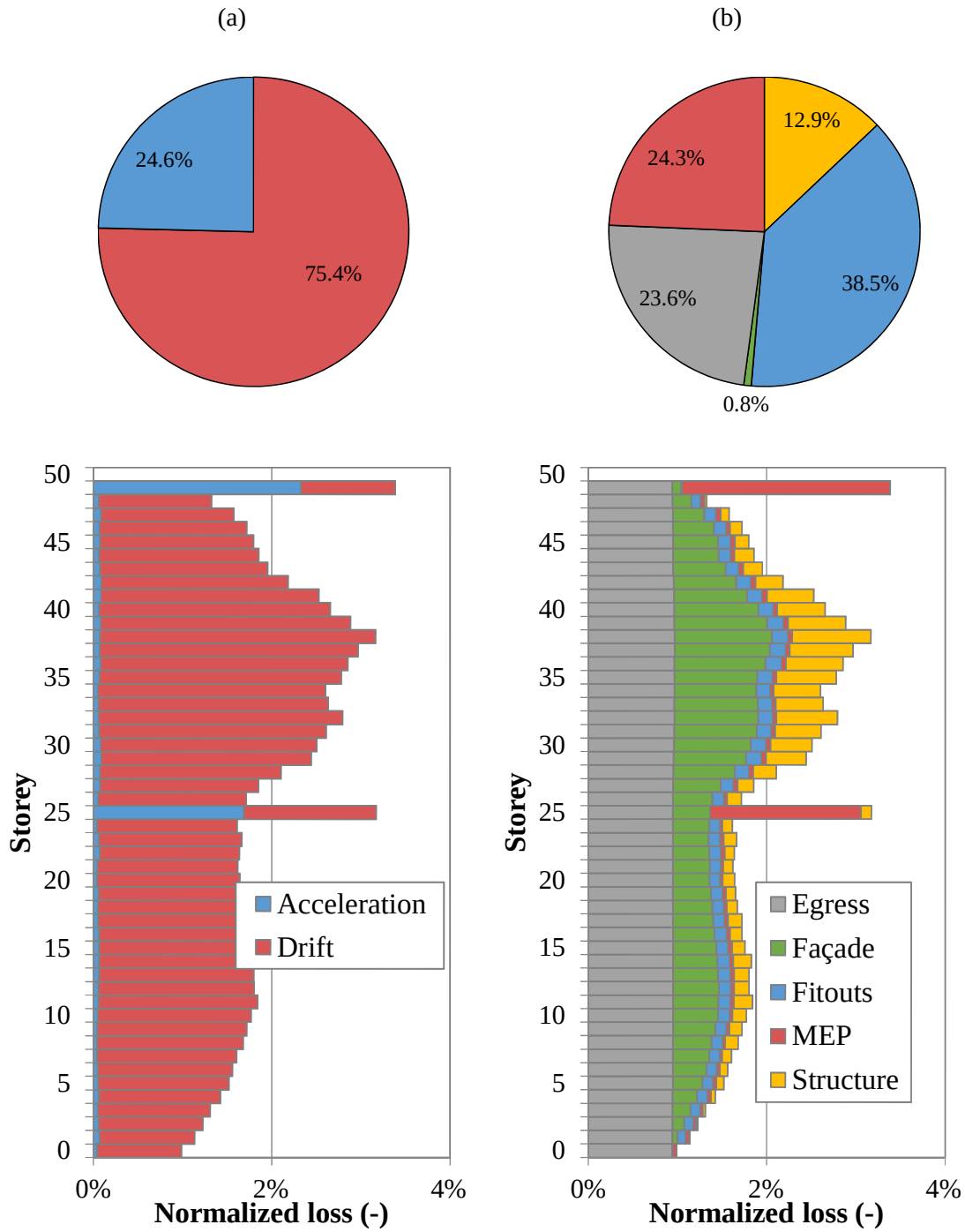

Figure H14: Contribution of acceleration versus drift-sensitive (a) and different building component categories (b) to repairable damage under earthquake ground motion intensity e_6 for the 2012 archetype.

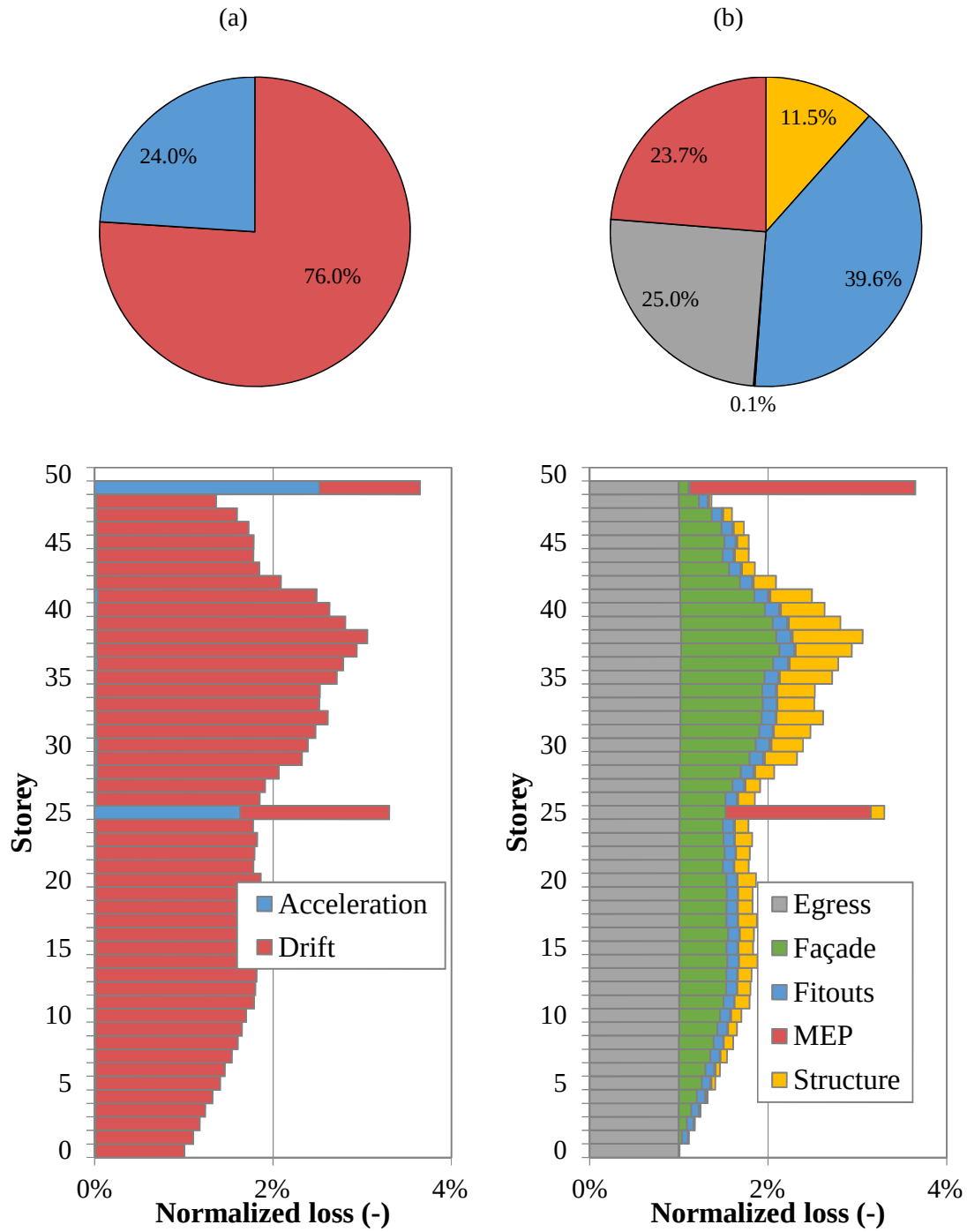

Figure H15: Contribution of acceleration versus drift-sensitive (a) and different building component categories (b) to repairable damage under earthquake ground motion intensity e_7 for the 2012 archetype.

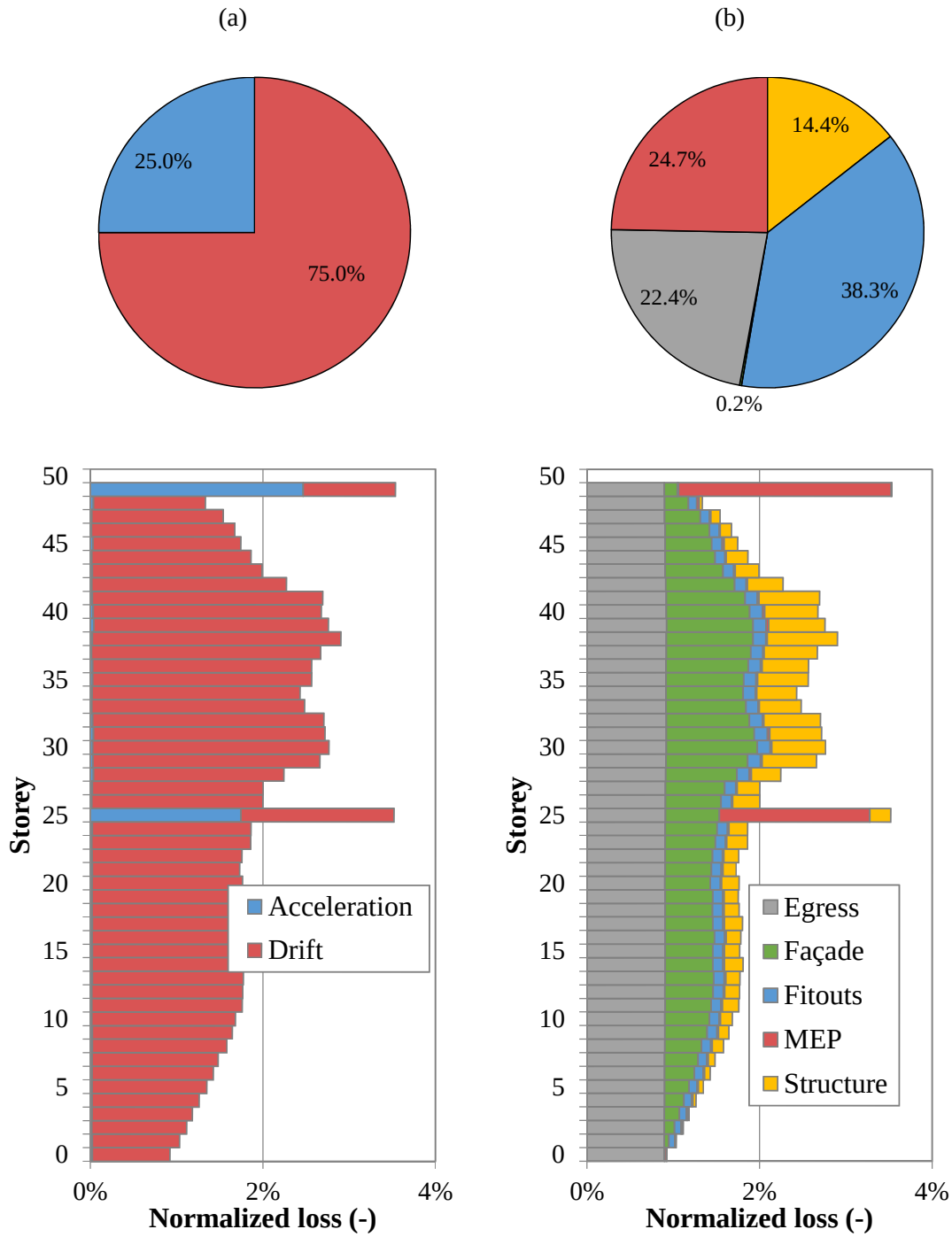

Figure H16: Contribution of acceleration versus drift-sensitive (a) and different building component categories (b) to repairable damage under earthquake ground motion intensity e_8 for the 2012 archetype.

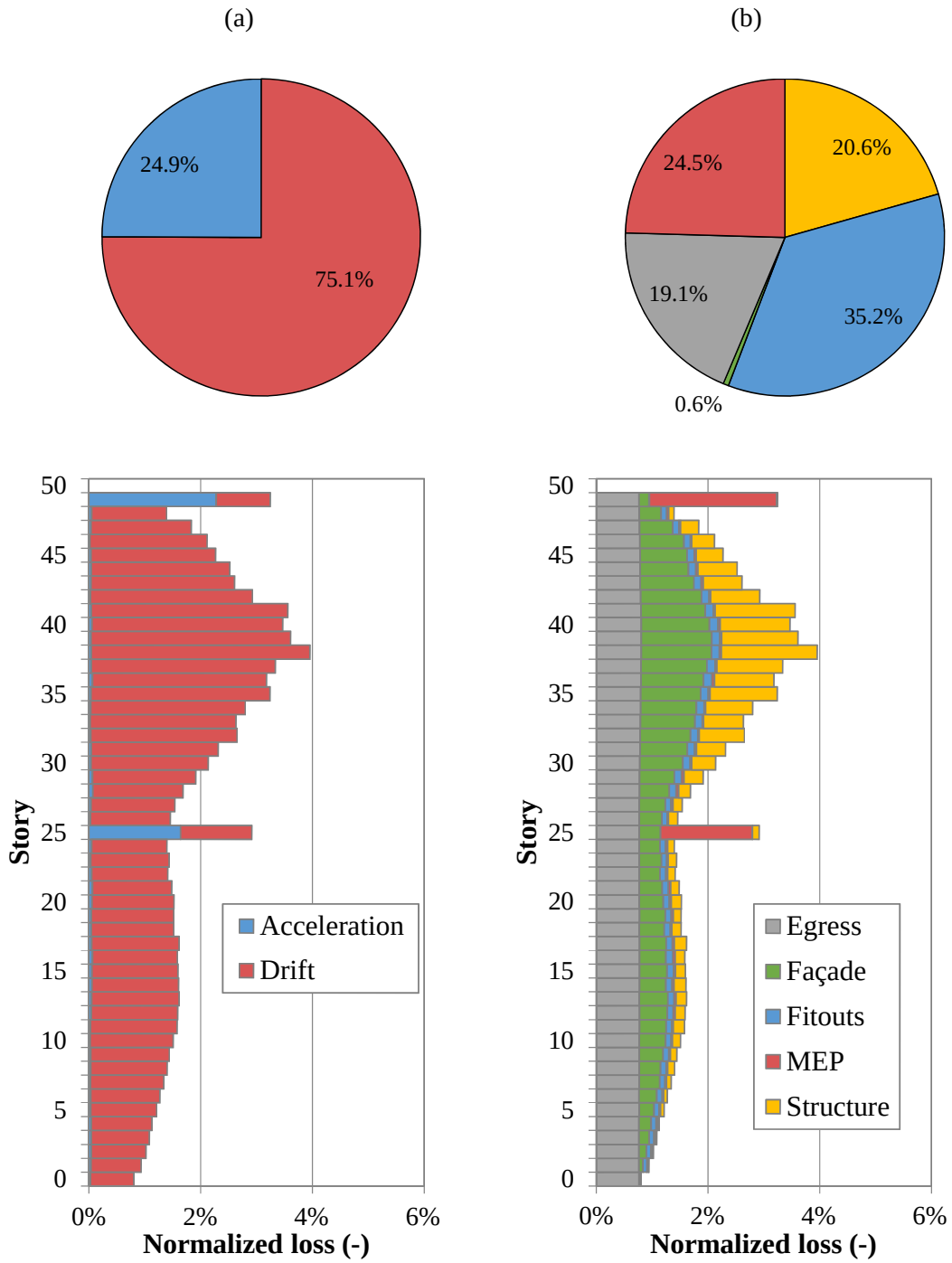

Figure H17: Contribution of acceleration versus drift-sensitive (a) and different building component categories (b) to repairable damage under earthquake ground motion intensity e_{8A} for the 2012 archetype.

This page is intentionally left blank.